

Special Issue Reprint

Recycled Materials for Concrete and Other Composites

Edited by
Malgorzata Ulewicz

[mdpi.com/journal/materials](https://www.mdpi.com/journal/materials)

Recycled Materials for Concrete and Other Composites

Recycled Materials for Concrete and Other Composites

Editor

Malgorzata Ulewicz



Basel • Beijing • Wuhan • Barcelona • Belgrade • Novi Sad • Cluj • Manchester

Editor

Malgorzata Ulewicz
Czestochowa University of
Technology
Czestochowa, Poland

Editorial Office

MDPI
St. Alban-Anlage 66
4052 Basel, Switzerland

This is a reprint of articles from the Special Issue published online in the open access journal *Materials* (ISSN 1996-1944) (available at: https://www.mdpi.com/journal/materials/special_issues/recycle_mat.concret.compos).

For citation purposes, cite each article independently as indicated on the article page online and as indicated below:

Lastname, A.A.; Lastname, B.B. Article Title. <i>Journal Name</i> Year , <i>Volume Number</i> , Page Range.
--

ISBN 978-3-0365-9542-9 (Hbk)

ISBN 978-3-0365-9543-6 (PDF)

doi.org/10.3390/books978-3-0365-9543-6

© 2023 by the authors. Articles in this book are Open Access and distributed under the Creative Commons Attribution (CC BY) license. The book as a whole is distributed by MDPI under the terms and conditions of the Creative Commons Attribution-NonCommercial-NoDerivs (CC BY-NC-ND) license.

Contents

About the Editor	ix
Preface	xi
Malgorzata Ulewicz Recycled Materials for Concrete and Other Composites Reprinted from: <i>Materials</i> 2021 , <i>14</i> , 2279, doi:10.3390/ma14092279	1
Mohammad R. Irshidat and Nasser Al-Nuaimi Industrial Waste Utilization of Carbon Dust in Sustainable Cementitious Composites Production Reprinted from: <i>Materials</i> 2020 , <i>13</i> , 3295, doi:10.3390/ma13153295	5
Zdzisława Owsiak, Przemysław Czapik and Justyna Zapala-Sławeta Properties of a Three-Component Mineral Road Binder for Deep-Cold Recycling Technology Reprinted from: <i>Materials</i> 2020 , <i>13</i> , 3585, doi:10.3390/ma13163585	19
Katarzyna Borek, Przemysław Czapik and Ryszard Dachowski Recycled Glass as a Substitute for Quartz Sand in Silicate Products Reprinted from: <i>Materials</i> 2020 , <i>13</i> , 1030, doi:10.3390/ma13051030	31
Guoqing Jing, Gang Huang and Wenjun Zhu An Experimental Study on Water Permeability of Architectural Mortar Using Waste Glass as Fine Aggregate Reprinted from: <i>Materials</i> 2020 , <i>13</i> , 1110, doi:10.3390/ma13051110	43
Wan Wang, Huixia Wu, Zhiming Ma and Ruixue Wu Using Eco-Friendly Recycled Powder from CDW to Prepare Strain Hardening Cementitious Composites (SHCC) and Properties Determination Reprinted from: <i>Materials</i> 2020 , <i>13</i> , 1143, doi:10.3390/ma13051143	57
Teeranai Srimahachota, Hiroshi Yokota and Yoshikazu Akira Recycled Nylon Fiber from Waste Fishing Nets as Reinforcement in Polymer Cement Mortar for the Repair of Corroded RC Beams Reprinted from: <i>Materials</i> 2020 , <i>13</i> , 4276, doi:10.3390/ma13194276	75
Seth Kane, Abby Thane, Michael Espinal, Kendra Lunday, Hakan Armağan, Adrienne Phillips, et al. Biom mineralization of Plastic Waste to Improve the Strength of Plastic-Reinforced Cement Mortar Reprinted from: <i>Materials</i> 2021 , <i>14</i> , 1949, doi:10.3390/ma14081949	89
Yanlei Wang, Guipeng Chen, Baolin Wan and Baoguo Han Compressive Behavior of Circular Sawdust-Reinforced Ice-Filled Flax FRP Tubular Short Columns Reprinted from: <i>Materials</i> 2020 , <i>13</i> , 957, doi:10.3390/ma13040957	109
Lan Liu, Lei He, Zhi Cheng, Xiaoyi Wang, Zhe Ma and Xinrong Cheng Interface Bonding Behavior of Concrete-Filled Steel Tube Blended with Circulating Fluidized Bed Bottom Ash Reprinted from: <i>Materials</i> 2021 , <i>14</i> , 1529, doi:10.3390/ma14061529	131
Weifeng Bai, Wenhao Li, Junfeng Guan, Jianyou Wang and Chenyang Yuan Research on the Mechanical Properties of Recycled Aggregate Concrete under Uniaxial Compression Based on the Statistical Damage Model Reprinted from: <i>Materials</i> 2020 , <i>13</i> , 3765, doi:10.3390/ma13173765	143

Se-Jin Choi, Young-Uk Kim, Tae-Gue Oh and Bong-Suk Cho Compressive Strength, Chloride Ion Penetrability, and Carbonation Characteristic of Concrete with Mixed Slag Aggregate Reprinted from: <i>Materials</i> 2020 , <i>13</i> , 940, doi:10.3390/ma13040940	167
Malgorzata Ulewicz and Alina Pietrzak Properties and Structure of Concretes Doped with Production Waste of Thermoplastic Elastomers from the Production of Car Floor Mats Reprinted from: <i>Materials</i> 2021 , <i>14</i> , 872, doi:10.3390/ma14040872	177
Md Jihad Miah, Md. Munir Hossain Patoary, Suvash Chandra Paul, Adewumi John Babafemi and Biranchi Panda Enhancement of Mechanical Properties and Porosity of Concrete Using Steel Slag Coarse Aggregate Reprinted from: <i>Materials</i> 2020 , <i>13</i> , 2865, doi:10.3390/ma13122865	189
Magdalena Dobiszewska and Ahmet Beycioğlu Physical Properties and Microstructure of Concrete with Waste Basalt Powder Addition Reprinted from: <i>Materials</i> 2020 , <i>13</i> , 3503, doi:10.3390/ma13163503	209
Sungchul Yang and Hyewon Lee Drying Shrinkage and Rapid Chloride Penetration Resistance of Recycled Aggregate Concretes Using Cement Paste Dissociation Agent Reprinted from: <i>Materials</i> 2021 , <i>14</i> , 1478, doi:10.3390/ma14061478	227
Abigail Landa-Sánchez, Juan Bosch, Miguel Angel Baltazar-Zamora, René Croche, Laura Landa-Ruiz, Griselda Santiago-Hurtado, et al. Corrosion Behavior of Steel-Reinforced Green Concrete Containing Recycled Coarse Aggregate Additions in Sulfate Media Reprinted from: <i>Materials</i> 2020 , <i>13</i> , 4345, doi:10.3390/ma13194345	245
Anna Król Mechanisms Accompanying Chromium Release from Concrete Reprinted from: <i>Materials</i> 2020 , <i>13</i> , 1891, doi:10.3390/ma13081891	265
Michał Ryms, Katarzyna Januszewicz, Paweł Kazimierski, Justyna Łuczak, Ewa Klugmann-Radziemska and Witold M. Lewandowski Post-Pyrolytic Carbon as a Phase Change Materials (PCMs) Carrier for Application in Building Materials Reprinted from: <i>Materials</i> 2020 , <i>13</i> , 1268, doi:10.3390/ma13061268	277
Jacek Gołaszewski, Tomasz Ponikiewski, Aleksandra Kostrzanowska-Siedlarz and Patrycja Miera The Influence of Calcareous Fly Ash on the Effectiveness of Plasticizers and Superplasticizers Reprinted from: <i>Materials</i> 2020 , <i>13</i> , 2245, doi:10.3390/ma13102245	295
Ahmet Beycioğlu, Orhan Kaya, Zeynel Baran Yıldırım, Baki Bağrıaçık, Magdalena Dobiszewska, Nihat Morova and Suna Çetin Use of GRP Pipe Waste Powder as a Filler Replacement in Hot-Mix Asphalt Reprinted from: <i>Materials</i> 2020 , <i>13</i> , 4630, doi:10.3390/ma13204630	319
Edgar H. Sánchez-Cotte, Carlos Albeiro Pacheco-Bustos, Ana Fonseca, Yaneth Pineda Triana, Ronald Mercado, Julián Yepes-Martínez and Ricardo Gabriel Lagares Espinoza The Chemical-Mineralogical Characterization of Recycled Concrete Aggregates from Different Sources and Their Potential Reactions in Asphalt Mixtures Reprinted from: <i>Materials</i> 2020 , <i>13</i> , 5592, doi:10.3390/ma13245592	335

Luca Lavagna, Roberto Nisticò, Matteo Sarasso and Matteo Pavese An Analytical Mini-Review on the Compression Strength of Rubberized Concrete as a Function of the Amount of Recycled Tires Crumb Rubber Reprinted from: <i>Materials</i> 2020 , <i>13</i> , 1234, doi:10.3390/ma13051234	353
Glaydson Simões dos Reis, Marco Quattrone, Weslei Monteiro Ambrós, Bogdan Grigore Cazacliu and Carlos Hoffmann Sampaio Current Applications of Recycled Aggregates from Construction and Demolition: A Review Reprinted from: <i>Materials</i> 2021 , <i>14</i> , 1700, doi:10.3390/ma14071700	369

About the Editor

Malgorzata Ulewicz

Malgorzata Ulewicz graduated from the Czestochowa University of Technology and the Higher Pedagogical School in Czestochowa. She completed her PhD degree and training at the Faculty of Engineering, Process, Materials and Applied Physics at the Czestochowa University of Technology. She is employed as a professor at the Czestochowa University of Technology and is the vice-dean of the Faculty of Civil Engineering.

Her research interests are related to materials engineering, in particular, the process of recycling materials, the use of waste materials in the synthesis of new materials, metal separation techniques, and environmental protection. Her didactic interests include the processes of the utilization and recycling of materials, sustainable construction, management, and social ecology.

Malgorzata Ulewicz is the author or co-author of 250 articles, including 9 books and monographs, 100 articles in journals, 15 chapters in monographs, and a number of papers based on original material research results presented at national and international conferences. She is the Editor-in-chief of the *Construction of Optimized Energy Potential* journal and a member of the Environmental Protection and Waste Management Committee of the Polish Academy of Sciences and the Building Engineering Committee of the Polish Academy of Sciences. She is also a member of several scientific committees for conferences and journals.

Preface

This Special Issue on “Recycled Materials for Concrete and Other Composites” focuses on the preparation and characterization of composites containing recycled materials that could be used in specific engineering applications, especially in the building industry. Using materials obtained through recycling is a key part of decreasing current waste. In composites, the materials used are mainly, but not only, recycled materials such as plastics, steel and other metals, glass, ceramics, and industrial wastes. Unfortunately, the synthesis of composite materials made from waste, by-products, or recycled materials requires research, which creates challenges for material engineers and chemists. For this reason, this Special Issue presents the results of the latest research in the field of the synthesis of composite materials, in particular cement-based composites and their properties. The topics of the published articles also include other issues that are important for engineers in the field of the physical and mechanical properties of mortars, concrete, and ceramic materials produced using waste or recycled materials, and their impact on the natural environment. The obtained research results clearly highlight the important direction of the use of such waste, which is consistent with the idea of sustainable development.

Malgorzata Ulewicz

Editor

Recycled Materials for Concrete and Other Composites

Malgorzata Ulewicz

Faculty of Civil Engineering, Czestochowa University of Technology, Dabrowskiego 69 Street,
PL 42-201 Czestochowa, Poland; malgorzata.ulewicz@pcz.pl; Tel.: +48-343-250-935

In recent years, industry, including the construction sector, has been focused on effectively reducing the consumption of natural resources, in compliance with the idea of sustainable development. The definition of “sustainable development” from the report “Our Common Future”, published in April 1987 by the World Commission on Environment and Development, defines sustainable development as “development that meets the needs of the present without compromising the ability of future generations to meet their own needs”. Therefore, the design and production of materials, including building materials, should be carried out with due regard to environmental protection requirements and with future generations in mind. It is particularly important to reduce the consumption of natural resources in the production of materials such as these, by using the latest technology, which can be replaced by waste materials and recycled building materials from the construction sector or waste materials from other industries.

Within this Special Issue of “Recycled materials for concrete and other composites”, there are published the latest results of scientific research on the use of recycled materials and post-production waste in the production of concrete and other composite materials. Research in this field is being carried out in many centers and universities around the world, including the USA, Colombia, Poland, Turkey, Jordan, Japan, China, India, Italy, Bangladesh, Spain, Korea, Mexico, Greece, Sweden, France, Qatar and South Africa.

This issue currently contains twenty-one original research papers and two review articles. The subject areas of these articles cover many aspects, including the production of composite materials containing recycled materials, their physicochemical and mechanical properties, corrosion resistance, elution of ions and their interactions with plasticizers or superplasticizers. Both interesting and practical solutions and the results of laboratory tests are presented. Irshidat and Al-Nuaimi [1] present the effect of utilizing carbon dust, generated as an industrial waste from aluminum factories, in the production of cementitious composites. Owsiak et al. [2] determine the physical properties of a three-component mineral binder containing hydrated lime, and cement bypass dust as a by-product derived from cement production. An interesting solution for the use of waste glass in composite products, including sand–lime, is described by Borek et al. [3]. Ternary mixtures of lime, sand and recycled waste glass had a higher compressive strength and lower density compared to the control sample, and the increase in the parameters was proportional to the amount of the replacement in these mixtures. Glass waste was also used by Jing et al. [4] as a fine aggregate in architectural mortar, while Wang et al. [5] investigated the micro-properties and mechanical properties of strain hardening cementitious composites containing recycled brick powder. It is worth paying attention to the work of Srimahachota et al. [6], which shows that recycled nylon fibers from waste fishing nets have great potential to be used as a strengthening fiber in cementitious material. Another way of using plastic waste is presented by Kane et al. [7] who have researched and examined the impact of biomineralization of plastic on the strength of plastic-reinforced mortar. In turn, Wang et al. [8] investigated the micro-properties and mechanical properties of cementitious composites containing sawdust and Liu et al. [9] present interface bonding behavior between the steel tube and the core concrete of a concrete-filled steel tube with circulating fluidized bed bottom ash.

Citation: Ulewicz, M. Recycled Materials for Concrete and Other Composites. *Materials* **2021**, *14*, 2279. <https://doi.org/10.3390/ma14092279>

Received: 24 April 2021

Accepted: 27 April 2021

Published: 28 April 2021

Publisher’s Note: MDPI stays neutral with regard to jurisdictional claims in published maps and institutional affiliations.



Copyright: © 2021 by the author. Licensee MDPI, Basel, Switzerland. This article is an open access article distributed under the terms and conditions of the Creative Commons Attribution (CC BY) license (<https://creativecommons.org/licenses/by/4.0/>).

A number of works in this Special Issue present the latest achievements in the synthesis of innovative concrete-containing recycled waste and materials and their properties. Bai et al. [10] determine the mechanical properties of recycled aggregate concrete under uniaxial compression based on a statistical damage model. Choi et al. [11] determine the compressive strength, chloride ion penetrability, and carbonation characteristics of concrete with both ferronickel slag and blast furnace slag. The physical and mechanical properties of concrete composites containing waste thermoplastic elastomer from the production process of car floor mats is presented by Ulewicz et al. [12]. Miah et al. [13] present the effect of steel slag aggregate as a substitute for conventionally used brick aggregate on the physical, mechanical and durability performances of concretes. In turn, Dobiszewska and Beycioğlu [14] show that waste basalt powder, which is a by-product of the production of mineral–asphalt mixtures, used as a partial sand replacement, increases the compressive strength of concretes. According to microstructural analyses, the presence of basalt powder in concrete mixes is beneficial for cement hydration products, and basalt powder-substituted concretes have lower porosity within the interfacial transition zone. The durability of concrete with recycled concrete aggregate (from precast concrete), treated by a coating of a cement paste dissociation agent, depends, as shown by Yang and Lee [15], on mixing methods. Additionally, Landa-Sánchez et al. [16] determine the corrosion resistance of green concrete (GC) admixtures containing recycled coarse aggregate and reinforced with AISI 1080 carbon steel and AISI 304 stainless steel. In turn, Król [17] presents the result of leaching of chromium from concretes made of Portland cement CEM I and slag cement CEM III/B containing 75% granulated blast furnace slag.

It is worth paying attention to the article by Ryms et al. [18] wherein the authors cover a new application for char as a carrier of phase-change materials (PCMs) used as an additive to building materials. Thus far, no one has tried to utilize pyrolytic biochar with a well-developed internal surface for permanent PCM adsorption. Gołaszewski et al. [19] present the influence of raw and ground calcareous fly ash on rheological properties and other effects of admixtures (plasticizers and superplasticizers), in particular, the amount of air in the mixture and the level of heat of hydration.

Recycled materials can also be successfully used as an additive to asphalt mixtures. Beycioğlu et al. [20] present the possibilities of using waste powder from glass fiber-reinforced polyester (GRP) pipes (GRP-WPs) for asphalt mixtures as a filler and Sánchez-Cotte et al. [21] present the implicational possibilities of using recycled concrete aggregate (recycled concrete aggregate of a building and recycled concrete aggregate from a pavement) as a replacement for natural aggregates in road construction. This research concludes that the studied recycled concrete aggregates might be used as replacements for coarse aggregate in asphalt mixtures since their chemical properties do not affect the overall chemical stability of the asphalt mixture.

This Special Issue is completed by a review article by Lavagna et al. [22]. This analytical mini-review presents the compression strength of rubberized concrete as a function of the amount of recycled tire crumb rubber. Glaydson dos Reis [23] discusses the generation and recycling of construction and demolition wastes (CDWs) as well as their main uses as raw materials for the construction engineering sector.

All the articles published in this Special Issue have been reviewed by recognized experts in the relevant fields of science. As Guest Editor, I would like to acknowledge all the authors for their valuable contributions. I would also like to thank the reviewers for their comments and suggestions that have greatly improved the quality of the papers. Last, but not least, I would also like to thank the Section Managing Editor, Ms. Freda Zhang, for her kind assistance in the preparation of this Special Issue of the journal.

Funding: This research received no external funding.

Conflicts of Interest: The authors declare no conflict of interest.

References

1. Irshidat, M.R.; Al-Nuaimi, N. Industrial Waste Utilization of Carbon Dust in Sustainable Cementitious Composites Production. *Materials* **2020**, *13*, 3295. [CrossRef]
2. Owsiak, Z.; Czapiak, P.; Zapała-Sławeta, J. Properties of a Three-Component Mineral Road Binder for Deep-Cold Recycling Technology. *Materials* **2020**, *13*, 3585. [CrossRef] [PubMed]
3. Borek, K.; Czapiak, P.; Dachowski, R. Recycled Glass as a Substitute for Quartz Sand in Silicate Products. *Materials* **2020**, *13*, 1030. [CrossRef] [PubMed]
4. Jing, G.; Huang, G.; Zhu, W. An Experimental Study on Water Permeability of Architectural Mortar Using Waste Glass as Fine Aggregate. *Materials* **2020**, *13*, 1110. [CrossRef]
5. Wang, W.; Wu, H.; Ma, Z.; Wu, R. Using Eco-Friendly Recycled Powder from CDW to Prepare Strain Hardening Cementitious Composites (SHCC) and Properties Determination. *Materials* **2020**, *13*, 1143. [CrossRef] [PubMed]
6. Srimahachota, T.; Yokota, H.; Akira, Y. Recycled Nylon Fiber from Waste Fishing Nets as Reinforcement in Polymer Cement Mortar for the Repair of Corroded RC Beams. *Materials* **2020**, *13*, 4276. [CrossRef]
7. Kane, S.; Thane, A.; Espinal, M.; Lunday, K.; Armağan, H.; Phillips, A.; Heveran, C.; Ryan, C. Biomineralization of plastic waste to improve the strength of plastic-reinforced cement mortar. *Materials* **2021**, *14*, 1949. [CrossRef]
8. Wang, Y.; Chen, G.; Wan, B.; Han, B. Compressive Behavior of Circular Sawdust-Reinforced Ice-Filled Flax FRP Tubular Short Columns. *Materials* **2020**, *13*, 957. [CrossRef]
9. Liu, L.; He, L.; Cheng, Z.; Wang, X.; Ma, Z.; Cheng, X. Interface Bonding Behavior of Concrete-Filled Steel Tube Blended with Circulating Fluidized Bed Bottom Ash. *Materials* **2021**, *14*, 1529. [CrossRef]
10. Bai, W.; Li, W.; Guan, J.; Wang, J.; Yuan, C. Research on the Mechanical Properties of Recycled Aggregate Concrete under Uniaxial Compression Based on the Statistical Damage Model. *Materials* **2020**, *13*, 3765. [CrossRef]
11. Choi, S.-J.; Kim, Y.-U.; Oh, T.-G.; Cho, B.-S. Compressive Strength, Chloride Ion Penetrability, and Carbonation Characteristic of Concrete with Mixed Slag Aggregate. *Materials* **2020**, *13*, 940. [CrossRef]
12. Ulewicz, M.; Pietrzak, A. Properties and Structure of Concretes Doped with Production Waste of Thermoplastic Elastomers from the Production of Car Floor Mats. *Materials* **2021**, *14*, 872. [CrossRef] [PubMed]
13. Miah, M.J.; Patoary, M.M.H.; Paul, S.C.; Babafemi, A.J.; Panda, B. Enhancement of Mechanical Properties and Porosity of Concrete Using Steel Slag Coarse Aggregate. *Materials* **2020**, *13*, 2865. [CrossRef] [PubMed]
14. Dobiszewska, M.; Beycioğlu, A. Physical Properties and Microstructure of Concrete with Waste Basalt Powder Addition. *Materials* **2020**, *13*, 3503. [CrossRef] [PubMed]
15. Yang, S.; Lee, H. Drying Shrinkage and Rapid Chloride Penetration Resistance of Recycled Aggregate Concretes Using Cement Paste Dissociation Agent. *Materials* **2021**, *14*, 1478. [CrossRef] [PubMed]
16. Landa-Sánchez, A.; Bosch, J.; Baltazar-Zamora, M.A.; Croche, R.; Landa-Ruiz, L.; Santiago-Hurtado, G.; Moreno-Landeros, V.M.; Olguin-Coca, J.; López-Léon, L.; Bastidas, J.M.; et al. Corrosion Behavior of Steel-Reinforced Green Concrete Containing Recycled Coarse Aggregate Additions in Sulfate Media. *Materials* **2020**, *13*, 4345. [CrossRef] [PubMed]
17. Król, A. Mechanisms Accompanying Chromium Release from Concrete. *Materials* **2020**, *13*, 1891. [CrossRef] [PubMed]
18. Rymys, M.; Januszewicz, K.; Kazimierski, P.; Łuczak, J.; Klugmann-Radziemska, E.; Lewandowski, W.M. Post-Pyrolytic Carbon as a Phase Change Materials (PCMs) Carrier for Application in Building Materials. *Materials* **2020**, *13*, 1268. [CrossRef]
19. Gołaszewski, J.; Ponikiewski, T.; Kostrzanowska-Siedlarz, A.; Miera, P. The Influence of Calcareous Fly Ash on the Effectiveness of Plasticizers and Superplasticizers. *Materials* **2020**, *13*, 2245. [CrossRef]
20. Beycioğlu, A.; Kaya, O.; Yıldırım, Z.B.; Bağrıaçık, B.; Dobiszewska, M.; Morova, N.; Çetin, S. Use of GRP Pipe Waste Powder as a Filler Replacement in Hot-Mix Asphalt. *Materials* **2020**, *13*, 4630. [CrossRef]
21. Sánchez-Cotte, E.H.; Pacheco-Bustos, C.A.; Fonseca, A.; Triana, Y.P.; Mercado, R.; Yepes-Martínez, J.; Lagares Espinoza, R.G. The Chemical-Mineralogical Characterization of Recycled Concrete Aggregates from Different Sources and Their Potential Reactions in Asphalt Mixtures. *Materials* **2020**, *13*, 5592. [CrossRef] [PubMed]
22. Lavagna, L.; Nisticò, R.; Sarasso, M.; Pavese, M. An Analytical Mini-Review on the Compression Strength of Rubberized Concrete as a Function of the Amount of Recycled Tires Crumb Rubber. *Materials* **2020**, *13*, 1234. [CrossRef] [PubMed]
23. dos Reis Glaydson, S.; Quattrone, M.; Ambrós, W.M.; Cazacliu, B.G.; Sampaio, C.H. Current applications of recycled aggregates from construction and demolition: A review. *Materials* **2021**, *14*, 1700. [CrossRef]

Article

Industrial Waste Utilization of Carbon Dust in Sustainable Cementitious Composites Production

Mohammad R. Irshidat ^{*,†} and Nasser Al-Nuaimi

Center for Advanced Materials (CAM), Qatar University, P.O. Box 2713, Doha, Qatar; anasser@qu.edu.qa

* Correspondence: mirshidat@qu.edu.qa

† On leave from Jordan University of Science and Technology (JUST), Jordan.

Received: 3 July 2020; Accepted: 21 July 2020; Published: 24 July 2020

Abstract: This paper experimentally investigates the effect of utilization of carbon dust generated as an industrial waste from aluminum factories in cementitious composites production. Carbon dust is collected, characterized, and then used to partially replace cement particles in cement mortar production. The effect of adding different dosages of carbon dust in the range of 5% to 40% by weight of cement on compressive strength, microstructure, and chemical composition of cement mortar is investigated. Scanning electron microscopy (SEM), X-ray diffraction (XRD), and X-ray fluorescence (XRF) analysis are used to justify the results. Experimental results show that incorporation of carbon dust in cement mortar production not only reduces its environmental side effects but also enhances the strength of cementitious composites. Up to 10% carbon dust by weight of cement can be added to the mixture without adversely affecting the strength of the mortar. Any further addition of carbon dust would decrease the strength. Best enhancement in compressive strength (27%) is achieved in the case of using 5% replacement ratio. SEM images show that incorporation of small amount of carbon dust (less than 10%) lead to produce denser and more compact-structure cement mortar.

Keywords: carbon dust; industrial waste; cement mortar; strength; microstructure

1. Introduction

Growing industrialization and urbanization are recently noticed all over the world. This growing is associated with high production of industrial by-products. The huge amount of industrial by-products generated from the wide range of industries cause serious concerns to the environment and health. One of the industrial wastes is the carbon dust generated during the production of aluminum in the aluminum companies. Carbon dust is a by-product of anode manufacturing process usually generated during crushing of anode butts and cleaning of bath material during shot blasting process. It is super fine black powder. Aluminum companies usually generate large quantities of carbon dust. The carbon dust represents a main challenge to get rid of because of its environmental side effects such as air pollution due to its fineness, and the possible leaching to the groundwater. In addition, the carbon dust is usually dumped in landfills. The handling and transportation of the dust are also problematic. The high generation rate, the purity, and the finer particle size of this by-product lead to potential utilization in concrete production.

Since the civil infrastructures around the world are mostly made of reinforced concrete (RC), the production and use of concrete increase rapidly. The high production and consumption rate of concrete make it a good option to recycle the industrial wastes. On the other hand, cement industry contributes about five to eight percent of the annual greenhouse gas emissions. The production of one ton of Portland cement generates about one ton of CO₂ [1]. Cement replacement with supplementary cementitious materials (SCM) or industrial byproducts make it possible considerably to reduce the greenhouse gas emissions, reduce the environmental impacts, and decrease the consumption of natural resources.

Various industrial by-products and solid wastes such as fly ash, slag, ceramic waste, bottom ash, granite dust, and marble dust are efficiently used in concrete production. The researchers studied this topic from different aspects. Some studies focused on the effect of using industrial byproducts on the strength of concrete. El-Dieb et al. [1] investigated the feasibility of using ceramic waste powder (CWP) to replace cement on concrete production. Their results indicated that CWP could be used to replace cement in concrete mixes and to enhance its behavior based on the replacement level. They concluded that partially replacement of cement by 10% CWP was suitable for strength enhancement, between 10% and 20% was adequate to enhance the workability while a 40% replacement was sufficient to improve the durability. Elahi et al. [2] investigated the mechanical and durability properties of high performance concretes containing SCM. Their results showed that silica fume performs better than other SCM used in the study for the strength development and bulk resistivity. Ali et al. [3] investigated the feasibility of using waste carbon black as a filler in producing lightweight concrete. They concluded that the lightweight concrete produced by substituting sand by carbon black could be used in both structural and non-structural purposes. Chitra et al. [4] showed that using carbon powder to replace cement enhanced the mechanical strengths of concrete and reduced its permeability. Schulze et al. [5] examined the ability of using natural calcined clay with different levels of quality as a cement constituent. Their results showed that natural calcined clays are suitable to be used as SCM in cement production.

Other studies focused on the effect of these materials on the durability of concrete. Ashish [6] studied the feasibility of using marble powder (MP) combined with SCM in concrete production. Two types of SCM namely silica fume and metakaolin were used to replace cement while the MP was used to replace sand. His results showed an enhancement in the durability of concrete because of 15% replacement of sand with MP combined with the use of SCM. Shah et al. [7] investigated the carbonation resistance of cements containing SCMs. Their results showed that the carbonation rate was ruled by the clinker replacement level, relative humidity and w/c ratio. Slag showed superior carbonation resistance ability compared to the other used SCMs. Farnam et al. [8] investigated the effect of SCM on damage caused by calcium oxychloride formation. They used several types of SCM to partially replace cement in cement paste production. Their results indicated that SCM improved the damage behavior of cementitious materials when exposed to CaCl_2 . Mangi et al. [9] studied the behavior of concrete with coal bottom ash (CBA) as SCM exposed to seawater. Their results showed that the compressive strength of concrete with SCM increased about 12% and 9% compared to control mix in water and seawater respectively at 180 days.

Other studies focused on the environmental aspect of waste utilization in concrete production. Zhang et al. [10] evaluated the environmental impact of concrete with SCMs using proposed integrated functional unit combining durability and compressive strength. The results revealed that adding fly ash or silica fume enhanced the environmental behavior compared to the ordinary concrete. Yang et al. [11] studied the feasibility of using various SCMs such as fly ash (FA), ground granulated blast-furnace slag (GGBS), and silica fume (SF) in reducing CO_2 emissions from concrete. Their results showed that the intensity of CO_2 decreased with increasing the dosage of the SCMs up to 15–20% replacement ratio. Vargas et al. [12] investigated the environmental impacts of using copper-treated tailings (CTT) as SCM. Their results showed that at higher mechanical behavior, CTT mixtures owned better environmental indicators than mixtures without CTT. Viet et al. [13] showed the ability of using fly ash (FA) generated from the thermal treatment solid waste as a CO_2 sequester and as SCM to develop green construction materials.

Other researchers focused on studying the feasibility of waste utilization in high strength concrete production. Pyo et al. [14] investigated the feasibility of using two types of quartz-based mine tailings to substitute silica powder and silica sand in ultra-high performance concrete (UHPC) production. They found that the shape and size of tailings particles affected the characteristics of the UHPC. They concluded that even though adding the tailings materials negatively affected the strength of the UHPC, these materials showed the capability to minimize the limitations due to the high production cost of the raw materials. Kim et al. [15] investigated the effect of using untreated coal bottom ash on

the hydration kinetics of high-strength concrete. They found that incorporation of bottom ash in high-performance concrete for internal curing increased the degree of hydration in the cement matrix.

The above-mentioned studies reflect that utilization of industrial wastes in concrete production, which is a massive construction material, is considered a good solution for solving the environmental impact of these materials. The high generation rate, the purity, and the finer particle size of carbon dust encourage the authors to investigate the feasibility of using it in cementitious composites production to partially replace cement. The aim of this study is to characterize the carbon powder generated as a by-product by aluminum factories with respect to its chemical composition, morphology, and particle size distribution. In addition, comprehensive study was conducted to evaluate the use of carbon powder as cement replacement on the strength and microstructure of cement mortar.

2. Materials and Methods

2.1. Materials

Portland cement, fine aggregate, and tap water were used in this study to prepare the control cement mortar specimens. The cement was commercially available with chemical composition shown in Table 1. The fine aggregate was washed sand from a local supplier with properties listed in Table 2. The carbon dust was provided by Qatar Aluminum Company (Qatalum, Doha, Qatar). It is super fine black talcum powder with a density of 1.9 g/cm^3 . The high generation rate, the purity, and the finer particle size of this waste by-product lead to potential utilization in concrete production. It was used as-received from Qatalum. Comprehensive characterization was performed to explore its properties as shown in Section 3.1.

Table 1. Constituents of cement.

Compound Name	Content Percentage
CaO	6.4%
SiO ₂	18.4%
Fe ₂ O ₃	6.1%
SO ₃	3.0%
Al ₂ O ₃	2.2%
MgO	1.4%
Na ₂ O	0.8%
LOI	1.7%

Table 2. Fine aggregate properties.

Material	Fineness Modulus	Specific Gravity	Density (kg/m ³)	Water Absorption (%)	Moisture Content (%)
Sand	2.31	2.564	2558.3	1.87	3.00

2.2. Carbon Dust Characteristics

The main properties of carbon dust used in this study such as particle size distribution, particles' shape, morphology, and chemical composition were investigated. The chemical composition analysis was conducted through X-ray diffraction (XRD) and X-ray fluorescence (XRF) test procedures. The carbon dust was sieved to pass through a 325-mesh sieve. The powder was placed on the JSX 3201M (Jeol) spectroscopy machine (JEOL, Peabody, MA, USA) to conduct the elemental tests. The morphology of the carbon dust was examined by scanning electron microscopy (SEM) technique using NOVA NanoSEM 450 device (Hillsboro, OR, USA) at high voltage of 5 kV and 20 kV and working distance ranging from 4.6 to 9 mm.

2.3. Mix Design and Test Specimens

Mortar mixes with different amounts of carbon dust were cast. Five replacement levels by weight of cement were studied 5%, 10%, 20%, 30%, and 40%. The mixtures were identified with the letters CD and two number, the letters refer to the carbon dust, and the numbers refer to the replacement ratio and the age of the specimen at the time of testing, respectively. For example, CD10-28 represents the mixture with 10% replacement ratio of carbon dust tested at 28 days. Table 3 summarizes the mix proportions and specimens designations. ASTM standard C305 was followed to mix and cast the cement mortars. For compressive strength test, the cement mortar was mixed and cast in 50-mm cube molds. Twenty-four hours after casting, the specimens were demolded and cured in lime-saturated water for different periods until the time of testing.

Table 3. Mix proportions and specimen's designation.

Specimen Designation	CD0	CD5	CD10	CD20	CD30	CD40
Replacement ratio (%)	0	5	10	20	30	40
Cement (kg/m ³)	731	694	658	585	512	439
Carbon powder (kg/m ³)	0.0	37	73	146	219	292
Sand (kg/m ³)	2010	2010	2010	2010	2010	2010
Water (kg/m ³)	355	355	355	355	355	355

2.4. Test Methods

The effect of carbon dust on the development of compressive strength of cement mortar with age was studied. Compressive strength test was performed after 3, 7, and 28 days of curing. Three specimens were tested for each mix at each age according to the ASTM 109/C109M. The test was performed using universal testing machine with loading rates of 1.3 kN/s. The compressive strength test setup is shown in Figure 1.



Figure 1. Compressive strength test setup.

At the end of the compressive strength test, scanning electron microscopy (SEM) imaging test was performed on selected specimens to explore the effect of carbon dust on the microstructure and morphology of cement mortar. Small fragments were extracted from different locations of the selected specimens to represent the entire sample. To enhance the conductivity of the mortar fragments, the surface of the fragments was coated with gold. After coating, the SEM analysis was conducted according to the ASTM C1723-10 using NOVA NanoSEM 450 device at high voltage of 5 kV and 20 kV and working distance ranging from 4.6 to 9 mm.

In addition, X-ray fluorescence (XRF) and X-ray diffraction (XRD) tests were conducted to investigate the effect of carbon dust on the chemical composition of cement mortar. Selected cement mortar specimens were crushed into size that can pass sieve size 150 μm . To make sure that the results are representative, the powder of each specimen was carefully mixed, and enough amount was taken to run the test. The powder was then placed on the JSX 3201M (Jeol) spectroscopy machine to conduct the analysis.

3. Results and Discussion

3.1. Carbon Dust Characteristics

The particle size distribution (PSD) of cement and carbon dust are shown in Figure 2. The figure reveals that both cement and carbon dust have continuous graded PSDs. Some of the carbon dust particles are finer than the cement particles, whereas some other particles are coarser. Almost 20% of the carbon dust particles are smaller than 30 μm , whereas 50% of the particles are smaller than 80 μm . SEM images of the carbon dust show that it has angular and irregular shapes and very small size particles (powder), as shown in Figure 3.

Table 4 summarizes the results of the chemical composition analysis of the carbon dust using XRF analysis. It is clear that the carbon dust is mainly composed of carbon. It presents almost 85% of the total mass. Moreover, very small percentages of other materials such as iron, fluoride, and sodium are observed. The mineralogical composition of carbon dust was investigated using XRD analysis. It is clear from the XRD patterns shown in Figure 4 that the carbon dust shows a very broad carbon peak at $2\theta = 25^\circ$ that can be attributed to two different forms of carbon, turbostratic carbon (carbon black) and graphene carbon (graphitic structure) [16,17]. These results support the XRF results mentioned previously.

Table 4. XRF analysis of carbon dust.

Name	Concentration (%)
Carbon	85
Iron	7
Fluoride	4
Sodium	2.5
Sulphur	1
Silicon	0.5

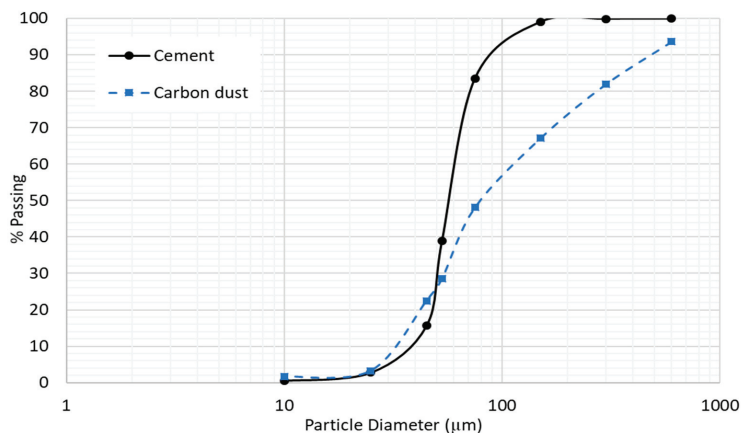


Figure 2. Particle size distribution of cement and carbon dust.

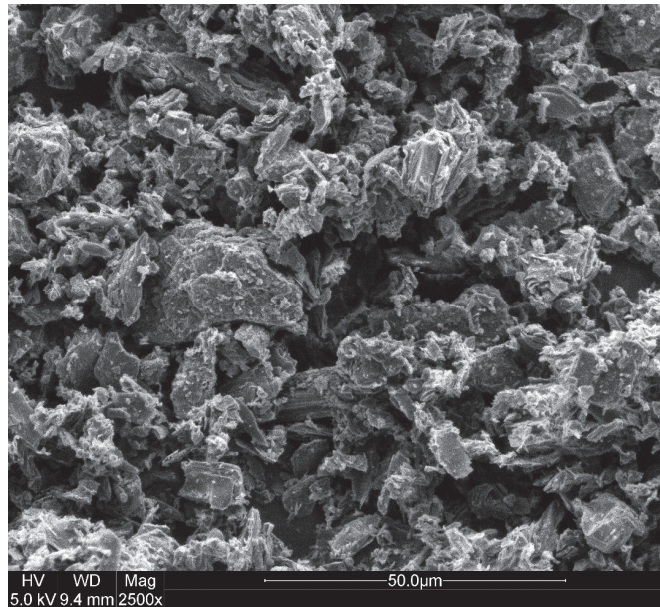


Figure 3. SEM image of carbon dust particles.

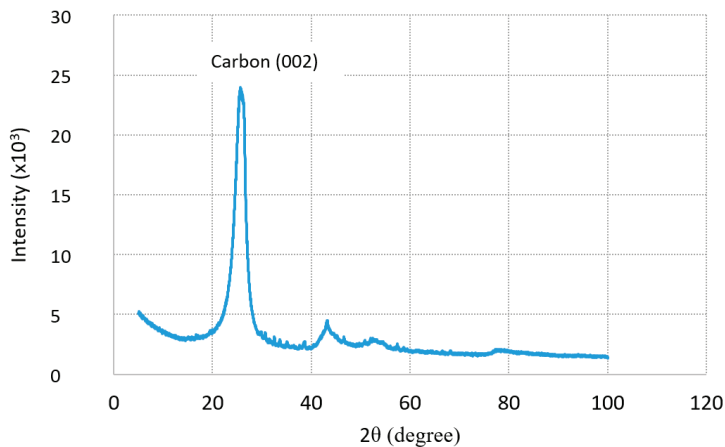
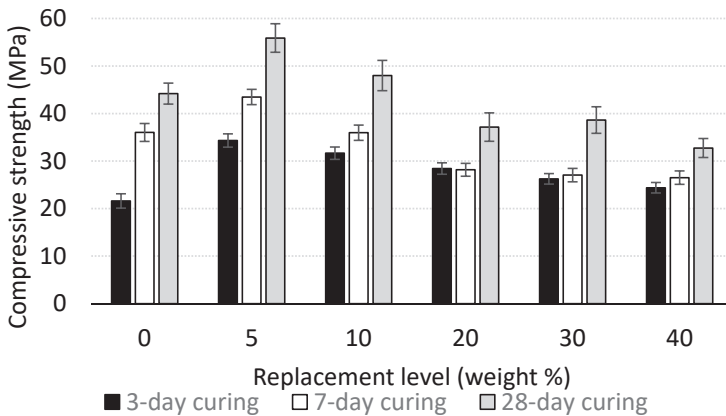


Figure 4. XRD pattern of carbon dust.

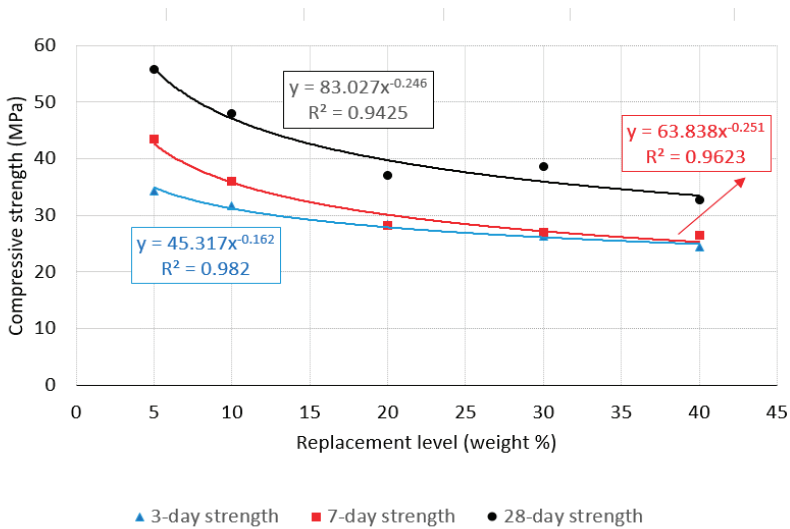
3.2. Compressive Strength Results

The influence of carbon dust on the compressive strength of cement mortar at different ages is shown in Table 5 and Figure 5. It is clear that incorporation of carbon dust significantly enhances the compressive strength of cement mortar at early age (3-day strength) for all replacement ratios 5%, 10%, 20%, 30%, and 40% compared to the control specimen. The highest enhancement in the 3-day strength is achieved in the case of 5% replacement ratio with about 59% compared to the control specimen. The enhancement in the compressive strength of the mortar at early age because of carbon dust incorporation could be attributed to the micro-filling ability of the carbon dust because of its small particle size [1,18]. For the 28-day strength, partially replacing cement with 5% and 10% carbon dust

enhances the compressive strength of the mortar by 27% and 9%, respectively. For replacement ratio of 20% and higher, incorporation of the carbon dust reduces the compressive strength of the mortar. Similar results are reported in other studies [1,4,6]. The enhancement in the 28-day compressive strength of the mortar due to carbon dust incorporation could be attributed to many reasons: (1) The micro-filling ability (filler effect) of the carbon dust that helped in forming a denser mixture [1,6,19,20] and improved the transition zone and cement matrix property [21]; (2) the carbon dust particles worked as nucleation spots for the hydration products [1]. The reduction in compressive strength when using high replacement ratio of carbon dust could be attributed to the following reasons: (1) The dilution effect where replacing cement with carbon dust negatively affect the strength development; (2) the micro-filling effect of carbon dust could not balance the reduction in the cement content [1].



(a)



(b)

Figure 5. Compressive strength development for mortar with different replacement ratios; (a) experimental results, (b) best fit curves.

3.3. Correlation between Compressive Strength and Replacement Ratio

Statistical analysis is very helpful in analyzing the variation of the experimental results. For this purpose, the standard deviation and regression analysis are used to investigate the trending of the results. The standard deviation for compressive strength of specimens contain various dosages of carbon dust and cured for different periods are listed in Table 5. According to the standard deviation values, the variability of the data is considerably small. The correlations between the carbon dust dosages and the compressive strength for specimens cured at various periods are shown in Figure 5b. Best-fit curves determined according to the data of each curing period are also presented in the figure. The results reveal that satisfactory power relationship exist between the dosage of the carbon dust and the compressive strength values for all curing periods. In addition, the R-square values of 0.98, 0.96, and 0.94 reflect the strong correlations between the compressive strength and the carbon dust replacement ratio for specimens cured for 3, 7, and 28 days, respectively.

Table 5. Compressive strength results.

Specimen		CD0	CD5	CD10	CD20	CD30	CD40
Replacement %		0%	5%	10%	20%	30%	40%
3-day curing	Strength (MPa)	21.6	34.3	31.7	28.4	26.3	24.4
	Standard deviation (\pm)	1.5	1.7	1.4	1.3	1.2	1.1
	Enhancement (%)	NA	58.9	46.6	31.6	21.5	12.9
7-day curing	Strength (MPa)	36.0	43.5	36.0	28.2	27.0	26.5
	Standard deviation (\pm)	1.9	2.0	1.6	1.6	1.35	1.4
	Enhancement (%)	NA	20.8	-0.1	-21.8	-24.9	-26.4
28-day curing	Strength (MPa)	44.2	55.9	48.0	37.2	38.6	32.7
	Standard deviation (\pm)	2.2	2.0	3.0	3.2	3.0	2.8
	Enhancement (%)	NA	26.5	8.6	-16.0	-12.6	-25.9

3.4. Chemical Composition of Cement Mortar

The effect of carbon dust replacement ratio on the chemical composition of cement mortar at 28-day age was investigated through XRF analysis. The results are summarized in Table 6. It is clear that for 5% replacement ratio, the CaO percentage decreased and the SiO₂ percentage increased, compared to the control specimen. This finding reflected the reduction in CH and replacement of C-S-H in the case of carbon dust addition. As the replacement ratio increased to be 10%, the CaO percentage increased compared to the 5% specimen but still below the value of the control specimen. In addition, the SiO₂ percentage decreased compared to the 5% specimen but still above the value of the control specimen. For higher replacement ratios such as 20%, the CaO percentage increased above the control specimen and the SiO₂ percentage decreased below the control specimen. These results could be used to clarify the compressive strength test results reported in the previous section.

Table 6. XRF analysis of mortar with carbon dust.

Replacement Ratio	0%	5%	10%	20%
SiO ₂	58.5	62.6	60.1	52.3
CaO	31.5	26.3	29.8	34.5
Fe ₂ O ₃	3.3	4.5	5.9	3.6
SO ₃	1.9	1.8	3	2.6
Al ₂ O ₃	2.3	2.5	2.2	3.4
K ₂ O	0.6	0.8	0.4	0.6
Na ₂ O	1.1	0.7	1.8	1.8
Ca/SiO ₂	0.54	0.42	0.50	0.66

The CaO/SiO₂ ratio is usually used to compare the quality of hydration. It is clear in Table 6 that the CaO/SiO₂ ratio for specimens with 5% and 10% replacement ratios is less than that of the control specimen. The reduction in the ratio reflected more consumption of the CH and more formulation of the C-S-H in the presence of carbon dust. Furthermore, the lower ratio of CaO/SiO₂ indicated the suitable quantities of C3S and C2S in the microstructure, thus improved strength development [22]. This result explains the enhancement in the compressive strength of the mortar with 5% and 10% replacement ratio compared to the control specimen.

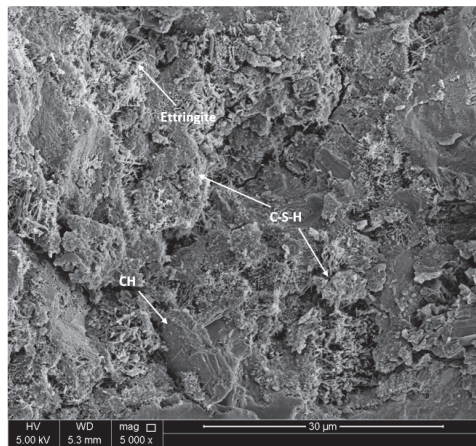
3.5. Microstructure of Cement Mortar

To investigate the effect of carbon dust on the microstructure of cement mortar, scanning electron microscopy (SEM) imaging was conducted. Figure 6 shows the microstructure of mortar specimens with different amount of carbon dust cured for 28 days. The SEM micrograph of control specimen made without carbon dust reflects the formation of the main hydration products such as calcium hydroxide (CH) platelets, calcium silicate hydrate (CSH), and calcium sulphoaluminate hydrate (Ettringite) needles as shown in Figure 6a. The SEM micrograph of specimens with low replacement ratio such as 5% and 10% carbon dust reflects the formation of more dense and compact structure with the presence of well-formed and dense clusters of C-S-H as compared to that of control specimen as shown in Figure 6b. The dense structure could be mainly attributed to many reasons such as (1) the formation of an excessive amount of CSH with consumption of CH in the present of carbon dust. These hydration products filled the microspores and resulted in less porous and denser structure [1]. (2) The carbon dust particles served as nucleus for hydration products [4,23]. This observation supports the compressive strength results. In addition, the ettringite needles are revealed to be in abundance. The well-formed ettringite crystals signal toward the healthy mix of cement mortar [22].

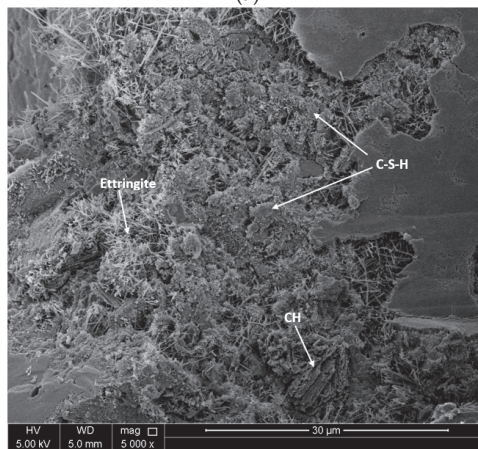
Figure 6c shows the microstructure of cement mortar specimen with high replacement ratio of carbon dust (40%). The microstructure of this specimen looks different than the previous ones, which explains the reduction in its compressive strength. It is clear that the clinker-shaped particles of CH that appears like the structure of un-hydrated clinkers of cement. The clusters of un-hydrated clinkers of Portlandite is formed due to the unavailability of water for proper hydration of concrete. Adding large amount of carbon dust led to absorb some of the water that should be used to complete the hydration process. In addition, the micro-filling effect of carbon dust could not balance the reduction in the cement content. The un-hydrated clinker particles have lower bonding capacity than well hydrated C-S-H and ettringite, thus, reducing the strength of the mortar.

3.6. Cement Content and Mortar Sustainability

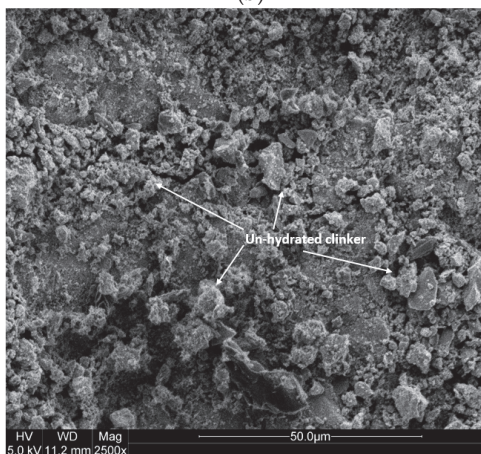
To connect between the simultaneous changes in cement content and strength of cement mortar, Figure 7 shows the variation in the 28-day compressive strength of cement mortar with various dosages of carbon dust. The horizontal line represents the 28-day strength of control specimen (without carbon dust). The figure reveals that maximum of 96 kg/m³ of cement content could be replaced with carbon dust (equivalent to 13% replacement ratio) without negatively affecting the 28-day compressive strength of the mortar. Any further cement replacement by carbon dust would decrease the strength to be less than that of control specimen. So, the filler technology of adding carbon dust to decrease the cement content in mortar mix could be applicable to certain limit without negatively affecting its strength.



(a)



(b)



(c)

Figure 6. SEM images for selected mortar specimens with (a) 0% carbon dust, (b) 5% carbon dust, (c) 40% carbon dust.

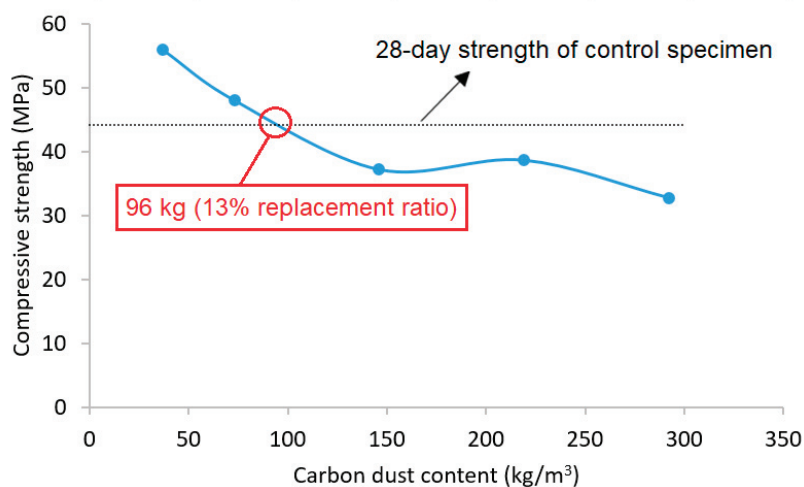


Figure 7. Carbon dust content versus compressive strength of mortar.

The recycling of carbon dust in cement mortar production has four major benefits in order to produce sustainable construction materials. First, replacing cement by carbon dust reduces the amount of cement needed for mortar production. That will significantly reduce the carbon footprint of cement mortar production since the major contribution of carbon footprint (about 90%) comes from cement production. Second, replacing cement with carbon dust reduces the cost of concrete due to the high price of cement compared with carbon dust (which is waste materials). Third, using carbon dust in cement mortar production thus in concrete would considerably reduce the amount of carbon dust that is disposed to landfills because of the huge consumption of concrete as construction material. That will extend the life period of limited capacity landfill used to store these wastes thus mitigate the environmental issues with difficulties to find new sites for landfills. Finally, replacing cement by carbon dust will not only improve the environmental sustainability but also enhance the compressive strength of cement mortar. However, it is important to run comprehensive durability study to investigate the effect of carbon dust on the durability properties of cement mortar and concrete.

4. Conclusions

The effect of utilization of carbon dust generated as an industrial waste from aluminum factories in cement mortar production was studied in this research. Experimental program was conducted to characterize the carbon dust, and then to investigate the effect of partially replacement of cement by carbon dust in the strength, microstructure, and chemical composition of cement mortar. The following conclusions could be drawn:

1. Partially replacing cement with small amount of carbon dust (5% and 10%) enhanced the compressive strength of the mortar. The maximum enhancement was 27% for 5% replacement ratio. For higher replacement ratio (more than 20%), incorporation of the carbon dust reduced the compressive strength of the mortar.
2. For low replacement ratio (5% and 10%), incorporation of carbon dust led to the formation of more dense and compact structure with the presence of well-formed and dense clusters of C-S-H as compared to the control specimen.
3. The microstructure of cement mortar with high replacement ratio (more than 20%) of carbon dust showed large quantities of un-hydrated clinkers reflecting improper hydration of concrete.

4. The maximum reduction in cement content that can be considered without negatively affecting the 28-day strength of the mortar was 96 kg/m³ (equivalent to 13% replacement ratio). Further cement replacement would decrease the strength.
5. Adding carbon dust as cement replacement would help in reducing the carbon footprint associated with concrete production and help in extending the life period of limited capacity landfill used to store these wastes thus mitigating the related environmental issues.

Author Contributions: M.R.I. and N.A.-N. conceived and designed the experiments; M.R.I. performed the experiments; M.R.I. analyzed the data; M.R.I. wrote the manuscript. All authors have read and agreed to the published version of the manuscript.

Funding: The experimental work presented in this study was funded by the Office of Research and Graduate Studies at Qatar University under project (QUCG-CAM-20/21-5).

Acknowledgments: The authors would like to thank Qatar Aluminum Company (Qatalum), Qatar for providing the carbon dust materials.

Conflicts of Interest: The authors declare no conflict of interest.

References

1. El-Dieb, A.S.; Kanaan, D.M. Ceramic waste powder an alternative cement replacement—Characterization and evaluation. *Sustain. Mater. Technol.* **2018**, *17*, e00063. [CrossRef]
2. Elahi, A.; Basheer, P.A.M.; Nanukkuttan, S.V.; Khan, Q.U.Z. Mechanical and durability properties of high performance concretes containing supplementary cementitious materials. *Constr. Build. Mater.* **2010**, *24*, 292–299. [CrossRef]
3. Ali, F.; Khan, M.A.; Qurashi, M.A.; Shah, S.A.R.; Khan, N.M.; Khursheed, Z.; Rahim, H.S.; Arshad, H.; Farhan, M.; Waseem, M. Utilization of Pyrolytic Carbon Black Waste for the Development of Sustainable Materials. *Processes* **2020**, *8*, 174. [CrossRef]
4. Chitra, D.G.; Selvi, P.V.; Vijayalakshmi, D.D. Carbon Black as an Additive in Conventional Concrete. *Int. J. Emerg. Technol. Adv. Eng.* **2014**, *4*, 194–201.
5. Schulze, S.E.; Rickert, J. Suitability of natural calcined clays as supplementary cementitious material. *Cem. Concr. Compos.* **2019**, *95*, 92–97. [CrossRef]
6. Ashish, D.K. Concrete made with waste marble powder and supplementary cementitious material for sustainable development. *J. Clean. Prod.* **2019**, *211*, 716–729. [CrossRef]
7. Shah, V.; Bishnoi, S. Carbonation resistance of cements containing supplementary cementitious materials and its relation to various parameters of concrete. *Constr. Build. Mater.* **2018**, *178*, 219–232. [CrossRef]
8. Farnam, Y.; Zhang, B.; Weiss, J. Evaluating the use of supplementary cementitious materials to mitigate damage in cementitious materials exposed to calcium chloride deicing salt. *Cem. Concr. Compos.* **2017**, *81*, 77–86. [CrossRef]
9. Mangi, S.A.; Wan Ibrahim, M.H.; Jamaluddin, N.; Arshad, M.F.; Shahidan, S. Performances of concrete containing coal bottom ash with different fineness as a supplementary cementitious material exposed to seawater. *Eng. Sci. Technol. Int. J.* **2019**, *22*, 929–938. [CrossRef]
10. Zhang, Y.; Zhang, J.; Luo, W.; Wang, J.; Shi, J.; Zhuang, H.; Wang, Y. Effect of compressive strength and chloride diffusion on life cycle CO₂ assessment of concrete containing supplementary cementitious materials. *J. Clean. Prod.* **2019**, *218*, 450–458. [CrossRef]
11. Yang, K.-H.; Jung, Y.-B.; Cho, M.-S.; Tae, S.-H. Effect of supplementary cementitious materials on reduction of CO₂ emissions from concrete. *J. Clean. Prod.* **2015**, *103*, 774–783. [CrossRef]
12. Vargas, F.; Lopez, M.; Rigamonti, L. Environmental impacts evaluation of treated copper tailings as supplementary cementitious materials. *Resour. Conserv. Recycl.* **2020**, *160*, 104890. [CrossRef]
13. Bui Viet, D.; Chan, W.-P.; Phua, Z.-H.; Ebrahimi, A.; Abbas, A.; Lisak, G. The use of fly ashes from waste-to-energy processes as mineral CO₂ sequesters and supplementary cementitious materials. *J. Hazard. Mater.* **2020**, *398*, 122906. [CrossRef] [PubMed]
14. Pyo, S.; Tafesse, M.; Kim, B.-J.; Kim, H.-K. Effects of quartz-based mine tailings on characteristics and leaching behavior of ultra-high performance concrete. *Constr. Build. Mater.* **2018**, *166*, 110–117. [CrossRef]

15. Kim, H.K.; Lee, H.K. Hydration kinetics of high-strength concrete with untreated coal bottom ash for internal curing. *Cem. Concr. Compos.* **2018**, *91*, 67–75. [CrossRef]
16. de Moura Souza, F.; Pollo Paniz, F.; Pedron, T.; Coelho dos Santos, M.; Lemos Batista, B. A high-throughput analytical tool for quantification of 15 metallic nanoparticles supported on carbon black. *Helvion* **2019**, *5*, e01308. [CrossRef]
17. Wu, G.; Chen, Z.; Artyushkova, K.; Garzon, F.H.; Zelenay, P. Polyaniline-derived Non-Precious Catalyst for the Polymer Electrolyte Fuel Cell Cathode. *ECS Trans.* **2008**, *16*, 159–170. [CrossRef]
18. Heidari, A.; Tavakoli, D. A study of the mechanical properties of ground ceramic powder concrete incorporating nano-SiO₂ particles. *Constr. Build. Mater.* **2013**, *38*, 255–264. [CrossRef]
19. Irshidat, M.R.; Al-Saleh, M.H.; Sanad, S. Effect of Nanoclay on the Expansive Potential of Cement Mortar due to Alkali-Silica Reaction. *ACI Mater. J.* **2015**, *112*, 801–808. [CrossRef]
20. Irshidat, M.R.; Al-Saleh, M.H. Thermal performance and fire resistance of nanoclay modified cementitious materials. *Constr. Build. Mater.* **2018**, *159*, 213–219. [CrossRef]
21. Singh, M.; Srivastava, A.; Bhunia, D. An investigation on effect of partial replacement of cement by waste marble slurry. *Constr. Build. Mater.* **2017**, *134*, 471–488. [CrossRef]
22. Khaliq, W.; Javaid, W. Efficiency Comparison of Conventional and Unconventional Curing Methods in Concrete. *Mater. J.* **2017**, *114*, 285–294. [CrossRef]
23. Jeyashree, T.M.; Chitra, G. Experimental studies on concrete elements using waste carbon black as filler material. *Asian J. Civ. Eng. (BHRC)* **2017**, *18*, 21–30.



© 2020 by the authors. Licensee MDPI, Basel, Switzerland. This article is an open access article distributed under the terms and conditions of the Creative Commons Attribution (CC BY) license (<http://creativecommons.org/licenses/by/4.0/>).

Article

Properties of a Three-Component Mineral Road Binder for Deep-Cold Recycling Technology

Zdzisława Owsiak, Przemysław Czapik * and Justyna Zapala-Sławeta *

Faculty of Civil Engineering and Architecture, Kielce University of Technology, 25-314 Kielce, Poland; owsiak@tu.kielce.pl

* Correspondence: p.czapik@tu.kielce.pl (P.C.); j.zapala@tu.kielce.pl (J.Z.-S.)

Received: 8 July 2020; Accepted: 11 August 2020; Published: 13 August 2020

Abstract: This study examined the physical properties of a three-component mineral binder that is typically used in deep-cold recycling. Test binders were produced using Portland cement, hydrated lime, and cement bypass dust (CBPD) as a byproduct derived from cement production. The suitability of CBPD for use in road binders was assessed. Effects of the three-component binder composition on the setting time, soundness, consistency, and tensile and compressive strengths of the cement pastes and mortars were determined. The pastes and mortars of the same consistency obtained at different w/b ratios were tested. On this basis, the mixture proportions resulting in road binders satisfying the requirements of PN-EN 13282-2:2015 were determined. By mixing cement, lime, and CBPD during the tests, binder classes N1 to N3 were obtained. The replacement of 40% of cement mass with the CBPD high in free lime produced road binders suitable for recycled base layers. The total content of CBPD and hydrated lime in the road binder should not exceed 50% by mass. The potential risk of mortar strength reduction due to KCl recrystallization was discussed.

Keywords: cement bypass dust; cement paste; mortar; mixed mineral binder; physical properties

1. Introduction

Bituminous road surfaces are subject to degradation due to various environmental impacts. Permanent deformation generated in the foundation or mineral base layers is the distress that requires extensive maintenance. One of the techniques recommended for eliminating the cause of permanent deformation is the environmentally friendly deep-cold recycling technology (CR) [1–4]. Pavement lower layers produced using CR are semi-rigid base courses that are typically made with bituminous binders (such as emulsion or foamed bitumen) and mineral binders (Portland cement, hydrated lime, fly ash, or cementitious dusts) [5,6]. Mineral binders make the base course stiffer, thereby minimizing the possibility of the regeneration of permanent deformation in the layer. On the other hand, an excessive strength of the binder can contribute to over-stiffening of the recycled layer and cause the formation of cracks running through all the layers of the bituminous pavement [2,5]. To counteract this effect and make the mixture more flexible, an appropriate amount of bituminous binder is added [7]. The stiffness of the layer can also be reduced by replacing cement with supplementary cementing materials (SCMs), such as hydrated lime, and with byproducts of the cement manufacturing process, such as cement kiln dust (CKD) and cement bypass dust (CBPD) [8–15].

The use of cement with the addition of byproducts generated during cement manufacture is a relatively recent innovation and requires undertaking further studies. Dusts, such as CKD or CBPD, especially those generated at lower temperatures in modern furnace systems, may have binding properties as they contain clinker phases [8,9]. They may also contain unreacted free lime [9,13]. The presence of these dusts can thus significantly affect the properties of the binder used in the base layer. Reduced reliance on landfill as a dust management option is an additional advantage of this

solution [10,13,16]. The quantity of CKD and CBPD generated in the cement clinker manufacturing process is largely dependent on the technology applied. It is usually between 0 and 25% of the clinker mass, as reported by researchers [16,17]. According to the Polish Cement Association, the amount of dust produced during cement manufacturing is decreasing. Their latest report found that the annual quantity of dusts from cement kilns in Poland was about 1200 tons [18]. Compared to 25,000 tons in Oman, 2.7–3.5 million tons in Egypt, 8 million tons in the UK, and 2.5–12 million tons in the US [16,19–21], the amount of 1200 tons appears minor. However, as a single cement plant is capable of producing 1000 tons of CBPD daily [22], the reported dust emission rate is not the same as the total dust quantity generated in Polish cement plants and does not include the CKD and CBPD that are recycled back into the kiln system. The amount of dust so used in Poland is much higher and ranges from 9000 to 25,000 tons a year [23]. In 2016, 15,071 tons of CKD and CBPD were reused in the cement production process [24]. However, as recycled dusts lower the cement quality, research is being conducted into new opportunities for dust management [16].

There is a strong body of research exploring alternatives to CBPD utilization [8,11,14,16]. One of important research directions is soil stabilization [13,16,17,25]. According to data reported in 2006, the USA uses more CKD for this purpose than for cement production. The same source mentions the use of dusts in road pavement construction. A number of researchers [21,26,27] have investigated the application of CKD as a filler in asphalt mixtures. Cement bypass dust is not an inert material as it contains phases that have binding properties [9,13,17]. Therefore, it can be used in the production of mineral binders. The high content of chloride and alkalis [9] prevents CBPD from being widely utilized in the production of the classical cement concrete [16]. Other uses for this material are being studied, such as its incorporation in alkali-activated binders [17,19] and in the binders that are not required to have high strength characteristics [17]. The latter mineral binders are chosen for deep-cold recycling [28–30].

Proper selection of the proportions of cold recycled mixture components is of key importance in terms of the required base course properties. The semi-rigid base must protect the pavement against permanent deformations, reflective cracking [2,10], and the local reduction in subgrade load support due to groundwater. The required properties of the base layer are achieved primarily by using appropriate proportions of mineral and bituminous binders of known characteristics [2]. The identification of mineral binder properties is problematic when it is composed of different materials [31–34]. The most popular binder used in CR is Portland cement. Cement increases the stiffness of the recycled base mixture, thereby increasing the risk of reflection crack formation under service loads. Together with the hydrated lime, CBPD is used to reduce the stiffness of the hardened composite [2]. Stiffness reduction with CBPD is associated with strength lowering, as the CBPD provides a weaker skeleton despite its binding properties [9,12,13]. The ability of CBPD to swell while setting is an interesting property [9,11,12] that balances the shrinkage of Portland cement and hydrated lime at the setting stage. By mixing these three binders, setting-related volume changes can be controlled.

The cement used alone is not capable of ensuring proper moisture and frost resistance. Cement binder parameters are commonly improved with a range of mineral additives. These are often waste products and byproducts of various industries. The use of these products in road binders has an additional advantage in terms of sustainable development [35].

This study aimed at investigating the properties of a three-component mineral binder that can be used in cold recycled mixtures. In addition to conventional components, such as Portland cement and hydrated lime, the binder contained CBPD. The three-component binder consisting of cement, hydrated lime, and CBPD has not as yet been studied for use in deep cold recycling. The experimental plan proposed by Atkinson and Donev [36] was adopted to design the composition of three-component mixtures. The plan involved determining an optimum composition of the cement-lime-CBPD binder with respect to its use for cold recycled base course mixtures. Physical and mechanical properties of the pastes and mortars prepared with seven binder blends were determined, as required by PN-EN 13282-2:2015 [37].

2. Materials and Methods

2.1. Properties of the Components Used in the Binder Preparation

The input materials used for composing the mineral road binders were Portland cement CEM I 32.5R (Cement Ożarów, Ożarów, Poland), hydrated lime (ZSChIM "PIOTROWICE II", Sitkówka, Poland), and CBPD with a high content of free lime (Cement Ożarów, Ożarów, Poland). The chemical composition of the materials is shown in Table 1. The phase compositions determined using X-ray diffraction are presented in the form of X-ray patterns in Figure 1 and in the form of tabulated results of the quantitative analysis in Table 2. The particle size distribution of raw materials is compiled in Figure 2.

Table 1. Chemical composition of Portland cement CEM I 32.5R and cement bypass dust (CBPD).

Material	Content (%)										
	SiO ₂	Al ₂ O ₃	Fe ₂ O ₃	CaO	MgO	Na ₂ O	K ₂ O	Na ₂ O _e	Cl	SO ₃	LOI
CEM I 32.5R	19.70	4.28	2.44	64.50	1.60	0.14	0.79	0.66	0.043	3.33	3.50
CBPD	15.44	3.42	1.77	52.17	1.31	0.26	6.03	4.22	3.53	1.65	14.40

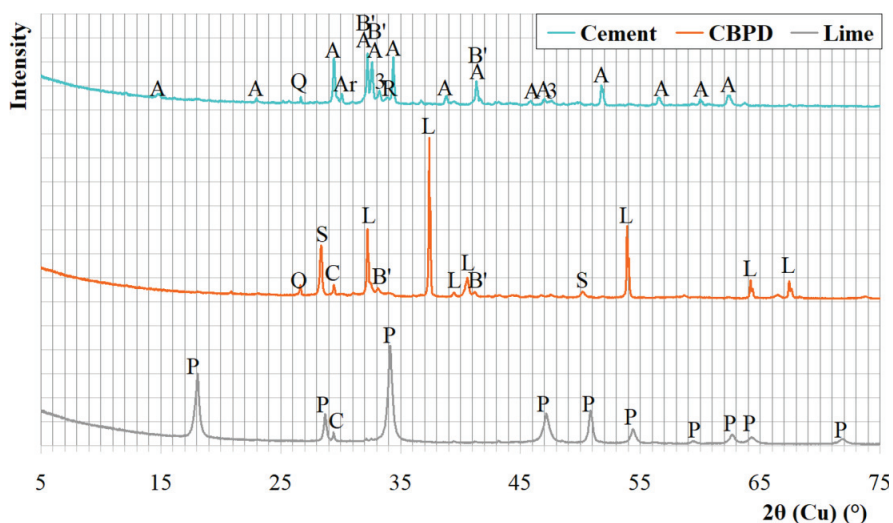


Figure 1. The X-ray patterns of cement CEM I 32.5R, CBPD, and hydrated lime. Designations: A—alite, B’—belite, R—brownmillerite, 3—C₃A, Ar—arcanite, Q—quartz, G—gypsum, L—free CaO, S—sylvine, P—portlandite, C—calcite.

Table 2. Phase composition of the road binder components (%).

CEM I 32.5R		CBPD		Lime	
C ₃ S (alite)	65.3	Free lime	42.8	Portlandite	97.4
β-C ₂ S (belite)	10.0	Sylvine	16.2	Calcite	2.6
C ₄ AF	4.4	C ₂ S (belite)	33.3		
C ₃ A	9.3	Calcite	5.9		
Arcanite	1.3	Quartz	2.7		
Gypsum	1.0				
Calcite	7.7				
Quartz	1.0				

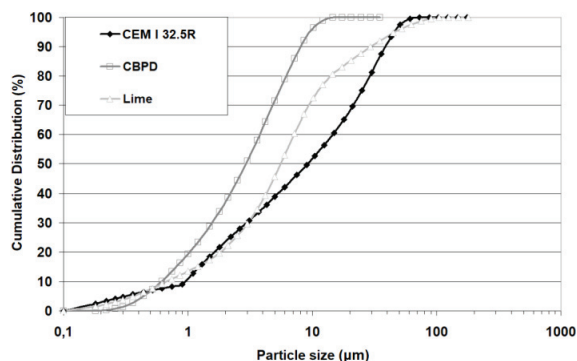


Figure 2. Raw materials' particle size distributions.

Each of the test results of the cement mineralogy revealed a phase composition typical of each respective material. In the CBPD, two phases indicating binding properties were present: CaO and C₂S, accompanied by sylvine (potassium chloride) and calcite, which were derived from the feed that was calcined before it entered the kiln or were transferred from the kiln by the air stream carrying bridged chlorine compounds. The minor amount of calcite in the hydrated lime may be due to the presence of non-decarbonated raw material or partial carbonation of portlandite. The high content of free lime in the CBPD that was tested is noteworthy when comparing it to other dusts [13].

The particle size distribution of the hydrated lime was found to be similar to that of Portland cement, i.e., from 0 to 100 µm, with lime having more particles in the range of 3 to 45 µm. The inflection above 12 µm on the lime grading curve was probably associated with the formation of lime particle agglomerates. Lime particles larger than 200 µm were excluded from the analysis and were regarded as small particle agglomerates that could reach tens of millimeters. The finest particles, from 0.20 to 18.5 µm, were found in the CBPD. Compared to the cement and lime, the CBPD had more particles in the 0.50 to 18.5 µm range but fewer particles in the 0.20 to 0.50 µm range. All components of the hydraulic binder met the EN 13282-2 [20] standard requirements. The recommended limit for the content of particles more than 90 µm in size is 15%. The cement and the CBPD met the standard requirements with respect to their compositions.

2.2. Methodology

2.2.1. Experimental Plan

Fitting the response surfaces to the mixture results is performed in the same way as fitting to the data from the central composite design. However, the mixture data are constrained in that the sum of all the mixture components is always 100%. The three-component mixture can be determined by providing a point in the triangular coordinate system defined by three variables. All experimental designs based on the mixture design require vertex points, that is, mixtures consisting of only one component. In practice, these systems may not be feasible due to cost or other technological constraints. In this experiment, constrained mixture designs were used, i.e., the basic mixture design was modified so that the amount of each component was in the range of 20% to 60%. Ultimately, the research program was subordinated to the constrained mixture design based on the simplex-centroid design [38].

The effect of the hydraulic binder composition on its properties was determined by preparing seven different road binders based on the experimental plan. The principles of simplex-centroid design by Atkinson and Donev [36] were adopted to describe the binder composition. The experimental plan assumes the assessment of the effect of the content of individual components and interactions between them on the properties of the binder and allows for evaluating the effect of the binder composition on the specified property at any point within the analyzed region of the experimental plan.

The simplex-centroid design is shown in Figure 3. Furthermore, the designations and compositions of the hydraulic binders are shown in Table 3.

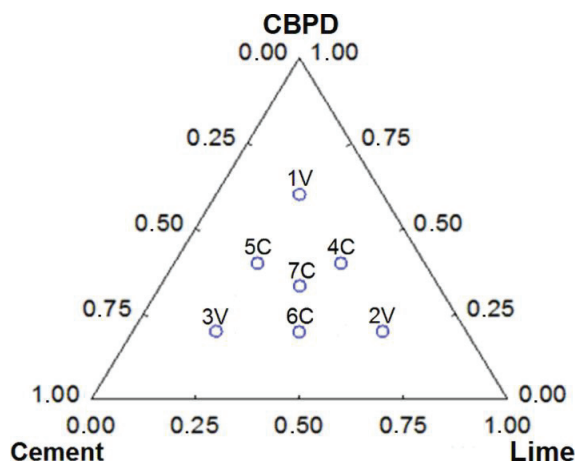


Figure 3. Simplex-centroid design.

Table 3. Designations and compositions of binders (mass%).

Binders	Components		
	Cement	Lime	CBPD
Ref.	1.00	0	0
1V	0.20	0.20	0.60
2V	0.20	0.60	0.20
3V	0.60	0.20	0.20
4C	0.20	0.40	0.40
5C	0.40	0.20	0.40
6C	0.40	0.40	0.20
7C	0.33	0.33	0.33

Seven road binders were prepared based on the experimental design to comprehensively evaluate the effects of binder components on the properties of hardened mortar. Pure Portland cement was used as the reference binder.

Figure 3 shows the code marking locations for the combination of components included in the universal binder and the method of determining the percentage value of those components. The amount of a given component in the triangle in Figure 3 is the length of the segment, which is the bisector between the neighboring sides of the triangle. The constrained mixture design consisted of estimating pseudo-components and treating the constrained region as the complete design. In practice, an experiment analysis with the use of mixture designs is the multiple (multivariate) regression with the constant component reduced to zero. The effect of the mixture composition on the properties of the innovative binder was assessed based on the analysis of the adequacy of the type of the approximated function of the test object and the estimation of the function coefficients.

The polynomial function was adopted as the approximating function. The degree of the polynomial was dependent on the significance of its form for explaining the variability of the test results. The next stage of the analysis was the estimation of the polynomial coefficients with the degree determined on the basis of the analysis of variance. Parameter approximation was based on the least-squares method (LSM).

2.2.2. Paste and Mortar

The chemical composition of the input materials was analyzed as per PE-EN 196-2 [39]. The phase composition was identified using X-ray diffraction (XRD) on the powder samples. The Empyrean diffractometer (PANalytical, Almelo, Netherlands) was used. The 2θ angle range of 5° to 75° was analyzed with a step size of 0.0167° and a count time of 60 s. The PANalytical XRD analysis software HighScore 4.6 with the International Center for Diffraction Data (ICDD) database PDF-2 was used for phase identification. Particle-size analysis of the binders was performed using laser diffraction with a Hellos KR laser diffractometer (Sympatec, Clausthal-Zellerfeld, Germany).

The proper amount of mixing water, the initial and final setting times, and changes in the binder volume were determined using the Le Chatelier test (Institute of Ceramics and Building Materials, Cracow, Poland) in accordance with PN-EN 196-3 [40]. The Blaine test (Institute of Ceramics and Building Materials, Cracow, Poland) was used as per PN-EN 196-6 [41] to measure the specific surface area of the binders. These test methods were used to explain the influence of individual constituents on the consistency of the prepared mortars.

The mortar consistency was determined using the penetration test according to PN 85/B-04500 [42] and the flow table test according to PN-EN 1015-3 [43].

These tests were performed to determine the water to binder ratios (w/b) required for the appropriate consistency of the mortars. It is known that the surface area and hence the water demand varies considerably between cement, hydrated lime, and CBPD. Moreover, the presence of a significant amount of free lime found in the composition of the CPBD can contribute to the evaporation of a portion of the mixing water as a result of heat release during hydration [9,12], thereby reducing the effective w/b ratio. There is thus a need to determine the w/b ratio for each binder, which produces pastes and mortars suitable for testing, and in the longer term for use in cold recycling.

Mortar compressive and flexural strengths were measured on $40 \times 40 \times 160$ mm bars at 28 and 56 days according to PN-EN 196-1 [44]. Determining the 56-day strength is essential for checking whether the mixtures meet the requirements for road binders set forth in PN-EN 13282-2:2015 [37]. The 28-day tests are classical strength tests performed for various cement composites and are widely discussed in the literature [44].

3. Test Results of Binder Physical and Mechanical Properties

3.1. Determination of the Density, Specific Surface, Proper Amount of Water, and Setting Time of Binders

Table 4 presents the results of the tests for density, specific surface, water amount, setting time and binder volume stability.

Table 4. Proper amount of water, setting times of individual binders, and the results of the binder volume stability determined in the Le Chatelier ring.

Binder Type	Ref.	1V	2V	3V	4C	5C	6C	7C
Density (kg/dm ³)	3.05	2.85	2.57	2.89	2.74	2.86	2.75	2.76
Specific area (m ² /kg)	377	534	576	466	555	501	521	520
w/b	0.27	0.70	0.67	0.45	0.61	0.57	0.50	0.55
Initial setting time (min)	200	265	1050	160	310	265	380	450
Final setting time (min)	265	305	1620	190	630	460	710	800
Setting time (min)	65	40	570	30	320	195	330	350
Soundness (mm)	9	54	22	21	53	17	9	17

The density and specific surface of the binders depended on the percentages of the input components. Lime or bypass dusts used as the replacement for cement increased the water demand of the binder. This was related to the considerably lower specific surface and higher density of the cement [17,44]. The presence of CBPD increased the water demand more than the addition of hydrated

lime. The initial setting time for all binders was more than 150 min, which is consistent with the requirements of the standard. The presence of hydrated lime in the binder had the strongest effect on the setting-time extension. The shortest setting time was observed for the 3V binder. In addition to cement as the main component, the 3V binder contained small quantities of lime and CBPD. The action of alkalis and free lime present in the CBPD contributed to the faster setting of the binder compared to the Portland cement. At small quantities, the alkalis and free lime can act as cement-setting activators. Likewise, the rise in the sample temperature resulting from the free lime hydration can promote faster setting. As a rule, however, the setting time of the prepared three-component binders was extended. This was due to the fact that the setting times of hydrated lime and CBPD were much longer than that of cement [17,25].

The standard requirement for cement binders is that the change in the Le Chatelier soundness should not exceed 30 mm. Binders 1V and 4C did not meet this condition; all the other binders exhibited swelling within acceptable limits. It was thus evident that a high content of CBPD in binders led to significant changes in their volume. The results obtained for 4C and 5C could be compensated for by adding cement, while the addition of hydrated lime had a negligible effect. The CBPD material was the major contributor to the increase in the binder water demand.

3.2. Determining the Mortar Consistency

Mortars containing particular binders having compositions as specified for standard mortars in PN-EN 196-1 were used in the tests for consistency. Table 5 compiles the mean values from three measurements.

Table 5. Consistency of mortars under analysis.

Binders	w/b	Flow Table Test (cm)	Penetration Test (cm)
Ref.	0.50	13.5	4.2
1V	0.79	13.5	3.5
2V	0.76	13.5	3.2
3V	0.60	13.5	4.2
4C	0.75	14.0	3.5
5C	0.68	14.0	3.5
6C	0.62	13.5	3.8
7C	0.66	14.0	3.4

Mortars were tested at different w/b values, and the consistency results obtained for mortars with the designed binders were compared with those for the mortar prepared with the cement binder. As in the paste consistency tests, the water demand of the binders increased with a decrease in the cement content. Unlike in the case of pastes, the differences were smaller because the consistency of mortars was largely related to the water demand of the aggregates and the quantity of aggregates was the same in each sample [44]. These results do not confirm the beneficial effect of CBPD on the fluidity of mortars, as found by Sreekrishnavilasam and Santagata [17] for low strength materials. These results confirm the concrete analysis findings presented by Siddique [25], who reported a thicker consistency with the increased content of CKD.

3.3. Test Results of Mortar Compressive and Flexural Strengths

Figures 4 and 5 show the results of flexural and compressive strength tests of mortar bars at 28 and 56 days. The results of the strength tests indicate that the use of lime and dust byproducts in the binder led to a significant strength reduction. The mechanical parameters of the reference sample after 28 days were significantly higher than those of other samples. The flexural and compressive strengths of the 3V sample containing 40% less cement were 50% and 55% less, respectively, than the reference sample. Thus, it can be seen that the dependence of strength on the cement content was not linear. The strength

of mortars was particularly affected by the addition of hydrated lime to the binder. The presence of CBPD in the binder also reduced the strength of mortars, as confirmed by other studies [14,17,25]. After 56 days, all mixtures except the 2V mixture with the highest proportion of hydrated lime met the standard strength requirements for hydraulic road binders, reaching a minimum strength of 2.5 MPa, thus representing class N1. The highest compressive strength, 23.7 MPa at 56 days, was achieved by the 3V binder, in which Portland cement was the dominant component, representing classes N2 and N3.

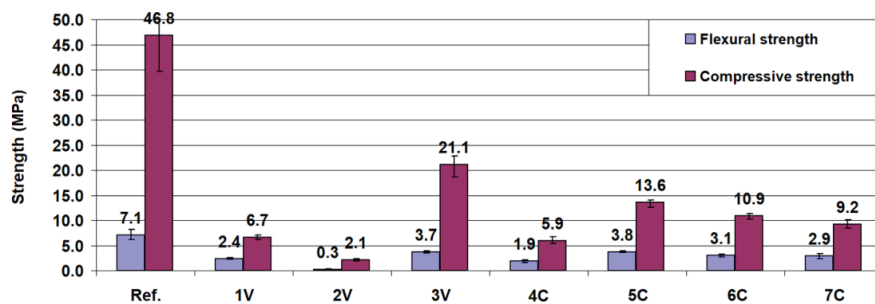


Figure 4. The 28-day compressive and flexural strengths of mortar bars made with the road binder.

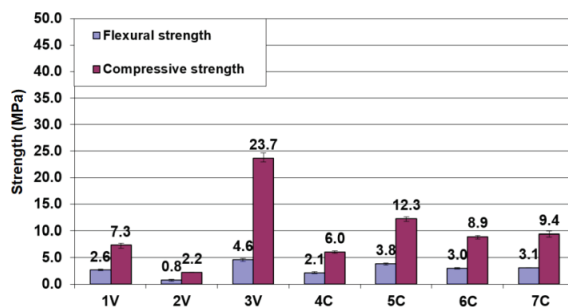


Figure 5. The 56-day compressive and flexural strengths of mortar bars made with the road binder.

In most cases, the comparison between the 28-day and 56-day tests showed only slight strength changes. It can thus be concluded that the binders tested behaved like ordinary Portland cement binders with the strength increase occurring mainly in a period shorter than 28 days. Generally, the changes taking place after this time resulted in an increase in strength, except for binders 5C and 6C. The observed decrease in the strength of these binders may be related to the progressing concrete degradation due to the influence of chlorides from the CBPD [14,17,45].

Within the first 2 days, a white deposit crystallized on the surface of the bars with the high content of cement dust (1V). The X-ray diffraction test results (Figure 6) revealed that the deposit was composed of sylvine crystals. The X-ray pattern also showed single, very weak peaks of other phases in the cement-based mortar, quartz, and calcite.

These findings confirm the recrystallization of sylvine during the setting and hardening of the binder containing CBPD, as found in previous studies [9,12]. In the previous studies, the sylvine recrystallization inside the paste was found to change its microstructure. Small KCl crystals and films formed. As was demonstrated, the crystalline film could also form on the surface of samples, taking the form of large crystals visible to the naked eye. The formation of such large crystals in the limited space of the paste matrix could damage it and thus reduce its strength. This may explain the strength decrease in the period between days 28 and 56 observed for binders 5C and 6C and the lack of dimensional stability of the hardened samples [14,17].

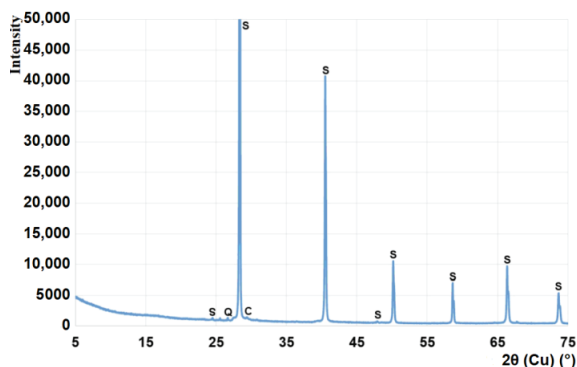


Figure 6. The X-ray pattern of the deposit on the surface of the road binder mortar bars. Q—quartz, S—sylvine, C—calcite.

4. Discussion

A simplex-centroid experimental design was applied to evaluate the results obtained. The second-degree and third-degree models (special cubic) were used to describe the variables. Figure 7 shows the response surfaces of the binder components and their interaction effects on the flexural and compressive strengths of the mortar bars.

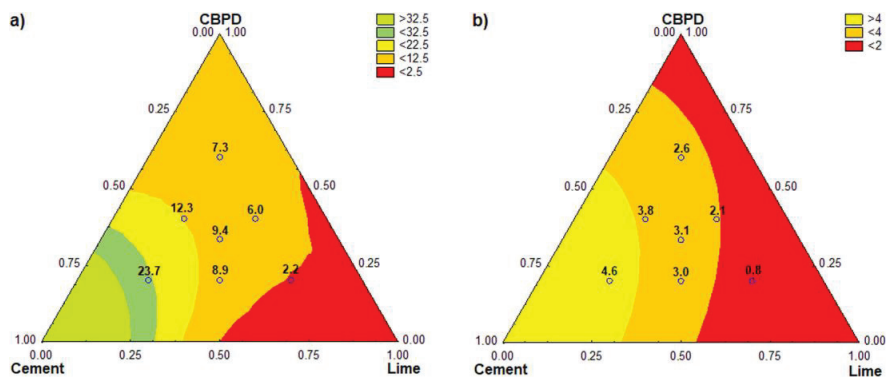


Figure 7. Response surfaces for the variables: (a) compressive strength of mortar bars at 56 days and (b) flexural strength of mortar bars at 56 days.

Figure 7 shows the road binder composition optimization with respect to strength. Analysis of the effect of the binder composition on its compressive strength (Figure 7a) indicated that cement was primarily responsible for the beneficial properties of the three-component road binder. To meet the requirements of EN 13282-2:2015 for class N1, the road binder must contain up to 60% of hydrated lime at the CBPD content of about 30%, but these proportions were not optimal due to the setting time. Considering the strength parameters, CBPD could replace cement in greater quantities. In theory, all cement could be replaced by CBPD in road binders. This was not possible because of the failure to meet the soundness requirement for binders. For this reason, the CBPD content in the road binder should not be higher than 40% (Table 4). This value, however, is still two times as large as the recommended maximum dosage value for CPBD used as a mineral additive for cement [8]. It is also remarkably larger than the amount (12%) recommended as the requirements for the road binder water resistance [29].

Replacing cement with hydrated lime and CBPD often leads to a significant reduction in binder compressive strength, allowing it to be classified as class N1 only. In order to obtain a higher-class road binder, the minimum required amount of cement should be 50% by mass of the binder.

The flexural strength of concrete was observed to be generally lower than that of the mortar; therefore, the mortar determined the upper limit of the concrete flexural strength [45]. This finding is important when designing pavements on the basis of flexural strength values and plays a role in the case of recycled base course layers. There are no requirements concerning the flexural strength of mortars with a hydraulic road binder.

The results (Figure 7b) show that compared to CBPD, the reduction in flexural strength due to lime was much greater. Theoretically, for the mortar strength to fall below 2 MPa, it is sufficient to replace 55% of the cement CEM 32.5R with hydrated lime. To obtain the same effect with CBPD, the cement replacement quantity should be at least 85%.

5. Conclusions

The test results obtained from this study show that:

- An appropriate combination of hydraulic road binder components resulted in the optimal composition for the required mechanical and physical performance in the recycled base course layer.
- An addition of CBPD and hydrated lime to Portland cement allowed for obtaining a mineral road binder class N1 to N3 that met the requirements of EN 13282 2: 2015.
- The presence of CBPD in the mineral binder increased its water demand and volume during setting. It also caused the potassium chloride crystallization that occurred after the binder had set, which was manifested by the formation of a white deposit on the mortar surface.
- The presence of hydrated lime contributed primarily to the extended setting time and reduced the flexural and compressive strength of the mortar.
- The Portland cement content was the primary factor that increased the strength of the cement-lime-CBPD mortar.
- The replacement of Portland cement with 50% hydrated lime and CBPD ensured maintaining the required physical and mechanical properties, as demonstrated by the optimization of the hydraulic road binder composition. For road binder production, the CBPD should not be used in an amount greater than 40% of the binder mass.
- The presence of CBPD reduced the strength of the mortars due to KCl recrystallization.

Author Contributions: Conceptualization, Z.O.; methodology, Z.O., P.C., and J.Z.-S.; validation, Z.O., P.C., and J.Z.-S.; formal analysis, Z.O. and P.C.; investigation, P.C. and J.Z.-S.; resources, Z.O., P.C., and J.Z.-S.; data curation, Z.O., P.C., and J.Z.-S.; writing—original draft preparation, Z.O., P.C., and J.Z.-S.; writing—review and editing, Z.O., P.C., and J.Z.-S.; visualization, P.C.; supervision, Z.O.; project administration, Z.O.; funding acquisition, Z.O. All authors have read and agreed to the published version of the manuscript.

Funding: The research results were developed as part of the project entitled “The innovative technology used for the binding agent optimization that provides the long service life of the recycled base course” (TECHMATSTRATEG1/349326/9/NCBR/2017) within the scientific undertaking of the Strategic Research and Development Program entitled “Modern Materials Technology” (TECHMATSTRATEG I), which is financed by the National Center for Research and Development (Polish NCBR).

Conflicts of Interest: The authors declare no conflict of interest.

References

1. Buczyński, P.; Iwański, M. The Influence of a Polymer Powder on the Properties of a Cold-Recycled Mixture with Foamed Bitumen. *Materials* **2019**, *12*, 4244. [CrossRef] [PubMed]
2. Iwański, M.; Chomicz-Kowlaska, A. Laboratory Study on Mechanical Parameters of Foamed Bitumen Mixture in the Cold Recycling Technology. *Procedia Eng.* **2013**, *57*, 433–442. [CrossRef]
3. Iwański, M.; Chomicz-Kowalska, A. Application of the Foamed Bitumen and Bitumen Emulsion to the Road Base Mixes in the Deep Cold Recycling Technology. *Baltic J. Road Bridge Eng.* **2016**, *11*, 93–101. [CrossRef]

4. Iwański, M.; Buczyński, P.; Mazurek, G. The use of gabbroic dust in the cold recycling of asphalt paving mixes with foamed bitumen. *Bull. Pol. Acad. Sci. Tech. Sci.* **2016**, *64*, 763–773. [CrossRef]
5. Chomicz-Kowalska, A.; Maciejewski, K. Performance and viscoelastic assessment of high-recycle rate cold foamed bitumen mixtures produced with different penetration binders for rehabilitation of deteriorated pavements. *J. Clean. Prod.* **2020**, *23*, 120517. [CrossRef]
6. Kukielka, J. Deep cold recycling on local asphalt road. *Materiały Budowlane* **2014**, *12*, 11–13.
7. Judycki, J.; Dołżycki, B.; Hunik, K.; Stienss, M. *Weryfikacja Zasad Projektowania Mieszanek Mineralno-Cementowo-Emulsyjnych*; Gdańsk University of Technology: Gdańsk, Poland, 2006; pp. 7–48.
8. Barnat-Hunek, D.; Góra, J.; Suchorab, Z.; Łagód, G. 5—Cement kiln dust. In *Waste and Supplementary Cementitious Materials in Concrete: Characterization, Properties and Applications*; Sissique, R., Cachim, P., Eds.; Woodhead Publishing: Cambridge, UK, 2018; pp. 149–180. [CrossRef]
9. Czapik, P.; Zapala-Sławeta, J.; Owsiak, Z.; Stepień, P. Hydration of cement by-pass dust. *Constr. Build Mat.* **2020**, *231*, 117139. [CrossRef]
10. Iwański, M.; Buczyński, P.; Mazurek, G. Optimization of the road binder in the layer the road construction. *Constr. Build Mat.* **2016**, *125*, 1044–1054. [CrossRef]
11. Nocuń-Wczelik, W.; Stolarska, K. Calorimetry in the studies of by-pass cement kiln dust as an additive to the calcium aluminate cement. *J. Therm. Anal. Calorim.* **2019**, *138*, 4561–4569. [CrossRef]
12. Owsiak, Z.; Czapik, P.; Zapala-Sławeta, J. Testing the cement, hydrated lime and cement by-pass dust mixtures hydration. *Roads Bridges—Drogi i Mosty* **2020**, *19*, 135–147. [CrossRef]
13. Peethamparan, S.; Olek, J.; Lovell, J. Influence of chemical and Physical characteristics of cement kiln dusts (CKDs) on their hydration behavior and potential suitability for soil stabilization. *Cem. Concr. Res.* **2008**, *38*, 803–815. [CrossRef]
14. Stryczek, S.; Gonet, A.; Czapik, P. Developing technological properties of sealing slurries with the use of cement dust. *AGH Drill. Oil Gas* **2009**, *26*, 345–354.
15. Seo, M.; Lee, S.-Y.; Lee, C.; Cho, S.-S. Recycling of Cement Kiln Dust as Raw Material for Cement. *Environments* **2019**, *6*, 113. [CrossRef]
16. Adaska, W.S.; Taubert, D.H. Beneficial Uses of Cement Kiln Dust. In Proceedings of the 2008 IEEE Cement Industry Technical Conference Record, Miami, FL, USA, 18–28 May 2008. [CrossRef]
17. Sreekrishnavilasam, A.; Santagata, M.C. Report No. FHWA/IN/JTRP-2005/10 *Development of Criteria for the Utilization of Cement Kiln Dust (CKD) in Highway Infrastructures*; Joint Transportation Research Program; Purdue University: West Lafayette, IN, USA, 2006.
18. 2012—INFORMATOR SPC—Przemysł Cementowy w liczbach”, Polish Cement Association reports. Available online: <https://www.polskicement.pl/2012-informator-spc-przemysl-cementowy-w-liczbach/> (accessed on 27 July 2020).
19. Abdel-Ghani, N.T.; El-Sayed, H.A.; El-Habak, A.A. Utilization of by-pass cement kiln dust and air-cooled blast-furnace steel slag in the production of some “green” cement products. *HBRC J.* **2018**, *14*, 408–414. [CrossRef]
20. Darweesh, H.H.M. A Review Article on the Influence of the Electrostatic Precipitator Cement Kiln Dust Waste on the Environment and Public Health. *Am. J. Biol. Environ. Stat.* **2017**, *3*, 36–43. [CrossRef]
21. Taha, R.; Al-Rawas, A.; Al-Harthy, A.; Qatan, A. Use of Cement Bypass Dust as Filler in Asphalt Concrete Mixture. *J. Mater. Civil Eng.* **2002**, *14*, 338–343. [CrossRef]
22. Khater, G.A. Use of bypass cement dust for production of glass ceramic materials. *Adv. Appl. Ceram.* **2006**, *105*, 107–111. [CrossRef]
23. Uliasz-Bocheńczyk, A. Chemical characteristics of dust from cement kilns. *Gospod. Surowcami Min.* **2019**, *35*, 87–102. [CrossRef]
24. 2019—Informator SPC—Przemysł Cementowy w iczbach, Polish Cement Association reports. Available online: <https://www.polskicement.pl/2019-informator-spc-przemysl-cementowy-w-liczbach/> (accessed on 27 July 2020).
25. Siddique, R. Utilization of cement kiln dust (CKD) in cement mortar and concrete-an overview. *Resour. Conserv. Recycl.* **2006**, *48*, 315–338. [CrossRef]
26. Orešković, M.; Trifunović, S.; Mladenović, G. Use of hydrated lime and cement bypass dust as alternative fillers in hot mix asphalt. In Proceedings of the 17th Colloquium Asphalt, Bitumen and Pavements, Bled, Slovenia, 27–29 November 2019.

27. Khodary, F.; Abd El-Sadek, M.S.; El-Shestawy, H.S. Nano-Size Cement Bypass as Asphalt Modifier in Highway Construction. *Int. J. Eng. Res. Appl.* **2013**, *3*, 645–648.
28. Buczyński, P.; Iwański, M. The Influence of Hydrated Lime, Portland Cement and Cement Dust on Rheological Properties of Recycled Cold Mixes with Foamed Bitumen. In Proceedings of the “Environmental Engineering” 10th International Conference, Vilnius, Lithuania, 27–28 April 2017. [CrossRef]
29. Buczyński, P.; Iwański, M.; Mazurek, G. The water resistance of a recycled base with foamed bitumen in the aspect of road binder composition. *Bud. Arch.* **2016**, *15*, 19–29. [CrossRef]
30. Omrani, M.A.; Modarres, A. Emulsified cold recycled mixtures using cement kiln dust and coal waste ash-mechanical-environmental impacts. *J. Clean. Prod.* **2018**, *199*, 101–111. [CrossRef]
31. Bahar, R.; Benazzoug, M.; Kenai, S. Performance of compacted cement-stabilised soil. *Cem. Concr. Compos.* **2004**, *26*, 811–820. [CrossRef]
32. Mahamedi, A.; Khemissa, M. Stabilization of an expansive overconsolidated clay using hydraulic binders. *HBRC J.* **2015**, *11*, 82–90. [CrossRef]
33. Pérez, P.; Agrela, F.; Herrador, R.; Ordoñez, J. Application of cement-treated recycled materials in the construction of a section of road in Malaga, Spain. *Constr. Build. Mat.* **2013**, *44*, 593–599. [CrossRef]
34. Pizon, J.; Łaźniewska-Piekarczyk, B. Efficiency assessment of admixtures and cement kiln dust with cooperation with different phase composition slag blended cements. *IOP Conf. Ser. Mater. Sci. Eng.* **2019**, *603*, 032088. [CrossRef]
35. Czarniecki, L.; Kurdowski, W. Tendencje kształtujące przyszłość betonu. *Budownictwo Technologie Architektura* **2007**, *1*, 50–55.
36. Atkinson, A.C.; Donev, A.N. *Optimum Experimental Designs*, Oxford Science Publications; Clarendon Press: Oxford, UK, 1992.
37. Polish Committee for Standardization. *Hydraulic Road Binders. Normal Hardening Hydraulic Road Binders. Composition, Specifications and Conformity Criteria*; PN-EN 13282-2:2015; Polish Committee for Standardization: Warsaw, Poland, 2015.
38. Lazić, Ž.R. *Design of Experiments in Chemical Engineering: A Practical Guide*; Wiley-VCH: Weinheim, Germany, 2004.
39. Polish Committee for Standardization. *Methods of Testing Cement. Chemical Analysis of Cement*; PN-EN 196-2:2013; Polish Committee for Standardization: Warsaw, Poland, 2013.
40. Polish Committee for Standardization. *Methods of Testing Cement. Determination of Setting Times and Soundness*; PN-EN 196-3:2016; Polish Committee for Standardization: Warsaw, Poland, 2016.
41. Polish Committee for Standardization. *Methods of Testing Cement. Determination of Fineness*; PN-EN 196-6:2018; Polish Committee for Standardization: Warsaw, Poland, 2018.
42. Polish Committee for Standardization. *Building Mortars—Testing of Physical and Mechanical Properties*; PN 85/B-04500; Polish Committee for Standardization: Warsaw, Poland, 1985.
43. Polish Committee for Standardization. *Methods of Test for Mortar for Masonry. Determination of Consistence of Fresh Mortar (by Flow Table)*; PN-EN 1015-3:2000/A1:2005; Polish Committee for Standardization: Warsaw, Poland, 2005.
44. Polish Committee for Standardization. *Methods of Testing Cement. Determination of Strength*; PN-EN 196-1:2016; Polish Committee for Standardization: Warsaw, Poland, 2016.
45. Neville, A.M. *Properties of Concrete*, 5th ed.; Pearson: Harlow, UK, 2011.



© 2020 by the authors. Licensee MDPI, Basel, Switzerland. This article is an open access article distributed under the terms and conditions of the Creative Commons Attribution (CC BY) license (<http://creativecommons.org/licenses/by/4.0/>).

Article

Recycled Glass as a Substitute for Quartz Sand in Silicate Products

Katarzyna Borek *, Przemysław Czapiak and Ryszard Dachowski

Civil Engineering and Architecture Department, Kielce University of Technology, Al. 1000-lecia PP 7, 25-314 Kielce, Poland; p.czapiak@tu.kielce.pl (P.C.); tobrd@tu.kielce.pl (R.D.)

* Correspondence: kkomisarzyk@tu.kielce.pl

Received: 23 January 2020; Accepted: 20 February 2020; Published: 25 February 2020

Abstract: In 2016, an average of 5.0 tons of waste per household was generated in the European Union (including waste glass). In the same year, 45.7% of the waste glass in the EU was recycled. The incorporation of recycled waste glass in building materials, i.e., concrete, cements, or ceramics, is very popular around the world because of the environmental problems and costs connected with their disposal and recycling. A less known solution, however, is using the waste glass in composite products, including sand-lime. The aim of this work was to assess the role of recycled container waste glass in a sand-lime mix. The waste was used as a substitute for the quartz sand. To verify the suitability of recycled glass for the production of sand-lime products, the physical and mechanical properties of sand-lime specimens were examined. Four series of specimens were made: 0%, 33%, 66%, and 100% of recycled waste glass (RG) as a sand (FA) replacement. The binder mass did not change (8%). The research results showed that ternary mixtures of lime, sand, and recycled waste glass had a higher compressive strength and lower density compared to the reference specimen. The sand-lime specimen containing 100% (RG) increased the compressive strength by 287% compared to that of the control specimen. The increase in the parameters was proportional to the amount of the replacement in the mixtures.

Keywords: silicate products; brick; sand; lime; glass; microstructure; tobermorite

1. Introduction

Managing wastes and resources is one of the main topics of research developing in the scientific community. Minimizing the necessity for extracting raw materials and maximizing the material life by promoting the reuse and recycling is a program that European and global markets are working on and gradually implementing. The concept behind this program is to turn waste into a valuable resource by designing products that can be easily recovered and reused as a raw material for the same, or a similar, industry [1]. Actions like these are an effective way to avoid pollution, reduce waste emissions, and gradually increase the environmental performance [2].

In Europe, the recycling of glass is one of the most advanced. In some European countries, almost 85% of glass containers—bottles and jars—are made from recycled material. Unfortunately in Poland, both used containers and crushed glass are mostly sent to municipal or illegal landfills. Managing waste, despite many attempts and undertakings, has not been acceptably resolved to this day [3].

To reduce the load on landfills, some of the recycled waste glass is used as a replacement for aggregate in building materials, being an effective recycling alternative [4–8]. Many scientists used waste glass in concrete as a substitute for fine or coarse aggregate in order to improve its features [9–11]. Arezki [12] used glass sand as an alternative for quartz sand in ultra-high-performance concrete to select the optimal glass sand (GS) combination, not only based on the highest packing density, but also based on producing optimal concrete properties (workability and compressive strength). Mixing glass

with Portland cement can, however, cause a decline in concrete strength due to the alkaline reaction, which depends on time [13]. However, the almost zero porosity and non-hygroscopic character of waste glass, as a substitute for natural sand, improves the properties of self-compacting cement mortar, such as increased workability and penetration resistance of chloride ions, reduced drying shrinkage, and improved compressive strength after being exposed to elevated temperatures [14–16]

Using RG in cement materials is not without its downsides. The disadvantage of glass with a smooth surface is the weak bond between RG and the cement paste. Consequently, a concrete or mortar specimen usually shows higher porosities [17,18]. An increased size and volume of voids in the transition zone reduce the mechanical properties, such as compressive and flexural strength [19–21].

Such common failures limit the wider use of RG in cement materials. To promote the use of RG in construction, and particularly in the building materials market, it is essential to seek alternative building materials that do not only include cement, but also recycled aggregate, and other materials, such as tires and other production waste. This is economically advantageous and is part of the Green Public Procurement (GPP) strategy [22]. For some EU countries, the use of construction materials with a percentage of recycled material is mandatory in the construction of public works [23].

Soda-lime glass is rich in silica and can potentially be used in materials that are rich in this raw material, such as in the external and internal walls of buildings. They are sand-lime products. They match the idea of sustainable development [24] and allow for creating a healthy living space for people without causing degradation of the natural environment. The raw materials that build the sand-lime products are quartz sand (over 90%), quenched lime (8%), and water. After forming, the material is subjected to a hydrothermal treatment, i.e., a temperature of around 180–200 °C and a water vapor pressure of about 16 bar. As a result of the reaction between the sand, lime, and water, crystalline phases are created in silicates.

The phase composition in the sand-lime products is a vital factor because it influences the performance of the compressive strength, porosity, and absorption capacity [25]. The products of synthesis include the C-S-H (Calcium Silicate Hydrate) phase, most often found in sand-lime products, as well as tobermorite and xonotlite. According to the literature [14], 11.3 A tobermorite includes a significant amount of water, but at temperatures above 300 °C, it decomposes to 9 A tobermorite. Xonotlite is similar to 11.3 A tobermorite in terms of structure, but it contains 5 times less water than tobermorite and is shaped at a temperature of ≈ 220 °C–380 °C.

The fundamental composition of silicate products is subject to modification. Fang et al. [26] successfully used a sand substitute in the form of low-SiO₂-content copper tailing.

The research conducted for the purposes of this article covered the characteristics of sand-lime products in which the basic source of active silica sand (FA) was substitute with household recycled waste glass (RG) from grinding jars. The goal of the research was to obtain sand-lime bricks with similar or better features and optimize the production costs by reducing energy consumption and decreasing the autoclaving temperature.

2. Materials and Methods

2.1. Lime

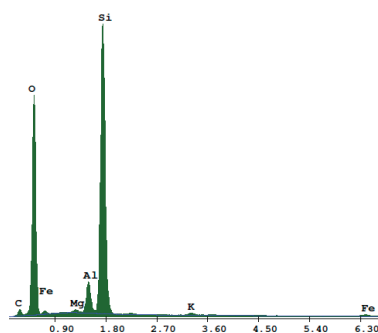
Lime is one of the binders that act as plasticizers. In this case, the binder was derived from the Trzuskawica Production Plant (Nowiny, Poland). Declared values of the basic properties of lime are presented in the Table 1.

Table 1. Summary of the basic properties of highly reactive burnt lime [27].

Functional Features of Burnt Lime	Declared Value
CaO + MgO (%)	≥91
MgO (%)	≤2.0
CO ₂ (%)	≤3.0
SO ₃ (%)	≤0.5
Screening through a 0.09 mm sieve (%)	≥90
Reactivity at 60 °C	≤2.0

2.2. Sand

Quartz sand of natural origin was the raw material, which was the source of silica, and at the same time, acted as an aggregate. It was obtained from deposits exploited at the Silicates Production Plant in Ludynia (Poland). Granulation was tested in accordance with the PN-EN 933-1 [28] standard for control purposes (Figures 1 and 2). The analysis of the glaurometric composition was carried out using the sieve method. Based on this, it was stated that fine quartz sand of natural origin with a maximum grain size of less than 0.5 mm would be used for the test. According to the Unified Soil Classification System, this kind of sand with less than 5% fines is designated with the SW symbol. The mean density was 2.63 g/cm³. The result indicates the average value of two measurements carried out in accordance with PN-EN-1097-6: 2013-11 [29].

**Figure 1.** Grains of quartz sand.**Figure 2.** Energy dispersion spectroscopy (EDS) analysis of the quartz sand.

2.3. Recycled Waste Glass

Transparent white recycled glass waste was obtained from the mechanical grinding of food storage jars. Transparent jars that were washed, dried, and crushed were received from households. The size of the glass particles was adjusted to the size of the quartz sand particles in the reference sand-lime product. The shape of the glass particles (Figure 3) was polyhedral and irregular. Based on the EDS analysis shown in Figure 4, the recycled waste glass had a high content of Si, Na, Mg, Al, Ca, K, S, and C. The mean density was 2.47 g/cm^3 (mean value of six results, determined using a helium pycnometer, manufacturer: Quantachrome Instruments Headquarters, Boynton Beach, Florida).

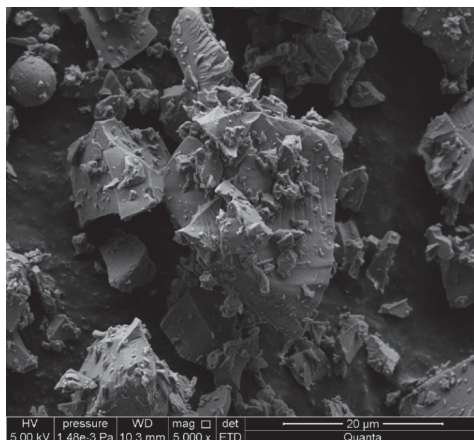


Figure 3. Recycled waste glass.

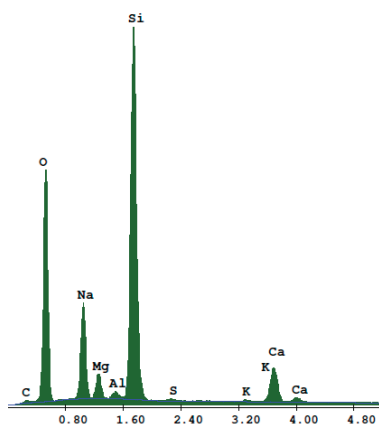


Figure 4. EDS analysis of the recycled waste glass particles.

2.4. Preparing the Sand-Lime Specimens with the Addition of Waste Glass

Proper amounts of raw materials were weighed for particular series (Figure 5, Table 2). Highly reactive burnt lime was mixed with the fine aggregate, which included different mixtures of FA and RG (RG33%, RG66%, RG100%). Water was added to the mixed ingredients of the raw material in a quantity sufficient to put out the lime. The mixture was placed in a sealed glass vessel and dried in the dryer at $65 \text{ }^\circ\text{C}$ for 1 h. After the mixture reached the ambient temperature, water was added again in the amount necessary to obtain a mass with 6–8% moisture. Then, cylindrical specimens with a diameter and height of 25 mm were formed using two-stage and two-sided compression with

inter-venting at a pressure of 10 MPa and 20 MPa. The specimens were autoclaved at 180 °C and at a saturated steam pressure of 1.002 MPa. Heating of the specimens at this temperature lasted 2.5 h, while proper hardening took 8 h. The specimens were taken from the autoclave after 12 h to cool the autoclave down and bring the samples to an ambient temperature of approx. 21 °C.

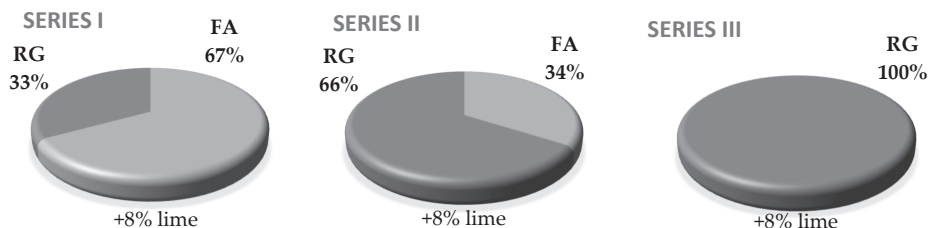


Figure 5. Quantitative summary of the raw material mix in particular series. FA: Sand, RG: Recycled Glass.

Table 2. Quantitative summary of FA and RG content, including the fractions.

Sieve Size	Series I RG33%		Series II RG66%		Series III RG100%	
	FA (g)	RG (g)	FA (g)	RG (g)	FA (g)	RG (g)
0	0.11	0.05	0.05	0.11	0	0.16
0.063	4.56	2.24	2.31	4.49	0	6.8
0.125	57.38	28.26	29.12	56.52	0	85.64
0.25	155.36	76.52	78.84	153.04	0	231.88
0.5	49.45	24.35	25.09	48.71	0	73.8
1.0	1.15	0.57	0.58	1.14	0	1.72

2.5. Testing Methods

The experimental specimens were tested for their physical and mechanical parameters. Mechanical tests were conducted in laboratory conditions at room temperature using a hydraulic press, model Controls 50-C9030 (manufacturer Controls, Warsaw, Poland). According to PN-EN 772-1: 2011 [30], compressive strength was tested 21 days after conducting the autoclaving process; the results are presented as the arithmetic mean of six measurements including the standard deviation.

The water absorption was determined according to PN-EN 772-21:2011 [31], where the volume density was determined through hydrostatic method. The specific density was determined using a helium pycnometer (manufacturer Quantachrome Instruments Headquarters, Boynton Beach, Florida). The density results were determined using the average of four measurements.

Morphological studies were conducted with a scanning electron microscopy (SEM-type Quanta 250 FEG, FEI, Hillsboro, Oregon, USA) using signals gathered by secondary electron (SE) and backscattered (BSE) detectors. The acceleration voltage was 5 kV. The pictures from the scanning areas were enriched by establishing the semi-quantitative chemical composition of the observed phases using X-ray energy dispersion spectroscopy (EDS, manufacturer FEI, Hillsboro, Oregon, USA). The measurements were conducted on flat cut surfaces. Samples were not covered with the metallic layer.

The analytical X-ray diffractometry (XRD) method was used in order to identify the phases appearing in the tested specimens, using an Empyrean PANALYTICAL device (manufacturer Panalytical, Almelo, Netherlands) with a Cu lamp.

3. Results

The following graphs (Figures 6–8) provide the average values of the obtained test results, including the standard deviations. Figure 6 shows the change in compressive strength of the sand-lime products depending on the amount of RG in the specimen. The compressive strength increased with the amount of waste glass in the specimen. The strength for RG100% was found to be more than 7 MPa higher than the reference sample (R). A small increase in strength of 1.4 MPa was observed with RG33% in the specimen.

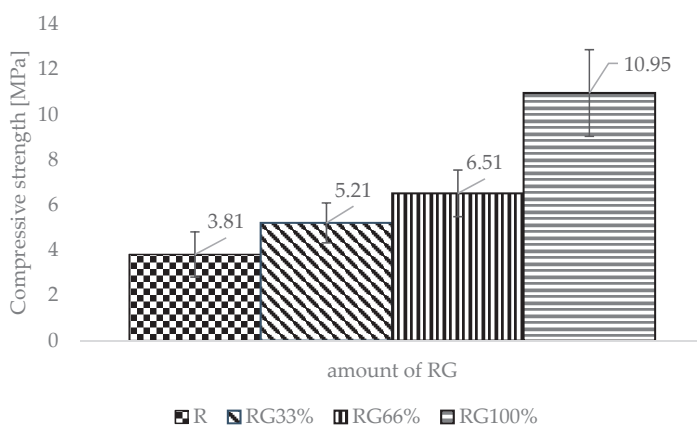


Figure 6. Compressive strength results.

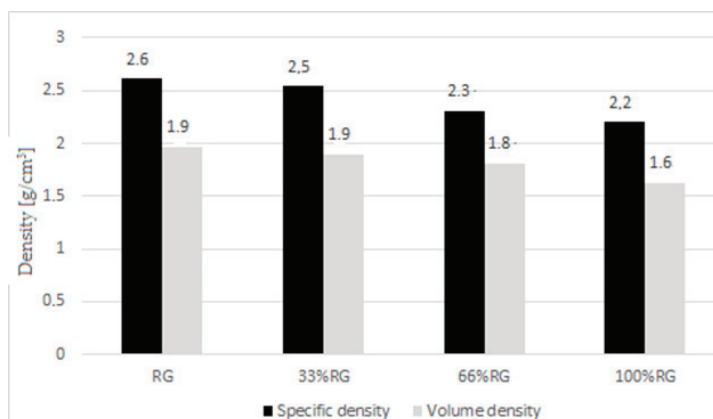


Figure 7. Density results.

The volume density decreased with the increase of the RG content in the specimen (Figure 7). The R specimen had a volume density of 1.9 g/cm^3 . The volume density of RG100% was lower at 1.6 g/cm^3 . The addition of RG in silicates also reduced the specific density of the finished sand-lime products. The R specimen had a value of 2.6 g/cm^3 , while RG100% had a 15.7% lower specific density (2.2 g/cm^3). Therefore, the difference in the density of the silicate samples tested was greater than the difference in aggregates used to make them (sand and white glass amounted to 6.1%). It can therefore be concluded that the density of glass was only one of the factors affecting the decrease in the specific and volume density. It can also be influenced by the construction of the contact zone between the binder and the aggregate, as well as the reaction of the aggregate used with the binder, which may affect the porosity of the silicate. Changes in the binder–aggregate contact zone have also been noticed

in the work Powęzka and Szulej [32]. However, by considering the results of water absorption, it was found that the proportion of open pores increased considerably (Figure 8). The increase of RG content in the specimen reduced the amount of closed intra-grain pores. This was connected with the structure of the glass. Sharp-edged and smooth surfaces, however, made the formation of a compact structure more difficult. Expanding the knowledge on the porosity of finished sand-lime products with the inclusion of RG is the next stage of research.

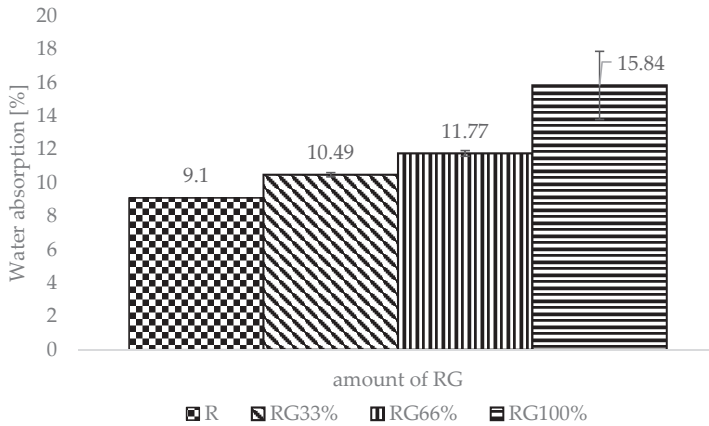


Figure 8. Water absorption results.

Figure 9 compares the diffractograms obtained for silicates R, RG33%, RG66%, and RG100%. For all cases, except for the specimen without sand, the main obtained peaks were quartz and calcite. Portlandite was also discovered in all samples containing recycled waste glass. Its remnant suggests that during the autoclaving, not all the lime was able to react.

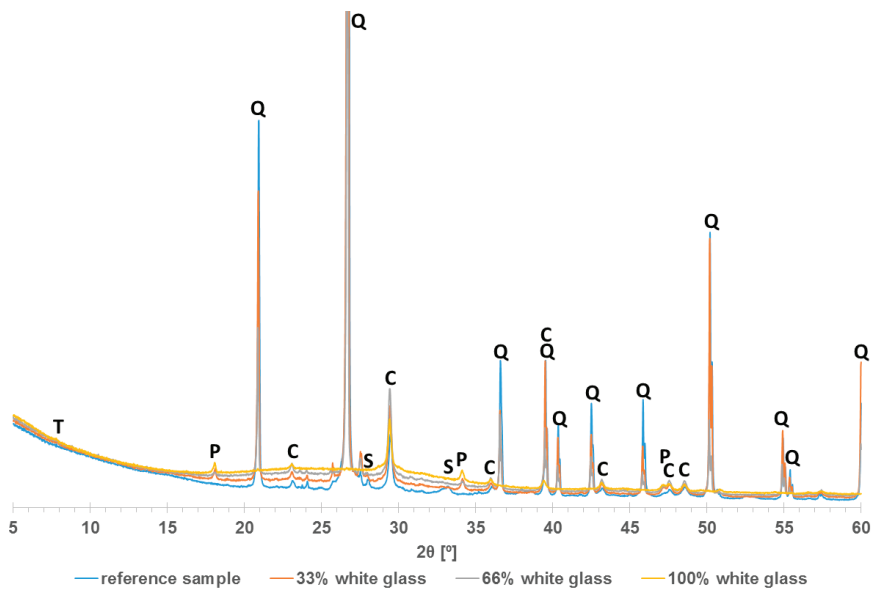


Figure 9. Diffractograms of silicate with different content of recycled waste glass. C—calcite, Q—quartz, P—portlandite, S—spurrite, T—tobermorite.

The intensity of the quartz peaks decreased along with the increase of the glass content in the specimen, until they disappear completely when 100% of the sand was replaced with glass. Simultaneously, as the amount of glass increased, the background diffractograms in the 2θ angle range = 15° – 40° increased as well. This proved the replacement of crystalline quartz present in sand with the amorphous glass.

Figure 10 shows the BSE of the RG100% specimens. Cracked glass particles slowly reacting under hydrothermal conditions were visible. Light particles (1) were unreacted sodium glass grain cores with the main components of silicon, sodium, and oxygen (Figure 11). Darker glass particles (2), with increased calcium content, became separated from the core (Figure 12). The increased content of lime may have resulted from its attachment to the glass during the autoclaving process. Inside the cracks between the glass particles (3), lime-rich glass reacting with products in the presence of lime, were visible (Figure 13).

Figure 14 presents a picture of a RG33% microstructure. At the surface with RG particles (1), there was both a spongy amorphous C-S-H phase (2) and tobermorite crystals (3), similar to thin plates and at unevenly set needles. The tobermorite crystals had different shapes. The result indicates that adding RG did not slow down the formation of phases that are characteristic of silicate products.

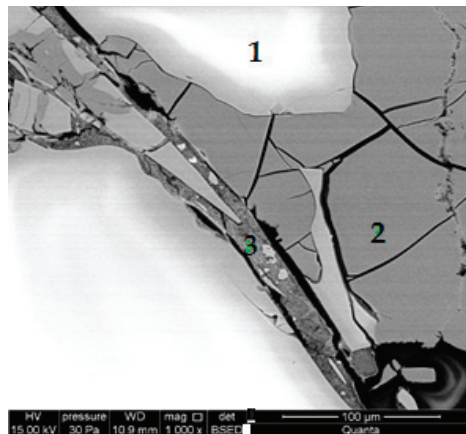


Figure 10. Backscattered electron (BSE) image of a RG100% specimen.

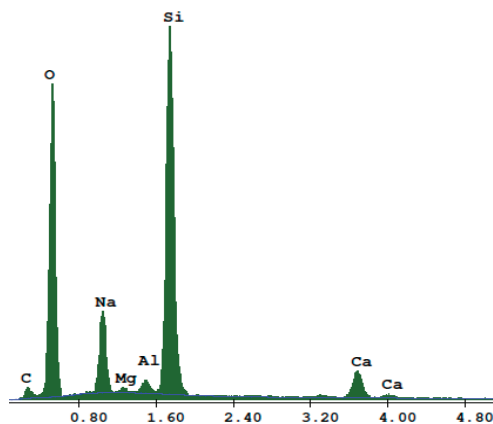


Figure 11. EDS analysis for point 1 in a RG100% sample.

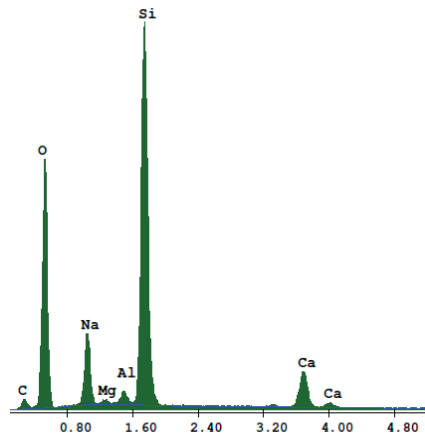


Figure 12. EDS analysis for point 2.

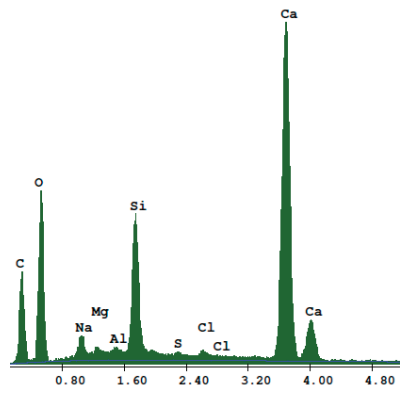


Figure 13. EDS analysis for point 3.

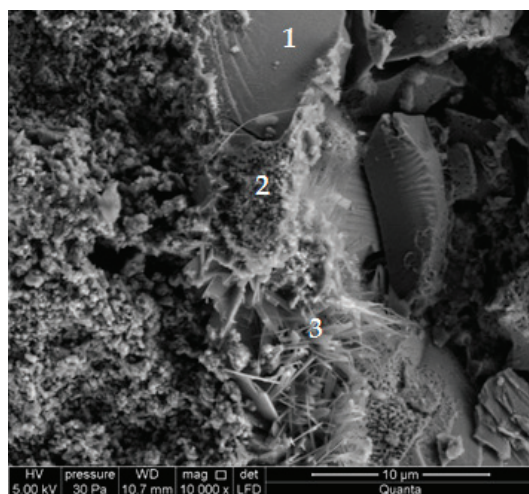


Figure 14. Microstructure of a RG33% specimen.

4. Conclusions

Based on the above results, the following conclusions can be drawn:

- RG can be used as a substitute for quartz sand in sand-lime products. A noteworthy increase in compressive strength compared with the reference specimen indicated that it was possible to completely replace the quartz sand in the silicate mix with the recycled waste aggregate. The larger compressive strength was obtained while reducing the density. This fits the current trends in the development of building materials, which are based on both economic and construction considerations: less material consumption, easier transport, the possibility of building taller buildings, and decreasing the cross-section of structural elements.
- For the strength properties and density, the point of view for the silicates production, completely replacing the quartz sand with waste glass was the most advantageous. This operation allowed for obtaining a silicate with a 287% higher compressive strength with a decrease in density by more than 15% compared to a traditional silicate.
- The increase in the content of RG in sand-lime products caused a significant increase in water absorption.
- Research on the microstructure showed that the exchange of quartz sand for recycled waste glass did not influence the formation of the C-S-H phase and tobermorite in autoclaved silicate products.
- The properties of small silicate samples were analyzed in this research. To better understand the silicates' properties in practice, further research will be carried out on larger volume samples. Comparing the impact of different types of glass on the sand-lime properties is also planned.

Author Contributions: Conceptualization, K.B., P.C., and R.D.; methodology, K.B.; formal analysis, K.B. and P.C.; investigation, K.B. and P.C.; writing—original draft preparation, K.B.; writing—review and editing, K.B.; visualization, K.B.; supervision, P.C. and R.D.; project administration, K.B. All authors have read and agreed to the published version of the manuscript.

Funding: This research received no external funding.

Acknowledgments: The project is supported by the program of the Minister of Science and Higher Education under the name: “Regional Initiative of Excellence” in 2019–2022 project number 025/RID/2018/19 financing amount PLN 12,000,000.



Conflicts of Interest: The authors declare no conflict of interest.

References

1. Rok, B. Rok w zamkniętym obiegu. In *Gospodarka Obiegu Zamkniętego*; Karwacka, M., Ed.; Koalicja na Rzecz Gospodarki Obiegu Zamkniętego Reconomy: Warsaw, Poland, 2017; pp. 10–14.
2. Dales, J.H. *Pollution. Property and Prices: An Essay in Policy-Making and Economics*; Edward Elgar Publishing: Toronto, ON, Canada, 2002.
3. Kuśnierz, A. Glass recycling. *Sci. Works Inst. Ceram. Constr. Mater.* **2010**, *6*, 22–33.
4. Ibrahim, S.; Meawad, A. Assessment of waste packaging glass bottles as supplementary cementitious materials. *Constr. Build. Mater.* **2018**, *182*, 451–458. [CrossRef]
5. Du, H.; Tan, K.H. Properties of high volume glass powder concrete. *Cem. Concr. Compos.* **2017**, *75*, 22–29. [CrossRef]
6. Shao, Y.; Lefort, T.; Moras, S.; Rodriguez, D. Studies on concrete containing ground waste glass. *Cem. Concr. Res.* **2000**, *30*, 91–100. [CrossRef]
7. Meawad, A.; Ibrahim, S. Novel bifunctional dispersing agents from waste PET packaging materials and interaction with cement. *Waste Manag.* **2019**, *85*, 563–573. [CrossRef]
8. Nergis, D.D.B.N.; Abdullah, M.M.A.B.; Sandu, A.V.; Vizureanu, P. XRD and TG-DTA study of new alkali activated materials based on fly ash with sand and glass powder. *Materials* **2020**, *13*, 343. [CrossRef]

9. Ling, T.C.; Poon, C.S. Feasible use of recycled CRT funnel glass as heavyweight fine aggregate in barite concrete. *J. Clean. Prod.* **2012**, *33*, 42–49. [CrossRef]
10. Lee, G.; Poon, C.S.; Wong, Y.L.; Ling, T.C. Effects of recycled fine glass aggregates on the properties of dry-mixed concrete blocks. *Constr. Build. Mater.* **2013**, *38*, 638–643. [CrossRef]
11. Topçu, İ.B.; Canbaz, M. Properties of concrete containing waste glass. *Cem. Concr. Res.* **2004**, *34*, 267–274. [CrossRef]
12. Soliman, N.A.; Arezki, T.H. Using glass sand as an alternative for quartz sand in UHPC. *Constr. Build. Mater.* **2017**, *145*, 243–252. [CrossRef]
13. Mostofinejad, D.; Hosseini, S.M.; Nosouhian, F.; Ozbakkaloglu, T.; Tehrania, B.N. Durability of concrete containing recycled concrete coarse and fine aggregates and milled waste glass in magnesium sulfate environment. *J. Build. Eng.* **2020**. [CrossRef]
14. Ling, T.C.; Poon, C.S. Feasible use of large volumes of GGBS in 100% recycled glass architectural mortar. *Cem. Concr. Compos.* **2014**, *53*, 350–356. [CrossRef]
15. Guo, M.Z.; Maury-Ramirez, A.; Poon, C.S. Versatile photocatalytic functions of self-compacting architectural glass mortars and their inter-relationship. *Mater. Des.* **2015**, *88*, 1260–1268. [CrossRef]
16. Guo, M.Z.; Chen, Z.; Ling, T.C.; Poo, C.S. Effects of recycled glass on properties of architectural mortar before and after exposure to elevated temperatures. *J. Clean. Prod.* **2015**, *101*, 158–164. [CrossRef]
17. Ling, C.; Poon, C.S. Properties of architectural mortar prepared with recycled glass with different particle sizes. *Mater. Des.* **2011**, *32*, 2675–2684. [CrossRef]
18. Ling, T.C.; Poon, C.S. Effects of particle size of treated CRT funnel glass on properties of cement mortar. *Mater. Struct.* **2013**, *46*, 25–34. [CrossRef]
19. Zhao, H.; Poon, C.S.; Ling, T.C. Utilizing recycled cathode ray tube funnel glass sand as river sand replacement in the high-density concrete. *J. Clean. Prod.* **2013**, *51*, 184–190. [CrossRef]
20. Park, S.B.; Lee, B.C.; Kim, J.H. Studies on mechanical properties of concrete containing waste glass aggregate. *Cem. Concr. Res.* **2004**, *34*, 2181–2189. [CrossRef]
21. Ling, T.C.; Poon, C.S. A comparative study on the feasible use of recycled beverage and CRT funnel glass as fine aggregate in cement mortar. *J. Clean. Prod.* **2012**, *29–30*, 46–52. [CrossRef]
22. Uttam, K.; Balfors, B.; Faith-Ell, C. Green public procurement (GPP) of construction and building materials. In *Eco-Efficient Construction and Building Materials*; Pacheco-Torgal, F., Cabeza, L.F., Labrincha, J., de Magalhães, A., Eds.; Woodhead Publishing: Cambridge, UK, 2014; pp. 166–195. [CrossRef]
23. Manzone, F.; Rebaudengo, M.; Lorenzo Zaccaro, V. The Italian Response to Sustainability in Built Environment: The Match between Law and Technical Assessment. In *Proceedings of the Third International Congress on Information and Communication Technology*, London, UK, 27–28 February 2018; Yang, X.-S., Sherratt, S., Dey, N., Joshi, A., Eds.; Springer Nature Singapore Pte Ltd. Publishing: London, UK, 2019. [CrossRef]
24. Stępień, A.; Sitarz, M.; Leśniak, M. A sustainable autoclaved material made of glass sand buildings. *Buildings* **2019**, *9*, 232. [CrossRef]
25. Li, J.; Lv, Y.; Jiao, X.; Sun, P.; Li, J.; Wuri, L.; Zhang, T.C. Electrolytic manganese residue based autoclaved bricks with Ca(OH)₂ and thermal-mechanical activated K-feldspar additions. *Constr. Build. Mater.* **2020**, *230*. [CrossRef]
26. Fang, Y.; Gu, Y.; Kang, Q.; Wen, Q.; Dai, P. Utilization of copper tailing for autoclaved sand–lime brick. *Constr. Build. Mater.* **2011**, *25*, 867–872. [CrossRef]
27. Komisarczyk, K.; Czapik, P.; Komisarczyk, K. Quartz bentonite sandmix in sand-lime products. *Open Eng.* **2019**, *9*, 363–373. [CrossRef]
28. *PN-EN 933-1:2012 Tests for Geometrical Properties of Aggregates—Part 1: Determination of Particle Size Distribution—Sieving Method*; Comite Europeen de Normalisation: Warsaw, Poland, 2012.
29. *PN-EN-1097-6: 2013-11 Tests for Mechanical and Physical Properties of Aggregates—Part 6: Determination of Particle Density and Water Absorption*; Comite Europeen de Normalisation: Warsaw, Poland, 2013.
30. *PN-EN 772-1+A1:2015-10 Methods of Test for Masonry Units—Part 1: Determination of Compressive Strength*; Comite Europeen de Normalisation: Warsaw, Poland, 2015.

31. PN-EN 772-21:2011 *Methods of Test for Masonry Units—Part 21: Determination of Water Absorption of Clay and Calcium Silicate Masonry Units by Cold Water Absorption*; Comite Europeen de Normalisation: Warsaw, Poland, 2011.
32. Powęzka, A.; Szulej, J.; Ogrodnik, P. Effect of high temperatures on the impact strength of concrete based on recycled aggregate made of heat-resistant cullet. *Materials* **2020**, *13*, 465. [CrossRef] [PubMed]



© 2020 by the authors. Licensee MDPI, Basel, Switzerland. This article is an open access article distributed under the terms and conditions of the Creative Commons Attribution (CC BY) license (<http://creativecommons.org/licenses/by/4.0/>).

Article

An Experimental Study on Water Permeability of Architectural Mortar Using Waste Glass as Fine Aggregate

Guoqing Jing ¹, Gang Huang ¹ and Wenjun Zhu ^{2,*}

¹ School of Civil Engineering, Beijing Jiaotong University, Beijing 100044, China

² Shanghai Key Laboratory of Rail Infrastructure Durability and System Safety, Department of Transportation Engineering, Tongji University, Shanghai 201804, China

* Correspondence: xxdhzwj@gmail.com

Received: 5 January 2020; Accepted: 17 February 2020; Published: 2 March 2020

Abstract: This paper investigates the water permeability, consistency and density of architectural mortar with various contents of glass sand as fine aggregate. To reduce the effect of alkali-silica-reaction (ASR), metakaolin (MK) was used as supplementary cementitious material (SCM) instead of a component of white cement. The microstructure of glass sand mortar was visualized by means of scanning electron microscope (SEM) images. The experimental results showed that the permeability of the mortar increased with the glass sand, reaching its maximum at about 60–80% glass sand content. The optimum MK content varied with the content of glass sand, and higher content of MK was required for 60% glass sand. In addition, the consistency and density of mortar had a negative correlation with the increase of glass sand.

Keywords: waste glass; water permeability; metakaolin; architectural mortar; microstructure

1. Introduction

Waste glass is one of the most important components of municipal solid waste (MSW), and has caused a heavy burden on the disposal in many cities all over the world [1]. In 2010, waste glass accounted for 4.6% of MSW in the United States [2]. In 2014, the waste glass produced by the EU reached 18.5 million tons [3]. In 2010, the waste glass produced in Hong Kong was over 370 tons per day, but only 3.3% was recycled and the rest was landfilled [1]. In 2018, the total amount of waste glass in China was about 18.8 million tons, including 9 million tons of flat glass, accounting for 48.9% [4]. On the one hand, the compositions and melting points of different glasses vary significantly, which results in the difficulty for remelting of the mixtures. The main obstacle to recycling was to separate different types of glass [5], as the discarding of waste glass is cheaper [6]. On the other hand, glass is non-degradable when used in landfills, so glass landfill is not a fundamental solution for waste glass. One possible method for the recycling of waste glass is to use it as building materials, as over 70% of the glass is SiO₂ [5].

According to the particle size of broken waste glass, there are generally two recycling applications: glass powder as supplementary cementitious material (SCM) to replace cement, and glass cullet to replace natural aggregates in concrete or mortar [7]. A great deal of research has been done on the properties of concrete and mortar with waste glass. A considerable number of studies have focused on the alkali-silica reaction during cement hydration [7,8]. For instance, in concrete with 100% waste glass aggregate, ground granulated blast furnace slag (GGBS) can be used to partly replace white cement to reduce the alkali-silica reaction and improve the performance of concrete, including the working performance, flexural strength at 28 days, dry shrinkage, ASR risk and acid resistance of concrete [9].

Compared to metakaolin (MK), silica fume (SF), fly ash (FA) and palm oil fuel ash (POFA), glass powder has similar properties to SCM in glass aggregate concrete [8,10,11], but the bending strength, acid resistance, and mechanical performance after heating at 800 °C are even greater. It is possible to produce mortar with better performance by replacing part of cement with glass powder [12,13]. To develop the application of waste glass with different particle sizes, a series of experimental studies using glass cullet and powder in mortar were conducted by Lu et al. [14,15]. It was found that fine glass powder was able to suppress the ASR expansion caused by waste glass aggregate and enhance the strength obviously due to the pozzolanic effect and the ability to fill the microstructure.

The effects of different types of waste glass as fine aggregate on the properties of mortar or concrete have also been investigated recently. Tan et al. [16,17] studied the effects of different colors on the freshness, mechanical and durability properties and alkali-silica reactions of mortars and proposed that the mechanical properties and flowability were reduced for the glass sand as fine aggregate, but the resistance to chloride ion penetration increased. The ASR expansion was promoted for the clear glass sand, but was reduced with the green and brown glass sand. The color separation of waste glass was still considered to be one of the technical challenges to the recycling of waste glass, so waste glass with various colors is more common [18]. Special types of glass have also been studied. Choi et al. [19] investigated the feasibility of recycled heavyweight waste glass as fine aggregate in mortar. With the increase of glass content, the ASR expansion increased gradually due to the permitted value of fly ash or blast furnace slag. Wang [20] focused on liquid crystal display (LCD) glass sand concrete and found that the durability of concrete with 20% glass sand was the best, and was superior to that of the control concrete. Moreover, a slump loss was found in LCD glass sand concrete, which was consistent with the results of Ismail et al. [21]. The slump decreased by 23% and 33% at 10% and 20% glass sand content, respectively. In addition to the above characteristics, water infiltration in mortar or concrete can cause degradation or some aesthetic problems; thereby, the long-term performance and the service life of the structure were decreased [22,23]. However, only a few researchers have paid attention to permeability. For example, Lu et al. [24] studied the effect of recycled concrete aggregate and waste glass aggregate on permeability and found that waste glass aggregate concrete has a lower impermeability. Bisht et al. [25] tested the permeability of waste glass aggregate concrete at various substitution levels (18%, 19%, 20%, 21%, 22%, 23% and 24%). The results showed that with the increase of glass sand content, the permeability decreased.

Moreover, as one of the important indicators of durability of cement-based materials, research on the impermeability of glass sand concrete has not been comprehensive enough. For example, the substitution percentage was not from 0% to 100%, and the reason for permeability change was not clear because of the different gradations of natural sand and glass sand. To study the influence of the waste glass as a fine aggregate on the permeability of the mortar, an experimental investigation was conducted in this paper.

2. Experimental Program

2.1. Materials

2.1.1. Cement (C)

White ordinary Portland cement (P.W 32.5) was used in order to achieve the aesthetics of the mortar. The chemical compositions of the cement are presented in Table 1. The physical and mechanical properties of the cement are presented in Table 2.

Table 1. Chemical compositions of cement and MK.

Chemical Composition (%)	Cement	MK
SiO ₂	15.31	52 ± 2
Al ₂ O ₃	1.67	45 ± 2
Fe ₂ O ₃	0.28	<0.4
CaO	63.83	<0.4
MgO	6.82	<0.2
SO ₃	2.19	-

Table 2. Physical and mechanical properties of cement.

Analysis	Results
Fineness	460 m ² /kg
Normal consistency	26.7%
Initial setting time	150 min
Whiteness	90.2
Compressive strength (1d)	13.3 MPa
Compressive strength (3d)	23.5 MPa
Compressive strength (28d)	36.5 MPa

2.1.2. Metakaolin (MK)

MK is a kind of pozzolanic material, which usually acts as a suppressor agent to mitigate the ASR. The color is white, consistent with that of cement. The chemical compositions of MK are also included in Table 1, with an average particle size of 10 µm.

2.1.3. Aggregates

Both natural sand with ISO standard and the glass sand are applied as fine aggregates, as shown in Figure 1. Figure 2 shows the waste flat glass in China, which accounted for 48.9% of the total amount of waste glass in China in 2018 [4]. The flat glass was crushed into particles with a size smaller than 3 mm by a hammer crusher. The particles were sieved with special gradations of 0–2 mm according to the gradation of ISO standard sand. The gradation curve of aggregate is shown in Figure 3. The fineness modulus of aggregate is 2.1.

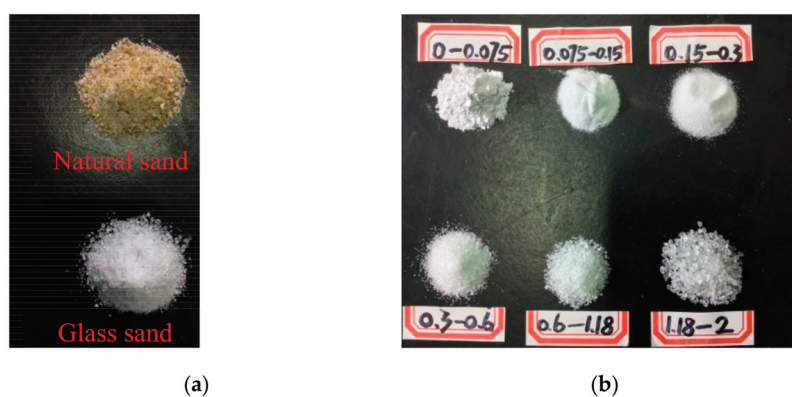


Figure 1. ISO standard sand and glass sand with different particle sizes. (a) Natural sand and glass sand; (b) Glass sand with different particle sizes.



Figure 2. Waste flat glass.

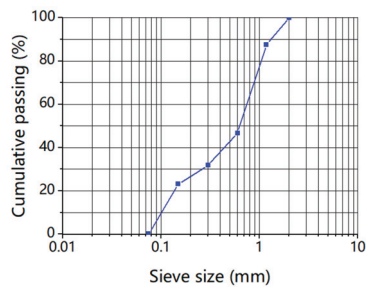


Figure 3. Gradation curve of aggregate.

2.2. Mix Proportions

The glass sand was used as a substitute for natural sand at six proportions (0%, 20%, 40%, 60%, 80%, 100%) by weight. MK accounted for 5%, 10% and 15% of the weight of cementitious materials (C + MK), respectively. The water-to-binder (W/B) ratio in this experiment was 0.4. The superplasticizer with about 0.5% of the weight of cementitious materials was adopted for the mortar to improve the workability of the mortar. Table 3 shows the details of the 20 mix proportions, including the relative weight of cementitious materials. Moreover, the figure without unit in the table is the ratio between materials.

Table 3. Mix proportions of mortar.

Type	C	MK	ISO Sand	GS	Water	SP
G0-M0	1	0	3	0	0.4	0.005
G0-M5	0.95	0.05	3	0	0.4	0.005
G0-M10	0.90	0.10	3	0	0.4	0.005
G0-M15	0.85	0.15	3	0	0.4	0.005
G20-M5	0.95	0.05	2.4	0.6	0.4	0.005
G20-M10	0.90	0.10	2.4	0.6	0.4	0.005
G20-M15	0.85	0.15	2.4	0.6	0.4	0.005
G40-M5	0.95	0.05	1.8	1.2	0.4	0.005
G40-M10	0.90	0.10	1.8	1.2	0.4	0.005
G40-M15	0.85	0.15	1.8	1.2	0.4	0.005
G60-M5	0.95	0.05	1.2	1.8	0.4	0.005
G60-M10	0.90	0.10	1.2	1.8	0.4	0.005
G60-M15	0.85	0.15	1.2	1.8	0.4	0.005
G80-M5	0.95	0.05	0.6	2.4	0.4	0.005
G80-M10	0.90	0.10	0.6	2.4	0.4	0.005
G80-M15	0.85	0.15	0.6	2.4	0.4	0.005
G100-M0	1.00	0	0	3	0.4	0.005
G100-M5	0.95	0.05	0	3	0.4	0.005
G100-M10	0.90	0.10	0	3	0.4	0.005
G100-M15	0.85	0.15	0	3	0.4	0.005

Note: GS: glass sand; SP: superplasticizer.

2.3. Preparation of Specimens

The fresh mortar paste with 20 mix proportions was cast and transferred in a room with a temperature of 20 ± 5 °C for 24 h before being demoulded. The specimens were in the shape of a truncated cone, as shown in Figure 4, with a height of 30 mm, and a diameter of the upper and lower surfaces of 70 and 80 mm, respectively, and were stored in a room with the temperature of 20 ± 2 °C and humidity over 90% for 3, 7, 14, and 28 days, respectively. A glue of paraffin rosin was applied to the side of the specimen. When the mortar paste was mixed, the water permeability test was conducted simultaneously, as well as the consistency and density tests.

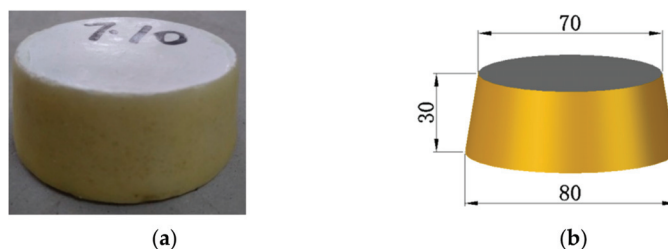


Figure 4. Specimen for water permeability test. (a) Mortar coated with sealing material; (b) Specimen size.

2.4. Experimental Methods

2.4.1. Mortar Consistency Test

Mortar consistency tester is mainly composed of a cone and a container. Prior to the test, the tip of the cone (with a height of 145 mm, diameter of 75 mm, and weight of 300 ± 2 g) was placed in contact with the surface of the fresh paste in the conical container (180 mm \times 150 mm). After the preparation, the fastener was opened to let the cone fall freely. When the cone had sunk in the mortar for 10 seconds, the fastener was closed and the sinking value recorded. All operations were completed within 15 min according to the Chinese national standard JGJ/T70-2009 (standard for test method of performance on building mortar [26]). The average value of the two results was taken as the consistency value. The fresh mortar with high consistency showed better workability.

2.4.2. Mortar Density Test

The density test of fresh mortar was used to study the effect of different glass sand content and MK content on density. According to Chinese national standard JGJ/T70-2009 [26], a steel container (1 L) was used to load fresh mortar. After that, the container filled with fresh mortar was put on a platform vibrator for 10 s. Finally, the density was deduced by the weight of the mortar, and the average value of two repeated tests was taken.

2.4.3. Water Permeability Test

20 different mix proportions were conducted as listed in Tables 3 and 4 at various ages: 3, 7, 14, and 28 days. Eighty groups in total and six specimens per group were evaluated based on the Chinese national standard JGJ/T70-2009 [26].

Table 4. The result of regression analysis.

Age	Z0	B	C	D	Adj-R ²
28d	1.48	35.16	28.54	6.38	0.93
14d	1.08	21.99	32.77	6.12	0.88
7d	0.98	22.65	26.92	4.84	0.89
3d	0.75	22.84	27.69	4.19	0.91

The mortar permeability tester with a capacity of six specimens per group (as shown in Figure 5) was used to investigate the water permeability of the mortar. When the six specimens were installed on the permeability tester, the machine gradually increased the water pressure to an initial value of 0.2 MPa, which was then maintained at 0.2 MPa for 2 h. According to the established program, the hydraulic pressure automatically rose by 0.1 MPa per hour until the upper surface of the third specimen became wet. The time of wetting of the third specimen was considered as the impermeability value of this group.

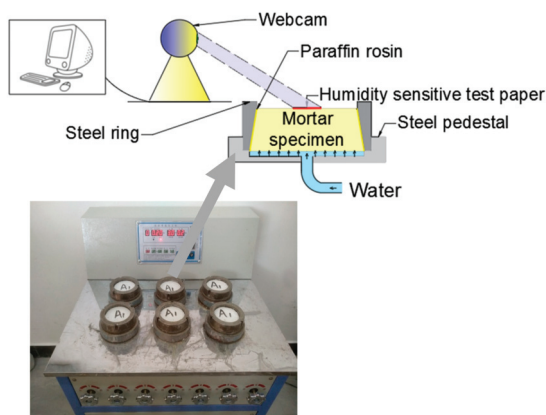


Figure 5. Water permeability test.

An original method was proposed for this experiment during the observation. As shown in Figure 5, a humidity-sensitive test paper attached to the upper surface of the specimen was used to indicate water seepage; when the water had completely penetrated the specimen, test paper would turn from white to red (shown in Figure 6). Moreover, a webcam was adopted in this experiment to monitor the progress of the test online. As a result, the color change of the test paper was detected by the webcam, and the test data could be acquired from the computer.



Figure 6. The color comparison of test paper.

3. Results and Discussions

3.1. Consistency of Mortar

The consistency of fresh mortar with different percentages of glass sand and MK is shown in Figure 7. The consistency was reduced more significantly with the increase of the glass sand. Compared with the mortar without glass sand; the consistency of mortar mixed with 100% glass sand decreased by 55% at the maximum, which was similar to the fluidity and workability of the fresh mortar. Tan et al. [16] pointed out that the fluidity of the fresh mortar decreased with the increase of glass sand, which was consistent with the test results. However, Lu et al. [27] and Ling et al. [28] found that the

addition of glass sand increased the fluidity of mortar. The reason for this was that the particle size of the glass sand used in the two tests was different, 0–2 mm in this experiment and a larger particle size in Lu et al.'s experiment. Compared with the natural sand, the particle size of glass sand had a higher aspect ratio and specific surface area, which increased the frictional resistance between particles and reduced the free water content in mortar.

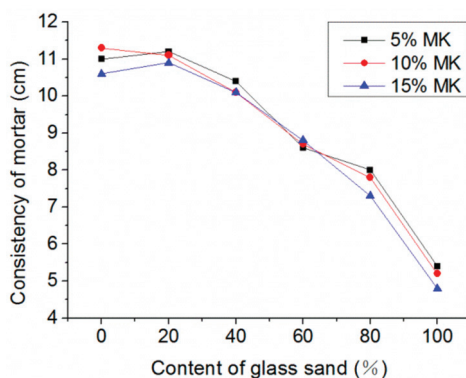


Figure 7. Influence of glass sand on the consistency of fresh mortar.

Additionally, mortar in most groups mixed with 5% MK showed a higher consistency, while the consistency of mortar mixed with 15% MK was the lowest. Courard et al. [29] also reported that 20% MK induced a decrease of consistency of 25%, but only in ordinary mortar. When the content of the glass sand and MK were 100% and 15%, respectively, the minimum mortar consistency of 4.7 cm was reached. Moreover, the consistency decreased from 5.4 cm to 4.7 cm in the group of 100% glass sand content when MK content increased from 5% to 15%.

3.2. The Fresh Density of Mortar

Figure 8 presents the density variation of fresh mortar with glass sand and MK. The density decreased with the addition of glass sand regardless of the different MK contents. The fresh density decreased by 2.7% and 7.9% at the maximum with the replacement percentage of 40% and 100%, respectively. Similarly, Tan et al. [16] reported that the density of mortars with different colors of glass as fine aggregates was decreased. Ismail et al. [21] also found the fresh density of concrete decreased when the glass sand was used instead of the natural fine aggregate. This was due to the angularity of glass sand [30]. The particle sizes of glass aggregates in these tests were different, but were able to reduce the density of mortar, except for special kinds of glass. From the relative position of the three curves, it can be seen that there was no obvious relationship between mortar density and MK content. The regression analysis was used to analyze the relationship between the fresh density of mortar and the percentage of glass sand. A model is proposed as follows:

$$Z = a \times x + b \quad (1)$$

where x is the percentage of glass sand, z is the fresh density of mortar, and a and b are the coefficients obtained by regression analysis. As a consequence of the analysis, $a = 2242.73$, $b = -1.79$. The correlation coefficient R^2 of this model is 0.94, which indicates that the results of the numerical model match well with those of the real test.

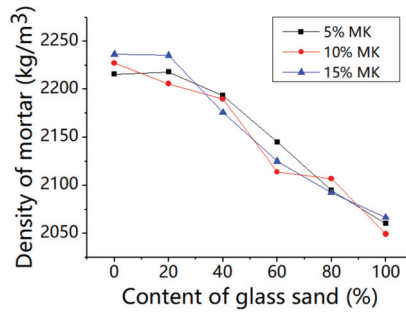


Figure 8. Influence on the density of the fresh mortar.

Figure 9 shows the scatter plot of the experiment and fitting results of the regressed mode (Adj-R² is 0.94, *p*-values of Intercept and *x* variable are 1.48×10^{-32} and 1.08×10^{-11} , respectively). A reduction in density of glass sand mortar, reported by Tan et al. [16], was also included, and the results showed that the predicted model matched well with the experimental results.

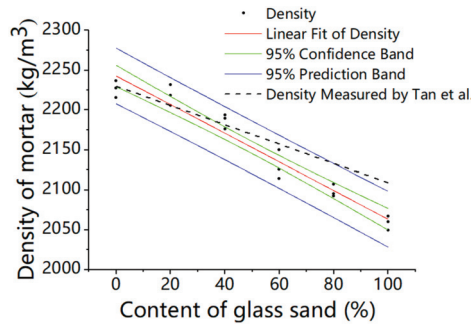


Figure 9. Regressed results of the fresh density.

The consistency of mortar is one of the most important factors affecting the pore structure of mortar, which has a significant effect on the density. The density increases in a linear way with the consistency of fresh mortar, as shown in Figure 10 (*p*-values of Intercept and *x* variable are 2.31×10^{-23} and 6.32×10^{-10} , respectively), which is similar to the fluidity of mortar. When the content of glass was changed in the range from 0% to 100%, the consistency value of the mortar increased by 50%, and the density of the mortar decreased from 2209 to 2065 kg/m³ in this regression model, which is in keeping with Tan’s [16] test results. Therefore, this model is also suitable for similar glass mortar.

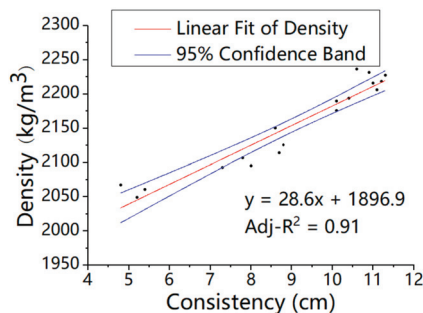


Figure 10. Relationship between the density and consistency of the mortar.

3.3. Water Permeability of the Mortar

3.3.1. The Relationship between Impermeability and the Content of Glass Sand with MK

Figure 11 shows the impermeability of the mortar with the glass and MK, respectively, which decreased sharply and then increased slightly with the content of the glass sand. The impermeability of the mortar with 5%, 10%, and 15% of MK at the age of 28 days reached its minimum value with glass content between 60% and 80%, and compared with 100% natural sand mortar, it was decreased by 94%, 83%, and 73%, respectively. Bisht et al. [25] reported a similar test in concrete, but the content of the glass sand only ranged from 18% to 24%. The reason for this could be the fact that there were more pores in glass sand mortar, including cracks and voids between glass and cement mortar, as the glass sand was more angular than the natural sand [25,30]. In addition, water absorption coefficient varied with the substitution level of glass sand, which characterizes the tendency of a porous material to absorb and transmit water through capillarity [31,32]. This was also supported by the results from SEM images, as shown in Figure 12. Compared with the natural sand in the group of G0-M15, the glass sand in the groups of G60-M5 and G100-M15 had a smoother surface and more edges and angles. Moreover, many cracks occurred in the interface transition zone (ITZ) of the glass sand and paste. Similar findings were found in glass particle mortar and concrete [33,34].

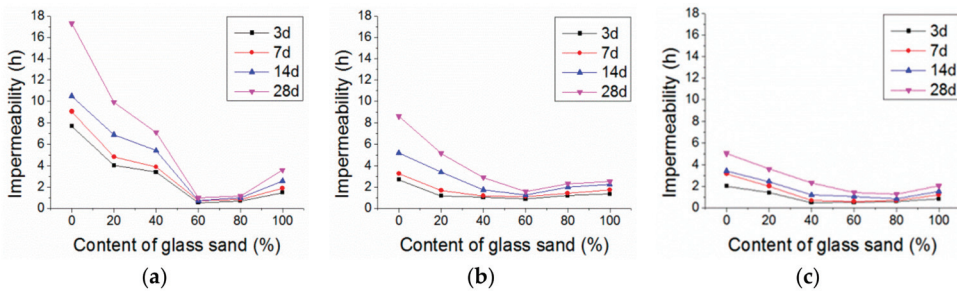


Figure 11. Impermeability with different content of glass sand. (a) 5% MK; (b) 10% MK; (c) 15% MK.

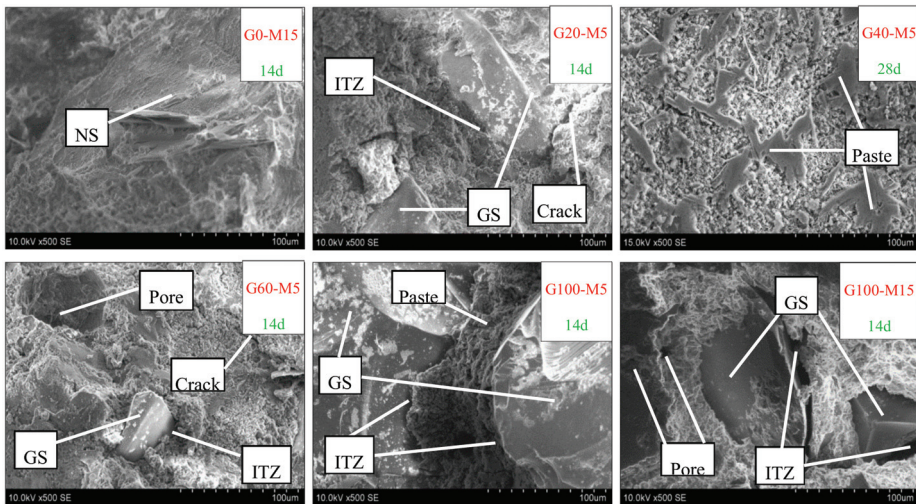


Figure 12. SEM images of mortar (magnification = 500, 14d: 14 days, 28d: 28 days).

Generally, the impermeability of the mortar decreased and then increased slightly, ranging from 12% to 27% in the 28d group. Penacho et al. [30] reported that the water retentivity of glass sand mortar was better because of the larger specific surface due to the cement hydration, which was supported by Neno et al. [35]. Ling et al. [28] reported that the permeable voids of the mortar increased with the content of the glass sand, but that permeable voids decreased when the content of the glass sand was high, which is directly related to the impermeability of mortar and gradually slowed down when the content of the glass sand was over 60%, and even increased with a percentage of 100%. The microstructures of mortars with different mix proportions were observed in this experiment. As shown in Figure 13, the mortar in group G60-M5 had more porous microstructures than other groups. Meanwhile, it could be found in Figure 12 that there were large pores in group G60-M5. Porous micro-structures led to lower impermeability of mortar with 60% and 80% glass sand content.

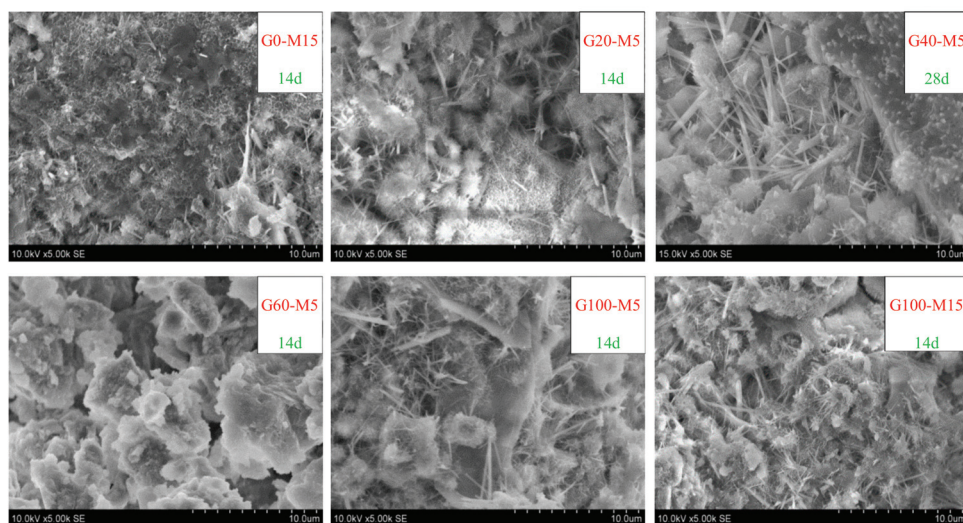


Figure 13. SEM images of mortar (magnification = 5000, 14d: 14days, 28d: 28 days).

In addition, compared with the fine aggregate used in other experiments [25,36], the size of glass sand in this experiment was smaller (0–2 mm). Glass particles with a diameter of 38–300 μm can be used as SCM. When the particle size of the glass sand was larger than 1 mm, a slight pozzolanic activity was also detected [8,37,38]. In this experiment, glass sand with a particle size no larger than 300 μm accounted for 31.8%. The characteristics of the glass sand contributed to better pore structures of mortar, especially when the content was more than 60%. On the other hand, compared with natural sand, the shape of glass sand was more irregular (as shown in Figure 12), and the particle tip of glass sand could fill large pores. Before the 60% content, there were fewer large pores, so the filling effect was not obvious. When the content of glass sand reached 60%, the large pores increased in number, and it became more obvious. Therefore, at 60%, there were the most pores and the weakest impermeability.

3.3.2. Influence of MK on the Water Impermeability

Figure 14 shows the impermeability of the mortars with the variation of MK and glass. When the glass content was 0%, 20%, 60%, and 100%, the optimum additions of MK were 5%, 5%, 10%, and 5% respectively. The optimum MK content increased before 60% glass sand, then decreased with the glass sand content. It was obvious that the optimum MK content varied with the glass sand content.

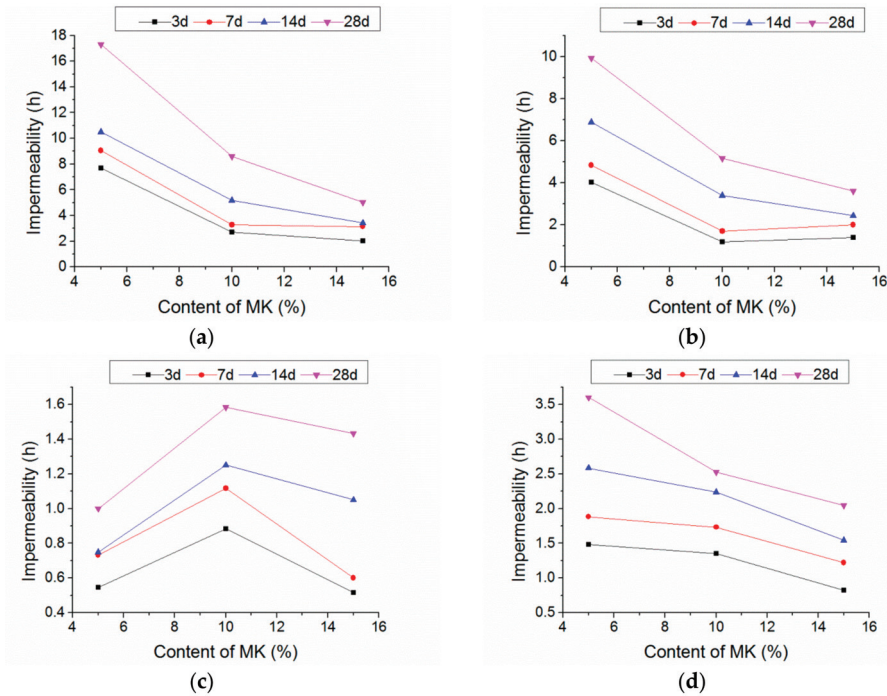


Figure 14. Variation in impermeability with content of MK. (a) Without glass sand; (b) 20% glass sand; (c) 60% glass sand; (d) 100% glass sand.

With the increase of the content of glass sand, the optimum MK content increased from 5% to 10%. This was caused by the “filler effect” [39] of MK as micro-aggregate. To suppress the alkali–aggregate reaction, the size of the MK particles was chosen to be only 10 μm in this test, providing the possibility for the MK particles to fill in the pores of the mortar. The pore structure of the mortar was subsequently improved, along with the compactness and impermeability. However, Ling et al. [28] investigated the effect of MK on the permeable voids of the glass sand mortar, and found that the use of MK as a cementitious material increased the pore structure of the mortar. Compared with the mortar containing 10% MK, permeable voids of 20% and 30% MK mortar increased by 16% and 39%, respectively. This contradiction might be induced by the MK composition, mix proportions and content. The MK could refine the pore size in mortar [39,40]. When the content of the glass sand was low, the pore size of the mortar was small, so the improvement of MK was not obvious. However, when the content of the glass sand reached 60%, the size and the number of pores became greater [30]. As a result, proper content of MK could improve the pore structure and the impermeability of the mortar. When the glass sand content reached 100%, more cement paste was required for the larger specific surface of the glass sand. Meanwhile, the hydration of MK was slower than that of cement. Consequently, the permeability of 100% glass sand mortar decreased with the MK.

3.3.3. Regression Analysis of Impermeability

As illustrated in Figure 11, a similar curve trend can be found at different MK contents. An effective regression model was established as follows:

$$z = Z_0 + B \times \exp\{-x/C - y/D\} \tag{2}$$

where x is the percentage of glass sand, y is the percentage of MK, z is the impermeability value. Z_0 is a coefficient related to curing age. B, C and D are the coefficients to be obtained by regression analysis as shown in Table 4. The values of adj- R^2 were between 0.88 and 0.93.

Figure 15 indicates the corresponding correlations between glass sand content, MK content and impermeability. This model can be used to estimate the impermeability value of similar mortar. Nevertheless, more experimental results and mix proportions are required to improve the application scope of the model.

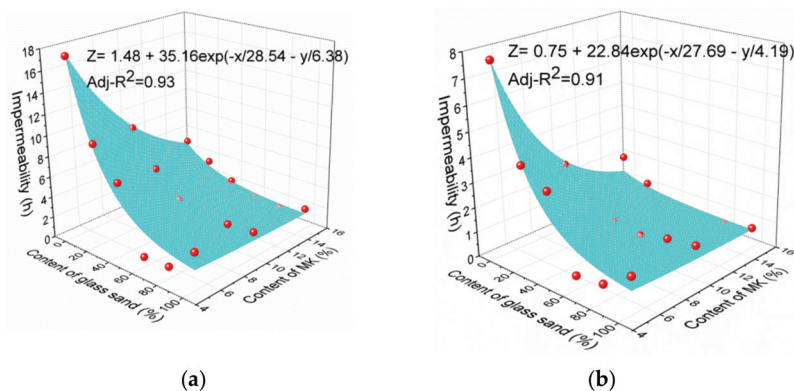


Figure 15. Regression models at different ages. (a) 28 days; (b) 3 days.

4. Conclusions

In this study, the waste glass was used as a fine aggregate instead of natural sand. Meanwhile, MK was used as SCM instead of the white cement with a substitution rate of 5%, 10% and 15%, which could reduce the alkali-silica reaction. The effect of MK and glass content on the properties of mortar was analyzed. The conclusions can be drawn as follows:

1. With the increase of glass and MK content, the consistency of mortar decreased. The glass content increased the trend of the decline. The consistency of mortar mixed with 100% glass sand decreased by 55% at the maximum. The density of fresh mortar decreased by 2.7% and 7.9% with the replacement percentage of 40% and 100%. There is a regression relationship (Adj- $R^2 = 0.91$) between consistency and density in order to predict the consistency.
2. The impermeability of mortar with glass sand decreased. However, it increased slightly when the glass sand reached 100%. The MK could improve the impermeability of glass sand mortar only when the glass sand content was about 60–80%.
3. SEM images showed that there was a crack between matrix and GS because of the smooth surface of glass sand, and more pore structures were found in mortar with 60% glass sand, leading to an increase of water permeability.
4. A regression model of impermeability was established that can predict the impermeability of glass sand mortar varying with glass sand content, MK content, and age.
5. As the addition of glass sand can significantly increase the permeability of mortar, glass sand mortar can be used as pervious material, and the optimum percentage is 60–80%.

Author Contributions: W.Z. conceived the experiments; W.Z. and G.J. designed the experiments; G.H. performed the experiments; W.Z., G.H. and G.J. analyzed the data; W.Z. and G.H. wrote the paper. All authors have read and agreed to the published version of the manuscript.

Funding: The paper was funded by the Natural Science Foundation of China (Grant No. 51578051 and Grant No. 51808033).

Conflicts of Interest: The authors declare no conflict of interest.

References

1. Ling, T.; Poon, C.; Wong, H. Management and recycling of waste glass in concrete products: Current situations in Hong Kong. *Resour. Resour. Conserv. Recycl.* **2013**, *70*, 25–31. [CrossRef]
2. Rashad, A.M. Recycled waste glass as fine aggregate replacement in cementitious materials based on Portland cement. *Constr. Build. Mater.* **2014**, *72*, 340–357. [CrossRef]
3. Silva, R.V.; Brito, J.; Lye, C.Q.; Dhir, R.K. The role of glass waste in the production of ceramic-based products and other applications: A review. *J. Clean. Prod.* **2017**, *167*, 346–364. [CrossRef]
4. MOFCOM. Development Report of Chinese Recycling Industry. 2019. Available online: <http://huanbao.bjx.com.cn/news/20191025/1015853-2.shtml> (accessed on 14 January 2020).
5. Heriyanto; Pahlevani, F.; Sahajwalla, V. From waste glass to building materials—An innovative sustainable solution for waste glass. *J. Clean. Prod.* **2018**, *191*, 192–206. [CrossRef]
6. Meyer, C. The greening of the concrete industry. *Cem. Concr. Compos.* **2009**, *31*, 601–605. [CrossRef]
7. Shi, C.; Zheng, K. A review on the use of waste glasses in the production of cement and concrete. *Resour. Conserv. Recycl.* **2007**, *52*, 234–247. [CrossRef]
8. Mirzahosseini, M.; Riding, K.A. Influence of different particle sizes on reactivity of finely ground glass as supplementary cementitious material (SCM). *Cem. Concr. Compos.* **2015**, *56*, 95–105. [CrossRef]
9. Ling, T.; Poon, C. Feasible use of large volumes of GGBS in 100% recycled glass architectural mortar. *Cem. Concr. Compos.* **2014**, *53*, 350–356. [CrossRef]
10. Federico, L.M.; Chidiac, S.E. Waste glass as a supplementary cementitious material in concrete—Critical review of treatment methods. *Cem. Concr. Compos.* **2009**, *31*, 606–610. [CrossRef]
11. Hossain, M.M.; Karim, M.R.; Hasan, M.; Hossain, M.K.; Zain, M.F.M. Durability of mortar and concrete made up of pozzolans as a partial replacement of cement: A review. *Constr. Build. Mater.* **2016**, *116*, 128–140. [CrossRef]
12. Lu, J.; Zhan, B.; Duan, Z.; Poon, C.S. Improving the performance of architectural mortar containing 100% recycled glass aggregates by using SCMs. *Constr. Build. Mater.* **2017**, *153*, 975–985. [CrossRef]
13. Shi, C.; Wu, Y.; Riefler, C.; Wang, H. Characteristics and pozzolanic reactivity of glass powders. *Cem. Concr. Res.* **2005**, *35*, 987–993. [CrossRef]
14. Lu, J.; Duan, Z.; Poon, C.S. Combined use of waste glass powder and cullet in architectural mortar. *Cem. Concr. Compos.* **2017**, *82*, 34–44. [CrossRef]
15. Lu, J.; Zhan, B.; Duan, Z.; Poon, C.S. Using glass powder to improve the durability of architectural mortar prepared with glass aggregates. *Mater. Des.* **2017**, *135*, 102–111. [CrossRef]
16. Tan, K.H.; Du, H. Use of waste glass as sand in mortar: Part I—Fresh, mechanical and durability properties. *Cem. Concr. Compos.* **2013**, *35*, 109–117. [CrossRef]
17. Du, H.; Tan, K.H. Use of waste glass as sand in mortar: Part II—Alkali-silica reaction and mitigation methods. *Cem. Concr. Compos.* **2013**, *35*, 118–126. [CrossRef]
18. Taha, B.; Nounu, G. Properties of concrete contains mixed colour waste recycled glass as sand and cement replacement. *Constr. Build. Mater.* **2008**, *22*, 713–720. [CrossRef]
19. Choi, S.Y.; Choi, Y.S.; Yang, E.I. Characteristics of volume change and heavy metal leaching in mortar specimens recycled heavyweight waste glass as fine aggregate. *Constr. Build. Mater.* **2018**, *165*, 424–433. [CrossRef]
20. Wang, H. A study of the effects of LCD glass sand on the properties of concrete. *Waste Manag.* **2009**, *29*, 335–341. [CrossRef]
21. Ismail, Z.Z.; AL-Hashmi, E.A. Recycling of waste glass as a partial replacement for fine aggregate in concrete. *Waste Manag.* **2009**, *29*, 655–659. [CrossRef]
22. Muhammad, N.Z.; Keyvanfar, A.; Majid, M.Z.A.; Shafaghat, A.; Mirza, J. Waterproof performance of concrete: A critical review on implemented approaches. *Constr. Build. Mater.* **2015**, *101*, 80–90. [CrossRef]
23. Basheer, L.; Kropp, J.; Cleland, D.J. Assessment of the durability of concrete from its permeation properties: A review. *Constr. Build. Mater.* **2001**, *15*, 93–103. [CrossRef]
24. Lu, J.; Yan, X.; He, P.P.; Poon, C. Sustainable design of pervious concrete using waste glass and recycled concrete aggregate. *J. Clean. Prod.* **2019**, *234*, 1102–1112. [CrossRef]
25. Bisht, K.; Ramana, P.V. Sustainable production of concrete containing discarded beverage glass as fine aggregate. *Constr. Build. Mater.* **2018**, *177*, 116–124. [CrossRef]

26. China Architecture & Building. *Standard for Test Method of Performance on Building Mortar*; China Architecture & Building Press: Beijing, China, 2009.
27. Lu, J.; Poon, C.S. Use of waste glass in alkali activated cement mortar. *Constr. Build. Mater.* **2018**, *160*, 399–407. [CrossRef]
28. Ling, T.; Poon, C.; Kou, S. Feasibility of using recycled glass in architectural cement mortars. *Cem. Concr. Compos.* **2011**, *33*, 848–854. [CrossRef]
29. Courard, L.; Darimont, A.; Schouterden, M.; Ferauche, F.; Willem, X.; Degeimbre, R. Durability of mortars modified with metakaolin. *Cem. Concr. Res.* **2003**, *33*, 1473–1479. [CrossRef]
30. Penacho, P.; Brito, J.D.; Rosário Veiga, M. Physico-mechanical and performance characterization of mortars incorporating fine glass waste aggregate. *Cem. Concr. Compos.* **2014**, *50*, 47–59. [CrossRef]
31. Candamano, S.; De Luca, P.; Frontera, P.; Crea, F. Production of Geopolymeric Mortars Containing Forest Biomass Ash as Partial Replacement of Metakaolin. *Environments* **2017**, *4*, 74. [CrossRef]
32. De Luca, P.; De Luca, P.; Candamano, S.; Macario, A.; Crea, F.; Nagy, J. Preparation and Characterization of Plasters with Photodegradative Action. *Buildings* **2018**, *8*, 122. [CrossRef]
33. Lu, J.; Poon, C.S. Improvement of early-age properties for glass-cement mortar by adding nanosilica. *Cem. Concr. Compos.* **2018**, *89*, 18–30. [CrossRef]
34. Du, H.; Tan, K.H. Properties of high volume glass powder concrete. *Cem. Concr. Compos.* **2017**, *75*, 22–29. [CrossRef]
35. Neno, C.; Brito, J.D.; Veiga, R. Using fine recycled concrete aggregate for mortar production. *Mater. Res.* **2013**, *17*, 168–177. [CrossRef]
36. Hui, Z.; Poon, C.S.; Ling, T.C. Properties of mortar prepared with recycled cathode ray tube funnel glass sand at different mineral admixture. *Constr. Build. Mater.* **2013**, *40*, 951–960. [CrossRef]
37. Idir, R.; Cyr, M.; Tagnit-Hamou, A. Pozzolanic properties of fine and coarse color-mixed glass cullet. *Cem. Concr. Compos.* **2011**, *33*, 19–29. [CrossRef]
38. Shao, Y.X.; Lefort, T.; Moras, S.; Rodriguez, D. Studies on concrete containing ground waste glass. *Cem. Concr. Res.* **2000**, *30*, 91–100. [CrossRef]
39. Siddique, R.; Klaus, J. Influence of metakaolin on the properties of mortar and concrete: A review. *Appl. Clay Sci.* **2009**, *43*, 392–400. [CrossRef]
40. Harbi, R.; Derabla, R.; Nafa, Z. Improvement of the properties of a mortar with 5% of kaolin fillers in sand combined with metakaolin, brick waste and glass powder in cement. *Constr. Build. Mater.* **2017**, *152*, 632–641. [CrossRef]



© 2020 by the authors. Licensee MDPI, Basel, Switzerland. This article is an open access article distributed under the terms and conditions of the Creative Commons Attribution (CC BY) license (<http://creativecommons.org/licenses/by/4.0/>).

Article

Using Eco-Friendly Recycled Powder from CDW to Prepare Strain Hardening Cementitious Composites (SHCC) and Properties Determination

Wan Wang ^{1,3}, Huixia Wu ^{2,3}, Zhiming Ma ^{2,*} and Ruixue Wu ²

¹ Department of Civil Engineering, Tongji Zhejiang College, Jiaxing 314051, China; wangwan@tongji.edu.cn

² College of civil science and engineering, Yangzhou University. Yangzhou 225127, China; dyyang_sub@163.com (H.W.); Ruixue_WuQT@163.com (R.W.)

³ Department of Structural Engineering, Tongji University, Shanghai 200092, China

* Correspondence: 1410218@tongji.edu.cn

Received: 7 February 2020; Accepted: 29 February 2020; Published: 4 March 2020

Abstract: Using eco-friendly recycled brick powder (RBP) derived from waste brick to prepare strain hardening cementitious composites (SHCC) provides a new way of recycling the construction and demolition waste (CDW), and the dosage of cement in SHCC can be decreased. This paper investigated the micro-properties and mechanical properties of SHCC containing RBP by a series of experiments. The results showed that RBP had typical characteristics of supplementary cementitious material (SCM). The addition of RBP increased the SiO₂ content and decreased the hydration products in cementitious materials; in this case, the mechanical properties of mortar decreased with increasing RBP replacements, and a linear relationship was observed between them. It was noticed that the adverse effect of RBP on the mechanical properties decreased with increasing PVA fiber content in mortar. For SHCC containing various RBP replacements, the ultimate load increased, and the ultimate displacement decreased with increasing curing days. When using RBP to replace cement by weight, the ultimate displacement increased with the addition of RBP. Meanwhile, there was no significant reduction in the ultimate load of SHCC. When using RBP to replace fly ash (FA) by weight, the incorporation of RBP decreased the ultimate displacement of SHCC, whereas the ultimate load was improved. For example, the ultimate load and displacement of SHCC with 54%RBP were 17.6% higher and 16.4% lower, respectively, than those of SHCC with 54% FA.

Keywords: strain hardening cementitious composites (SHCC); construction and demolition waste (CDW); recycled brick powder (RBP); properties determination

1. Introduction

The rapid onset of global urbanization has resulted in a massive number of construction and demolition wastes (CDW) [1]. In China, the output of CDW reached approximately 1.8 billion tons per year, and it will be kept at a high level in the next few years [2]. Because of CDW containing some hazardous substances, the traditional disposal of CDW by dumping has inevitably resulted in environmental pollution, such as soil and water pollution [3,4]. Therefore, disposing such CDW in effective and eco-friendly ways has become an important issue around the world [5]. In recent years, recycling technologies for CDW are developed, and the waste concrete and brick are recycled into recycled aggregate and used to prepare recycled aggregate concrete [6,7]. The properties of recycled aggregate from waste concrete are similar to those of natural aggregate, the recycled aggregate has been widely used in the construction engineering, and the high-quality recycled aggregate can also be employed in the preparation of high performance recycled concrete [8,9], self-compacting recycled concrete [10], and structural recycled concrete [11]. Moreover, the improvement technology

for the recycled concrete aggregate and prepared concrete has also developed in recent years, whereby excellent properties can be obtained after enhancement treatment [12,13]. Being different from the recycled concrete aggregate, the utilization of recycled brick aggregate in construction engineering is very scarce because of recycled brick aggregate containing high porosity and water absorption; in this case, the recycling rate of waste brick was much lower than that of waste concrete in CDW [14].

Forcing on the challenge of recycling the waste brick in CDW, some scholars proposed using waste bricks to prepare recycled brick powder that can be used as supplementary cementitious material (SCM) in the preparation of cement and concrete products, which was a sustainable cement-based material [15,16]. Some investigations have been conducted to study the properties of RBP and prepared concrete. For example, findings have been reported that the main compositions of RBP are similar to those of fly ash; attributed to RBP containing high content of amorphous phase and vitreous phase, the high fineness RBP has a satisfied pozzolanic activity [17,18]. Incorporating an appropriate content of high activity RBP has less impact on the mechanical properties of prepared concrete, and even a slight increase in the mechanical properties can be observed with the addition of high fineness RBP. However, the incorporation of high-volume RBP significantly decreases the mechanical properties [19]. For example, Olofinnade et al. [20] found that the compressive strength and tensile strength of concrete with 10% RBP were respectively 32% and 2% higher than those of the plain concrete after 90 d curing. In addition, the RBP concrete has a better durability performance than the plain concrete, as Ma et al. [21] and Ge et al. [22,23] found that the RBP concrete has better water penetration and sulfate attack resistance than the plain concrete. Therefore, using RBP as SCM to prepare concrete is appropriate, and the RBP is sustainably recycled material.

To address the brittleness issue on the ordinary concrete materials, the strain hardening cementitious composites (SHCC) have been developed due to the fiber-bridging action of multiple cracking behaviors and ultra-high ductility [24,25]. Investigations reported that the SHCC possessed excellent mechanical properties and durability performance [26–28]. However, it is noticed that more than half of SHCC component, according to the mix proportion by weight, is the cement and the SCM of fly ash (FA) or silica fume (SF) [29,30]; in this case, the preparation cost is increased, and SHCC is not eco-friendly due to the addition of massive cement. Thus, an eco-friendly and sustainable SHCC is urged to be developed. Considering that the RBP could be used as the SCM, one can expect that the RBP could be further used in the preparation of SHCC. The utilization of RBP in SHCC not only decreases the dosage of cement and FA in SHCC, but also promotes the recycling rate of the waste brick in CDW, which is eco-friendlier and more sustainable.

Based on the introductions above, this paper was developed to investigate the properties of SHCC containing RBP. The RBP was respectively used to replace the cement and FA in SHCC by weight, and the micro-properties of cementitious materials and the mechanical properties of SHCC with RBP were determined. The authors hope the findings in this paper are helpful to further research on the SHCC and CDW recycling.

2. Materials and Experimental Details

2.1. Preparation of the RBP Derived from the CDW

Figure 1 shows the flow of using waste bricks to prepare high fineness RBP. The waste bricks were first collected from the CDW by machine or manual sorting, and then, they were crushed into the recycled brick aggregates with a maximum size of 10 mm by a jaw crusher (SANME, Shanghai, China). Subsequently, the recycled brick aggregates were ground to low fineness RBP with a maximum size of 150 μm by a ball grinding mill (SANME, Shanghai, China), and the obtained RBP were further ground to high fineness RBP with a maximum size of 45 μm by a planetary ball mill (Jingxin, Shanghai, China). The high fineness RBP was used in the preparation of SHCC. Furthermore, Figure 1 shows the test flow in this paper. The effects of fiber content and RBP replacements on the properties of cementitious materials were considered in the experiment design. The micro properties of cementitious materials

containing RBP were determined to reveal the feasibility of using RBP as SCM in the SHCC preparation, and the compressive and flexural strength were tested to investigate the mechanical properties of SHCC with RBP.

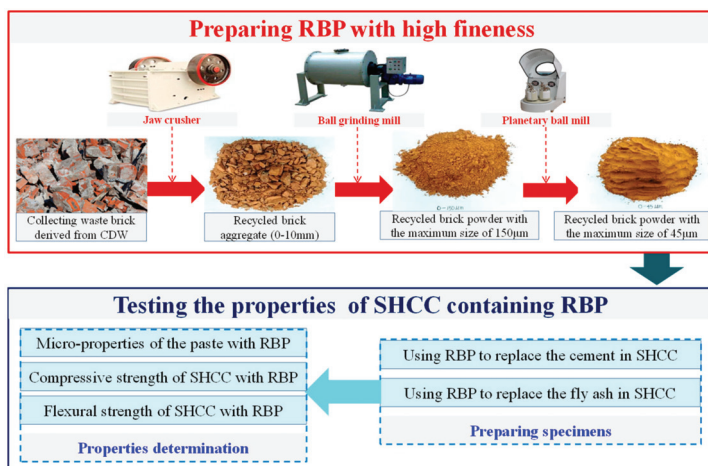


Figure 1. Flow diagram of using the waste bricks in CDW to prepare RBP.

2.2. Mix Proportion and Specimens Preparation

Table 1 gives the mix proportion of the mortar and SHCC with RBP. The mortar specimens were prepared, to quantify the effects of RBP and fiber on the properties of cementitious materials. The mix proportion of SHCC with RBP was proposed according to that of SHCC with FA by the previous studies; the total content of binding materials was 1200 g, and the content of water, sand and PVA fiber is respectively 395 g, 550 g, and 26 g [31–34]. On the one side, the RBP was used to replace the cement in SHCC by weight, and the replacement ratios (weight) were 0% (0 g), 18% (216 g), 36% (432 g), and 54% (650 g), which aimed to investigate the effects of RBP content on the properties of SHCC, such as, the sample titled SHCC-54%RBP represents that 54% of cement in SHCC was replaced by the same weight of RBP. On the other side, the RBP was used to replace the FA by weight, which aimed to investigate the potential of using RBP to replace the FA in the preparation of SHCC; for example, the sample SHCC-27%RBP + 27%FA represented that the RBP and FA replacements are both 27%.

Table 1. Mix proportion of the mortar and SHCC with RBP (g).

Sample	Cement	RBP	FA (Class I)	Water	Sand	PVA Fiber
Mortar-0%RBP	1200	0				
Mortar-18%RBP	984	216				
Mortar-36%RBP	768	432	0	395	550	0
Mortar-54%RBP	550	650				
Mortar-0 F						0
Mortar-6.5 F						6.5
Mortar-13 F	550	650	0	395	550	13
Mortar-26 F						26
SHCC-0%RBP	1200	0				
SHCC-18%RBP	984	216				
SHCC-36%RBP	768	432	0	395	550	26
SHCC-54%RBP	550	650				
SHCC-27%RBP + 27%FA	550	325	325	395	550	26
SHCC-54%FA	550	0	650			

It is noticed that the mix proportion of the mortar is corresponding to the mix proportion of SHCC in this paper, and the mortar is also titled as the SHCC without PVA fiber; in this case, the effect of PVA fiber content on the mechanical properties of SHCC can be well quantified. Besides, the pozzolanic activity of RBP is also determined according to British standard BS EN 450-1 and Chinese standard GB/T 1596-2017, to prove the feasibility of using RBP as SCM in SHCC. The amount of cement, RBP, water and sand in this mix proportion is respectively 315, 135, 225 and 1350 kg/m³, and the pozzolanic activity index of RBP is determined as the value of 89.6% by a compressive strength test. Therefore, the high fineness RBP used in this study has high pozzolanic activity.

Referring to the related references on the determination of SHCC properties, the sample size was 40 × 40 × 160 mm, and a three-point bending test was conducted to determine the flexural strength and ductility of SHCC with RBP [35,36]. All the specimens were first prepared according to the mix proportion shown in Table 1, and the specimens after 24 h hardening were placed in the standard curing room (T = 20 ± 2 °C, RH ≥ 95%) for 3 d, 14 d, and 28 d. When reaching the targeted curing days, the mechanical properties of the mortar and SHCC samples were determined.

2.3. Micro Properties and Mechanical Properties Determination

The paste with RBP was used in testing the micro properties of cementitious materials. The test of SEM (scanning electron microscope, Hitachi, Tokyo, Japan) was applied to show the micro-structure of cementitious materials, and the elemental map was further presented to quantify the elemental composition of cementitious materials; moreover, the XRD (X-ray diffraction, Bruker AXS, Karlsruhe, Germany) test and TG (thermogravimetric, PerkinElmer, Waltham, MA, USA) test were conducted to reveal the effect of RBP incorporation on the hydration products of cementitious materials [37,38]. The mortar and SHCC samples were used to test the mechanical properties, including the compressive strength and flexural strength, and the mechanical test was conducted according to Chinese standard GB50081 (2019) and American standard ASTM-C78 (2005). The applied load in the bending test was controlled by the displacement, and the loading rate was kept at 0.05 mm/min until the sample failure. The applied force and displacement were simultaneously obtained by the testing machine (MTS, Eden Prairie, MN, USA); and in this case, the force-displacement curves can be obtained, and the ultimate force and ultimate displacement were used in this paper to evaluate the mechanical properties of SHCC containing RBP.

3. Results and Discussion

3.1. Micro-Properties of the Cementitious Materials Containing RBP

This section aims to investigate the feasibility of using RBP as SCM in SHCC preparation. The high fineness powder frequently results in a high activity, and the high fineness powder is helpful to promote the micro-aggregate filling effect of cementitious materials [39]. Considering that the RBP is derived from the waste brick and no hydrated substance contained in it, the fineness of RBP should be higher than that of the cement and FA, which is beneficial to improve the activity of RBP when using RBP as SCM to replace the cement or FA in SHCC. Figure 2a shows the particle size distribution of cement, FA and RBP used in this paper, and the results show that their median diameter (D₅₀) is approximately 19 μm, 15 μm, and 11.5 μm. Figure 2b shows the XRD results, whereby the SiO₂ content in RBP is much higher than that in cement and FA, and there are no hydrated compounds (such as CaO, Ca(OH)₂) in RBP. Attributed to the SiO₂ being the main component that takes part in the pozzolanic reaction of cementitious materials, the high fineness RBP can be used as the SCM in the cementitious materials [40]. Figure 2b further shows the SEM images of RBP, and an irregular micro-structure can be observed.

Figure 3 shows the micro-structure of the paste with RBP. Most C-S-H can be observed when the RBP replacement is 0%, whereas the content of C-S-H and Ca(OH)₂ decrease with increasing RBP replacement. The content of ettringite and RBP micro-particle increases with the increase of RBP content, and the RBP micro-particle connects with the C-S-H in the paste. Attributed to the dilution

effect and nucleation of RBP, the addition of RBP promotes the hydration reaction rate of cementitious materials. However, the RBP has higher SiO₂ content and lower CaO content than the cement, and thus, incorporating RBP leads to a reduction in the hydration products when using RBP to partially replace the cement in the paste, and a similar phenomenon is obtained by previous studies [41,42]. When the RBP replacement is 18%, there is no obvious difference for the micro-structure of Paste-0%RBP and Paste-18%RBP, and this may be because the micro-aggregate filling effect of RBP filled the pores and meanwhile the reduction of hydration products in cementitious materials is not obvious. However, with a significant reduction of the hydration products in cementitious materials, the micro-structure of paste-54%RBP is looser than that of the paste-0%RBP, which indicates that the addition of high-volume RBP is adverse to the properties of prepared mortar and concrete.

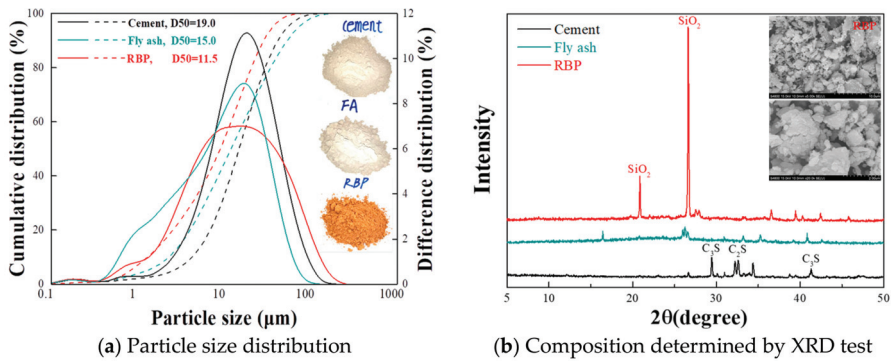


Figure 2. Properties of CBP used in the preparation of SHCC. (a) Particle size distribution; (b) Composition determined by XRD test.

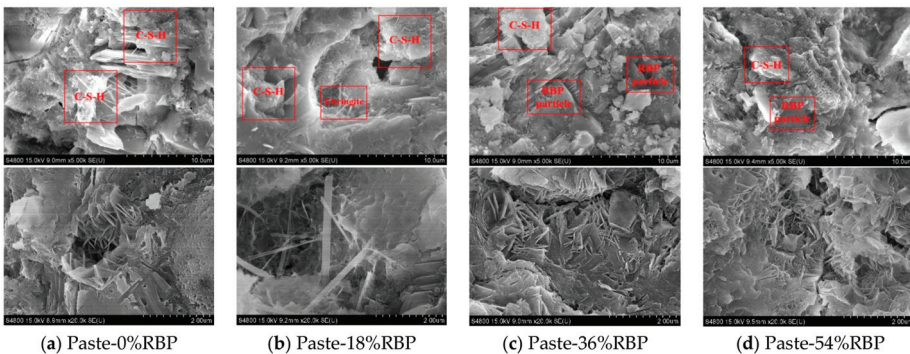


Figure 3. SEM images of paste with various replacements of RBP. (a) Paste-0%RBP; (b) Paste-18%RBP; (c) Paste-36%RBP; (d) Paste-54%RBP.

Figure 4 shows the elemental maps of the paste with various RPB replacements. When the RBP replacement ratios are below 36%, the calcium content is higher than the silicon, and the calcium content decreases, and the silicon content increases with the increase of RBP replacement ratios. In particular, the calcium content is lower than the silicon when the RBP replacement ratios are 54%. This may be because the RBP contains higher silicon content and lower calcium content than the cement, the silicon content increases, and the calcium content decreases with the addition of RBP in the paste. The appropriate calcium-silicate ratio is beneficial to the properties of cementitious materials, whereas the excessively low of calcium-silicate ratio results in the reduction of hydration products and is adverse to the properties of cementitious materials [43,44].

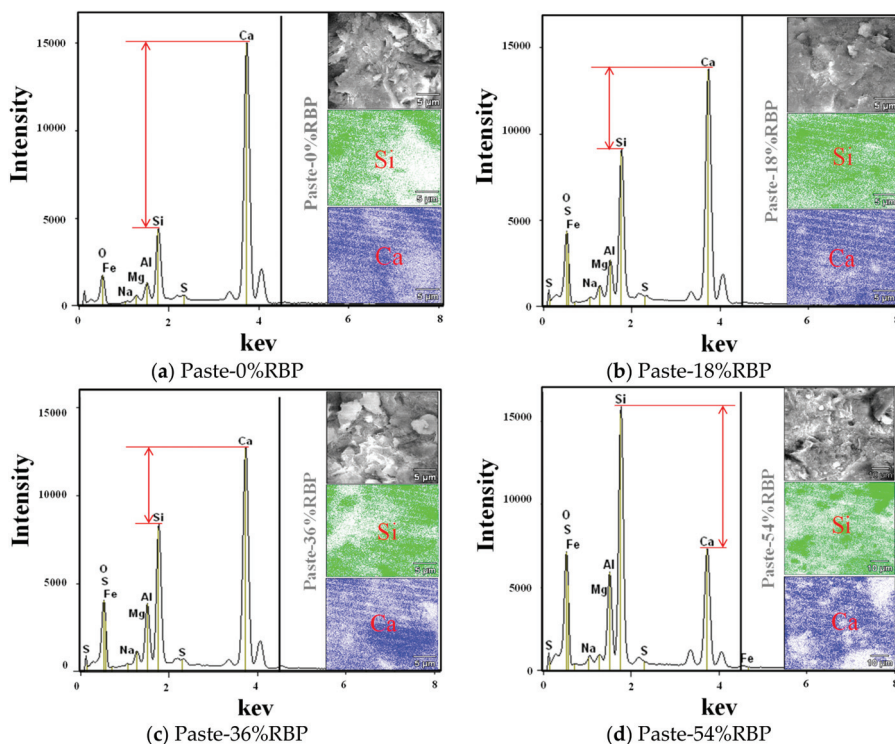


Figure 4. Elemental maps of the paste with various RBP replacements. (a) Paste-0%RBP; (b) Paste-18%RBP; (c) Paste-36%RBP; (d) Paste-54%RBP.

Figure 5 shows the XRD results of the paste containing RBP. The incorporation of RP increases the content of SiO_2 in the paste, while the content of $\text{Ca}(\text{OH})_2$ and CaCO_3 decreases with the addition of RBP. The $\text{Ca}(\text{OH})_2$ and CaCO_3 are the main hydration products of cementitious materials; thus, incorporating RBP reduces the hydration products of cementitious materials [41,45]. Attributed to RBP containing higher SiO_2 content and lower CaO content compared with the cement, the addition of RBP increases the SiO_2 content when using the RBP to replace the cement by weight in the paste. The micro-particle SiO_2 is the main compound that takes part in the pozzolanic reaction; thus, incorporating RBP promotes the pozzolanic reaction of cementitious materials, and the high fineness possesses an excellent micro-aggregate filling effect. However, the incorporation of RBP reduced the hydration products in the paste, which is adverse to the properties of cementitious materials. Therefore, the positive and negative effects of RBP on the micro-properties should be both considered in the performance analysis of SHCC.

Figure 6 shows the DTG (derivative thermogravimetric analysis) results of the paste with RBP after 28 d curing. Three peaks around 100°C , 450°C and 700°C can be seen from the DTG curves. The first peak presents the dehydration of C-S-H gel, and incorporating RBP reduces the content of C-S-H gel in paste, which further proved that the incorporation of RBP decreases the hydration reaction of cementitious materials. The content of $\text{Ca}(\text{OH})_2$ and CaCO_3 in the Paste-54%RBP is much lower than that in the Paste-0%, and a similar conclusion can also be obtained from Figure 5. As shown in Figures 2–5, the micro-properties results of the RBP and prepared paste highlight that the high fineness RBP can be used as the SCM in the preparation of cement products. One can expect that the RBP can also be used in the preparation of SHCC, and the mechanical properties of SHCC containing RBP are discussed in the following sections.

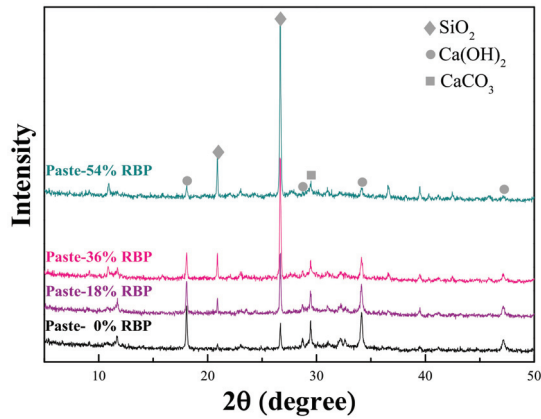


Figure 5. Compound composition of paste with various replacement of RBP by XRD test.

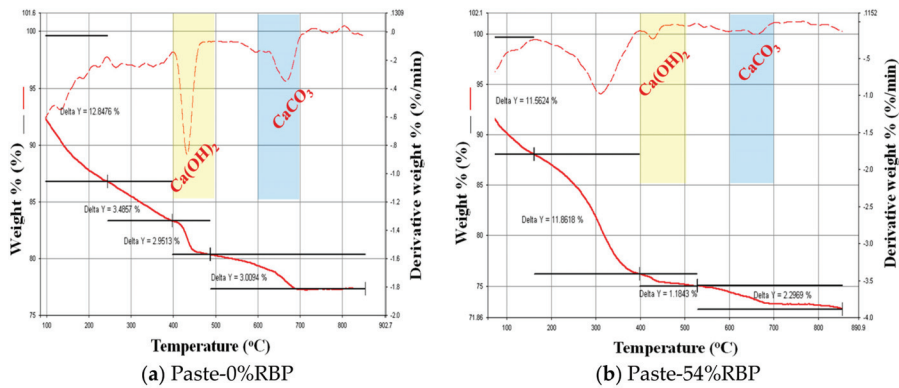


Figure 6. Hydration product analysis for the paste with RBP by DTG test. (a) Paste-0%RBP; (b) Paste-54%RBP.

3.2. Compressive Strength of the Mortar and SHCC Containing RBP

The effects of RBP and PVA fiber content on the compressive strength of prepared mortar are first determined, and the results are shown in Figure 7. The compressive strength of the mortar with and without RBP both increased with increasing curing days. However, after undergoing the same curing days, the addition of RBP decreases the compressive strength; such as, the compressive strength of the mortar with 18% RBP, 36% RBP, and 54% RBP is 8.8%, 23.9%, and 31.4% lower respectively, than that of the control group without RBP. This may be because the incorporation of RBP decreases the hydration products in mortar and then the compressive strength is decreased. Besides, a linear relationship can be observed between the RBP replacement ratios and compressive strength of prepared mortar and the specific equation is described in Figure 7a, where the F_{RBP} and F_0 represent the compressive strength of the mortar with and without RBP, in MPa; P_{RBP} is the RBP replacement ratios, in %.

Figure 7b shows the compressive strength of the Mortar-54%RBP with various PVA fiber contents. It can be seen that the compressive strength of Mortar-54%RBP first increases and then decreases with increasing PVA fiber content, and the Mortar-54%RBP with 6.5 g PVA fiber has the highest compressive strength compared with that with the other contents of PVA fiber; such as, the compressive strength of Mortar-54%RBP with 6.5 g, 13 g, and 26 g PVA fiber is 6.6% higher, 2.1% higher, and 1.8% lower, respectively, than that without PVA fiber. This may be because the appropriate content of PVA fiber improves the integrity of prepared mortar and thus the compressive strength is increased; however,

the high content of PVA fiber results in an obvious weak interface between the fiber and the paste, which is adverse to the compressive strength of prepared mortar [46].

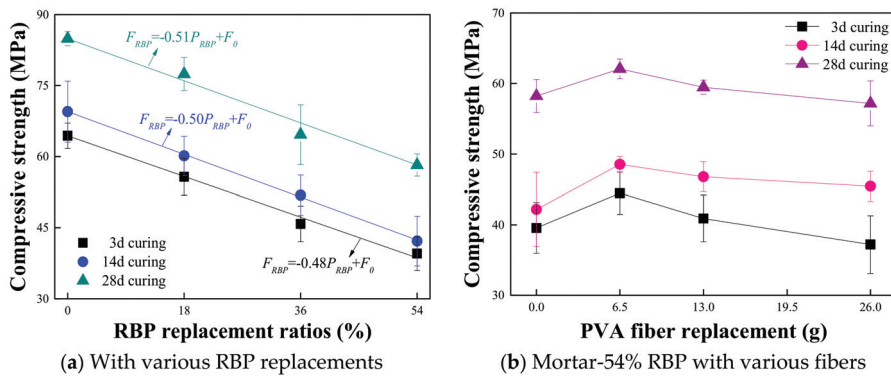


Figure 7. Compressive strength of mortar with various contents of RBP and PVA fiber. (Displayed values are the mean values of three measurements). (a) With various RBP replacements; (b) Mortar-54% RBP with various fibers.

Figure 8a shows the compressive strength of SHCC when using RBP to replace cement by weight. The results show that the compressive strength of SHCC decreases with the increase of RBP replacements after undergoing the same curing days; such as, the compressive strength of SHCC-18%RBP, SHCC-36%RBP, and SHCC-54%RBP is 3.2%, 11.2%, and 20.0% lower, respectively, than that of the control group without RBP after 28d curing. Compared with the results in Figures 7a and 8a, the adverse effect of RBP replacement on the SHCC strength is lower than that on the mortar strength; such as, the compressive strength of Mortar-54%RBP and SHCC-54%RBP is 23.9% and 20.0% lower than the control group after 28 d curing. Figure 8b further shows the compressive strength of SHCC when using RBP to replace the FA by weight. The addition of RBP increases the compressive strength of the SHCC with FA; such as, the compressive strength of SHCC-54%RBP and SHCC-27%RBP + 27%FA is 14.7% and 7.0% higher than that of SHCC-54%FA. This may be due to that RBP contained higher content of micro-particle SiO₂ than the FA, and the incorporation of SiO₂ with high micro-hardness is helpful to the strength of prepared SHCC. Therefore, when the replacement ratios of RBP and FA are the same, the compressive strength of SHCC with RBP is better than that of SHCC with FA.

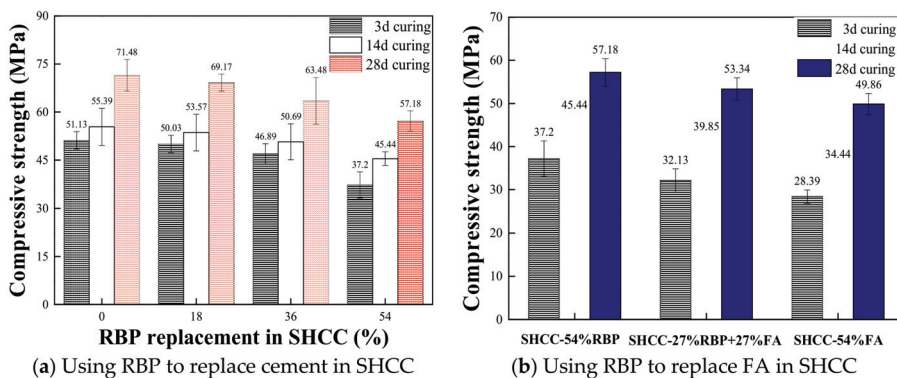


Figure 8. Compressive strength of SHCC with various RBP replacements. (Displayed values are the mean values of three measurements). (a) Using RBP to replace cement in SHCC; (b) Using RBP to replace FA in SHCC.

3.3. Flexural Strength of SHCC When Using RBP to Replace Cement by Weight

The flexural strength of the mortar with various RBP contents was first determined, and the results are shown in Figure 9. The ultimate load of the mortar decreases with the increase of RBP replacements; such as, the ultimate load of Mortar-18%RBP, Mortar-36%RBP, and Mortar-54%RBP is 8.5%, 18.1%, and 29.3% lower, respectively, than that of Mortar-0%RBP when the curing duration is 28 d. In particular, a linear relationship can be observed between the RBP replacement and ultimate load of prepared mortar, and the detailed equation is also described in this figure, where the F_{RBP} and F_0 represent the ultimate load of the mortar with and without RBP, in kN; the P_{RBP} is the RBP content, in %. Figure 9 further shows the force-displacement curves of the mortar with various RBP replacements, and a similar ascent stage can be observed when the RBP replacements are below 36%; however, the ascent stage of Mortar-54%RBP was lower than that of the other samples, and possibly because the significant reduction of hydration products in mortar and the cementation is obviously decreased.

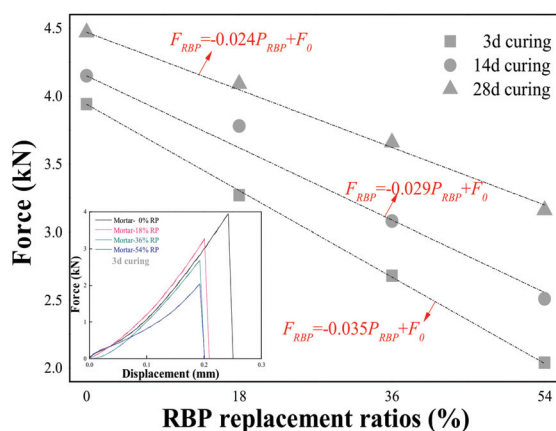


Figure 9. Flexural strength of mortar containing RBP after various curing days. (Displayed values are the mean values of three measurements).

Figure 10 shows the force-displacement curves of the mortar with various PVA fiber contents under the application of flexural load. The results highlight that the ultimate load and displacement increase with increasing PVA fiber content in mortar; such as, after 3 d curing, the ultimate load of Mortar-6.5F, Mortar-13F, and Mortar-26F is 24.8%, 53.7%, and 140.3% higher, respectively than that of Mortar-0F, and the results are 115.0%, 190.0%, and 505.0% for the ultimate displacement. This is because the bridging effect provided by the PVA fiber in cementitious materials, and the ultimate strength and strain are improved [47]. Compared with the results in Figure 10a–c, the increasing curing days improve the ultimate load of the mortar with RBP, whereas the ultimate displacement decreases with increasing curing days. In Figure 10a–c, for the plain mortar without RBP, a strain-softening curve can be observed, and there is only one peak in the force-displacement curve. For the mortar with 6 g and 13 g of PVA fiber, two peaks can be observed from the force-displacement curve, and the first peak is the highest point for the Mortar-6F, however, the second peak was the highest point for the Mortar-13F. For the mortar with 26 g of PVA fiber as well as titled SHCC sample, an obvious strain hardening curves can be observed from the force-displacement curve of Mortar-26F. Because of the existence of high content of PVA fiber in cementitious materials, the applied flexural load can be well dispersed by the bridging stress between the PVA fiber and cementitious materials, more micro cracks, rather than the large crack, are produced in cementitious materials, and thus the strain hardening characteristic appears [48–50].

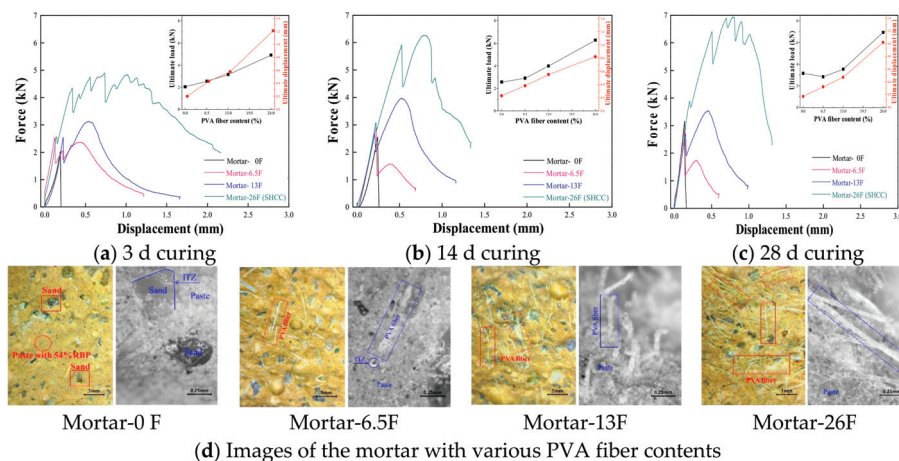


Figure 10. Force-displacement curves of mortar with various content of PVA fiber. (a) 3d curing; (b) 14 d curing; (c) 28 d curing; (d) Images of the mortar with various PVA fiber contents.

To investigate the effect of curing duration on the flexural performance of SHCC with RBP, Figure 11 shows the force-displacement curves of SHCC with RBP after various curing days. The results indicate that the ultimate load increases with increasing curing days; for example, when the curing duration is after 3 d, 14 d, and 28 d, the ultimate load of the SHCC-0%RBP is respectively 5.18 kN, 6.22 kN, and 7.70 kN, and the results are 4.9 kN, 6.28 kN, and 6.94 kN for the SHCC-54%RBP. It is noticed that the ultimate displacement generally decreases with increasing curing days, and this is due to the appearance of embrittlement with aging [51]. Compared with the results in Figure 11a–d, the adverse effects of embrittlement on the ultimate displacement of the SHCC-0%RBP is higher than that of the SHCC with RBP; for example, there are only three peaks in the force-displacement curve of SHCC-0%, whereas there are six peaks in the force-displacement curve of SHCC-54% after 28d curing. This is because the hydration products in SHCC are decreased with increasing RBP replacements, and thus, the adverse impact of embrittlement caused by the increasing hydration reaction is reduced.

To investigate the effects of RBP replacements on the flexural performance of SHCC, Figure 12 shows the force-displacement of SHCC containing various RBP contents. When the curing duration are 3 d, the ultimate load of SHCC-18%RBP and SHCC-36%RBP is higher than the SHCC-0%; however, when the RBP replacement ratios are 54%, the ultimate load of SHCC-54%RBP is lower than that of the SHCC-0%. This is because there is enough hydrated substance in the cementitious materials at the early age of curing; in this case, the appropriate content of RBP with high fineness and micro-hardness is beneficial to the mechanical properties of prepared SHCC. However, the addition of high-volume RBP results in a significant reduction in the hydration products, and thus the mechanical properties of SHCC are decreased. When the curing duration are 28 d, the ultimate load of SHCC with RBP is lower than the SHCC without RBP; this mainly due to that the hydrated substance decreases with the addition of RBP at the late period of curing, and the mechanical properties of prepared SHCC are decreased. Compared with the results in Figures 9 and 12, the adverse effect of RBP replacement on the ultimate load of SHCC is much lower than that of the mortar after undergoing the same curing days; for example when the curing duration are 28 d, the ultimate load of the mortar with 18–54% RBP is 8.5–29.3% lower than that of the mortar without RBP, whereas the ultimate load of SHCC with 18–54%RBP is 5.2–9.9% lower than that of SHCC without RBP. Therefore, using RBP as SCM to prepare SHCC is more feasible than using RBP to prepare mortar and concrete.

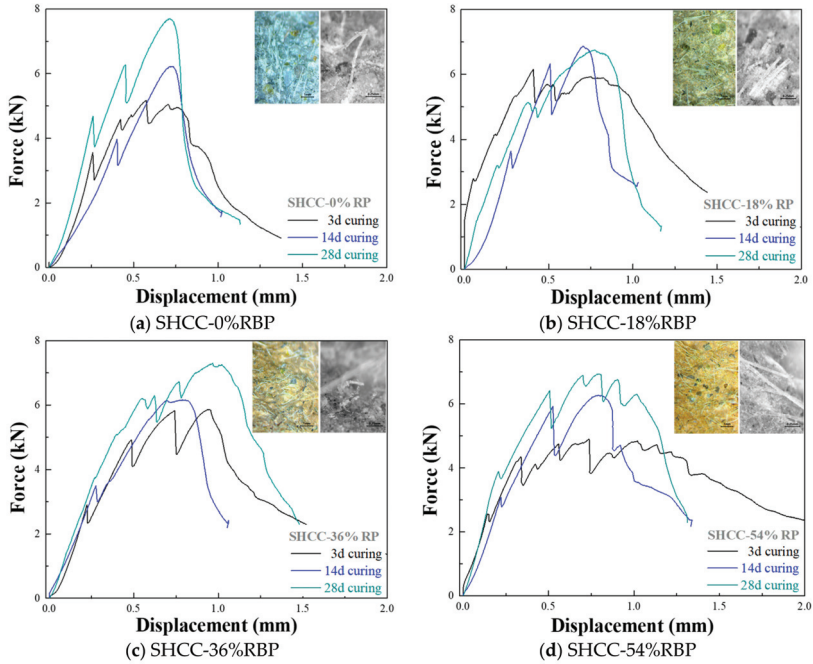


Figure 11. Force-displacement curves of SHCC containing RBP after various curing days. (a) SHCC-0%RBP; (b) SHCC-18%RBP; (c) SHCC-36%RBP; (d) SHCC-54%RBP.

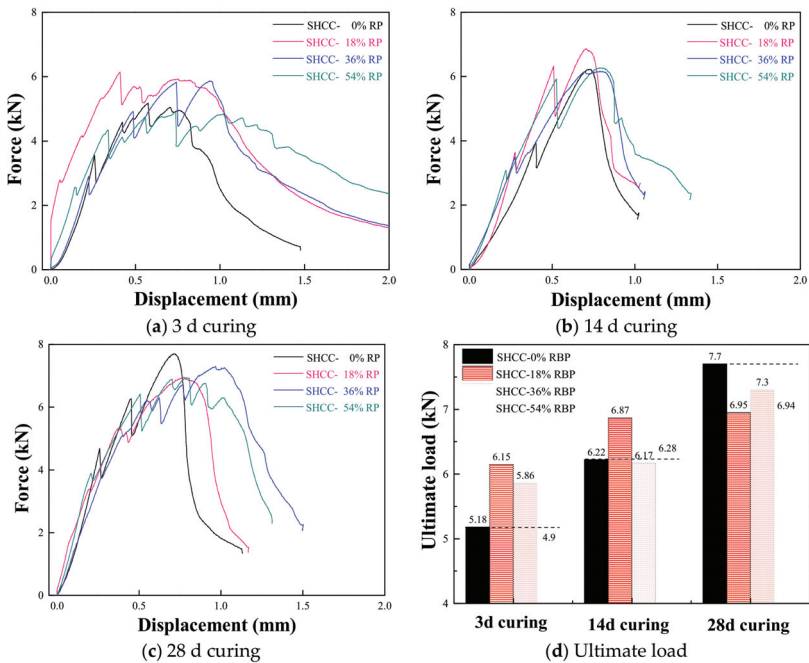


Figure 12. Force-displacement curves of SHCC with various RBP replacements. (a) 3 d curing; (b) 14 d curing; (c) 28 d curing; (d) Ultimate load.

Considering Figure 12, the ultimate displacement of SHCC increases with increasing RBP replacements after undergoing the same curing days; for example, the ultimate displacement of SHCC-18%, SHCC-36%, and SHCC-54% is 12.3%, 30.1%, and 65.8% higher respectively, than that of the SHCC-0%RBP after 3 d curing, and the results are 8.3%, 34.7%, and 41.7% after 28 d curing. This may be because the high micro-hardness of SiO_2 , contained in RBP, with irregular and amorphous structure improves the bridging stress between the PVA fiber and cementitious materials, and thus the strain hardening properties of SHCC are improved with the addition of RBP. Furthermore, Figure 13 shows the relationship between the relative ultimate displacement of SHCC and the RBP replacements, and a linear relationship can be observed between them. The specific equation is also described in Figure 13, where the D_R represents the relative value of the ultimate displacement of SHCC with RBP; R_{RBP} is the RBP replacement ratios, in %.

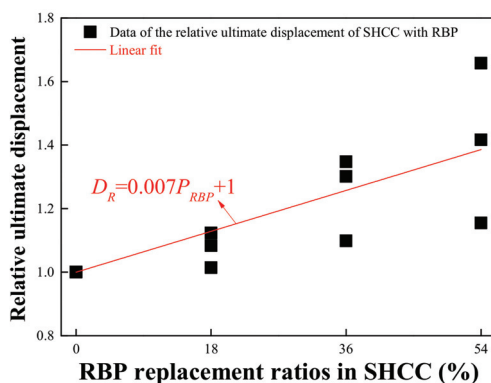


Figure 13. Relationship between the ultimate displacement of SHCC and and RBP replacements.

When using RBP to partially replace the cement by weight in SHCC, the results in this section highlight that the incorporation of RBP improves the strain hardening properties of prepared SHCC. In addition, compared with the flexural performance of SHCC without RBP, there is no obvious decrease in the ultimate load when the RBP replacement ratios are 54% in SHCC. Thus, using RBP as SCM to prepare SHCC is feasible, and the high-volume replacements of RBP derived from CDW decrease the demand of cement and provide an effective way of recycling the waste bricks in CDW.

3.4. Flexural Strength of SHCC when Using RBP to Replace Fly Ash by Weight

This section investigates the flexural performance of SHCC, when using RBP to replace FA by weight in SHCC. Figure 14 shows the force-displacement curves of SHCC with FA and RBP after various curing days, and the results show that the ultimate load increases and the ultimate displacement decreases with the increase of curing days. Figure 15 further shows the force-displacement curves of SHCC when replacing FA with various contents of RBP. The ultimate load of SHCC with RBP is higher than that of SHCC with FA; for example, the ultimate load of SHCC-54%RBP after 3 d, 14 d and 28 d curing were 9.8%, 5.8%, and 17.6% higher, respectively, than that of SHCC-54%FA. This is because the content of SiO_2 micro-particle in RBP is higher than that in FA (as shown in Figure 2b), and the higher fineness SiO_2 with high micro-hardness is beneficial to the mechanical properties of SHCC. However, the ultimate displacement of SHCC with RBP is lower than that of SHCC with FA after undergoing the same curing days. In particular, the difference between the ultimate displacement of SHCC with FA and RBP is decreased with increasing curing days. For example, the ultimate displacement of SHCC-27%RBP + 27%FA and SHCC-54%RBP were 5.6% and 38.6% lower than that of SHCC-54%FA after 3 d curing, and the results were 6.6% and 16.4% after 28 d curing.

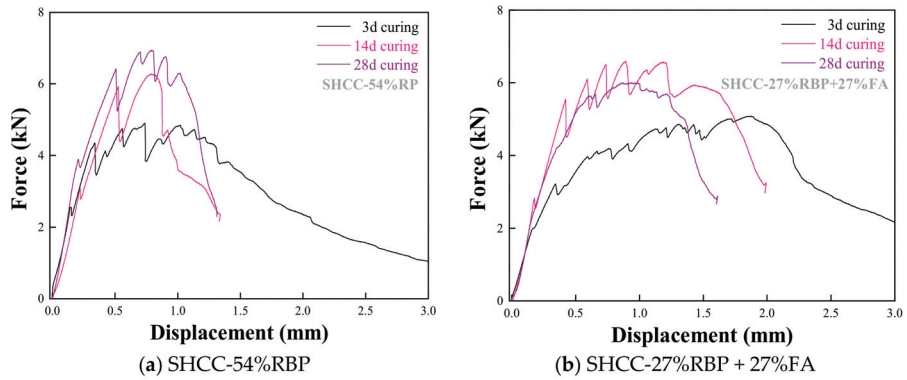


Figure 14. Force-displacement curves of SHCC with RBP and FA after various curing days. (a) SHCC-54%RBP; (b) SHCC-27%RBP + 27%FA.

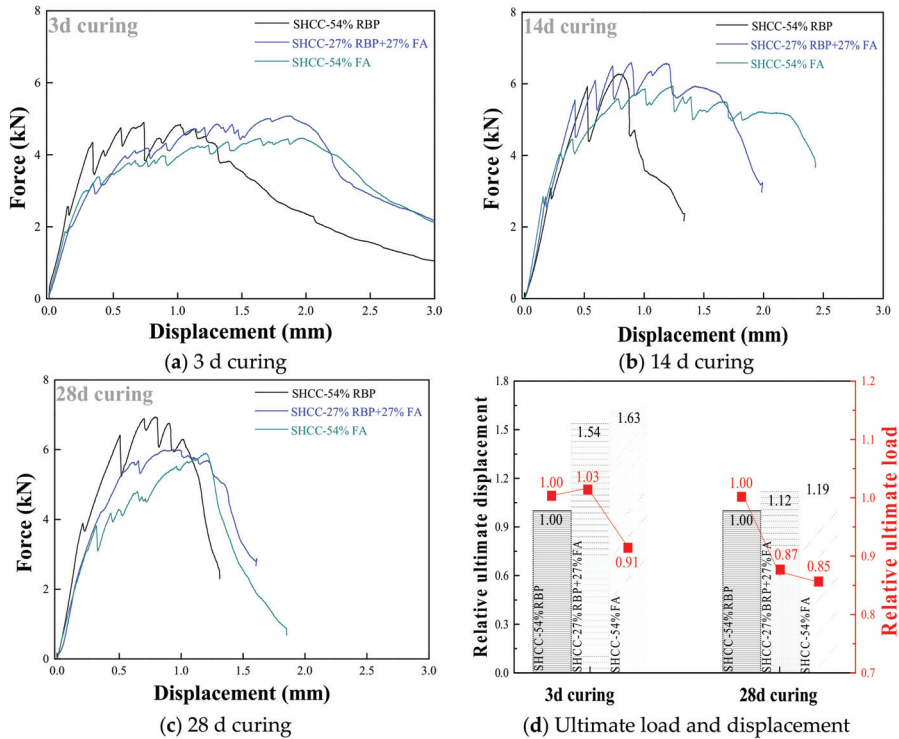


Figure 15. Force-displacement curves of SHCC when replacing FA with various RBP replacements. (a) 3 d curing; (b) 14 d curing; (c) 28 d curing; (d) Ultimate load and displacement.

The mechanism of the improvement in the strain hardening characteristic is different for the SHCC with FA and RBP. For the SHCC with FA, the microsphere structure of FA well disperses the PVA fibers in SHCC, and the addition of FA improves the ductility of cementitious materials. Thus, the strain hardening characteristic of SHCC increases with the incorporation of FA [52,53]. However, for the SHCC with RBP, the improvement in the strain hardening characteristic is mainly contributed to its amorphous structure and high micro-hardness; in this case, the bridging stress between the fiber and cementitious materials is improved, and the ultimate stress and strain are both improved. Therefore,

the ultimate load of SHCC with RBP is higher than that with FA, whereas a contrary phenomenon is observed for the ultimate displacement. When using RBP to completely replace the FA in SHCC, the ultimate load and displacement of SHCC-54%RBP are 17.6% higher and 16.4% lower than that of SHCC-54%FA. Therefore, the RBP was an appropriate SCM to prepare SHCC; especially for the SHCC may suffer a high ultimate load, the applicability of RBP is higher than that of FA in SHCC preparation.

Besides, the economic and environmental benefits of CBP preparation are higher than that of cement preparation [54]. The previous findings report that the energy consumption, CO₂ emission and cost of cement production are respectively 5.5 MJ/kg, 0.930 kg/kg, and 500 RMB/ton, and the results are 0.1–1.2 MJ/k, 0.028–0.333 kg/kg, and 30–330 RMB/ton for the preparation of RBP with various particle sizes [55]. Therefore, the CBP is an eco-friendly recycled material, and the utilization of CBP in SHCC preparation has excellent economic and environmental benefits.

4. Conclusions

Using RBP as SCM to prepare SHCC provides a new way of recycling the CDW and decreases the dosage of cement in SHCC preparation. The micro and mechanical properties of SHCC with RBP were determined in this paper. Based on the results and discussions, the following conclusions can be obtained.

- (1) The RBP has higher silicon content and lower calcium content than the cement and FA. The addition of RBP increases the content of SiO₂ in the cementitious materials, however, the hydrated compound and hydration products are decreased with the addition of RBP. The high fineness RBP has the typical characteristic of SCM, and it is feasible to use RBP as SCM in the preparation of cementitious composites.
- (2) The incorporation of RBP decreases the compressive strength and flexural strength of the prepared mortar, and a linear relationship can be observed between them. However, the adverse effect of RBP on the mechanical properties is decreased with increasing PVA fiber content; moreover, the ultimate load and displacement both increases with the increase of PVA fiber content, and an excellent strain hardening characteristic appears when the content of PVA fiber is 26 g.
- (3) Using RBP as SCM to partially replace the cement in SHCC: The ultimate load increases and the ultimate displacement decreases with increasing curing days. There is no obvious reduction in the ultimate load of SHCC with the addition of RBP. The ultimate displacement of SHCC increases with increasing RBP replacements, which indicates that the incorporation of RBP improves the ductility of SHCC. The ultimate displacement of SHCC-54%RBP is 41.7–65.8% higher than that of SHCC-0% after various curing days.
- (4) When using RBP to replace FA in SHCC: Although replacing FA by the same weight of RBP decreases the ultimate displacement of SHCC, the ultimate load is increased. The ultimate load and displacement of SHCC-54%RBP are 17.6% higher and 16.4% lower than that of SHCC-54%FA. Under some specific conditions (such as those with a requirement of high strength), the SHCC with RBP is more suitable applied in the construction than the SHCC with FA.
- (5) Although this paper proved the feasibility of using RBP to prepare SHCC, there still exist some shortcomings which should be studied in the future. For example, the particle size and types of recycled powder, derived from CDW, may significantly impact the micro and mechanical properties of prepared SHCC. Moreover, the uniaxial tensile test should be employed in the determination of properties.

Author Contributions: Conceptualization, Z.M.; methodology, Z.M.; validation, W.W. and H.W.; formal analysis, R.W.; investigation, W.W. and H.W.; data curation, R.W.; writing—original draft preparation, W.W., H.W. and R.W.; writing—review and editing, W.W., H.W. and R.W.; supervision, Z.M.; funding acquisition, Z.M. All authors have read and agreed to the published version of the manuscript.

Funding: This research was funded by National Key R&D Program of China (2018YFD1101002-05) and China Postdoctoral Science Foundation (2019M651579).

Conflicts of Interest: The authors declare no conflict of interest.

References

1. Liu, T.J.; Wang, Z.Z.; Zou, D.J.; Zhou, A.; Du, J. Strength enhancement of recycled aggregate pervious concrete using a cement paste redistribution method. *Cem. Concr. Res.* **2019**, *122*, 72–82. [CrossRef]
2. Liang, C.; Ma, H.; Pan, Y.; Ma, Z.; Duan, Z.; He, Z. Chloride permeability and the caused steel corrosion in the concrete with carbonated recycled aggregate. *Constr. Build. Mater.* **2019**, *218*, 506–518. [CrossRef]
3. Yu, D.; Duan, H.; Song, Q.; Li, X.; Zhang, H.; Zhang, H.; Wang, J. Characterizing the environmental impact of metals in construction and demolition waste. *Environ. Sci. Pollut. R.* **2018**, *25*, 13823–13832. [CrossRef] [PubMed]
4. Bao, J.; Li, S.; Zhang, P.; Ding, X.; Xue, S.; Cui, Y.; Zhao, T. Influence of the incorporation of recycled coarse aggregate on water absorption and chloride penetration into concrete. *Constr. Build. Mater.* **2020**, *239*, 117845. [CrossRef]
5. Guo, H.; Shi, C.; Guan, X.; Zhu, J.; Ding, Y.; Ling, T.C.; Wang, Y. Durability of recycled aggregate concrete—A review. *Cem. Concr. Compos.* **2018**, *89*, 251–259. [CrossRef]
6. Zhang, J.; Shi, C.; Li, Y.; Pan, X.; Poon, C.S.; Xie, Z. Influence of carbonated recycled concrete aggregate on properties of cement mortar. *Constr. Build. Mater.* **2015**, *98*, 1–7. [CrossRef]
7. Ma, Z.; Liu, M.; Tang, Q.; Liang, C.; Duan, Z. Chloride permeability of recycled aggregate concrete under the coupling effect of freezing-thawing, elevated temperature or mechanical damage. *Constr. Build. Mater.* **2020**, *237*, 117648. [CrossRef]
8. Kou, S.C.; Poon, C.S. Effect of the quality of parent concrete on the properties of high performance recycled aggregate concrete. *Constr. Build. Mater.* **2015**, *77*, 501–508. [CrossRef]
9. Pedro, D.; DeBrito, J.; Evangelista, L. Durability performance of high-performance concrete made with recycled aggregates, fly ash and densified silica fume. *Cem. Concr. Compos.* **2018**, *93*, 63–74. [CrossRef]
10. González-Taboada, I.; González-Fontebo, B.; Martínez-Abella, F.; Seara-Paz, S. Thixotropy and interlayer bond strength of self-compacting recycled concrete. *Constr. Build. Mater.* **2018**, *161*, 479–488. [CrossRef]
11. Wang, C.; Xiao, J.; Wang, C.; Zhang, C. Nonlinear damping and nonlinear responses of recycled aggregate concrete frames under earthquake loading. *Eng. Struct.* **2019**, *201*, 109575. [CrossRef]
12. Liang, C.; Pan, B.; Ma, Z.; He, Z.; Duan, Z. Utilization of CO₂ curing to enhance the properties of recycled aggregate and prepared concrete: A review. *Cem. Concr. Compos.* **2020**, *105*, 103446. [CrossRef]
13. Shi, C.; Li, Y.; Zhang, J.; Li, W.; Chong, L.; Xie, Z. Performance enhancement of recycled concrete aggregate—A review. *J. Clean. Prod.* **2016**, *112*, 466–472. [CrossRef]
14. Ma, Z.; Tang, Q.; Yang, D.; Ba, G. Durability Studies on the Recycled Aggregate Concrete in China over the Past Decade: A Review. *Adv. Civ. Eng.* **2019**, *2019*, 4073130. [CrossRef]
15. Shao, J.; Gao, J.; Zhao, Y.; Chen, X. Study on the pozzolanic reaction of clay brick powder in blended cement pastes. *Constr. Build. Mater.* **2019**, *213*, 209–215. [CrossRef]
16. Lin, K.L.; Chen, B.Y.; Chiou, C.S.; Cheng, A. Waste brick's potential for use as a pozzolan in blended portland cement. *Waste Manag. Res.* **2010**, *28*, 647–652. [CrossRef]
17. Hwang, C.L.; Damtie, Y.M.; Vo, D.H.; Huynh, T.P. Development of high-strength alkali-activated pastes containing high volumes of waste brick and ceramic powders. *Constr. Build. Mater.* **2019**, *218*, 519–529. [CrossRef]
18. Navrátilová, E.; Rovnaníková, P. Pozzolanic properties of brick powders and their effect on the properties of modified lime mortars. *Constr. Build. Mater.* **2016**, *120*, 53–539. [CrossRef]
19. Letelier, V.; Ortega, J.; Muñoz, P.; Tarela, E.; Moriconi, G. Influence of waste brick powder in the mechanical properties of recycled aggregate concrete. *Sustainability* **2018**, *10*, 1037. [CrossRef]
20. Olofinnade, O.M.; Ede, A.N.; Booth, C.A. Sustainability of waste glass powder and clay brick powder as cement substitute in green concrete. In *Handbook of Environmental Materials Management*; Springer International Publishing: Cham, Switzerland, 2018; pp. 1–22.
21. Ma, Z.; Liu, M.; Duan, Z.; Liang, C.; Wu, H. Effects of active waste powder obtained from C&D waste on the microproperties and water permeability of concrete. *J. Clean. Prod.* **2020**, *257*, 120518.
22. Ge, Z.; Wang, Y.; Sun, R.; Wu, X.; Guan, Y. Influence of ground waste clay brick on properties of fresh and hardened concrete. *Constr. Build. Mater.* **2015**, *98*, 128–136. [CrossRef]

23. Ge, Z.; Meng, F.B.; Yue, H.Y.; Hu, Y.Z. Durability study of PET-brick powder mortar. *J. Shandong Univ.* **2014**, *44*, 76–79.
24. Lu, C.; Yu, J.; Leung, C.K. Tensile performance and impact resistance of Strain Hardening Cementitious Composites (SHCC) with recycled fibers. *Constr. Build. Mater.* **2018**, *171*, 566–576. [CrossRef]
25. Jun, P.; Mechtcherine, V. Behaviour of strain-hardening cement-based composites (SHCC) under monotonic and cyclic tensile loading: Part 2—Modelling. *Cem. Concr. Compos.* **2010**, *32*, 810–818. [CrossRef]
26. Paul, S.C.; Babafemi, A.J. A review of the mechanical and durability properties of strain hardening cement-based composite (SHCC). *J. Sustain. Cement-Based Mater.* **2018**, *7*, 57–78. [CrossRef]
27. Choi, W.C.; Jang, S.J.; Yun, H.D. Bond and cracking behavior of lap-spliced reinforcing bars embedded in hybrid fiber reinforced strain-hardening cementitious composite (SHCC). *Compos. Part B Eng.* **2017**, *108*, 35–44. [CrossRef]
28. Gao, S.; Jin, J.; Hu, G.; Qi, L. Experimental investigation of the interface bond properties between SHCC and concrete under sulfate attack. *Constr. Build. Mater.* **2019**, *217*, 651–663. [CrossRef]
29. Ma, Z.; Zhu, F.; Ba, G. Effects of freeze-thaw damage on the bond behavior of concrete and enhancing measures. *Constr. Build. Mater.* **2019**, *196*, 375–385. [CrossRef]
30. Arain, M.F.; Wang, M.; Chen, J.; Zhang, H. Experimental and numerical study on tensile behavior of surface modified PVA fiber reinforced strain-hardening cementitious composites (PVA-SHCC). *Constr. Build. Mater.* **2019**, *217*, 403–415. [CrossRef]
31. Van Zijl, G.P.; Wittmann, F.H.; Oh, B.H.; Kabele, P.; Filho, R.D.T.; Fairbairn, E.M.; Altmann, F. Durability of strain-hardening cement-based composites (SHCC). *Mater. Struct.* **2012**, *45*, 1447–1463. [CrossRef]
32. Van Zijl, G.P.; Slowik, V.; Filho, R.D.T.; Wittmann, F.H.; Mihashi, H. Comparative testing of crack formation in strain-hardening cement-based composites (SHCC). *Mater. Struct.* **2016**, *49*, 1175–1189. [CrossRef]
33. Zhang, P.; Dai, Y.Q.; Ding, X.Y.; Zhou, C.S.; Xue, X.; Zhao, T. Self-healing behaviour of multiple microcracks of strain hardening cementitious composites (SHCC). *Constr. Build. Mater.* **2018**, *169*, 705–715. [CrossRef]
34. Ma, Z.M.; Zhao, T.J.; Xiao, J.Z.; Wang, P.G. Effect of applied loads on water and chloride penetrations of strain hardening cement-based composites. *J. Mater. Civil Eng.* **2016**, *28*, 04016069. [CrossRef]
35. Arain, M.F.; Wang, M.; Chen, J.; Zhang, H. Study on PVA fiber surface modification for strain-hardening cementitious composites (PVA-SHCC). *Constr. Build. Mater.* **2019**, *197*, 107–116. [CrossRef]
36. Tosun, K.; Felekoğlu, B.; Baradan, B. Multiple cracking response of plasma treated polyethylene fiber reinforced cementitious composites under flexural loading. *Cem. Concr. Compos.* **2012**, *34*, 508–520. [CrossRef]
37. Mei, J.; Tan, H.; Li, H.; Ma, B.; Liu, X.; Jiang, W.; Li, X. Effect of sodium sulfate and nano-SiO₂ on hydration and microstructure of cementitious materials containing high volume fly ash under steam curing. *Constr. Build. Mater.* **2018**, *163*, 812–825. [CrossRef]
38. Kim, H.; Lee, C.H.; Ann, K.Y. Feasibility of ferronickel slag powder for cementitious binder in concrete mix. *Constr. Build. Mater.* **2019**, *207*, 693–705. [CrossRef]
39. Chindaprasirt, P.; Jaturapitakkul, C.; Sinsiri, T. Effect of fly ash fineness on compressive strength and pore size of blended cement paste. *Cem. Concr. Compos.* **2005**, *27*, 425–428. [CrossRef]
40. Li, S.; Li, Q.; Zhao, X.; Luo, J.; Gao, S.; Yue, G.; Su, D. Experimental Study on the Preparation of Recycled Admixtures by Using Construction and Demolition Waste. *Materials* **2019**, *12*, 1678. [CrossRef]
41. Ma, Z.; Duan, Z.; Ba, G. Effects of an Applied Load on the Chloride Penetration of Concrete with Recycled Aggregates and Recycled Powder. *Adv. Civ. Eng.* **2019**, *2019*, 1340803. [CrossRef]
42. Yu, K.Q.; Zhu, W.J.; Ding, Y.; Lu, Z.D.; Yu, J.T.; Xiao, J.Z. Micro-structural and mechanical properties of ultra-high performance engineered cementitious composites (UHP-ECC) incorporation of recycled fine powder (RFP). *Cem. Concr. Res.* **2019**, *124*, 105813. [CrossRef]
43. L'Hôpital, E.; Lothenbach, B.; Kulik, D.A.; Scrivener, K. Influence of calcium to silica ratio on aluminium uptake in calcium silicate hydrate. *Cem. Concr. Res.* **2016**, *85*, 111–121. [CrossRef]
44. Kunther, W.; Ferreira, S.; Skibsted, J. Influence of the Ca/Si ratio on the compressive strength of cementitious calcium-silicate-hydrate binders. *J. Mater. Chem. A* **2017**, *5*, 17401–17412. [CrossRef]
45. Li, Z.; Zhang, Y.; Zhao, H.; Chen, H.; He, R. Structure characteristics and composition of hydration products of coal gasification slag mixed cement and lime. *Constr. Build. Mater.* **2019**, *213*, 265–274. [CrossRef]

46. Mohammadhosseini, H.; Awal, A.S.M.A.; Yatim, J.B.M. The impact resistance and mechanical properties of concrete reinforced with waste polypropylene carpet fibres. *Constr. Build. Mater.* **2017**, *143*, 147–157. [CrossRef]
47. Ranjbarian, M.; Mechtcherine, V. Influence of loading parameters in cyclic tension-compression regime on crack-bridging behaviour of PVA microfibres embedded in cement-based matrix. *Constr. Build. Mater.* **2019**, *228*, 116760. [CrossRef]
48. Müller, S.; Mechtcherine, V. Fatigue behaviour of strain-hardening cement-based composites (SHCC). *Cem. Concr. Res.* **2017**, *92*, 75–83. [CrossRef]
49. Zhang, P.; Wang, P.; Hou, D.; Liu, Z.; Haist, M.; Zhao, T. Application of neutron radiography in observing and quantifying the time-dependent moisture distributions in multi-cracked cement-based composites. *Cem. Concr. Compos.* **2017**, *78*, 13–20. [CrossRef]
50. Yu, J.; Chen, Y.; Leung, C.K. Mechanical performance of Strain-Hardening Cementitious Composites (SHCC) with hybrid polyvinyl alcohol and steel fibers. *Compos. Struct.* **2019**, *226*, 111198. [CrossRef]
51. Paul, S.C.; van Zijl, G.P. Mechanically induced cracking behaviour in fine and coarse sand strain hardening cement based composites (SHCC) at different load levels. *J. Adv. Concr. Technol.* **2013**, *11*, 301–311. [CrossRef]
52. Liu, C.C.; Yuan, Y.Z.; Yuan, H. Mechanical properties of pva-ecc with high volume fly ash and mechanism analysis of fly ash. *Bull. Chin. Ceram. Soc.* **2017**, *36*, 3739–3744.
53. Yu, J.; Leung, C.K. Strength improvement of strain-hardening cementitious composites with ultrahigh-volume fly ash. *J. Mater. Civ. Eng.* **2017**, *29*, 05017003. [CrossRef]
54. He, X.Y.; Zheng, Z.Q.; Yang, J.; Su, Y.; Wang, T.W.; Strnadel, B. Feasibility of incorporating autoclaved aerated concrete waste for cement replacement in sustainable building materials. *J. Clean. Prod.* **2019**, *250*, 119455. [CrossRef]
55. Zhao, Y.; Gao, J.; Liu, C.; Chen, X.; Xu, Z. The particle-size effect of waste clay brick powder on its pozzolanic activity and properties of blended cement. *J. Clean. Prod.* **2020**, *242*, 118521. [CrossRef]



© 2020 by the authors. Licensee MDPI, Basel, Switzerland. This article is an open access article distributed under the terms and conditions of the Creative Commons Attribution (CC BY) license (<http://creativecommons.org/licenses/by/4.0/>).

Article

Recycled Nylon Fiber from Waste Fishing Nets as Reinforcement in Polymer Cement Mortar for the Repair of Corroded RC Beams

Teeranai Srimahachota ^{1,*}, Hiroshi Yokota ² and Yoshikazu Akira ³¹ Graduate School of Engineering, Hokkaido University, Sapporo 001-0014, Japan² Faculty of Engineering, Hokkaido University, Sapporo 001-0014, Japan; yokota@eng.hokudai.ac.jp³ Faculty of Engineering, Kagoshima University, Kagoshima 890-0065, Japan; akira@oce.kagoshima-u.ac.jp

* Correspondence: agartoon@eis.hokudai.ac.jp; Tel.: +81-(0)11-706-6204

Received: 29 August 2020; Accepted: 24 September 2020; Published: 25 September 2020

Abstract: Waste fishing nets were utilized as recycled nylon (RN) short fiber to improve the mechanical properties of cement mortar. RN and manufactured polyethylene (PE) fibers were added to polymer cement mortar (PCM) as a reinforcement, and fiber-reinforced PCM was sprayed on the section of reinforced concrete (RC) beams. Normal RC beams and the upgraded RC beams were placed in the tidal zone for 14 months to induce rebar corrosion. Consequently, a repair operation took place by the removal of the concrete cover then spraying fiber-reinforced PCM. The tested RC beams were subjected to four-point flexural tests to study their load-carrying capacity. It was found that the fibers helped transfer stresses through cracks and distribute stresses by transforming a single wide crack into many small cracks. Overall, the experimental results showed that recycled nylon fibers from waste fishing nets have great potential to be used as a strengthening fiber in cementitious material.

Keywords: fiber reinforcing mortar; polymer cement mortar; recycled fiber; waste fishing nets

1. Introduction

Marine ecosystems are deteriorating due to derelict fishing gear (DFG). Fishing gears including lines, ropes and fishing nets that were discarded or lost in the ocean become traps, leading to the deaths of many marine species. It was estimated that DFG causes the deaths of 380,000 marine animals annually, especially whales, sea lions and turtles [1]. It is estimated that 5.7% of fishing nets, 8.6% of traps and 29% of lines from global fishery industries were lost into the ocean in 2017 [2]. DFG becomes the most common material entangling marine life, as well as causing damage to coral reefs [3]. For example, more than 58,000 cases of entanglement by DFG were reported in Korean seas, causing economic losses over 90 million USD [4]. Therefore, finding suitable solutions for collecting and recycling those fishing nets is an urgent issue to mitigate environmental impact.

Fishing nets are usually made of strong and durable materials, such as nylon, polyamide (PA) and high-density polyethylene (HDPE), which are non-biodegradable and require a lot of resources and energy, as well as emitting greenhouse gases, for their recycling [5]. Waste fishing nets can be recycled into many products, such as textiles, clothes, footwear and accessories [6,7]. In the concrete engineering field, synthetic fibers have been widely used as reinforcement in cementitious materials. For instance, polypropylene (PP), polyvinyl alcohol (PVA) and polyethylene terephthalate (PET) fibers were found to improve the mechanical properties and durability of concrete, such as flexural capacity, flexural toughness, shrinkage resistance and freeze-thaw resistance [8–18], and adding fibers was found to have a significant effect on the crack bridging and the failure behavior [19–21]. Moreover, it was found that adding PP fibers improves sulfate resistance and alkali-silica reaction (ASR) expansions [22–26].

The usage of nylon fibers in cementitious materials was found to lead to superior performance compared to the usage of PP fibers in terms of compressive strength, splitting tensile strength, modulus of rupture, impact resistance and shrinkage cracks resistance [27]. Recycled PET, PP and HDPE fibers have also been applied to cementitious mortar and found to effectively improve mechanical properties such as toughness, impact load, energy absorption [28–37].

Currently, the usage of recycled fibers from waste fishing nets is gaining attention among civil engineers, as they have shown the potential to improve the performance of concrete structures [38]; however, only limited research has been conducted. The recycled nylon fibers from waste fishing nets maintains mechanical properties of the virgin fibers [39], and exhibits stability under the high alkaline conditions in concrete [40]. It was found that the addition of recycled nylon fibers from waste fishing nets in cementitious materials increase the tensile strength of mortar under axial load, ductility, and toughness index, and improves flexural capacity in the range of 22–41% [41–43]. However, high fiber contents resulted in a reduction of the compressive strength of mortar [40].

This paper investigates the application of polymer cement mortar (PCM) reinforced with recycled nylon (RN) fibers from waste fishing nets for repairing corroded reinforced concrete (RC) beams, with a focus on the restorability of load-carrying capacity of the RC beams exposed to a natural corrosion environment. RC beams were placed in the tidal zone for 14 months to induce steel corrosion, then repairs were carried out by spraying PCM reinforced with RN fiber or manufactured polyethylene (PE) microfiber. The load-carrying capacity, crack openings and final crack formation of the RC beams were extensively investigated to evaluate the effectiveness of the repair.

2. Experimental Program

2.1. Testing Materials

A total of 12 RC beams measuring 900 mm long, 100 mm wide and 150 mm high were produced. The water-to-cement ratio of the concrete was 0.5, and the design strength was 33 MPa. Galvanized coated steel bars were used for the top (compressive) reinforcement and the stirrups so that the corrosion concentrated on the bottom (tensile) reinforcement. The beams were cured by a wet towel for 7 days, and then placed in the respective environments explained later. Figure 1a shows the geometry and reinforcement details of the RC beams.

The waste fishing nets used in this study were obtained from local fishermen in Hokkaido. The fishing nets were washed by soaking in water, dried, and then manually cut into specified lengths to make RN fiber. Only the straight part of the net was used to prevent the formation of fiber clumps during mixing and to maintain flowability of the fresh mortar. Two types of fiber were used in this study: RN fiber and manufactured PE fibrillated microfiber (Figure 2). PE fibers were produced in the form of bundles, but they separated into individual fibers during mixing with the diameter of 0.01 to 0.1 mm. PCM and PE fibers were supplied from Sumitomo Osaka Cement Co., Ltd., Tokyo, Japan for research purposes.

The uniaxial tensile test was carried out for RN fiber according to the American Society for Testing and Materials (ASTM) C1557 [44], and the properties of the fibers are given in Table 1. Spadea et al. [40] previously confirmed that nylon fiber from waste fishing nets can be safely applied to cementitious materials, with only a slightly drop in tensile strength of around 4% between virgin and used fishing nets.

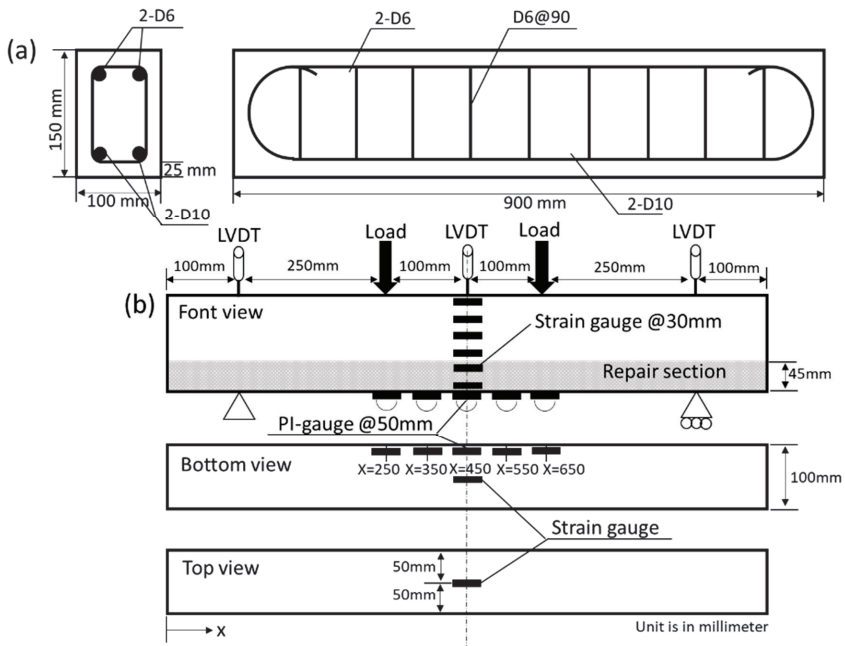


Figure 1. Tested beam: (a) geometry and reinforcement details; (b) experimental setup.

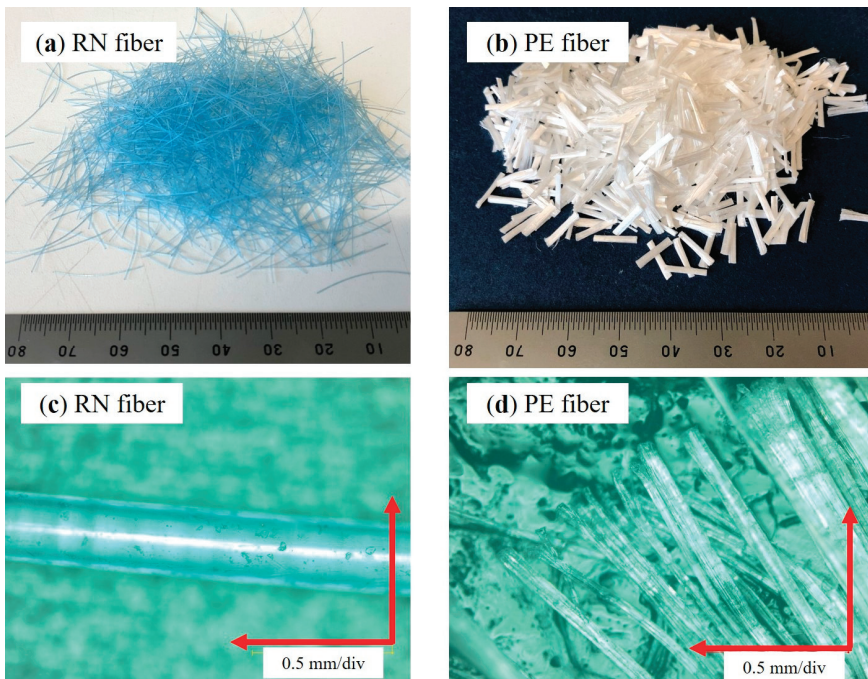


Figure 2. Types of fibers: (a) recycled nylon (RN) fiber; (b) polyethylene (PE) fiber, and microscope images ($\times 200$) of (c) RN fiber; (d) PE fiber.

Table 1. Properties of the fibers.

Fiber	Diameter (mm)	Length (mm)	Density (g/cm ³)	Tensile Strength (MPa)
Recycled nylon (RN)	0.24	20	1.13	440
Polyethylene (PE)	0.01–0.1	9	1.05	n/a

2.2. Exposure and Repair Operations

The tested RC beams were divided into 3 groups: group A beams were stored in the laboratory room for 10 months and then tested; group B beams (normal and upgraded RC beams) were exposed to the tidal zone for 14 months; and group C beams (normal RC beams only) were repaired after the 14-month tidal exposure. The normal RC beam was directly exposed to the tide, and repairs were made at the end of the exposure period. The upgraded RC beams underwent repair operations before starting the exposure, and were not further repaired even after the exposure. The details of the tested beams are listed in Table 2.

Table 2. Name and conditions of the tested RC beams.

Specimen Name	Condition	Tidal Exposure	Sprayed Material
Group A	RC0	Normal RC	-
	RN0	Upgraded RC	PCM–RN
	PE0	Upgraded RC	PCM–PE
Group B	RC1	Normal RC	14 months
	RN1	Upgraded RC	14 months
	PE1	Upgraded RC	14 months
Group C	RC1–NF	Normal RC	14 months
	RC1–RN	Normal RC	14 months
	RC1–PE	Normal RC	14 months

For groups B and C beams, steel corrosion was induced naturally by placing the beams in the tidal zone for 14 months. The corrosion progress of the steel rebars was periodically monitored by half-cell potential in accordance with the Japan Society of Civil Engineers (JSCE) E 601 [45].

Repair operations were conducted by removing the bottom concrete cover up to 20 mm over the tensile rebar and subsequently spraying acrylic type PCM reinforced with fibers (Figure 3). Three mixes of PCM were used: PCM without fiber added, or non-fiber, PCM (PCM–NF); PCM reinforced with recycled nylon fiber (PCM–RN); and PCM reinforced with polyethylene fiber (PCM–PE). The water-to-binder ratio of PCM was 0.2, and the fiber fractions by volume for RN and PE fibers were 1.0% and 1.1%, respectively. Mix proportions are indicated in Table 3. It should be noted that the fiber fraction of PE was calculated from the manufacturer in order to simplify the mixing onsite.

**Figure 3.** Spraying PCM on the removed section of RC beams.

Table 3. Mix proportion of PCM (in 25 kg of PCM).

Mix	Water (kg)	Fiber (g)
PCM–NF	4.93	-
PCM–RN	4.93	0.164
PCM–PE	4.93	0.160

PCM was prepared by mixing PCM powder with water for 1 min, followed by air removal agent. Fibers were subsequently added at the designated amount while continuing mixing. The mixing was continued for 2–3 min to ensure uniform fiber distribution and that no fiber clusters have formed. After concluding the mixing, PCM was pumped and sprayed through a nozzle on the removed section of RC beams. PCM specimens were also cast by directly spraying in the 40 mm × 40 mm × 160 mm prism molds and the 50 mm × 100 mm cylinder molds for flexural and compressive tests, respectively.

2.3. Loading Tests

Four-point flexural tests, in accordance with Japanese Industrial Standards (JIS) A 1106 [46], were conducted on tested RC beams using 1000 kN type universal testing machine made by Shimadzu Corporation, Tokyo, Japan. Linear variable differential transformers (LVDTs) brand Tokyo Measuring Instruments Laboratory Co., Ltd., Tokyo, Japan with the capacity of 100 mm were used to measure the deflection of the beams at midspan and the end supports. Concrete surface strains were measured using 8 strain gauges with a 30 mm gauge length: 6 gauges attached in the midspan at 30 mm intervals, 1 gauge on the top surface of the midspan, and 1 gauge on the bottom surface. A series of 5 pi-type gauges with 50 mm gauge length were installed at the bottom surface of the beam for measuring crack openings. Figure 1b shows the experimental setup for the tested RC beams.

Flexural strength tests as per JIS R 5201 [47] and the compressive strength tests following JIS A 1108 [48] were conducted on PCM specimens using an autograph-type universal testing machine made by Jacom co., Ltd., Tokyo, Japan with the capacity of 250 kN. These specimens were air cured for 28 days before testing.

3. Results and Discussion

3.1. Mechanical Behavior of Polymer Cement Mortar (PCM) Specimens

3.1.1. Flowability

Flow diameters of PCM were measured onsite following JIS R 5201 [47], and the results are listed in Table 4. The addition of RN fibers slightly reduced the flow diameter of fresh mortar. For the case of RN fiber in PCM, the reduction in flowability may be negligible; however, further confirmation is needed. A slight reduction of 5–10% in the flowability of fresh mortar was also previously found in the case of the ordinary Portland cement mortar using nylon fiber [40,43]. PCM–PE showed a considerable reduction of 24% in flow diameter compared to PCM–NF. This reduction was likely due to the fibrillated characteristic of the PE fibers, which have a comparatively higher surface area. PE fibers also have lower density than RN fibers; therefore, more fibers are needed to obtain the same volume fraction.

Table 4. Flow diameters.

Specimen Name	Flow Diameter (mm)	%ΔFlow Diameter
PCM–NF	165	-
PCM–RN	164	−0.7
PCM–PE	126	−23.7

3.1.2. Compressive and Flexural Strengths

The compressive and flexural test results of PCM specimens are summarized in Table 5. The reported values are the average of three samples. The addition of RN fiber resulted in a considerable reduction of both compressive and flexural strengths. However, increases of 24.3% and 39.2% were found for the compressive and flexural strengths, respectively, of PCM-PE. Ozger, et al. [36] suggested that short fiber plays an important role in enhancing the lateral tensile strength of concrete during the load. However, the addition of fibers can increase the voids inside the cement matrix and reduce the modulus of elasticity [12]. It should be noted that the compressive strength tests for PCM-RN were taken from the sawed prism specimen after the bending test.

Table 5. Compressive strength tests and flexural strength tests results.

Specimen Name	Compressive Strength Tests			Flexural Strength Tests			
	f'_c (MPa)	SD	$\% \Delta f'_c$	P_{cr} (kN)	f_b (MPa)	SD	$\% \Delta f_b$
PCM-NF	32.7	3.65	-	1.69	4.77	0.14	-
PCM-RN	24.0 ¹	3.53	-31.4	1.56	4.37	0.72	-8.4
PCM-PE	43.5	1.41	24.3	2.36	6.64	0.82	39.2

Note: f'_c is the compressive strength, SD is the standard deviation, $\% \Delta f'_c$ is the percent difference in compressive strength compared to PCM-NF, P_{cr} is the maximum load, f_b is the flexural strength, and $\% \Delta f_b$ is the percent difference in flexural strength compared to PCM-NF. ¹ Obtained with 40 mm cube specimens taken out from the beam.

3.1.3. Failure Behavior

Three-point flexural tests were performed on 40 mm × 40 mm × 160 mm prism specimens, with the load-midspan deflection curves of the beams shown in Figure 4. PCM-PE showed the highest peak load, followed by PCM-RN and PCM-NF. PCM-NF exhibited a brittle failure mode as the load suddenly decreased to zero, while PCM-PE and PCM-RN retained some load after the yield point. A hardening stage was found for PCM-PE in which the load increased after the peak; therefore, it can be confirmed that PE fibers transferred stresses after the cracks occurred.

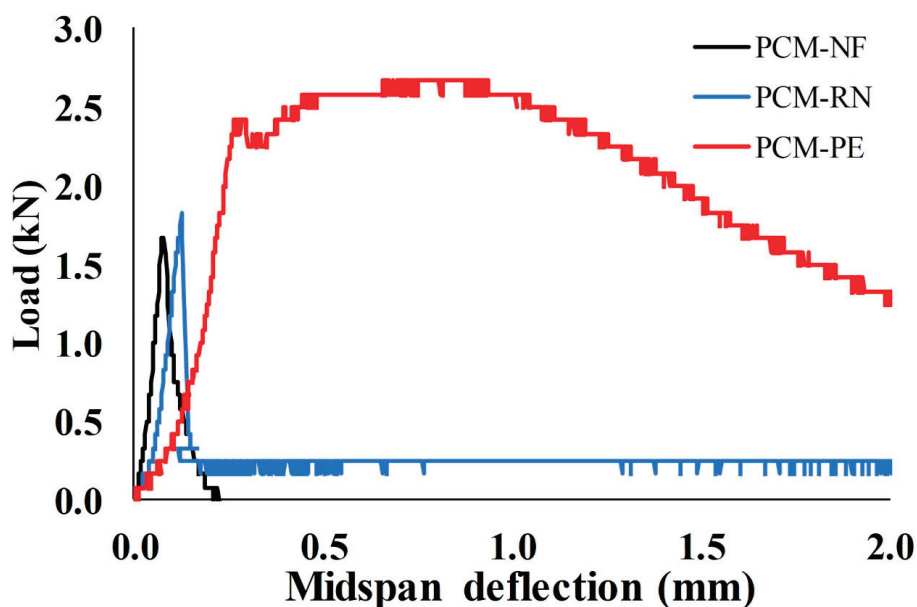


Figure 4. Load-midspan deflection curves of PCM-NF, PCM-RN and PCM-PE.

For PCM–RN, the load suddenly decreased after the yield point, but still sustained a small residual load of approximately 13.6% of the yield load. Even though the residual load of PCM–RN was lower than that of PCM–PE, RN fiber prevented abrupt failure of the beam. The lower residual load was likely due to weak bonding of the RN fiber, as it has a smooth surface compared to PE fiber. Test results of PCM–RN and PCM–PE correspond to the experiment by Orasutthikul, et al. [43].

The final cracks on the bottom surface of the beam after the test are shown in Figure 5. PCM–RN had a wide single crack while PCM–PE had many small cracks. This phenomenon confirmed that PE fiber transfers stresses by dispersing damage from a wide single crack into many small cracks. No breakage of fiber was observed in the case of RN fiber, and RN fibers were pulled out rather than elongated. It is concluded that RN fiber transfers stresses through wide cracks while PE fiber bridges small or micro cracks.

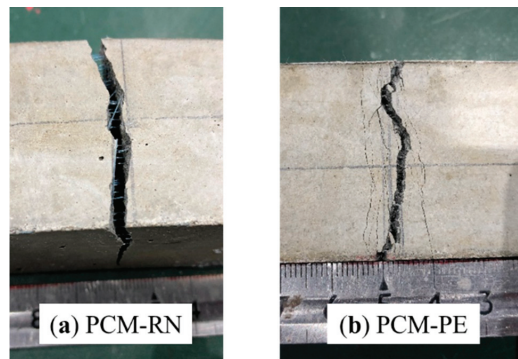


Figure 5. Crack pattern at the bottom surface of the beam: (a) PCM–RN; (b) PCM–PE.

3.2. Mechanical Behavior of Reinforced Concrete (RC) Beams

3.2.1. Flexural Capacity

Results from the four-point flexural tests are summarized in Table 6, and the load-midspan displacement curves are shown in Figure 6. As the flexural capacities of group A beams indicate, the respective two beams having the identical test parameters have an uncertainty of less than 10%. Therefore, the relative trends can be discussed based on the series of tests although only one beam was tested with each set of test parameters for groups B and C beams. For group A, RN0 showed flexural capacity approximately 8% lower than RC0, while PE0 was 7% higher. RN fiber seemed to provide no contribution to the flexural capacity. In addition, the shorter curing period of the beams in group A may be another reason for the decrease in flexural capacity.

For group B, RN1 and PE1 gained 10% and 34% more flexural capacity than RC0, respectively. The increase in flexural capacity of RN1 and PE1 was attributed to the sprayed PCM. The beams sprayed with PCM–RN (RN0 and RN1) tended to express flexural-shear failure mode, likely due to the fact that RN fiber reduces shear capacity by adding voids in the PCM matrix.

For group C, RC1–PE gave highest yield load at 28% higher than that of RC0, but RC1–RN gave a comparable yield load to RC1–NF. The ultimate load of all the beams are similar to each other in the range of 15–17%. PE fibers showed greater contribution to the flexural capacity of the repaired beams than RN fibers; however, flexural capacity of the repaired beams were compensated by spraying PCM. The results of tested RC beams with respect to the sprayed PCM correspond to the mechanical properties of PCM specimens in Section 3.1.2. We conclude from the results that spraying PCM reinforced with RN and PE fibers can restore the load-carrying capacity of the rebar-corroded beams to their original performance.

Table 6. Four-point flexural test results.

Specimen Name	P_y (kN)	P_u (kN)	$\% \Delta P_y$	$\% \Delta P_u$	Failure Type	Mass Loss of Each Tensile Bar (%)		
Group A	RC0 (1)	49.1	59.6	-	-	Flexural	-	-
	RC0 (2)	48.1	60.9	-	-	Flexural	-	-
	RN0 (1)	41.4	55.4	-14.8	-8.0	Flexural-shear	-	-
	RN0 (2)	45.1	58.0	-7.2	-3.7	Flexural-shear	-	-
	PE0 (1)	58.5	61.0	20.4	1.2	Flexural	-	-
	PE0 (2)	60.7	64.2	24.9	6.6	Flexural-shear	-	-
Group B	RC1	45.2	56.2	-7.0	-6.7	Flexural	0.9	1.8
	RN1	48.3	66.5	-0.6	10.4	Flexural-shear	0.8	0.7
	PE1	64.6	81.1	32.9	34.6	Flexural	0.6	0.7
Group C	RC1-NF	49.1	70.8	1.0	17.5	Flexural-shear	0.6	0.5
	RC1-RN	50.2	69.9	3.3	16.0	Flexural	0.6	0.5
	RC1-PE	62.0	69.7	27.6	15.7	Flexural	0.8	0.9

Note: P_y is the yield load and P_u is the ultimate load and $\% \Delta P_y$ and $\% \Delta P_u$ are the percent difference in P_y and P_u compared to the average of RC0 (1) and RC0 (2), respectively.

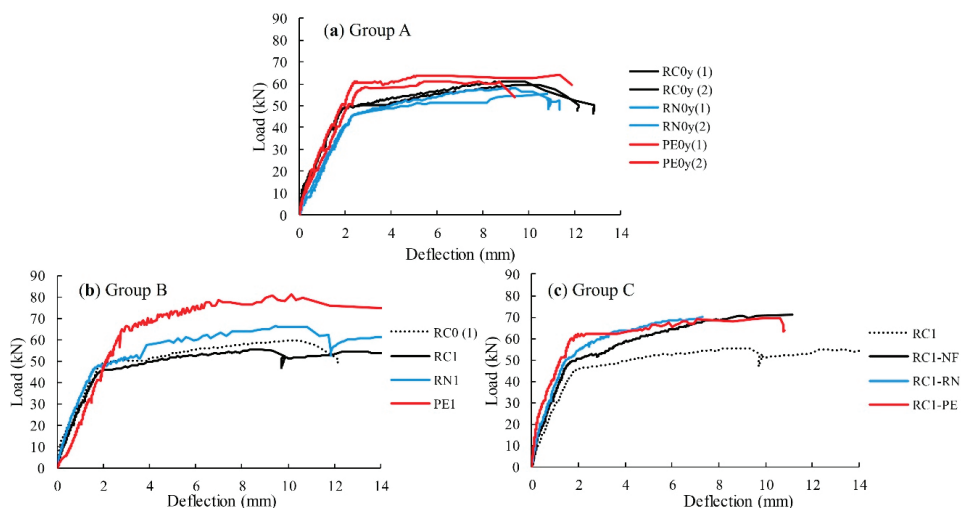


Figure 6. Load-midspan deflection curves of RC beams: (a) Group A; (b) Group B; and (c) Group C.

In general, a section repair is conducted by removal of the deteriorated concrete section and corroded rebars; however, with the usage of reinforced PCM, a section repair can be done without the removal of rebars. The early repair for slightly rebar-corroded beams is intended in this study. Adding fibers was found to compensate the tensile stresses that had been carried by corroded tensile rebars. The beams sprayed with PCM-RN could restore flexural capacity of the corroded RC beams, but were still less effective than PCM-PE.

3.2.2. Strain Distribution

Concrete strain was measured on the side surfaces of the beams at the midspan with the spacing of 30 mm. Strain distributions of the RC beams in group A are shown in Figure 7. PE0 showed almost linear strain distribution while RC0 and RN0 showed unbalanced strain distributions. For PE0, strain seems to increase linearly as the load increased, indicating that no separation occurred between PCM and the substrate concrete. The same tendency of uniform distribution of strain is also observed in groups B and C. The addition of fiber—especially PE—seems to help distribute strain throughout the beam. However, in some cases, cracks propagated outside the measurement area, and the strain gauge could only measure strain before it broke. Therefore, it is difficult to explain the actual phenomenon of the strain during the loading.

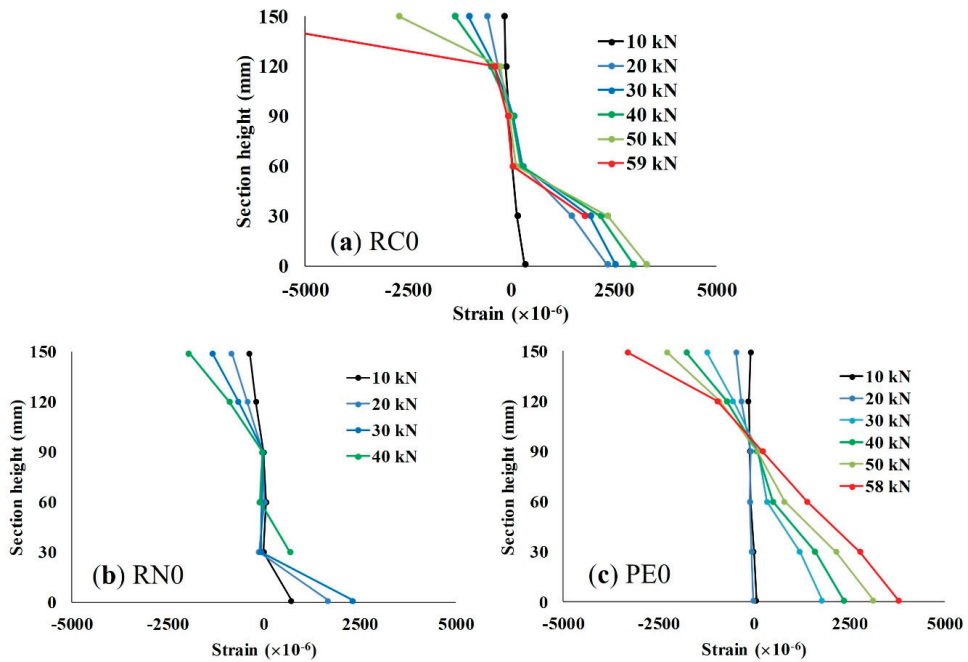


Figure 7. Strain distributions at the midspan of group A beams: (a) RC0; (b) RN0; and (c) PE0.

3.2.3. Crack Formation

The sides of the test beams were divided into many small grids for observing crack formation. Cracks were drawn manually on the beam just after the experiment, then plotted on a spreadsheet. Although only the cracks on the front side of the beams are reported, it was observed that the crack patterns on the back side of the beams were similar. Figure 8 shows the final crack formations on the side surface of the beams after the four-point bending test.

Crack openings on the bottom surface of the beams were also measured at the location of 25, 35, 45, 55, and 65 cm from the end of the beam, with the results plotted in Figure 9. It should be noted that for RC1–NF, RC1–RN and RC1–PE, the locations of the pi-type gauges were changed to 35, 40, 45, 50, and 55 cm because cracks tended to concentrate at the midspan of the beam.

The beams sprayed with PCM–RN and PCM–PE fibers showed more distributed cracks comparing to the normal RC beam. Especially for PE0 and RC1–PE, many small cracks were observed. For RN0 and RC1–RN, cracks were widely distributed and spread towards the support, rather than concentrated near the midspan of the beam. In contrast, cracks were observed to be most concentrated at the midspan for RC0 and RC1–NF. Adding fiber seems to facilitate stress transfer through cracks; therefore, fibers prevent serious damage from wider cracks by distributing into many small cracks. However, it should be noted that cracks formed in the outer side of the gauge-covered areas cannot be measured, which makes it difficult to evaluate the total increment rate of the crack opening.

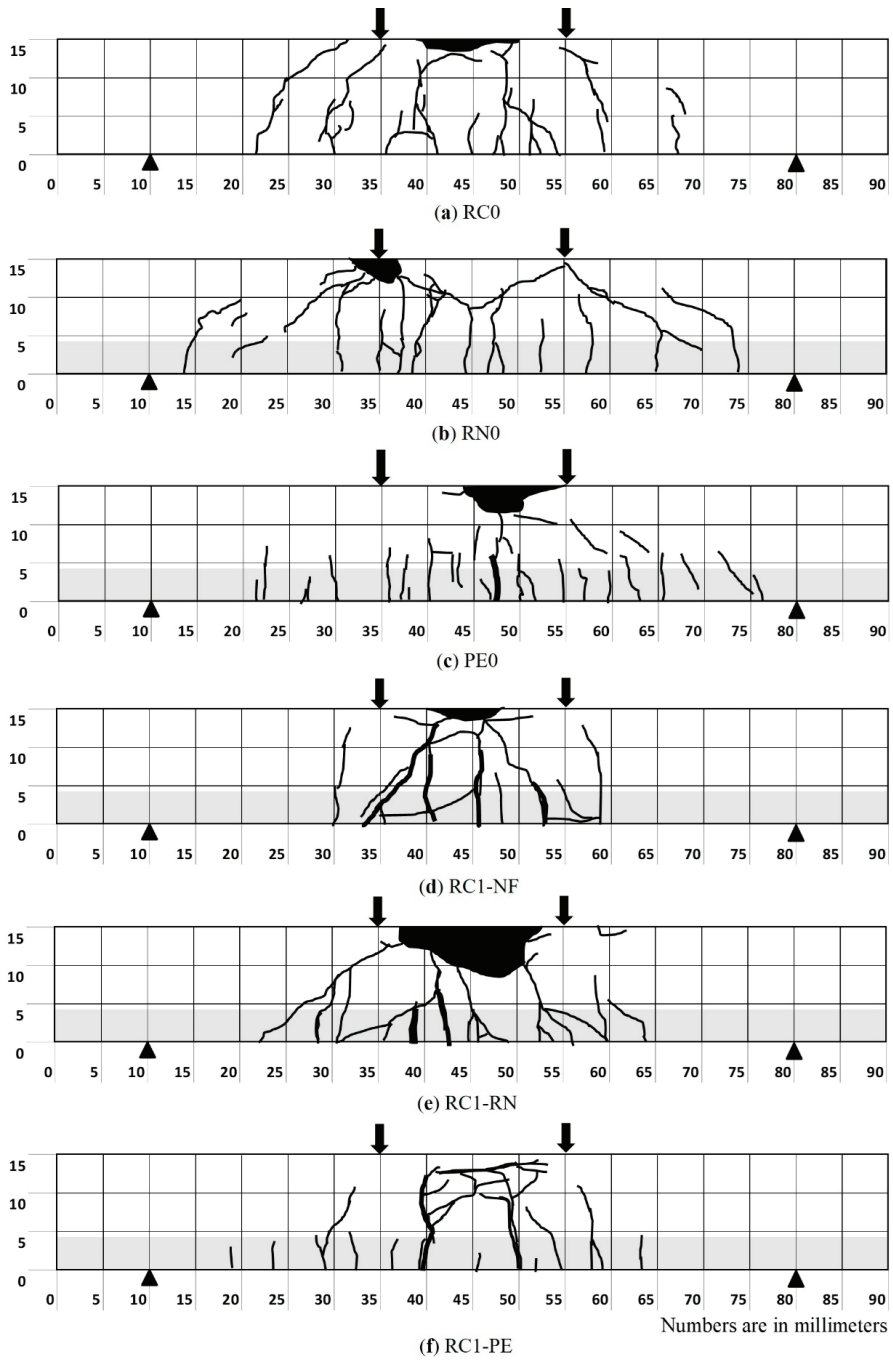


Figure 8. Final crack formation of the tested beams. (a) RC0; (b) RN0; (c) PE0; (d) RC1-NF; (e) RC1-RN; (f) RC1-PE.

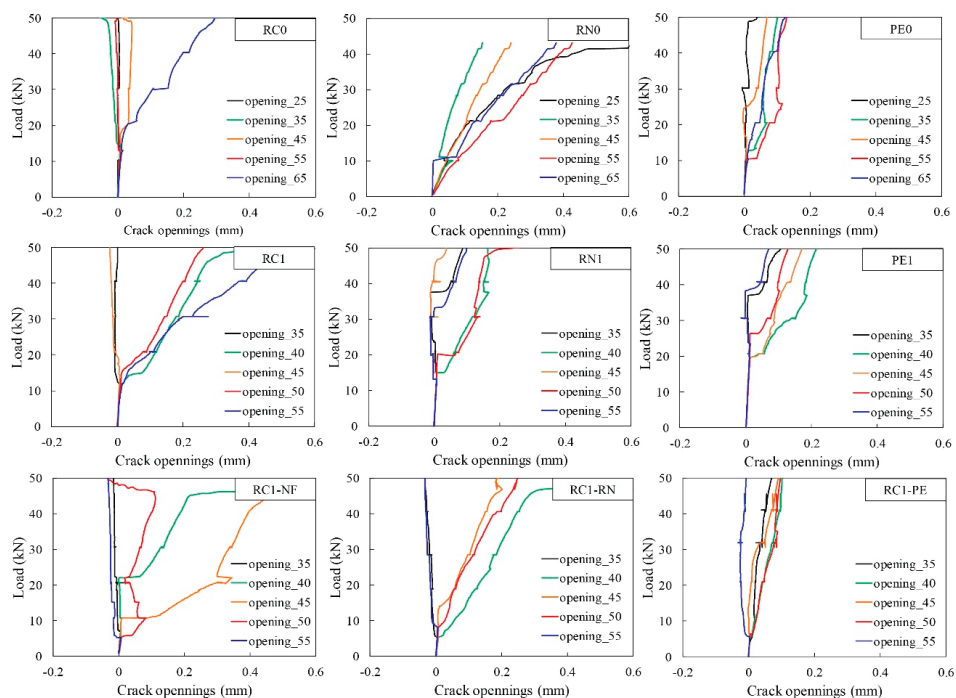


Figure 9. Crack openings at the bottom surface of the tested beams.

3.2.4. Rebar Mass Loss

All the beams were demolished after the flexural tests, and the tensile rebars were carefully collected. The rebars were washed using diammonium hydrogen citrate solution, and the mass of the remaining tensile rebar was measured. The percent mass losses of each tensile rebar are listed in Table 6. All the exposed beams had an average mass loss of 0.5% to 0.8% with RC1 exhibiting a slightly higher loss of 1.8%. The mass losses of RN1 and PE1 are slightly lower than that of RC1, likely due to the effect of fibers that reduce permeability and mitigate steel corrosion; however, further investigation is needed. Rebar mass loss confirmed that all exposed beams had almost the same level of corrosion.

4. Conclusions

This experimental study on PCM reinforced with RN and PE fiber for the repair of corroded RC beams reveals several findings. Results confirmed that recycled nylon fibers from waste fishing nets have great potential for the effective repair and upgrading RC structures, as they showed performance comparable to the manufactured PE fibers. As such, application of recycled fiber for civil engineering is a possible way of utilizing waste fishing nets. From this study, the following conclusions were drawn:

1. The addition of RN seems to have no noticeable effect on the flowability of fresh PCM. However, the addition of PE fiber results in a reduction of flowability of PCM up to 23.7% due to the geometry and surface property of PE fiber.
2. The addition of RN fiber results in a reduction of compressive strength and flexural capacity of PCM. In contrast, the addition of PE fiber increases the compressive and flexural strengths of PCM up to 24% and 39%, respectively.
3. The addition of RN and PE fibers enables the PCM to sustain more flexural loads after the peak. PCM-RN retains a stable post-peak load of approximately 13.6% of the yield load, while the use

- of PCM-PE led to an increase in the load after the yield point. The addition of RN short fiber helps prevent abrupt failure of the beams; however, its flexural strength is inferior to those of PE.
4. RN and PE fibers can be used as a reinforcement material for the repair of lightly corroded RC beams. Spraying reinforced PCM can compensate the flexural capacity that deteriorated due to the corrosion of tensile rebar; however, the effectiveness of the RN fibers is inferior to that of PE fibers.
 5. Adding fibers helps distribute stresses throughout the beam under the bending load. RN fiber helps transfer stresses through wide cracks and spreads the cracks toward the support of the beams. PE fiber prevents severe damage of the beams by distributing damage from a wide crack to many small cracks.
 6. The rate of crack openings is reduced in the RC beams repaired by PCM reinforced with fiber. The beams that were repaired with PCM-PE exhibit the lowest crack opening and the rate of crack openings, followed by PCM–RN.

The recycled nylon fibers from waste fishing nets tested in this study have been proven effective for reinforcing cementitious materials, and for repairing lightly corroded RC beams. It must be noted that, even though the effectiveness of using RN fiber is slightly inferior to the manufactured PE fiber, the use of recycled fiber promotes waste utilization from the ocean.

Further studies are still necessary in terms of pre-treatment, quality control of the recycled fiber, and durability against longer exposure. At the experimental scale, RN fibers were manually cut by hand, which is time consuming and not suitable for real applications. Processing machines need to be developed for mass production of RN fibers. Pre-treatment of fiber is also necessary to improve bond behavior between fibers and the cement substrate. Finally, factors affecting the durability are yet to be investigated, such as permeability, pore distribution and the chloride ion resistivity of the fiber-reinforced mortar.

Author Contributions: Methodology, Investigation and Writing—Original Draft Preparation, T.S.; Writing—Review and Editing, Supervision and Project Administration, H.Y.; Supervision, Validation, Resources and Investigation, Y.A. All authors have read and agreed to the published version of the manuscript.

Funding: This research was funded by JSPS Grant-in-Aid for Scientific Research (B), grant number 17H03293.

Acknowledgments: Shanya Orasuttikul, Hokkaido University, Haruka Matsuura, Hokkaido University, and Makoto Yamamoto, Sumitomo Osaka Cement Co., Ltd. are greatly appreciated for their supports and advice during this research.

Conflicts of Interest: The authors declare no conflict of interest.

References

1. Daily Mail Online. Available online: <https://www.dailymail.co.uk/sciencetech/article-7201755/Ocean-cleanup-effort-drags-5-TON-ghost-net-Pacific-Ocean-Garbage-Patch.html> (accessed on 28 August 2020).
2. Richardson, K.; Hardesty, B.D.; Wilcox, C. Estimates of fishing gear loss rates at a global scale: A literature review and meta-analysis. *Fish Fish.* **2019**, *20*, 1218–1231. [[CrossRef](#)]
3. Valderrama, L.B.; Matthews, J.L.; Hoeksema, B.W. Pollution and coral damage caused by derelict fishing gear on coral reefs around Koh Tao, Gulf of Thailand. *Mar. Pollut. Bull.* **2018**, *135*, 1107–1116. [[CrossRef](#)] [[PubMed](#)]
4. Hong, S.; Lee, J.; Lim, S. Navigational threats by derelict fishing gear to navy ships in the Korean seas. *Mar. Pollut. Bull.* **2017**, *119*, 100–105. [[CrossRef](#)] [[PubMed](#)]
5. National Geographic. Available online: <https://www.nationalgeographic.com/magazine/2018/06/plastic-planet-waste-pollution-trash-crisis/> (accessed on 28 August 2020).
6. Charter, M.; Carruthers, R.; Femmer, S.J. Products from Waste Fishing Nets Accessories, Clothing, Footwear, Home Ware, Recreation. *Circular Ocean.* **2018**.
7. Wang, Y. Fiber and textile waste Utilization. *Waste Biomass Valori.* **2010**, *1*, 135–143. [[CrossRef](#)]
8. Afroughsabet, V.; Ozbakkaloglu, T. Mechanical and durability properties of high-strength concrete containing steel and polypropylene fibers. *Constr. Build. Mater.* **2015**, *94*, 73–82. [[CrossRef](#)]

9. Alhozaimy, A.; Soroushian, P.; Mirza, F. Mechanical properties of polypropylene fiber reinforced concrete and the effects of pozzolanic materials. *Cem. Concr. Compos.* **1996**, *18*, 85–92. [[CrossRef](#)]
10. Allan, M.; Kukacka, L. Strength and durability of polypropylene fibre reinforced grouts. *Cem. Concr. Res.* **1995**, *25*, 511–521. [[CrossRef](#)]
11. Fallah, S.; Nematzadeh, M. Mechanical properties and durability of high-strength concrete containing macro-polymeric and polypropylene fibers with nano-silica and silica fume. *Constr. Build. Mater.* **2017**, *132*, 170–187. [[CrossRef](#)]
12. Karahan, O.; Atiş, C. The durability properties of polypropylene fiber reinforced fly ash concrete. *Mater. Des.* **2011**, *32*, 1044–1049. [[CrossRef](#)]
13. Ramezani-pour, A.; Esmaili, M.; Ghahari, S.; Najafi, M. Laboratory study on the effect of polypropylene fiber on durability, and physical and mechanical characteristic of concrete for application in sleepers. *Constr. Build. Mater.* **2013**, *44*, 411–418. [[CrossRef](#)]
14. Söylev, T.; Özturan, T. Durability, physical and mechanical properties of fiber-reinforced concretes at low-volume fraction. *Constr. Build. Mater.* **2014**, *73*, 67–75. [[CrossRef](#)]
15. Toutanji, H.; McNeil, S.; Bayasi, Z. Chloride permeability and impact resistance of polypropylene-fiber-reinforced silica fume concrete. *Cem. Concr. Res.* **1998**, *28*, 961–968. [[CrossRef](#)]
16. Zheng, Z.; Feldman, D. Synthetic Fibre-reinforced Concrete. *Prog. Polym. Sci.* **1995**, *20*, 185–210. [[CrossRef](#)]
17. Zhang, P.; Li, Q. Effect of polypropylene fiber on durability of concrete composite containing fly ash and silica fume. *Compos. B. Eng.* **2013**, *45*, 1587–1594. [[CrossRef](#)]
18. Özkan, Ş.; Demir, F. The hybrid effects of PVA fiber and basalt fiber on mechanical performance of cost effective hybrid cementitious composites. *Constr. Build. Mater.* **2020**, *263*. [[CrossRef](#)]
19. Lee, S. Effect of Nylon Fiber Addition on the Performance of Recycled Aggregate Concrete. *Appl. Sci.* **2019**, *9*, 767. [[CrossRef](#)]
20. Ozger, O.; Girardi, F.; Giannuzzi, G.; Salomoni, V.; Majorana, C.; Fambri, L.; Baldassino, N.; Di Maggio, R. Effect of nylon fibres on mechanical and thermal properties of hardened concrete for energy storage systems. *Mater. Des.* **2013**, *51*, 989–997. [[CrossRef](#)]
21. Qin, Y.; Zhang, X.; Chai, J. Damage performance and compressive behavior of early-age green concrete with recycled nylon fiber fabric under an axial load. *Constr. Build. Mater.* **2019**, *209*, 105–114. [[CrossRef](#)]
22. Alimrani, N.S.; Balazs, G.L. Synthetic fibres or fibre cocktail in terms of shear capacity of concrete after elevated temperatures. *Mech. Mater.* **2020**, *148*, 103504. [[CrossRef](#)]
23. Algin, Z.; Gerginci, S. Freeze-thaw resistance and water permeability properties of roller compacted concrete produced with macro synthetic fibre. *Constr. Build. Mater.* **2020**, *234*, 117382. [[CrossRef](#)]
24. Bankir, M.B.; Korkut Sevim, U. Performance optimization of hybrid fiber concretes against acid and sulfate attack. *J. Build. Eng.* **2020**, *32*, 101433. [[CrossRef](#)]
25. Wang, J.; Dai, Q.; Si, R.; Guo, S. Mechanical, durability, and microstructural properties of macro synthetic polypropylene (PP) fiber-reinforced rubber concrete. *J. Clean. Prod.* **2019**, *234*, 1351–1364. [[CrossRef](#)]
26. Simões, T.; Costa, H.; Dias-da-Costa, D.; Júlio, E. Influence of type and dosage of micro-fibres on the physical properties of fibre reinforced mortar matrixes. *Constr. Build. Mater.* **2018**, *187*, 1277–1285. [[CrossRef](#)]
27. Song, P.; Hwang, S.; Sheu, B. Strength properties of nylon- and polypropylene-fiber-reinforced concretes. *Cem. Concr. Res.* **2005**, *35*, 1546–1550. [[CrossRef](#)]
28. Merli, R.; Preziosi, M.; Acampora, A.; Lucchetti, M.C.; Petrucci, E. Recycled fibers in reinforced concrete: A systematic literature review. *J. Clean. Prod.* **2020**, *248*, 119207. [[CrossRef](#)]
29. Fraternali, F.; Farina, I.; Polzone, C.; Pagliuca, E.; Feo, L. On the use of R-PET strips for the reinforcement of cement mortars. *Compos. B. Eng.* **2013**, *46*, 207–210. [[CrossRef](#)]
30. Foti, D. Preliminary analysis of concrete reinforced with waste bottles PET fibers. *Constr. Build. Mater.* **2011**, *25*, 1906–1915. [[CrossRef](#)]
31. Pereira De Oliveira, L.; Castro-Gomes, J. Physical and mechanical behaviour of recycled PET fibre reinforced mortar. *Constr. Build. Mater.* **2011**, *25*, 1712–1717. [[CrossRef](#)]
32. Silva, D.; Betioli, A.; Gleize, P.; Roman, H.; Gómez, L.; Ribeiro, J. Degradation of recycled PET fibers in Portland cement-based materials. *Cem. Concr. Res.* **2005**, *35*, 1741–1746. [[CrossRef](#)]
33. Al-Hadithi, A.I.; Noaman, A.T.; Mosleh, W.K. Mechanical properties and impact behavior of PET fiber reinforced self-compacting concrete (SCC). *Compos. Struct.* **2019**, *224*, 111021. [[CrossRef](#)]

34. Adnan, H.M.; Dawood, A.O. Strength behavior of reinforced concrete beam using re-cycle of PET wastes as synthetic fibers. *Case Stud. Constr.* **2020**, *13*, e00367.
35. Pešić, N.; Živanović, S.; Garcia, R.; Papastergiou, P. Mechanical properties of concrete reinforced with recycled HDPE plastic fibres. *Constr. Build. Mater.* **2016**, *115*, 362–370. [[CrossRef](#)]
36. Yin, S.; Tuladhar, R.; Riella, J.; Chung, D.; Collister, T.; Combe, M.; Sivakugan, N. Comparative evaluation of virgin and recycled polypropylene fibre reinforced concrete. *Constr. Build. Mater.* **2016**, *114*, 134–141. [[CrossRef](#)]
37. Mohammadhosseini, H.; Abdul Awal, A.S.M.; Mohd Yatim, J.B. The impact resistance and mechanical properties of concrete reinforced with waste polypropylene carpet fibres. *Constr. Build. Mater.* **2017**, *143*, 147–157. [[CrossRef](#)]
38. Maria, I.; Bertelsen, G.; Ottosen, L. Engineering properties of fibres from waste fishing nets Materials, Systems and Structures in Civil Engineering Circular Ocean. In Proceedings of the International RILEM Conference on Materials, Systems and Structures in Civil Engineering: Conference Workshop on Cold Region Engineering, Copenhagen, Denmark, 22–24 August 2016.
39. Gurutz, M.; Galder, K.; Eider, M.; Nekane, G.; Aitor, A.; Cristina, P.R. Thermomechanical recycling of polyamide 6 from fishing nets waste. *J. Appl.* **2020**, *137*, 48442.
40. Spadea, S.; Farina, I.; Carrafiello, A.; Fraternali, F. Recycled nylon fibers as cement mortar reinforcement. *Constr. Build. Mater.* **2015**, *80*, 200–209. [[CrossRef](#)]
41. Park, J.K.; Kim, D.J.; Kim, M.O. Mechanical behavior of waste fishing net fiber-reinforced cementitious composites subjected to direct tension. *J. Build. Eng.* **2021**, *33*, 101622. [[CrossRef](#)]
42. Ottosen, L.M.; Svensson, S.J.; Bertelsen, I.M.G. Discarded nylon fishing nets as fibre reinforcement in cement mortar. *WIT Trans. Ecol.* **2019**, *231*, 245–256.
43. Orasutthikul, S.; Unno, D.; Yokota, H. Effectiveness of recycled nylon fiber from waste fishing net with respect to fiber reinforced mortar. *Constr. Build. Mater.* **2017**, *146*, 594–602. [[CrossRef](#)]
44. ASTM C1557-03, *Standard Test Method for Tensile Strength and Young's Modulus of Fibers*; ASTM International: West Conshohocken, PA, USA, 2003.
45. JSCE E 601, *Test Method for Half-Cell Potential of Uncoated Rebars in Concrete Structures*; Japan Society of Civil Engineers: Tokyo, Japan, 2002.
46. JIS A 1106, *Method of Test for Flexural Strength of Concrete*; Japan Standards Association: Tokyo, Japan, 2019. (In Japanese)
47. JIS R 5201, *Physical Testing Methods for Cement*; Japan Standards Association: Tokyo, Japan, 2015. (In Japanese)
48. JIS A 1108, *Method of Test for Compressive Strength of Concrete*; Japan Standards Association: Tokyo, Japan, 2018. (In Japanese)



© 2020 by the authors. Licensee MDPI, Basel, Switzerland. This article is an open access article distributed under the terms and conditions of the Creative Commons Attribution (CC BY) license (<http://creativecommons.org/licenses/by/4.0/>).

Article

Biom mineralization of Plastic Waste to Improve the Strength of Plastic-Reinforced Cement Mortar

Seth Kane ^{1,2,*}, Abby Thane ², Michael Espinal ^{1,2}, Kendra Lunday ³, Hakan Armağan ⁴,
Adrienne Phillips ^{2,5}, Chelsea Heveran ^{1,2} and Cecily Ryan ^{1,2}

¹ Mechanical and Industrial Engineering Department, Montana State University, Bozeman, MT 59717, USA; michael.espinal@student.montana.edu (M.E.); chelsea.heveran@montana.edu (C.H.); cecily.ryan@montana.edu (C.R.)

² Center for Biofilm Engineering, Montana State University, Bozeman, MT 59717, USA; abbyathane@gmail.com (A.T.); adrienne.phillips@montana.edu (A.P.)

³ Capital High School, Helena, MT 59601, USA; klunday@helenaschools.org

⁴ Omaha Burke High School, Omaha, NE 68154, USA; sezai.armagan@ops.org

⁵ Civil Engineering Department, Montana State University, Bozeman, MT 59717, USA

* Correspondence: sethkane@montana.edu; Tel.: +1-907-750-6364

Abstract: The development of methods to reuse large volumes of plastic waste is essential to curb the environmental impact of plastic pollution. Plastic-reinforced cementitious materials (PRCs), such as plastic-reinforced mortar (PRM), may be potential avenues to productively use large quantities of low-value plastic waste. However, poor bonding between the plastic and cement matrix reduces the strength of PRCs, limiting its viable applications. In this study, calcium carbonate biom mineralization techniques were applied to coat plastic waste and improved the compressive strength of PRM. Two biom mineralization treatments were examined: enzymatically induced calcium carbonate precipitation (EICP) and microbially induced calcium carbonate precipitation (MICP). MICP treatment of polyethylene terephthalate (PET) resulted in PRMs with compressive strengths similar to that of plastic-free mortar and higher than the compressive strengths of PRMs with untreated or EICP-treated PET. Based on the results of this study, MICP was used to treat hard-to-recycle types 3–7 plastic waste. No plastics investigated in this study inhibited the MICP process. PRM samples with 5% MICP-treated polyvinyl chloride (PVC) and mixed type 3–7 plastic had compressive strengths similar to plastic-free mortar. These results indicate that MICP treatment can improve PRM strength and that MICP-treated PRM shows promise as a method to reuse plastic waste.

Citation: Kane, S.; Thane, A.; Espinal, M.; Lunday, K.; Armağan, H.; Phillips, A.; Heveran, C.; Ryan, C. Biom mineralization of Plastic Waste to Improve the Strength of Plastic-Reinforced Cement Mortar. *Materials* **2021**, *14*, 1949. <https://doi.org/10.3390/ma14081949>

Academic Editor: Malgorzata Ulewicz

Received: 28 February 2021

Accepted: 7 April 2021

Published: 13 April 2021

Publisher's Note: MDPI stays neutral with regard to jurisdictional claims in published maps and institutional affiliations.



Copyright: © 2021 by the authors. Licensee MDPI, Basel, Switzerland. This article is an open access article distributed under the terms and conditions of the Creative Commons Attribution (CC BY) license (<https://creativecommons.org/licenses/by/4.0/>).

Keywords: plastic waste; cement; concrete; microbial-induced calcium carbonate precipitation; valorization; plastic-reinforced concrete; plastic recycling

1. Introduction

Plastic is one of the world's largest and fastest-growing waste streams, with 368 million tons of plastic waste generated in 2019 [1]. Plastic recycling rates remain low, with only 9% of plastics recycled, despite strong public interest [2]. The amount of plastic recycled is economically limited by the low cost of virgin plastic and the high costs associated with recycling processes such as transportation, sorting, cleaning, and extrusion. This limitation leads to low-value type 3–7 plastics typically being routed to the landfill or being improperly managed, thereby contaminating the environment. New approaches are urgently needed to reduce the volume of plastic waste sent to landfills and entering the environment.

The addition of waste materials to concrete has the potential to reuse large volumes of diverse waste streams including glass, plastic, and industrial waste [3–6]. The addition of waste to concrete provides the dual benefits of redirecting waste away from the landfill and reducing greenhouse gas emissions associated with cement production. In particular, plastic-reinforced cementitious materials (PRCs), such as plastic-reinforced mortar

(PRM), may allow for the repurposing of mixed-type plastic waste of varying geometries, eliminating the costly sorting process required for conventional plastic recycling [3,7–15]. The use of PRCs is currently limited by the low strength of these composites relative to conventional concrete [3,10]. This decrease in strength further declines with increasing volumes of plastic addition, constraining the amount of plastic waste that can be added to PRC. Three mechanisms have been proposed to explain this decrease in strength: (1) stress concentrations due to the low modulus of plastic relative to the cement matrix, (2) increased porosity with plastic addition, and (3) poor bonding between the plastic and cement matrix [3]. Several studies have attempted to improve the strength of PRC by improving the interfacial strength via pretreatment of the plastic [8,16–18]. One particularly promising treatment is the deposition of calcium carbonate (CaCO_3) onto the surface of the plastic. Both microbial and abiotic methods have been used to deposit CaCO_3 . Both methods increase the interfacial strength between polypropylene and the cement matrix and bending strength and locally increase cement hydration [17,18]. However, critical gaps remain in further evaluating the potential of CaCO_3 treatment to improve PRM strength. Notably, it is unknown how the method of CaCO_3 deposition used affects PRC strength, including the potential impacts of biofilms formed during microbial CaCO_3 treatment. Past studies have also been limited by examining only CaCO_3 treatment of polypropylene plastic. It is necessary to examine whether CaCO_3 pretreatment of other plastic types with limited markets for recycling would also benefit PRM strength.

Biom mineralization is one method to deposit CaCO_3 onto plastic. During CaCO_3 biom mineralization, the urease enzyme catalyzes the hydrolysis of urea to precipitate CaCO_3 . In the microbially induced calcium carbonate precipitation (MICP) process, the urease enzyme is produced by microorganisms, such as the soil bacterium *Sporosarcina pasteurii* (*S. pasteurii*) [19–21]. If urease enzymes are instead sourced from *Canavalia ensiformis* (i.e., jack bean), the process is termed enzymatically induced calcium carbonate precipitation (EICP) [22]. Both techniques have been applied to repair cracks in concrete and to seal leaky oil wells [19,23–27]. Either EICP or MICP could potentially be leveraged to control the deposition of CaCO_3 onto waste plastic, and both may be easier to scale at low cost than past techniques to deposit CaCO_3 onto plastic [17]. Prior to this study, it was not yet known if EICP- and MICP-precipitated CaCO_3 may differently affect the strength of PRM.

In this study, we examine the impact of CaCO_3 biom mineralization of plastic on PRM. We first compared EICP and MICP biom mineralization techniques to determine the impact of the biofilm in MICP treatment on CaCO_3 deposition onto plastic and the strength of the resulting PRM. To this end, mortar samples were reinforced with 1% and 5% of untreated polyethylene terephthalate (PET), MICP-treated PET, and EICP-treated PET and the compressive strength of the resulting PRM was evaluated. We then explored the feasibility of creating a CaCO_3 coating on the surfaces of type 3–7 and mixed type plastic, which have limited recycling markets. These plastics were mineralized with MICP to determine if any plastic types are inhibitory to the mineralization process. MICP-treated plastics were then added to cement mortar at 5% plastic, and the compressive strength of the resulting PRM was compared with untreated PRM and non-reinforced (plastic-free) mortar. We hypothesized that MICP treatment of waste plastic would improve the compressive strength of PRM relative to PRM prepared with unmineralized plastics. This study further develops CaCO_3 biom mineralization as a method to improve the strength of PRM by identifying the impact of biofilm formation on CaCO_3 deposition. By examining the application of MICP treatment to more plastic types than have been examined in past studies, this study establishes MICP as a potential treatment for other hard-to-recycle plastic types.

2. Materials and Methods

2.1. Materials

2.1.1. Plastic

Polyethylene terephthalate (PET) plastic additive was prepared by grinding PET clamshell food containers in a commercial laboratory blender (Model # 34BL97, Waring, Stamford, CT, USA) for two minutes at medium speed. The ground particles were passed through a 2 mm sieve followed by a 0.85 mm sieve to achieve a size fraction between these two values. This ensured that particle sizes were relatively uniform and did not exceed one-third of the minimum dimension of the mold that would be used to make future mortar specimens [28].

For batch-test comparisons to test for potential inhibition to the biomineralization process by uncommonly recycled plastic, polyvinyl chloride (PVC, type 3), low-density polyethylene (LDPE, type 4), polypropylene (PP, type 5), polystyrene (PS, type 6), and acrylonitrile butadiene styrene (ABS, type 7) plastic flakes were provided by Northwest Polymers (Molalla, OR, USA).

These flakes differed in geometry by plastic type. To directly compare the amount and morphology of biomineral formed on each plastic type during mineralization, the flakes were molded into disks of uniform size and thickness. Constant volumes of flakes were hot-pressed between two films of mylar into thin sheets on a hot press (Model # LCB1015-3, Auplex, Fuzhou, Fujian, China) at the temperatures shown in Table S1. Disk samples of 0.6 cm in diameter were cut from the thin sheets using a standard paper hole punch.

The geometries of ground, recycled plastic flakes for type 3–7 plastics varied by plastic type. To eliminate this uncontrolled variable of flake geometry, chopped 1.75 mm plastic filament was used to examine the effect of mineralization on PRM reinforced with type 3–7 plastics. Plastic filament was purchased from Filaments.ca (Mississauga, ON, Canada, accessed on 4 August 2020) Canada) for the PVC (Filamentum Vinyl 303 PVC—Black), LDPE (Filaments.ca LLDPE Filament—Natural), PP (Centaur Polypropylene Filament—White), PS (NefilaTek 100% Recycled HIPS Filament—Black), and ABS (NefilaTek 100% Recycled ABS Filament—Black) plastic types. The filament was cut into approximately 0.8 cm lengths with a goal upper limit of 1.6 cm using a paper cutter fitted with a 3D-printed cutting jig. This length was chosen to meet the fiber length reinforcement requirements specified for beam samples in ASTM International C1609 [28]. Before use, all plastics were disinfected by submerging in 70% ethanol for ten minutes and by rinsing three times with sterile deionized (DI) water. The density, tensile strength, and elastic modulus of each polymer fiber is described in Table S1.

For each type of plastic, random samples of 50 fibers were measured with calipers to estimate their overall length distribution. A normal Gaussian fit of the distribution of fiber lengths for each plastic type is shown in Figure S2. All mean lengths were within one standard deviation of the 8 mm goal length.

2.1.2. Mineralization Solutions

All chemicals were purchased through Fisher Scientific unless otherwise noted. The following solutions were used to grow *S. pasteurii*: brain heart infusion (BHI) media composed of 37 g/L brain heart infusion broth spiked with 20 g/L urea and calcium mineralizing media containing 3 g/L nutrient broth, 10 g/L ammonium chloride, 20 g/L urea (CMM−), adjusted to pH 6.15 and spiked with 49 g/L calcium chloride dihydrate (CMM+). All solutions were prepared with DI water and filtered with sterile syringe filters with 0.2 µm cellulose acetate membrane (VWR part # 28145-475, Radnor, PA, USA) before use.

For EICP tests, a similar solution composed of urea (20 g/L) and calcium chloride dihydrate (49 g/L) (U + C) in DI water that did not include nutrients necessary for microbial growth was used. This solution was prepared immediately before use and was not filter sterilized.

2.2. Batch Testing for Microbial Growth and Plastic Biomineralization

Batch tests were completed for the PET flakes and type 3–7 disks (1) to determine if *S. pasteurii* cells can attach to the surface of each plastic during MICP, (2) to evaluate if the addition of plastics inhibits biomineralization processes, and (3) to examine the physical characteristics and amount of precipitates on each type of plastic. No inhibition batch tests were performed on the EICP process as it was observed that the MICP process was not inhibited under the conditions and time scale tested.

2.2.1. MICP Biomineralization of PET

The following conditions were tested in triplicate using PET flakes: (1) *S. pasteurii* with PET (test condition), (2) *S. pasteurii* without PET (positive control), and (3) PET without *S. pasteurii*. (negative control) (Table 1). An *S. pasteurii* (ATCC 11859) starter culture was prepared in brain heart infusion (BHI) and precipitation was promoted using calcium mineralizing medium (CMM) as described in past studies [29,30].

Table 1. Experimental matrix for both polyethylene terephthalate (PET) and plastic types 3–7 microbially induced calcium carbonate precipitation (MICP) batch study.

	Attachment Phase	Mineralization Phase
Test condition	<i>S. pasteurii</i> , plastic, CMM–	Plastic (with biofilm), CMM+
Positive control	<i>S. pasteurii</i> , CMM–	None
Negative control	Plastic, CMM–	Plastic (no biofilm), CMM+

PET plastic flakes (1 g) and either 1 mL of *S. pasteurii* culture or no bacteria (negative control) were added to Erlenmeyer flasks filled with 100 mL BHI. The flasks were incubated on a shaking table at room temperature (Innova 2400 Platform Shaker, New Brunswick Scientific, Enfield, CN, USA). The samples were collected for optical density at 600 nm (OD_{600}) measured in triplicate on 200 μ L in a 96-well plate by a Biotek spectrophotometer at 0, 1, 2, 4, 8, and 24 h, and pH and urea concentration were measured at 0, 8, and 24 h (Fisher Accumet probe, AR20 Accumet pH and conductivity meter, Fisher Scientific, Waltham, MA, USA). The samples were filtered (VWR sterile syringe filters with 0.2 μ m cellulose acetate membrane) and stored at 4 °C before assessment of the urea concentration using a modified Jung colorimetric assay [31,32].

2.2.2. Types 3–7 Biomineralization Comparisons

More extensive batch tests were completed for plastic types 3–7. The tests were conducted in two phases: (1) a 24 h attachment phase to evaluate biofilm growth on plastics and (2) a 24 h mineralization phase to assess biomineral formation. Three conditions (Table 1) were tested in triplicate. In phase 1, twenty plastic discs were added to each of the test and negative control flasks filled with 100 mL CMM for each of type 3–7 plastics. The flasks were incubated and sampled at 0, 4, 8, and 24 h for pH, OD_{600} , and urea concentration as described above.

After the 24 h biofilm growth phase, 19 disks from each flask were transferred to 250 mL flasks with 100 mL CMM+ for the mineralization phase. The flasks were shaken for 24 h at room temperature. At 0 and 24 h, the samples were collected for pH and urea concentration analysis as described above.

2.2.3. Calcium Digests

A calcium digest was performed to estimate the mass of calcium carbonate formed on the plastic. For PET plastic mineralized with MICP, 10 g PET flakes were added to 100 mL BHI inoculated with a 1 mL *S. pasteurii* cryo-stock and shaken at 150 rpm and 30 °C for 24 h. The plastic was then transferred to 100 mL CMM+ and shaken for an additional 24 h. For PET plastic mineralized with EICP, 5 g PET flakes were added to 100 mL U + C with 5 g/L jack bean meal (jack bean fine powder, Sigma-Aldrich product #J0125, St Louis, MO,

USA) as the urease source and shaken at room temperature for 24 h. After mineralization, the plastic was dried at room temperature for 24 h. Three samples of plastic weighing 1 g each were acid digested using the procedure described above to assess the mass of calcium.

For plastic types 3–7, three disks from each flask were weighed and added to a 15 mL centrifuge tube containing 5 mL 10% trace metal grade nitric acid (Fisher Scientific, A509-P212). The tubes were vortexed and left for 24 h at room temperature. The supernate was then removed from each tube, serially diluted, and analyzed for calcium concentration using a colorimetric calcium assay [33]. The disks were dried at room temperature for 24 h and weighed a second time. The weight difference before and after digestion was compared to the mass of calcium carbonate calculated from the concentration found in the supernate.

2.2.4. X-ray Diffraction Spectroscopy

Untreated PET, EICP-PET, and MICP-PET samples were analyzed with a SCINTAG X1 X-ray Powder Diffraction Spectrometer (XRD) to identify calcium carbonate polymorphs. The samples were held on a glass slide with Vaseline and analyzed from 2θ of $3\text{--}75^\circ$.

2.3. Preparation and Testing of Plastic-Reinforced Mortar Specimens

Cement mortar cylinder specimens were prepared for the test conditions described in Table 2. The impacts of EICP- and MICP-treated PET were assessed at 1 and 5 wt.%; for plastic types 3–7 individually and mixed, and the impact of MICP-treated plastics were only evaluated at 5 wt.%.

Table 2. Cement mortar cylinder specimen experimental matrix.

Plastic Type (s)	Mineralization Method	wt.% Replacement
PET	EICP	1%, 5%
PET	MICP	1%, 5%
PET	None	1%, 5%
Types 3–7	MICP	5%
Types 3–7	None	5%
None (control)	None	0%

2.3.1. Mineralization of Plastic

PET flakes were mineralized via EICP as described in Section 2.2.1.

PET flakes were treated with MICP by adding flakes to flasks containing BHI inoculated with *S. pasteurii*. After shaking at 150 rpm and 30°C for 24 h, the fluid was strained out of the BHI culture and drained, and CMM+ was added for an additional 24 h treatment at room temperature. The plastic was then strained out of the solution and dried at room temperature.

Type 3–7 plastics (treated individually and as an equal mass mixture) were treated with MICP by placing 121 g of plastic into a mesh bag that was submerged in 700 mL of CMM+ in a 1 L beaker on a stir plate (MIRAK, Barnstead Thermolyne), mixing at 140 rpm (Figure S1). The beakers were inoculated with 14 mL of an *S. pasteurii* culture. The beakers were covered loosely with aluminum foil and incubated for 48 h at room temperature. After mineralization, the fluid was drained and the plastic fibers were dried at room temperature for 24 h.

2.3.2. Cement Mortar Production

Cement mortar cylinders are prepared for the experimental conditions shown in Table 2. Mortar specimens were prepared following a procedure based on ASTM International C109 [34]. Each batch was mixed with 2500 g of ordinary Portland cement (Quikrete, commercial grade) with 0 wt.%, 1 wt.%, or 5 wt.% of cement replaced with the equivalent weight of plastic. To control for the amount of plastic between untreated and mineralized

plastic, the plastic was weighed pre-mineralization. A cement:sand ratio of 0.8 and a water:cement ratio of 0.46 were used for all batches. Cement mortar was mixed following the procedure described in ASTM International C305 [35].

Cylinder molds (2 in D × 4 in H (5.08 cm × 10.1 cm); Bio-cylinder, Deslauriers Inc., La Grange Park, IL, USA) were sprayed with a thin coat of vegetable oil before the addition of cement mortar. The mortar was added to the molds following the procedure described ASTM C192 [36]. After molding, the specimens were stored in a concrete curing room at 100% relative humidity until testing. Specimens were demolded 24 h after mixing and returned to the cement curing room until testing.

2.3.3. Cement Mortar Compressive Testing

Strength testing was completed for cylinder specimens with an MTS Criterion Model 64 load frame on days 14 and 28 of curing. Due to instrument maintenance issues, PET specimens and their controls were tested on day 35 rather than day 28. Specimen strengths are not expected to change after 28 days of curing. Neoprene caps were placed over the end of the cylinder specimens, and the specimens were compressed between the lower crosshead and the test table. Compression was performed at a constant rate of 0.127 mm/s (0.005 in/s) until failure.

2.4. Microscopy

Mineralized plastic samples and PRM samples were examined on a Field Emission Scanning Electron Microscope (FESEM). The samples were placed on carbon sticky dots, sputter-coated with gold on an Emitech K-875X Sputter Coater, and examined on a Zeiss Supra 55VP FESEM at 1 kV and a working distance of 3.9–5.3 mm with an SE2 detector.

Confocal images of *S. pasteurii* attachment to PET were collected using a Leica CS upright confocal microscope (TCS SP5 IIDM6000, Leica Microsystems, Buffalo Grove, IL, USA), as described in Section S1.1 of the Supplementary Materials.

2.5. Characterization of Cement Hydration and Structure

Cement paste samples were prepared to determine the effect of MICP-produced biomineral on the degree of hydration and cement crystalline structure. Mixed type 3–7 plastics were mineralized following the submersion method in Section 2.3.1. To obtain a macroscopically homogeneous cement paste sample, the biomineral was scraped off of the plastic and ground to a powder. The cement paste samples were prepared with a 0.46 water:cement ratio and no sand, with 0%, 1%, and 5% of the cement replaced with biomineral. Sample mixture followed the procedure described in Section 2.3.2. Samples were molded in weigh boats (Thermo Scientific, part #08-732-112) and cured as in Section 2.3.2. After 1, 7, 14, and 28 days of curing, a sample of each mineral amount was removed from the curing room, allowed to dry, and ground into a powder with a mortar and pestle for use in the thermogravimetric analysis (TGA) and XRD measurements.

TGA was performed on a TA Instruments Q5000-IR TGA (TA Instruments Inc., New Castle, DE, USA) to determine the degree of hydration of the cement paste samples. Triplicate samples of 40–50 mg of cement paste powder were placed in TA Instruments high-temperature platinum TGA pans for each of the 0%, 1%, and 5% biomineral samples. The samples were heated from 30 °C to 1000 °C at 10 °C/min. Weight loss data were analyzed to determine the degree of hydration following the method described by Monteagudo et al., with modification of decarbonation beginning at 390 °C rather than 400 °C to include the full TGA derivative peak observed at that temperature [37,38]. A value of 24% was used to correspond to complete hydration [38].

XRD measurements were taken of the cement paste samples as in Section 2.2.4. Jade (Materials Data Inc., Livermore, CA, USA) was used to identify the peaks associated with the phases present within both the biomineral and hydrated cement phases. Whole pattern matching was used to determine the relative semi-quantitative phase composition of the hydrated cement with and without biomineralized plastic [39–43].

2.6. Data Analysis

All statistical analyses were performed in Minitab (vers. 19.2020.1, Minitab LLC, State College, PA, USA). Critical alpha was set a priori to 0.05 for all analyses. The effect of the addition of untreated PET on mortar compressive strength was evaluated using one-way ANOVA. Two-factor ANOVA evaluated the effects of the amount of PET and type of mineralization treatment (MICP and EICP) on the dependent variables of compressive strength and modulus. Additional models compared the effects of plastic type and mineralization type on PRM strength and modulus. For all models, the residuals satisfied the assumptions of normality and homoscedasticity. Follow-up testing was performed using the Bonferonni method, where critical alpha was divided by the number of comparisons to control family-wise error.

3. Results and Discussion

3.1. Comparison of EICP and MICP Treatment of PET

In the first study comparing EICP and MICP treatment, PET did not impair the growth of *S. pasteurii* in a flask culture. This was shown by OD₆₀₀ and pH measurements that matched those of the no-PET control over a 24 h growth study (Figure S3). Urea concentration decreased and pH increased at similar rates over time both with and without PET (Figure S3), indicating that the reaction was not impaired by plastic. Attachment of *S. pasteurii* to the PET flakes was observed via both confocal microscopy and FESEM (Figure 1). This demonstrates that *S. pasteurii* was successful in forming biofilms on the PET flakes under the conditions tested.

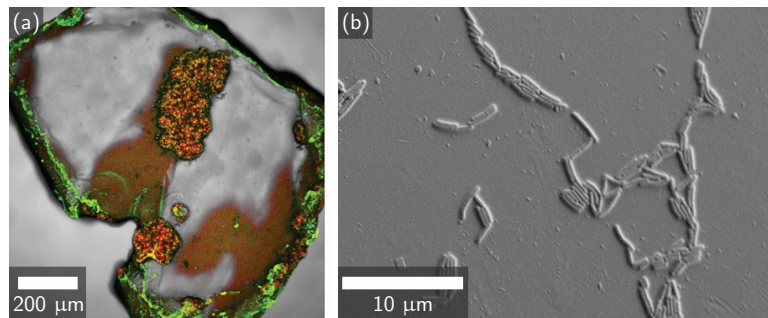


Figure 1. (a) Confocal image of *S. pasteurii* attachment and CaCO₃ precipitation of a MICP-treated PET flake at 10× magnification. The *S. pasteurii* biofilm is stained green, biomineral deposits are stained red, and yellow represents regions where both the biofilm and biomineral are present. (b) FESEM image of *S. pasteurii* bacteria attachment to a PET flake at 4700× magnification.

Both MICP and EICP formed a CaCO₃ coating on PET flakes. MICP treatment deposited more CaCO₃ on PET than EICP treatment as measured by both calcium assay and mass change (Figure 2a). XRD measurements showed similar spectra for both EICP and MICP. Both mineralization methods were observed to have calcite and vaterite phases of CaCO₃ (Figure 2b). The observed broad amorphous bands are attributed to the PET. No other phases of CaCO₃ or other minerals were identified. This finding is consistent with past work that found that EICP can produce the calcite phase of CaCO₃ [44,45] while MICP may precipitate vaterite as a transient, meta-stable, lower-modulus phase that eventually transforms to calcite [44,46,47]. FESEM imaging of the biomineral shows evidence that EICP produced faceted polycrystals with a length of approximately 1–5 μm (Figure 3a). In contrast, images of MICP-treated PET showed evidence of predominantly large, rounded structures composed of very small polycrystals (<1 μm facets) (Figure 3b).

The differences between EICP and MICP biomineral morphology may depend on the influence of bacteria. Smaller CaCO₃ crystals are produced at higher saturation states, and microorganisms in MICP would locally increase saturation state [46]. During EICP, urease

enzyme from jack bean would be expected to affect the solution more uniformly [46]. Furthermore, these bacteria can produce extra polymeric substances that may stabilize forming surfaces [19,23]. This proposed mechanism is shown in Figure 4. MICP's greater deposition of CaCO_3 on PET could result from the attachment of bacteria to PET (Figures 1 and 4) and then nucleation of CaCO_3 on bacterial cell walls [20,21,48]. In contrast, during EICP, CaCO_3 forms without these benefits from microbial cells.

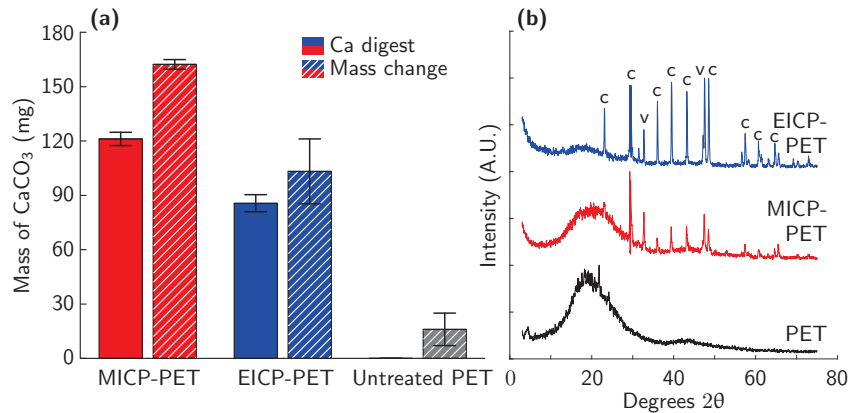


Figure 2. (a) Calcium assay and mass change means for MICP-treated PET flakes, enzymatically induced calcium carbonate precipitation (EICP)-treated PET flakes, and a control sample of untreated PET flakes. The error bars indicate one standard deviation. (b) XRD spectra for PET flakes (black), EICP-treated PET flakes (blue), and MICP-treated PET flakes (red). Peaks labeled c represent the calcite phase of CaCO_3 , while peaks labeled v represent the vaterite phase. No aragonite phases or other minerals were observed.

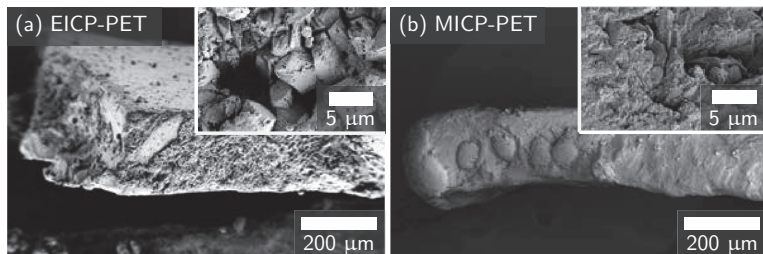


Figure 3. FESEM images of EICP-treated PET (a) and MICP-treated PET (b) at approximately 300 \times magnification. Inset images show details of the CaCO_3 texture at approximately 10k \times magnification. An image of an untreated control sample is shown in Figure S4.

After 35 days of curing, compressive strength decreased for PRM with untreated PET ($p < 0.001$, Figure 5a). PRM samples with 5% PET showed a larger decrease in strength than PRM samples with 1% PET (Table 3, $p < 0.01$). This is consistent with prior reports of losses in strength for similar additions of untreated PET to cement mortar [3]. Two-way ANOVA testing showed a significant interaction ($p < 0.05$) between the effect of the amount of PET replacement and mineralization technique (EICP or MICP) on PRM compressive strength. Post hoc testing found that PRM samples with 1% EICP-treated PET and 1% MICP-treated PET both show similar compressive strengths to non-reinforced mortar samples (Table 3, $p > 0.05$ for each). In contrast, PRM samples with untreated PET were found to have significantly lower compressive strength than non-reinforced mortar samples (Table 3, $p < 0.05$). At the 5% PET level, EICP-treated PET and untreated PET reinforced mortar show similar compressive strengths ($p > 0.05$) while PRM samples with MICP-treated PET

show significantly higher strength than either EICP-treated PET or untreated PET ($p < 0.05$ for both). No treatments or amounts of PET added to PRM samples had a significant effect on compressive modulus ($p > 0.05$, Figure 5b). Similar trends are seen for compressive strength and modulus measurements taken after 14 days (Table S2).

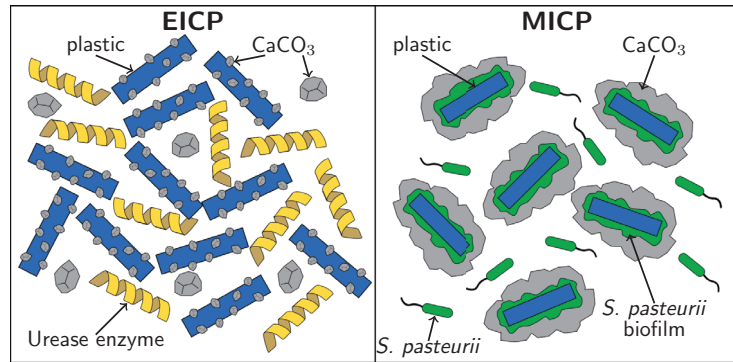


Figure 4. Proposed mechanism for the differences between EICP and MICP biomineralization of plastic. The formation of a biofilm on the plastic in MICP localizes CaCO_3 precipitation to the surface of the plastic, while EICP biomineralization is more evenly distributed throughout the solution.

Table 3. Change in mean cement mortar compressive strength relative to the mean for non-reinforced mortar control when reinforced with untreated PET, EICP-treated PET, or MICP-treated PET at 1% or 5% replacement after 35 days of curing.

Plastic Replacement	Change in Compressive Strength Relative to Control		
	Untreated PET	EICP-PET	MICP-PET
1%	−14.6%	−3.74%	−2.54%
5%	−30.1%	−29.2%	−11.9%

One possible explanation for the strength differences could be that the untreated PET was not well bonded to the cement matrix. FESEM imaging of the failure interface of PRM with untreated PET provides evidence to support this explanation, with a gap visible at the interface for the assessed sample (Figure 6a). In contrast, images of both EICP-treated PET (Figure 6b) and MICP-treated PET (Figure 6c) showed a continuous interface between the mineralized plastic and the surrounding cement matrix. This improved contact along with the observed increase in compressive strength supports the hypothesis that biomineralization of plastic waste could improve the interfacial strength between plastic waste and cement. However, additional work directly measuring the effect of mineralization on interfacial strength is needed to further test this hypothesis.

These results show that, at 1% plastic replacement, both EICP and MICP mineralization of PET results in comparable PRM compressive strengths that are higher than those of mortar reinforced with untreated PET. Because MICP requires additional infrastructure to culture cells, this indicates that EICP may be an appropriate biomineralization choice for low-volume PET applications. An important result is that mortar reinforced with 5% treated PET shows significant improvements in strength over both EICP-treated PET and untreated PET, with compressive strengths similar to 1% untreated PET-reinforced mortar. This result shows that MICP treatment allows for the use of higher volumes of plastic, with less loss in strength than would be expected in untreated plastic. In applications where density is of concern, 5% MICP-treated PET mortar shows even more promise due to the decrease in density with the addition of higher quantities of PET [3].

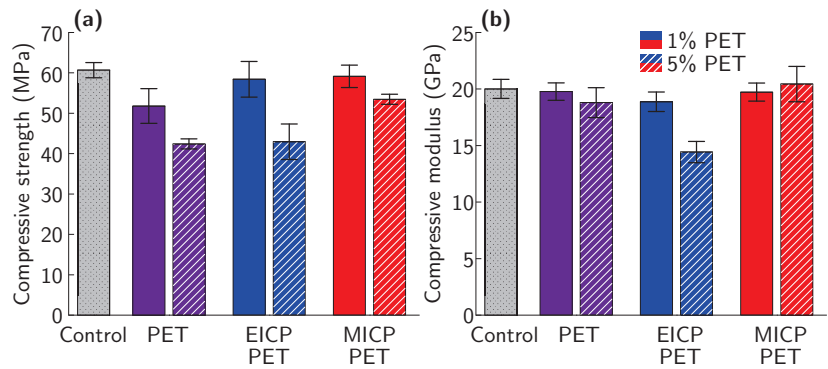


Figure 5. Comparison of (a) compressive strength and (b) compressive modulus for non-reinforced mortar and mortar reinforced with 1% and 5% untreated PET, 1% and 5% EICP-treated PET, and 1% and 5% MICP-treated PET after 35 days of curing. Values for 14 and 35 day compressive strength and modulus are listed in Table S2. Representative stress-strain curves for these sample types are shown in Figure S6.



Figure 6. FESEM images of the interface between PET flakes and the cement mortar for (a) untreated PET, (b) EICP-treated PET, and (c) MICP-treated PET.

We hypothesize that the observed difference in compressive strength of PRM between EICP and MICP treatments is due to the increased deposition of CaCO_3 with MICP treatment (Figure 2). Hao et al. found that a higher mass of CaCO_3 coating on plastic increased the fiber pullout strength of plastic from cement mortar up to a peak value, after which pullout strength rapidly decreased [18]. Another potential mechanism is that the increased texture of MICP CaCO_3 could provide more surface area for interaction with the cement matrix during cement hydration and mechanical loading. Further work is required to explore these hypotheses.

3.2. Comparison of MICP Treatment of Type 3–7 Plastics

The results of the EICP and MICP comparison (Section 3.1) were used to inform mineralization strategies for type 3–7 plastics. MICP was chosen to mineralize type 3–7 plastics as it resulted in higher strength PRMs than EICP treatment in comparisons of PET. We chose 5% plastic replacement of cement for type 3–7 plastics based on the results of our PET study. While a modest strength decrease is seen with 5% plastic replacement, it is much lower with MICP treatment compared with untreated plastic and allows for the use of more plastic waste.

All plastic types 3–7 were successfully biomineralized. OD_{600} , pH (Figure S5), and urea concentration measurements (Figure 7a) all show the biomineralization reaction progressing to the same degree as the plastic-free positive control. However, the amount of CaCO_3 deposited on the plastic varies by plastic type (Figure 7b). MICP-treatment deposited the least amount of CaCO_3 on ABS when measured with both mass change and calcium assay, while PVC sees the highest amount of CaCO_3 deposition with both measurements. PP, PS, and PVC have large variations in the mass of CaCO_3 deposited, indicating that the mineralization of these samples may not be uniform. Representative FESEM images for each type of plastic show that different MICP-treated plastics have

different mineral morphologies (Figure 8). FESEM images of MICP-treated PVC show a uniform mineral coating, with a consistent mineral structure. MICP-treated ABS has more scattered and clumped mineralization. MICP-treated LDPE, PP, and PS each show a unique mineral structure, with LDPE and PP showing consistent mineral structures, similar to PVC, while PS shows a scattered mineral coating, more similar to ABS. The crystal morphology also differs by plastic type, with ABS and PS showing sharp crystals approximately 5 μm in size, while PVC, LDPE, and PP all show smaller, more rounded crystals.

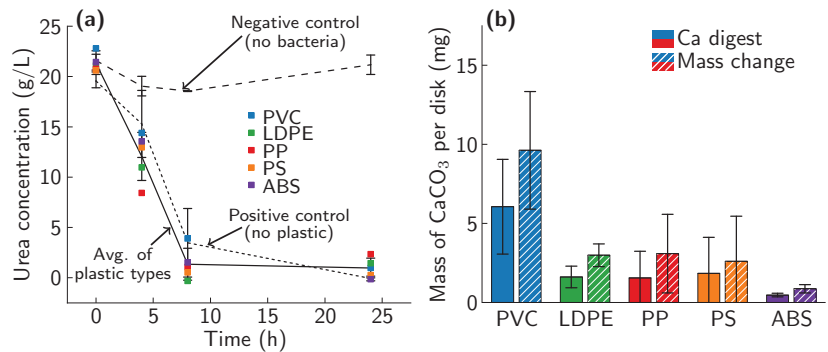


Figure 7. (a) Urea concentration results for each plastic type batch test, a no-bacteria negative control, and a plastic-free positive control. (b) Mean amount of CaCO_3 present for each plastic type as measured by mass change (dashed) and calcium assay (solid). Error bars indicate one standard deviation.

For the submersion method, on average, 0.22 ± 0.01 mg CaCO_3 was deposited per mm of fiber length for all plastic types except ABS (Figure 9). ABS had an average of 0.13 mg CaCO_3 /mm of fiber length. Additionally, 14% of ABS fibers measured were found to have no mineral, compared to 6% for PP, 4% for PVC, and 0% for all other plastic types. Additional evidence from the batch tests (Figure 7) and FESEM imaging (Figure 8) leads us to hypothesize that MICP may be less effective at mineralizing ABS than other plastic types. However, additional work is needed to further support this hypothesis and to understand the mechanisms behind the observed differences. Less variation in CaCO_3 mass between plastic types is observed in these samples than in batch tests (Figure 7a). This demonstrates the success of the submersion method in more uniformly coating plastics than the plastic-in-solution method used in the batch tests.

The amount of CaCO_3 deposited on plastic with the submersion method was found to be greater than that observed in past studies of plastic treatment with MICP. Hao et al. reported that mineralization of PP with MICP formed 0.026 g CaCO_3 per g PP after 24 h of mineralization and increasing amounts at longer mineralization times [18]. Our MICP-treated PP shows an average value of 0.098 g CaCO_3 /g PP after 24 h of mineralization. Similarly, PVC (0.064 g CaCO_3 /g PVC), LDPE (0.105 g CaCO_3 /g LDPE), PS (0.086 g CaCO_3 /g PS), and ABS (0.052 g CaCO_3 /g ABS) show more CaCO_3 deposition than the method used by Hao et al. deposited in 24 h for PP. The mass of CaCO_3 deposited by the submersion method is similar to the 0.096 g CaCO_3 /g plastic that Hao et al. found to provide the largest increase in fiber pullout strength from cement mortar [18].

MICP treatment increased compressive strength for some, but not all, plastic types (Figure 10a). An interaction between MICP treatment and plastic type was observed for compressive strength of PRM reinforced with untreated and MICP-treated type 3–7 plastics. Post hoc testing shows a significant increase in compressive strength for mortar samples reinforced with MICP-treated PVC relative to mortar samples reinforced with untreated PVC (18% increase, $p < 0.05$). LDPE, PP, PS, ABS, and mixed plastic all show no statistically significant change in PRM for samples treated with MICP relative to untreated plastic of the same type ($p > 0.05$ for all). Mortar reinforced with 5% MICP-treated PVC shows

promising strength, with an average compressive strength at 97% of the average of the plastic-free control mortars. Mortar reinforced with 5% mixed type 3–7 plastics also shows high compressive strength, at 91% of the average of the non-reinforced mortar controls. As mixed plastic waste has the advantage of avoiding costly plastic waste sorting, this is an especially promising result. Only untreated LDPE samples show a significant change in compressive modulus relative to the plastic-free controls ($p < 0.05$), indicating that neither the addition of most types of plastic nor mineralization has a significant impact on compressive modulus (Figure 10b). Similar trends are seen for compressive strength and modulus measurements taken after 14 days (Table S2).

FESEM imaging of the interface between plastic and cement at the fracture surface show evidence supporting a reduction in the gap at the interface between plastic and cement with mineralization (Figure 11 and Figure S8). In images of one sample of PVC, which sees the largest increase in compressive strength with MICP treatment, MICP-treated PVC was observed to have a cement matrix on the surface of the plastic after failure, while untreated PVC does not (Figure 11). This may indicate improved bonding between PVC and the cement matrix. To better understand the failure mechanisms of mineralized PRM and to explain the differences observed between plastic types, additional work is needed to quantify the fiber pullout strength of each plastic type with and without mineralization.

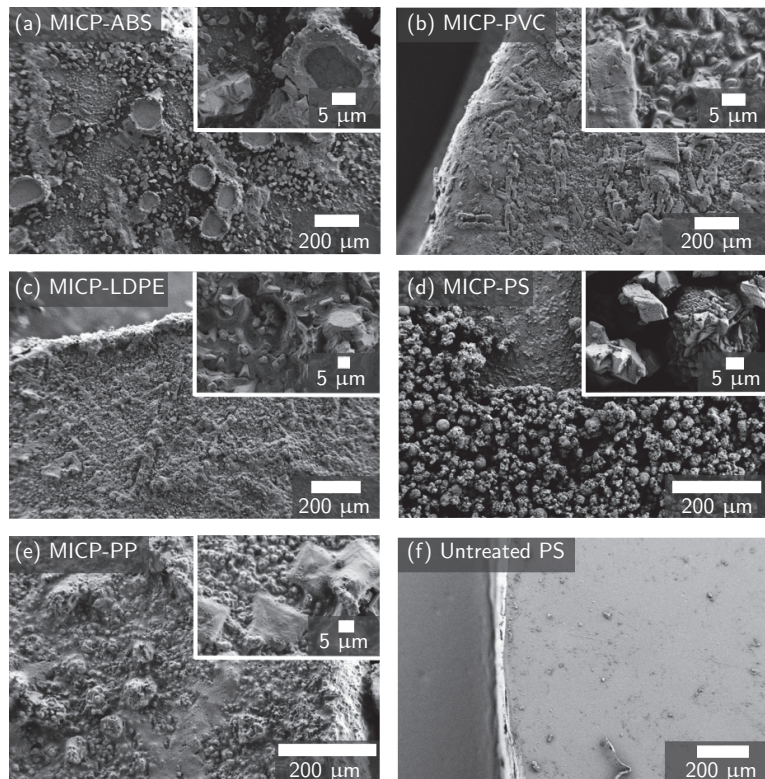


Figure 8. FESEM images of MICP-produced calcium carbonate crust on the surface of (a) ABS, (b) PVC, (c) LDPE, (d) PS, and (e) PP plastic disks at approximately 300 \times magnification, with insets at approximately 2500 \times magnification. Calcium assay results (Figure 7b) show that ABS had the least CaCO_3 deposition while PVC had the most. (f) An untreated PS plastic disk at approximately 300 \times magnification shows little surface roughness. All other untreated plastics show a similarly smooth surface to PS.

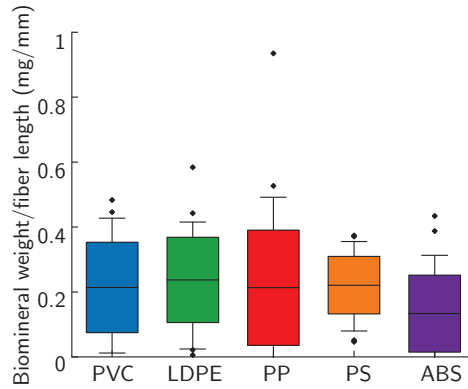


Figure 9. Weight of CaCO_3 per fiber length on fibers mineralized with MICP via the submersion method. The center line is the median, the colored boxes are the middle 50% of data points, the whiskers contain 95% of data points and the \blacklozenge are outliers.

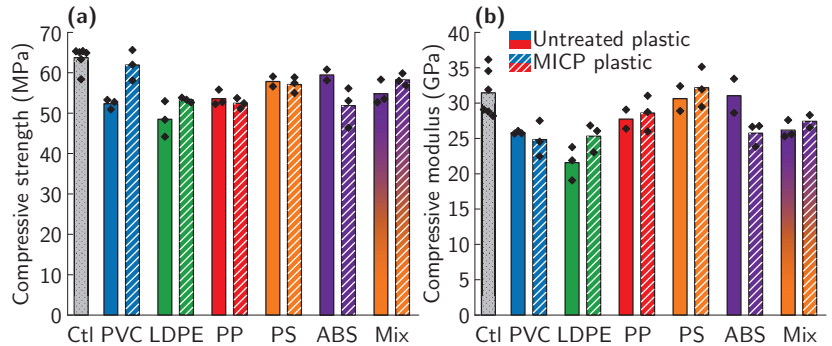


Figure 10. Comparison of compressive strength (a) and modulus (b) for non-reinforced mortar (Ctl) and MICP-treated and untreated PVC, LDPE, PP, PS, ABS, and mixed-type plastic reinforced mortar. Bars represent mean values and \blacklozenge are individual data points. Exact compressive strength and modulus values are shown in Table S2, and representative stress–strain curves are shown in Figure S7.

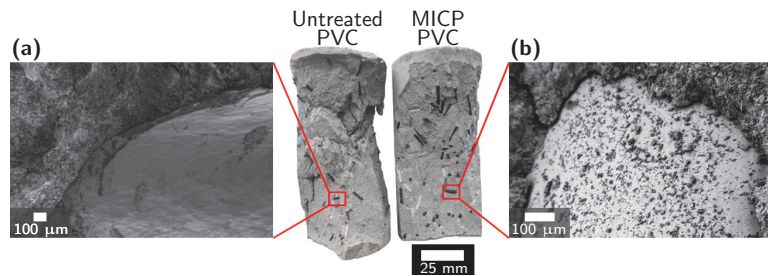


Figure 11. Photos of failed mortar cylinders and FESEM images of the failure surface of cement mortar cylinders reinforced with (a) untreated PVC and (b) MICP-treated PVC. The interface between plastic and cement is shown. PVC, LDPE, PS, and ABS failure interfaces are shown in Figure S8.

The compressive strengths measured in this study demonstrate that, for PET and PVC plastic, MICP treatment can produce a significant increase in PRM compressive strength while, in other plastic types, little change in compressive strength was seen with mineralization. MICP-treated PP PRM had a statistically insignificant change in compressive strength compared untreated PP, a finding consistent with the compressive

strength testing performed by Hao et al. [18]. It is not yet fully understood why these differences exist between plastic types. The differences in strength between plastic types do not appear to only be related to a change in CaCO_3 mass and may also be impacted by factors including plastic surface roughness, fiber modulus, or CaCO_3 surface geometry. Past studies have identified increases in fiber pullout strength, an indicator of improved compressive strength, with MICP treatment of plastic [18] and application of CaCO_3 to plastic [17]. However, this work is the first to examine the impact of both plastic type and biomineralization on the compressive strength of PRM. Due to MICP previously being used to repair cracks in concrete and seal oil wells [19,23–27], we expect that MICP treatment of plastic has the potential to be scalable for treating plastic waste. An important limitation of the current work is that the influence of each biomineralization method and plastic type on mechanical properties other than compressive strength, such as flexural strength and toughness, workability, and durability, was not examined. Additionally, it would be valuable to examine different plastic geometries and higher plastic volumes to determine optimal geometries for MICP-treated PRM and to maximize the amount of plastic waste used. Importantly, increases in strength over what was observed in this study would be expected if MICP-treated plastics were applied in plastic-reinforced concrete rather than mortar. Based on the compressive strengths for PRM with MICP treatment of PVC, PET, and mixed-type plastic observed in this study, we would expect plastic-reinforced concrete with these treated plastics to have sufficiently high strength for important construction applications, such as concrete slabs, footpaths, and walls [49].

3.3. Effect of Biomineral on Cement Hydration

Cement hydration plays an important role in the mechanical properties of cement mortar and concrete. Changes in cement hydration may play a role in the increases in compressive strength with MICP treatment observed in this study [17]. After 1 day of curing, cement hydration, as measured via TGA, increases with the amount of biomineral added (Figure 12b). This increase in measured rate of hydration is consistent with the formation of a denser cement matrix at the interface around biomineralized fibers that has been observed in past studies of CaCO_3 -treated PRM [17]. The largest difference in cement hydration was found at a curing time of 1 day, with small increases in hydration observed at 7, 14, and 28 days. The increase in hydration with biomineral after 1 day of curing was observed as being due to an increase in mass loss during the dehydration, dehydroxylation, and decarbonation degradation regions (Figure 12a). At longer curing times, similar amounts of mass loss are seen in the decarbonation and dehydration regions for 0%, 1%, and 5% biomineral samples.

The 5% biomineral sample experienced a larger mass loss than 0% and 1% biomineral samples in the dehydroxylation region and a larger mass loss in the decomposition of the CaCO_3 region (Figure 12a) [37]. This contribution to the mass loss indicates that, in the 5% biomineral cement paste samples, more portlandite was formed than at 1% and 0% biomineral. Calcium present in the CaCO_3 biomineral can participate in the cement hydration reaction [50]. The presence of an additional mass loss in the decomposition of the CaCO_3 region indicates that a portion of the biomineral has not participated in the hydration reaction and that unreacted CaCO_3 remains [50]. We hypothesize that, as biomineral concentrations will be greater than 5% in the regions immediately surrounding biomineralized plastic in the mortar, some inert biomineral will remain surrounding the plastic and a similar effect will be seen on the cement matrix of biomineralized PRM as in the 5% biomineral cement paste sample.

The XRD results show only minor differences between cement paste samples with 0%, 1%, and 5% biomineral after 7 days of curing (Figure 13). As in TGA measurements, the largest change is observed between 1 and 7 days, with only small differences over time after 7 days of curing (hydration at 1 and 7 days shown in Figure 13 and at 14 and 28 days in Figure S10). Calcite, portlandite, and alite peaks are observed as major phases for all cement paste samples. Ettringite and belite shift between major and minor phases,

with the relative phase composition changing with hydration between time points. The monocarboaluminate and hemicarboaluminate phases are observed in small quantities. The XRD spectrum of the biomineral shows a majority calcite structure, with a minor vaterite phase, confirming the results for MICP mineral seen on PET flakes (Figure 2a). Past work by Monteiro et al. on abiotic vaterite-containing carbonate precipitates found that the addition of both calcite and vaterite to cement paste leads to the formation of monocarboaluminate and hemicarboaluminate phases [39]. The XRD results further support an incomplete reaction of the CaCO_3 polymorphs as cement hydration progresses that was observed in TGA measurements, as evidenced by the remaining calcite and vaterite present in the hydrated samples.

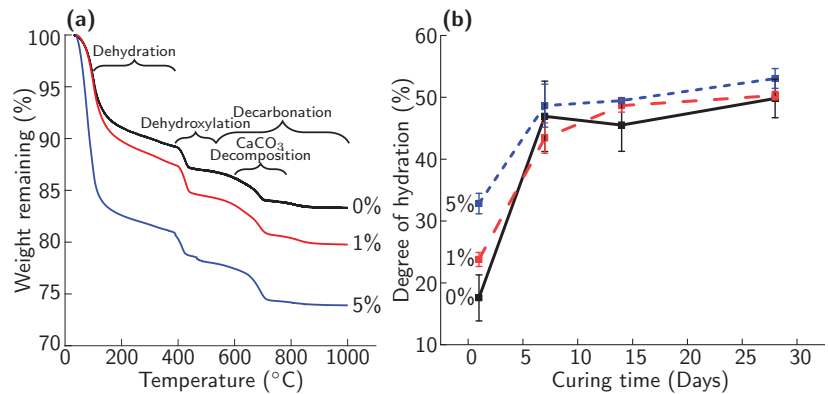


Figure 12. (a) Thermogravimetric analysis (TGA) curve of 0% (black), 1% (red), and 5% (blue) biomineral cement paste samples after 1 day of curing; 7, 14, and 28 day and replicate TGA curves are shown in (Figure S9). (b) Degree of hydration of 0% (black), 1% (red), and 5% (blue) biomineral cement paste over time, as determined from TGA measurements.

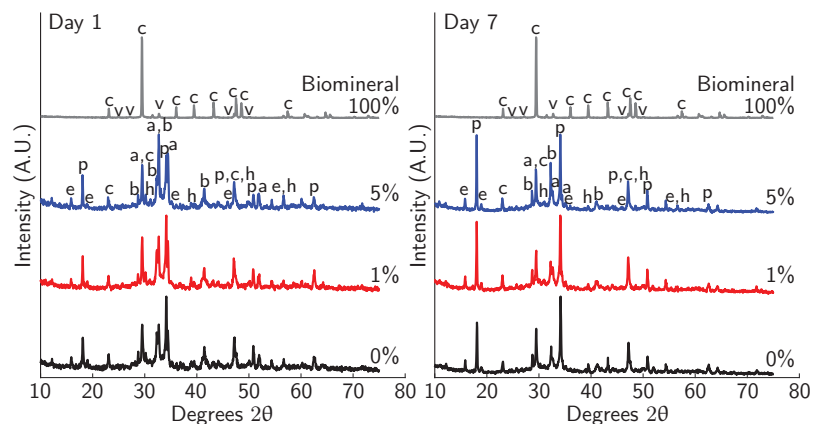


Figure 13. XRD spectrum for cement paste after 1 and 7 days of curing with 0%, 1%, and 5% MICP biomineral added and 100% MICP biomineral. The peaks present are alite (a), belite (b), calcite (c), portlandite (p), ettringite (e), and hemicarboaluminate (h), with labels corresponding to the first letter of the mineral. Little change was seen after 7 days, and XRD spectra for 14 and 28 days are included in the Supplementary Materials (Figure S10).

4. Conclusions

In this study, we show that biomineralization can improve the strength of plastic-reinforced mortar. A key finding of this study was that none of the examined plastics

(PET, PVC, LDPE, PP, PS, or ABS) inhibited *S. pasteurii* growth under the biomineralization conditions tested in this study. MICP treatment deposited more CaCO₃ on the surface of PET plastic than EICP treatment, resulting in PRM with 5% MICP-treated PET having 88% of the compressive strength of the plastic-free mortar. Importantly, PRM reinforced with 5% MICP-treated PET, PVC, and mixed type 3–7 plastics had strengths similar to that of plastic-free mortar and showed sufficient strength for application in engineering structures.

Together, these results indicate that MICP treatment allows for the reuse of larger volumes of plastic waste in PRM. At constant values of plastic addition, MICP also increases the strength of PRM, which may be valuable in applications where high strength is a concern. As mixed type 3–7 plastic is a low-value, often landfilled plastic waste stream, this treatment is a promising option to reduce the amount of plastic waste sent to landfills. Biomineralized mixed-type PRM shows similar strength to non-reinforced mortar, indicating that mixed-plastic waste may be added in many concrete applications to reuse this low value waste stream.

Additional work is needed to better understand why MICP treatment affects the compressive strength of PRM differently in each plastic type. This study observed an increase in cement hydration and a visually improved interface between plastic waste and cement mortar with MICP treatment. To better understand the mechanisms behind the differences in strengths observed in this study, further work is needed to directly establish the impact of MICP treatment on interfacial strength. Increased knowledge of these mechanisms may allow additional improvement in the strength of PRCs with MICP treatment. These improvements would further establish biomineralized PRC as a high-volume method to reuse plastic waste.

Supplementary Materials: The following are available at <https://www.mdpi.com/1996-1944/14/8/1949/s1>, Table S1: Plastic properties, Figure S1: Submersion method setup, Figure S2: Plastic fiber length, Figure S3: PET additional batch test data, Figure S4: Untreated PET FESEM image, Figure S5: Type 3–7 additional batch test data, Table S2: Full PRM strength data, Figure S6: PET PRM stress-strain curves, Figure S7: Type 3–7 PRM stress-strain curves, Figure S8: Type 3–7 PRM interface FESEM images, Figure S9: Cement hydration TGA curves, and Figure S10: Cement hydration XRD spectra.

Author Contributions: Conceptualization, A.P., C.H. and C.R.; data curation, S.K., A.T., M.E., K.L. and H.A.; formal analysis, S.K.; funding acquisition, A.P., C.H. and C.R.; investigation, S.K., A.T., M.E., K.L. and H.A.; methodology, S.K., A.T., M.E., K.L. and H.A.; project administration, A.P., C.H. and C.R.; resources, A.P.; software, S.K.; supervision, A.P., C.H. and C.R.; visualization, S.K.; writing—original draft, S.K., A.T., C.H. and C.R.; writing—review and editing, S.K., A.P., C.H. and C.R. All authors have read and agreed to the published version of the manuscript.

Funding: This research was funded by The Hawthorn Foundation (Recycled Plastics Industry in Wyoming-Feasibility Study) and startup funds from Montana State University. This material is partially based upon work supported by the National Science Foundation Research Experience for Teachers Program under grant No. EEC-1610089 awarded to the MSU Western Transportation Institute. Any opinions, findings, and conclusions or recommendations expressed in this material are those of the authors and do not necessarily reflect the views of the National Science Foundation. Seth Kane's contribution was funded in part by the Environmental Research and Education Foundation. This work was performed in part at the Montana Nanotechnology Facility, a member of the National Nanotechnology Coordinated Infrastructure (NNCI), which is supported by the National Science Foundation (grant# ECCS-1542210). Microscopy at the Center for Biofilm Engineering was made possible by awards from the Murdock Charitable Trust and the National Science Foundation.

Data Availability Statement: The data presented in this study are openly available in Dryad at <https://doi.org/10.5061/dryad.79cnp5hvg>.

Acknowledgments: The authors thank Mike Berry and Kirsten Matteson for assistance with the compression testing, Elif Roehm and Nathaniel Rieders for performing XRD measurements, Sobia Anjum for taking confocal images, Francis Kerins and Ashlee Buller for their techno-economic analysis in support of the Hawthorn Foundation grant, and Farli Boden and Kylee Rux for assistance with biomineralization and plastic cutting. The authors would also like to acknowledge the graphical illustrations provided by Jill Story (CBE). The authors would like to thank We Recycle Montana, Four Corners Recycling and Northwest Polymers for the consultations on regional plastic recycling and for providing materials.

Conflicts of Interest: The authors declare no conflict of interest. The funders had no role in the design of the study; in the collection, analyses, or interpretation of data; in the writing of the manuscript; or in the decision to publish the results.

References

1. Plastics Europe. *Plastics—The Facts 2020*; Plastics Europe: Brussels, Belgium, 2020.
2. United Nations Environment Programme. *Single-Use Plastics: A Roadmap for Sustainability*; United Nations Environment Programme: Washington, DC, USA, 2018.
3. Babafemi, A.; Šavija, B.; Paul, S.; Anggraini, V. Engineering Properties of Concrete with Waste Recycled Plastic: A Review. *Sustainability* **2018**, *10*, 3875. [CrossRef]
4. Jani, Y.; Hogland, W. Waste glass in the production of cement and concrete—A review. *J. Environ. Chem. Eng.* **2014**, *2*, 1767–1775. [CrossRef]
5. Kishore, K.; Gupta, N. Application of domestic & industrial waste materials in concrete: A review. *Mater. Today Proc.* **2019**, *26*, 2926–2931. [CrossRef]
6. Miller, S.A. Supplementary cementitious materials to mitigate greenhouse gas emissions from concrete: Can there be too much of a good thing? *J. Clean. Prod.* **2018**, *178*, 587–598. [CrossRef]
7. Yina, S.; Tuladhar, R.; Sheehan, M.; Combe, M.; Collister, T. A life cycle assessment of recycled polypropylene fibre in concrete footpaths. *J. Clean. Prod.* **2016**, *112*, 2231–2242. [CrossRef]
8. Kim, S.B.; Yi, N.H.; Kim, H.Y.; Kim, J.H.J.; Song, Y.C. Material and structural performance evaluation of recycled PET fiber reinforced concrete. *Cem. Concr. Compos.* **2010**, *32*, 232–240. [CrossRef]
9. Pešić, N.; Živanović, S.; Garcia, R.; Papastergiou, P. Mechanical properties of concrete reinforced with recycled HDPE plastic fibres. *Constr. Build. Mater.* **2016**, *115*, 362–370. [CrossRef]
10. Sharma, R.; Bansal, P.P. Use of different forms of waste plastic in concrete—A review. *J. Clean. Prod.* **2016**, *112*, 473–482. [CrossRef]
11. Yin, S. Development of Recycled Polypropylene Plastic Fibres to Reinforce Concrete. Ph.D. Thesis, James Cook University, Douglas, Australia, 2017. [CrossRef]
12. Ochi, T.; Okubo, S.; Fukui, K. Development of recycled PET fiber and its application as concrete-reinforcing fiber. *Cem. Concr. Compos.* **2007**, *29*, 448–455. [CrossRef]
13. Saikia, N.; De Brito, J. Use of plastic waste as aggregate in cement mortar and concrete preparation: A review. *Constr. Build. Mater.* **2012**, *34*, 385–401. [CrossRef]
14. Al-Tulaian, B.S.; Al-Shannag, M.J.; Al-Hozaimy, A.R. Recycled plastic waste fibers for reinforcing Portland cement mortar. *Constr. Build. Mater.* **2016**, *127*, 102–110. [CrossRef]
15. Jacob-Vaillancourt, C.; Sorelli, L. Characterization of concrete composites with recycled plastic aggregates from postconsumer material streams. *Constr. Build. Mater.* **2018**, *182*, 561–572. [CrossRef]
16. Naik, T.R.; Singh, S.S.; Huber, C.O.; Brodersen, B.S. Use of post-consumer waste plastics in cement-based composites. *Cem. Concr. Res.* **1996**, *26*, 1489–1492. [CrossRef]
17. Feng, J.; Yang, F.; Qian, S. Improving the bond between polypropylene fiber and cement matrix by nano calcium carbonate modification. *Constr. Build. Mater.* **2021**, *269*, 121249. [CrossRef]
18. Hao, Y.; Cheng, L.; Hao, H.; Shahin, M.A. Enhancing fiber/matrix bonding in polypropylene fiber reinforced cementitious composites by microbially induced calcite precipitation pre-treatment. *Cem. Concr. Compos.* **2018**, *88*, 1–7. [CrossRef]
19. Phillips, A.J.; Gerlach, R.; Lauchnor, E.; Mitchell, A.C.; Cunningham, A.B.; Spangler, L. Engineered applications of ureolytic biomineralization: A review. *Biofouling* **2013**, *29*, 715–733. [CrossRef]
20. Bachmeier, K.L.; Williams, A.E.; Warmington, J.R.; Bang, S.S. Urease activity in microbially-induced calcite precipitation. *J. Biotechnol.* **2002**, *93*, 171–181. [CrossRef]
21. Stocks-Fischer, S.; Galinat, J.K.; Bang, S.S. Microbiological precipitation of CaCO₃. *Soil Biol. Biochem.* **1999**, *31*, 1563–1571. [CrossRef]
22. Hommel, J.; Akyel, A.; Frieling, Z.; Phillips, A.J.; Gerlach, R.; Cunningham, A.B.; Class, H. A Numerical Model for Enzymatically Induced Calcium Carbonate Precipitation. *Appl. Sci.* **2020**, *10*, 4538. [CrossRef]

23. De Muynck, W.; De Belie, N.; Verstraete, W. Microbial carbonate precipitation in construction materials: A review. *Ecol. Eng.* **2010**, *36*, 118–136. [CrossRef]
24. Phillips, A.J.; Cunningham, A.B.; Gerlach, R.; Hiebert, R.; Hwang, C.; Lomans, B.P.; Westrich, J.; Mantilla, C.; Kirksey, J.; Esposito, R.; et al. Fracture Sealing with Microbially-Induced Calcium Carbonate Precipitation: A Field Study. *Environ. Sci. Technol.* **2016**, *50*, 4111–4117. [CrossRef]
25. Wang, J.Y.; Soens, H.; Verstraete, W.; De Belie, N. Self-healing concrete by use of microencapsulated bacterial spores. *Cem. Concr. Res.* **2014**, *56*, 139–152. [CrossRef]
26. Lee, Y.S.; Park, W. Current challenges and future directions for bacterial self-healing concrete. *Appl. Microbiol. Biotechnol.* **2018**, *102*, 3059–3070. [CrossRef]
27. Dakhane, A.; Das, S.; Hansen, H.; O'Donnell, S.; Hanoon, F.; Rushton, A.; Perla, C.; Neithalath, N. Crack Healing in Cementitious Mortars Using Enzyme-Induced Carbonate Precipitation: Quantification Based on Fracture Response. *J. Mater. Civ. Eng.* **2018**, *30*, 04018035. [CrossRef]
28. ASTM International. *C1609/C1609M-19a Standard Test Method for Flexural Performance of Fiber-Reinforced Concrete (Using Beam with Third-Point Loading)*; Standard; ASTM International: West Conshohocken, PA, USA, 2019. [CrossRef]
29. Phillips, A.J.; Lauchnor, E.; Eldring, J.; Esposito, R.; Mitchell, A.C.; Gerlach, R.; Cunningham, A.B.; Spangler, L.H. Potential CO₂ leakage reduction through biofilm-induced calcium carbonate precipitation. *Environ. Sci. Technol.* **2013**, *47*, 142–149. [CrossRef]
30. Thrane, L.W.; Daily, R.L.; Thane, A.; Kirkland, C.M.; Mccarney, E.R.; Dykstra, R.; Codd, S.L.; Phillips, A.J. Detecting Microbially Induced Calcium Carbonate Precipitation in Porous Systems Using Low-Field Nuclear Magnetic Resonance Relaxometry. *J. Geotech. Geoenviron. Eng.* **2020**, *146*, 04020012. [CrossRef]
31. Jung, D.; Biggs, H.; Erikson, J.; Ledyard, P.U. New Colorimetric reaction for end-point, continuous-flow, and kinetic measurement of urea. *Clin. Chem.* **1975**, *21*, 1136–1140. [CrossRef]
32. Phillips, A.J. Biofilm-Induced Calcium Carbonate Precipitation: Application in the Subsurface. Ph.D. Thesis, Montana State University, Bozeman, MT, USA, 2013.
33. Frieling, Z. Urease Immobilization for Advancing Enzyme-Induced Calcium Carbonate Precipitation Applications. Master's Thesis, Montana State University, Bozeman, MT, USA, 2019.
34. ASTM International. *C109/C109M-20b Standard Test Method for Compressive Strength of Hydraulic Cement Mortars (Using 2-in. or [50 mm] Cube Specimens)*; Standard; ASTM International: West Conshohocken, PA, USA, 2020. [CrossRef]
35. ASTM International. *C305-20 Standard Practice for Mechanical Mixing of Hydraulic Cement Pastes and Mortars of Plastic Consistency*; Standard; ASTM International: West Conshohocken, PA, USA, 2020. [CrossRef]
36. ASTM International. *ASTM C192: Standard Practice for Making and Curing Concrete Test Specimens in the Laboratory*; Standard; ASTM International: West Conshohocken, PA, USA, 2019. [CrossRef]
37. Monteagudo, S.M.; Moragues, A.; Gálvez, J.C.; Casati, M.J.; Reyes, E. The degree of hydration assessment of blended cement pastes by differential thermal and thermogravimetric analysis. Morphological evolution of the solid phases. *Thermochim. Acta* **2014**, *592*, 37–51. [CrossRef]
38. Deboucha, W.; Leklou, N.; Khelidj, A.; Oudjit, M.N. Hydration development of mineral additives blended cement using thermogravimetric analysis (TGA): Methodology of calculating the degree of hydration. *Constr. Build. Mater.* **2017**, *146*, 687–701. [CrossRef]
39. Monteiro, P.J.; Clodic, L.; Battocchio, F.; Kanitpanyacharoen, W.; Chae, S.R.; Ha, J.; Wenk, H.R. Incorporating carbon sequestration materials in civil infrastructure: A micro and nano-structural analysis. *Cem. Concr. Compos.* **2013**, *40*, 14–20. [CrossRef]
40. Stutzman, P.E.; Feng, P.; Bullard, J.W. Phase Analysis of Portland Cements by Combined Quantitative X-ray Powder Diffraction and Scanning Electron Microscopy. *NIST J. Res.* **2016**, *121*, 47–107. [CrossRef]
41. Ipavec, A.; Gabrovšek, R.; Vuk, T.; Kaučič, V.; Maček, J.; Meden, A. Carboaluminate Phases Formation During the Hydration of Calcite-Containing Portland Cement. *J. Am. Ceram. Soc.* **2011**, *94*, 1238–1242. [CrossRef]
42. Jeong, Y.; Hargis, C.W.; Chun, S.; Moon, J. Effect of Calcium Carbonate Fineness on Calcium Sulfoaluminate-Belite Cement. *Materials* **2017**, *10*, 900. [CrossRef]
43. Runčevski, T.; Dinnebir, R.E.; Magdysyuk, O.V.; Pöllmann, H. Crystal structures of calcium hemicarboaluminate and carbonated calcium hemicarboaluminate from synchrotron powder diffraction data. *Acta Crystallogr. Sect. B* **2012**, *68*, 493–500. [CrossRef]
44. Sondi, I.; Salopek-Sondi, B. Influence of the primary structure of enzymes on the formation of CaCO₃ polymorphs: A comparison of plant (*Canavalia ensiformis*) and bacterial (*Bacillus pasteurii*) ureases. *Langmuir* **2005**, *21*, 8876–8882. [CrossRef]
45. Almajed, A.; Tirkolaei, H.K.; Kavazanjian, E.; Hamdan, N. Enzyme Induced Biocemented Sand with High Strength at Low Carbonate Content. *Sci. Rep.* **2019**, *9*, 1135. [CrossRef]
46. Heveran, C.M.; Liang, L.; Nagarajan, A.; Hubler, M.H.; Gill, R.; Cameron, J.C.; Cook, S.M.; Srubar, W.V. Engineered Ureolytic Microorganisms Can Tailor the Morphology and Nanomechanical Properties of Microbial-Precipitated Calcium Carbonate. *Sci. Rep.* **2019**, *9*, 14721. [CrossRef]
47. Dhami, N.K.; Mukherjee, A.; Reddy, M.S. Micrographical, mineralogical and nano-mechanical characterisation of microbial carbonates from urease and carbonic anhydrase producing bacteria. *Ecol. Eng.* **2016**, *94*, 443–454. [CrossRef]
48. Achal, V.; Pan, X.; Özyurt, N. Improved strength and durability of fly ash-amended concrete by microbial calcite precipitation. *Ecol. Eng.* **2011**, *37*, 554–559. [CrossRef]

49. International Code Council. The Strength of Concrete. In *2015 Concrete Manual*; International Code Council: Washington, DC, USA, 2015; Chapter 3, p. 25.
50. Matschei, T.; Lothenbach, B.; Glasser, F.P. The role of calcium carbonate in cement hydration. *Cem. Concr. Res.* **2007**, *37*, 551–558. [CrossRef]

Article

Compressive Behavior of Circular Sawdust-Reinforced Ice-Filled Flax FRP Tubular Short Columns

Yanlei Wang ^{1,*}, Guipeng Chen ¹, Baolin Wan ² and Baoguo Han ¹

¹ State Key Laboratory of Coastal and Offshore Engineering, School of Civil Engineering, Dalian University of Technology, Dalian 116024, China; chenguipeng1993@163.com (G.C.); hanbaoguo@dlut.edu.cn (B.H.)

² Department of Civil, Construction and Environmental Engineering, Marquette University, Milwaukee, WI 53201, USA; baolin.wan@marquette.edu

* Correspondence: wangyanlei@dlut.edu.cn

Received: 26 December 2019; Accepted: 18 February 2020; Published: 20 February 2020

Abstract: Sawdust-reinforced ice-filled flax fiber-reinforced polymer (FRP) tubular (SIFFT) columns are newly proposed to be used as structural components in cold areas. A SIFFT column is composed of an external flax FRP tube filled with sawdust-reinforced ice. The compressive behavior of circular SIFFT short columns was systematically investigated. Four types of short columns with circular sections, including three plain ice specimens, three sawdust-reinforced ice specimens (a mixture of 14% sawdust and 86% ice in weight), nine plain ice-filled flax FRP tubular (PIFFT) specimens and nine SIFFT specimens, were tested to assess the concept of the innovative composite columns. The test variables were the thickness of flax FRP tubes and the type of ice cores. The test results indicated that the lateral dilation and the development of cracks of the ice cores were effectively suppressed by outer flax FRP tubes, thus causing a considerable enhancement in the compressive strength. Moreover, the compressive behavior, energy-absorption capacity, and anti-melting property of sawdust-reinforced ice cores were better than those of plain ice cores confined by flax FRP tubes with the same thicknesses. The proposed equations for estimating ultimate bearing capacities of PIFFT and SIFFT short columns were shown to provide reasonable and accurate predictions.

Keywords: flax fiber; FRP; sawdust; ice; tubular column; confinement

1. Introduction

The low temperature in cold areas tremendously limits the use of traditional building materials, especially concrete. Water freezing causes detrimental effect on hydration reaction of the cement, resulting in severe deterioration of mechanical properties of the resulting concrete. Furthermore, the local environment will be easily polluted due to the use of concrete in construction. Therefore, there is a particular need to find a potential construction material with cost-effective and environmentally friendly advantages to replace concrete in such areas.

In fact, the local ice has served as a cleaner construction material since ancient times in cold areas, such as the igloos built up by Inuit people. In addition, the compressive properties of ice have been investigated by many researchers (e.g., [1–4]). Ice belongs to a brittle material relatively strong under compression but very weak under tension, which is very similar to concrete [4]. However, the cylinder compressive of plain ice at $-2\text{ }^{\circ}\text{C}$ is less than 1/10 of that of normal concrete specimen with the same size [5]. Therefore, appropriate measures need to be taken to ameliorate the mechanical properties of plain ice. A variety of materials including alluvium [6], sand [7], and fiberglass net and cloth [8] were introduced into plain ice as reinforcement. The test results demonstrated that the mechanical properties of plain ice were enhanced after introducing the aforementioned materials in ice. For example, the compressive strength of the ice specimens modified by 2% volumetric content of fiberglass net was twice as large as that of the plain ice at $-20\text{ }^{\circ}\text{C}$ [8]. Moreover, sawdust is another

popular reinforcing material for the modification of plain ice. Vasiliev et al. [9] studied the compressive and flexural behaviors of ice specimens reinforced by sawdust, wood chips, and wood shavings at $-18\text{ }^{\circ}\text{C}$. The test results revealed that the compressive and bending strengths of plain ice were enhanced from 3.18 and 1.24 MPa to 12.45 and 3.74 MPa, respectively, after introducing 10.5% sawdust in weight. However, the compressive strength of the reinforced ice is still weaker than that of normal concrete, which severely restricts its further application. Furthermore, the surrounding chemicals might have a detrimental impact on the long-term mechanical properties of the reinforced ice when directly exposed to environmental attack without an outer protective jacket. Therefore, it is desired to find ways to overcome such shortcomings.

More recently, fiber-reinforced polymer (FRP) composites have been increasingly used in civil engineering because of their high strength-to-weight ratios, good design flexibility, and excellent corrosion resistance even under harsh environment [10–22]. In the 1990s, Mirmiran and Shahawy [23] proposed concrete-filled FRP tubular (CFFT) columns. For a CFFT column, the pre-fabricated tube made of FRP composites acts as permanent formworks for fresh concrete without concern for possible corrosion. Furthermore, the outer FRP tube offers additional confinement to the concrete core. Many researches (e.g., [24–30]) have been carried out on the axial compressive behavior of CFFT columns, which demonstrated the excellent structural performance of such members. However, the majority of the reinforcing fibers in current FRP belong to synthetic fibers (e.g., carbon and glass fibers), which will consume large amounts of energy.

In consideration of environmental protection and sustainable development, natural fibers have attracted the attention of many researchers as substitutable reinforcements for traditional synthetic fibers due to their advantages such as low cost, high specific strength, environmental friendliness and bio-degradability, ease of fabrication, and good structural rigidity [31–33]. Dittenber and Gangarao [34] compared over 20 common natural fibers (e.g., sisal, ramie, kenaf, jute, hemp, flax, coir, cotton, etc.) with glass fibers in terms of specific modulus, cost per weight, as well as cost per unit length (capable of resisting 100 kN load). It revealed that flax fibers possess the optimum combination of advantages among these natural fibers. More recently, flax FRP tubes were used to provide lateral confinement to concrete columns (e.g., [35–37]). Yan and Chouw [35] investigated the axial compressive performance of the coir fiber-reinforced concrete-filled flax FRP tubes, which revealed that the compressive strength and the ductility of the coir fiber-reinforced concrete cores were substantially improved by the additional confinement from flax FRP tubes. Xia et al. [37] studied the behavior of self-compacting concrete-filled flax FRP tubular columns under static and cycle compression, which confirmed that the compressive strength and the ultimate axial strain of filament-wound flax FRP-confined concrete were increased with the increase of tube thickness. In view of the similarities between ice and concrete, it might be a good way to study the compressive responses of the flax FRP-confined ice based on the well understanding of the behavior of flax FRP-confined concrete.

Based on previous researches on sawdust-reinforced ice [9] and concrete-filled flax FRP tubes (e.g., [35–37]), sawdust-reinforced ice-filled flax FRP tubular (SIFFT) columns are innovatively proposed in this paper to dramatically improve the compressive properties of plain ice. They are composed of flax FRP tubes filled with sawdust-reinforced ice. The compressive strength of inner ice is expected to be greatly improved by the flax FRP confinement. In addition, the melting of inner ice might be delayed due to the inclusion of sawdust. Furthermore, the isolation of flax FRP tube, with a low thermal conductivity of around $0.04\text{ W}/(\text{m}\cdot\text{K})$ for flax fibers [38], might also contribute to the improvement of thermal insulation property. Additionally, the flax FRP tubes can be filled with sea ice without any corrosion concern, which is a significant advantage over traditional steel tubes. Finally, the proposed SIFFT column is a novel structural member with less environmental pollution: (a) ice is a clean material, readily available in cold areas, which becomes water after melting without pollution [39]; (b) natural fibers (i.e., flax fibers and wood waste sawdust) used in this study are biodegradable materials. The novel SIFFT columns are expected to be potentially used in the piers of a bridge built in remote

cold regions. Moreover, the outer steel columns of the structures of the existing scientific research station in polar areas might be replaced by the proposed SIFFT columns with better durability.

Experimental studies were conducted to assess the axial compressive behavior of the newly proposed SIFFT column and to verify the possibility of this column to be used as a compression member in cold regions. Effects of the thickness of flax FRP tube and the inclusion of sawdust in ice were discussed. Equations were proposed to predict the ultimate bearing capacities of circular plain ice-filled flax FRP tubular (PIFFT) short columns and circular sawdust-reinforced ice-filled flax FRP tubular (SIFFT) short columns.

2. Experimental Program

2.1. Specimens

A total of 18 circular short composite columns, including nine plain ice-filled flax FRP tubular (PIFFT) specimens and nine sawdust-reinforced ice-filled flax FRP tubular (SIFFT) specimens, were tested subjected to axial compression. In addition, three unconfined plain ice specimens and three unconfined sawdust-reinforced ice specimens were prepared as control specimens. Each series included three nominally identical specimens. All test specimens had a height of 300 mm and a nominal diameter of 150 mm, measured at the surface of ice cores. The test variables included the number of FRP layers in flax FRP tubes and the type of ice cores. It has been well established that the compressive property of ice will be improved after the inclusion of sawdust in ice due to the fiber bridging effect. However, it does not mean that more sawdust will always contribute to better compressive property of the sawdust-reinforced ice. In fact, the workability of the water–sawdust mixture will decrease when the volume fraction of sawdust exceeds a certain level, leading to more initial defects in the prepared sawdust-reinforced ice. Therefore, a decrease in the compressive property of the sawdust-reinforced ice might occur corresponding to such a large reinforcing amount. Based on the results of trial tests on sawdust-reinforced ice specimens with different volume fractions of sawdust (i.e., 14.3%, 19.8%, 26.6%, and 32.8%, respectively), the sawdust-reinforced ice with a volume fraction of 26.6% sawdust was confirmed to have the best compressive properties. Based on conversion, the optimal weight ratio of the sawdust and water was 14:86 corresponding to this volume fraction. Therefore, the sawdust-reinforced ice used in this study was a mixture of 14% pine sawdust with a dry density of 0.45 g/mm^3 and 86% water in weight. Table 1 shows the details of all test specimens.

The naming rule of test specimens was described as follows. (1) It began with PI, SI, IF, and SF to indicate different specimen series (i.e., plain ice column, sawdust-reinforced ice column, PIFFT column, and SIFFT column, respectively). (2) The Arabic numeral denoted the number of plies of fiber fabric in flax FRP tubes. (3) The Roman numeral was introduced to distinguish three nominally identical specimens. Taking specimen SF2-I as an example, it represented an SIFFT specimen with two FRP layers in flax FRP tube and it was the first specimen within the same series.

2.2. Material Properties

Unidirectional flax fiber sheet with a surface density of 210 g/m^2 was supplied by Nanjing Hitech Composites Co., Ltd., China. The nominal thickness of the sheet was 0.135 mm. The matching epoxy resin was obtained from Shanghai Sanyou Resin Co., Ltd., China. Considering that the proposed composite column would serve in cold areas, this type of epoxy resin was selected in this study due to the fact that its mechanical properties are not sensitive to the low temperature. However, low temperature will affect the viscosity and curing properties of the selected epoxy resin. So, the flax FRP tubes used in the paper were fabricated and cured at room temperature. The epoxy L-500 AS (main agent) was assisted by the hardener L-500 BS with a mix ratio of 2:1. According to ASTM D3039/D3039M-17 [40], flat coupon tensile tests were conducted to determine the mechanical properties of flax FRP. The test results showed that the tensile stress vs. strain featured approximately linear shape, which was similar to conventional FRP with synthetic fibers. The average elastic modulus E_f ,

tensile strength f_u , and ultimate tensile strain ε_f of the flax FRP used in this study were 72.3 GPa, 784 MPa, and 1.34%, respectively. The average and standard deviation of elastic modulus E_f , tensile strength f_u , and ultimate tensile strain ε_f of the flax FRP used in this study were 72.3 ± 3.43 GPa, 784 ± 54.0 MPa, and $1.34\% \pm 0.16\%$, respectively. It was noticed that the material properties including the elastic modulus and the tensile strength of the flax FRP in this paper are much larger than the test results reported by some researchers [e.g., 35–37], which can be explained as follows. It is difficult to precisely control the actual thickness of FRP specimens when they are prepared by hand layup process. In order to better evaluate the tensile properties of FRP fabricated by hand layup process, the tensile stress of FRP is generally calculated through the tensile load divided by the nominal thickness (ignoring the thickness of resin matrix) of the fiber fabric instead of the actual thickness (considering the thickness of resin matrix) of FRP laminate [41], thus trying to eliminate the discreteness caused by the variation of resin thickness during hand layup process. This calculation method is also adopted in this paper. In this way, both the tensile strength and the deduced elastic modulus reported in this study are overestimated compared to their true values. One may argue that the nominal modulus is larger than its true value. However, such treatment is widely accepted especially when the FRP tube prepared via wet layup process is used as a confining jacket (e.g., FRP-confined concrete members) because the nominal thickness and the nominal elastic modulus of FRP make up a couple and always appear simultaneously in the equation of determining the confining stress of the FRP tubes. Such treatment will effectively eliminate the difference and is more familiar to the engineers during the design of a certain member confined by FRP.

Table 1. Details of specimens and main test results.

Series	Specimen	Type of Ice Core	Flax FRP Tube				Test Results		
			Ply	t (mm)	t_a (mm)	N_e (kN)	Average N_e (kN)	Average N_f (kN)	$\frac{N_e}{N_e + N_f}$
PI	PI0-I	PI	-	-	-	49.79	48.98	-	-
	PI0-II					48.18			
	PI0-III					48.96			
SI	SI0-I	SI	-	-	-	74.82	75.61	-	-
	SI0-II					75.62			
	SI0-III					76.38			
IF2	IF2-I	PI	2	0.27	3.00	123.27	122.00	82.66	0.927
	IF2-II					121.13			
	IF2-III					121.61			
SF2	SF2-I	SI	2	0.27	3.00	187.09	179.61	82.66	1.364
	SF2-II					178.24			
	SF2-III					173.50			
IF4	IF4-I	PI	4	0.54	3.75	168.01	169.72	103.01	1.117
	IF4-II					172.51			
	IF4-III					168.65			
SF4	SF4-I	SI	4	0.54	3.75	250.01	245.98	103.01	1.618
	SF4-II					247.95			
	SF4-III					239.98			
IF6	IF6-I	PI	6	0.81	4.86	250.94	245.39	135.56	1.330
	IF6-II					241.21			
	IF6-III					244.03			
SF6	SF6-I	SI	6	0.81	4.86	332.02	331.36	135.56	1.796
	SF6-II					325.18			
	SF6-III					336.88			

Note: t = nominal thickness of flax FRP tube without considering the thickness of resin matrix; t_a = actual thickness of flax FRP tube; N_e = bearing capacity of test specimens; N_f = bearing capacity of flax FRP rings; N_i = bearing capacity of plain ice or sawdust-reinforced ice specimens. For the type of ice core, PI = plain ice; SI = sawdust-reinforced ice.

In addition, in order to evaluate the bearing contribution of outer flax FRP tubes in composite columns, two nominally identical flax FRP rings with three different thicknesses, with a height of 50 mm and an inner diameter of 150 mm, were prepared and axially loaded until failure following Chinese standard GB/T 5350-2005 [42]. The naming rule of flax FRP ring specimens was described as

follows. It began with FR representing FRP rings, followed by a number indicating the number of FRP layers in flax FRP rings. The last Roman numeral was used for differentiating two nominally identical specimens. The test results of the flax FRP rings were presented in the next section.

2.3. Preparation of Specimens

The main preparation processes of plain ice and sawdust-reinforced ice specimens included the following steps: (1) A PVC tube with an inner diameter of 150 mm and a height of 300 mm was capped with a wooden plate by epoxy resin, which was used as the formwork for preparing ice specimens (Figure 1a). (2) Four hollow PVC hoses with sealed bottoms were symmetrically placed in the formwork (Figure 1b). The volume expansion during ice formation would squeeze the voids of the hollow hoses. Therefore, the radical pressure during water freezing process would be significantly released, leading to a great decrease in the number of cracks in ice [5,43]. (3) For sawdust-reinforced ice specimens, the sawdust was uniformly mixed with the water at the weight ratio of 14 (the sawdust) to 86 (the water) via mechanical stirrer. Considering the high water absorption of sawdust, the mixture should stay for at least three hours at ambient temperature to ensure that the sawdust was fully saturated in water. (4) Water and the mixture of sawdust and water were poured into the formworks for plain ice and sawdust-reinforced ice specimens, respectively. For the sawdust-reinforced ice specimen, the mixture of sawdust and water should be compacted layer by layer (five layers in total) to avoid bubbles. (5) After the casting was finished, the formworks were placed in the refrigerator (AUCMA Inc., Qingdao, China) at $-15\text{ }^{\circ}\text{C}$ for 48 h. (6) Finally, five plies of 45-mm-wide duct tapes were used to strengthen the ends of plain ice column (Figure 1c) and sawdust-reinforced ice column (Figure 1d) to avoid any premature failure at such locations due to stress concentration during the test. As shown in Figure 1d, the sawdust was approximately evenly distributed in the sawdust-reinforced ice specimen corresponding to the selected volume fraction (i.e., 26.6%).

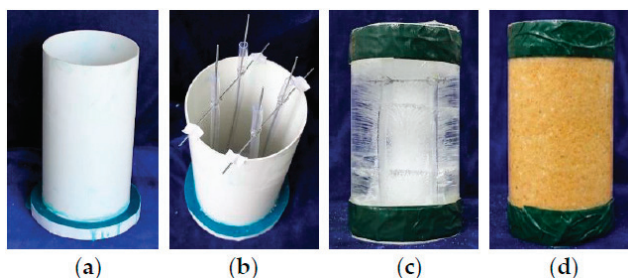


Figure 1. Preparation of plain ice and sawdust-reinforced ice specimens: (a) PVC formwork; (b) placement of hoses; (c) plain ice specimen; and (d) sawdust-reinforced ice specimen.

The preparation of PIFFT and SIFFT specimens was similar to that of aforementioned unconfined ice specimens. Firstly, the flax FRP tube was prepared via wet layup process by wrapping resin-impregnated flax fiber fabric around a cylindrical steel mold with fibers oriented in the hoop direction, with an overlapping length of 150 mm. Each end of flax FRP tube was strengthened by a 45-mm-wide carbon FRP strip to avoid any premature failure at the ends. In order to constitute a formwork, one end of the prepared flax FRP tube was capped with a circular wooden plate (Figure 2a). The following procedures, including the installation of hollow hoses (Figure 2b), the casting of water or the mixture of sawdust and water into flax FRP tubes, and the freezing in refrigerators were the same as those of unconfined plain ice and sawdust-reinforced ice columns.

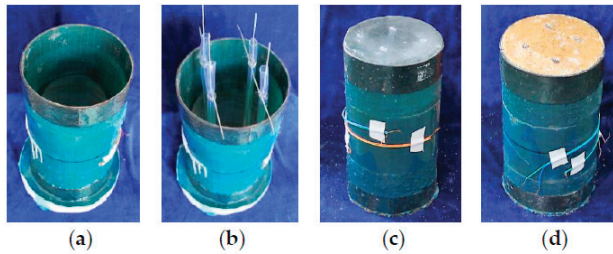


Figure 2. Preparation of plain ice-filled flax fiber-reinforced polymer tubular (PIFFT) and sawdust reinforced ice-filled flax fiber-reinforced polymer tubular (SIFFT) specimens: (a) flax fiber-reinforced polymer (FRP) tube; (b) placement of hoses; (c) PIFFT specimen; and (d) SIFFT specimen.

2.4. Test Setup and Instrumentation

All axial compression tests were conducted in winter. Prior to the compression test, the temperature of all specimens should be stabilized at $-3\text{ }^{\circ}\text{C}$, which is equal to the temperature inside the laboratory, to avoid the heat exchange between the specimens and surrounding environment during the axial compression loading. It should be admitted that the difference between the specimen preparation temperature (i.e., $-15\text{ }^{\circ}\text{C}$) and specimen compression temperature (i.e., $-3\text{ }^{\circ}\text{C}$) might cause some internal damage of the ice, which was ignored in this study. A more accurate experimental program remained to be conducted in the authors’ future study to take this influence into consideration. All specimens were axially loaded under displacement control at a loading rate of 1.5 mm/min. As shown in Figure 3a, two insulating plates were placed between the testing machine and specimen’s each end to block the heat transfer between them [39]. Two linear variable displacement transducers (LVDTs, Liyang Instrument and Meter Inc., Liyang, China) were installed to monitor the overall axial shortening of the specimen (Figure 3a). In addition, for each PIFFT or SIFFT specimen, four strain gauges (Zhejiang Huangyan Testing Instrument Inc., Taizhou, China) with a gauge length of 20 mm were mounted on the surface of the outer flax FRP tube at the mid-height region to monitor the hoop strains. One (i.e., SG4) was placed within the overlapping zone and the remaining three (i.e., SG1, SG2, and SG3) were symmetrically distributed at 90° outside the overlapping zone (Figure 3b).

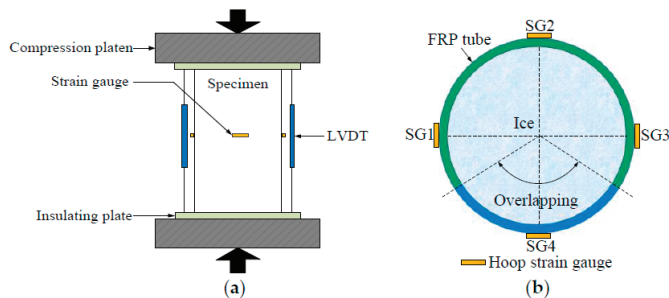


Figure 3. Test setup and instrumentation: (a) Test setup and linear variable displacement transducers (LVDTs); and (b) layout of strain gauges.

2.5. Melting Tests

In addition to axial compression tests, melting tests were also designed in this study to evaluate the melting rate of different types of specimens. As shown in Figure 4, four representative specimens, including plain ice short column (PI), sawdust-reinforced ice short column (SI), PIFFT short column (IF6), and SIFFT short column (SF6), were placed on the roof of the laboratory to conduct the melting tests. The specimen naming rule was identical to that proposed for the specimens in the compression

tests. For PIFFT and SIFFT specimens, considering that the heat insulation effect might be better when a thicker FRP tube was used, flax FRP tubes with six FRP layers were used in the melting tests. A circular wooden plate was placed on the bottom of each specimen to avoid direct contact between the specimen and the ground. Moreover, a rubber cap with a diameter of 160 mm was set on the top of each specimen to avoid direct sunlight based on the consideration that the top surface of the ice column in an actual structure should not be directly exposed to the surrounding environment. The melting tests were carried out from March 22, 2018 at 10:00 to March 25, 2018 at 13:00. The outdoor temperature and the weight of each specimen were simultaneously recorded twice per hour in the first 12 h and then once per hour in the following 63 h.



Figure 4. Melting specimens.

3. Results and Discussions

3.1. General Observations

Many longitudinal cracks were developed through the whole height of the plain ice specimen during compression, which was followed by significant dilation near the mid-height region at failure (Figure 5a). By contrast, the number of cracks in the sawdust-reinforced ice specimen after the compression tests was dramatically decreased (Figure 5b). This might be interpreted by sawdust fiber bridging effect, which played a significant role on reducing and holding cracks in ice. In addition, pronounced dilation occurred near the ends of sawdust-reinforced ice specimen, while the lateral deformation at mid-height region was relatively small, which was probably attributed to the excellent plastic deformability of reinforced ice after the modification of sawdust.

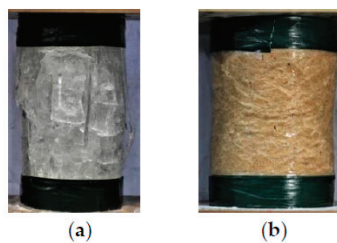


Figure 5. Typical failure modes of (a) plain ice specimen and (b) sawdust-reinforced ice specimen.

The typical failure modes of PIFFT and SIFFT specimens after the compression tests are shown in Figure 6. Both PIFFT and SIFFT specimens failed by the sudden rupture of flax FRP tubes outside the additional confinement zone at two ends accompanied by a loud popping noise, which was very similar to the failure mode of concrete-filled flax FRP tubular (CFFT) short columns under axial compression reported by Xia et al. [44]. The flax FRP tubes were carefully removed after finishing the tests. The lateral dilation of confined plain ice at mid-height was observed to be much smaller than that of unconfined plain ice because of the effective confinement of the outer FRP tube. Some minor longitudinal cracks developed in the plain ice cores corresponding to the rupture zone of the outer flax FRP tube. By contrast, few cracks were observed in sawdust-reinforced ice core. Furthermore,

the dilation of confined sawdust-reinforced ice near mid-height region was more significant than that of each end due to the additional confinement from the carbon FRP strip, which was tremendously different from the failure mode of unconfined sawdust-reinforced ice specimen (Figure 5b).

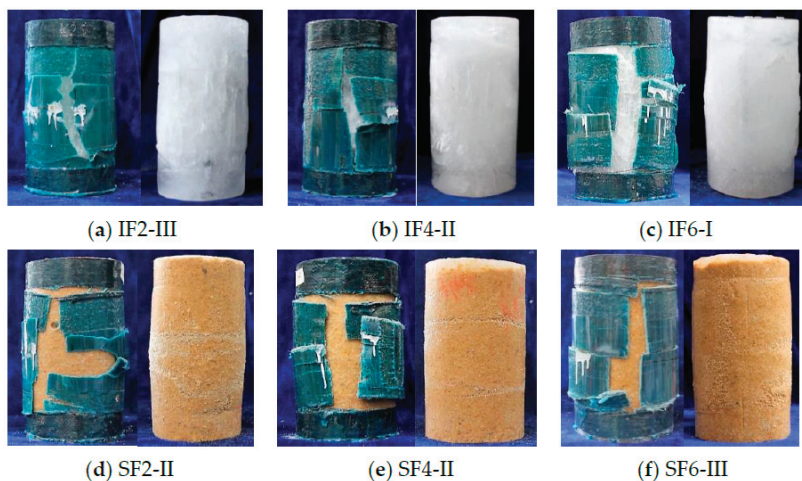


Figure 6. (a–f) Typical failure modes of PIFFT and SIFFT specimens (IF and SF representing PIFFT and SIFFT, respectively; Arabic numeral representing the number of flax FRP layers; and Roman numeral differentiating three nominally identical specimens).

3.2. Axial Load vs. Strain Response

Figure 7 shows the axial load vs. axial strain responses of the plain ice and sawdust-reinforced ice specimens. Unless otherwise specified, the axial strain in this study was obtained based on the total shortening of the test specimen. As shown in Figure 7, the initial compressive stiffness of the plain ice specimens was slightly higher than that of the sawdust-reinforced ice specimens. The average elastic moduli of the plain ice and sawdust-reinforced ice were 0.36 and 0.28 GPa, respectively. The average bearing capacity and the corresponding axial strain of the plain ice specimens were 48.98 kN and 1.13%, respectively, while 75.61 kN and 2.41% for the sawdust-reinforced ice specimens. As for the descending branch, the axial load of the sawdust-reinforced ice specimens decreased much more slowly than that of the plain ice specimens, which confirmed that the ductility of ice was considerably improved due to the introduction of sawdust. Overall, the sawdust-reinforced ice column was observed to have higher bearing capacity and better deformability compared with the plain ice column when tested under axial compression. The compression tests were continued until the resistance of the plain ice specimens dropped to around 65% of the peak load, while the compression tests on the sawdust-reinforced specimens were terminated manually when the axial shortening reached around 30 mm due to their excellent deformability.

In a concrete-filled FRP tubular (CFFT) column, the axial bearing contribution of the outer FRP tube to the total load carried by the composite column would be very limited if the fibers are mainly oriented in the hoop direction. In fact, the compressive strength of an FRP tube in the orthogonal direction to the reinforcing fibers is mainly dependent on its resin matrix [45]. Therefore, the axial contribution of such FRP tube to a CFFT column is usually omitted during the calculation process. However, given that the elastic moduli of unconfined plain ice (0.36 GPa) and sawdust-reinforced ice (0.28 GPa) tested in this study were much smaller than that of the normal concrete (around 30 GPa), the compressive bearing contribution of outer flax FRP tubes in PIFFT and SIFFT columns should be taken into consideration.

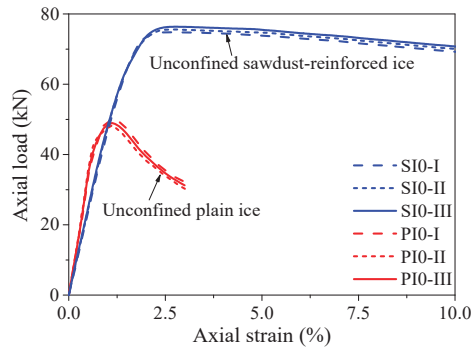


Figure 7. Axial load vs. strain responses of the plain ice and sawdust reinforced ice columns.

It was observed that the local buckling of the outer flax FRP tube in PIFFT and SIFFT specimens was effectively suppressed by the corresponding plain ice and sawdust-reinforced ice cores before rupture. Similarly, the local buckling of the axially loaded flax FRP rings was also not observed before reaching their peak loads. In the present study, it was assumed that the compressive behavior of the outer flax FRP tube in PIFFT and SIFFT columns can be reflected by the axial load vs. axial strain curves of the flax FRP ring specimens (Figure 8). As shown in Figure 8, the initial compressive stiffness and the bearing capacity of the flax FRP rings increased with the wall thickness. The average bearing capacities of the flax FRP rings with two, four, and six FRP layers were 82.66, 103.01, and 135.56 kN, respectively. The axial strains at peak loads of the flax FRP rings with three different numbers of FRP layers, with an average value of 3.84%, were close to each other. It was obvious that the peak loads of the flax FRP rings were larger than those of the unconfined plain (i.e., 48.98 kN) and sawdust-reinforced ice (i.e., 75.61 kN) specimens, which confirmed the necessity of considering the compressive contribution of outer flax FRP tubes to composite columns in this study.

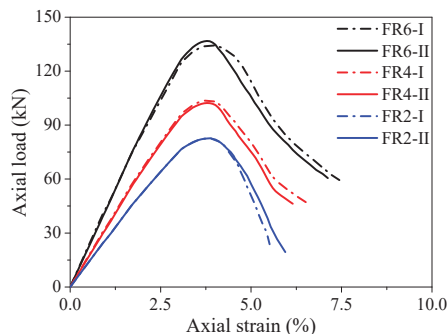


Figure 8. Axial load vs. strain responses of flax FRP rings.

Figure 9 shows the axial load vs. strain responses of PIFFT and SIFFT columns. The hoop strain was the average value of the readings of three hoop strain gauges (i.e., SG1, SG2, and SG3) outside the overlapping zone (Figure 3b). The ultimate condition of the composite column was characterized by the hoop rupture of outer flax FRP tubes in PIFFT and SIFFT columns. The axial load vs. axial strain responses of composite columns terminated at the peak point when the absolute value of hoop strain reached its maximum value (i.e., hoop rupture strain). The peak loads of PIFFT and SIFFT specimens were obviously greater than those of the corresponding unconfined plain ice and sawdust-reinforced ice column, respectively. As shown in Table 1 and Figure 9, the peak loads of PIFFT and SIFFT specimens increased with the increasing thickness of outer flax FRP tubes. In addition, the peak load, hoop rupture strain, and ultimate axial strain of SIFFT column were obviously larger than that of PIFFT

column with the same tube thickness. It should be noted that the deformability of the unconfined sawdust-reinforced ice specimen (within SI series) was so excellent that its axial strain was just plotted from 0% to 5% in Figure 9.

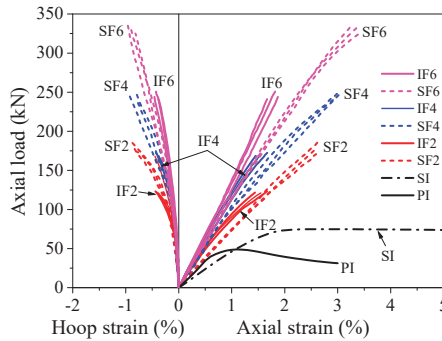


Figure 9. Axial load vs. strain responses of PIFFT and SIFFT specimens.

3.3. Axial Stress vs. Strain Behavior of Confined Ice

The axial load was simultaneously shared by the outer flax FRP tube and the plain or sawdust-reinforced ice core when a PIFFT or SIFFT column was tested under axial compression. Based on the static equilibrium as well as the axial deformation compatibility between outer tube and inner ice, the load carried by the ice core was believed to be equal to the difference between the load resisted by the composite column and the load carried by the flax FRP tube at the same axial strain, and the latter was obtained through the compression tests on flax FRP rings (Figure 8). It is worth mentioning that the hollow flax FRP ring specimens and the outer flax FRP tubes in composite columns had different stress states, because the latter also suffered hoop tension apart from axial compression. However, this distinction was ignored for simplification in this study. Based on the simplified assumption, the axial stress vs. axial strain responses of the flax FRP-confined plain ice and sawdust-reinforced ice were obtained, as shown in Figure 10.

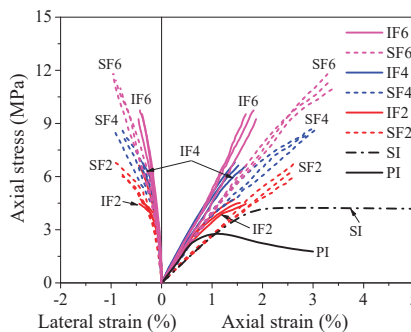


Figure 10. Axial stress vs. strain responses of the confined plain ice and sawdust-reinforced ice.

In terms of hoop strain, in an FRP-confined concrete column, the FRP jacket and inner concrete were believed to have compatible deformation in the circumferential direction. In this study, the hoop strain of the flax FRP tube in PIFFT and SIFFT columns was also employed to assess the lateral strain of the confined plain ice and sawdust-reinforced ice due to the fact that the inner ice was well confined by the outer flax FRP tube until rupture. The axial stress vs. lateral strain responses of the plain ice cores and sawdust-reinforced ice cores are also exhibited in Figure 10 to demonstrate their lateral dilation during the loading process.

The main test results of the plain ice cores and sawdust-reinforced ice cores in PIFFT and SIFFT specimens are summarized in Table 2, including the axial compressive strength f'_{ic} , ultimate axial strain ϵ_{iu} , and the hoop rupture strain $\epsilon_{h,rupt}$ of outer flax FRP tubes. The strength and strain enhancement ratios (i.e., f'_{ic}/f'_{io} and $\epsilon_{iu}/\epsilon_{io}$), together with the ratios between hoop rupture strains of flax FRP tubes and material ultimate tensile strains of flat coupons (i.e., $\epsilon_{h,rupt}/\epsilon_f$), are also shown in Table 2. It can be seen that the strength enhancement ratio of confined sawdust-reinforced ice was smaller than that of the confined plain ice corresponding to the same number of flax FRP layers. Moreover, the strain enhancement ratio was observed to have a similar trend. Additionally, the average hoop rupture strain of flax FRP tubes in SIFFT specimens was around twice as large as that of flax FRP tubes in PIFFT specimens.

Table 2. Test results of confined plain ice and sawdust-reinforced ice.

Series	Specimen	f'_{ic} (MPa)	Average f'_{ic} (MPa)	f'_{ic}/f'_{io}	ϵ_{iu} (%)	Average ϵ_{iu} (%)	$\epsilon_{iu}/\epsilon_{io}$	$\epsilon_{h,rupt}$ (%)	Average $\epsilon_{h,rupt}$ (%)	$\epsilon_{h,rupt}/\epsilon_f$
IF2	IF2-I	4.46			1.67			0.44		
	IF2-II	4.52	4.56	1.65	1.55	1.55	1.37	0.38	0.42	0.310
	IF2-III	4.71			1.44			0.42		
SF2	SF2-I	6.78			2.65			0.91		
	SF2-II	6.34	6.37	1.49	2.60	2.63	1.09	0.84	0.84	0.628
	SF2-III	6.01			2.65			0.78		
IF4	IF4-I	6.63			1.52			0.45		
	IF4-II	6.60	6.68	2.41	1.67	1.55	1.37	0.43	0.42	0.313
	IF4-III	6.80			1.45			0.38		
SF4	SF4-I	8.78			3.02			0.81		
	SF4-II	8.64	8.60	2.01	3.04	2.99	1.24	0.94	0.85	0.633
	SF4-III	8.39			2.91			0.79		
IF6	IF6-I	9.74			1.82			0.43		
	IF6-II	9.53	9.50	3.43	1.67	1.79	1.58	0.39	0.42	0.316
	IF6-III	9.24			1.87			0.46		
SF6	SF6-I	11.43			3.35			0.90		
	SF6-II	10.99	11.40	2.66	3.41	3.35	1.39	0.82	0.90	0.668
	SF6-III	11.78			3.29			0.96		

Note: f'_{io} = compressive strength of unconfined ice (2.77 MPa for plain ice and 4.28 MPa for sawdust-reinforced ice); and ϵ_{io} = peak axial strain of unconfined ice (1.13% for plain ice and 2.41% for sawdust-reinforced ice).

As shown in Table 2, the compressive strengths of the confined plain ice and sawdust-reinforced ice were obviously greater than those of the corresponding unconfined plain ice and sawdust-reinforced ice, and they increased approximately linearly with the number of flax FRP layers in this study, which was also observed in self-luminous glass FRP-confined ice [39]. In addition, the compressive strengths and peak axial strains of the unconfined and confined sawdust-reinforced ice were larger than those of the corresponding unconfined and confined plain ice with the same thickness of flax FRP tube, which indicated the compressive properties of ice would be effectively enhanced after the introduction of sawdust. It was noticed that the number of FRP layers in flax FRP tubes had only a marginal effect on the peak strains of the confined plain ice, while a slightly linear increase was observed for confined sawdust-reinforced ice with the increasing flax FRP layers. Overall, the axial compressive properties including compressive strength and corresponding peak axial strain of the sawdust-reinforced ice were better than those of the plain ice regardless of the existence of flax FRP tubes.

3.4. Lateral Dilatation Behavior of Confined Ice

It is generally accepted that the lateral dilatation (hoop strain) of confined concrete is a function of the axial strain. Meanwhile, the dilatation of the concrete core is restricted by the confining pressure

provided by steel stirrups and/or FRP jackets. Therefore, the confining pressure is dependent on the axial strain and some analytical models have been established based on this understanding [46–48]. Similarly, the development of the confining pressure provided the flax FRP tube in this study is also expected to be a function of the axial strain of the confined ice. Considering that the flax FRP is a linear elastic material, as a simplification, the relationship between the lateral strain (instead of confining pressure from the flax FRP tube) and the axial strain of the plain ice cores and sawdust-reinforced ice cores are presented in Figure 11. It was observed that the lateral strain vs. axial strain responses of all ice cores were close to each other when their axial strains were within 0.5%. After that, the absolute values of the lateral strains of the plain ice cores were greater than those of sawdust-reinforced ice cores at a given axial strain, especially for plain ice cores confined by two and four FRP layers in flax FRP tubes. This observation indicated that the lateral dilation of the confined sawdust-reinforced ice was more effectively suppressed due to the fiber bridging effect after the introduction of sawdust in ice.

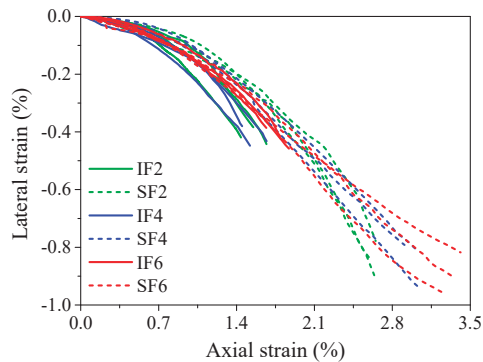


Figure 11. Lateral strain vs. axial strain responses of confined ice.

3.5. Hoop Strain Distribution of FRP Tube

The uniformity of the lateral dilation of flax FRP-confined might be reflected by the hoop strain distribution of outer flax FRP tube around the circumference. Figure 12 shows the distribution of the hoop strains of flax FRP tubes in PIFFT and SIFFT specimens corresponding to the peak loads. The hoop strains were monitored by the four hoop strain gauges around the circumference of the outer flax FRP tube (Figure 3b). It was observed that the hoop strain distribution of flax FRP tubes in SIFFT specimens was more non-uniform compared with that in PIFFT columns. Similarly, the hoop strain distribution of FRP jacket in FRP-confined concrete columns tested under axial compression was also observed to be non-uniform [41]. It might be attributed to the fact that both the sawdust-reinforced ice and the concrete are a mixture of at least two constituent materials, and there is an unavoidable regional heterogeneity in the body of the specimen even though it is carefully prepared. By contrast, the plain ice was prepared using one component material (i.e., water), thus causing a much more uniform distribution of the hoop strains of flax FRP tubes in PIFFT columns in this study. In addition, the hoop strains within the overlapping zone of flax FRP tubes in PIFFT and SIFFT specimens were observed to be slightly smaller than those outside the overlapping zone, which was similar to the observations in axially loaded FRP-confined concrete columns [41].

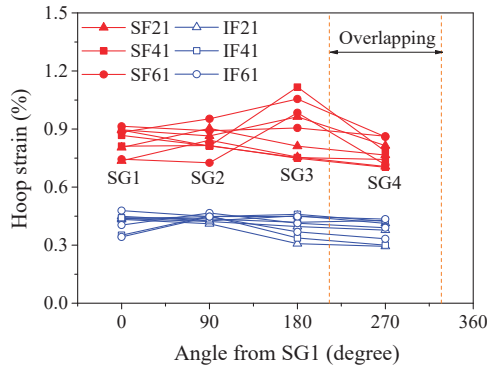


Figure 12. Distribution of hoop strains of FRP tubes in PIFFT and SIFFT specimens at peak loads.

It was also of great significance to investigate the hoop strain distribution of outer flax FRP tubes in the composite columns at different loading period. In this study, specimens IF2-II and SF4-II were selected as representatives to evaluate the distribution of the hoop strains of the flax FRP tubes in PIFFT and SIFFT specimens at different loading level, respectively. In order to clearly present the variation of hoop strains obtained even at the smallest axial load, all hoop strains were normalized by the readings of SG1 at each level of loading. As shown in Figure 13a, the normalized hoop strain distribution curves of flax FRP tubes in PIFFT specimens generally had a similar trend regardless of the variation of axial load. By contrast, the normalized hoop strain distribution in SIFFT specimens (Figure 13b) was observed to become more uniform with the increase of axial load. The phenomenon might be explained by the fact that the confined sawdust–ice mixture with more initial defects than plain ice becomes denser with the increase of axial load and lateral confinement. As a result, a more evenly distributed hoop strains were observed in the more homogeneous sawdust-reinforced ice with the increasing loading level. Moreover, the hoop strains within the overlapping zone of FRP tubes in PIFFT and SIFFT columns were smaller than those outside the overlapping zone at different loading level.

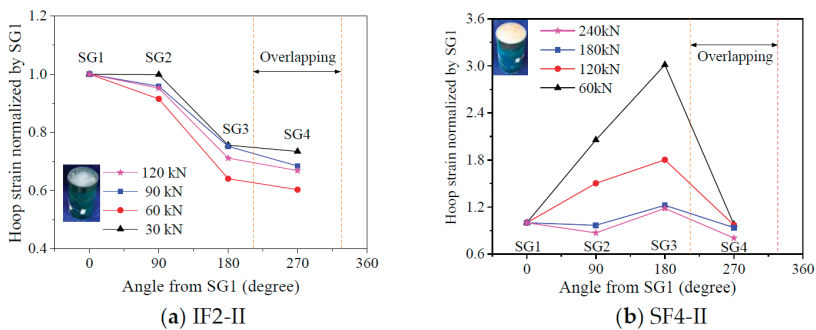


Figure 13. Distribution of normalized hoop strains of FRP tubes in PIFFT and SIFFT specimens at different loads.

3.6. Energy-Absorption Capacity

As we all know, a good structural member is required to have high bearing capacity, good deformability, and large energy-absorption capacity. In this study, the flax FRP composites were almost elastic until failure without yielding characteristic and the axial load vs. strain responses of PIFFT and SIFFT columns were approximately linear before reaching the ultimate state. Therefore, it was unsuitable to use peak load or ultimate axial strain alone to evaluate the energy-absorption capacity of the composite columns. In order to solve this problem, one parameter termed energy index was

initially proposed by Yan and Chou [36] for flax FRP-confined concrete. In this paper, it was defined as the ratio of the fracture energy of the confined plain ice or sawdust-reinforced ice divided by the fracture energy of the unconfined plain ice. The fracture energy was the area under axial stress (from zero to peak value) vs. strain curve of confined ice. It was observed that the area of the confined sawdust-reinforced ice in SIFFT specimen was obviously larger than that of the confined plain ice in the corresponding PIFFT specimen with the same tube thickness.

The average energy indexes of confined plain ice and sawdust-reinforced ice are shown in Figure 14. According to the definition, the value of the energy index for the unconfined plain ice specimens was equal to one. The energy index of the unconfined sawdust-reinforced ice specimens was 3.25 times as large as that of the unconfined plain ice specimens. The energy indexes of the confined body in PIFFT and SIFFT specimens were roughly linearly increased with the increase of flax FRP layers. In addition, the energy index of the confined sawdust-reinforced ice in the SIFFT specimen was larger than that of the confined plain ice in the corresponding PIFFT specimen with the same tube thickness. The energy indexes of the confined plain ice in PIFFT specimens with two, four, and six plies of FRP layers were 2.10, 2.77, and 3.94, respectively, while 4.34, 7.20, and 10.14 for the confined sawdust-reinforced ice with the same tube thickness, respectively. In summary, it confirmed that the energy-absorption capacity of confined ice would be considerably improved if sawdust was introduced into ice or a thicker flax FRP tube was used.

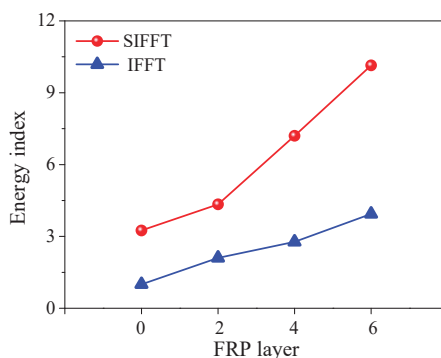


Figure 14. Energy index of confined plain ice and sawdust-reinforced ice.

3.7. Melting Rate

Figure 15 shows the melting ratio of four representative specimens (Figure 4) and the corresponding outdoor temperature with increasing time periods. The melting ratio was defined as the weight reduction of each specimen divided by its original weight of its involved ice. The weights of the non-melting bodies (i.e., PVC hoses, sawdust and flax FRP tubes) were deducted during the calculation. As shown in Figure 15, during the daytime, the melting rates of the four specimens were relatively fast due to the solar radiation and increase of outdoor temperature, especially at the initial stage of the melting tests. At night, the melting rates of the specimens were much slower because of the absence of sunlight and lower temperature (around 4 °C). Moreover, the melting rate of the specimen PI was faster than that of the specimens SI and IF6, which confirmed that the melting of plain ice was effectively delayed by the inclusion of sawdust as well as the insulation of outer flax FRP tube.

In addition, the melting rates of specimens SI and SF6 were close to each other, which indicated that flax FRP tube has little influence on the melting rate of sawdust-reinforced ice specimen. This phenomenon might be explained by the melting mechanism of sawdust-reinforced ice in SIFFT column, as shown in Figure 16. The unconfined or confined sawdust-reinforced ice was surrounded by a layer of dry wood fiber with a very low thermal conductivity after the initial melting, which insulated the inner frozen sawdust-ice mixture from solar radiation. Sawdust-reinforced ice specimen

itself had so excellent melting-resistant properties that the insulating effect of the outer flax FRP tube in SIFFT specimen was not dominant. The specimen PI was totally melted at 50.26 h while 74.93 h for the specimen IF6. The melting rates of the specimens SI and SF6 were so slow that their monitoring was stopped at 75 h, with the corresponding final melting ratios of 51.7% and 48.3%, respectively. Finally, it should be noted that the melting test is a relatively rough exploratory test. In addition to the temperature, many other factors such as the heat flow are not taken into consideration in this paper due to the limitation of experimental conditions, which will be improved by the authors in future study.

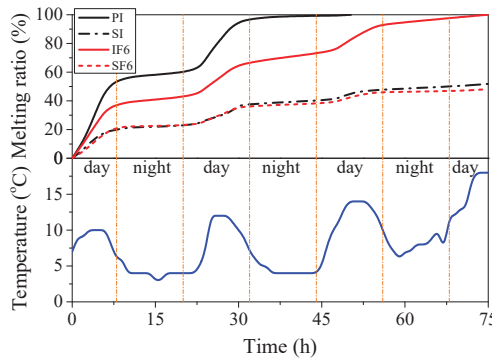


Figure 15. Melting rate of representative specimens and variation of temperature with increasing time.

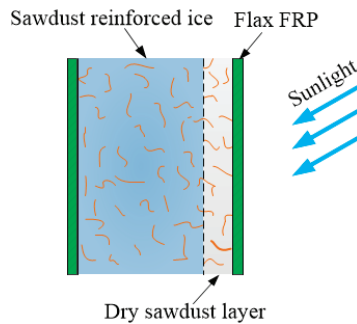


Figure 16. Melting mechanism of sawdust-reinforced ice in SIFFT specimen.

4. Ultimate Bearing Capacity of Short Columns

Taking the bearing contribution of outer flax FRP tubes into consideration, the ultimate bearing capacity N_u of the proposed PIFFT and SIFFT short column with circular sections can be calculated as following:

$$N_u = \beta f_f A_f + f'_{ic} A_i \tag{1}$$

in which A_f and A_i = actual cross-sectional areas of flax FRP tube and plain ice or sawdust-reinforced ice core, respectively; f_f = compressive strength of flax FRP tubes (57.2 MPa in this study) obtained by the compression tests on hollow flax FRP rings based on the actual thickness t_a (Table 1). β is a reduction factor proposed based on the consideration that the hollow FRP rings and ice cores do not simultaneously reach their axial peak loads. The compressive strength of outer FRP tube in composite columns will be overestimated if the bearing capacity of hollow FRP rings is directly used. f'_{ic} is the compressive strength of the confined plain ice and sawdust-reinforced ice, which is obtained through regression analysis (Figure 17). It was noticed from Figure 17 that the slope of trend line for PIFFT specimens was larger than that observed for SIFFT specimens, which might be attributed to the fact

that the plain ice with relatively weak compressive strength is much more sensitive to the lateral confinement from flax FRP tubes compared with sawdust-reinforced ice.

$$\frac{f'_{ic}}{f'_{io}} = \begin{cases} 1 + 1.93 \frac{f_l}{f'_{io}} & \text{for PIFFT} \\ 1 + \frac{f_l}{f'_{io}} & \text{for SIFFT} \end{cases} \quad (2)$$

in which f'_{io} = compressive strength of the unconfined plain ice or sawdust-reinforced ice, with values of 2.77 and 4.28 MPa, respectively, in this study; f_l = maximum confining stress of flax FRP tubes at rupture and it is given by

$$f_l = \frac{2E_f \varepsilon_{h,rupt} t}{D} \quad (3)$$

in which E_f = hoop tensile elastic modulus of flax FRP tube; t = nominal thickness of flax FRP tube; D = diameter of confined ice; $\varepsilon_{h,rupt}$ = hoop rupture strain of flax FRP tube and it can be determined by

$$\varepsilon_{h,rupt} = k_\varepsilon \varepsilon_f \quad (4)$$

in which ε_f = ultimate tensile strain of flax FRP laminates obtained via flat coupon tests; k_ε = FRP efficiency factor initially proposed by Pessiki et al. [49] for FRP-confined concrete, which was used in this study to evaluate the utilization rate of the strain capacity of the flax FRP in PIFFT and SIFFT columns. Figure 18 shows that the mean values of k_ε were 0.313 and 0.643, respectively, for PIFFT and SIFFT specimens.

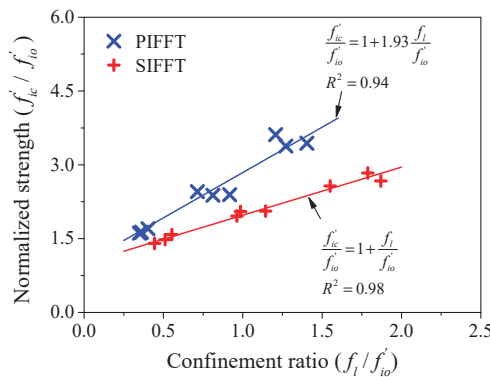


Figure 17. Regression of the compressive strength of confined ice.

It can be seen from Figures 8 and 9 that the peak axial strains of the confined plain ice and sawdust-reinforced ice in corresponding PIFFT and SIFFT short columns were smaller than those of flax FRP rings, which indicated that it was unsuitable to predict the axial bearing capacity of the composite short column using the simple superposition of the peak loads of the confined ice and FRP ring. Therefore, a reduction factor β was incorporated to assess the compressive strength of the outer flax FRP tube in PIFFT and SIFFT specimens more accurately. It was defined as the ratio of axial load of flax FRP ring corresponding to peak strain of the composite short column to the bearing capacity of flax FRP ring. Figure 19 shows the relationship between the reduction factor β and the diameter-to-thickness (D/t_a) ratio of flax FRP tube. The value of β was around 0.53 for PIFFT short columns and approximately linearly decreased with D/t_a ratio for SIFFT short columns. The value of β was determined using Equation (5).

$$\beta = \begin{cases} 0.53 & \text{for PIFFT} \\ 1.21 - 0.0078 \frac{D}{t_a} & \text{for SIFFT} \end{cases} \quad (5)$$

Figure 20 shows the comparison of ultimate bearing capacities between predicted and experimental results. The ratio of the calculated ultimate bearing capacities N_u to the experimental results N_e was close to one, which indicated that the proposed equation achieved good evaluation of the ultimate bearing capacities of circular PIFFT and SIFFT short columns. It is noteworthy that the equations for evaluating the bearing capacities of PIFFT and SIFFT stub columns are proposed based on the test results of fairly limited specimens tested in this study. Therefore, the accuracy of these equations remains to be verified by more test results reported by other researchers. However, to the best of the authors' knowledge, composite columns consisting of natural FRP composites (e.g., flax FRP) and ice have not been documented in the literature. Therefore, more reasonable equations with enough accuracy need to be established on the basis of more detailed experimental results and more in-depth theoretical analysis in future study. In addition, it should be noted that axial compression tests are very sensitive to boundary conditions, which would cause non-pure compressive state in the specimens. Furthermore, the lateral confining stress provided by the flax FRP tube further complicates the internal stress in the ice core of the specimens. In order to take these factors into consideration, finite element modeling might be a good technique that could be used to study and identify this complex internal stress state of the confined ice. The related work will be incorporated in the authors' future study.

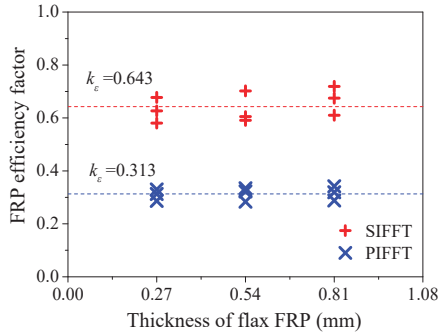


Figure 18. Strain efficiency factor in PIFFT and SIFFT specimens.

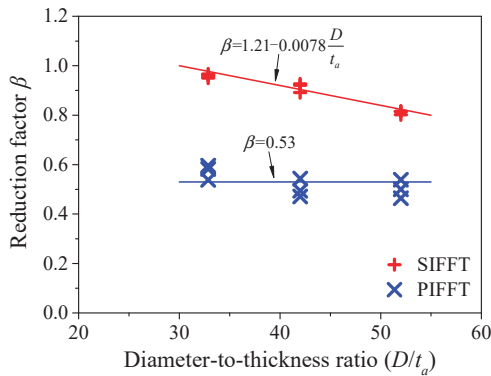


Figure 19. Relationship between β and D/t_a in PIFFT and SIFFT specimens.

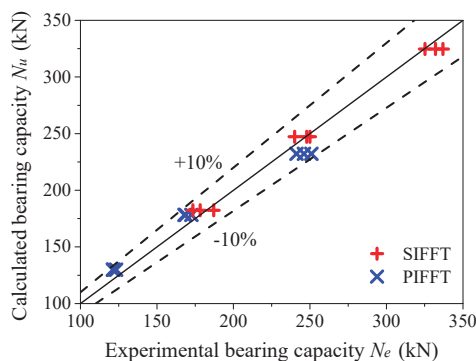


Figure 20. Comparison of ultimate bearing capacities between calculated and experimental results.

5. Conclusions

This paper presents an exploratory investigation on the axial compressive behavior of circular sawdust-reinforced ice-filled flax FRP tubular (SIFFT) short columns. In addition to SIFFT short columns, three types of short columns including the plain ice specimens, the sawdust-reinforced ice specimens, and the plain ice-filled flax FRP tubular (PIFFT) specimens were also tested to make comparisons between different specimen series. It confirmed that the proposed SIFFT columns hold great potential to be used as compression members in cold areas due to its good compressive behavior. Moreover, the SIFFT column is innovatively achieved by three types of recycled constituent materials (i.e., flax fiber, ice, and sawdust), which might lead to a more sustainable and environmentally friendly solution. The results and discussions presented in this study allow the following conclusions to be drawn:

- (1) Both PIFFT and SIFFT specimens fail by the rupture of flax FRP tubes outside the additional confinement zone. The lateral dilation and the development of cracks of the ice cores are effectively suppressed by the outer flax FRP tubes. Overall, the PIFFT and SIFFT specimens exhibit relatively brittle behavior.
- (2) Different from the typically bilinear curves of FRP-confined concrete, the axial stress vs. strain curves of flax FRP-confined ice are quite linear. The compressive strength of confined plain ice and sawdust-reinforced ice is approximately linearly enhanced with the increasing number of FRP layers in flax FRP tubes. Sawdust-reinforced ice cores have greater compressive strength, ultimate axial strain, and energy-absorption capacity compared with plain ice cores confined by flax FRP tubes with the same thicknesses.
- (3) At a given axial strain, the lateral dilation of confined sawdust-reinforced ice is smaller than that of confined plain ice. The hoop strain distribution in SIFFT specimens is more non-uniform than that observed in PIFFT specimens.
- (4) The melting of plain ice specimen is effectively delayed by the inclusion of sawdust and the insulation of outer flax FRP tube, while the melting rate of unconfined sawdust-reinforced ice is close to that of confined sawdust-reinforced ice due to the insulation of a layer of dry wood fiber with a low thermal conductivity after the initial melting.
- (5) Equations are proposed to estimate ultimate bearing capacities of PIFFT and SIFFT short columns with circular sections. The predictions are shown to be in reasonable agreement with the test results.

Author Contributions: Conceptualization, Y.W.; methodology, Y.W. and B.W.; software, G.C.; validation, B.H.; formal analysis, G.C.; investigation, G.C. and Y.W.; resources, Y.W.; data curation, G.C.; writing—original draft preparation, G.C.; writing—review and editing, Y.W., B.W., and B.H.; visualization, G.C.; supervision, Y.W., B.W.

and B.H.; project administration, Y.W.; funding acquisition, Y.W. All authors have read and agreed to the published version of the manuscript.

Funding: This research was funded by the National Key R&D Program of China (Project No. 2017YFC0703000), the National Natural Science Foundation of China (Project Nos. 51778102 and 51978126), the Fundamental Research Funds for the Central Universities (Project No. DUT18LK35) and the Natural Science Foundation of Liaoning Province of China (Project No. 20180550763).

Acknowledgments: The authors wish to thank six undergraduate students including Shuo Chen, Pinqing Wang, Yitong Ji, Jinlei Gao, Haidong Guo and Peng Li for their valuable assistance in the experimental work.

Conflicts of Interest: The authors declare no conflict of interest.

References

1. Schulson, E.M. Brittle failure of ice. *Eng. Fract. Mech.* **2001**, *68*, 1839–1887. [CrossRef]
2. Timco, G.W.; Weeks, W.F. A review of the engineering properties of sea ice. *Cold Reg. Sci. Technol.* **2010**, *60*, 107–129. [CrossRef]
3. Wu, X.; Prakash, V. Dynamic strength of distill water and lake water ice at high strain rates. *Int. J. Impact Eng.* **2015**, *76*, 155–165. [CrossRef]
4. Masterson, D.M. State of the art of ice bearing capacity and ice construction. *Cold Reg. Sci. Technol.* **2009**, *58*, 99–112. [CrossRef]
5. Wang, Y.; Chen, G.; Wan, B.; Lin, H.; Zhang, J. Behavior of innovative circular ice filled steel tubular stub columns under axial compression. *Constr. Build. Mater.* **2018**, *171*, 680–689. [CrossRef]
6. Nixon, W.A. Alluvium-reinforced ice: A preliminary report of bending strength tests. *Cold Reg. Sci. Technol.* **1989**, *16*, 309–313. [CrossRef]
7. Nixon, W.A.; Weber, L.J. Reinforcement percentage effects on bending strength of soil-ice mixtures. *J. Cold Reg. Eng.* **1995**, *9*, 152–163. [CrossRef]
8. Vasiliev, N.K. On development of fibre-ice-composites. *Cold Reg. Sci. Technol.* **1993**, *21*, 195–199. [CrossRef]
9. Vasiliev, N.K.; Pronk, A.D.C.; Shatalina, I.N.; Janssen, F.H.M.E.; Houben, R.W.G. A review on the development of reinforced ice for use as a building material in cold regions. *Cold Reg. Sci. Technol.* **2015**, *115*, 56–63. [CrossRef]
10. Bai, Y.; Yan, Z.; Ozbakkaloglu, T.; Han, Q.; Dai, J.; Zhu, D. Quasi-static and dynamic tensile properties of large-rupture-strain (LRS) polyethylene terephthalate fiber bundle. *Constr. Build. Mater.* **2020**, *232*, 117241. [CrossRef]
11. He, J.; Xian, G.; Zhang, YX. Effect of moderately elevated temperatures on bond behaviour of CFRP-to-steel bonded joints using different adhesives. *Constr. Build. Mater.* **2020**, *241*, 118057. [CrossRef]
12. Huang, H.; Jia, B.; Lian, J.; Wang, W. Experimental investigation on the tensile performance of resin-filled steel pipe splices of BFRP bars. *Constr. Build. Mater.* **2020**, *242*, 118018. [CrossRef]
13. Zhang, B.; Feng, G.; Wang, Y.; Lai, C.; Wang, C.; Hu, X. Elliptical FRP-concrete-steel double-skin tubular columns under monotonic axial compression. *Adv. Polym. Technol.* **2020**, *2020*, 7573848. [CrossRef]
14. Lu, M.; Xiao, H.; Liu, M.; Li, X. Improved interfacial strength of SiO₂ coated carbon fiber in cement matrix. *Cem. Concr. Compos.* **2018**, *91*, 21–28. [CrossRef]
15. Wang, Y.; Wang, Y.; Han, B.; Wan, B.; Cai, G.; Chang, R. In situ strain and damage monitoring of GFRP laminates incorporating carbon nanofibers under tension. *Polymers* **2018**, *10*, 777. [CrossRef]
16. Wang, Y.; Wang, Y.; Wan, B.; Han, B.; Cai, G.; Chang, R. Strain and damage self-sensing of basalt fiber reinforced polymer laminates fabricated with carbon nanofibers/epoxy composites under tension. *Compos. Part A Appl. Sci. Manuf.* **2018**, *113*, 40–52. [CrossRef]
17. Li, J.; Xie, J.; Liu, F.; Lu, Z. A critical review and assessment for FRP-concrete bond systems with epoxy resin exposed to chloride environments. *Compos. Struct.* **2019**, *229*, 111372. [CrossRef]
18. Zhai, K.; Fang, H.; Fu, B.; Wang, F.; Hu, B. Mechanical response of externally bonded CFRP on repair of PCCPs with broken wires under internal water pressure. *Constr. Build. Mater.* **2020**, *239*, 117878. [CrossRef]
19. Wei, Y.; Zhang, X.; Wu, G.; Zhou, Y. Behaviour of concrete confined by both steel spirals and fiber-reinforced polymer under axial load. *Compos. Struct.* **2018**, *192*, 577–591. [CrossRef]

20. Wang, Y.; Zhang, X.; Cai, G.; Wan, B.; Waldmann, D.; Qu, Y. A new thickness-based accelerated aging test methodology for resin materials: Theory and preliminary experimental study. *Constr. Build. Mater.* **2018**, *186*, 986–995. [CrossRef]
21. Zhang, Y.; Wei, Y.; Bai, J.; Zhang, Y. Stress-strain model of an FRP-confined concrete filled steel tube under axial compression. *Thin Walled Struct.* **2019**, *142*, 149–159. [CrossRef]
22. Zhang, X.; Wang, Y.; Wan, B.; Cai, G.; Qu, Y. Effect of specimen thicknesses on water absorption and flexural strength of CFRP laminates subjected to water or alkaline solution immersion. *Constr. Build. Mater.* **2019**, *208*, 314–325. [CrossRef]
23. Mirmiran, A.; Shahawy, M. A new concrete-filled hollow FRP composite column. *Compos. Part B* **1996**, *27*, 263–268. [CrossRef]
24. Zeng, J.; Gao, W.; Duan, Z.; Bai, Y.; Guo, Y.; Ouyang, L. Axial compressive behavior of polyethylene terephthalate/carbon FRP-confined seawater sea-sand concrete in circular columns. *Constr. Build. Mater.* **2020**, *234*, 117383. [CrossRef]
25. Bai, Y.; Dai, J.; Mohammadi, M.; Lin, G.; Mei, S. Stiffness-based design-oriented compressive stress-strain model for large-rupture-strain (LRS) FRP-confined concrete. *Compos. Struct.* **2019**, *223*, 110953. [CrossRef]
26. Pi, Z.; Xiao, H.; Du, J.; Liu, M.; Li, H. Interfacial microstructure and bond strength of nano-SiO₂-coated steel fibers in cement matrix. *Cem. Concr. Compos.* **2019**, *103*, 1–10. [CrossRef]
27. Cao, Q.; Tao, J.; Ma, Z.J.; Wu, Z. Axial compressive behavior of CFRP-confined expansive concrete columns. *ACI Struct. J.* **2017**, *114*, 475–485. [CrossRef]
28. Cao, Q.; Tao, J.; Wu, Z.; Ma, Z.J. Behavior of FRP-steel confined concrete tubular columns made of expansive self-consolidating concrete under axial compression. *J. Compos. Constr.* **2017**, *21*, 04017037. [CrossRef]
29. Wang, Y.; Cai, G.; Li, Y.; Waldmann, D.; Larbi, A.S.; Tsavdaridis, K.D. Behavior of circular fiber-reinforced polymer-steel-confined concrete columns subjected to reversed cyclic loads: Experimental studies and finite-element analysis. *J. Struct. Eng.* **2019**, *145*, 04019085. [CrossRef]
30. Dong, Z.; Wu, G.; Zhao, X.; Zhu, H.; Wei, Y.; Yan, Z. Mechanical properties of discrete BFRP needles reinforced seawater sea-sand concrete-filled GFRP tubular stub columns. *Constr. Build. Mater.* **2020**, *244*, 118330. [CrossRef]
31. Alkbir, M.F.M.; Sapuan, S.M.; Nuraini, A.A.; Ishak, M.R. Fibre properties and crashworthiness parameters of natural fibre-reinforced composite structure: A literature review. *Compos. Struct.* **2016**, *148*, 59–73. [CrossRef]
32. Bachtari, E.V.; Kurkowiak, K.; Yan, L.; Kasal, B. Thermal stability, fire performance, and mechanical properties of natural fibre fabric-reinforced polymer composites with different fire retardants. *Polymers* **2019**, *11*, 699. [CrossRef] [PubMed]
33. Wang, Y.; Wang, Y.; Wan, B.; Han, B.; Cai, G.; Li, Z. Properties and mechanisms of self-sensing carbon nanofibers/epoxy composites for structural health monitoring. *Compos. Struct.* **2018**, *200*, 669–678. [CrossRef]
34. Dittenber, D.B.; Gangarao, H.V.S. Critical review of recent publications on use of natural composites in infrastructure. *Compos. Part A Appl. Sci. Manuf.* **2012**, *43*, 1419–1429. [CrossRef]
35. Yan, L.; Chouw, N. Experimental study of flax FRP tube encased coir fibre reinforced concrete composite column. *Constr. Build. Mater.* **2013**, *40*, 1118–1127. [CrossRef]
36. Yan, L.; Chouw, N. Compressive and flexural behaviour and theoretical analysis of flax fibre reinforced polymer tube encased coir fibre reinforced concrete composite. *Mater. Des.* **2013**, *52*, 801–811. [CrossRef]
37. Xia, Y.; Xian, G.; Wang, Z.; Li, H. Static and cyclic compressive properties of self-compacting concrete-filled flax fiber-reinforced polymer tubes. *J. Compos. Constr.* **2016**, *20*, 04016046. [CrossRef]
38. Kymäläinen, H.R.; Sjöberg, A.M. Flax and hemp fibres as raw materials for thermal insulations. *Build. Environ.* **2008**, *43*, 1261–1269. [CrossRef]
39. Wang, Y.; Chen, G.; Wan, B.; Cai, G.; Zhang, Y. Behavior of circular ice-filled self-luminous FRP tubular stub columns under axial compression. *Constr. Build. Mater.* **2020**, *232*, 117287. [CrossRef]
40. ASTM International. *Standard Test Method for Tensile Properties of Polymer Matrix Composite Materials (ASTM D3039/D3039M-17)*; ASTM International: West Conshohocken, PA, USA, 2017.
41. Lam, L.; Teng, J.G. Ultimate condition of fiber reinforced polymer-confined concrete. *J. Compos. Constr.* **2004**, *8*, 539–548. [CrossRef]
42. Standards Press of China. *Fiber-Reinforced Thermosetting Plastic Composites Pipe-Determination for Longitudinal Compressive Properties (GB/T 5350-2005)*; Standards Press of China: Beijing, China, 2005.

43. Wang, Y.; Chen, G.; Wan, B.; Lin, H. Axial compressive behavior of square ice filled steel tubular stub columns. *Constr. Build. Mater.* **2018**, *188*, 198–209. [CrossRef]
44. Xia, Y.; Xian, G.; Kafodya, I.; Li, H. Compression behavior of concrete cylinders externally confined by flax fiber reinforced polymer sheets. *Adv. Struct. Eng.* **2014**, *17*, 1825–1833. [CrossRef]
45. Al-saadi, A.U.; Aravinthan, T.; Lokuge, W. Structural applications of fibre reinforced polymer (FRP) composite tubes: A review of columns members. *Compos. Struct.* **2018**, *204*, 513–524. [CrossRef]
46. D’Amato, M.; Braga, F.; Gigliotti, R.; Kunnath, S.; Laterza, M. A numerical general-purpose confinement model for non-linear analysis of R/C members. *Comput. Struct.* **2012**, *102*, 64–75. [CrossRef]
47. Laterza, M.; D’Amato, M.; Braga, F.; Gigliotti, R. Extension to rectangular section of an analytical model for concrete confined by steel stirrups and/or FRP jackets. *Compos. Struct.* **2017**, *176*, 910–922. [CrossRef]
48. Mander, J.B.; Priestley, M.J.N.; Park, R. Theoretical stress-strain model for confined concrete. *J. Struct. Eng.* **1988**, *114*, 1804–1826. [CrossRef]
49. Pessiki, S.; Harries, K.A.; Kestner, J.T.; Sause, R.; Ricles, J.M. Axial behavior of reinforced concrete columns confined with FRP jackets. *J. Compos. Constr.* **2001**, *5*, 237–245. [CrossRef]



© 2020 by the authors. Licensee MDPI, Basel, Switzerland. This article is an open access article distributed under the terms and conditions of the Creative Commons Attribution (CC BY) license (<http://creativecommons.org/licenses/by/4.0/>).

Article

Interface Bonding Behavior of Concrete-Filled Steel Tube Blended with Circulating Fluidized Bed Bottom Ash

Lan Liu, Lei He, Zhi Cheng *, Xiaoyi Wang, Zhe Ma and Xinrong Cheng

School of Science, North University of China, Taiyuan 030051, China; yunvln@163.com (L.L.); 18434367366@163.com (L.H.); 18404912146@163.com (X.W.); mz605810831@163.com (Z.M.); 18234162820@163.com (X.C.)

* Correspondence: chengzhi@nuc.edu.cn

Abstract: The interface bonding behavior between the steel tube and the concrete of concrete-filled steel tube (CFST) blended with circulating fluidized bed bottom ash (CFB-BA) was investigated in this study. A total of 8 groups of CFSTs stub columns were prepared with different dosage of CFB-BA, water-binder ratio (W/B), and interface bonding length. A series of push-out tests were carried out to acquire the data representing the interface bonding behavior. The results show that the dosage of CFB-BA has a direct effect on interface bonding behavior of CFST. CFB-BA can improve the interface bonding behavior of CFST. The highest ultimate bonding load and strength are achieved when the dosage of CFB-BA is 30%. When the dosage of CFB-BA increases to 50%, its interface bonding behavior decreases, but is still better than that of CFST without CFB-BA. W/B has a negative correlation with the interface bonding behavior of CFST. While the W/B increases, the interface bonding load and strength of CFST decreases. The increase of the interface bonding length can improve the interface bonding load, but cannot improve the interface bonding strength.

Citation: Liu, L.; He, L.; Cheng, Z.; Wang, X.; Ma, Z.; Cheng, X. Interface Bonding Behavior of Concrete-Filled Steel Tube Blended with Circulating Fluidized Bed Bottom Ash. *Materials* **2021**, *14*, 1529. <https://doi.org/10.3390/ma14061529>

Academic Editor:
Malgorzata Ulewicz

Received: 22 February 2021
Accepted: 16 March 2021
Published: 20 March 2021

Publisher's Note: MDPI stays neutral with regard to jurisdictional claims in published maps and institutional affiliations.



Copyright: © 2021 by the authors. Licensee MDPI, Basel, Switzerland. This article is an open access article distributed under the terms and conditions of the Creative Commons Attribution (CC BY) license (<https://creativecommons.org/licenses/by/4.0/>).

Keywords: concrete-filled steel tube; circulating fluidized bed bottom ash; push-out test; bonding strength; bonding load

1. Introduction

Concrete-filled steel tube (CFST) is composed of steel tube and core concrete working together [1,2]. It has the characteristics of high bearing capacity, large lateral rigidity, good ductility and high construction efficiency [3–8]. CFST has been widely applied as the large load-bearing components in the construction because it can reduce the component size, save resources, speed up construction efficiency, and protect the environment [9,10].

The interface bonding force of the CFST consists of chemical bonding force, mechanical biting force, and frictional resistance [11]. There are many factors that affect the interface bonding strength of CFST, such as the shrinkage of concrete, water-to-binder ratio, and additives [12,13]. Xiushu Qu [14] studied the influence of factors such as the amount of concrete expansion agent and compressive strength of concrete on the bonding strength of concrete. The test results show that the compressive strength of concrete and the amount of expansion agent are the main factors affecting the interface bonding strength. Raed Abendeh [15] observed the bonding behavior by changing the material composition with rubber wire, and found that the shrinkage of concrete is also a vital factor affecting the bonding strength of CFSTs. The shrinkage of concrete can reduce the bonding strength of CFSTs, and even separate the steel tube and core concrete. Chang Xu [16] studied the interface bonding behavior of CFSTs with the expansive cement, and found that expansive cement can significantly enhance the bonding strength of CFSTs. The reduction of concrete shrinkage can improve the bonding strength of CFSTs.

Circulating fluidized bed bottom ash (CFB-BA) is a waste product from the bottom of circulating fluidized bed combustion in thermal power plants. CFB technology has been widely used due to its advantages such as good fuel adaptability, high efficient combustion,

and low NO_x emissions [17–19]. The annual emissions of CFB-BA are very large, but its utilization rate is low [20]. Different from ordinary coal-fired fly ash, the particles of CFB-BA are loose and porous inside, so it has larger water absorption. Just like fly ash, CFB-BA also contain SiO₂ and Al₂O₃, so it also has pozzolanic activity [21]. Researches have shown that CFB-BA has expansibility, which is closely related to the content of anhydrite and f-CaO [22–24]. To avoid the damage caused by expansion, the CFB-BA should be treated or the amount should be controlled during use. Mechanical grinding is a useful modified method for CFB-BA, which can improve the CFB-BA's utilization and optimize its performance [22]. Zhi Cheng et al. [23] studied the expansion and load-deformation behavior of self-compacting concrete-filled steel tube stub column of CFB-BA. The results show that CFB-BA can improve the bearing capacity of concrete-filled steel tube stub columns.

The aforementioned works indicate that CFB-BA has expansibility, which is beneficial for compensating the shrinkage of concrete. This paper presents the interface bonding behavior between the steel tube and the core concrete of CFST, which can contribute to the application of CFB-BA in CFST. In the paper, a controlled variable method was used to design a total of 8 groups of CFSTs, and push-out tests were carried out. The dosage of CFB-BA, the water-binder ratio and the interface bonding length are considered to be the main influencing factor. Load-slip curves, longitudinal strain distribution, and other data were obtained to analyze the interface bonding behavior of the CFSTs.

2. Experiment Part

2.1. Materials

Grade P.O 42.5 Portland Cement (PC) (Chihoi, Taiyuan, China) was used in the experiment. The physical and mechanical properties of the PC are shown in Table 1. The CFB-BA from Pingshuo Coal Gangue Power Plant of Shuozhou, China was applied as well. After grinding with a ball mill for 39 min, it was passed through an 80 μm square hole sieve to gain a fine CFB-BAs. The main chemical compositions of CFB-BA are shown in Table 2. The ground CFB-BA was used as a mixture, which partly replaced PC. The surface area of the ground CFB-BA was 400 m²/kg. Particle size distribution of ground CFB-BA is shown in Table 3. Figure 1 shows the images of the raw CFB-BA and the ground CFB-BA.

Table 1. Properties of Portland Cement.

Setting Time (min)		Flexural Strength (MPa)		Compressive Strength (MPa)		Density (kg/m ³)	Surface Area (m ² /kg)
Initial	Final	3 d	28 d	3 d	28 d		
183	234	5.5	7.6	26.1	45.9	3100	350

Table 2. Main chemical compositions of CFB-BA (%).

SiO ₂	Al ₂ O ₃	CaO	SO ₃	Fe ₂ O ₃	MgO	K ₂ O	P ₂ O ₅	Na ₂ O	Loss on Ignition
42.19	25.9	10.1	5.91	3.1	1.35	0.79	0.12	0.06	6.09

Table 3. Particle size distribution of ground CFB-BA.

Grinding Time (min)	Specific Surface Area (cm ² /g)	×10 (μm)	×50 (μm)	×90 (μm)	×98 (μm)
39	400	1.40	15.07	63.86	97.23

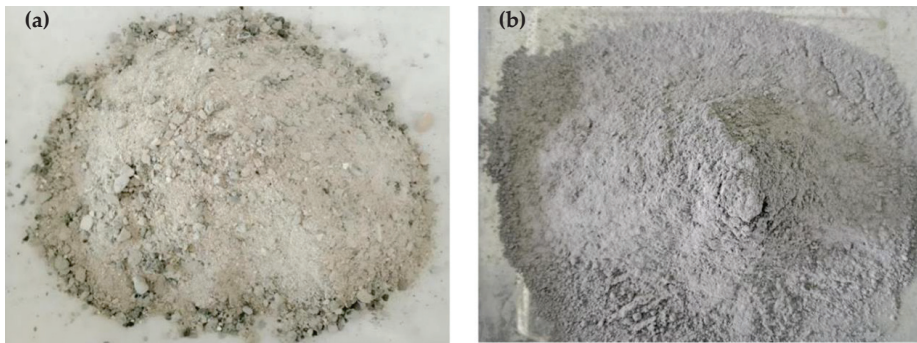


Figure 1. Digital images (a) Raw CFB-BA (b) Ground CFB-BA.

The crushed stone (G) (5–20 mm) was used as the coarse aggregate, which meets the demand of the Chinese Industry Standard “GB/T 14685-2011 Pebble and crushed stone for construction” [25]. The fine aggregate was the natural sand (S) with a fineness module of 2.86–2.94, and the apparent density and bulk density were 2590 kg/m³ and 1550 kg/m³, respectively. The sand was sieved in compliance with the Chinese Industry Standard “GB/T 14684-2011 Construction sand” [26]. All aggregates were air-dried before use.

The polycarboxylate superplasticizer (PS) was from Baoding Muhu Hengyuan New Building Material Company (Baoding, China). Grade Q235 circular steel tubes with a straight slit (Tangshan Iron & Steel Group, Tangshan, China) were adopted to fabricate the test specimens. The steel tube was 2.5 mm in thickness and 89 mm in outer diameter. The material properties of steel are shown in Table 4.

Table 4. Properties of the steel tubes.

Thickness (mm)	Elastic Modulus (GPa)	Yield Strength (MPa)	Ultimate Strength (MPa)	Poisson's Ratio
2.5	206	312	441	0.3

2.2. Preparation of the Specimens

A total of 8 groups CFSTs were fabricated with a dosage of CFB-BA, W/B, and interface bonding length as variables. Each group contained two specimens, and the final test results were averaged accordingly. The self-compacting concretes (SCCs) were prepared, and the values of slump flow all exceed 650 mm. Before pouring the specimens, both ends of the steel tubes were polished, and the bottom was sealed with thin-film plastic to prevent the poured concrete from flowing out. The specimens were fabricated in the laboratory with a temperature of 20 ± 2 °C and a relative humidity of 50%. Three standard test cubes were reserved for each group to test the compressive strength of SCCs. The Mix proportions of SCCs is shown in Table 5, and the component parameters of CFSTs is shown in Table 6.

Table 5. Mix proportions of SCCs.

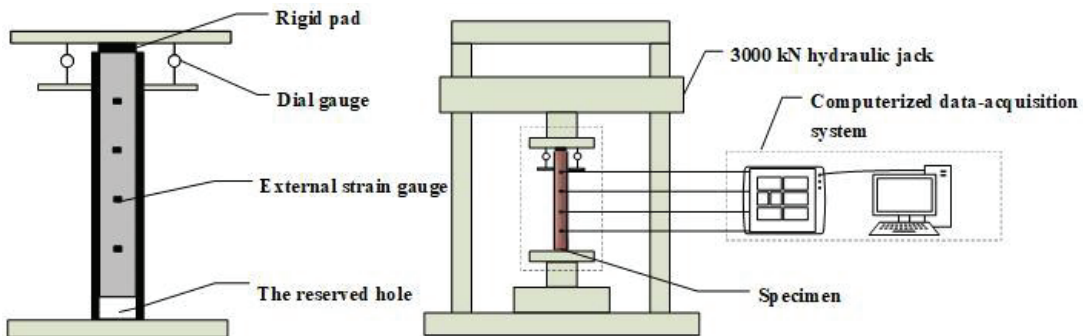
SCC	CFB-BA (%)	W/B	PC (kg)	CFB-BA (kg)	W (kg)	S (kg)	G (kg)	PS (%)
SCC-1	0	0	548.8	0.0	164.6	790.6	885.5	1
SCC-2	10	0.3	493.7	54.9	164.7	785.4	877.8	1.2
SCC-3	30	0.3	383.6	164.4	164.4	784.7	976.9	1.3
SCC-4	50	0.3	274.3	274.3	164.6	782.2	872.2	1.7
SCC-5	30	0.34	365.8	156.8	177.7	784.7	876.9	1.3
SCC-6	30	0.38	350.7	150.3	190.4	784.5	877.1	1.2

Table 6. Component parameters of CFSTs.

Group	SCC	CFB-BA (%)	W/B	Bonding Length (mm)	D × T × L (mm)
GP1	SCC-1	0	0.3	250	89 × 2.5 × 300
GP2	SCC-2	10	0.3	250	89 × 2.5 × 300
GP3	SCC-3	30	0.3	250	89 × 2.5 × 300
GP4	SCC-4	50	0.3	250	89 × 2.5 × 300
GP5	SCC-5	30	0.34	250	89 × 2.5 × 300
GP6	SCC-6	30	0.38	250	89 × 2.5 × 300
GP7	SCC-5	30	0.3	200	89 × 2.5 × 300
GP8	SCC-3	30	0.3	150	89 × 2.5 × 300

2.3. Test Setup and Instrument

The static grading load method was adopted in the push-out test. The test device model is shown in Figure 2. The steel tube at the free end of the test specimen was compressed. The core concrete at the loading end was also compressed. A rigid pad with a diameter slightly smaller than the steel tube was placed at the bottom of the core concrete at the loading end. Slippage occurred, and the core concrete was pushed out. Strain gauges were affixed every 50 mm in the longitudinal height of the steel tube specimen to measure the strain value along with the height. Two dial gauges were symmetrically arranged on the surface of the pressure plate to measure the relative slip between the steel tube and the concrete. Figure 3 shows the actual test device system, and Figure 4 shows the specimen before loading and after loading.

**Figure 2.** Test device model of CFST.

The loading process of the CFST specimen is divided into two stages, known as the pre-loading stage and formal loading stage.

During the process of test loading, the 5 kN load was pre-applied. The upper and lower pressure plates, specimens and pads of the press were in close contact so that the core concrete was evenly stressed.

In the formal loading stage, the load was graded, the rate was lower than 200 N/s, and the load was recorded every 5 kN load until the test specimens failed. At the beginning of loading, there was no change in the value displayed by the dial gauge and strain gauge. As the load increased, the loading process was gradually stabilized, and a small amount of slippage occurred at the end of the loading process. The relative amount of slippage became even larger as the load increased from the initial stage. The produce of the slippage means the chemical bonding force failure between the steel tube and the CFB-BA concrete [23]. In the later loading process, the load remained unchanged. The value of the dial gauge continued to increase, and the rigid pad has a pivotal displacement change, but the steel

tube did not collapse. At this time, the bonding force at the interface of the CFST, and the specimens were broken. The test results of the specimens are shown in Table 7.

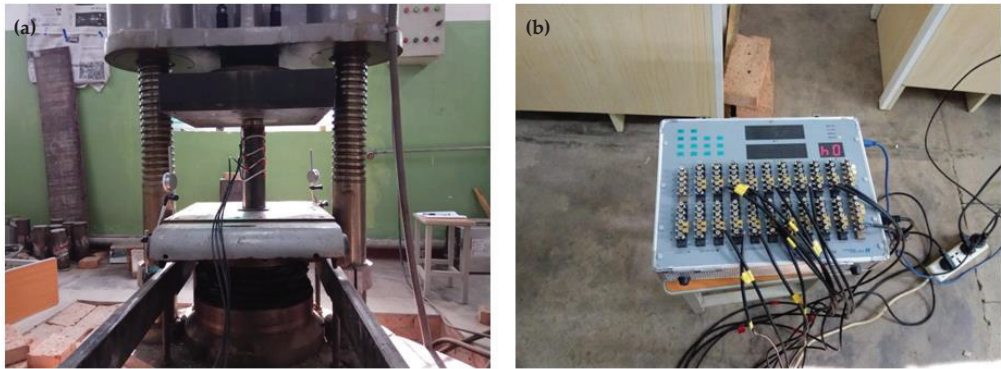


Figure 3. Test device system of CFST (a) loading system (b) data collection system.



Figure 4. Comparison of CFST specimen (a) before loading (b) after loading.

Table 7. Test results of specimens.

Group	CFB-BA (%)	W/B	Bonding Length (mm)	Compressive Strength at 28 d Age (MPa)	Ultimate Bonding Load (kN)	Ultimate Bonding Strength (MPa)	Relative Slip Value (mm)
GP1	0	0.3	250	57.1	134.1	1.97	2.514
GP2	10	0.3	250	52.4	164.5	2.42	2.486
GP3	30	0.3	250	55.5	169.6	2.50	2.286
GP4	50	0.3	250	48.8	136.1	2.00	1.200
GP5	30	0.34	250	46.6	155.0	2.13	2.199
GP6	30	0.38	250	37.1	134.4	1.92	2.097
GP7	30	0.3	200	55.5	125.2	2.54	1.573
GP8	30	0.3	150	55.5	102.5	2.51	1.017

3. Results and Discussions

3.1. Load-Slip Curves of CFST

The load-slip curves of CFST are shown in Figure 5. It can be seen that the shape of the load-slip curve of each group is similar to that of concrete-filled steel-tube without CFB-BA (GP1). In the entire process of interface adhesion from occurrence to destruction, the common characteristics can be concluded.

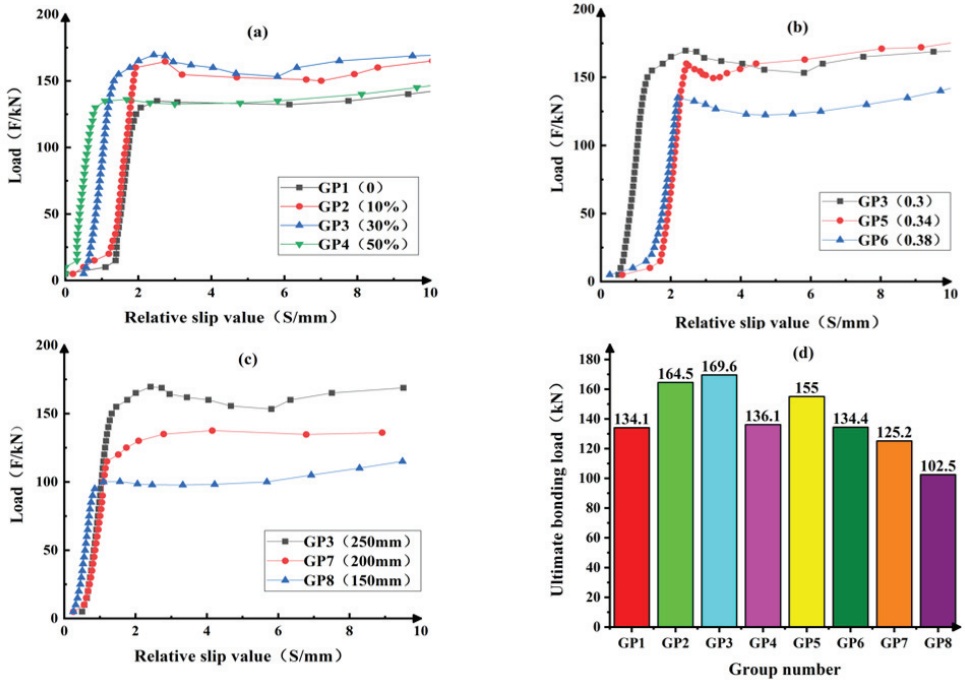


Figure 5. Load-slip curves of CFST (a) different dosage of CFB-BA (b) different W/B (c) different bonding length (d) ultimate bonding load.

During the initial loading, slip occurs on a small scale between the concrete and the steel tube, because the core concrete is in direct contact with the loading slab. The core concrete produces the elastic compression deformation, causing slip afterward. As the load increases, the relative slip between the steel tube and the core concrete undergoes a process from slight slip to partial slip, and finally to full slip. When the load is increased to the failure load of the component interface bonding, the load-slip curve grows almost linearly. Besides, the interface bonding force is continuous along with the component length. With the increase of the load, the relative slip also increases with the speed lower than the load speed. When the applied load is close to the interface failure load, the relative curvature of the load-displacement curve becomes smaller. Load-slip curve shows an evident inflection point. With the increasing of component relative slip, the load has no significant change. The curve stays at a certain level for a period of time.

Figure 6 shows the load-slip curve model of CFST. As seen in Figure 6, the curve is consisted by four sections, which are OA, AB, BC and CD.

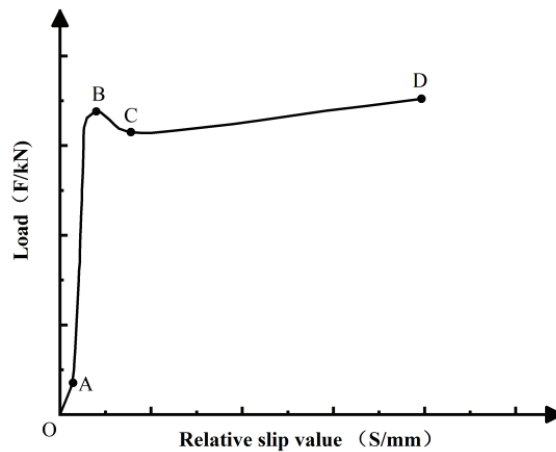


Figure 6. Load-slip curve model of CFST.

In the OA section, the initial load is rather small, and the specimens have a slight relative slip. At this time, the interface bonding force of the CFST is mainly borne by the chemical bonding force. The main factors affecting the chemical bonding force are cement dosage, concrete strength, and water binder ratio [23]. The chemical bonding force is small. When the applied load is low, an insignificant local relative slip occurs between the steel tube and the core concrete. At this time, the chemical bonding force of the part where the relative slip occurs has failed.

In the AB section, when the load continues increasing, a relatively large slip occurs between the core concrete and the steel tube. The local relative slip becomes more evident. At this time, the load on the specimen increases faster than the increase of relative slip. The interface bonding force is mainly caused by part of the chemical bonding force and mechanical biting force. When the chemical bonding force and mechanical biting force on the interface reach the maximum value, the load is near to the ultimate bonding load (F_U). The load shows approximate linear distribution before the load is near to point B.

In the BC section, when the load reaches point B, the relative slip of the CFST interface enters a nonlinear phase. The core concrete has slipped to the steel tube. At this time, the chemical bonding force and mechanical bite force have failed. The interface bonding force is mainly borne by the friction between the steel tube and the core concrete. In this stage, even if a small load is applied, the displacement between the steel tube and the core concrete will be significantly changed.

In the CD section, as the slippage continues to develop, the concrete expands circumferentially under axial compression, and lateral extension produces. The concrete's lateral extension results in the increase of the steel tube's lateral pressure, which enlarges the sliding friction on the interface, so the CD section shows an upward trend.

3.2. Longitudinal Strain Distribution of CFST

The curve of longitudinal strain distribution of CFST is shown in Figure 7. It can be seen from Figure 7 that at the initial loading process, the longitudinal strain along the height of the steel tube shows no difference under the small load. The force transmission between the steel tube and the concrete in the specimens are relatively uniform. As the load gradually increases, the longitudinal strain along the height of the component also increases. Then, the continuity of the force transmission between the steel tube and the core concrete is gradually broke, which means that the bonding strength between the steel tube and the core concrete is damaged. A relative slip occurs between the steel tube and the core concrete. From the analysis on the strain curve of each specimen, it can be obtained

that the largest longitudinal strain on the steel tube appears at its free end, and the smallest strain appears at its loading end.

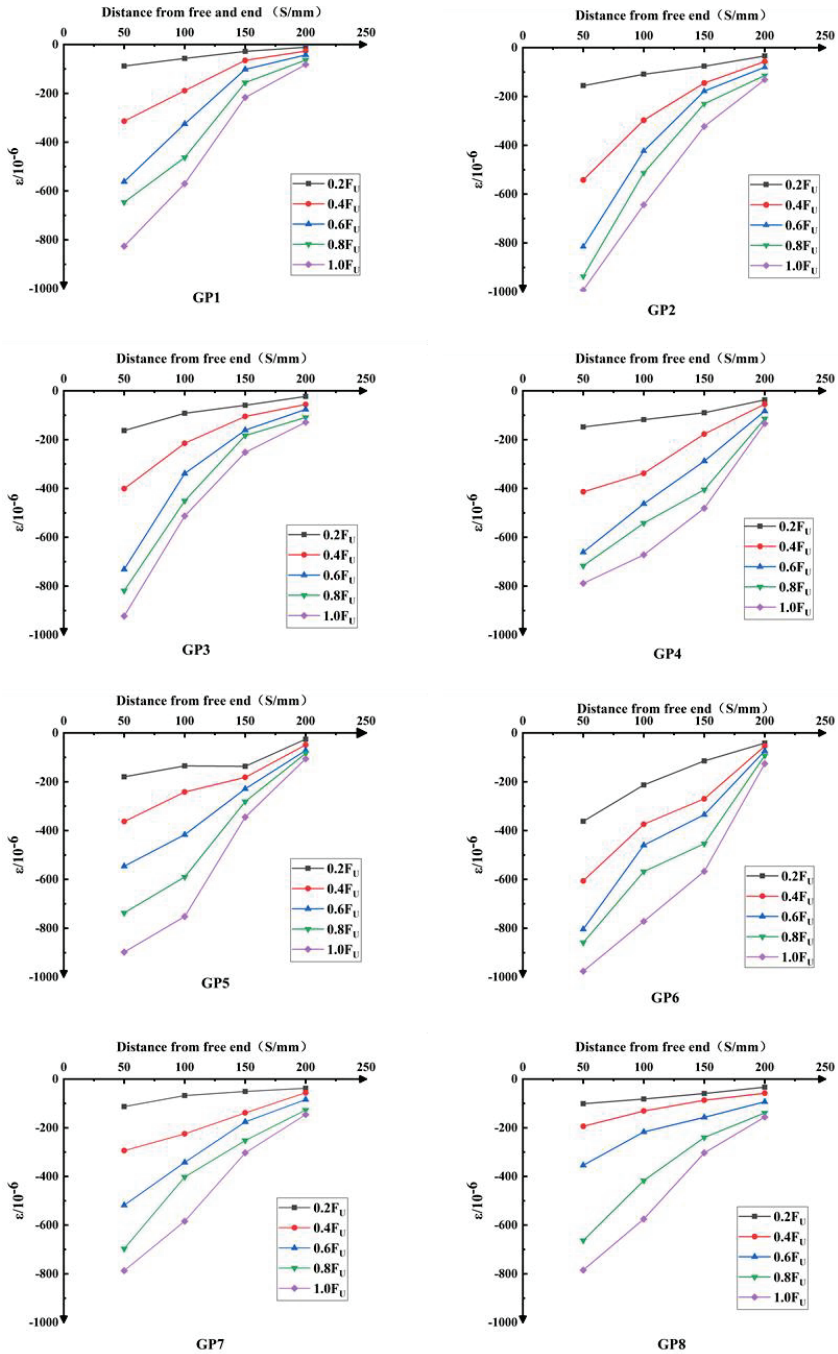


Figure 7. The curve of longitudinal strain distribution of CFST. Note: F_U means the ultimate bonding load.

Throughout the testing process, the steel tube was assumed to be always in the elastic stage before the specimen was damaged. In this test, the elastic modulus E of the steel tube is regarded as a fixed value. From the analysis of the stress state, when the core concrete in the steel tube is pushed out, it will produce a particular lateral squeeze on the steel tube with the action of thrust. The lateral squeeze makes the circular steel tube located in a circumferential tension state, causing a certain elastic deformation in the circumference of the steel tube. A small pushing load is applied to the test piece so that the core concrete can closely make contact with the steel tube. At this time, the core concrete exerted a specific lateral compression on the steel tube, which can increase the longitudinal strain of the steel tube. The core concrete is effectively restrained, which leads to an increase in the bonding stress. The increase of bonding stress is conducive to the cooperation of the steel tube and the concrete under external load.

3.3. Influence Factors on the Interface Bonding Behavior of CFST

Figure 8 shows the dependence of CFB-BA dosage on the interface bonding behavior. It can be seen from Figure 8 that when the amount of CFB-BA is 30%, the bonding load reaches the maximum. Comparing with the concrete filled steel tube without CFB-BA, its ultimate bonding load increased by 26.5%. The ultimate bonding loads of the concrete filled steel tube with 10% and 50% CFB-BA were higher than those without CFB-BA by 22.7% and 1.5%, respectively. The bonding strength of the group GP2 with 10% CFB-BA, the group GP3 with 30% CFB-BA, the group GP4 with 50% CFB-BA are 22.8%, 26.9%, 1.5%, respectively, which are all higher than that of the group GP1 without CFB-BA. CFB-BA contains II-CaSO_4 and f-CaO . In the hydration process of the cementitious system, f-CaO can hydrate to Ca(OH)_2 , and II-CaSO_4 can hydrate to gypsum. Gypsum can continue to react with Ca(OH)_2 and hydrated calcium aluminate, and then produce ettringite. The ettringite can fill the pores and improve the compactness of the core concrete, and even produce self-stress in the CFST. So dosage of CFB-BA can improve the compressive strength of the core concrete, and make the core concrete and steel tube closer. But too much CFB-BA can lead to great expansion and anhydrite cannot hydrate completely, which decrease the compressive strength of the core concrete. So there exists a reasonable amount of CFB-BA. When the amount of CFB-BA is 30%, the CFST gains the maximum bonding load and maximum bonding strength [24].

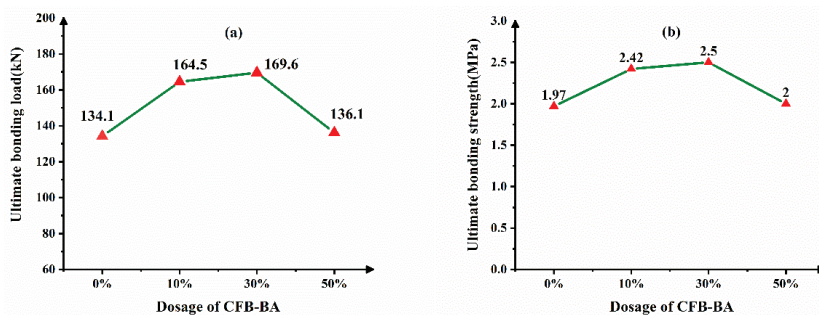


Figure 8. Dependence of CFB-BA dosage on the interface bonding behavior (a) ultimate bonding load (b) ultimate bonding strength.

Figure 9 shows the dependence of W/B on the interface bonding behavior. It can be seen from Figure 9 that when the amount of CFB-BA and the bonding length are fixed, the bonding load will reach the maximum with the water-cement ratio of 0.3. The bonding strength also reaches the maximum 2.50 MPa. With the increase of W/B , the bonding strength decreases by varying degrees. When the W/B is 0.34, the bonding strength is reduced by 14.8%. When the W/B is 0.38, the bonding strength is reduced by 23.2%. It can be seen from Table 6 that the measured compressive strength of the concrete cube

decreases as the water-cement ratio increases. Cement mainly provides the cohesive force for the concrete. As the water-to-binder ratio increases, the actual amount of cement decreases, and the pores left by the sand and gravel aggregate cannot be filled. The porosity increases, the concrete is not dense, and the strength decreases. With higher water-cement ratio, the excess water may remain in the cement or evaporate to form pores or channels after the hardening process, resulting in a decrease in mechanical strength. The reduction in the strength of the core concrete will bring a decrease in the bonding strength of the CFST interface.

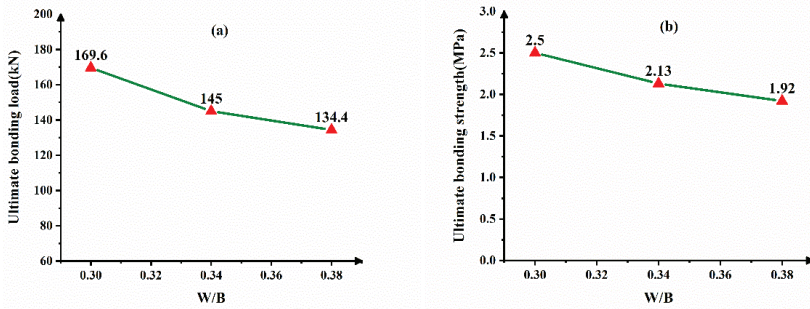


Figure 9. Dependence of W/B on the interface bonding behavior (a) ultimate bonding load (b) ultimate bonding strength.

Figure 10 shows the dependence of bonding length on the interface bonding behavior. As shown in Figure 10, when the amount of CFB-BA and W/B is constant, the longer the interface bonding length, the higher the bonding load. However, the interface bonding strength shows no notable change. The reason is that, while the interface bonding length increases, the bonding force between the core concrete and the steel tube also increases. Thus, the increase of interface bonding length cannot improve the interface bonding strength.

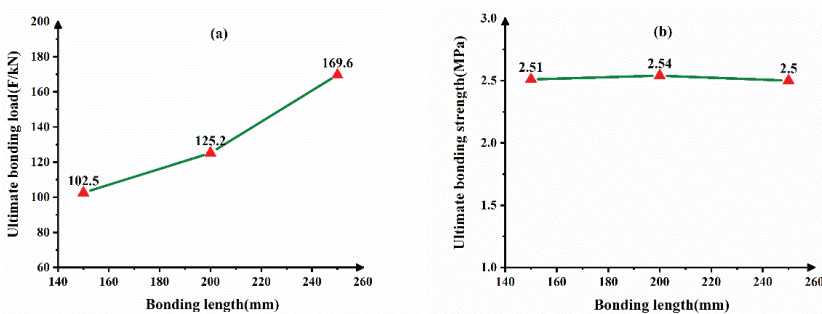


Figure 10. Dependence of bonding length on the interface bonding behavior (a) ultimate bonding load (b) ultimate bonding strength.

4. Conclusions

The interface bonding behavior of CFST blended with CFB-BA was studied in the paper, and a total of 8 groups of CFST were designed for the push-out test. Several conclusions can be drawn as the following:

- The load slip curve of CFST blended with CFB-BA can be divided into four stages. The strains along the longitudinal height of the steel tube are the same as the ordinary CFST without CFB-BA.
- Adding CFB-BA within a certain range has a positive effect on the bonding strength of CFST. When the dosage of CFB-BA is 10%, 30% and 50%, the interface bonding strength of CFST increased by 22.8%, 26.9% and 1.5%, respectively. The micro-expansion

property of the CFB-BA can make the concrete squeeze on the sidewall of the steel tube to improve the interface bonding strength. However, too much CFB-BA in concrete will reduce the strength of the concrete, thereby reducing the bonding strength of CFST.

- The W/B has an important influence on the interface bonding strength of CFST with CFB-BA. When the dosage of CFB-BA and the interface bonding length are constant, the higher the W/B, the lower the interface bonding strength of the CFST. W/B has negative correlation with the interface bonding load and bonding strength. When the W/B is 0.3, the interface bonding strength of the CFST reached the maximum, the value reaches 2.50 MPa.
- Bonding length has a significant effect on the ultimate bonding load of CFST. However, because the force-bearing area increases with the increase of the bonding length, the bonding strength of CFST is basically unaffected.

Author Contributions: Conceptualization, L.L. and Z.C.; methodology, L.L.; writing—original draft preparation, X.W. and L.H.; writing—review and editing, L.L.; visualization, Z.M. and X.C.; supervision, Z.C.; funding acquisition, Z.C. and L.H. All authors have read and agreed to the published version of the manuscript.

Funding: This work was financially supported by the Science Fundamental Research Projects of Shanxi Province (Nos. 201901D111169 and 201801D221233), and the Graduate Student Education Innovation Projects of Shanxi Province (No. 2020SY384).

Informed Consent Statement: Not applicable.

Data Availability Statement: The data presented in this study are available on request from the corresponding author.

Conflicts of Interest: The authors declare no conflict of interest.

References

1. Lai, M.H.; Ho, J.C.M. Confinement effect of ring-confined concrete-filled-steel-tube columns under uni-axial load. *Eng. Struct.* **2014**, *67*, 123–141. [CrossRef]
2. Milan, C.C.; Albareda-Valls, A.; Carreras, J.M. Evaluation of structural performance between active and passive preloading systems in circular concrete-filled steel tubes (CFST). *Eng. Struct.* **2019**, *194*, 207–219. [CrossRef]
3. Han, L.-H.; Li, W.; Bjorhovde, R. Developments and advanced applications of concrete-filled steel tubular (CFST) structures: Members. *J. Constr. Steel Res.* **2014**, *100*, 211–228. [CrossRef]
4. Ibañez, C.; Hernández-Figueirido, D.; Piquer, A. Shape effect on axially loaded high strength CFST stub columns. *J. Constr. Steel Res.* **2018**, *147*, 247–256. [CrossRef]
5. Yu, Z.-W.; Ding, F.-X.; Cai, C.S. Experimental behavior of circular concrete-filled steel tube stub columns. *J. Constr. Steel Res.* **2007**, *63*, 165–174. [CrossRef]
6. Nie, J.-G.; Wang, Y.-H.; Fan, J.-S. Experimental study on seismic behavior of concrete filled steel tube columns under pure torsion and compression–torsion cyclic load. *J. Constr. Steel Res.* **2012**, *79*, 115–126. [CrossRef]
7. Wang, R.; Han, L.-H.; Hou, C.-C. Behavior of concrete filled steel tubular (CFST) members under lateral impact: Experiment and FEA model. *J. Constr. Steel Res.* **2013**, *80*, 188–201. [CrossRef]
8. Roeder, C.W.; Lehman, D.E.; Bishop, E. Strength and Stiffness of Circular Concrete-Filled Tubes. *J. Struct. Eng.* **2010**, *136*, 1545–1553. [CrossRef]
9. Xiong, M.; Xiong, D.; Liew, J.Y.R.J.E.S. Axial performance of short concrete filled steel tubes with high- and ultra-high- strength materials. *Eng. Struct.* **2017**, *136*, 494–510. [CrossRef]
10. Zhang, X.; Gao, X. The hysteretic behavior of recycled aggregate concrete-filled square steel tube columns. *Eng. Struct.* **2019**, *198*. [CrossRef]
11. Virdi, K. *Bond Strength in Concrete Filled Steel Tubes*; Int Assoc for Bridge & Structural Eng: Zürich, Switzerland, 1980.
12. Lyu, W.-Q.; Han, L.-H. Investigation on bond strength between recycled aggregate concrete (RAC) and steel tube in RAC-filled steel tubes. *J. Constr. Steel Res.* **2019**, *155*, 438–459. [CrossRef]
13. Tao, Z.; Song, T.-Y.; Uy, B.; Han, L.-H. Bond behavior in concrete-filled steel tubes. *J. Constr. Steel Res.* **2016**, *120*, 81–93. [CrossRef]
14. Qu, X.; Liu, Q. Bond strength between steel and self-compacting lower expansion concrete in composite columns. *J. Constr. Steel Res.* **2017**, *139*, 176–187. [CrossRef]
15. Abende, R.; Ahmad, H.S.; Hunaiti, Y.M. Experimental studies on the behavior of concrete-filled steel tubes incorporating crumb rubber. *J. Constr. Steel Res.* **2016**, *122*, 251–260. [CrossRef]
16. Chang, X.; Huang, C.; Jiang, D.; Song, Y. Push-out test of pre-stressing concrete filled circular steel tube columns by means of expansive cement. *Constr. Build. Mater.* **2009**, *23*, 491–497. [CrossRef]

17. Topper, J.M.; Cross, P.J.I.; Goldthorpe, S.H. Clean coal technology for power and cogeneration. *Fuel* **1993**, *73*, 1056–1063. [CrossRef]
18. Beer, J.M. Combustion technology developments in power generation in response to environmental challenges. *Prog. Energy Combust. Sci.* **2000**, *26*, 301–327. [CrossRef]
19. Sondreal, E.A.; Benson, S.A.; Hurley, J.P.; Mann, M.D.; Pavlish, J.H.; Swanson, M.L.; Weber, G.F.; Zygarlicke, C.J.J.F.P.T. Review of advances in combustion technology and biomass cofiring. *Fuel Process. Technol.* **2001**, *71*, 7–38. [CrossRef]
20. Lv, S.Z.; Chen, X.M.; Lu, Z.Y.; Peng, Y.H. Study on high belite cement clinker calcination with ashes from circulating fluidized bed combustion. *New Build. Mater.* **2011**, *8*, 1–3.
21. Tang, S.X.; Wang, Z.; He, Y.F.; Chen, R. Changes of coal ash properties and its effect on concrete. *New Build. Mater.* **2018**, *45*, 103–106+132.
22. Li, X.G.; Chen, Q.B.; Huang, K.Z.; Ma, B.G.; Wu, B. Cementitious properties and hydration mechanism of circulating fluidized bed combustion (CFBC) desulfurization ashes. *Constr. Build. Mater.* **2012**, *36*, 182–187. [CrossRef]
23. Cheng, Z.; Pei, X.; Hou, H.; Han, T.; Liu, L.; Wang, H.; Han, Y. Expansive Behavior in Circular Steel Tube Stub Columns of SCC Blended with CFB Bottom Ashes. *J. Mater. Civ. Eng.* **2019**, *31*. [CrossRef]
24. Cheng, Z.; Cheng, Z.; Hou, H.; Han, T.; Liu, L. Engineering. Research on the Expansion Characteristics and Compressive Strength of Mortars Containing Circulating Fluidized Bed Combustion Desulfurization Slag. *Adv. Mater. Sci. Eng.* **2018**, *2018*, 1–11.
25. China Aggregates Association; Beijing University of Civil Engineering and Architecture; Technical Supervision and Research Center of Building Materials Industry. *Pebble and Crushed Stone for Construction. General Administration of Quality Supervision, Inspection and Quarantine of the People's Republic of China; Standardization Administration: Beijing, China, 2011; p. 32.*
26. China Aggregates Association; Beijing University of Civil Engineering and Architecture; Technical Supervision and Research Center of Building Materials Industry. *Construction Sand. General Administration of Quality Supervision, Inspection and Quarantine of the People's Republic of China; Standardization Administration: Beijing, China, 2011; p. 36.*

Article

Research on the Mechanical Properties of Recycled Aggregate Concrete under Uniaxial Compression Based on the Statistical Damage Model

Weifeng Bai ¹, Wenhao Li ¹, Junfeng Guan ^{1,*}, Jianyou Wang ^{2,*} and Chenyang Yuan ¹

¹ School of Water Conservancy, North China University of Water Resources and Electric Power, Zhengzhou 450046, China; yf9906@163.com (W.B.); a675615151@163.com (W.L.); chenyang_yuan@yeah.net (C.Y.)

² School of Water Conservancy Engineering, Zhengzhou University, Zhengzhou 450001, China

* Correspondence: junfengguan@ncwu.edu.cn (J.G.); wangjianyou@zzu.edu.cn (J.W.)

Received: 20 July 2020; Accepted: 20 August 2020; Published: 26 August 2020

Abstract: In this paper, uniaxial compression tests were carried out for recycled aggregate concrete with water cement ratios of 0.38, 0.49, and 0.66 and replacement ratios of 0%, 25%, 50%, 75%, and 100%, respectively. The influence of the replacement ratio of recycled aggregate and water cement ratio on the strength, elastic modulus, and deformation characteristics of concrete was discussed. The results show that the replacement rate of recycled aggregate has a significant effect on the macro stress–strain behavior of concrete. In the case of a constant water cement ratio, the peak nominal stress first decreases and then increases with the increase of the replacement rate; while the water cement ratios equal 0.38, 0.49, and 0.66, the corresponding transition states are 25%, 50%, and 50% of the replacement rate, respectively. The deformation and failure is characterized by two stages: distributed damage and local failure. Combined with the statistical damage mechanics, the influence of the aggregate replacement rate on the damage evolution mechanism of recycled concrete on a mesoscopic scale was explored. Two mesoscopic damage modes, fracture and yield, are considered. Their cumulative evolutions are assumed to follow triangular probability distributions, which could be characterized by four parameters. The peak nominal stress state and the critical state are distinguished, and the latter is defined as a precursor to local failure. With the increase of the replacement rate of recycled aggregate, the inhomogeneous evolution of mesoscopic damage shows obvious regular change, which is consistent with the internal chemical and physical mechanism and macro nonlinear stress–strain behavior.

Keywords: recycled aggregate concrete; uniaxial compression; stress–strain curve; mesoscopic damage mechanism; statistical damage mechanics

1. Introduction

In recent years, with the construction of new buildings and demolition of abandoned buildings, a large amount of construction waste has been generated in cities. The amount of construction waste is increasing rapidly year by year, which is more obvious in developing countries such as China and India [1]. Currently, construction waste in many countries is mainly recycled in the form of roadbed bedding and recycled bricks. Unfortunately, these methods not only waste limited resources, but are generally inefficient. On the other hand, with the further acceleration of urbanization, the consumption of natural resources is increasing, and there is an urgent need for a sustainable construction waste utilization method [2].

The application of recycled aggregate has become a priority project in various countries, and recycled aggregate concrete (RAC) is widely regarded as a new channel for sustainable development

of the construction industry [3]. Precisely because of the application of RAC, a large number of construction waste disposal difficulties and the resulting negative impact on the environment and other problems have been solved, and the exploitation of natural resources is reduced at same time, which could protect the ecological environment [4–6]. RAC is a new type of concrete, which is made up of recycled aggregate obtained from crushing, screening, cleaning, and other processes of construction waste, water, cement, sand, and other admixtures in a certain proportion. The biggest difference between RAC and NAC (natural aggregate concrete) is that the selected coarse aggregate is recycled aggregate rather than natural coarse aggregate, which leads to some differences in their mechanical properties. Many scholars at home and abroad have conducted a large number of experimental studies on the performance of RAC. On the one hand, there are many pore defects in recycled aggregate, resulting in the weak contact surface between recycled aggregate and old mortar in RAC, and the strength of recycled aggregate is lower than that of ordinary concrete, which is widely recognized by the public [7–9]. On the other hand, many micro-cracks in the recycled aggregate surface will absorb new cement particles, which makes the contact area comprehensively hydrated and increases the compactness of RAC, thus the mechanical properties of concrete have been improved [10–13]. Owing to the above two factors and the discreteness of concrete test results, scholars draw different conclusions through similar experiments.

Kapoor et al., GF Belén et al., Beltrán et al., and Xiao et al. respectively carried out the mechanical test of RAC under uniaxial compression with different replacement rates of recycled aggregate, and the full stress–strain curves of RAC were obtained. The results showed that, with the increase of the replacement rate, the compressive strength and elastic modulus of RAC show a gradually decreasing trend, and the peak strain increased monotonously. The corresponding stress–strain curves have similar shape characteristics in test [14–18]. Shi et al. proposed that, as a joint result of the water absorption and replacement rate of recycled aggregate, the increase of the total water absorption of the aggregate is the primary cause of the reduction in compressive strength, and the compressive strength of RAC can be improved in an appropriate water content [19]. Gupta concluded that, when the water cement ratio is low, the compressive strength of RAC will be lower than that of NAC, otherwise it is the opposite [20]. Chen et al. carried out uniaxial compression tests for recycled pebble and gravel concrete, and believed that the deformation and energy dissipation performance of RAC were inferior to that of NAC [21,22]. Du et al. found that the peak stress, peak strain, peak secant modulus, and elasticity modulus of RAC increase with the increase of concrete strength level [23]. Xiao et al. reported the relationship between the mechanical properties of recycled coarse aggregate and the single origin of recycled coarse aggregate, and believed that, when the recycled coarse aggregate is composite, the failure characteristics are the same, but the descending section of the full stress–strain curve is obviously affected [24]. Poon et al. compared the compressive strength of RAC at the ages of 3 d, 7 d, and 28 d, and found that it increases at first and then decreases with the increase of replacement rate at each age [25]. Tabsh and Abdelfatah hold that using RAC as high-strength concrete material is feasible if compressive strength, flexural strength, and elastic modulus can meet the needs of engineering characteristics, and it is necessary to establish a new standard for the use of recycled aggregate under different conditions, which can effectively reduce costs and protect the environment [4]. The interface transition zone (ITZ) is widely regarded as an important area affecting the mechanical properties of RAC, and it is the joint place between aggregate and cement slurry, which is usually weaker than aggregate or hydrated cement slurry. Li et al., Lotfi et al., and Kou et al. attribute the low specific strength of recycled aggregate to the existence of new and old ITZ [26–28].

Owing to the limitation of test technology, the studies on mechanical properties of RAC in the literature are mostly focused on the experimental analysis of macro mechanical properties, while the studies on microscopic damage mechanism are scarce. Moreover, most of the constitutive relations established are macroscopic phenomenological, focusing on the empirical fitting of test data, and could not establish an effective relationship between microscopic damage mechanism and macroscopic nonlinear constitutive behavior. In fact, the deformation and failure of quasi brittle materials (such as

concrete and rock) is essentially a microscopic to macroscopic trans-scale damage evolution process, involving the nucleation, initiation, and propagation of micro defects (micro cracks and micro holes). The macroscopic nonlinear stress–strain behavior is determined by the heterogeneity of microstructure and the nonlinear damage evolution on a micro scale. Meanwhile, damage localization is a common phenomenon for quasi-brittle solid that macroscopic ultimate failure is caused by damage evolution and accumulation. Localization behavior deepens the complexity of material deformation and failure and the difficulty of analysis. On the basis of the catastrophe theory, Bai et al. divided the deformation and failure of quasi brittle solids into two stages: distributed damage accumulation and local disaster [29]. They pointed out that this kind of macro failure phenomenon caused by the accumulation of micro-damage has mutation characteristics. When the microscopic damage accumulates to a certain critical state, the damage develops rapidly and leads to the ultimate failure of the material, which reflects the process from quantitative change to qualitative change.

Statistical damage mechanics is developed from continuous damage mechanics and has gradually become a research hotspot in the field of damage mechanics. It provides an effective method for studying the meso damage mechanism of quasi-brittle materials such as concrete. These kinds of models abstract quasi-brittle materials into a complex system composed of countless meso-elements (micro bar or micro spring). By assuming that the characteristic parameters of the meso-elements obey some form of statistical distribution, such as Weibull and normal, the heterogeneity in the microstructure of material could be introduced. In this way, both the complicated physical details of damage process and the complicated calculation of statistical mechanics could be avoided. It can be used to build a bridge between the meso damage mechanism and the macroscopic nonlinear mechanical behavior of quasi-brittle materials. Considering that there are two fundamental damage modes (fracture and yield) in the microstructure of concrete, the statistical damage models of concrete under uniaxial and multiaxial loading were proposed by Chen et al. and Bai et al. [30–34]. They further put forward the theory of intrinsic mechanical properties exert mechanism, suggesting that the deformation and failure of quasi brittle materials is not only a “degradation” process of the mechanical properties involving the initiation and propagation of micro-cracks and the decrease of macroscopic elastic modulus, but also a “strengthening” process manifesting that continuous optimization and adjustment of the effective stress skeleton in the microstructure to adapt to the change of external load environment.

In the second chapter, the basic assumption of the statistical damage theory is introduced. It describes the mesoscopic damage mechanism and macroscopic nonlinear mechanical behavior of concrete under uniaxial compression in detail, as well as the statistical damage model of concrete under uniaxial compression. The basic situation of the experiment, including the experimental scheme with three water cement ratios and five replacement rates, is demonstrated in the third chapter. Then, in Section 4, the test results are discussed. The influences of the water cement ratio and recycled aggregate replacement rate on the stress–strain curve, elastic modulus, compressive strength, peak strain, and failure mode are studied. In Section 5, the influence of the water cement ratio and replacement rate on the meso damage mechanism is analyzed based on the statistical damage model. In Section 6, the summary and prospect of the study are presented. In this paper, the tensile stress and strain are expressed as positive, while the compressive stress and strain are expressed as negative.

2. Statistical Damage Theory

2.1. Basic Assumption

According to the theory of intrinsic mechanical properties exert mechanism [30,32,33], the deformation and failure of quasi-brittle materials, such as concrete and rock, is essentially a self-organized process in which the potential mechanical capacity of the material system is constantly developed and released to adapt to the changes of the external load environment. As shown in Figure 1, at the meso scale, there are two mechanisms of concrete under uniaxial compression: the degradation effect and strengthening effect.

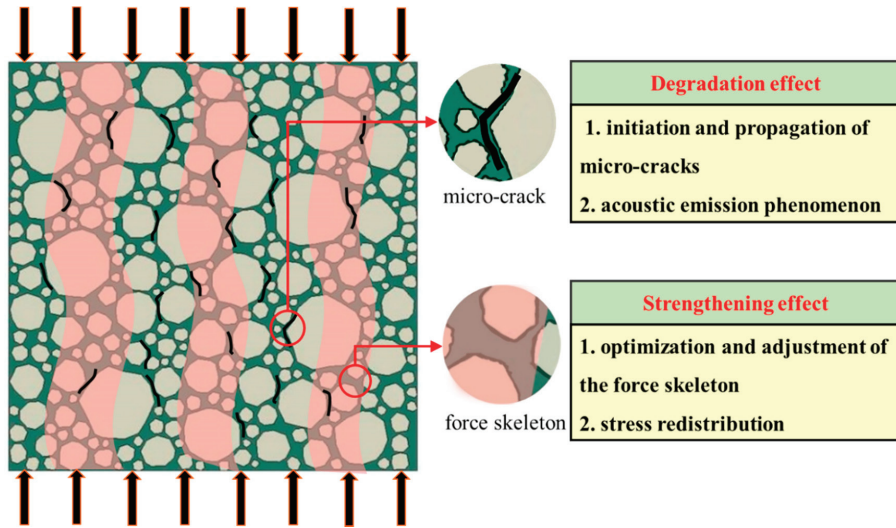


Figure 1. “Degradation” and “strengthening” in microstructure under uniaxial compression.

2.1.1. Degradation Effect

Owing to the existence of micro-cracks, micro-holes, and other micro-defects in the concrete matrix before the force is applied, the micro-cracks will further expand with the increase of deformation under the external load. At the same time, new micro-cracks will be generated in the weak parts of the specimen because of local tensile strain exceeding the limit, accompanied by acoustic emission phenomenon in microstructure, which is called the degradation effect. This effect is known as the physical basis of traditional damage mechanics.

2.1.2. Strengthening Effect

Along with the degradation effect, the strengthening effect may also occur in the microstructure. At the initial stress stage, the stress skeleton in the microstructure is not optimal. With the nucleation and penetration of micro-cracks, the weak parts in the microstructure will gradually withdraw from the stress state. Meanwhile, stress redistribution will occur in the microstructure, and the stress skeleton is further optimized and adjusted, resulting in the potential mechanical capacity of the material being further liberated to be able to withstand greater external loads (effective stress). When the effective stress skeleton is adjusted to the optimum, it indicates that the potential mechanical capacity of materials is fully released. After that, the material will not be able to withstand greater effective stresses, leading to local catastrophes. It is worth noting that this effect is ignored by traditional damage mechanics.

In conclusion, in the process of damage evolution of concrete materials, the deterioration phenomena such as the initiation and propagation of micro-cracks in microstructure are just external representations. Meanwhile, the reinforcement effect generated by further optimization and adjustment of the force skeleton (further development of potential mechanical capacity) should be regarded as the internal motivation, which determines the whole course.

2.2. Uniaxial Compression

2.2.1. Meso Damage Mechanism

Under uniaxial compression, the compression direction is denoted as the main direction, and the corresponding nominal stress, effective stress, and compressive strain are marked as σ , σ_E , and ε ,

respectively. The orthogonal directions on both sides are marked as direction 1 and 2, and the corresponding tensile strains are marked as ε_1 and ε_2 . As shown in Figure 2a, the typical nominal stress–strain curve and predicted effective stress–strain curve of concrete under uniaxial compression are presented. It includes four typical states, A, B, C, and D, where A is the state of limit proportion, B is the peak nominal stress state, C is the critical state, and D is the local failure state. The corresponding nominal stress and effective stress are noted as $\sigma_A, \sigma_B, \sigma_C, \sigma_D$ and $\sigma_{EA}, \sigma_{EB}, \sigma_{EC}, \sigma_{ED}$, respectively. Figure 2b shows the meso damage evolutions in the microstructure of concrete specimen corresponding to the four typical states, A, B, C, and D.

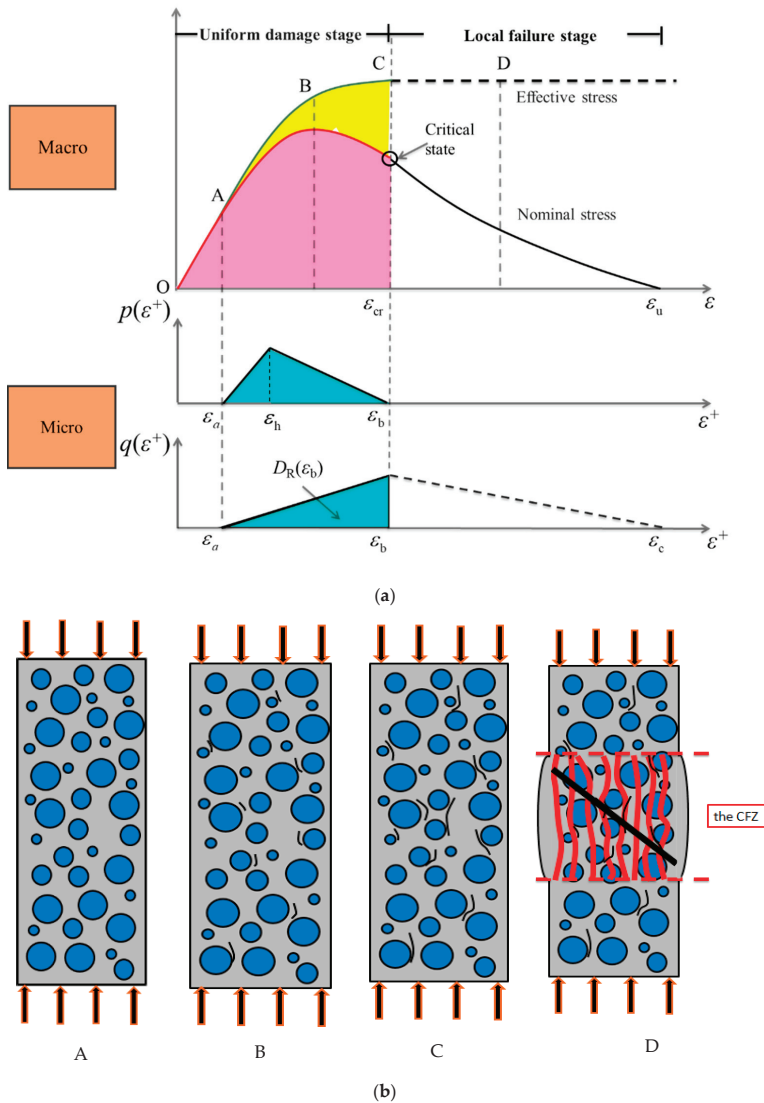


Figure 2. Uniaxial compression. CFZ, compression failure zone. (a) Meso damage mechanism and macro nonlinear stress–strain relationship; (b) Schematic diagram of mesoscopic damage evolution in typical states.

During the loading process, owing to the Poisson effect, the concrete specimen will produce transverse tensile strain in directions 1 and 2. Micro-cracks will occur randomly at certain weak parts (such as the interface between aggregate and cement mortar) in the microstructure of concrete, when its tensile strain exceeds the limit [33,34]. The orientation of the micro-crack surface is roughly parallel to the pressure direction. At the same time, with the exit of the weak part from the stress state, the stress redistribution in the microstructure is realized, and the effective force skeleton is further optimized and adjusted to ensure that it can withstand more effective stress.

During the loading process from the initial to state C ($O \rightarrow A \rightarrow B \rightarrow C$), the density of micro-cracks increases gradually; the effective stress skeleton in microstructure could be further optimized and adjusted by means of the initiation and propagation of micro-cracks. Thus, the material system can obtain greater bearing capacity to maintain the balance with each load increment state. The effective stress σ_E increases monotonically with the increase of compression deformation. At state C, the effective force skeleton in the microstructure has been adjusted to the optimum, and σ_E reaches its maximum. The nominal stress σ first increases and then decreases with the increase of compression deformation, and reaches its maximum at state B. At this stage, the formation and penetration of micro-cracks were random and disorderly in the whole range of the specimen, with the micro-crack density in a small degree. The whole specimen can approximate in a state of uniform damage and deformation. Thus, we define it as the uniform damage phase.

After state C, the force skeleton of the microstructure cannot be further optimized by means of micro-crack generation and propagation, which indicates the potential mechanical capacities of the material have been played to the limit, and then the specimen will enter a failure stage characterized by local catastrophe. Damage localization will appear, forming the local compression failure zone (CFZ). In the CFZ, the compression damage will further aggravate with the expansion of macroscopic longitudinal tensile cracks; at state D, the localized shear band will further occur, which finally leads to the failure. Meanwhile, the rest of the specimen will unload and remain a continuum [35,36]. At this stage, the localized behavior of damage evolution deepens the complexity of catastrophic failure and the difficulty of prediction. Localization makes it difficult to describe the behavior of solids in terms of the global average [29]. The nominal stress–strain curve experimentally obtained has an obvious size effect and cannot be regarded as a pure material property. Here, state C is further taken as a precursor to local failure, and the whole process is divided into the uniform (distributed) damage stage and local failure stage [31,33,34].

Van Geel studied the damage localization of concrete under compression [36]. On the basis of the photographic observations along the different stages of the descending branch of the stress–strain curve, he indicated that the localization occurs after the peak and on the steeper part of the softening branch, where the macroscopic longitudinal tensile cracks start to extend toward the center of the specimen. The remaining region of the specimen does not unload at the peak state, but will only start to unload after a certain post-peak deformation, meaning the rest of the region still contributes to the deformation of softening section, to some extent. This is consistent with the assumption of the position of state C (critical state) in this paper.

2.2.2. Statistical Damage Constitutive Model

The above analysis shows that the deformation and failure of concrete under uniaxial compression is essentially a continuous damage evolution process in three-dimensional space [31,34]. The damage in the compression direction is controlled by the lateral tensile damage process caused by the Poisson effect, which can be simulated by the improved parallel bar system model (IPBS) [30]. The variable ε^+ ($\varepsilon^+ > 0$, orthogonal to the compression direction) is defined as the equivalent transfer tension damage strain corresponding to the compression direction. It can be expressed as a function of the lateral tensile strains ε_1 and ε_2 . For uniaxial compression, it satisfies $\varepsilon^+ = -\nu\varepsilon$, where ν is Poisson's ratio.

As shown in Figure 2a, the macroscopic nonlinear stress–strain behavior (nominal/effective stress–strain curve) of concrete in the compression direction is controlled by two kinds of mesoscopic

damage evolution, fracture and yield [31,34]. They can be characterized by the fracture and yield of micro-bars in the IPBS, and represent the initiation and propagation of micro-cracks and the optimization and adjustment of the force skeleton of microstructures, respectively. It should be emphasized here that the yield damage mode also reflects the “strengthening” effect in microstructure, that is, the further development of the potential mechanical capacities.

$q(\varepsilon^+)$ and $p(\varepsilon^+)$ are defined as the probability density functions of mesoscopic fracture and yield damage, respectively. To simplify the analysis, they are assumed to follow independent triangular distributions [31,33,34]. For easy description, the strains of the x-coordinate are denoted by ε and ε^+ , respectively.

The characteristic tensile strains corresponding to ε^+ include ε_a , ε_h , and ε_b , where ε_a is the initial damage strain; ε_h is the peak strain of $p(\varepsilon^+)$; ε_b is the maximum yield damage strain, and also the peak strain of $q(\varepsilon^+)$; and ε_{cr} is the compressive strain corresponding to the critical state, satisfying $\varepsilon_b = -\nu\varepsilon_{cr}$. The constitutive relation corresponding to the uniform damage stage ($0 \leq \varepsilon^+ \leq \varepsilon_b$ and $\varepsilon_{cr} \leq \varepsilon \leq 0$) can be expressed as follows [31,34]:

$$\sigma = E(1 - D_y)(1 - D_R)\varepsilon \tag{1}$$

$$\sigma_E = E(1 - D_y)\varepsilon \tag{2}$$

$$D_y = \int_0^{\varepsilon^+} p(\varepsilon^+)d\varepsilon^+ - \frac{\int_0^{\varepsilon^+} p(\varepsilon^+)\varepsilon^+d\varepsilon^+}{\varepsilon^+} \tag{3}$$

$$D_R = \int_0^{\varepsilon^+} q(\varepsilon^+)d\varepsilon^+ \tag{4}$$

$$E_v = \int_0^{\varepsilon^+} p(\varepsilon^+)d\varepsilon^+ \tag{5}$$

$$p(\varepsilon^+) = \begin{cases} 0 & (\varepsilon^+ \leq \varepsilon_a) \\ \frac{2(\varepsilon^+ - \varepsilon_a)}{(\varepsilon_h - \varepsilon_a)(\varepsilon_b - \varepsilon_a)} & (\varepsilon_a < \varepsilon^+ \leq \varepsilon_h) \\ \frac{2(\varepsilon_b - \varepsilon^+)}{(\varepsilon_b - \varepsilon_h)(\varepsilon_b - \varepsilon_a)} & (\varepsilon_h < \varepsilon^+ \leq \varepsilon_b) \end{cases} \tag{6}$$

$$q(\varepsilon^+) = \begin{cases} 0 & (\varepsilon^+ \leq \varepsilon_a) \\ \frac{2H(\varepsilon^+ - \varepsilon_a)}{(\varepsilon_b - \varepsilon_a)^2} & (\varepsilon_a < \varepsilon^+ \leq \varepsilon_b) \end{cases} \tag{7}$$

$$H = D_R(\varepsilon_b) \tag{8}$$

where E is the initial modulus of elasticity; D_R and D_y are the accumulated damage variables related to mesoscopic fracture and yield damage, respectively; E_v is the evolution factor to describe the “strengthening” process in the microstructure, corresponding to the yield damage mode; and H is the fracture damage value corresponding to the critical state.

E_v could be used to assess the extent to which the potential mechanical capacity (adjustment capacity of force skeleton in microstructure) of materials is developed, ranging from 0 to 1. When $E_v = 0$, it corresponds to the initial undamaged state. When $E_v = 1$, it corresponds to the critical state, at which point the potential adjustment capacity of materials reaches its limit, σ_E reaches its maximum, and then the materials enter into the local catastrophic stage. The whole process embodies the characteristics of “quantum” to “qualitative”, in which the yield damage mode plays a key role.

S is defined as the energy absorption capacity, which represents the energy absorbed by concrete in the process of stress and deformation [37,38], and the expression is as follows:

$$S = \int_0^{\varepsilon} \sigma d\varepsilon \tag{9}$$

$$S_p = \int_0^{\varepsilon_p} \sigma d\varepsilon \quad (10)$$

$$S_{cr} = \int_0^{\varepsilon_{cr}} \sigma d\varepsilon \quad (11)$$

where S_p and S_{cr} are the energy absorption capacity corresponding to peak nominal stress state and critical state, respectively; and σ_p and ε_p are the nominal stress and strain corresponding to the peak nominal stress state, respectively.

2.2.3. Method of Parameter Determination

Each stress–strain curve needs to determine the following five parameters: E , ε_a , ε_h , ε_b , and H . E can be obtained directly from the test curve, and its value is the secant modulus from 0.2–0.4 times the peak nominal stress point to the origin point. ε_a , ε_h , ε_b , and H are obtained by the multivariate regression analysis of the genetic algorithm module in Matlab toolbox. The specific steps are as follows [34]:

1. Create a fitness function, including four parameters, ε_a , ε_h , ε_b , and H . The optimization criterion is the minimum sum of squares of the deviation between the predicted stress and the measured stress;
2. Set the initial search interval of four parameters;
3. Genetic algorithm is implemented to obtain the optimal parameter solution of this iteration. Adjust or narrow the parameter search interval according to the result;
4. Repeat step 3 until obtaining the optimal solution.

3. Experimental Descriptions

3.1. Materials

The cement used in this test is ordinary Portland cement produced by Henan Fengbo Tianrui Company (Zhengzhou, China), and its performance indicators are shown in Table 1. The sand is natural river sand (fineness modulus 2.92, medium sand) according to Chinese standard [39]. The natural coarse aggregate is collected from continuous graded natural gravel, and the recycled coarse aggregate is obtained by crushing and screening the abandoned concrete pavement of the school (the sampling strength is about 35 MPa). The particle size range is 5 mm~20 mm, which can be regarded as a single source. Figures 3 and 4 present the grain gradation curve and the apparent characteristics of coarse aggregate, respectively. The physical properties of coarse aggregate are shown in Table 2, as measured by the test methods provided in Chinese code [39].

Table 1. Performance indicators of cement.

Specific Surface Area (m ² /Kg)	Coagulation Time/min		28d Strength/MPa		Chloride Ion Content/%	Loss on Ignition/%
	Initial Coagulation	Final Coagulation	Flexural Strength	Compressive Strength		
348.7	176	244	7.1	48.6	0.022	3.2

Table 2. Basic properties of coarse aggregates.

Aggregate Type	Particle Size Range/mm	Moisture Content/%	Water Absorption Rate/%	Crushing Index/%	Tight Packing Density/(kg·m ⁻³)	Apparent Density/(kg·m ⁻³)
Natural	5~20	0.23	0.65	10.07	1570.23	2722.27
Recycled	5~20	3.85	4.98	19.63	1272.67	2493.50

It can be seen from Table 2 that the moisture content, water absorption, and crushing value of natural aggregate are lower than those of recycled aggregate, while the tight packing density and

apparent density are higher. The apparent density of recycled aggregate conforms to the Type I standard (apparent density $> 2450 \text{ kg/m}^3$) recommended in Chinese code [40], and the crushing index, water absorption rate, and air void rate all conform to the Type II standard (crushing index $< 20\%$, water absorption rate $< 5\%$, air void rate $< 5\%$). The grain grading curve of coarse aggregate basically satisfies the requirements of the continuous grain grading of Chinese standard [40]. In general, the recycled coarse aggregate used in this experiment has relatively high quality.

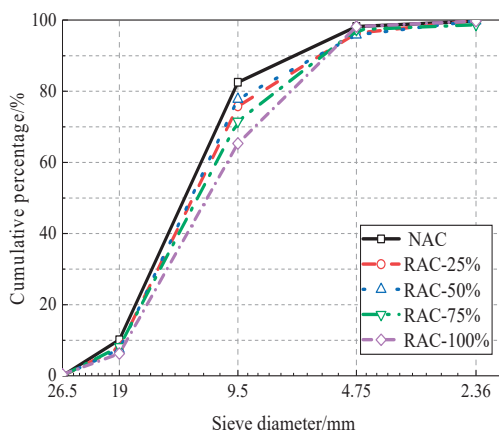


Figure 3. Particle grading curve of coarse aggregate. NAC, natural coarse aggregate; RAC, recycled coarse aggregate.



Figure 4. Apparent characteristics of coarse aggregate. (a) Recycled coarse aggregate; (b) Natural coarse aggregate.

3.2. Mix Proportion

According to the test equipment conditions, cylinder specimens with a diameter of 100 mm and a height of 200 mm were selected. Considering the dispersion of the experimental results, five specimens were prepared for each group of tests. It is generally believed that the strength of concrete is very sensitive to the water cement ratio. The surface of recycled aggregate is covered with an old cement mortar compared with natural aggregate, resulting in higher water absorption of recycled aggregate, which will inevitably have a greater impact on the mechanical properties of RAC. Therefore, it is necessary to consider additional water in the mix design to balance the water cement ratio according to Chinese code [40]. In order to fully consider cement hydration, the specimens were placed in a standard curing room for 90 days. The mix proportion of three kinds of concrete with different water

cement ratios is shown in Table 3, where RAC-I, RAC-II, and RAC-III correspond to concrete with water cement ratios of 0.66, 0.49, and 0.38, respectively.

Table 3. Experiment mix ratio. RAC, recycled coarse aggregate; W/C, water/cement.

Specimen Type	Replacement Rate of Recycled Aggregate	W/C	Cement	Sand	Coarse Aggregate		Water	
					Natural	Recycled	Mixed Water	Additional Water
RAC-I	0%	0.66	311	735	1149	-	205	-
	25%	0.66	311	735	861.5	287.5	205	3.94
	50%	0.66	311	735	574.5	574.5	205	7.87
	75%	0.66	311	735	287.5	861.5	205	11.80
	100%	0.66	311	735	-	1149	205	15.74
RAC-II	0%	0.49	418	613	1164	-	205	-
	25%	0.49	418	613	873	291	205	4.01
	50%	0.49	418	613	582	582	205	8.02
	75%	0.49	418	613	291	873	205	12.03
	100%	0.49	418	613	-	1164	205	16.04
RAC-III	0%	0.38	539	563	1143	-	205	-
	25%	0.38	539	563	857.2	285.8	205	3.57
	50%	0.38	539	563	571.5	571.5	205	7.88
	75%	0.38	539	563	285.8	857.2	205	11.81
	100%	0.38	539	563	-	1143	205	15.75

Unit: Kg/m³.

3.3. Test Setup and Loading

The WAW-1000 electro hydraulic servo universal testing machine produced by Shanghai Hualong Company (Shanghai, China) was used in the test, as shown in Figure 5. Before the test, the end face of the specimen is ground and an anti-friction agent is applied. The specimen should be preloaded before the formal loading test. Displacement control is adopted in the loading mode and the quasi-static loading rate was 0.36 mm/min. The preloading end point is 40% of the designed strength. The uniaxial compression test should start after three repeats of preloading. Quasi static loading is used for uniaxial compression, and the loading rate is 0.36 mm/min with displacement loading mode. The longitudinal deformation and axial force of the specimen are automatically collected by the testing system of the testing machine, and the displacement meter measures the displacement at both ends of the specimen. The experimental operation was conducted by referring to Chinese code [41].



Figure 5. Universal testing machine.

4. Experimental Results

After the test, five stress–strain curves were obtained for each group. Two curves with the maximum and minimum peak stress were eliminated first, and the average stress–strain curve of the middle three curves after average treatment is taken as the representative value of this group of tests. The test parameters of the middle three curves are shown in Table 4.

Table 4. Characteristic parameter.

Specimen	Peak Stress (MPa)				Peak Strain (10 ⁻³)				Elastic Modulus (10 ⁻⁴ MPa)						
	Sample 1	Sample 2	Sample 3	Average	St. dev	Sample 1	Sample 2	Sample 3	Average	St. dev	Sample 1	Sample 2	Sample 3	Average	St. dev
RAC-I-0%	-24.74	-22.98	-21.44	-23.03	1.651	-2.318	-1.677	-1.948	-1.981	0.321	1.692	1.898	1.501	1.697	0.198
RAC-I-25%	-23.26	-22.78	-21.04	-22.36	1.168	-2.876	-2.332	-2.451	-2.553	0.285	1.262	1.475	1.189	1.308	0.148
RAC-I-50%	-21.5	-20.43	-19.01	-20.31	1.249	-2.567	-3.705	-3.303	-3.191	0.577	0.898	0.873	0.944	0.905	0.036
RAC-I-75%	-23.32	-22.01	-21.69	-22.34	0.863	-4.18	-3.619	-3.016	-3.605	0.582	0.94	0.973	0.982	0.965	0.022
RAC-I-100%	-28.04	-24.87	-22.17	-25.02	2.938	-3.657	-4.636	-3.701	-3.998	0.552	0.981	0.858	0.844	0.894	0.075
RAC-II-0%	-31.05	-28.06	-25.71	-28.27	2.676	-1.618	-2.263	-2.302	-2.061	0.384	2.045	1.997	2.408	2.151	0.224
RAC-II-25%	-30.63	-27.44	-25.44	-27.83	2.617	-2.778	-3.408	-2.914	-3.033	0.331	1.62	1.66	1.386	1.555	0.148
RAC-II-50%	-27.89	-26.78	-21.72	-25.46	3.288	-3.875	-3.381	-2.693	-3.316	0.593	0.811	0.895	0.985	0.897	0.087
RAC-II-75%	-28.69	-28.17	-25.46	-27.44	1.734	-2.385	-2.115	-1.802	-2.101	0.291	1.834	2.192	2.261	2.095	0.229
RAC-II-100%	-34.47	-32.73	-29.87	-32.35	2.322	-1.871	-1.448	-1.188	-1.733	0.246	2.546	2.876	2.159	2.527	0.358
RAC-III-0%	-45.5	-40.84	-38.74	-41.69	3.459	-1.695	-2.396	-2.097	-2.062	0.351	2.258	2.828	2.427	2.504	0.292
RAC-III-25%	-38.87	-35.51	-29.78	-34.72	4.596	-2.806	-3.398	-3.754	-3.319	0.478	1.219	1.275	1.136	1.21	0.069
RAC-III-50%	-44.06	-39.81	-38.09	-40.65	3.071	-2.989	-3.23	-2.42	-2.879	0.415	1.948	1.786	1.748	1.827	0.106
RAC-III-75%	-44.62	-42.96	-37.85	-41.81	3.528	-2.879	-2.318	-3.247	-2.814	0.467	1.716	1.793	2.151	1.886	0.232
RAC-III-100%	-51.79	-47.6	-44.67	-48.02	3.578	-2.296	-3.221	-2.171	-2.562	0.573	2.075	2.458	2.342	2.291	0.196

"St. dev" represents the standard deviation of the specimen.

The average nominal stress–strain curves corresponding to five different replacement rates and three different water cement ratios are as shown in Figure 6. It can be seen that the stress–strain curves conform to the basic characteristics of the classic uniaxial compression test: good continuity and smoothness. The stress–strain curves of different replacement rates are similar in shape and have good regularity in curve trend. The pre-peak ascending phase of stress–strain from the origin to 50~70% of the peak stress can be considered as a linear elastic stage, after which the slope of the curve gradually slows down, and then the curve declines rapidly after reaching the peak stress. In the post-peak descending phase, when the stress drops to 75–85% of the peak stress, the curve appears an inflection point, and its shape changes from convex to concave, with the decreasing rate gradually slowing down.

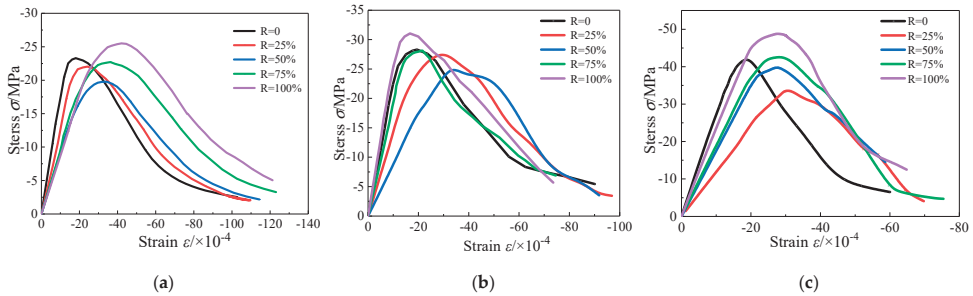


Figure 6. Stress–strain full curves under uniaxial compression. (a) RAC-I; (b) RAC-II; (c) RAC-III.

4.1. Compressive Strength

As shown in Figure 7, peak stress of RAC-I, RAC-II, and RAC-III (with water cement ratio of 0.66, 0.49, and 0.38) decreases first and then increases with the increase of the replacement rate *R*. With *R* = 50% as the bound, when the replacement rate increases in the interval [0%, 50%], the compressive strength of RAC-I and RAC-II decreases monotonously, and then shows an upward trend in the interval [50%, 100%]. In addition to the different inflexion point (*R* = 25%), the compressive strength of RAC-III also conforms to the law of decreasing first and then increasing. At *R* = 100%, the compressive strength of RAC-I, RAC-II, and RAC-III increases by 9.7%, 10.8%, and 11.8% compared with NAC (*R* = 0%), respectively.

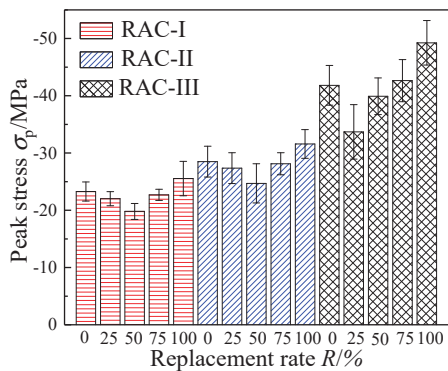


Figure 7. Summary of compressive strength.

Compared with NAC, there are two types of ITZ in RAC, namely old aggregate and old mortar, as well as regenerated aggregate and new mortar, as shown in Figure 8. The change of macro mechanical properties of RAC is closely related to the composition of material microstructures and the physical and chemical reactions within RAC. There are two main mechanisms:

- Degradation effect: old cement mortar is attached to the surface of recycled aggregate, ITZ of new and old cement slurry is a weak area of mechanical properties [8], and there are many micro-cracks in the production process of recycled aggregate under external force, which lead to the degradation of mechanical properties [42].
- Strengthening effect: the high porosity of recycled aggregate means RAC contains more water and plays an internal curing role, which makes the later hydration reaction more thorough [43]. Meanwhile, the remaining unhydrated old cement adheres to the surface of RAC particles and reacts with water to improve the development rate of strength and the density of microstructure [44]. In addition, the porous properties of recycled aggregate allow it to bond better with new mortar and absorb more water from ITZ, so as to reduce the water cement ratio of ITZ and effectively improve the rigidity of local areas [10]. Moreover, the surface of recycled aggregate is rough and angular, which increases the mutual friction and mechanical biting between aggregates [45,46].

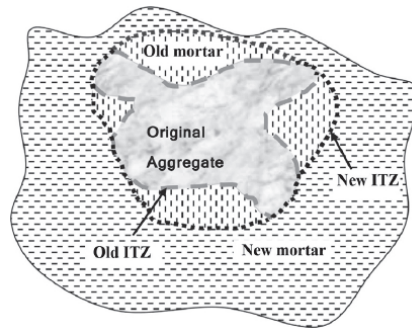


Figure 8. Schematic of the old and new interface transition zone (ITZ) in RAC [8].

In this experiment, when R is in the range of 0–50% (RAC-III: 0–25%), the degradation effect is dominant, and the strength of RAC decreases with the increase of the replacement rate, while R at the range of 50–100% (RAC-III: 75–100%) shows the opposite situation to the one above.

Experiment dates of uniaxial compression obtained by different scholars for test blocks with standard maintenance for 28 days are shown in Figure 9 [18,21,25]. As can be seen, the compressive strength increases with the increase of the RAC replacement rate, or decreases first and then increases. Relatively speaking, the change of compressive strength in this experiment is more obvious. According to relevant experimental reports, the strength development rate of RAC concrete is higher than NAC, especially in anaphase (28 days and later) [25,44,47]. As residues of unhydrated old cement adhere to the surface of RAC particles, these particles react with water, so as to increase the strength and development rate.

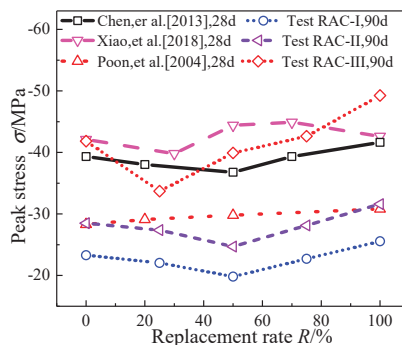


Figure 9. Compressive strength statistics.

4.2. Peak Strain

ϵ_p is the peak strain corresponding to the nominal peak stress. Figure 10 shows the change rule of peak strain with replacement rate. The peak strain of RAC-I increases from -1.80×10^{-3} to -4.15×10^{-3} , with an increased monotonically trend. For RAC-II, with $R = 50\%$ as the limit, the peak strain first increases from -1.94×10^{-3} to -3.28×10^{-3} , and then decreases to -1.66×10^{-3} . It can also be seen clearly that, when the peak strain of RAC-III is bounded by $R = 25\%$, it first increases from -1.89×10^{-3} to -3.15×10^{-3} and then decreases to -2.55×10^{-3} .

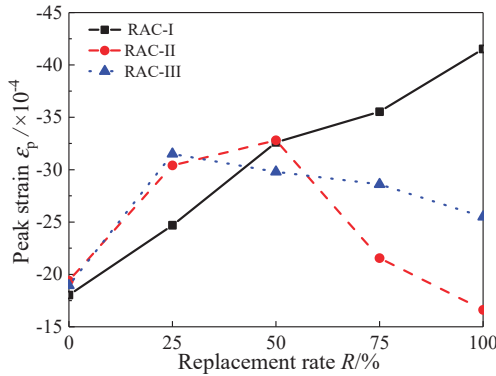


Figure 10. Peak strain.

4.3. Elastic Modulus

Figure 11 presents the trend and fitting curve of the initial elastic modulus E for RAC-I, RAC-II, and RAC-III with the replacement rate, respectively. It can be seen that the curve has obvious regularity. For RAC-I, E decreases by 51.3% from 17.96 GPa to 8.74 GPa, showing a trend of rapid decline first and then to level, with the inflection point at $R = 50\%$. As for the change trends of E for RAC-II and RAC-III, they decrease first and then increase with the replacement rate. When the replacement rate is 100%, E of RAC-II increases by 17.7% from 22.3 GPa to 26.24 GPa, and E of RAC-III decreases from 26.2 GPa to 22.32 GPa with a 14.8% reduction.

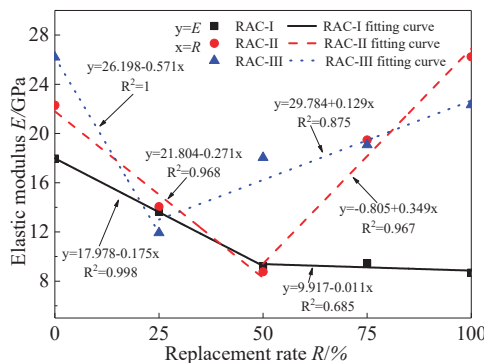


Figure 11. Elastic modulus.

4.4. Deformation and Failure Characteristics

During the uniaxial compression test, the specimens will undergo several typical stages, each of them corresponding to different mechanical characteristics. Figure 12 shows the typical deformation view of the specimen at different stages. In Figure 12a, the whole specimen is in the stage of uniform

deformation and damage; there are no macroscopic cracks here. At the post-peak softening section of the stress–strain curve, when the stress of specimen decreases to 80–90% of the peak stress, a series of columnar macro-cracks will appear in the middle of the specimen, forming an obvious local bulging region (i.e., the CFZ), as shown in Figure 12b. Continuing loading, the compressive deformation and damage are further increased in the local bulging zone, and the inclined shear cracks will appear when the stress decreases to 50%~60% of the peak stress, as shown in Figure 12c, leading to the ultimate failure of the specimen. Xiao et al. obtained similar results [17,18].

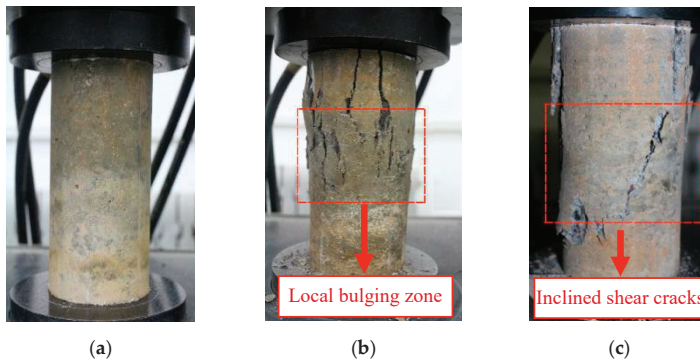


Figure 12. Typical characteristics under uniaxial compression. (a) Uniform deformation; (b) Local bulging; (c) Shear failure.

On the basis of catastrophe theory, the quasi-brittle solid failure is divided into the distributed damage accumulation stage and local catastrophe stage by Bai et al. [29]. They pointed out that the macroscopic failure of materials caused by the accumulation of micro damage has the characteristics of mutation. When the damage accumulation reaches a certain critical value, the damage develops rapidly and leads to final local failure of the material, which embodies the process from quantitative change to qualitative change. Van Geel et al. studied the damage localization of concrete under compression based on the photographic observations along the different stages of the softening branch of the stress–strain curve [36]. They concluded that the damage localization occurs after the peak and on the steeper part (about 90% of the peak stress) of the descending branch, which is related to concrete type, aggregate size, and other factors. It was also observed that the concrete continuum outside the CFZ does not unload at the peak, but will only start unloading after a certain post-peak deformation, which has a certain contribution to the deformation of softening branch. In this paper, the state when local bulging happens is taken as the critical state, and the deformation and failure of concrete under uniaxial compression are divided into two stages: distributed damage and local failure, corresponding to the catastrophe theory.

5. Analysis of Mesoscopic Damage Mechanism

Nonlinear mechanical behavior of concrete is the macroscopic representation of meso-heterogeneous damage evolution, and the macroscopic stress–strain curve contains effective information of mesoscopic damage evolution process. On the basis of the statistical damage model, the influence of recycled aggregate replacement rate on the mesoscopic damage evolution of concrete under uniaxial compression is studied according to the experimental curve. The intrinsic relationship between the physical-chemical mechanism, the mesoscopic damage evolution mechanism, and the macroscopic nonlinear mechanical behavior is discussed. Referring to Chinese code [39], Poisson's ratio is 0.2.

5.1. The Fitting of the Nominal Stress–Strain Curve

The nominal stress–strain curves fitted by the statistical damage model are presented in Figure 13, and the calculation parameters are shown in Table 5. Moreover, the effective stress–strain curves are also predicted using the model in this paper, as shown in Figure 14. The deformation and failure of concrete under uniaxial compression can be better understood by this model from the perspective of effective stress. In the distributed damage phase, nominal stress first increases and then decreases, containing the peak nominal stress state. Meanwhile, the effective stress monotonously increases, reaching the maximum at the critical state. After the critical state, the specimen will enter the local failure stage characterized by the damage localization. The envelopes of the predicted nominal and effective strain curves are as shown in Figures 15 and 16, respectively. As can be seen, with $R = 50\%$ (RAC-III: $R = 25\%$) as the boundary, the envelope shapes of RAC-I, RAC-II, and RAC-III show obvious rules with the increase of the replacement rate.

Table 5. The results of the calculation parameters.

Specimen Type	R/%	E/GPa	$\epsilon_a/\times 10^{-4}$	$\epsilon_h/\times 10^{-4}$	$\epsilon_b/\times 10^{-4}$	H
RAC-I	0	17.96	0.955	2.101	5.891	0.208
	25	13.65	0.853	3.379	7.046	0.259
	50	9.22	0.572	6.309	9.662	0.366
	75	9.54	1.705	5.436	10.684	0.329
	100	8.69	2.984	5.117	12.620	0.317
RAC-II	0	22.3	0.877	2.207	5.623	0.231
	25	14.05	1.770	3.913	8.510	0.258
	50	8.77	3.078	6.144	11.060	0.353
	75	19.47	1.341	3.550	7.022	0.280
	100	26.24	0.597	2.909	4.908	0.197
RAC-III	0	26.2	2.337	2.924	5.437	0.307
	25	11.93	4.189	6.606	8.697	0.329
	50	18.04	2.860	5.050	7.655	0.315
	75	19.07	2.787	4.917	7.591	0.297
	100	22.32	2.706	4.824	7.472	0.258

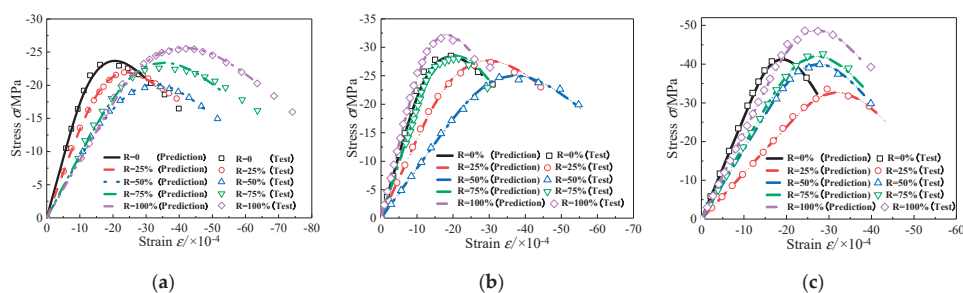


Figure 13. Nominal stress–strain curve (plan view). (a) RAC-I; (b) RAC-II; (c) RAC-III.

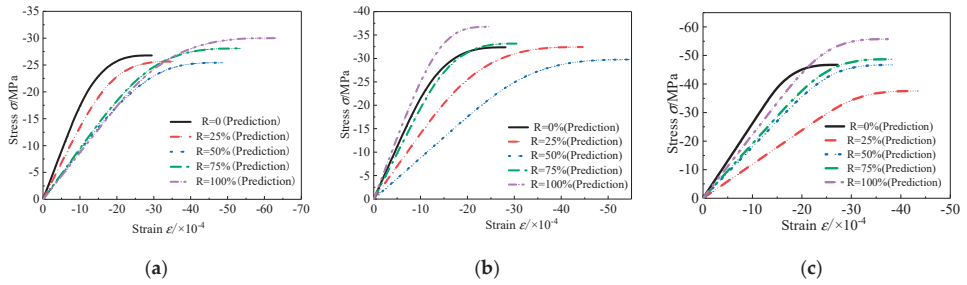


Figure 14. Effective stress–strain curve (plan view). (a) RAC-I; (b) RAC-II; (c) RAC-III.

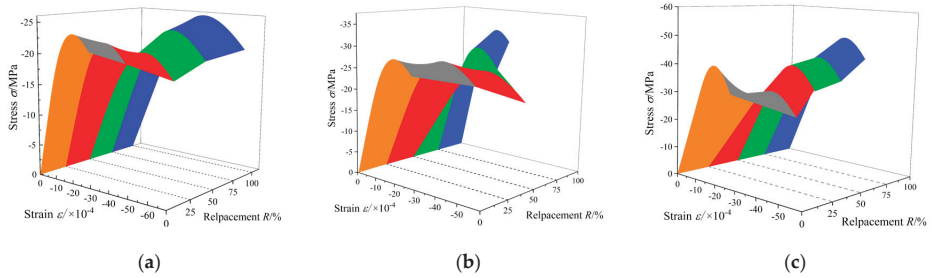


Figure 15. Nominal stress–strain curve envelope surface (3D view). (a) RAC-I; (b) RAC-II; (c) RAC-III.

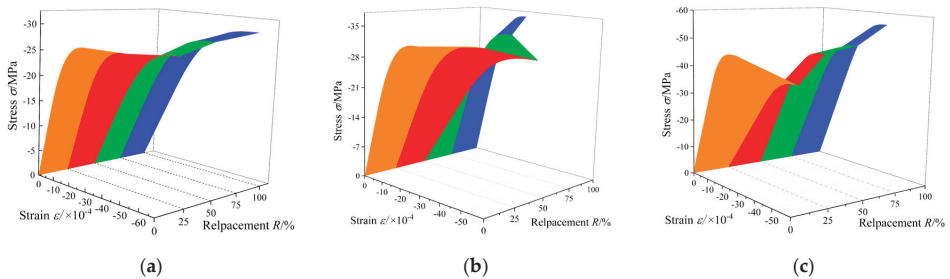


Figure 16. Effective stress–strain curve envelope surface (3D view). (a) RAC-I; (b) RAC-II; (c) RAC-III.

5.2. Mesoscopic Damage Mechanism

According to the four characteristic parameters (ε_a , ε_h , ε_b , and H), the specific shapes of triangular probability distributions corresponding to the mesoscopic damage evolution of yield and fracture could be determined, and the vivid physical pictures will be presented.

The change curves of yield damage related parameters, ε_a , ε_h , and ε_b , of RAC-I, RAC-II, and RAC-III are indicated in Figure 17. It clearly shows the change rules of the yield damage parameters with the replacement rate, when the water cement ratio is 0.38, 0.49, and 0.66, respectively. As shown, when the water cement ratio is invariant, with the increase of the recycled aggregate replacement rate, the changes of these three characteristic parameters show obvious regularity. Especially for RAC-II and RAC-III, three parameters show the similar change law; that is, with $R = 50\%$ ($R = 25\%$) as the boundary, they present a trend of linear increase and then linear decrease. As for RAC-I, with $R = 50\%$ as the boundary, ε_a first decreases and then increases, while ε_h displays the opposite; ε_b increases linearly from 5.81×10^{-4} at $R = 0\%$ to 12.62×10^{-4} at $R = 100\%$, as the critical state strain increases monotonously with the replacement rate. The yield damage pattern reflects the process of optimization and adjustment of the stress skeleton of concrete microstructure. Unfortunately, it cannot

be measured effectively by the existing experimental techniques. In Figure 18a–c, the influence curves of the replacement rate R of recycled aggregate on ε_a , ε_h , and ε_b are exhibited respectively. On the basis of regression analysis, the expressions of the three parameters changing with the replacement rate are obtained. The correlation coefficient R^2 between the predicted and fitted values of the parameters is also given in the figures.

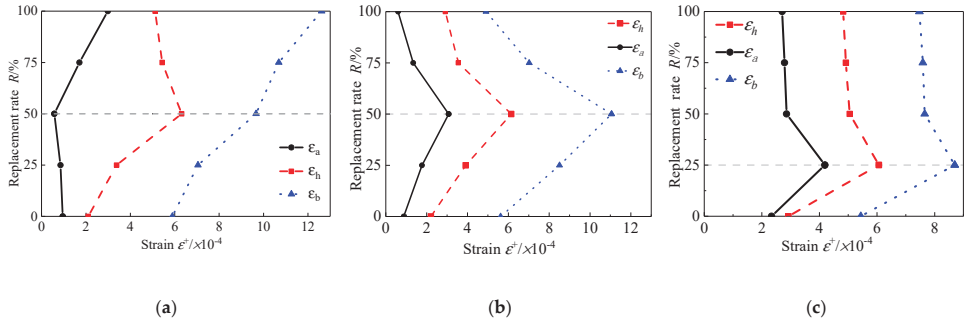


Figure 17. R - ε_a , ε_h , ε_b curves. (a) RAC-I; (b) RAC-II; (c) RAC-III.

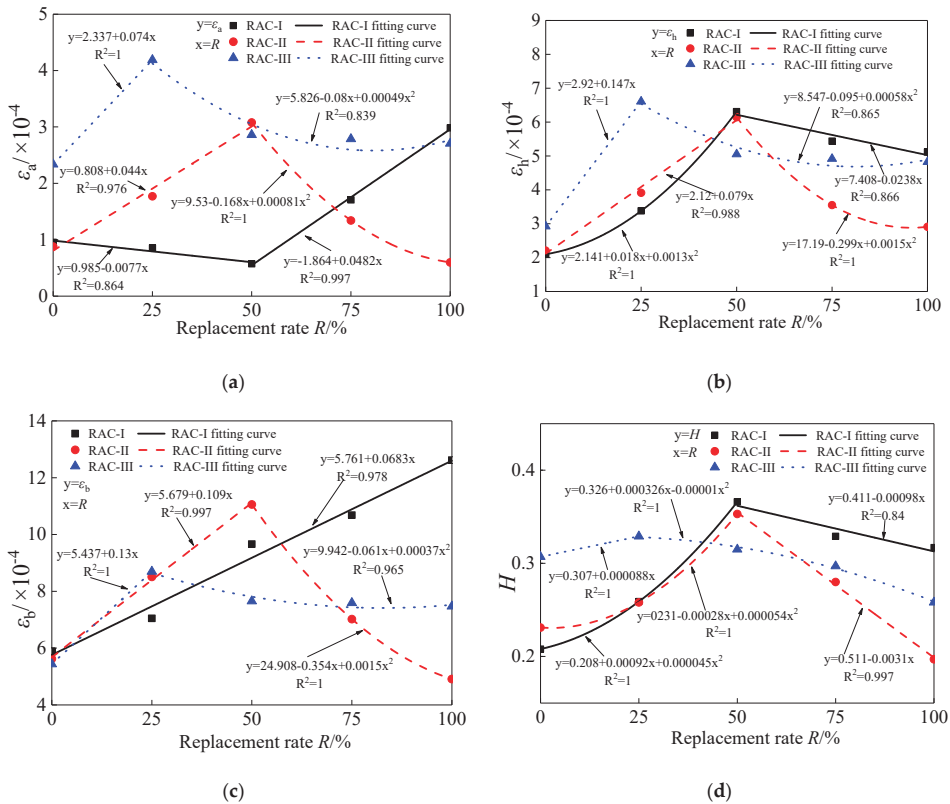


Figure 18. ε_a , ε_h , ε_b , H - R curves. (a) ε_a - R curve; (b) ε_h - R curve; (c) ε_b - R curve; (d) H - R curve.

The change curves of fracture damage related parameter H of RAC-I, RAC-II, and RAC-III are shown in Figure 18d. They show obvious similar regularity with the increase of the replacement rate. The fitting formula is obtained by regression analysis, and the correlation coefficient R^2 between the

predicted and fitted values is also given. With $R = 50\%$ (RAC-III: $R = 25\%$) as the boundary, H shows a trend of linear increase and then linear decrease. The fracture damage pattern of concrete is associated with the density of micro-crack, and also closely related to the physical and chemical reactions in concrete. As mentioned above, recycled aggregate has both a degradation and strengthening effect on concrete. Taking RAC-II as an example, when R is in the interval $[0, 50\%]$, the degradation effect (more microdefects and the existence of the old ITZ) of recycled aggregate is dominant, manifesting the reduction of microstructure density and the deterioration of mechanical properties of concrete. With the increase of the replacement rate, H increases linearly from 0.231 to 0.353. When R is in the interval $[50\%, 100\%]$, the strengthening effect (the further hydration of old cement and the roughness of aggregate boundary) of recycled aggregate is dominant, manifesting the increase of microstructure density and the improvement of mechanical properties of concrete. With the increase of the replacement rate, H decreases linearly from 0.353 to 0.197.

In Figure 19, the evolution curves of evolution factor E_v of RAC-I, RAC-II, and RAC-III are presented, respectively. E_v is related to yield damage and reflects the degree of potential mechanical properties of concrete, that is, the degree of optimization and adjustment of the stress skeleton of the material microstructure. It plays a decisive role in the evolution of material damage, and increases from 0 to 1 in the uniform damage stage. After the use of recycled aggregate to replace natural aggregate, the process of micro-crack initiation and propagation and the optimization and adjustment of stress skeleton in concrete microstructure will be changed during the stress process, which finally lead to the change of the macroscopic nonlinear mechanical behavior of concrete. For RAC-I, the increase of replacement rate of recycled aggregate significantly delays the evolution process of E_v , thus increasing the ductility of concrete. The ductility is maximized at $R = 100\%$. For RAC-II, with $R = 50\%$ as the bound, the evolution process is first delayed and then accelerated with the increase of the replacement rate. When $R = 50\%$, the ductility reaches the maximum. RAC-III is similar to RAC-II, except that the threshold replacement rate is changed to $R = 25\%$. When $E_v = 1$, this means that the effective stress skeleton of the microstructure is adjusted to the optimal, while the potential mechanical properties of the material are exerted to the limit, and the effective stress reaches the maximum. The specimen then enters the failure stage characterized by damage localization. The whole damage evolution process reflects the transformation from quantitative change to qualitative change.

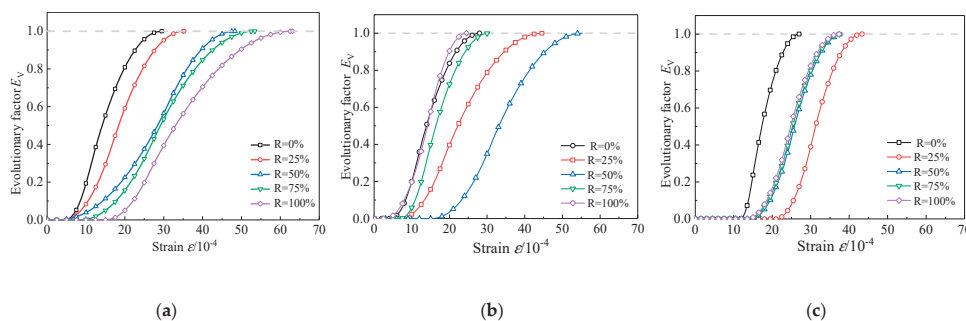


Figure 19. E_v - ϵ curves. (a) RAC-I; (b) RAC-II; (c) RAC-III.

The evolution curves of fracture damage variable D_R of RAC-I, RAC-II, and RAC-III are shown in Figure 20. For RAC-I, with the increase of the replacement rate of recycled aggregate, the ductility of the uniform damage stage of concrete is improved, which retards the process of micro-crack initiation and propagation. The fracture damage value H corresponding to the critical state first increases and then decreases with the increase of the replacement rate, and reaches a maximum value of 0.366 at $R = 50\%$. For RAC-II, with $R = 50\%$ as the boundary, the ductility of uniform damage stage increases first and then decreases, which leads to the result that the growth of micro-cracks is slowed down and then accelerated. H reaches its maximum of 0.353 at $R = 50\%$. RAC-III is similar to RAC-II, except that

the boundary value of R is changed to 25%. H reaches its maximum of 0.329 at $R = 25\%$. It can be seen that, at the critical state, the micro-crack density still remains in a relatively small range. In this experiment, the replacement of recycled aggregate can improve the ductility of concrete. For concrete with a water cement ratio of 0.66, 0.49, and 0.38, the replacement rates corresponding to the maximum ductility are 100%, 50%, and 25%, respectively.

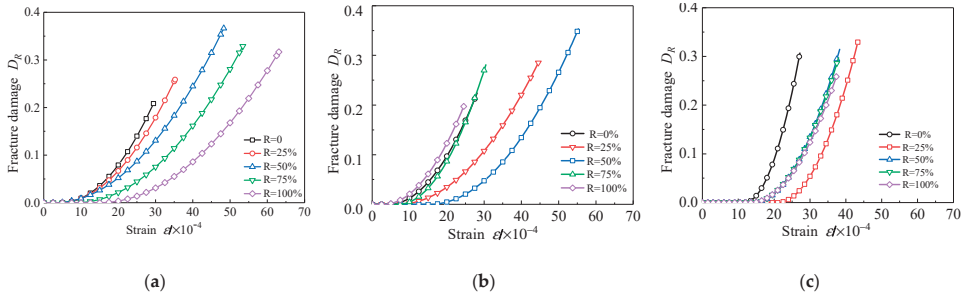


Figure 20. D_R - ϵ curves. (a) RAC-I; (b) RAC-II; (c) RAC-III.

The change curves of energy absorbing capacity S of RAC-I, RAC-II, and RAC-III with the replacement rate of recycled aggregate are shown in Figure 21, where S_p and S_{cr} are the energy absorbing capacities corresponding to the nominal peak stress state and the critical state, respectively. In previous studies, S_p was often used to characterize the energy absorption capacity of concrete before failure [37,38]. In this paper, in order to fully consider the ductility and bearing potential of the material at the uniform damage stage, S_{cr} is proposed to characterize the energy absorption capacity of concrete before local failure. It can be seen that, for RAC-I and RAC-III, S_p and S_{cr} are monotonically increasing with the increase of the replacement rate. For RAC-II, however, S_p and S_{cr} show a trend of increasing first and then decreasing, and reached the peak value at $R = 50\%$. Obviously, the replacement of recycled aggregate effectively improves the energy absorbing capacity of the material.

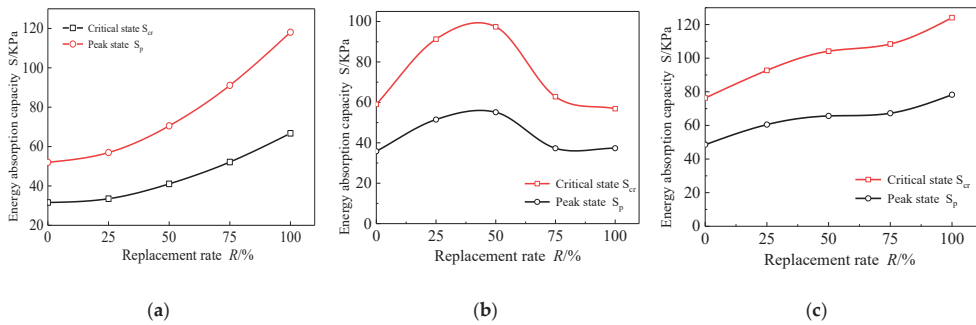


Figure 21. Energy absorption capacity. (a) RAC-I; (b) RAC-II; (c) RAC-III.

Figure 22a shows the ratios of critical state strain ϵ_{cr} to peak strain ϵ_p under different replacement rates. Their values range from 1.28 to 1.65, with an average of 1.47. Figure 22b shows the ratios of critical state stress σ_{cr} to peak stress σ_p under different replacement rates. Their values range from 0.74 to 0.91, with an average of 0.83. The water cement ratio and the replacement rate of recycled aggregate have no obvious effect on the above ratios. Xiao et al. [17] proposed to define the state in the descending section of the curve with 85% of the peak stress as the ultimate state, so as to fully consider the ductility of the softening section and to avoid too much consideration of the size effect of the local failure stage. It is found that the position of the critical state defined in this paper is almost

consistent with that of the ultimate state defined by Xiao. Meanwhile, the mechanical mechanism of this softening section is explained as part of the uniform damage phase.

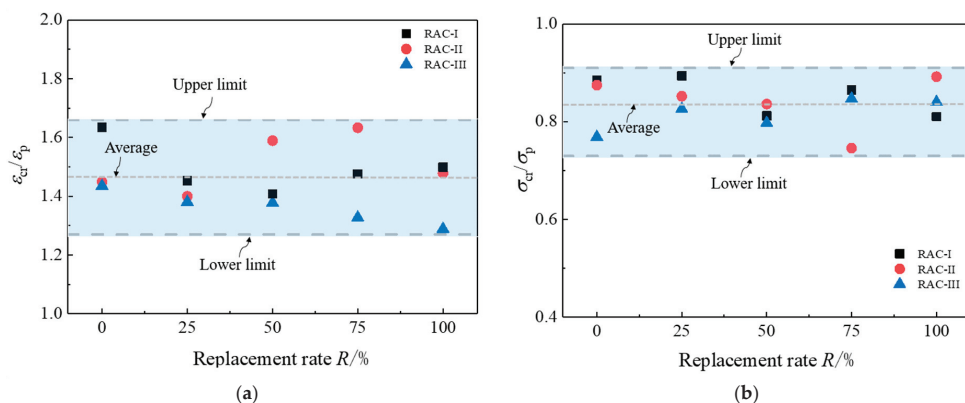


Figure 22. Comparison of the peak stress state and critical state. (a) $\varepsilon_{cr}/\varepsilon_p$ - R relation; (b) σ_{cr}/σ_p - R relation.

6. Conclusions

1. Uniaxial compression tests of recycled concrete with three levels of water cement ratio (0.66, 0.49, and 0.38) and five levels of recycled aggregate replacement rate (0, 25%, 50%, 75%, and 100%) were conducted in this paper. The test results show that the nominal stress–strain full curves have similar shape features under the quasi-static loading. The change rules of compressive strength, elastic modulus, and peak strain of three kinds of concrete with recycled aggregate replacement rate were discussed. The mechanical properties of concrete are closely related to the composition of material microstructure and the internal physical and chemical reactions, which are jointly controlled by the strengthening and degradation effects of recycled aggregate.
2. There are similar failure modes between RAC and NAC. Macro cracks begin to appear in the middle of the concrete block after the peak nominal stress, and then the obvious bulging zone is formed in this part. Continuing loading, the deformation in local bulging zone is further increased, but unloading occurs in other parts. Inclined crack will appear in the middle, which leads to the ultimate failure of the concrete block. Taking the state when local bulging happens as the critical state, the deformation of concrete is divided into the distributed damage stage and local failure stage.
3. On the basis of the statistical damage model, the mesoscopic damage evolution law of RAC under different replacement rates is discussed quantitatively. It considers two meso damage modes, fracture and yield, which represent the initiation and propagation of micro-cracks and the optimization and adjustment of the stress skeleton of microstructure, respectively. Yield damage plays a key role in the whole process of deformation and failure. The results show that, with the increase of the replacement rate, four characteristic parameters, ε_a , ε_h , ε_b , and H , have obvious regularity. The meso damage evolution law reflected by the model is in good agreement with the internal chemical physical mechanism and the macro nonlinear stress–strain behavior. Distinguishing between the peak nominal stress state and the critical state, the average values of σ_{cr}/σ_p and $\varepsilon_{cr}/\varepsilon_p$ are 0.83 and 1.47, respectively. It is suggested that the critical state be taken as the ultimate failure state of the constitutive model, which can fully consider the ductility in the distributed damage stage of material and avoid the size effect in the local failure stage.
4. The mechanical properties of recycled concrete are affected by many factors, including mix proportion, source of recycled aggregate, replacement rate of aggregate, type of additive, age, test environment, strain rate, loading mode, and so on. Owing to the limitation of the length of this paper, only two factors, the water cement ratio and replacement rate, are considered.

The influence of various factors on the macro and micro mechanical properties of recycled concrete will be further studied in combination with micro test technology.

Author Contributions: Conceptualization, W.B.; Methodology, W.B. and J.G.; Data curation, validation, and writing—original draft preparation, W.L., J.W., and C.Y.; Writing—review and editing, W.B. and W.L. All authors have read and agreed to the published version of the manuscript.

Funding: The authors would like to express gratitude for the support of National Key R & D Program China (No. 2018YFC0406803), National Natural Science Foundation of China (No. 51679092; No. 51779095).

Conflicts of Interest: The authors declared that they have no conflict of interest to this work.

References

1. Rao, A.; Jha, K.N.; Misra, S. Use of aggregates from recycled construction and demolition waste in concrete. *Resour. Conserv. Recycl.* **2007**, *50*, 71–81. [CrossRef]
2. Shi, C.J. Recycled aggregate concrete. *J. Sustain. Cem. Mater.* **2017**, *6*, 1.
3. Ding, T.; Xiao, J.; Tam, V.W.Y. A closed-loop life cycle assessment of recycled aggregate concrete utilization in China. *Waste Manag.* **2016**, *56*, 367–375. [CrossRef] [PubMed]
4. Tabsh, S.W.; Abdelfatah, A.S. Influence of recycled concrete aggregates on strength properties of concrete. *Constr. Build. Mater.* **2009**, *23*, 1163–1167. [CrossRef]
5. Shi, C.J.; Cao, Z.J.; Xie, Z.B. Research progress in the mechanical properties of recycled aggregate concrete. *Mater. Rep.* **2016**, *30*, 96–103. (In Chinese)
6. Verian, K.P. Using Recycled Concrete as Coarse Aggregate in Pavement Concrete. Master's Thesis, Purdue University, West Lafayette, IN, USA, 2012.
7. Watanabe, T.; Nishibata, S.; Hashimoto, C.; Hashimoto, C.; Ohtsu, M. Compressive failure in concrete of recycled aggregate by acoustic emission. *Constr. Build. Mater.* **2007**, *21*, 470–476. [CrossRef]
8. Verian, K.P.; Ashraf, W.; Cao, Y. Properties of recycled concrete aggregate and their influence in new concrete production. *Resour. Conserv. Recycl.* **2018**, *133*, 30–49. [CrossRef]
9. Tam, V.W.Y.; Kotrayothar, D.; Xiao, J. Long-term deformation behaviour of recycled aggregate concrete. *Constr. Build. Mater.* **2015**, *100*, 262–272. [CrossRef]
10. Domingo-Cabo, A.; Lázaro, C.; López-Gayarre, F.; Serrano-López, M.A.; Serna, P.; Castaño-Tabares, J.O. Creep and shrinkage of recycled aggregate concrete. *Constr. Build. Mater.* **2009**, *23*, 2545–2553. [CrossRef]
11. Catarina, N.; De Brito, J.; Veiga, R. Using fine recycled concrete aggregate for mortar production. *Mater. Res.* **2014**, *17*, 168–177.
12. Topcu, I.B.; Bilir, R. Experimental investigation of drying shrinkage cracking of composite mortars incorporating crushed tile fine aggregate. *Mater. Des.* **2010**, *31*, 4088–4097. [CrossRef]
13. Braga, M.; De Brito, J.; Veiga, R. Incorporation of fine concrete aggregates in mortars. *Constr. Build. Mater.* **2012**, *36*, 960–969. [CrossRef]
14. Kapoor, K.M.E.; Singh, S.P.; Singh, B. Durability of self-compacting concrete made with Recycled Concrete Aggregates and mineral admixtures. *Constr. Build. Mater.* **2016**, *128*, 67–76. [CrossRef]
15. Belén, G.F.; Fernando, M.A.; Diego, C.L.; Sindy, S.-P. Stress–strain relationship in axial compression for concrete using recycled saturated coarse aggregate. *Constr. Build. Mater.* **2011**, *25*, 2335–2342. [CrossRef]
16. Beltrán, M.G.; Barbudo, A.; Agrela, F.; Galvín, A.P.; Jiménez, J.R. Effect of cement addition on the properties of recycled concretes to reach control concretes strengths. *J. Clean. Prod.* **2014**, *79*, 124–133. [CrossRef]
17. Xiao, J.; Li, J.; Zhang, C. Mechanical properties of recycled aggregate concrete under uniaxial loading. *Cem. Concr. Res.* **2005**, *35*, 1187–1194. [CrossRef]
18. Xiao, J.; Zhang, K.; Akbarnezhad, A. Variability of stress–strain relationship for recycled aggregate concrete under uniaxial compression loading. *J. Clean. Prod.* **2018**, *181*, 753–771. [CrossRef]
19. Shi, C.; Li, Y.; Zhang, J.; Li, W.; Chong, L.; Xie, Z. Performance enhancement of recycled concrete aggregate—A review. *J. Clean. Prod.* **2016**, *112*, 466–472. [CrossRef]
20. Gupta, S.M. Strength Characteristics of concrete made with demolition waste as coarse aggregate. In Proceedings of the Structural Engineering Convention, SEC-2001, Indian Institute of Technology Roorkee, Roorkee, India, 29–31 October 2001; pp. 364–373.

21. Chen, Z.; Xu, J.; Zheng, H.; Su, Y.; Xue, J.; Li, J. Basic mechanical properties test and stress-strain constitutive relation of recycled concrete. *J. Build. Mater.* **2013**, *16*, 24–32.
22. Chen, Z.; Zhou, C.; Chen, Y.; Huang, J. Mechanical properties and stress-strain constitutive relationship of recycled pebble aggregate concrete. *J. Appli. Found. Eng. Sci.* **2014**, *4*, 763–774. (In Chinese)
23. Du, T.; Wang, W.; Liu, Z.; Lin, H.; Guo, T. The complete stress-strain curve of recycled aggregate concrete under uniaxial compression loading. *J. Wuhan Univ. Technol.-Mater. Sci. Edit.* **2010**, *25*, 862–865. [CrossRef]
24. Xiao, J.Z.; Du, J.T. Complete stress-strain curve of concrete with different recycled coarse aggregates under uniaxial compression. *J. Build. Mater.* **2008**, *11*, 111–115.
25. Poon, C.T.; Poon, C.S.; Shui, Z.; Larm, L.; Fok, H.; Kou, S.C. Influence of moisture states of natural and recycled aggregates on the slump and compressive strength of concrete. *Cem. Concr. Res.* **2004**, *34*, 31–36. [CrossRef]
26. Li, W.; Xiao, J.; Sun, Z.; Kawashima, S.; Shah, S.P. Interfacial transition zones in recycled aggregate concrete with different mixing approaches. *Constr. Build. Mater.* **2012**, *35*, 1045–1055. [CrossRef]
27. Lotfi, S.; Deja, J.; Rem, P.; Mróz, R.; van Roekel, E.; van der Stelt, H. Mechanical recycling of EOL concrete into high-grade aggregates. *Resour. Conserv. Recycl.* **2014**, *87*, 117–125. [CrossRef]
28. Kou, S.C.; Poon, C.S.; Agrela, F. Comparisons of natural and recycled aggregate concretes prepared with the addition of different mineral admixtures. *Cem. Concr. Compos.* **2011**, *33*, 788–795. [CrossRef]
29. Bai, Y.L.; Wang, H.Y.; Xia, M.F.; Ke, F.J. Statistical Mesomechanics of Solid, Linking Coupled Multiple Space and Time Scales. *Appl. Mechan. Rev.* **2005**, *58*, 286–305. [CrossRef]
30. Chen, J.Y.; Bai, W.F.; Fan, S.L.; Lin, G. Statistical damage model for quasi-brittle materials under uniaxial tension. *J. Cent. South. Univ. Technol.* **2009**, *16*, 669–676. [CrossRef]
31. Bai, W.F.; Chen, J.Y.; Fan, S.L.; Lin, G. Statistical damage constitutive model for concrete materials under uniaxial compression. *J. Harbin Univ. Technol. (English edition)* **2010**, *17*, 338–344.
32. Bai, W.F.; Zhang, S.J.; Guan, J.F.; Chen, J.-Y. Study on orthotropic statistical damage constitutive model for concrete. *J. Hydraul. Eng.* **2014**, *45*, 607–618. (In Chinese)
33. Bai, W.F. Study on Damage Mechanism of Concrete and Mechanical Property of Saturated Concrete. Ph.D. Thesis, Dalian University of Technology, Dalian, China, 2008. (In Chinese)
34. Bai, W.F.; Liu, L.A.; Guan, J.F.; Yao, X.-H. Study on constitutive model of sulfate attack concrete based on statistical damage theory. *Eng. Mech.* **2019**, *36*, 69–80. (In Chinese)
35. Markeset, G.; Hillerborg, A. Softening of concrete in compression—Localization and size effects. *Cem. Concr. Res.* **1995**, *25*, 702–708. [CrossRef]
36. Van Geel, E. Concrete Behaviour in Multiaxial Compression: Experimental Research. Ph.D. Thesis, Eindhoven University, Eindhoven, The Netherlands, 1998.
37. Rostami, R.; Zarrebini, M.; Sanginabadi, K.; Mostofinejad, D.; Abtahi, S.M.; Fashandi, H. The effect of specific surface area of macro fibers on energy absorption capacity of concrete. *J. Text. Instit.* **2018**, *110*, 707–714. [CrossRef]
38. Saxena, R.; Siddique, S.; Gupta, T.; Sharma, R.K.; Chaudhary, S. Impact resistance and energy absorption capacity of concrete containing plastic waste. *Constr. Build. Mater.* **2018**, *176*, 415–421. [CrossRef]
39. GB/T 25177-2010. *Recycled Coarse Aggregate for Concrete*; China Architecture and Building Press: Beijing, China, 2010. (In Chinese)
40. JGJ 55-2011. *Specification for Mix Design of Ordinary Concrete*; China Architecture and Building Press: Beijing, China, 2011. (In Chinese)
41. SL 352-2006. *Test Code for Hydraulic Concrete*; China Water Resources and Hydropower Press: Beijing, China, 2006. (In Chinese)
42. Omary, S.; Ghorbel, E.; Wardeh, G.; Nguyen, M.D. Mix Design and Recycled Aggregates Effects on the Concrete's Properties. *Int. J. Civ. Eng.* **2018**, *16*, 973–992. [CrossRef]
43. Lei, B.; Li, Z.X.; Zou, J.; Xiong, J. Durability test of recycled concrete under the coupling action of load and corrosion freeze-thaw. *Trans. Chin. Soc. Agric. Eng. (Trans. CSAE)* **2018**, *34*, 169–174. (In Chinese)
44. Kurad, R.; Silvestre, J.D.; de Brito, J.; Ahmed, H. Effect of incorporation of high volume of recycled concrete aggregates and fly ash on the strength and global warming potential of concrete. *J. Clean. Prod.* **2017**, *166*, 485–502. [CrossRef]
45. Walraven, J.C. Aggregate interlock: A theoretical and experimental investigation. Ph.D. Thesis, College of Civil Engineering of Delft University of Technology, Delft, The Netherlands, 1980.

46. Walraven, J.C. Fundamental analysis of aggregate interlock. *J. Struct. Div. ASCE* **1981**, *107*, 2245.
47. Gesoglu, M.; Güneyisi, E.; Öz, H.O.; Taha, I.; Yasemin, M.T. Failure characteristics of self-compacting concretes made with recycled aggregates. *Constr. Build. Mater.* **2015**, *98*, 334–344. [CrossRef]



© 2020 by the authors. Licensee MDPI, Basel, Switzerland. This article is an open access article distributed under the terms and conditions of the Creative Commons Attribution (CC BY) license (<http://creativecommons.org/licenses/by/4.0/>).

Article

Compressive Strength, Chloride Ion Penetrability, and Carbonation Characteristic of Concrete with Mixed Slag Aggregate

Se-Jin Choi ^{1,*}, Young-Uk Kim ², Tae-Gue Oh ¹ and Bong-Suk Cho ³

¹ Department of Architectural Engineering, Wonkwang University, 460 Iksan-daero, Iksan 54538, Korea; alkjd3@naver.com

² Department of Architectural Engineering, Yonsei University, 50 Yonsei-ro Seodaemun-gu, Seoul 03722, Korea; yuk92@hanmail.net

³ Environment and Resources Research Group, Research Institute of Industrial Science and Technology, Pohang 37673, Korea; chos8@hanmail.net

* Correspondence: csj2378@wku.ac.kr; Tel.: +82-63-850-6789

Received: 2 February 2020; Accepted: 17 February 2020; Published: 20 February 2020

Abstract: The shortage of natural aggregates has recently emerged as a serious problem owing to the tremendous growth of the concrete industry. Consequently, the social interest in identifying aggregate materials as alternatives to natural aggregates has increased. In South Korea's growing steel industry, a large amount of steel slag is generated and discarded every year, thereby causing environmental pollution. In previous studies, steel slag, such as blast furnace slag (BFS), has been used as substitutes for concrete aggregates; however, few studies have been conducted on concrete containing both BFS and Ferronickel slag (FNS) as the fine aggregate. In this study, the compressive strength, chloride ion penetrability, and carbonation characteristic of concrete with both FNS and BFS were investigated. The mixed slag fine aggregate (MSFA) was used to replace 0, 25%, 50%, 75%, and 100% of the natural fine aggregate volume. From the test results, the highest compressive strength after 56 days was observed for the B/F100 sample. The 56 days chloride ion penetrability of the B/F75, and B/F100 samples with the MSFA contents of 75% and 100% were low level, approximately 34%, and 54% lower than that of the plain sample, respectively. In addition, the carbonation depth of the samples decreased with the increase in replacement ratio of MSFA.

Keywords: aggregate; blast furnace slag; ferronickel slag; compressive strength; chloride ion penetrability; carbonation

1. Introduction

Owing to the immense growth of the global concrete industry, the shortage of natural aggregates has emerged as a serious problem. In Korea, the lack of aggregates has often led to construction problems. Therefore, a considerable amount of social and research interest has been focused on finding alternative aggregate materials to replace natural aggregates [1–7]. Various types of steel slag can be considered as alternatives to aggregates for concrete. Ferronickel slag (FNS) is an industrial byproduct of the ferronickel production process. It is obtained after nickel ore and bituminous coal used as raw materials in the ferronickel smelting process are melted at a high temperature and separated from ferronickel [2]. The annual amount of FNS produced in South Korea is over 2 million tons. Most are discarded and cause serious environmental pollution. Generally, the FNS is used as a substitute material for foundry sand, abrasive, and serpentine [2]. In addition, studies were carried out on the use of FNS as fine aggregate for concrete [5–7].

Saha et al. [5] studied the strength and durability of cement mortar using FNS as the replacement of natural sand. The maximum compressive strength of cement mortar was obtained by replacing 50%

sand with FNS. In addition, X-ray diffraction test results showed that the pozzolanic reaction of fly ash helped to reduce the strength loss.

Choi et al. [6] investigated the alkali-silica reactivity of cementitious materials with FNS fine aggregate produced under different cooling conditions. The alkali-silica reactivity of mortar using FNS fine aggregate was dependent on the cooling speed and particle size of FNS.

Lee et al. [7] investigated the mechanical properties and resistances to freezing and thawing of concrete using an air-cooled ferronickel slag (ACFNS) fine aggregate. The compressive strength and static modulus of elasticity of the concrete with ACFNS fine-aggregate increased with increasing the replacement ratio of ACFNS.

Blast furnace slag (BFS) is also another steel industry byproduct that is obtained from blast furnaces used in the manufacturing of pig iron. The annual amount of produced BFS in Korea is approximately 15 million tons. The BFS has been extensively used as a successful replacement material for Portland cement in concrete materials to improve the durability and in the production of high-strength concrete, with environmental and economic benefits, such as resource conservation, CO₂ reduction, and energy savings [8–11]. In addition, BFS also can be used as the aggregate for cement mortar of concrete. In previous studies [12,13], BFS was used as a substitute material for concrete aggregate; however, few studies have been conducted on concrete with slag aggregate containing both FNS and BFS as the fine aggregate.

In this study, the slump, air content, compressive strength, resistance to chloride ions, and carbonation characteristic of concrete with both FNS and BFS as the fine aggregate were investigated to effectively utilize the mixed slag fine aggregate (MSFA) as a substitute material for the natural aggregate in the concrete industry.

2. Materials and Methods

2.1. Materials

An ASTM type I ordinary Portland cement manufactured by Asia Cement Co. (Seoul, Korea), BFS powder obtained from Daehan Slag Co., Ltd. (Gwangyang, Korea), and fly ash obtained from the Honam power plant in Korea were used as cementitious materials in this study. In addition, a crushed coarse aggregate (Granite, G_{max} 25 mm) with a density of 2.65 and fineness modulus of 6.49 was used.

Table 1 summarizes the chemical compositions of the cement, BFS powder, and fly ash used in the experiment. Natural, BFS, and FNS fine aggregates were used in the experiment. Natural sand (NS) was used as the natural fine aggregate with a maximum size of 5 mm and fineness modulus of 2.89. The BFS sand (BS) and FNS sand (FS) used as the slag fine aggregates were obtained from POSCO, Korea.

Table 1. Chemical composition and strength of cementitious materials.

Type	SiO ₂	Al ₂ O ₃	Fe ₂ O ₃	CaO	MgO	K ₂ O	Comp. str. (MPa)	
							7 day	28 day
Cement (C)	17.43	6.50	3.57	64.40	2.55	1.17	42.7	56.5
Blast furnace slag (BFS) powder	30.61	13.98	0.32	40.71	6.43	0.60	-	-
Fly ash (FA)	64.88	20.56	6.06	2.58	0.80	1.45	-	-

Figure 1 shows the used fine aggregate samples, while Table 2 summarizes their physical properties. Figure 2 shows the particle size distributions of the NS, BS, FS, and MSFA (B/F) with a BFS:FNS ratio of 5:5 by volume. The particle size distribution of each aggregate was compared with the standard proposed by KS F 2527. The fineness modulus of the BS was smaller than that of the NS, while that of the FS was higher than that of the NS. The fineness modulus of B/F was 2.94, similar to that of the NS.



Figure 1. Fine aggregate samples. (a) Natural sand (NS); (b) BFS sand (BS); (c) FNS sand (FS).

Table 2. Physical properties of fine aggregates.

Type	FM	Density (g/cm ³)	Water Absorption (%)	Unit Weight (kg/L)	Ratio of Absolute Volume (%)
Natural sand (NS)	2.89	2.63	1.1	1.645	62.56
BFS sand (BS)	2.37	2.81	2.1	1.737	61.80
FNS sand (FS)	3.51	3.04	0.6	1.871	61.56

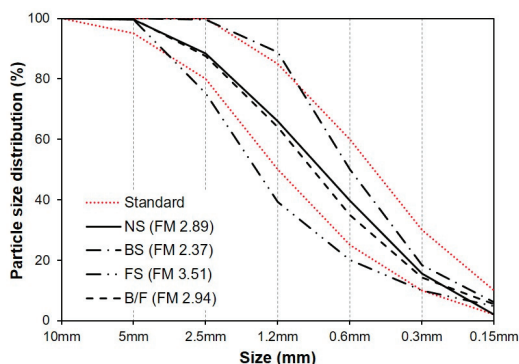


Figure 2. Particle size distribution of fine aggregate.

2.2. Mixing Proportions and Specimen Preparation

In this study, the MSFA with the BFS:FNS mixture ratio of 5:5 was used to replace 0 (plain), 25%, 50%, 75%, and 100% of the volume of the NS. A constant water-to-binder ratio of 0.518 was used. In all mixtures, the BFS powder and fly ash were used to replace 20% and 10% (weight) of the cement, respectively. The mixing proportions of the concrete samples are summarized in Table 3. In addition, a water-reducing agent (WRA; S Co., Seoul, Korea) was used to control the fluidities of all mixtures. The components of the concrete samples were mixed in a mechanical mixer. Cylindrical molds (Ø100 × 200 mm) were fabricated for the compressive strength test. After 24 h, the specimens were removed from their molds and cured at 20 °C in a water tank.

Table 3. Mix proportion of concrete.

Mix	W/B (%)	S/a (%)	Unit Weight (kg/m ³)							WRA (B*%)	
			Water	Cement	BFS Powder	Fly Ash	NS	BS	FS		Gravel
Plain			176	238	68	34	812	-	-	916	0.9
B/F25			176	238	68	34	609	109	117	916	0.7
B/F50	51.8	47	176	238	68	34	406	219	234	916	0.5
B/F75			176	238	68	34	203	328	351	916	0.3
B/F100			176	238	68	34	-	437	469	916	0.2

B*: Binder.

The slump and air content tests of the concrete samples were carried out in accordance with Korean Standards (KS) F 2402 [14] and KS F 2421 [15], respectively. The compressive strength test was carried out after 7, 14, 28, and 56 days in accordance with KS F 2405 [16]. The presented strength test values are the average values of three samples.

Chloride ion penetration tests were carried out after 7, 14, 28, and 56 days, according to ASTM 1202 C [17]. Specimens having dimensions of $\varnothing 100 \times 50$ mm, obtained by cutting the $\varnothing 100 \times 200$ mm cylindrical specimens, were used in the test. The specimen and equipment used in the chloride ion penetration test are shown in Figure 3.

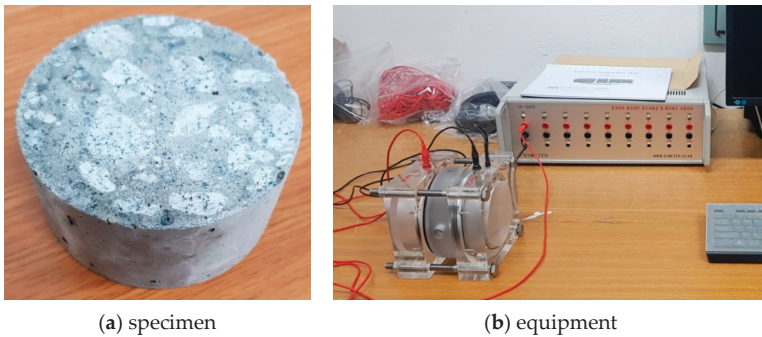


Figure 3. Specimen and equipment for chloride ion penetration test.

Accelerated-carbonation test (Figure 4) of the concrete samples ($\varnothing 100 \times 200$ mm) was carried out during 7, 28, and 56 days, according to KS F 2584 [18], by using an accelerated-carbonation chamber at a constant temperature of 20 ± 2 °C, constant humidity of $60 \pm 5\%$, and constant CO_2 concentration of $5 \pm 0.2\%$. During the testing period, the samples were split into two halves and the carbonation depth was measured by spraying an approximately 1% phenolphthalein solution on the broken surface of the sample, after the dust was removed.

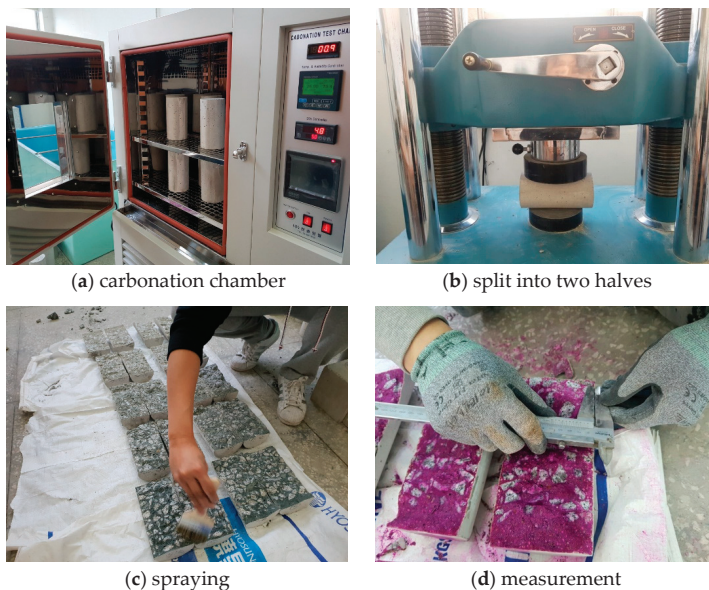


Figure 4. Accelerated carbonation test.

3. Results and Discussion

3.1. Slump and Air Content

Figure 5 shows the slumps and WRA dosages of the samples with the MSFAs. The slumps of all mixtures were similar, in the range of 200 to 210 mm, regardless of the replacement ratio of MSFA. In addition, the dosage of WRA used to control the fluidity of the plain sample with the NS was 0.9% of the binder weight. The WRA dosage decreased with the increase in replacement ratio of MSFA. The WRA dosage of the B/F100 sample (only with the MSFA) was 0.2% of the binder weight. The tendency that the fluidity of the mixture with the BFS fine aggregate is better than that of the mixture with the NS owing to the vitreous texture of the BFS particle is similar to those in previous reports [13,19].

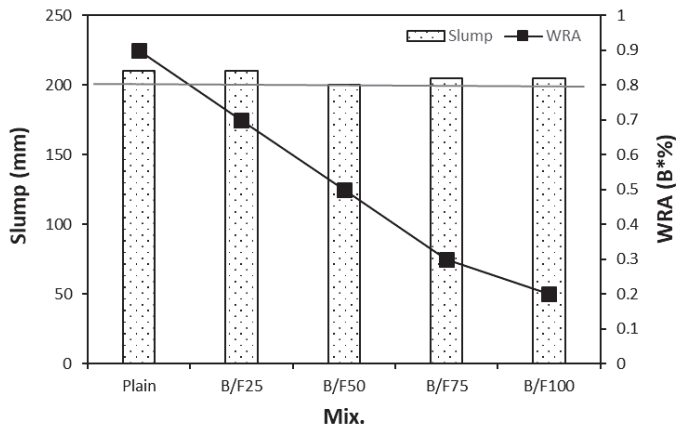


Figure 5. Slump and WRA dosage.

Figure 6 shows the variation in air content of the concrete sample with both BFS and FNS as the fine aggregate with the replacement ratio of MSFA. The air contents of the concrete samples were similar (2.3% to 2.6%), regardless of the replacement ratio of MSFA.

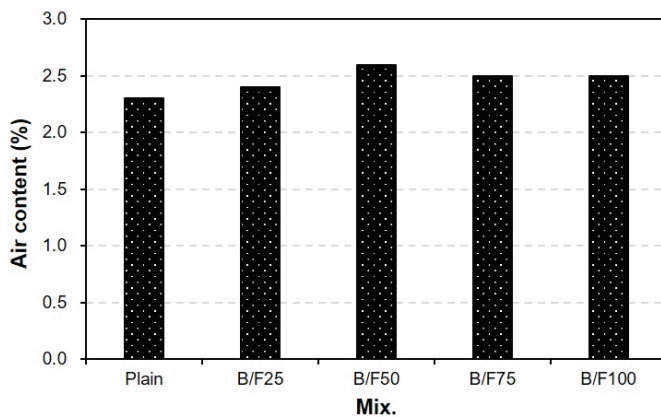


Figure 6. Air content.

3.2. Compressive Strength

Figure 7 shows the variation in compressive strength of the concrete sample with both BFS and FNS as the fine aggregate with the replacement ratio of MSFA. After seven days, the compressive

strength of the plain sample without MSFA was approximately 23.1 MPa, while those of the samples with the MSFAs were in the range of 21.2 to 23.5 MPa. After 14 days of curing, the compressive strengths of all samples, except the B/F75 sample, were similar (approximately 29 MPa). After 28 days of curing, the compressive strength of the plain sample was approximately 33.5 MPa, while those of the samples with the MSFAs were in the range of 32.2 to 34.3 MPa. The compressive strength of the sample with the MSFA increased with the replacement ratio of MSFA. After 56 days, the compressive strengths of all samples were increased; those of the samples with the MSFAs were in the range of 36.6 to 38.8 MPa. The highest compressive strength (approximately 38.8 MPa) was obtained for the B/F100 sample, which contained only the MSFA. The increase in compressive strength could be explained as the particle size distribution of the MSFA was similar to that of the NS and the formation of a secondary calcium silicate hydrated (CSH) gel was initiated [20].

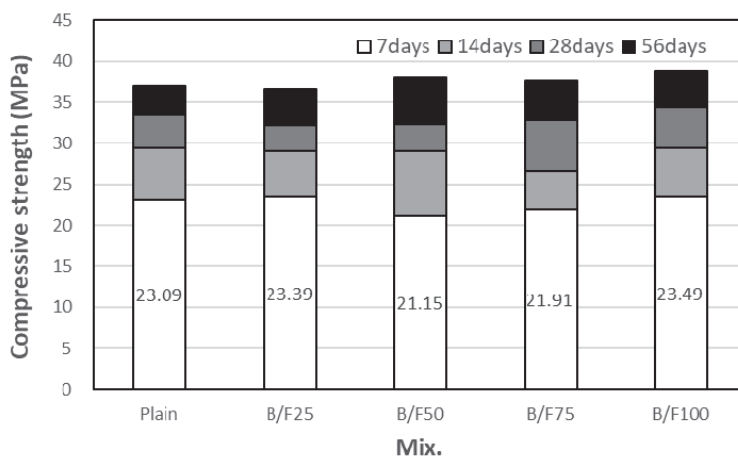


Figure 7. Compressive strength.

3.3. Chloride Ion Penetrability

Figure 8 shows the variation in chloride ion penetrability of the sample with both BFS and FNS as the fine aggregate. The total charge passed through the sample during the considered period was calculated according to ASTM C 1202. After seven days, the charge passed through the plain sample was approximately 9273 C. The charge passed through the B/F100 sample with 100% MSFA was the smallest, approximately 37% smaller than that of the plain sample. After 14 days of curing, the largest passed charge (approximately 8083 C) was observed for the plain sample, which contained only the NS. The charges passed through all samples with the MSFAs were smaller than that through the plain sample. The charge passed through the B/F100 sample was the smallest (4106 C), approximately 50% smaller than that through the plain sample (8084 C). After 28 days of curing, the charge passed through the sample decreased with the increase in replacement ratio of MSFA (3993 C (plain) to 2041 C (B/F100)). The chloride ion penetrabilities of all samples were moderate level (2000–4000 C; ASTM C 1202 [17]). After 56 days, the charge passed through the sample decreased with the increase in replacement ratio of MSFA. The chloride ion penetrabilities of B/F50, B/F75, and B/F100 with MSFA contents of 50%, 75%, and 100% were low level (1000–2000 C; ASTM C 1202), approximately 17%, 34%, and 54% lower than that of the plain sample, respectively. The resistances to penetration of chloride ions of the samples with the MSFAs were better than that of the plain sample. The tendency that the concrete with BFS has a good resistance to chloride ions is similar to those observed in previous studies [21,22].

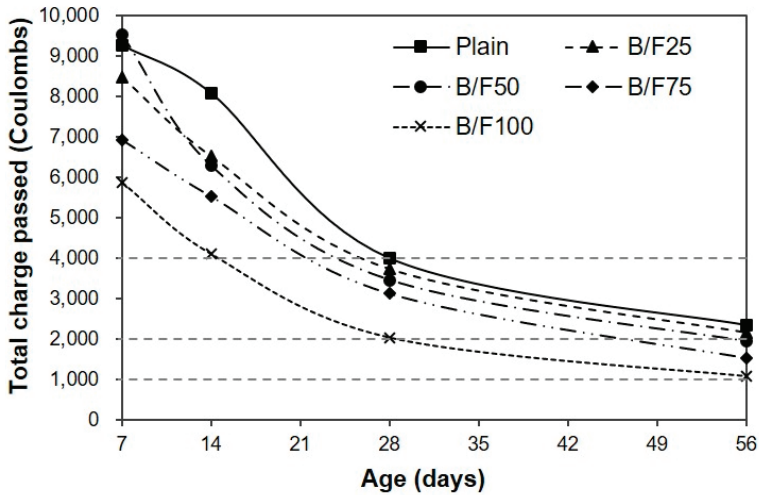


Figure 8. Chloride ion penetrability.

Figure 9 shows the relation between the compressive strength and chloride ion penetrability for the samples with different replacement ratios of MSFA. The chloride ion penetrability decreased with the increase in compressive strength. In addition, the chloride ion penetrabilities of the samples with the MSFAs were lower than that of the sample with the NS at the same compressive strength.

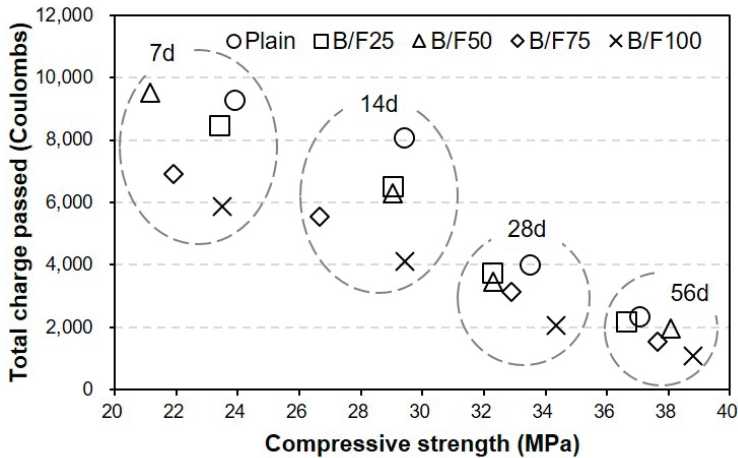


Figure 9. Relationship between compressive strength and chloride ion penetrability.

3.4. Carbonation Depth

Figure 10 shows the variation in carbonation depth of the sample with both BFS and FNS as the fine aggregate. A higher replacement ratio of MSFA led to a smaller carbonation depth. After seven days of treatment in the accelerated carbonation chamber, the carbonation depth of the plain sample was approximately 1.18 mm, while those of the samples with the MSFAs were approximately 45% to 69% (0.53 to 0.82 mm) of that of the plain sample. After 28 days, the carbonation depths of the plain, B/F25, B/F50, B/F75, and B/F100 samples were approximately 1.16, 0.94, 0.83, 0.76, and 0.68 mm, respectively. The carbonation depth of B/F100 was approximately 41% smaller than that of the plain sample. After 56 days of accelerated carbonation testing, the carbonation depths of all samples were increased. The largest carbonation depth (1.26 mm) was observed for the plain sample. The carbonation

depth decreased with the increase in replacement ratio of MSFA. The carbonation depth of B/F100 was the smallest (0.79 mm). The tendency that the resistance to carbonation of the concrete with the steel slag as the aggregate is better than that of the concrete with the natural aggregate is similar to that in a previous report [23]. This shows that the use of the MSFA in the mortar or concrete can be effective for the improvement in carbonation resistance.

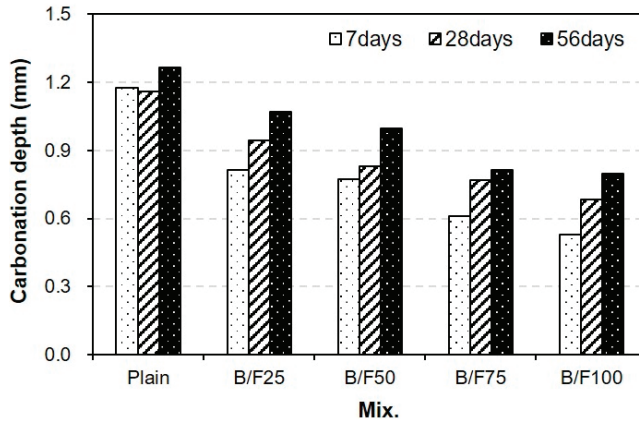


Figure 10. Carbonation depth.

Figure 11 shows the relation between the compressive strength and carbonation depth for the concrete samples with different replacement ratios of MSFA. With the increase in accelerated carbonation testing period, the carbonation depth increase was accompanied by an increase in compressive strength. In addition, the carbonation depths of the samples with the MSFAs were smaller than that of the plain sample at the same compressive strength.

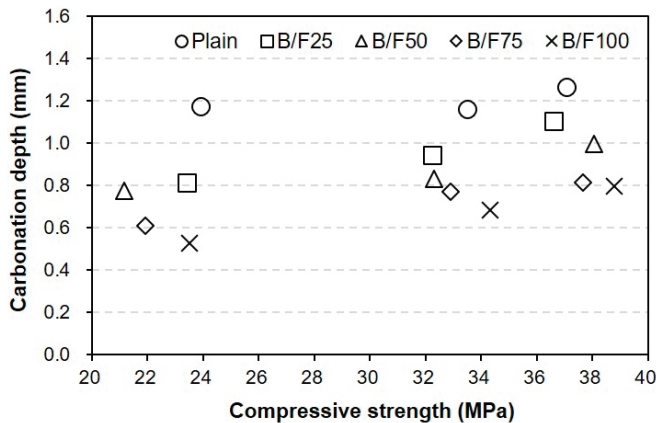


Figure 11. Relationship between compressive strength and carbonation depth.

4. Conclusions

The conclusions of this study can be summarized as follows.

- (1) The slumps of all mixtures were similar (200 to 210 mm), regardless of the replacement ratio of MSFA. The WRA dosage decreased with the increase in replacement ratio of MSFA.
- (2) The compressive strength of the plain sample was approximately 23.9 MPa, while those of the samples with the MSFAs were in the range of 21.2 to 23.5 MPa after seven days. After 56 days,

the highest compressive strength (approximately 38.8 MPa) was observed for the B/F100 sample. The increase in compressive strength could be explained as the particle size distribution of the MSFA was similar to that of the NS and the formation of the secondary CSH gel was initiated.

- (3) After seven days, the charge passed through B/F100 was the smallest, approximately 37% smaller than that through the plain sample. After 28 days of curing, the chloride ion penetrabilities of all samples were moderate level according to ASTM C 1202. After 56 days, the chloride ion penetrabilities of B/F50, B/F75, and B/F100 were low level, approximately 17%, 34%, and 54% lower than that of the plain sample, respectively.
- (4) The resistances to penetration of chloride ions of the samples with the MSFAs were better than that of the plain sample. The tendency that the concrete with BFS has a good resistance to chloride ions is similar to those in previous reports.
- (5) The chloride ion penetrability decreased with the increase in compressive strength. In addition, the chloride ion penetrabilities of the samples with the MSFAs were lower than that of the plain sample at the same compressive strength.
- (6) The higher replacement ratio of MSFA led to a smaller carbonation depth. The carbonation depth (0.79 mm) of B/F100 was the smallest after 56 days. The results show that the use of the MSFA in the mortar or concrete can be effective for the improvement in carbonation resistance.

However, further studies are needed to establish the strength development mechanism and respective relationships between the strength properties of mortar containing various slag aggregate and water-binder ratio, density, alkali content, and durability, etc.

Author Contributions: S.-J.C. conducted all of the experimental studies, analyzed the test data. Y.-U.K. and T.-G.O. conducted some experiments and wrote the manuscript. B.-S.C. advised the experimental work, and revised the manuscript. All authors have read and agreed to the published version of the manuscript.

Funding: This research was supported by Basic Science Research Program through the National Research Foundation of Korea (NRF) funded by the Ministry of Education (NRF-2019R111A3A01049510).

Acknowledgments: The authors gratefully acknowledge the National Research Foundation of Korea and Ministry of Education for the financial support of this work. The authors would like to thank Editage for English language editing.

Conflicts of Interest: The authors declare no conflict of interest.

References

1. Khatib, J.M. Properties of concrete incorporating fine recycled aggregate. *Cem. Concr. Res.* **2005**, *35*, 763–769. [CrossRef]
2. Cho, B.S.; Kim, Y.U.; Kim, D.B.; Choi, S.J. Effect of ferronickel slag powder on microhydration heat, flow, compressive strength, and drying shrinkage of mortar. *Adv. Civ. Eng.* **2018**, *2018*, 1–7. [CrossRef]
3. Maslehuddin, M.; Sharif, A.M.; Shameem, M.; Ibrahim, M.; Barry, M.S. Comparison of properties of steel slag and crushed limestone aggregate concretes. *Constr. Build. Mater.* **2003**, *17*, 105–112. [CrossRef]
4. Arellano Aguilar, R.; Burciaga Díaz, O.; Escalante García, J.I. Lightweight concretes of activated metakaolin-fly ash binders, with blast furnace slag aggregates. *Constr. Build. Mater.* **2010**, *24*, 1166–1175. [CrossRef]
5. Saha, A.K.; Sarker, P.K. Durability of Mortar Incorporating Ferronickel Slag Aggregate and Supplementary Cementitious Materials Subjected to Wet-Dry Cycles. *Int. J. Concr. Struct. Mater.* **2018**, *12*, 29. [CrossRef]
6. Choi, Y.C.; Choi, S. Alkali-silica reactivity of cementitious materials using ferro-nickel slag fine aggregates produced in different cooling conditions. *Constr. Build. Mater.* **2015**, *99*, 279–287. [CrossRef]
7. Lee, H.G.; Bae, S.H.; Lee, H.J.; Choi, Y.W.; Cho, B.S. Mechanical Properties and Resistance to Freezing and Thawing of Concrete Using Air-Cooled Ferronickel Slag Fine Aggregate. *J. Rec. Const. Resour.* **2018**, *6*, 319–323.
8. Ulubeyli, G.C.; Artir, R. Sustainability for Blast Furnace Slag: Use of Some Construction Wastes. *Procedia Soc. Behav. Sci.* **2015**, *195*, 2191–2198. [CrossRef]
9. Li, G.; Zhao, X. Properties of concrete incorporating fly ash and ground granulated blast-furnace slag. *Cem. Concr. Compos.* **2003**, *25*, 293–299. [CrossRef]

10. Sanjuán, M.Á.; Estévez, E.; Argiz, C.; del Barrio, D. Effect of curing time on granulated blast-furnace slag cement mortars carbonation. *Cem. Concr. Compos.* **2018**, *90*, 257–265. [CrossRef]
11. Yazici, H. The effect of curing conditions on compressive strength of ultra high strength concrete with high volume mineral admixtures. *Build. Environ.* **2007**, *42*, 2083–2089. [CrossRef]
12. Nataraja, M.C.; Dileep Kumar, P.G.; Manu, A.S.; Sanjay, M.C. Use of granulated blast furnace slag as fine aggregate in cement mortar. *Int. J. Struct. Civ. Eng. Res.* **2013**, *2*, 1–10.
13. Patra, R.K.; Mukharjee, B.B. Influence of incorporation of granulated blast furnace slag as replacement of fine aggregate on properties of concrete. *J. Clean. Prod.* **2017**, *165*, 468–476. [CrossRef]
14. KS F 2402. *Standard Test Method for Concrete Slump*; Korea Standards Association: Seoul, Korea, 2017.
15. KS F 2421. *Standard Test Method for Air Content of Fresh Concrete by the Pressure Method (Air Receiver Method)*; Korea Standards Association: Seoul, Korea, 2016.
16. KS F 2405. *Standard Test Method for Compressive Strength of Concrete*; Korea Standards Association: Seoul, Korea, 2017.
17. ASTM C1202. *Electrical Indication of Concrete's Ability to Resist Chloride Ion Penetration*; ASTM International: Philadelphia, PA, USA, 2000.
18. KS L 2584. *Standard Test Method for Accelerated Carbonation of Concrete*; Korea Standards Association: Seoul, Korea, 2015.
19. Valcuende, M.; Benito, F.; Parra, C.; Miñano, I. Shrinkage of self-compacting concrete made with blast furnace slag as fine aggregate. *Constr. Build. Mater.* **2015**, *76*, 1–9. [CrossRef]
20. Subathra Devi, V.; Gnanavel, B.K. Properties of concrete manufactured using steel slag. *Procedia Eng.* **2014**, *97*, 95–104. [CrossRef]
21. Leng, F.; Feng, N.; Lu, X. Experimental study on the properties of resistance to diffusion of chloride ions of fly ash and blast furnace slag concrete. *Cem. Concr. Res.* **2000**, *30*, 989–992. [CrossRef]
22. Yeau, K.Y.; Kim, E.K. An experimental study on corrosion resistance of concrete with ground granulate blast-furnace slag. *Cem. Concr. Res.* **2005**, *35*, 1391–1399. [CrossRef]
23. Mo, L.; Zhang, F.; Deng, M.; Jin, F.; Al-Tabbaa, A.; Wang, A. Accelerated carbonation and performance of concrete made with steel slag as binding materials and aggregates. *Cem. Concr. Compos.* **2017**, *83*, 138–145. [CrossRef]



© 2020 by the authors. Licensee MDPI, Basel, Switzerland. This article is an open access article distributed under the terms and conditions of the Creative Commons Attribution (CC BY) license (<http://creativecommons.org/licenses/by/4.0/>).

Article

Properties and Structure of Concretes Doped with Production Waste of Thermoplastic Elastomers from the Production of Car Floor Mats

Malgorzata Ulewicz * and Alina Pietrzak

Faculty of Civil Engineering, Czestochowa University of Technology, Dabrowskiego 69 Street, PL 42-201 Czestochowa, Poland; alina.pietrzak@pcz.pl

* Correspondence: malgorzata.ulewicz@pcz.pl; Tel.: +48-343250935

Abstract: This article presents physical and mechanical properties of concrete composites that include waste thermoplastic elastomer (TPE) from the production process of car floor mats. Waste elastomer (2–8 mm fraction) was used as a substitute for fine aggregate in quantities of 2.5, 5.0, 7.5, and 10% of the cement weight. For all series of concrete, the following tests were carried out: compression strength, bending tensile strength, splitting tensile strength, absorbability, density, resistance to water penetration under pressure, frost resistance, and abrasion resistance, according to applicable standards. Moreover, SEM/EDS analysis was carried out on the surface microstructure of synthesized concrete composites. It was proven that the use of production waste from the production process of car floor mats in the quantity of 2.5% does not influence the change of the concrete microstructure and it does not result in the decrease of the mechanical parameters of concrete modified with waste. All concrete modified with the addition of waste meet standards requirements after carrying out 15 cycles of freezing and thawing, and the average decrease in compression strength did not exceed 20%. Adding waste in the quantity of 2.5% allows for limiting the use of aggregate by about 5%, which is beneficial for the natural environment.

Keywords: waste thermoplastic elastomer; concrete; compression strength; frost resistance; microstructure

Citation: Ulewicz, M.; Pietrzak, A. Properties and Structure of Concretes Doped with Production Waste of Thermoplastic Elastomers from the Production of Car Floor Mats. *Materials* **2021**, *14*, 872. <https://doi.org/10.3390/ma14040872>

Academic Editor:
Francesco Colangelo

Received: 12 January 2021
Accepted: 5 February 2021
Published: 11 February 2021

Publisher's Note: MDPI stays neutral with regard to jurisdictional claims in published maps and institutional affiliations.



Copyright: © 2021 by the authors. Licensee MDPI, Basel, Switzerland. This article is an open access article distributed under the terms and conditions of the Creative Commons Attribution (CC BY) license (<https://creativecommons.org/licenses/by/4.0/>).

1. Introduction

Concrete, which is a composite material with a cement matrix, is commonly used in the construction industry. A systematic increase in the quantity of manufactured concrete causes the use of large quantities or natural aggregates, and the excessive use of natural resources results in environment degradation. Therefore, in recent years, many research centers have carried out tests concerning the possibility of using various waste materials, such as domestic and industrial waste [1], bottom ash [2], sanitary and utilitarian ceramic [3,4], cathode ray tube glass (CRT) [5], recycled glass sand aggregates [6], and slag aggregate [7]. Amongst various waste materials, there is a large focus on polymer waste [8–11]. According to the literature, one of the most tested materials in terms of waste use for the said purpose is polyethylene terephthalate (PET) used as aggregate [12–16] or fiber [17–19]. Recyclate obtained from PET waste has been used in concrete as the substitute for aggregate or in the form of fiber as reinforcement. The manner of PET recyclate preparation and its form have a large impact on the parameters of manufactured concrete. Recyclate with a smooth, spherical surface has less impact on the concrete workability than recyclate with an uneven form. As proven by most authors, adding waste PET to concrete results in decreasing compression strength, tensile strength, and bending strength of concrete, as well as the modulus of elasticity, irrespective of tested consistency and water–cement ratio.

Moreover, tests concerning the use of waste recyclate from polyethylene and polypropylene [20–23] as the substitute for aggregate or as the reinforcement of concrete have also

been carried out. Recycling mixtures of this material are characterized with various quality and mechanical properties [24,25]. Due to the fact that the properties of fibers from pure synthetic material are significantly different than the properties of fibers obtained from recycling material, fibers made of pure polypropylene or polyethylene are more often used in tests [26–28]. Concrete with polypropylene fibers in the quantity up to 1% present higher compression strength and splitting or bending strength than concrete that does not contain such material (standard concrete).

An increase in the quantity of synthetic fibers above such level results in the worsening of the mechanical properties of modified concrete. There is also much information on the use of waste polystyrene [29–32] and rubber [33–43] to manufacture concrete. Along with the increase in the quantity of rubber waste used as a substitute for sand, concrete mixtures are characterized with lower [36–41] or higher [34] workability. Concrete containing rubber recycle presents lower values of mechanical parameters than concrete manufactured without the addition of waste [35,36]. On the other hand, the use of rubber recycle together with waste glass powder or silica sand has a positive impact on the mechanical properties of manufactured concrete [44,45]. The mechanical properties of concretes can be improved, according to literature reports, by introducing polymer, sisal, or steel fibers into the concrete [46–48]. The compressive, tensile, and bending strength of concrete composites increases in comparison to normal concretes with an increase in the quantity of fibers amount.

Currently, a large quantity of polymer waste materials is available on the market, which are of no practical use. However, it is worth testing them to possibly use them in the production process of composite materials. This group covers waste thermoplastic elastomer from the production process of car floor mats. According to the waste catalogue [49], waste from the production of car floor mats is classified as waste group 12 01 05. Car floor mats are usually made of needle velour (polypropylene or polyamide) finished with rubber crumbs (e.g., polybutadiene or polyolefin). Moreover, car floor mats are also manufactured on the basis of polyethylene terephthalate and polyethylene–polypropylene copolymer. What is more, this material contains modifying additives, such as flame retardant agent, mineral fillings, reinforcing fillings, plasticizer, UV stabilizers, antioxidants, and coloring agents. The diverse composition of modifying additives and the diverse chemical structure of the main polymer makes segregation of this type of waste ineffective, and renders recycling impossible. Thus, the search for new possibilities for the use of waste thermoplastic elastomer from the production process of car floor mats is an essential topic due to environmental protection.

2. Materials and Methods

2.1. Materials

The following concrete was used for the tests: Portland cement CEM I 42.5R (Cemex, Rudniki, Poland), which meets the requirements of standard PN-EN 197-1, sand, gravel aggregate with 2–8 mm and 8–16 mm fractions, water, additives of CHRYSTO Plast 331, and CHRYSTO Air LB (the company CHRYSTO, Błonie, Poland), as well as waste thermoplastic elastomers from the production process of car floor mats at the production company Gumotest (Bielsko Białą, Poland). The waste used in this research was a thermoplastic elastomer (TPE-V; Bielsko Białą, Poland) based on an ethylene propylene diene blend (EPDM). Following initial crushing, production waste (Figure 1) was crushed into a 2–8 mm fraction in a granulator (SG-2417 SHINI, Donggung, China). With the use of the X-ray spectrometer WDXRF (Model S8 Tiger of the company Bruker, Billerica, USA), the elemental composition of the waste thermoplastic elastomer used in the tests was identified, which is presented in Table 1. For the tests, tap water from the water intake in Czestochowa was used, which meets the requirements of standard PN-EN 1008:2004 [50]. The average quantity of nitrate in the water was 37.0 mg/dm³, the average quantity of chlorides in the water was 31.5 mg/dm³, and the average quantity of sulphates in the water was 53.8 mg/dm³.

TGA-DTA analysis was carried out for the waste used in the tests. The test was carried out in the thermal analysis device Jupiter STA 449 F5 (of the company Netzsch, Netzsch, Selb, Germany) in the temperature range from 30 to 600 °C, with the temperature increase rate 10 °C/min in an air atmosphere, and with the gas flow rate 100 cm³/min. The results of thermogravimetric analysis (TG), differential thermogravimetric analysis (DTG), and differential scanning calorimetry (DSC) are presented in Figure 2. A loss of weight of the samples can be seen in a wide range of temperature from ca. 200 to 500 °C, and is ca. 11%. The processes connected with weight loss are endothermic.



Figure 1. Production waste from the production process of car floor mats: (a) initially crushed material; (b) material crushed to 2–8 mm fraction.

Table 1. Percentage content of the elements in the production waste.

Chemical Composition [% (m/m)]								
Ca	Si	Al	Zn	Mg	S	Ti	Fe	K
2.20	0.49	0.28	0.51	0.10	0.28	0.02	0.02	0.03

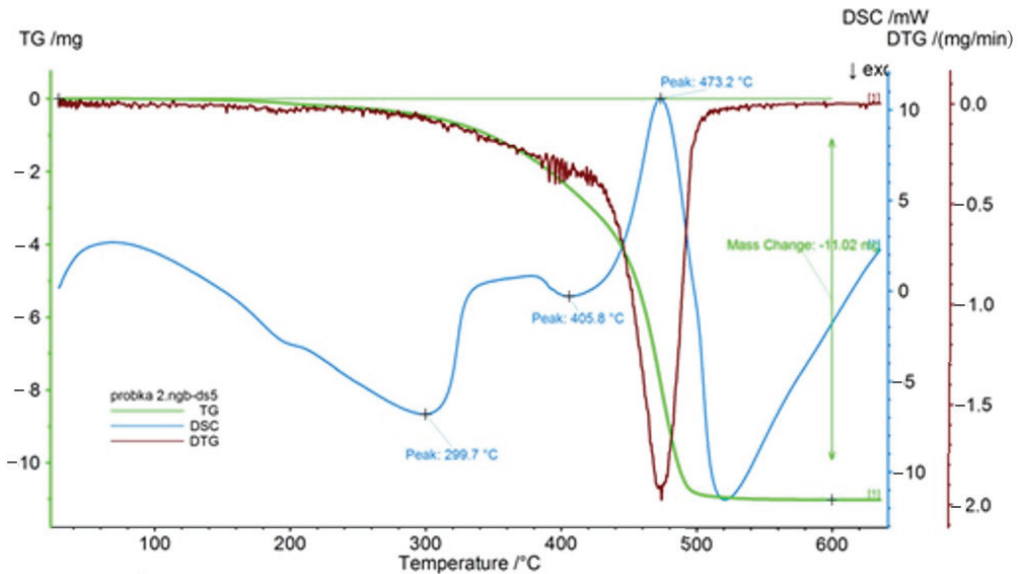


Figure 2. TGA–DTA thermogram for the waste thermoplastic elastomer.

2.2. Methods

Five series of concrete were prepared. To design the composition of the concrete mixture of the reference concrete (RC), an experimental method developed by Professor Kuczyński was used. It is the most popular Polish computational–experimental method of designing a concrete mix called the method of successive approximations or starting with iteration. It involves the calculation of three unknowns, i.e., the amount of cement, water, and aggregate, by using three basic equations: strength, tightness, and water demand (consistency). The obtained results are verified experimentally. The water–cement ratio was assumed to be 2:22 and the consistency class was assumed to be S2. To prepare the reference concrete, Portland cement CEM I 42.5R, the mixture of gravel–sand aggregates with a particle size distribution of 0–16 mm and a sand content of 33.1%, tap water and plasticizing admixture CHRYSTO Plast 331 in the quantity of 0.35% of the cement weight, and air entraining admixture CHRYSTO Air LB in the quantity of 0.2% of the cement weight were used. The reference concrete (RC) was modified with waste thermoplastic elastomer from the production process of car floor mats. The waste was added to concrete in the quantities of 2.5%, 5.0%, 7.5%, and 10% of the cement weight, adjusting the volume of gravel aggregate with a particle size distribution of 2–8 mm. The series of concrete were identified as S1-1, S1-2, S1-3, and S1-4, accordingly, and the composition of the designed mixtures is presented in Table 2. The waste thermoplastic elastomers from the production process of car floor mats were added directly to the mixer and pre-mixed with the aggregate. The workability of the mixture modified with waste did not change. The samples were shaped in accordance with the applicable standards, and then disassembled after 24 h and stored at a temperature of 18 ± 2 °C and relative humidity above 90%.

Table 2. The composition of the reference concrete and concrete modified with waste as the substitute for gravel aggregate with a particle size distribution of 2–8 mm.

Composition	Units	Series				
		SK	S1-1	S1-2	S1-3	S1-4
Cement	kg/m ³	327.50	327.50	327.50	327.50	372.5
Water	dm ³ /m ³	167.50	167.50	167.50	167.50	167.5
Sand	kg/m ³	463.70	463.70	463.70	463.70	463.7
Gravel 8–16	kg/m ³	776.20	776.20	776.20	776.20	776.2
Gravel 2–8	kg/m ³	635.10	593.90	552.80	511.70	470.5
Plasticizing admixture	dm ³ /m ³	1.30	1.30	1.30	1.30	1.30
Air entraining admixture	dm ³ /m ³	0.745	0.745	0.745	0.745	0.745
Production waste	kg/m ³	–	9.31	18.63	27.94	37.25

For all concrete mixtures, the consistency was defined according to standard PN-EN 12350-2:2011 [51], and the air quantity was defined according to standard PN-EN 12350-7:2011 [52]. On the other hand, concrete was tested for compression strength after 7, 28, and 56 days of the curing period according to standards PN-EN 206-1+A1:2016-12, PN-EN 12390-1:2013-03, PN-EN 12390-2:2019-07, PN-EN 12390-3:2019-07, and PN-EN 12390-4:2001 [53–57], and the following tests were carried out: bending tensile strength according to standard PN-EN 12390-5:2019-08 [58], and splitting tensile strength according to standard PN-EN 12390-6:2011 [59]. What is more, concrete absorbability was tested according to standard PN-B 06250 [60], density was tested according to standard PN-EN 206-1+A1:2016-12 [53], and resistance to water penetration under pressure was tested according to PN-EN 12390-8:2019-08 [61]. In addition, frost resistance was identified for the tested concretes: decrease in resistance and weight loss after frost resistance test according to standard PN-B 06250 [61], and abrasion resistance according to standard PN-EN 13892-3:2015 [62].

SEM/EDS analysis of the microstructure of the synthesized concrete composites that included the waste thermoplastic elastomer was also carried out. Scanning electron microscopy (SEM), LEO Electron Microscopy Ltd., Cambridge, UK) was used for the tests, which was equipped with a system for chemical composition analysis based on X-ray energy dispersion—EDS (energy dispersive spectroscopy, Bruker AXS, Karlsruhe, Germany).

3. Results and Discussion

For the concrete mixture of the reference concrete, an S2 consistency was assumed (concrete slump at 50–90 mm). After preparation of the concrete mixture, samples were collected to define the consistency class and air content in the concrete mixture. For the reference mixture (RC), the slump was 70 mm, which corresponds to the S2 class. Air content in this mixture was 3.5%. For concrete mixtures modified with the waste thermoplastic elastomer (S1-1–S1-4), the slump was between 50 and 75 mm, which also corresponds to the S2 consistency class (Table 3). The air content in the concrete mixtures modified with production waste was at the level of 3.65–4.1%.

Table 3. Consistency class and air content in concrete mixtures subject to tests.

Series	Consistence mm/Class	Air Content [%]
SK	70/S2	3.50
S1-1	55/S2	3.95
S1-2	55/S2	3.90
S1-3	50/S2	3.65
S1-4	75/S2	4.10

For each series of concrete, 18 cubic samples with a 150 mm side were prepared, which were subject to compression strength tests after 7, 28, and 56 days of the curing period under laboratory conditions. For the results obtained in the individual series, the standard deviation and confidence level at 95% were identified. The reference concrete (RC) after seven days of curing was characterized with an average compression strength of 46.6 ± 0.95 MPa, whilst after 28 days it was 57.0 ± 1.59 MPa, and 61.9 ± 1.19 MPa after 56 days (Table 4). The average compression strengths for the concretes modified with the waste thermoplastic elastomer in the quantity of 2.5% after seven days of curing period were at the level of the average compression strength of the reference concrete. On the other hand, the average compression strength of the concretes containing the waste elastomer in the quantities of 5.0%, 7.5%, and 10% was lower than in the case of the reference concrete. Therefore, from the point of view of compression strength tested after seven days of the curing period, only the use of the waste thermoplastic elastomer in the quantity below 2.5% does not cause a significant decrease in this parameter. The average compression strength for the concrete series S1-1 containing 2.5% of waste tested after 28 days of the curing period was at the level of the reference concrete (57.8 ± 0.36 MPa), whilst the other series of concrete (S1-2, S1-3, and S1-4) modified with waste presented a lower 28-day average compression strength than the reference series concrete. The decrease in the average compression strength for the individual concrete series was between 9.6% and 22.6%. After 56 days of the sample curing period, the reference concrete (RC) obtained an average compression strength higher by 8.5% than the 28-day average compression strength, which was 61.9 ± 1.19 MPa. In the event of the concrete series modified with waste, the compression strength increased compared to the strength obtained after 28 days. Concrete series S1-1 containing 2.5% waste obtained strength (62.1 ± 1.7 MPa) at the level of the reference concrete, whilst the other series of concrete, which are S1-2, S1-3, and S1-4, obtained lower average compression strengths compared to the reference concrete—from 11.3% to 24.3%.

Table 4. Compression strength of the tested concrete and the resistance class.

Series	Compression Strength [MPa]			Resistance Class
	After 7 Days	After 28 Days	After 56 Days	
SK	46.6	57.0	61.9	C40/50
S1-1	46.5	57.8	62.1	C40/50
S1-2	44.0	51.5	54.9	C35/45
S1-3	42.9	50.1	53.0	C35/45
S1-4	36.1	44.1	46.8	C30/37

The addition of the waste thermoplastic elastomer to concrete also influenced the bending strength and splitting tensile strength of the concrete (Table 5). Adding production waste, which was used as a substitute for aggregate with particle size distribution 2–8 mm, at the quantities of 2.5% and 5.0% to concrete had a positive impact on the tested parameters. For series S1-1 and S1-2, an increase in the average bending strength by 3.1% and 2.2%, accordingly, as compared to the reference concrete, was noted. For the other series of modified concrete (S1-3 and S1-4), a slight decrease in the average bending strength by 0.8% and 1.2%, accordingly, as compared to the reference concrete series, was noted. On the other hand, the average splitting tensile strength of the reference concrete was equal to 3.78 ± 0.98 MPa. In the event of concrete containing the addition of production waste in the quantities of 2.5% and 5.0% (series S1-1 and S1-2), an increase of the tested parameter by 13.5% and 9.0%, accordingly, as compared to the RC series, was noted. Meanwhile, in the event of other series (S1-3 and S1-4), a decrease in the average splitting tensile strength of concrete by 5.3% and 12.2%, accordingly, as compared to the reference series, was noted. The increase in bending tensile strength and splitting tensile strength is most likely related to the grain surface of the waste thermoplastic elastomer granulate and the surface of the natural aggregate grain. Both sand and gravel are natural pebble aggregates with a very smooth surface, while the waste granulate used had a much rougher surface, which perhaps resulted in better adhesion with the cement matrix and increased the mechanical properties of the concrete.

Table 5. Concrete bending tensile strength and splitting tensile strength.

Series	Bending Strength [MPa]	Splitting Tensile Strength [MPa]
SK	3.59	3.78
S1-1	3.70	4.29
S1-2	3.67	4.12
S1-3	3.56	3.58
S1-4	3.44	3.32

The next stage of tests was to determine the absorbability, density, water penetration under pressure, frost resistance, and abrasion resistance of the concrete (Table 6). The absorbability test was carried out after 28 days of curing the samples. In the event of the reference concrete (RC), the absorbability was 5.4%. A similar level of absorbability (from 4.9% to 5.6%) was presented by the concrete modified with production waste in the quantities of 2.5%, 5.0%, 7.5%, and 10%. According to standard PN-B 06250 [56], the absorbability of concrete exposed to environmental factors should not be higher than 5%, whilst concrete covered from the direct influence of environmental factors should not exceed 9%. Both the reference series concrete, as well as the concrete modified with the waste thermoplastic elastomer, obtained absorbability below 9%. This means that concrete manufactured with this type of production waste should be covered from the direct influence of environmental factors. Due to its density, which was 2271 kg/m^3 , the reference concrete was classified into a standard concrete category according to standard PN-EN 12390-4:2001 [53]. Similarly, all concretes modified with the waste thermoplastic elastomer were included in the standard concrete category, since their density was between 2000 and

2600 kg/m³. The reference concrete obtained an average depth of water penetration equal to 65 mm. For the series of concrete modified with the waste thermoplastic elastomer, the average depth of water penetration was from 60 to 67 mm. The lowest value of the tested parameter (60 mm) was obtained for series S1-1, in which 2.5% of production waste was used, whilst the highest value (67 mm) was obtained for concrete series S1-4, in which 10% of the said waste was used. In the event of the reference concrete (RC), the abrasion strength was 7.4 cm³/50 cm². For the concrete modified with the waste of thermoplastic elastomer, a lower abrasion strength was obtained than for the reference series concrete—it was 2.7–6.8%.

Table 6. Parameters tested for each series of concrete.

Series	Water Absorbability [%]	Density [kg/m ³]	Water Penetration [mm]	Abrasion Strength [cm ³ /50 cm ²]
SK	5.4	2271	65	7.4
S1-1	5.2	2258	60	6.9
S1-2	5.6	2218	63	6.7
S1-3	5.6	2214	65	7.0
S1-4	5.3	2172	67	7.2

A frost resistance test was carried out for all series of concrete. For each series of concrete, 12 cubic samples with a 100 mm side were prepared, of which six samples were subject to frost resistance tests, and six samples were left in water as the reference samples. In the event of the reference concrete, the average decrease in compression strength after 150 cycles of freezing and thawing was 4.4%, and the average weight loss was 0.34% (Figure 3).

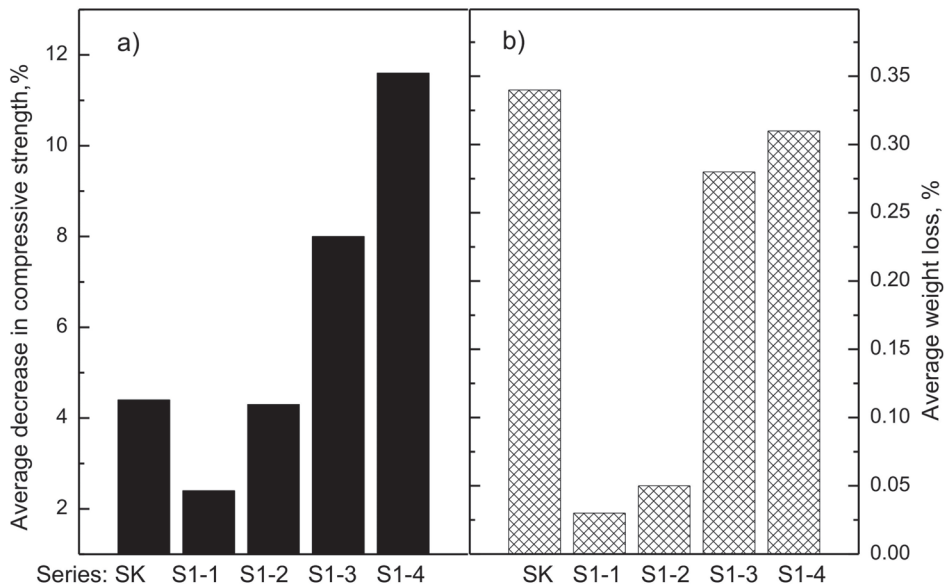


Figure 3. The average decrease in compression strength of the concrete after the frost strength test (a) and the average weight drop (b), both in %.

In the event of the concrete modified with the waste thermoplastic elastomer used as the substitute for gravel aggregate with particle size distribution 2–8 mm in the quantities of 2.5% and 5.0% of the cement weight, a lower average decrease in the compression strength than for the reference series concrete was noted. The average compression strength of the concrete after the frost resistance tests decreased, along with an increase of the amount of

production waste added to the concrete. The lowest decrease in the average compression strength after the frost resistance test was noted for concrete series with the addition of 2.5% production waste, where it was 2.4%, whilst the highest (11.6%) was noted for concrete containing 10% of production waste. After the frost resistance test, the average weight loss was at the level of 0.05–0.34%. None of the samples cracked and there were no scratches.

During the next stage of tests, analysis of the surface layer of the synthesized composites was carried out, mainly defining their morphology and elemental composition. Figure 4 presents a microscopic image for the reference concrete (RC) enlarged 80 times (Figure 4a), together with location maps of the dominant elements in this area (Figure 4b). In the reference concrete (RC), a lighter structure of concrete matrix is visible, as well as a darker area, which represents the aggregate based on silicon. The microstructure at the border of the aggregate with the cement matrix is of high density. According to EDS analysis of concrete surface visible on the image, in addition to calcium (33.06%; blue color), significant amounts of silicon (20.36%; green color) and iron (4.49%; pink color) are visible. At a quantity below 1.0%, the following elements are visible: aluminum, sulfur, potassium, magnesium, and carbon. In the event of concrete series S1-1 modified with the waste thermoplastic elastomer in the quantity of 2.5%, the microscopic images present a structure very similar to the reference series concrete (Figure 5). Equally located aggregate particles can be seen in the concrete. EDS analysis of the surface of the S1-1 series concrete shows the presence of calcium (23.48%; blue color), silicon (14.70%; green color), and carbon (4.71%; red color). In addition, the following elements are also present: iron and titanium in quantities of 7.07% and 6.54%, accordingly, as well as aluminum, magnesium, sulfur, potassium, sodium, and zinc in quantities below 1.0%. Similarly, in the event of the cement series S1-4 modified with the waste thermoplastic elastomer in the quantity of 10.0%, a structure very similar to the reference series concrete was observed. EDS analysis shows the presence of calcium (18.98%; blue color), silicon (16.35%; green color), and carbon (9.20%; red color). In addition, the following elements are also present: aluminum and iron in quantities of 1.19% and 1.0%, accordingly, as well as sulfur, magnesium, potassium, and zinc in quantities below 1.0%. The carbon quantity increased by 9.0% in series S1-4, which was caused by the increased quantity of waste in the concrete mixture. The structure of the concrete modified by elastomer waste did not differ significantly from the structure of control concrete. The bending and splitting strength of the concrete containing 2.5% and 5% of waste (amount of carbon < 5%) increased compared to control concrete. On the other hand, a greater amount of waste in the concrete (carbon content of 9.2%) had a negative impact on these strength parameters.

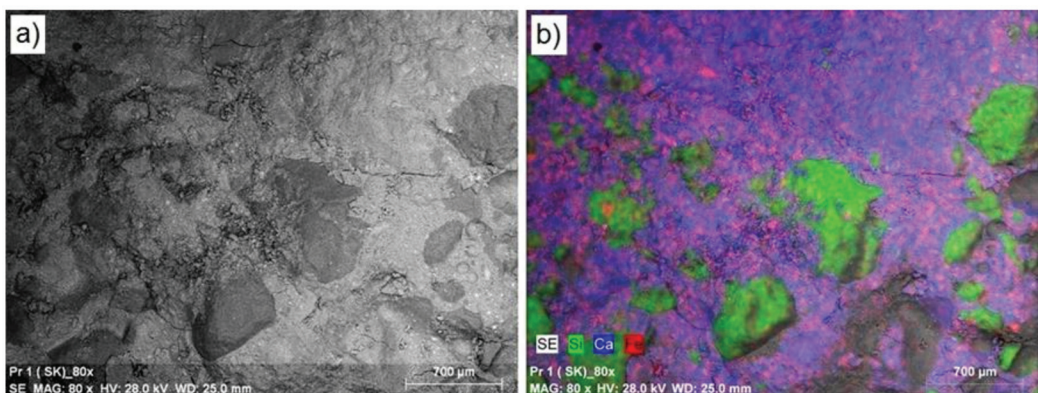


Figure 4. Microstructure of the controlled series concrete: (a) enlarged by 80×; (b) location map of the dominant elements in a given area.

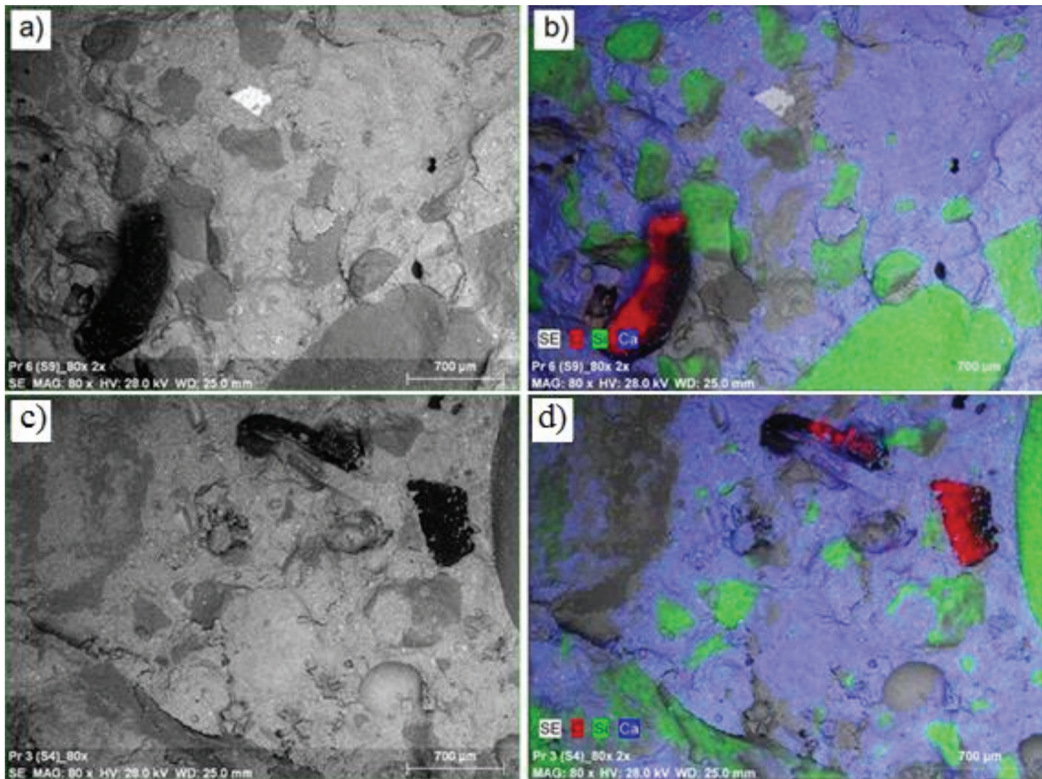


Figure 5. Concrete microstructure: (a) reference series S1-1 enlarged by 80×; (b) location map of the dominant elements in a given area, concrete series S1-1; (c) series S1-4 enlarged by 80×; (d) location map of the dominant elements in a given area, concrete series S1-4.

4. Conclusions

Tests of the properties and structures of concrete composites containing a waste thermo-plastic elastomer from the production process of car floor mats, as well as analysis of obtained results, showed the suitability of this waste type for the production of concrete. The early compression strength of concrete (tested after seven days of curing) modified with production waste in the quantity of 2.5% of the cement weight that was used as the substitute for fine gravel aggregate was similar to the compression strength of the reference concrete. On the other hand, in the event of concrete containing waste in the quantities of 5.0%, 7.5%, and 10% of the cement weight, a decrease of a seven-day compression strength was noted at the level between 5.5% to 11.3%. Similarly, the compression strength tested after 28 and 56 days of curing of samples of concrete modified with 2.5% additive of waste was comparable to the strength of the reference samples (increased by 0.3–1.4%). The addition of a higher quantity of waste resulted in a decrease in the values of this parameter by 9.6–22.6% in the event of samples tested after 28 days, and by 11.3–24.4% in the event of samples tested after 56 days of curing. The tests showed that adding a waste thermoplastic elastomer to concrete in the quantities of 2.5% and 5.0% of the cement weight as a substitute for fine gravel aggregate with a particle size distribution 2–8 mm had a positive impact on the increase of the bending strength of concrete. For concrete of these series, an increase in the bending strength by 3.1% and 2.2%, accordingly, as compared to the reference concrete, was noted. Concrete modified with waste in the quantities of 7.5% and 10% showed a decrease in bending strength by 0.8% and 4.2%, accordingly, as compared to the reference concrete. The addition of production waste in

the quantities of 2.5% and 5.0% also had a positive impact on the splitting tensile strength of concrete. For these series of concrete, this parameter was higher as compared to the reference concrete by 9.0% and 13.5%, accordingly. In the event of concrete modified with waste in the quantities of 7.5% and 10%, a decrease in the splitting tensile strength of the concrete by 5.3% and 12.3%, accordingly, as compared to the reference concrete, was noted.

All concretes modified with waste obtained lower densities than the reference concrete, which was between 2000 and 2600 kg/m³. This allowed for classifying them into the standard concrete category. Both the reference concrete and the concrete modified with waste thermoplastic elastomer obtained absorbability at the ca. 5.0% level. All concretes modified with the waste thermoplastic elastomer met the standard requirements. After 150 cycles of freezing and thawing, the average decrease in compression strength did not exceed 20%, and the average weight loss did not exceed 5%. Therefore, it may be concluded that it is beneficial to add a waste thermoplastic elastomer from the production process of car floor mats in the quantity of 2.5% of the cement weight to concrete, which allows for the saving of natural resources and decreases the costs of concrete manufacture by 20 kg/m³, which is about 5.0%.

Author Contributions: M.U.—conceptualization and methodology; A.P.—investigation and software; M.U.—analysis, writing—review and editing; writing—original draft preparation; A.P.—formal analysis and writing original draft preparation. All authors have read and agreed to the published version of the manuscript.

Funding: This research received no external funding.

Data Availability Statement: The data presented in this study are available on request from the corresponding author.

Acknowledgments: The authors would like to thank Gumotest Plant (Poland) for providing waste materials to research.

Conflicts of Interest: The authors declare no conflict of interest. The funders had no role in the design of the study; in the collection, analyses, or interpretation of data; in the writing of the manuscript, or in the decision to publish the results.

References

1. Kishore, K.; Gupta, N. Application of domestic & industrial waste materials in concrete: A review. *Mater. Today Proc.* **2020**, *26*, 2926–2931. [CrossRef]
2. Aggarwal, Y.; Siddique, R. Microstructure and properties of concrete using bottom ash and waste foundry sand as partial replacement of fine aggregates. *Constr. Build. Mater.* **2014**, *54*, 210–223. [CrossRef]
3. Halicka, A.; Ogrodnik, P.; Zegardlo, B. Using ceramic sanitary ware waste as concrete aggregate. *Constr. Build. Mater.* **2013**, *48*, 295–305. [CrossRef]
4. Ulewicz, M.; Halbiniak, J. Application of waste from utilitarian ceramics for production of cement mortar and concrete. *Physicochem. Probl. Miner. Process.* **2016**, *52*, 1002–1010.
5. Walczak, P.; Malolepszy, J.; Reben, M.; Rzepa, K. Mechanical properties of concrete mortar based on mixture of CRT glass cullet and fluidized fly ash. *Procedia Eng.* **2015**, *108*, 453–458. [CrossRef]
6. Bostanci, S.C.; Limbachiya, M.; Kew, H. Portland-composite and composite cement concretes made with coarse recycled and recycled glass sand aggregates: Engineering and durability properties. *Constr. Build. Mater.* **2016**, *128*, 324–340. [CrossRef]
7. Choi, S.-J.; Kim, Y.-U.; Oh, T.-G.; Cho, B.-S. Compressive Strength, Chloride Ion Penetrability, and Carbonation Characteristic of Concrete with Mixed Slag Aggregate. *Materials* **2020**, *13*, 940. [CrossRef]
8. Gu, L.; Ozbakkaloglu, T. Use of recycled plastics in concrete: A critical review. *Waste Manag.* **2016**, *51*, 19–42. [CrossRef]
9. Rashad, A.M. A comprehensive overview about recycling rubber as fine aggregate replacement in traditional cementitious materials. *Int. J. Sustain. Built Environ.* **2016**, *5*, 46–82. [CrossRef]
10. Tavakoli, D.; Hashempour, M.; Heidari, A. Use of Waste Materials in Concrete: A review. *Pertanika J. Sci. Technol.* **2018**, *26*, 499–522.
11. Sharma, R.; Bansal, P.P. Use of different forms of waste plastic in concrete—A review. *J. Clean. Prod.* **2016**, *112*, 473–482. [CrossRef]
12. Choi, Y.W.; Moon, D.J.; Chung, J.S.; Cho, S.K. Effects of waste PET bottlers aggregate on the properties of concrete. *Cem. Concr. Res.* **2005**, *35*, 776–781. [CrossRef]
13. Choi, Y.W.; Moon, D.J.; Kim, Y.J.; Lachemi, M. Characteristics of mortar and concrete containing fine aggregate manufactured from recycled waste polyethylene terephthalate bottles. *Constr. Build. Mater.* **2009**, *23*, 2829–2835. [CrossRef]

14. Nibudey, R.; Nagarnaik, P.; Parbat, D.; Pande, A. Strength and fracture properties of post consumed waste plastic fiber reinforced concrete. *Int. J. Civ. Struct. Environ. Infrastruct. Eng. Res. Dev.* **2013**, *3*, 9–16.
15. Rahmani, E.; Dehestani, M.; Beygi, M.H.A.; Allahyari, H.; Nikbin, I.M. On the mechanical properties of concrete contain-ing waste PET particles. *Constr. Build. Mater.* **2013**, *47*, 1302–1308. [CrossRef]
16. Ferreira, L.; De Brito, J.; Saikia, N. Influence of curing conditions on the mechanical performance of concrete containing recycled plastic aggregate. *Constr. Build. Mater.* **2012**, *36*, 196–204. [CrossRef]
17. Silva, R.; De Brito, J.; Saikia, N. Influence of curing conditions on the durability-related performance of concrete made with selected plastic waste aggregates. *Cem. Concr. Compos.* **2013**, *35*, 23–31. [CrossRef]
18. Saikia, N.; de Brito, J. Waste polyethylene terephthalate as an aggregate in concrete. *Mater. Res.* **2013**, *16*, 341–350. [CrossRef]
19. Ochi, T.; Okubo, S.; Fukui, K. Development of recycled PET fiber and its application as con-crete-reinforcing fiber. *Cement Concr. Compos.* **2007**, *29*, 448–455. [CrossRef]
20. Chaudhary, M.; Srivastava, V.; Agarwal, V. Effect of waste low density polyethylene on mechanical properties of concrete. *J. Acad. Ind. Res.* **2014**, *3*, 123.
21. Martínez-Barrera, G.; Viguera-Santiago, E.; Hernández-López, S.; Brostow, W.; Menchaca-Campos, C. Me-chemical improvement of concrete by irradiated polypropylene fibers. *Polym. Eng. Sci.* **2005**, *45*, 1426–1431. [CrossRef]
22. Abdelmoti, H.; Mustafa, A.M. Use of Polypropylene Waste Plastic Pellets as Partial Replacement for Fine Aggregate in Concrete. *Univ. Khartoum Eng. J.* **2019**, *9*, 37–43.
23. Wang, Y.; Wu, H.; Li, V.C. Concrete reinforcement with recycled fibers. *J. Mater. Civ. Eng.* **2000**, *12*, 314–319. [CrossRef]
24. Borovanska, I.; Dobrova, T.; Benavente, R.; Djoumalisky, S.; Kotzev, G. Quality assessment of recycled and modified LDPE/PP blends. *J. Elastomers Plast.* **2012**, *44*, 479–497. [CrossRef]
25. Kojnoková, T.; Markovičová, L.; Nový, F. The changes of LD-PE films after exposure in different media. *Prod. Eng. Arch.* **2020**, *26*, 185–189. [CrossRef]
26. Kakooei, S.; Akil, H.M.; Jamshidi, M.; Rouhi, J. The effects of polypropylene fibers on the properties of reinforced concrete structures. *Constr. Build. Mater.* **2012**, *27*, 73–77. [CrossRef]
27. Sivakumar, A.; Santhanam, M. A quantitative study on the plastic shrinkage cracking in high strength hybrid fibre reinforced concrete. *Cem. Concr. Compos.* **2007**, *29*, 575–581. [CrossRef]
28. Pietrzak, A.; Ulewicz, M. The impact of the length of polypropylene fibers on selected properties of concrete. *Acta Sci. Pol. Arch. Bud.* **2019**, *18*, 21–25. [CrossRef]
29. Tang, W.; Lo, Y.; Nadeem, A. Mechanical and drying shrinkage properties of structural-graded polystyrene aggregate con-crete. *Cem. Concr. Compos.* **2008**, *30*, 403–409. [CrossRef]
30. Herki, A.; Khatib, J.; Negim, E. Lightweight concrete made from waste polystyrene and fly ash. *World Appl. Sci. J.* **2013**, *21*, 1356–1360.
31. Babu, D.S.; Babu, K.G.; Tiong-Huan, W. Effect of polystyrene aggregate size on strength and moisture migration characteristics of lightweight concrete. *Cem. Concr. Compos.* **2006**, *28*, 520–527. [CrossRef]
32. Xu, Y.; Jiang, L.; Xu, J.; Li, Y. Mechanical properties of expanded polystyrene lightweight aggregate concrete and brick. *Constr. Build. Mater.* **2012**, *27*, 32–38. [CrossRef]
33. Sofi, A. Effect of waste tyre rubber on mechanical and durability properties of concrete—A review. *Ain Shams Eng. J.* **2018**, *9*, 2691–2700. [CrossRef]
34. Balaha, M.M.; Badawy, A.A.M.; Hashish, M. Effect of using ground tire rubber as fine aggregate on the behaviour of concrete mixes. *Indian J. Eng. Mater. Sci.* **2007**, *14*, 427–435.
35. Gesoğlu, M.; Güneyisi, E. Strength development and chloride penetration in rubberized concretes with and without silica fume. *Mater. Struct.* **2007**, *40*, 953–964. [CrossRef]
36. Albano, C.; Camacho, N.; Reyes, J.; Feliu, J.L.; Herná ndez, M. Influence of scrap rubber to Portland I concrete composites: Destructive and non-destructive testing. *Compos. Struct.* **2005**, *71*, 439–446. [CrossRef]
37. Holmes, N.; Dunne, K.; O'Donnell, J. Longitudinal shear resistance of composite slabs containing crumb rubber in concrete toppings. *Constr. Build. Mater.* **2014**, *55*, 365–378. [CrossRef]
38. Bravo, M.; de Brito, J. Concrete made with used tyre aggregate: Durability-related performance. *J. Clean. Prod.* **2012**, *25*, 42–50. [CrossRef]
39. Onuaguluchi, O.; Panesar, D.K. Hardened properties of concrete mixtures containing pre-coated crumb rubber and silica fume. *J. Clean. Prod.* **2014**, *82*, 125–131. [CrossRef]
40. Taha, M.M.R.; El-Dieb, A.S.; El-Wahab, M.A.A.; Abdel-Hameed, M.E. Mechanical, fracture, and microstructural investigations of rubber concrete. *J. Mater. Civ. Eng.* **2008**, *20*, 640–649. [CrossRef]
41. Batayneh, M.K.; Marie, I.; Asi, I. Promoting the use of crumb rubber concrete in developing countries. *Waste Manag.* **2008**, *28*, 2171–2176. [CrossRef]
42. Lavagna, L.; Nisticò, R.; Sarasso, M.; Pavese, M. An Analytical Mini-review on the compression strength of rubberized concrete as a function of the amount of recycled tires crumb rubber. *Materials* **2020**, *13*, 1234. [CrossRef]
43. Mercante, I.; Alejandrino, C.; Ojeda, J.P.; Chini, J.; Maroto, C.; Fajardo, N. Mortar and concrete composites with recycled plastic: A review. *Sci. Technol. Mater.* **2018**, *30*, 69–79. [CrossRef]

44. Pelisser, F.; Zavarise, N.; Longo, T.A.; Bernardin, A.M. Concrete made with recycled tire rubber: Effect of alkaline activation and silica fume addition. *J. Clean. Prod.* **2011**, *19*, 757–763. [CrossRef]
45. Ramdani, S.; Guettala, A.; Benmalek, M.L.; Aguiar, J.B. Physical and mechanical performance of concrete made with waste rubber aggregate, glass powder and silica sand powder. *J. Build. Eng.* **2019**, *21*, 302–311. [CrossRef]
46. Almeida, F.; Cunha, V.M.C.F.; Miranda, T.; Cristelo, N. Indirect tensile behaviour of fibre reinforced alkali-activated composites. *Fibers* **2018**, *6*, 30. [CrossRef]
47. Kytinou, V.K.; Chalioris, C.E.; Karayannis, C.G. Analysis of residual flexural stiffness of steel fiber-reinforced concrete beams with steel reinforcement. *Materials* **2020**, *13*, 2698. [CrossRef]
48. Babaie, R.; Abolfazli, M.; Fahimifar, A. Mechanical properties of steel and polymer fiber reinforced concrete. *J. Mech. Behav. Mater.* **2019**, *28*, 119–134. [CrossRef]
49. Commission Decision of amending Decision 2000/532/EC on the list of waste pursuant to Directive 2008/98/EC of the European Parliament and of the Council (2014/955/EU). European Parliament, Brussels. Available online: <https://eur-lex.europa.eu/legal-content/EN/TXT/?uri=CELEX%3A32014D0955> (accessed on 11 February 2021).
50. The Polish Committee for Standardization. *Specification of Sampling, Testing and Evaluation of the Suitability of Mixing Water for Concrete, Including Water Recovered from Concrete Production Processes*; The Polish Committee for Standardization: Warsaw, Poland, July 2002.
51. The Polish Committee for Standardization: PN-EN 12350-2:2011. *Testing Fresh Concrete—Part 2: Slump-Test*; The Polish Committee for Standardization: Warsaw, Poland, 2011.
52. The Polish Committee for Standardization: PN-EN 12350-7:2011. *Testing Fresh Concrete—Part 7: Air Content—Pressure methods*; The Polish Committee for Standardization: Warsaw, Poland, 2011.
53. The Polish Committee for Standardization: PN-EN 206-1+A1:2016-12. *Concrete—Requirements, Properties, Production and Compliance*; The Polish Committee for Standardization: Warsaw, Poland, 2016.
54. The Polish Committee for Standardization: PN-EN 12390-1:2013-03. *Testing Hardened Concrete—Part 1: Shape, Dimensions and other Requirements for Specimens and Moulds*; The Polish Committee for Standardization: Warsaw, Poland, 2013.
55. The Polish Committee for Standardization: PN-EN 12390-2:2019-07. *Testing Hardened Concrete—Part 2: Making and Curing Specimens for Strength Tests*; The Polish Committee for Standardization: Warsaw, Poland, 2019.
56. The Polish Committee for Standardization: PN-EN 12390-3:2019-07. *Testing Hardened Concrete—Part 3: Compressive Strength of Test Specimens*; The Polish Committee for Standardization: Warsaw, Poland, 2019.
57. The Polish Committee for Standardization: PN-EN 12390-4:2001. *Testing Hardened Concrete—Part 4: Compressive Strength—Requirements for Testing Machines*; The Polish Committee for Standardization: Warsaw, Poland, 2001.
58. The Polish Committee for Standardization: PN-EN 12390-5:2019-08. *Testing Hardened Concrete—Part 5: Bending Strength of Test Specimens*; The Polish Committee for Standardization: Warsaw, Poland, 2019.
59. The Polish Committee for Standardization: PN-EN 12390-6:2011. *Testing Hardened Concrete—Part 6: Tensile Strength when Splitting Test Samples*; The Polish Committee for Standardization: Warsaw, Poland, 2011.
60. The Polish Committee for Standardization: PN-B 06250. *Plain Concrete*; The Polish Committee for Standardization: Warsaw, Poland, 2003.
61. The Polish Committee for Standardization: PN-EN 12390-8:2019-08. *Testing Hardened Concrete—Part 8: The Depth of Penetration of Pressurized Water*; The Polish Committee for Standardization: Warsaw, Poland, 2019.
62. The Polish Committee for Standardization: PN-EN 13892-3:2015. *Methods of Testing Materials for Floor Screeds—Part 3: Determination of The Resistance to Abrasion According to Boehme*; The Polish Committee for Standardization: Warsaw, Poland, 2015.

Article

Enhancement of Mechanical Properties and Porosity of Concrete Using Steel Slag Coarse Aggregate

Md Jihad Miah¹, Md. Munir Hossain Patoary¹, Suvash Chandra Paul²,
Adewumi John Babafemi³ and Biranchi Panda^{4,*}

¹ Department of Civil Engineering, University of Asia Pacific, Dhaka 1205, Bangladesh; jihad.miah@uap-bd.edu (M.J.M.); 3dcometdesign@gmail.com (M.M.H.P.)

² Department of Civil Engineering, International University of Business Agriculture and Technology, Dhaka 1230, Bangladesh; suvashpl@iubat.edu

³ Department of Civil Engineering, Stellenbosch University, Private Bag X1, Matieland 7602, Stellenbosch, South Africa; ajbabafemi@sun.ac.za

⁴ Department of Mechanical Engineering, Indian Institute of Technology Guwahati, Assam 781039, India

* Correspondence: biranchipanda@tecnico.ulisboa.pt; Tel.: +91-3612582700

Received: 31 May 2020; Accepted: 22 June 2020; Published: 26 June 2020

Abstract: This paper investigates the possibility of utilizing steel slags produced in the steelmaking industry as an alternative to burnt clay brick aggregate (BA) in concrete. Within this context, physical, mechanical (i.e., compressive and splitting tensile strength), length change, and durability (porosity) tests were conducted on concrete made with nine different percentage replacements (0%, 10%, 20%, 30%, 40%, 50%, 60%, 80%, and 100% by volume of BA) of BA by induction of furnace steel slag aggregate (SSA). In addition, the chemical composition of aggregate through X-ray fluorescence (XRF) analysis and microstructural analysis through scanning electron microscopy (SEM) of aggregates and concrete were performed. The experimental results show that the physical and mechanical properties of concrete made with SSA were significantly higher than that of concrete made with BA. The compressive and tensile strength increased by 73% when SSA fully replaced BA. The expansion of concrete made with SSA was a bit higher than the concrete made with BA. Furthermore, a significant lower porosity was observed for concrete made with SSA than BA, which decreased by 40% for 100% SSA concrete than 100% BA concrete. The relation between compressive and tensile strength with the porosity of concrete mixes are in agreement with the relationships presented in the literature. This study demonstrates that SSA can be used as a full replacement of BA, which is economical, conserves the natural aggregate, and is sustainable building material since burning brick produces a lot of CO₂.

Keywords: steel slag aggregate; concrete; compressive and tensile strength; length change; porosity

1. Introduction

In the utilization of industrial residues as construction raw materials, the concrete industry can play an important role in sustainable development, leading to considerable environmental benefits. Generally, aggregates (coarse and fine) occupy about 60–85% of the total volume of hardened concrete [1]. Aggregates are important constituents in the concrete composite that help to improve the various properties of concrete, including reducing the shrinkage and providing workability, volume stability, strength, and durability to the concrete [2]. In the numerous countries of South Asia, the concrete industry mostly depends on burnt clay brick aggregate (BA) due to the shortage of natural stones [3]. The production process of BA increases CO₂ in the air, resulting in a large negative environmental impact and risk to human life. Though crushed stone aggregates are used in the concrete industry due to rapid urbanization, they are mostly imported from abroad, thereby, increasing the cost of concrete

production. Due to the aforementioned issues, indeed, it is necessary to find possible alternative construction raw materials that can be used as coarse and fine aggregates in concrete construction works [4–6].

Steel slag is a byproduct of the steelmaking process which is produced during the separation of the molten steel from impurities in the steelmaking furnace, and it is used as coarse aggregate in concrete. It was found that steel slag aggregate (SSA) has superior physical and mechanical properties as well as lower carbon footprint and reduced negative environmental effects [7,8]. The compressive strength of concrete containing steel slag at 28 days was about 35% higher than the reference concrete [9]. The incorporation of different replacement percentages (15%, 25%, 50%, 75%, and 100%) of natural stone aggregate by SSA increased compressive and flexural strength, while it reduced the chloride ion permeability from 40% to 70% compared to concrete made with natural stone aggregate [10]. Similarly, research demonstrated that the physical and mechanical properties of concrete made of slag aggregate were higher as compared to natural aggregate [11]. Conversely, the reduction in workability was observed for concrete containing SSA compared to natural aggregate.

Netinger et al. [12] investigated the mechanical properties and corrosion resistance of concrete made with SSA. It was found that SSA can be used in concrete since it provides acceptable mechanical properties and no risk of corrosion of reinforcement. It was found that the carbonation treatments can significantly improve the strength and volume stability of concrete made with carbonated granulated steel slag aggregate [13]. Abu-Eishah et al. [14] observed that the concrete made with steel SSA provides high-strength compared to similar conventional concrete mixtures, which could be due to the strong bond between the cement/mortar matrix and SSA. It has been observed that concrete made with SSA decreased the workability of fresh concrete; it was claimed that SSA particles were angularly resulting in a reduction of the flowability of concrete [13]. Similarly, Qasrawi [15,16] observed that the addition of SSA decreased the workability of concrete and produced an unacceptable flow when more than 50% SSA were used. The reduction in a slump of concrete containing SSA was also observed by Sheen et al. [17].

Several studies have been carried out to investigate the mechanical performance of concrete made with SSA, but few focused on durability (e.g., porosity). To the authors' knowledge, there seems to be no published work on concrete made with induction furnace SSA as a replacement of BA. This induction furnace slag is used mainly for landfills and sometimes as an alternative aggregate in road construction, which is not very common due to lack of research data. The lack of research data, limited information, and knowledge on the mechanical and durability performances of concrete made with SSA as a replacement for BA motivate this research work. Within this context, comprehensive experimental studies were conducted on the possibility of using induction furnace steel slag as coarse aggregate replacement for BA. This is with the goal to reduce the consumption of industrial-made brick (reduce CO₂) and natural aggregate which is mainly imported from abroad (reduce the cost of concrete and obtain a sustainable construction material). The aim of this research work is to investigate the physical, mechanical (i.e., compressive and splitting tensile strength), length change, and durability (porosity) performances of concrete made with nine different replacement percentages (0%, 10%, 20%, 30%, 40%, 50%, 60%, 80%, and 100% by volume of BA) of BA by induction furnace SSA. To gain a deeper understanding of the role of SSA on the performance of concrete, the relation between strength (compressive and tensile) and porosity of concrete mixes was discussed. Additionally, the chemical composition of aggregate through X-ray fluorescence (XRF) analysis was determined and microstructural analysis using scanning electron microscopy (SEM) of aggregates and concrete was performed.

2. Experimental Methodology

2.1. Material Characterization

2.1.1. Aggregates

Two types of coarse aggregates (first-class burnt clay brick and induction furnace SSA) were used in this study. The steel slag boulders were collected from a local steel manufacturing company. Two different types of steel slag boulders were found: some were light in weight with more voids (more porous, see Figure 1a), those were used in wastewater treatment [18], and others were denser with less voids (see Figure 1b). The SSAs with the denser structure were used in this study.



Figure 1. Induction furnace steel slag boulders: (a) steel slag with more void, (b) steel slag with less void; steel slag aggregate (SSA): (c) steel slag coarse aggregate, (d) close view of SSA; brick aggregate (BA): (e) brick coarse aggregate, (f) close view of BA.

The steel slag boulders were manually crushed to smaller sizes to be used as coarse aggregate in concrete (see Figure 1c). Similarly, the first-class burnt clay bricks were collected from the local market and then crushed into coarse aggregate (CA) (see Figure 1e). Thereafter, the slag and brick aggregates were sieved in the laboratory using the ASTM C136 standard sieves [19] and compared with the upper and lower limits recommended in the ASTM C33 standard [20]. To avoid the effect of grading on the mechanical and porosity performances of the concrete, similar gradation was used for both BA and SSA. The grading curves of coarse and fine aggregates are shown in Figure 2. For the physical properties of both BA and SSA, aggregates were tested for unit weight, voids, specific gravity, absorption capacity, and Los Angeles (LA) abrasion resistance as per ASTM standards. The aggregate

impact value, aggregate crushing value, angularity number, flakiness index, and elongation index were measured according to BS EN 1097-3:1998 [21].

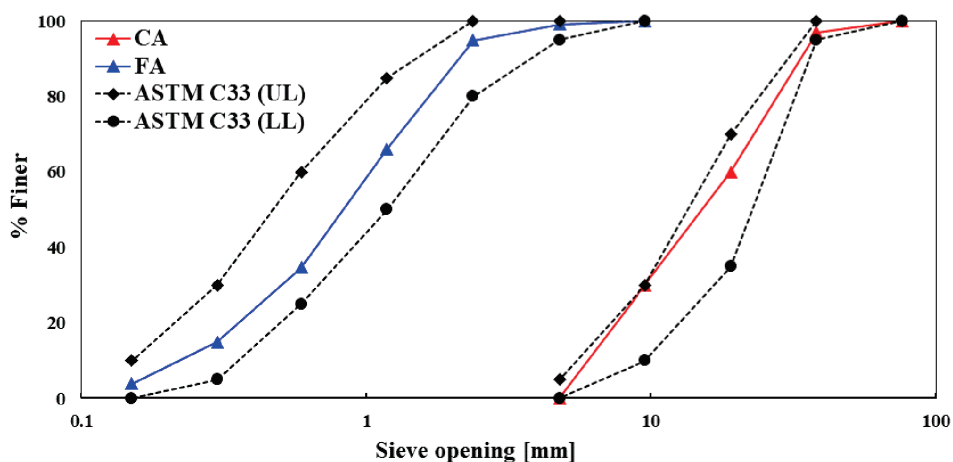


Figure 2. Grading curve of coarse aggregate (CA: BA and SSA) and fine aggregate (FA), and comparison with the upper limit (UL) and lower limit (LL) recommended in ASTM C33 standard [20].

The chemical composition of both BA and SSA was performed by using XRF analysis. The results of the XRF analyses are presented in Table 1. The SSA contains about 26% SiO₂, 44% Fe₂O₃, 4.9% Al₂O₃, and 4.9% CaO. By contrast, BA contains 60% SiO₂, 14% Fe₂O₃, 9.9% Al₂O₃, and 4.1% CaO. Indeed, the oxide percentage of steel slag or brick aggregates depends on the type, source, origin, and furnace systems. It can be seen that the Fe₂O₃ of SSA was quite higher than the BA, which could be responsible for the higher specific gravity and density of SSA (see Table 1).

Table 1. Chemical composition of brick and induction furnace steel slag.

Chemical Composition	BA (%)	SSA (%)
SiO ₂	60.43	26.18
Fe ₂ O ₃	14.27	44.39
Al ₂ O ₃	9.96	4.94
K ₂ O	5.23	0.56
CaO	4.18	4.94
TiO ₂	1.81	1.73
MgO	1.69	0.47
Na ₂ O	0.90	0.45
SO ₃	0.57	0.43
MnO	0.30	12.9
P ₂ O ₅	0.24	0.08
ZnO	0.10	2.33
ZrO ₂	0.05	0.11
SrO	0.05	0.09

2.1.2. Binder

CEM II cement was used as a binder for all mixes. The physical properties of cement such as normal consistency, initial and final setting time, as well as compressive strength were carried out as per ASTM C187 [22] ASTM C191 [23], and ASTM C109 [24], respectively. The physical and main constituents of cement are presented in Table 2.

Table 2. Physical and main constituents of cement.

Properties	Observed Values
Normal consistency (%)	27.50
Initial setting time (min)	110
Final setting time (min)	360
Compressive strength (MPa) at 3, 7, 14, and 28 days	15.20, 19.50, 25.80 and 31.74
Chemical composition:	
Clinker (%)	80–94
Slag and fly ash, limestone (%)	6–20
Gypsum (%)	0–5

2.2. Experimental Programs, Apparatus, and Test Procedures

All the concrete specimens were produced at constant water to cement ratio (w/c) of 0.45 and cement content of 350 kg/m³. The experimental programs were divided into two parts: mechanical properties and porosity tests. The SSA was used to replace BA at nine different replacement levels (0%, 10%, 20%, 30%, 40%, 50%, 60%, 80%, and 100% by volume of BA). Although no chemical treatment procedure was applied, the SSA was washed with tap water before use. The mixture proportions of the concrete mixes are summarized in Table 3. The workability of the concrete mixes was investigated by measuring the slump values of fresh concrete.

Table 3. Mixture proportion of concrete mixes (kg/m³).

Mix ID.	% SSA	% BA	Cement	Coarse Aggregate		Fine Aggregate	Water
				SSA	BA		
0% SSA	0	100	350	0	775	872	158
10% SSA	10	90	350	82	735	872	158
20% SSA	20	80	350	172	687	872	158
30% SSA	30	70	350	270	631	872	158
40% SSA	40	60	350	377	566	872	158
50% SSA	50	50	350	493	493	872	158
60% SSA	60	40	350	616	411	872	158
80% SSA	80	20	350	889	222	872	158
100% SSA	100	0	350	1196	0	872	158

In addition, the temperature of the fresh concrete mixes was measured at all replacement levels. Since SSA is the byproduct of the steelmaking industry, the rate of expansion (length change) of the hardened concrete was monitored. Specimens (three replicates each) from three concrete mixes containing 0%, 50%, and 100% (by volume of BA) SSA were used for the investigation of expansion. The measurement of the longitudinal deformation of the specimens was conducted at different ages according to the French standard, NF P18-454 [25], using prismatic specimens (70 mm × 70 mm × 280 mm) (see Figure 3). As a reference, the first value was taken right after 24 h of casting concrete samples. A high-accuracy digital dial gauge with a precision of 0.001 mm was used to monitor the longitudinal length change.

2.2.1. Mechanical Properties

A total of 216 cylindrical specimens (100 mm in diameter and 200 mm in length) for the nine different mixes was cast for compression and tensile (splitting) strength of the concrete mixes. Then, 24 h after casting, specimens were cured underwater (20 ± 2 °C) up to the day of the tests. The compressive and tensile strength tests were performed at 14, 28, 60, and 90 days to monitor the evolution of strength as per ASTM C39 [26] and ASTM 496 [27], respectively. During the compression test, the deformation of concrete specimens was measured by a strain measurement setup with dial gauges attached with an extensometer. The gauge length was 100 mm in the central part of the cylinder specimen.

Three specimens were used for each curing age and each mix of both compressive and splitting tensile strength tests, and then the average strength was calculated by the arithmetic mean of three specimens. Moreover, the dry density of concrete specimens was measured on the same specimens that were used for the mechanical tests. Finally, the fractured surfaces of the specimens after compression and tension tests were studied.



Figure 3. Measurement of concrete expansion made with 100% BA (a) and 100% SSA (b).

2.2.2. Porosity

The porosity of the concrete mixes was investigated using a technique based on water absorption porosity according to the French standard, NF P18-459 [28]. The porosity test was performed using concrete specimens of a quarter-cylinder, 104 mm in diameter and 50 mm in thickness (see Figure 4). To monitor the evolution of apparent porosity as a function of time, the porosity test was conducted at 14, 28, 60, and 90 days for all the mixes. Within the scope of the study, a total of 108 concrete specimens for the nine different mixes was tested. The porosity of concrete (in %) was calculated by measuring the mass of concrete specimens in three states of saturation: (i) mass of dry (M_{dry}) test specimen, (ii) apparent mass of immersed (M_{sat}^{imm}) test specimen, and (iii) mass of soaked (M_{sat}) test specimen. To do this, first, the specimens were dried in an oven at a temperature of $105\text{ }^{\circ}\text{C} \pm 5\text{ }^{\circ}\text{C}$ until a constant value of mass was reached, and the mass of the dry specimen was recorded. Then, the mass of the specimen was measured in a saturated state when it was immersed in water. In this stage, a vacuum pressure of 25 mbar was attained and maintained for 4 h. After that, the specimens were immersed in water for 24 h. Finally, the saturated specimens were removed from the water and a damp cloth was used to remove excess surface water. The mass of all specimens was measured, and the apparent porosity, P_a (%), was computed for the three states investigated according to Equation (1).

$$P_a = \frac{M_{sat} - M_{dry}}{M_{sat} - M_{sat}^{imm}} \quad (1)$$

where M_{dry} is the mass of dry test specimen, M_{sat}^{imm} is the apparent mass of immersed test specimen, and M_{sat} indicates the mass of the soaked test specimen.

2.2.3. Scanning Electron Microscopy (SEM)

Scanning electron microscopy (SEM) of the BA and SSA was performed to understand the pore structure and surface roughness of the aggregates. Indeed, pore structure and surface texture of the aggregates are very important for concrete since they influence the physical, mechanical, and durability performances of concrete. Furthermore, SEM observations were also carried out on the concrete

samples to detect possible cracking at the interface between BA/SSA and cement paste. Observed cracks could be correlated to the mechanical and durability performances of concrete made with these aggregates. All SEM tests were carried out using JEOL JSM-7600F Schottky Field Emission Scanning Electron Microscope. For the investigation of the interfacial transition zone (ITZ), completely dry concrete specimens were used, which had been polished with sandpaper and then submersed in ethanol solution.

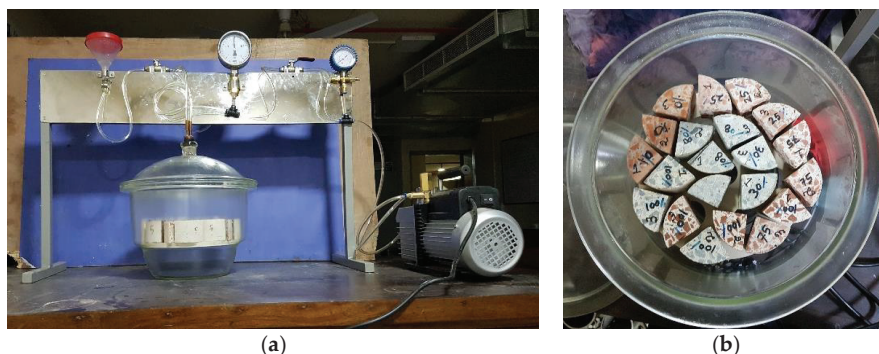


Figure 4. Test setup for porosity according to the French standard NF P18-459 [28] (a) and specimens for porosity test (b).

3. Experimental Results and Discussion

3.1. Physical Properties of Aggregates

The physical properties of the coarse and fine aggregates are summarized in Table 4. The specific gravity of the SSA was higher than the BA, which is believed to have been caused by its higher Fe_2O_3 content as shown in Table 1. Conversely, significantly lower values of LA abrasion, impact value, flakiness index, and elongation index were observed for SSA than BA, resulting in higher mechanical properties and durability of concrete made with SSA than BA (see Table 4). As regards the angularity number, SSA provides higher values than BA (9.13 for SSA and 11.20 for BA); therefore, on the one hand, SSA could reduce the workability of the concrete because of high stability due to better interlocking and friction. On the other hand, it could result in better ITZ between SSA and cement mortar, meaning higher strength and durability. Moreover, significantly lower absorption capacity was observed for SSA than BA (1% for SSA and 20% for BA). The lower absorption capacity of SSA could be explained by the impervious nature of SSA compared to BA, resulting in less permeable and durable concrete when SSA is used.

Table 4. Physical properties of coarse (SSA and BA) and fine (FA) aggregates.

Properties	BA	SSA	FA
Fineness modulus	6.35	6.35	2.92
*SSD unit weight (kg/m^3)	1120	1835	1530
Specific gravity in SSD condition	2.10	3.24	2.56
Absorption capacity (%)	20.00	1.00	3.10
Los Angeles (LA) abrasion (%)	42.70	19.40	-
Impact value (%)	28.10	8.95	-
Crushing value (%)	41.21	20.64	-
Angularity number	9.13	11.20	-
Flakiness index (%)	13.60	7.19	-
Elongation index (%)	40.67	24.19	-

Note: *SSD means saturated surface dry

3.2. Fresh Concrete Properties

The workability of different concrete mixes was evaluated by measuring the slump value of fresh concrete at the time of placing (Table 5). No segregation and bleeding were observed during and after the fresh concrete placement. It was observed that the concrete made with SSA had lower workability as compared to concrete made with BA. The slump values of concrete made with 0%, 50%, and 100% of SSA were 21.70 cm, 18.70 cm, and 16.20 cm, respectively. It was about 13% and 25% lower slump for concrete containing 50% and 100% SSA, respectively, as compared to concrete made with 100% BA. The visual observation of SSA shows that SSA was highly angular in shape with sharp edges and had a rougher surface texture than BA (see Figure 1d,f), resulting in the reduction of the flowability of concrete due to better interlocking in the mix. Similar results were found in the literature [7]. The reduction in the flowability could also be linked to the temperature of concrete at the time of placing. As shown in Table 5, as the temperature of the fresh concrete increases, the workability of the concrete decreases due to faster heat of hydration of cement paste. It was observed that the temperature of the fresh concrete at the time of placement was higher for SSA than BA.

Table 5. Slump and temperature of fresh concrete made with nine concrete mixes.

SSA	0%	10%	20%	30%	40%	50%	60%	80%	100%
Slump (cm)	21.70	20.40	21.00	20.90	19.50	18.70	18.30	16.90	16.20
Temperature (°C)	27.70	28.10	28.60	29.00	30.20	29.80	30.40	30.60	30.90

3.3. Concrete Expansion

The longitudinal expansion of concrete mixes as a function of time is presented in Figure 5. It was observed that the expansion of concrete made with 100% SSA was higher than the concrete made with 50% SSA and 0% SSA (100% BA). The average expansion of concrete made with 0% SSA, 50% SSA, and 100% SSA measured at 90 days was 0.012%, 0.014%, and 0.017%, respectively. These values of expansion of SSA concrete are consistent with the results found in previous studies [11,17,29]. The higher expansion of concrete made with SSA could be explained by the higher amount of calcium oxide (4.18% for BA and 4.94% for SSA, see Table 1). Several researchers reported that free calcium and magnesium oxides were the main reasons for the expansion of SSA concrete [11,17]. However, the expansion of SSA concrete was not significantly high as compared to BA concrete, which is consistent with the XRF results. In Table 1, it is reported that the calcium oxide content of SSA was very close to BA, while the magnesium oxide was much lower for SSA than BA (1.69 for BA and 0.47 for SSA, see Table 1). It is well-known that the expansion and cracking of concrete lead to loss of strength and slope of the stress–strain curve (i.e., modulus of elasticity). It should be noted that no cracking was observed at the ITZ of concrete made with SSA (see Section 3.7), and both compressive and tensile strength were also higher for SSA than BA, which is consistent with the expansion results.

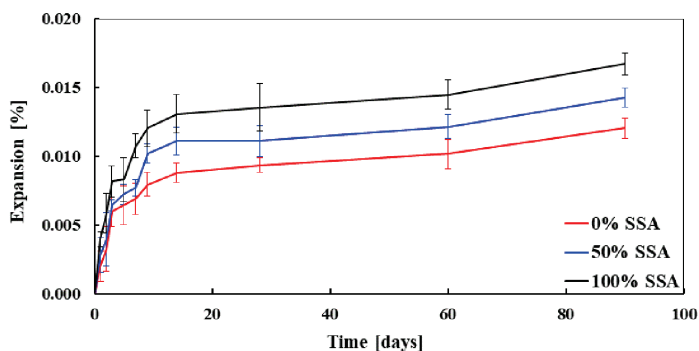


Figure 5. Longitudinal expansion of concrete mixes as a function of time.

3.4. Dry Density of Concrete Mixes

The dry density of concrete was measured on the same concrete cylinders that were used for the compressive strength tests. The average dry density and increase in dry density of hardened concrete are presented in Table 6. As expected, with an increase in the percentage replacement of BA by SSA, the density of hardened concrete also increases.

Table 6. The average dry density (ρ) and the increase in density of hardened concrete mixes.

Age	SSA	0%	10%	20%	30%	40%	50%	60%	80%	100%
14 days	ρ (Kg/m ³)	2078	2290	2405	2378	2429	2494	2540	2591	2633
	Increase (%)	0.00	10.20	15.80	14.50	16.90	20.0	22.30	24.70	26.70
28 days	ρ (Kg/m ³)	2132	2299	2351	2391	2439	2514	2555	2634	2668
	Increase (%)	0.00	7.90	10.30	12.20	14.40	18.00	19.90	23.60	25.20
60 days	ρ (Kg/m ³)	2117	2320	2373	2401	2465	2531	2571	2628	2691
	Increase (%)	0.00	9.60	12.10	13.40	16.40	19.60	21.50	24.20	27.10
90 days	ρ (Kg/m ³)	2145	2321	2385	2455	2487	2539	2595	2658	2724
	Increase (%)	0.00	8.20	11.20	14.50	15.90	18.40	21.00	23.90	27.00

The average density of concrete made with 0% SSA (100% BA), 50% SSA, and 100% SSA was 2132 kg/m³, 2514 kg/m³, and 2668 kg/m³, respectively, at 28 days and 2145 kg/m³, 2539 kg/m³, and 2724 kg/m³ accordingly at 90 days. The highest density was observed for the concrete made with 100% SSA, which was about 25–27% higher for all ages than the concrete made with 100% BA (without SSA). This higher density of concrete made with SSA is directly linked with the higher specific gravity (3.24 for SSA and 2.1 for BA, see Table 4) and better interlocking between SSA than BA. The higher density of concrete made with SSA was also reported by Adegoloye et al. [11].

3.5. Mechanical Properties

3.5.1. Stress–Strain Behavior of Concrete Mixes

The example of the stress–strain curves in compression of all concrete mixes performed at 28 days and 90 days is plotted in Figure 6. Although three specimens for each curing age and each mix were tested in compression, the curves presented in Figure 6 are the result of one specimen for each mix. The results show that the compressive strength and the modulus of elasticity increase with the increase of replacement percentage of BA by SSA. This behavior was more pronounced when the BA was fully replaced by SSA. The strain corresponding to the compressive strength decreases with the increase of compressive strength, especially for the concrete specimens made with a higher percentage of SSA (e.g., 80% and 100% SSA). This is attributed to higher stiffness and hardness of SSA than BA, which limits the deformation (i.e., cracking on the aggregate and at ITZ) of concrete. The results also indicate that the modulus of elasticity increases over time, which could be linked to the development of strength, porosity, and ITZ around the aggregates. A similar conclusion was drawn by Qasrawi [16].

3.5.2. Compressive Strength

The average compressive strength of concrete mixes measured at 14, 28, 60, and 90 days is reported in Figure 7a. It is clearly shown that the concrete made with SSA has significantly higher compressive strength at all curing ages as compared to 100% BA, and this behavior was more pronounced at later ages. It is noteworthy that none of the concrete specimens made with SSA shows lower strength in compression as compared to that of 100% BA. For example, the average compressive strength of concrete made with 0%, 50%, and 100% SSA was 22.24 MPa, 32.63 MPa, and 34.98 MPa at 28 days, respectively, and 28.03 MPa, 32.18 MPa, and 48.00 MPa at 90 days accordingly (see Figure 7a and

Table 7). The increase in the compressive strength of concrete mixes made with the nine different percentage replacements of BA by SSA for all curing ages was in the range of 10% to 70% of the strength of BA (see Figure 7b). The higher compressive strength of concrete made with SSA could be attributed to higher aggregate strength (LA abrasion: 19.4% for SSA and 42.7% for BA), higher crushing and impact resistance, impervious nature (i.e., lower porosity, see Figure 1d), higher angularity (angularity number: 11.20 for SSA and 9.13 for BA), and stronger bond with cement paste of SSA than BA.

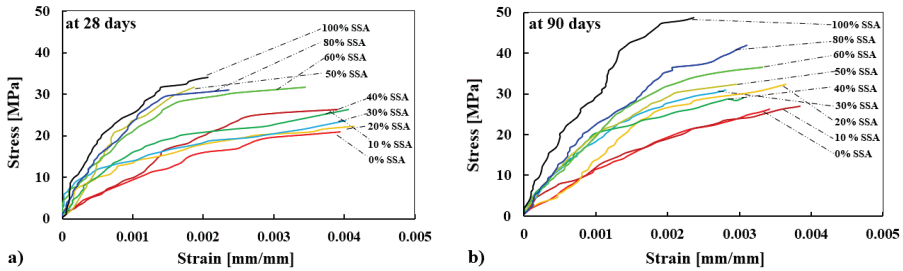


Figure 6. Stress–strain curves of concrete made with SSA measured at 28 days (a) and 90 days (b).

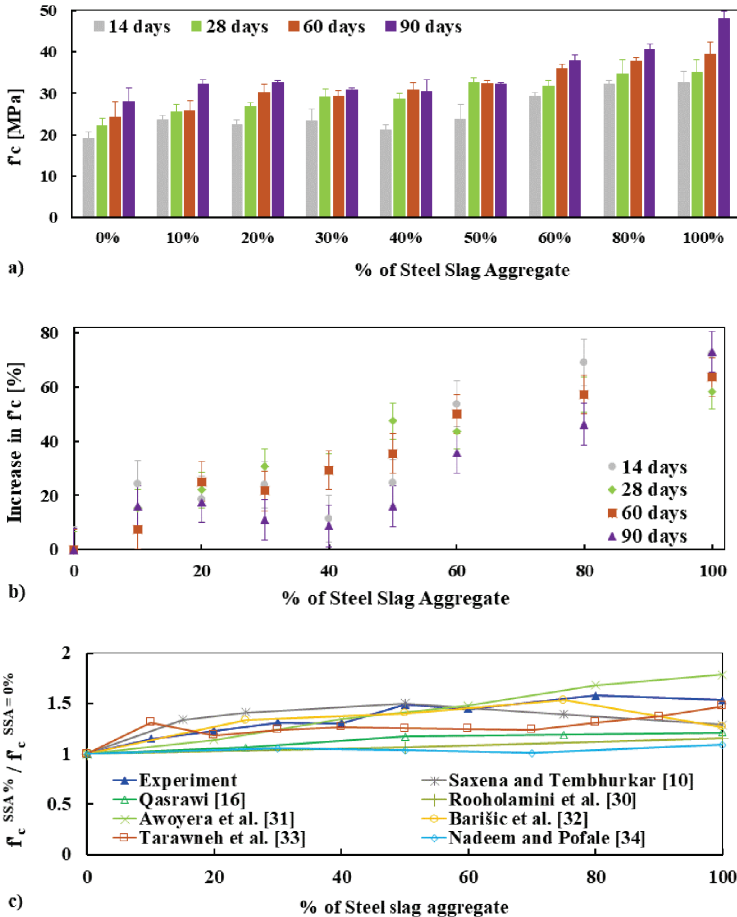


Figure 7. Compressive strength f'_c (a), an increase in f'_c as a function of SSA (b), and normalized f'_c of concrete mixes measured at 28 days were compared with other results found in the literature (c), respectively.

Table 7. The average compressive strength (f'_c) and coefficient of variation (CoV) of concrete.

Age	SSA	0%	10%	20%	30%	40%	50%	60%	80%	100%
14 days	f'_c (MPa)	19.08	23.60	22.47	23.37	21.11	23.82	29.24	32.09	32.63
	CoV (%)	8.94	4.98	4.61	11.72	6.68	14.60	3.35	2.88	8.39
28 days	f'_c (MPa)	22.24	25.63	26.98	29.02	28.57	32.63	31.73	34.67	34.98
	CoV (%)	8.06	7.00	2.51	7.01	4.94	3.17	4.27	9.84	9.03
60 days	f'_c (MPa)	24.30	25.85	30.15	29.24	30.83	32.41	36.02	37.60	39.41
	CoV (%)	15.13	9.21	6.87	4.82	5.53	2.09	2.87	2.75	7.16
90 days	f'_c (MPa)	28.03	32.18	32.63	30.83	30.37	32.18	37.83	40.54	47.99
	CoV (%)	11.63	3.22	1.20	1.27	9.73	1.22	3.58	3.34	3.74

By visual inspection it was observed that the SSA was highly angular in shape, had higher rough surface texture and lower flaky particles than the BA, which is the key feature to a stronger bond between the aggregate and cement paste in the concrete matrix. These results are consistent with the results available in existing studies [11]. For a uniaxially loaded concrete, on the one hand, the micro-cracks and cracks are open parallel to the applied loading direction; on the other hand, it decreases the crack opening that is perpendicular to the load [30,31]. Generally, the cracks are more pronounced for weak ITZ and weak aggregate. Therefore, the cracks were higher in BA concrete than SSA due to its softer and porousness behavior, thus providing a weak ITZ and then lower strength. Moreover, significant lower porosity was observed for the concrete made with SSA than BA (see Section 3.6), which could also explain the higher strength of SSA concrete.

The analysis of the fractured surfaces of concrete specimens after compressive strength tests shows that the failure plane passes through the SSA (see Figure 8a) and cement mortar (i.e., combined failure). This failure pattern confirmed the stronger bond between the aggregate and cement paste. Though a similar failure pattern was observed for the concrete made with BA (see Figure 8b), the relatively low strength, higher porosity, and flakier particles of BA than SSA restricted the concrete to gain higher strength.

To gain a deeper understanding of the role of different percentage replacement of BA by SSA on the compressive strength of concrete, normalized compressive strength at 28 days was calculated by dividing the 100% BA (SSA = 0%) concrete (i.e., $f'_c{}^{SSA\%} / f'_c{}^{SSA=0\%}$) and comparing it with the results found in the literature [10,16,32–36] (see Figure 7c). It was observed that the experimental results are in good agreement with the results found in the literature. Most of the researchers found similarities with this experimental work. Hence, it implies that without compromising the compressive strength, 100% BA can be replaced by SSA in concrete.

3.5.3. Tensile strength of Concrete Mixes

The splitting tensile strength of concrete mixes made with different percentage replacements of BA by SSA is presented in Figure 9a.

It is seen that the tensile strength increases with the increasing percentage of SSA for all curing ages, which is in good agreement with the results of the compressive strength as discussed in Section 3.5.2. The splitting tensile strength of the concrete made with 100% BA (0% SSA) and 100% SSA was 2.00 MPa and 3.40 MPa, respectively, at 28 days and 2.50 MPa and 4.00 MPa accordingly at 90 days (see Table 8). The increased strength in tension of all concrete mixes made with the nine different percentage replacements of BA by SSA for all curing ages was in the range of 15% to 73% of the tensile strength of BA (see Figure 9b), which is almost similar to the strength increase in compression (see Figure 7b). These results are consistent with the results available in the existing studies [29,32–34,36]. Figure 9c presents the normalized splitting tensile strength at 28 days of all concrete mixes and compares with the

results found in the literature. It shows that splitting tensile strength was increased with the increased amount of SSA and the results are consistent with the literature.

As described briefly in Section 3.5.2, this higher tensile strength of concrete made with SSA could be linked to the higher strength, higher angularity, and excellent surface roughness of SSA than the BA, which ensured strong ITZ around the SSA than the BA. It is noted that the combined (cement mortar and aggregate) failure occurs for both SSA and BA concrete, which shows good adherence and cohesion between aggregates and cement mortar (see Figure 8c,d). As mentioned earlier, the lower tensile strength of BA concrete could be attributed to the relatively softer and more porous behavior of BA than SSA. In addition, SEM observations show that BA has more cracks on the aggregate as well as at the ITZ, while no cracking of this type was observed for SSA, which could be another reason for lower tensile and compressive strength of concrete made with BA than SSA (see Section 3.7).

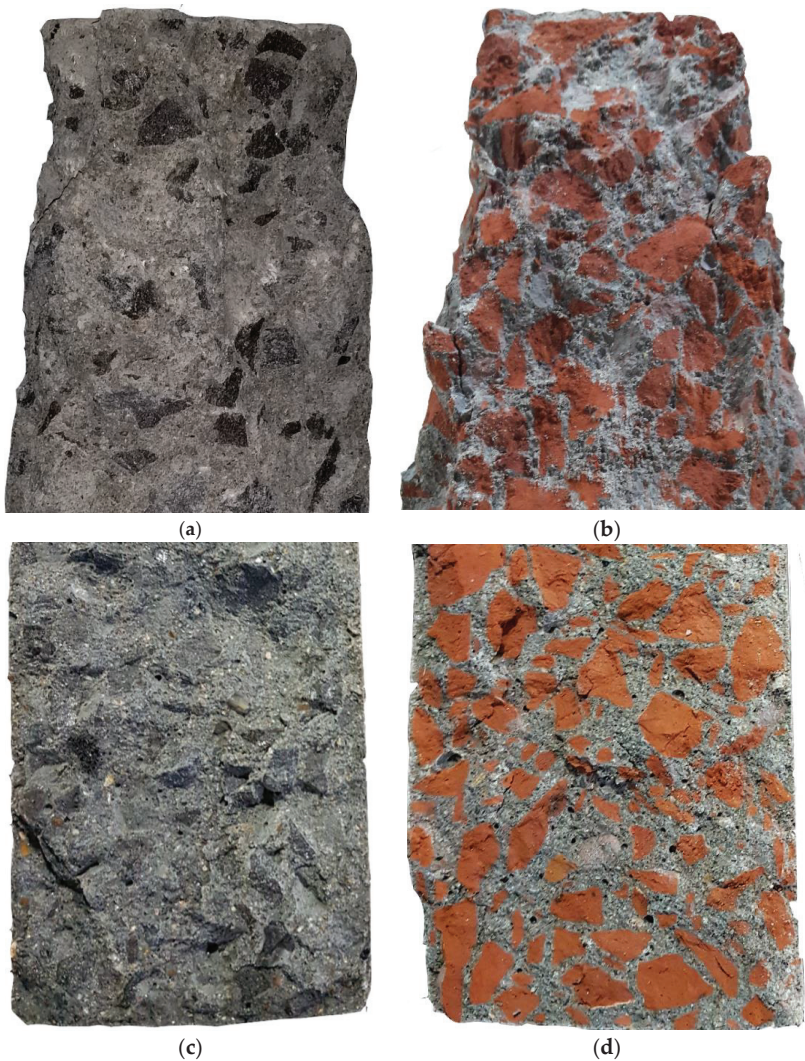


Figure 8. Fracture surface after compressive strength test of SSA concrete (a) BA concrete (b) and splitting tensile strength test of SSA concrete (c) and BA concrete (d) samples.

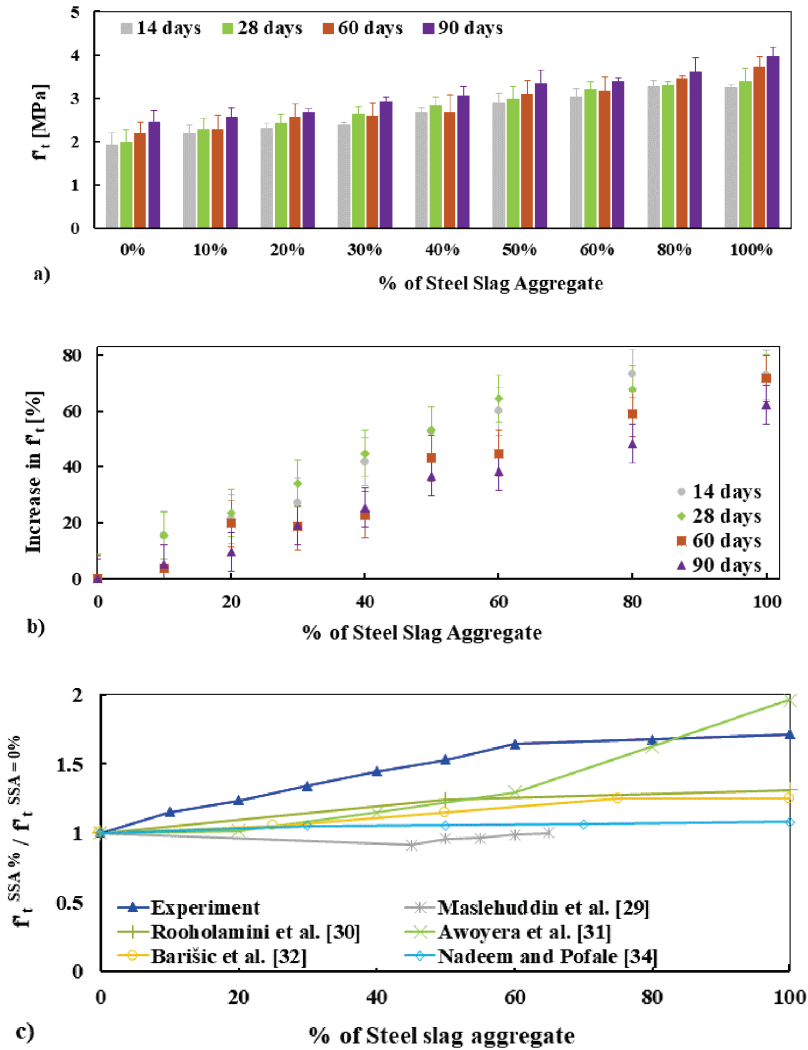


Figure 9. Tensile (splitting) strength: f'_t (a) and an increase in f'_t as a function of SSA (b), and normalized f'_t of concrete mixes measured at 28 days compared with other results found in the literature (c).

Table 8. The average tensile strength (f'_t) and coefficient of variation (CoV) of concrete.

Age	SSA	0%	10%	20%	30%	40%	50%	60%	80%	100%
14 days	f'_t (MPa)	1.91	2.19	2.29	2.39	2.67	2.90	3.02	3.27	3.26
	CoV (%)	15.28	9.48	6.36	2.31	4.29	7.21	6.40	4.39	1.49
28 days	f'_t (MPa)	1.98	2.28	2.42	2.63	2.83	2.99	3.21	3.29	3.38
	CoV (%)	14.56	11.70	8.63	6.88	7.02	9.09	5.51	2.79	9.04
60 days	f'_t (MPa)	2.19	2.27	2.57	2.59	2.68	3.10	3.15	3.44	3.72
	CoV (%)	11.68	14.99	12.04	12.13	14.83	9.55	10.64	2.45	6.45
90 days	f'_t (MPa)	2.46	2.56	2.67	2.91	3.06	3.33	3.38	3.61	3.96
	CoV (%)	10.04	8.83	3.57	3.85	6.83	9.43	2.37	9.18	5.71

3.6. Porosity of Concrete Mixes

To gain an understanding of the pore volume of the concrete mixes and the role played by SSA, the total porosity of concrete was measured by means of water absorption porosimetry, as reported in Figure 10a. It is seen that the porosity of the concrete mixes decreases for all ages with increasing percentage replacement of BA by SSA, see Figure 10b. This lower porosity of concrete made with SSA than BA is consistent with the higher compressive and tensile strength of concrete. The apparent porosity of the concrete made with 100% BA and 100% SSA was 30.20% and 18.30%, respectively, at 28 days and 23.40% and 12.60%, accordingly, at 90 days. The maximum decrease in porosity was observed for 100% SSA concrete, which was about 34%, 39%, 44.5%, and 45.8% at 14, 28, 60, and 90 days, respectively, lower than 100% BA concrete (see Figure 10b). This lower porosity of SSA concrete could be attributed to the dense microstructure (i.e., stronger due to lower LA abrasion, see Table 4) and lower voids (lower permeable and impermeable pores and lower connectivity of pores, see Figure 1d) of SSA than BA.

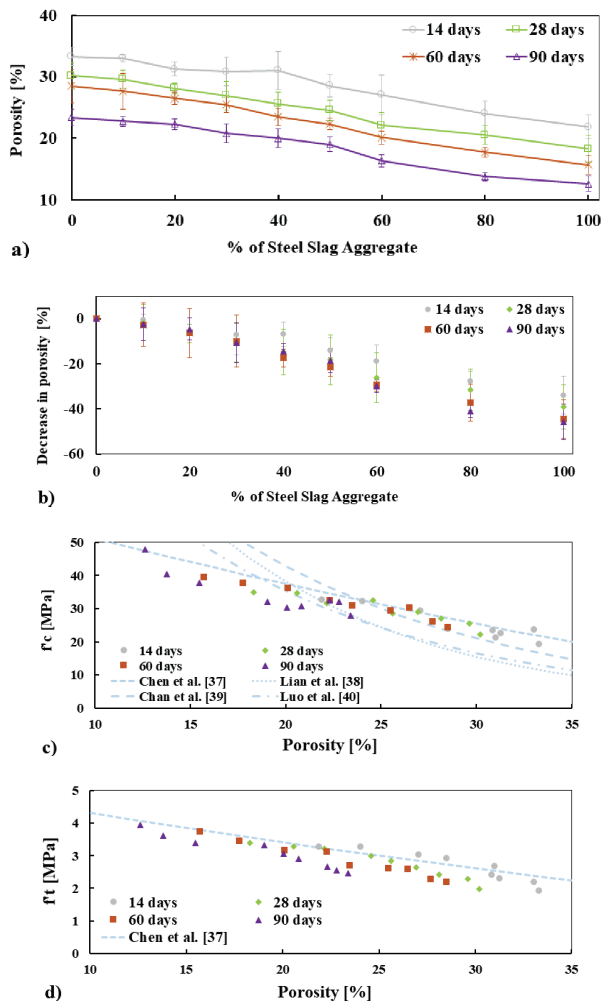


Figure 10. Apparent porosity (a), decrease in apparent porosity as a function of SSA (b), and the relation between f'_c and f'_t compared with different models/exponential relationships available in the literature (c,d), respectively.

It is well-known that porosity and permeability have a direct link [31]. Though permeability of concrete was not measured in this study, the lower porosity and better ITZ of SSA concrete imply that the permeability of SSA concrete could be lower, which could be an indication of higher durability. The relationship between porosity and both compressive and tensile strength of the concrete mixes are plotted in Figure 10c,d. The experimentally measured compressive and tensile strength of concrete mixes were compared with models/exponential relationships available in the literature [37–40]. As expected, as the porosity increases, the compressive strength decreases. It is noted that the relation between both compressive and tensile strength with the porosity of the concrete mixes for all ages are in agreement with the relationships presented in the literature (see Figure 10c,d). This relation implies that the measurement of both compressive strength and porosity are quite satisfactory.

3.7. Scanning Electron Microscopy (SEM) Analysis

The microstructure of concrete and aggregate is very important since it influences the mechanical and durability performances of concrete. The images captured by SEM analysis of SSA and BA are shown in Figure 11a,b. It is shown that the SSA was denser (i.e., strong), had a highly rough surface texture, and less voids than BA. This higher surface roughness is an important factor that affects the bonding between aggregate and cement paste (i.e., ITZ). SEM images of BA showed that it has more voids and internal cracks (see Figure 11b), while no cracking of this type was observed in SSA. These higher voids and cracks of BA affect the global strength and durability of concrete, which is in good agreement with the lower strength and higher porosity of concrete made with BA than SSA.

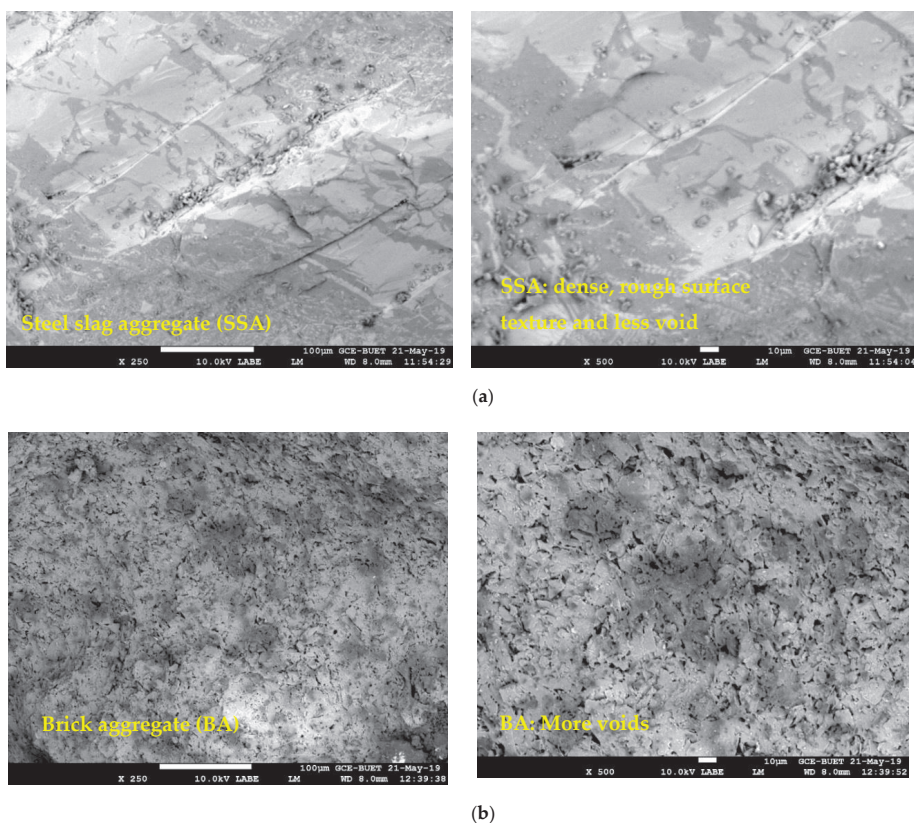


Figure 11. Cont.

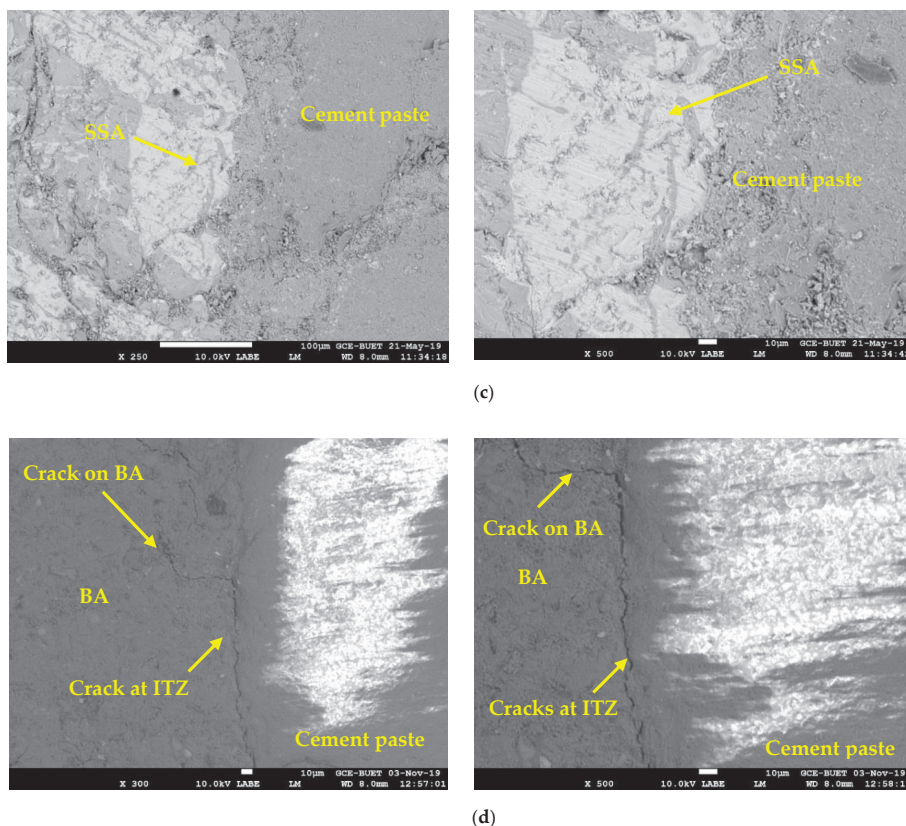


Figure 11. SEM images of SSA (a), BA (b), interfacial transition zone (ITZ) of concrete made with SSA (c) and ITZ of concrete made with BA (d), respectively.

To relate strength performance and possible cracks in the concrete, SEM observations were carried out on concrete samples made with 100% SSA and 100% BA at the interface between the aggregates (SSA and BA) and cement paste. The SEM images at the ITZ for both concrete mixes are presented in Figure 11c,d. A clear dense ITZ was observed around the SSA (see Figure 11c), which could be attributed to the rough surface texture of SSA (improving the bond between cement paste and SSA) that ensures better mechanical and higher durability of concrete. In contrast, it should be noted that more clear cracking through the BA and at the ITZ and more voids (see Figure 11b) are visible in BA concrete, which has a significant effect on the global strength and durability of the concrete. The cracking in the ITZ of cement paste and BA can be explained in two ways. Firstly, the compressive strength of BA is lower than the cement paste. Typically, BA has a compressive strength of about 20 MPa, and under the compression loading test, BA reaches its ultimate load capacity level before the cement paste. Thus, the cracks can be formed in the ITZ. Lastly, the higher water absorption capacity of BA can create a weak ITZ by absorbing water from its surrounding cement paste, which may increase the unhydrated binders in BA concrete. Therefore, under the compression load, these unhydrated binders can also lead to the cracking in the ITZ. Nevertheless, these cracks and voids should be the main reason for lower compressive and tensile strength as well as higher porosity of concrete made with BA than SSA.

4. Concluding Remarks

In this paper, the effect of steel slag aggregate (SSA) as a substitute for conventionally used brick aggregate (BA) on the physical, mechanical, and durability (i.e., porosity) performances of concretes was investigated. It is worth noting, however, that many studies have been conducted on the mechanical properties of concrete, while comparatively, few published data are available on the durability (e.g., porosity) as well as length change. To this end, nine concrete mixes made with different percentage replacements of BA by SSA were studied. The main findings of the influence of SSA on the physical, mechanical, and porosity of concrete can be summarized as follows:

- I. The use of SSA as a replacement for BA in concrete shows significantly higher compressive and tensile strength, which was 73% higher when BA was fully replaced by SSA.
- II. Lower workability was noticed for the concrete made with SSA than BA, which could be attributed to the higher rough surface texture and higher angularity of SSA than BA as well as better interlocking, which reduces the mobility of fresh concrete.
- III. The concrete made with SSA exhibited higher expansion than the concrete made BA.
- IV. A significantly lower porosity was observed for the concrete made with SSA than BA. The maximum decrease in porosity was observed when BA was fully replaced by SSA, and the decrease was 45.80% lower than BA concrete.
- V. A satisfactory relationship between strength (compressive and tensile) and porosity was observed, which is consistent with the literature.
- VI. SEM images showed that SSA was denser and has a stronger ITZ, which leads to the higher strength of concrete. By contrast, BA has more voids and cracks on aggregate as well as at the ITZ, which explains the lower strength of this concrete.
- VII. From the experimental results of the nine mixes, this study reveals that SSA can be used as a full replacement for BA since SSA is denser, less porous, higher angularity, and has excellent surface roughness, which provides better mechanical and durability performances. Furthermore, SSA concrete provides environmental solutions by reducing the dumping problem, economical, conservation of natural aggregate, and sustainable green construction material since burning brick produces a lot of CO₂.

Future research should focus on utilizing other industrial by products and sustainable technologies such as 3D concrete printing [41–43] without compromising the mechanical properties required for civil applications.

Author Contributions: M.J.M. conceptualization, methodology, analysis, experiment, writing—original draft; M.M.H.P. experiment; S.C.P., A.J.B., and B.P. writing—reviewing the manuscript. All authors have read and agreed to the published version of the manuscript.

Funding: This research did not receive any specific grant from funding agencies in the public, commercial, or not-for-profit sectors.

Acknowledgments: The authors acknowledge funding and facilities provided by the Institute for Energy, Environment, Research and Development (IEERD) and Department of Civil Engineering, UAP to undertake this research. A special thanks also to undergraduate candidates, Md. Ashraful Alam, Taukir Ahmed Shamim, and Mst. Anisa Sultana to the fulfillment of the requirements of their B.Sc. degree.

Conflicts of Interest: The authors declare no conflicts of interest.

References

1. Domone, P.; Illston, J. *Construction Materials: Their Nature and Behaviour*, 4th ed.; Spon Press 270 Madison Avenue: New York, NY, USA, 2010.
2. Mehta, P.K.; Monteiro, P.J. *Concrete Microstructure, Properties and Materials*; McGraw-Hill: New York, NY, USA, 2006.
3. Miah, M.J.; Miah, M.S.; Alam, W.B.; Lo Monte, F.; Li, Y. Strengthening of RC beams by ferrocement made with unconventional concrete. *Mag. Civ. Eng.* **2019**, *89*, 94–105.

4. Khern, Y.C.; Paul, S.C.; Kong, S.Y.; Babafemi, A.J.; Anggraini, V.; Miah, M.J.; Šavija, B. Impact of chemically treated waste rubber tire aggregates on mechanical, durability and thermal properties of concrete. *Front. Mater.* **2020**, *7*, 90. [CrossRef]
5. Miah, M.J.; Ali, M.K.; Paul, S.C.; Babafemi, A.J.; Kong, S.Y.; Šavija, B. Effect of recycled iron powder as fine aggregate on the mechanical, durability, and high temperature behavior of mortars. *Materials* **2020**, *13*, 1168. [CrossRef]
6. Miah, M.J.; Ali, M.K.; Paul, S.C.; Miah, M.S.; Haque, M.M.; Islam, M.S.; Islam, M.R. Impact of partial replacement of brick coarse aggregate by waste rubber tyre on the fresh and hardened properties of concrete. Key Engineering Materials (Accepted). ISSN: 1662-9795. In Proceedings of the 11th International Conference on Material and Manufacturing Technology (ICMMT 2020), Bangkok, Thailand, 24–26 April 2020.
7. Jiang, Y.; Ling, T.-C.; Shi, C.; Pan, S.-Y. Characteristics of steel slags and their use in cement and concrete—A review. *Resour. Conserv. Recycl.* **2018**, *136*, 187–197. [CrossRef]
8. Roychand, R.; Pramanik, B.K.; Zhang, G.; Setunge, S. Recycling steel slag from municipal wastewater treatment plants into concrete applications – A step towards circular economy. *Resour. Conserv. Recycl.* **2020**, *152*, 104533. [CrossRef]
9. San-José, J.T.; Vegas, I.; Arribas, I.; Marcos, I. The performance of steel-making slag concretes in the hardened state. *Mater. Des.* **2014**, *60*, 612–619. [CrossRef]
10. Saxena, S.; Tembhurkar, A.R. Impact of use of steel slag as coarse aggregate and wastewater on fresh and hardened properties of concrete. *Constr. Build. Mater.* **2018**, *165*, 126–137. [CrossRef]
11. Adegloye, G.; Beaucour, A.L.; Ortola, S.; Noumowé, A. Concretes made of EAF slag and AOD slag aggregates from stainless steel process: Mechanical properties and durability. *Constr. Build. Mater.* **2015**, *76*, 313–321. [CrossRef]
12. Netinger, I.; Bjegovic, D.; Vrhovac, G. Utilisation of steel slag as an aggregate in concrete. *Mater. Struct.* **2011**, *44*, 1565–1575. [CrossRef]
13. Pang, B.; Zhou, Z.; Xu, H. Utilization of carbonated and granulated steel slag aggregate in concrete. *Constr. Build. Mater.* **2015**, *84*, 454–467. [CrossRef]
14. Abu-Eishah, S.I.; El-Dieb, A.S.; Bedir, M.S. Performance of concrete mixtures made with electric arc furnace (EAF) steel slag aggregate produced in the Arabian Gulf region. *Constr. Build. Mater.* **2012**, *34*, 249–256. [CrossRef]
15. Qasrawi, H. Fresh properties of green SCC made with recycled steel slag coarse aggregate under normal and hot weather. *J. Clean. Prod.* **2018**, *204*, 980–991. [CrossRef]
16. Qasrawi, H. The use of steel slag aggregate to enhance the mechanical properties of recycled aggregate concrete and retain the environment. *Constr. Build. Mater.* **2014**, *54*, 298–304. [CrossRef]
17. Sheen, Y.-N.; Le, D.-H.; Sun, T.-H. Innovative usages of stainless steel slags in developing self-compacting concrete. *Constr. Build. Mater.* **2015**, *101*, 268–276. [CrossRef]
18. Saeed, T.; Miah, M.J.; Khan, T.; Ove, A. Pollutant removal employing tidal flow constructed wetlands: Media and feeding strategies. *Chem. Eng. J.* **2020**, *382*, 122874. [CrossRef]
19. ASTM. C136/C136M-14. *Standard Test Method for Sieve Analysis of Fine and Coarse Aggregates*; ASTM International: West Conshohocken, PA, USA, 2014.
20. ASTM. C33/C33M-18. *Standard Specification for Concrete Aggregates*; ASTM International: West Conshohocken, PA, USA, 2018.
21. BS EN 1097-3:1998. *Tests for Mechanical and Physical Properties of Aggregates—Determination of Loose Bulk Density and Voids*; British Standard Institutions: London, UK, 1998.
22. ASTM. C187-16. *Standard Test Method for Amount of Water Required for Normal Consistency of Hydraulic Cement Paste*; ASTM International: West Conshohocken, PA, USA, 2016.
23. ASTM. C191-19. *Standard Test Methods for Time of Setting of Hydraulic Cement by Vicat Needle*; ASTM International: West Conshohocken, PA, USA, 2019.
24. ASTM. C109/C109M-16a. *Standard Test Method for Compressive Strength of Hydraulic Cement Mortars (Using 2-in. or [50-mm] Cube Specimens)*; ASTM International: West Conshohocken, PA, USA, 2016.
25. NFP. 18-454. *Béton—Réactivité D'une Formule de Béton Vis-à-Vis de L'alcali-Réaction—Essai de Performance*; AFNOR: La Plaine, French, December 2004.
26. ASTM. C39/C39M-18. *Standard Test Method for Compressive Strength of Cylindrical Concrete Specimens*; ASTM International: West Conshohocken, PA, USA, 2018.

27. ASTM. C496/C496M-17. *Standard Test Method for Splitting Tensile Strength of Cylindrical Concrete Specimens*; ASTM International: West Conshohocken, PA, USA, 2017.
28. NFP. 18-459. *Essai Pour Béton durci-Essai De Porosité et De Masse Volumique*; AFNOR: La Plaine, France, 2010.
29. Maslehuddin, M.; Sharif, A.M.; Shameem, M.; Ibrahim, M.; Barry, M.S. Comparison of properties of steel slag and crushed limestone aggregate concretes. *Constr. Build. Mater.* **2003**, *17*, 105–112. [CrossRef]
30. Miah, M.J.; Kallel, H.; Carré, H.; Pimienta, P.; La Borderie, C. The effect of compressive loading on the residual gas permeability of concrete. *Constr. Build. Mater.* **2019**, *217*, 12–19. [CrossRef]
31. Miah, M.J. The Effect of Compressive Loading and Cement Type on the Fire Spalling Behaviour of Concrete. Ph.D. Thesis, Université de Pau et des Pays de l'Adour, Pau, France, 19 October 2017.
32. Rooholamini, H.; Sedghi, R.; Ghobadipour, B.; Adresi, M. Effect of electric arc furnace steel slag on the mechanical and fracture properties of roller-compacted concrete. *Constr. Build. Mater.* **2019**, *211*, 88–98. [CrossRef]
33. Awoyera, P.O.; Olofinnade, O.M.; Busari, A.A.; Akinwumi, I.I.; Oyefesobi, M.; Ikemefuna, M. Performance of steel slag aggregate concrete with varied water-cement ratio. *J. Teknol. (Sci. Eng.)* **2016**, *78*, 125–131. [CrossRef]
34. Barišić, I.; Dimter, S.; Rukavina, T. Strength properties of steel slag stabilized mixes. *Compos. Part B* **2014**, *58*, 386–391. [CrossRef]
35. Tarawneh, S.A.; Gharaibeh, E.A.; Saraireh, F.M. Effect of using steel slag aggregate on mechanical properties of concrete. *Am. J. Appl. Sci.* **2014**, *11*, 700–706. [CrossRef]
36. Nadeem, M.; Pofale, A.D. Utilization of industrial waste slag as aggregate in concrete applications by adopting taguchi's approach for optimization. *Open J. Civ. Eng.* **2012**, *2*, 96–105. [CrossRef]
37. Chen, X.; Wu, S.; Zhou, J. Influence of porosity on compressive and tensile strength of cement mortar. *Constr. Build. Mater.* **2013**, *40*, 869–874. [CrossRef]
38. Lian, C.; Zhuge, Y.; Beecham, S. The relationship between porosity and strength for porous concrete. *Constr. Build. Mater.* **2011**, *25*, 4294–4298. [CrossRef]
39. Chan, Y.N.; Luo, X.; Sun, W. Compressive strength and pore structure of high-performance concrete after exposure to high temperature up to 800 °C. *Cem. Concr. Res.* **2000**, *30*, 247–251. [CrossRef]
40. Luo, X.; Sun, W.; Chan, S.Y.N. Effect of heating and cooling regimes on residual strength and microstructure of normal strength and high-performance concrete. *Cem. Concr. Res.* **2000**, *30*, 379–383. [CrossRef]
41. Paul, S.C.; Tay, Y.W.D.; Panda, B.; Tan, M.J. Fresh and hardened properties of 3D printable cementitious materials for building and construction. *Arch. Civ. Mech. Eng.* **2018**, *18*, 311–319. [CrossRef]
42. Panda, B.; Singh, G.B.; Unluer, C.; Tan, M.J. Synthesis and characterization of one-part geopolymers for extrusion based 3D concrete printing. *J. Clean. Prod.* **2019**, *220*, 610–619. [CrossRef]
43. Panda, B.; Noor Mohamed, N.A.; Paul, S.C.; Bhagath Singh, G.V.P.; Tan, M.J.; Šavija, B. The effect of material fresh properties and process parameters on buildability and interlayer adhesion of 3D printed concrete. *Materials* **2019**, *12*, 2149. [CrossRef]



© 2020 by the authors. Licensee MDPI, Basel, Switzerland. This article is an open access article distributed under the terms and conditions of the Creative Commons Attribution (CC BY) license (<http://creativecommons.org/licenses/by/4.0/>).

Article

Physical Properties and Microstructure of Concrete with Waste Basalt Powder Addition

Magdalena Dobiszewska ^{1,*} and Ahmet Beycioğlu ²

¹ Faculty of Civil and Environmental Engineering and Architecture, UTP University of Science and Technology in Bydgoszcz, 85-304 Bydgoszcz, Poland

² Construction and Building Materials Division, AAT Science and Technology University, 01250 Adana, Turkey; abeycioglu@gmail.com

* Correspondence: magdalena.dobiszewsak@utp.edu.pl

Received: 14 June 2020; Accepted: 3 August 2020; Published: 8 August 2020

Abstract: The natural aggregates are one of the main components in the production of concrete. Although deposits of natural aggregates lie on the earth's surface or at low depths and belong to common deposits, the shortage of aggregate, especially natural sand, is presently observed in many countries. In such a situation, one is looking for other materials that can be used as a substitute for natural aggregates in mortars and concrete production. This paper presents the results of an experimental investigation carried out to evaluate the potential usage of waste basalt powder in concrete production. For this purpose, the waste basalt powder, which is a by-product of the production of mineral–asphalt mixtures, was substituted with 10%, 20%, and 30% sand replacement. In the experimental program, the workability, compressive strength, water transport properties, and microstructural performances were evaluated. The results showed that the production of concretes that feature a strong internal structure with decreased water transport behavior is possible with waste basalt usage. Furthermore, when waste basalt powder is used as a partial sand replacement, the compressive strength of concretes can be increased up to 25%. According to the microstructural analyses, the presence of basalt powder in concrete mixes is beneficial for cement hydration products, and basalt powder substituted concretes have lower porosity within the interfacial transition zone.

Keywords: concrete; waste basalt powder; compressive strength; water absorption; permeability; microstructure

1. Introduction

The economic development of the country is reflected, among other things, in the increasing demand for construction projects, and thus the increased production of construction materials. As a result, the demand for materials for construction projects is constantly growing, and the limitations resulting from the need to protect the environment significantly reduce the range of natural resource deposits that can be used for their production. Currently, the most frequently used building materials in the world are cement composites, among which the dominant role is played by structural concrete. One of natural raw materials used in the production of cement composites are natural aggregates.

The production and utilization of aggregates in Europe is about 4 billion tons per year, most of which, i.e., 91% comes from natural deposits [1]. Although deposits of natural aggregates lie on the earth's surface or at low depths and belong to common deposits, the shortage of aggregate, especially natural sand, is presently observed in many countries. There are also great problems with obtaining new deposits of natural resources despite relatively large geological resources of aggregate deposits. For example, the documented balance resources of natural aggregates in Poland are relatively large. However, based on the much smaller amount of industrial resources, the gravel-sand aggregate reserve is estimated to be only 18 years, and the broken and block stone reserve is estimated to be

only 42 years [2]. Due to resource losses, these numbers may be further reduced by 20–30% [3]. The establishment of the Natura 2000 European network of protected areas has resulted in more than 900 documented deposits, including about 500 exploited rock deposits, located in these areas in Poland. The need to comply with the principles of the EU Habitats Directive causes the reduction of approximately 35% of current extraction capacity [4].

In such a situation, one is looking for other materials that can be used as a substitute for natural aggregates in mortars and concrete production. As a partial substitute of fine aggregate, i.e., sand, the blast furnace slag and fly ash can be used. For this, there are many experimental studies available in the literature.

Bilir [5] investigated the effect of non-ground coal bottom ash and non-ground granulated blast furnace slag on the permeability properties of concretes. Rashad [6] reviewed more than 40 studies in the literature in the past 15 years before 2015, and he stated that the blast furnace slag and copper slag can be used as a partial/full replacement of natural fine aggregate in mortar and concrete. Yuksel and Genc [7] investigated the possibility of using granulated blast-furnace slag, furnace bottom ash, and their combination as fine aggregates in concrete. They used these powder materials without applying any preprocesses such as sieving and grinding, and they reported that concrete strength decreases with increasing replacement ratio with respect to reference concrete.

Bilir et al. [8] reported that the usage of a high volume of fly ash (at the ratio of 60–70%) as fine aggregate without causing significant changes on the properties of mortars is possible. Ravina [9] utilized a large quantity of Class F fly ash in structural concrete as a partial fine sand replacement and found that the fly ash has a good effect on the compressive strength, particularly at a later age. Besides, the author mentioned that the maximum penetration depth of water under the pressure of fly ash substituted mixtures is smaller than that of the reference mix. Siddique [10] substituted the class F fly ash with 10%, 20%, 30%, 40%, and 50% partial sand replacement, and he determined the compressive strength, splitting tensile strength, flexural strength, and the modulus of elasticity after 7, 14, 28, 56, 91, and 365 days of curing. According to the findings, the author mentioned that the C class fly ash can be effectively used in structural concrete.

The rock dust, which is a by-product obtained from the production process of crushed-stone aggregates, is another well-known powder material to be used in concrete. During rock extraction and mechanical processing, and due to their sorting, large quantities of waste material are produced in the form of rock dust. Similar dust waste is produced during the drying process of the aggregate used for the production of mineral–asphalt mixtures and at stonemason facilities. The storage of this type of fine material poses serious environmental problems. Dust released to the atmosphere significantly contributes to the accumulation and harmful dispersion of fine solids in air, water, and soil [11,12].

The chemical and mineral composition of dusts is the same as of the bedrock from which they originate. This makes them suitable for the production of cement mortars and concretes as a partial substitute of fine aggregate or even cement. Not only will it reduce the cost of construction production, it will also make the management of this waste more efficient. Such waste utilization is consistent with the principle of sustainable development that assumes an efficient management of non-renewable (consumable) natural resources and their replacement with recycled waste substitutes.

Most authors believe that the introduction of rock dust as a replacement for the part of sand contributes to the improvement of the mechanical properties of mortars and cement concretes (Figures 1 and 2) as well as durability. As early as 1976, Soroka and Stern [13] noted the beneficial effect of fillers on the mechanical properties of cement mortars. Strength increases with the dust share in sand mass and with the increase of its fineness. The same conclusions have been drawn by many authors who have studied mortars and concretes with the following additives as replacement for sand lime dust [14–18], marble dust [15,19–21], granite dust [12,22–26], and basalt dust [14,27].

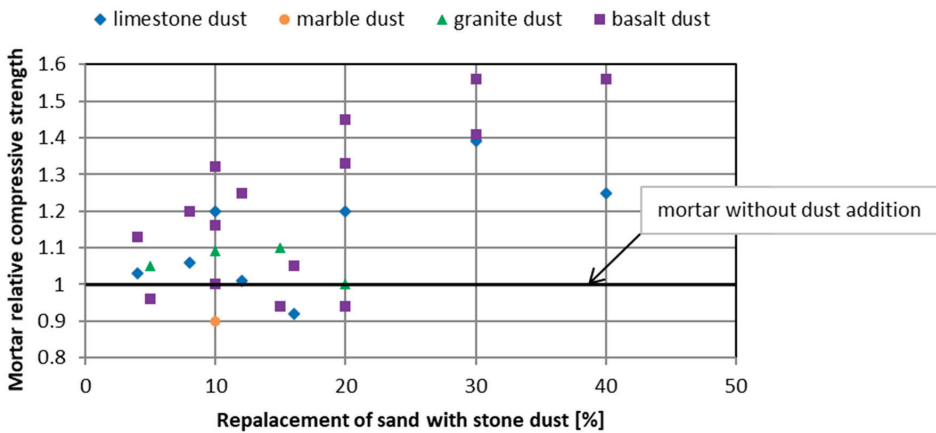


Figure 1. The influence of rock dust on the compressive strength of cement mortars after 28 days of hardening [14,21,24,27,28].

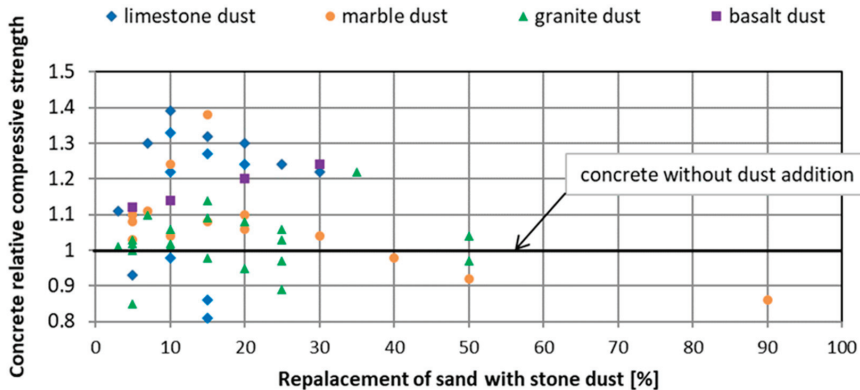


Figure 2. The influence of rock dust on the compressive strength of concrete after 28 days of hardening [12,15–20,22,23,25,26,29,30].

Abdelaziz et al. [14] studied the use of two different quarry dusts as cement and fine aggregate replacement materials and experimentally demonstrated the usability of quarry dust as fine aggregate replacement. It was concluded that the strength properties of blended cement mortars with quarry dusts are higher than those of the control mortars. Binici et al. [15] used marble dusts and limestone dusts instead of fine sand aggregate. The authors stated that higher abrasion resistant concrete can be produced by using this waste instead of sand. Furthermore, the authors reported that the sulfate resistance also increased in concretes containing this waste. The study of Çelik and Marar [16] revealed that the use of breaker powder in concrete has been worked on for a long time. The authors noticed that the addition of dust improved the compressive strength and abrasion resistance, while reducing the absorption and permeability of concrete. Eren and Marar [17] found a reduction in water permeability with the increasing replacement level of the crusher dust replacement in fine aggregate. Topçu and Uğurlu [18] used the mineral filler as a replacement for sand, and they investigated the effect of applying different amounts of mineral filler on concrete. They found that the addition of 7–10% of mineral filler to fine aggregate (0–2 mm) considerably improved the mechanical properties of concrete and decreased its permeability. Aliabdo et al. [19] studied the utilization of waste marble dust in cement and concrete production. They added the marble dust with 0.0%, 5.0%, 7.5%, 10.0%,

and 15.0% replacement ratios by weight of cement and sand. They concluded that concrete made of marble dust as a sand replacement indicated better performance compared to cement replacement. Alyamaç and Aydın [20] produced the concrete samples by replacing sand with marble powder at 10%, 20%, 30%, 40%, 50%, and 90% by volume. They concluded that using up to 40% marble powder in concrete had a positive effect on the mechanical properties of concrete, including abrasion resistance, and it also reduced water absorption. Corinaldesi et al. [21] used a by-product of marble sawing and shaping in concrete production and it was found that 10% substitution of sand with marble powder provided maximum compressive strength. Arivumangai and Felixkala [22] studied the usage of granite powder with 0, 25%, and 50% sand replacement. They mentioned that the concrete with increased performance in compressive strength as well as in the durability aspect can be produced. Bonavetti and Irassar [24] used the stone dusts of quartz, granite, and limestone in percentages ranging from 0 to 20% as a replacement for equal weights of sand. They found an improvement in mortar strength at early ages, and no detrimental effects were observed at later ages. Reddy et al. [25] and Divakar et al. [26] studied waste granite powder and concluded that locally available granite is a useful partial substitution material for concrete. This material can improve the compressive, tensile, and flexure strengths of concrete.

The improvement of properties of cement composites with rock dust additives is primarily related to the filler role of rock dust. The operation mechanism of chemically inert dust neither depends on the type of rock material the dust originates from nor its chemical composition [31,32]. Therefore, the dust grain size of rock dust is much more important in these cases. Fine dust material acts as an inert filler, which contributes to better filling of the intergranular free space in a composite. This results in a compact cement matrix structure with lower porosity and therefore greater strength and durability [24,33,34]. Apart from the dominant filler effect, the heterogeneous nucleation of C–S–H on rock dust grains plays a secondary role in shaping the microstructure of the hardened cement slurry, which leads to the increased content of hydrated calcium silicates [35,36]. This contributes to the additional sealing of the cement matrix and thus to its strength increase.

The use of waste materials in the production of cement composites, the properties and evaluation criteria of which have not been specified in the standards, requires a comprehensive analysis and evaluation of the properties of mortars and concretes produced with their use. Despite the growing interest in the use of various rock dust types in concrete production, many problems still remain unexplained. There is no literature related to basalt dust utilization as a partial sand substitute in concrete. The scientific goal of the research presented in the paper was to determine the effect of the basalt dust additive, partially replacing sand, on the properties of concrete. The influence of basalt dust on the technological properties of concrete mixtures, including the compressive strength, water absorption, permeability, and microstructure of hardened concrete with basalt dust additive were analyzed. The results of research on the concrete mechanical properties presented by the authors in this paper are consistent with those of other scientists who analyzed the influence of rock dusts of different mineral origin (lime, marble, and granite dusts) on concrete properties. Moreover, the presented analyses concerning the influence of basalt dust on the porosity and microstructure of the cement matrix supplement the knowledge deficiency, especially with regard to basalt dusts used in concrete as a sand substitute.

2. Materials and Methods

Waste basalt powder generated in the production process of asphalt mixtures with basalt aggregate was used. During the drying of the mineral aggregate, exhaust fumes leave the dryer with various powder particles. A coarser fraction of waste powder is collected in a special separator, while a very fine fraction is retained in a dryer filter. Asphalt mixture production leads to the formation of rock powder in an amount of about 5% of the aggregate mass used to produce the asphalt mixture. This very fine material is treated as a waste.

The chemical composition of the basalt powder used in this study is presented in Table 1. Figure 3 presents the particle size distribution of the basalt powder, which is similar to OPC (ordinary Portland cement). The range of the basalt powder particle diameters is 0.5 to 200 μm , and the average particle size is 20 μm in diameter. The basalt powder specific gravity is 2.99, and the specific surface area determined by the Blaine method is 3500 cm^2/g .

Basalt powder particles have a rough surface and an angular shape (the scanning electron microscope SEM image (Scanning Electron Microscope (SEM) Quanta 250 FEG by FEI (Hillsboro, OR, USA), equipped with the system of chemical content analysis based on the energy dispersion of the X-ray using Energy Dispersive X-ray Spectroscopy (EDS, Panalytical, Almelo, The Netherlands) by EDAX is presented in Figure 4). The mineralogical composition of the basalt powder was determined based on the XRD diffractogram (X-ray diffraction (XRD) method using a X'pert MPD X-ray diffractometer (Panalytical, Almelo, The Netherlands) with a goniometer PW 3020, Cu lamp and a graphite monochromator. Diffraction patterns were recorded by step scanning from 5 to 65, with a step size of 0.02° . HighScore Pro software version 4.1 (Panalytical, Almelo, The Netherlands) was used to process diffraction data. The identification of mineral phases was based on the PCPDFWIN ver. 1.30 formalized by JCPDS-ICDD (ICDD, Newtown, CT, USA)) (Figure 5). Plagioclase rich in anorthite particles (Ca-Plagioclase) dominates in the mineral composition of basalt powder, as well as pyroxene and amphibole. There is a small amount of illite, which is probably the effect of plagioclases weathering.

Table 1. Chemical composition of basalt powder.

Chemical Composition (%)	
SiO ₂	42.61
Al ₂ O ₃	12.90
Fe ₂ O ₃	14.05
CaO	13.00
MgO	7.82
SO ₃	0.07
K ₂ O	1.15
Na ₂ O	1.76
Cl ⁻	0.10
P ₂ O ₅	1.80
MnO	0.25

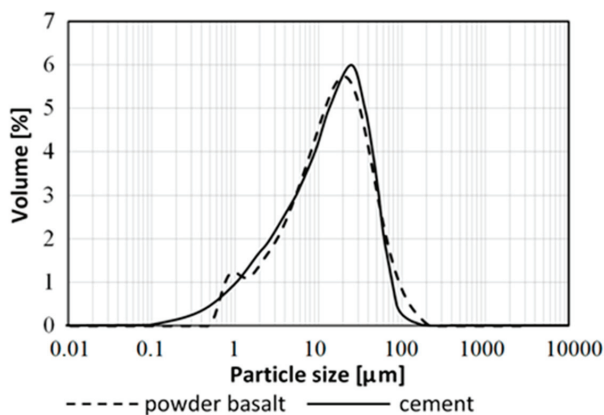


Figure 3. Particle size distribution of basalt powder and Portland cement.

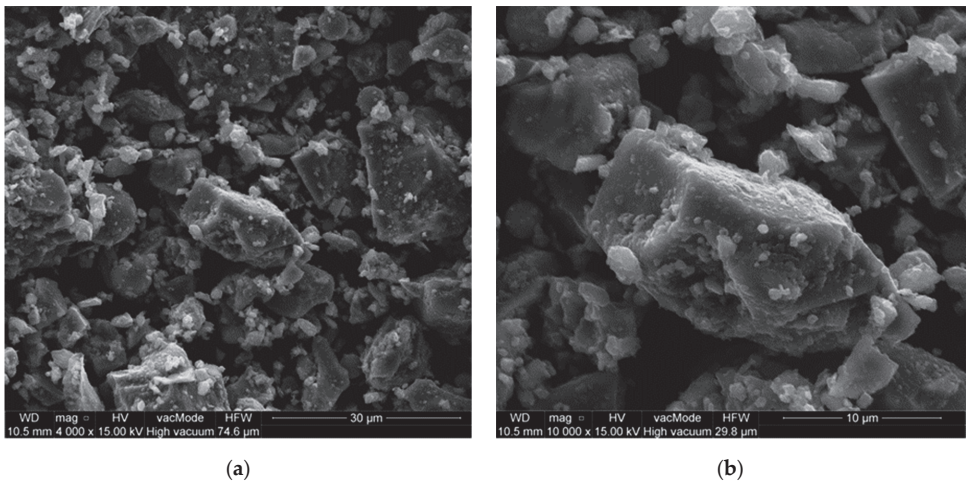


Figure 4. Scanning electron microscope image of basalt powder: (a) mag. ×4000; (b) mag. ×10000.

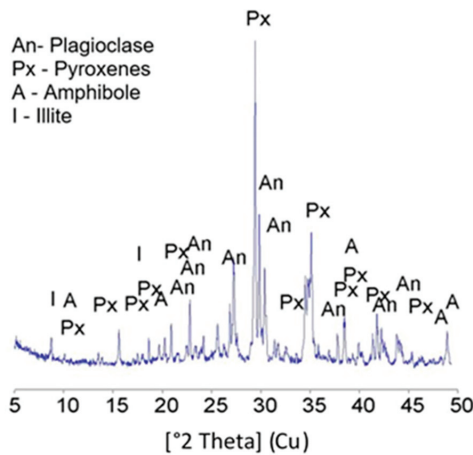


Figure 5. XRD diffractogram of the basalt powder.

The concrete mixtures were prepared with the use of ordinary Portland cement CEM I 42.5R (Lafarge Cement Plant Kujawy in Bielawy, Poland). Table 2 presents the chemical and mineral composition of the OPC. The particle size distribution of cement is shown in Figure 3. The ordinary Portland cement specific gravity is 3.13, and the specific surface area determined by the Blaine method is 3500 cm²/g. As a coarse aggregate (CA) (Pędzewo, Zławieś Wielka, Poland), the gravel of the group of fractions 2/16 was used, and as a fine aggregate (FA) (Pędzewo, Zławieś Wielka, Poland), river sand (Pędzewo, Zławieś Wielka, Poland) was used. In order to obtain the desired workability of concrete mixtures, the high-range water-reducing (HRWR) admixture was added.

Table 2. Chemical and mineral composition of cement.

Chemical Composition (%)		Mineral Composition (%)	
SiO ₂	19.39		
Al ₂ O ₃	4.67	C ₃ S	59.7
Fe ₂ O ₃	3.34		
CaO	63.17		
MgO	1.24	C ₂ S	12.4
SO ₃	2.95		
K ₂ O	0.62	C ₃ A	2.8
Na ₂ O	0.17		
Cl ⁻	0.07	C ₄ AF	11.8
P ₂ O ₅	0.12		

To analyze the effect of basalt powder on the properties and microstructure of concrete, four concrete mixes were prepared. The reference concrete, i.e., concrete without waste basalt powder, was named C0, and the concretes with different amount of basalt powder replacing 10%, 20%, and 30% of the sand by mass were named C10, C20, and C30, respectively. The comparison between the properties and microstructure of reference concrete without basalt powder and concretes containing different amounts of waste basalt powder was made. The composition of the concrete mixtures is presented in Table 3. The water/cement ratio was maintained constant at 0.4.

To analyze the technological properties of concrete mixtures, the concrete slump test according to European Standard EN-12350-2:2011 was performed. Maintaining the same consistency and similar workability level of each concrete mixture was assumed, therefore with increasing basalt powder content, the high-range water-reducing admixture amount was increased.

Table 3. Concrete mixture proportions. C10, C20, and C30: concretes with different amount of basalt powder replacing 10%, 20%, and 30% of the sand by mass, CA: coarse aggregate, HRWR: high-range water-reducing.

Concrete	Cement (kg/m ³)	Water (kg/m ³)	Basalt Powder (kg/m ³)	Fine Agg. (kg/m ³)	CA		HRWR Admix. (kg/m ³)
					2/8 mm (kg/m ³)	8/16 mm (kg/m ³)	
C0			0	676			4.6
C10			68	608			5.6
C20	350	140	135	541	512	640	7.7
C30			203	473			11.6

To assess the influence of different amounts of basalt powder on the physical properties of concrete, the compressive strength, permeability, and water absorption were analyzed. Compressive strength and permeability were conducted according to European Standards EN-12390-3:2011 and EN-12390-8:2011. The compression tests were performed using a computer-controlled test machine of 3000 kN capacity. The hardness value of the compressive test machine loading heads is 550 HV 30 (HRC 53), which conforms to the EN12390-4. For tests, the loading rate was selected constant as 0.5 MPa/s. The permeability of concrete was determined with a measuring device designed to determine the depth of water penetration in hardened concrete specimens under pressure. Research was conducted in accordance with the procedure set out in EN 12390-8. The measuring device enables the transfer of water pressure to the test area and its current indications. Water absorption was determined based on the relative mass loss of samples dried up to constant mass compared with samples fully saturated with water. Cube specimens 100 mm × 100 mm × 100 mm and 150 mm × 150 mm × 150 mm (for permeability determination) were prepared for each concrete, i.e., the reference concrete and concretes with waste basalt powder. A laboratory mixer was used to prepare concrete mixtures. After placing in the molds, concrete specimens were consolidated in two layers by using mechanical vibration. Until

demolding, all specimens were kept covered in a chamber at controlled temperature 20 ± 2 °C for 24 h. After demolding, specimens were stored in water until testing. The testing of compressive strength was conducted at 7, 14, 28, 90, 180 and 360 days, the testing of permeability was conducted at 28 days, and the testing of water absorption was conducted at 28, 180, and 360 days.

In order to determine the effect of basalt powder on the cement matrix microstructure, the scanning electron microscope (SEM) observation and energy-dispersive spectroscopy (EDS) analysis were performed. SEM analyses were performed with Quanta 250 FEG by FEI (Hillsboro, OR, USA) instrument, equipped with the system of chemical content analysis based on the energy dispersion of the X-ray using Energy Dispersive X-ray Spectroscopy (EDS, Panalytical, Almelo, The Netherlands) by EDAX. Fractured samples were specially prepared. The phases presented in the interfacial transition zone and bulk hydrated cement paste were identified based on EDS analysis.

3. Results and Discussion

The partial replacement of sand with basalt dust leads to a change in two parameters of the analyzed concrete, i.e., the particle size distribution of the aggregate and rock material (quartz on basalt). The introduction of basalt dust into the concrete mix in exchange for the corresponding sand dust fraction allows maintaining the same screening curve of the aggregate mix and analyzing the impact of the type of rock material on the properties of concrete. However, in such a situation, it is difficult to talk about the physical effect of the additive, i.e., the effect of the filler, because the sand dust fraction is replaced with the same dust fraction. The addition of mineral dust as a substitute exclusively for the fine aggregate dust fraction will affect the properties of concrete when this additive has a clear activity in relation to the solution in the pores of the hardened cement paste. Conducting research with the substitution of sand with basalt dust allowed, first of all, to analyze the influence of aggregate mixture sealing on the properties of mortars and concretes.

3.1. Properties of Concrete Mixtures

The change in concrete mix consistency, measured with a slump cone test, when the level of sand substitution with basalt dust at constant and variable fluidizing admixture content increases is presented in Figure 6. Incorporating dust in the concrete mix leads to a change toward a less liquid mix consistency, as well as to a deterioration of workability.

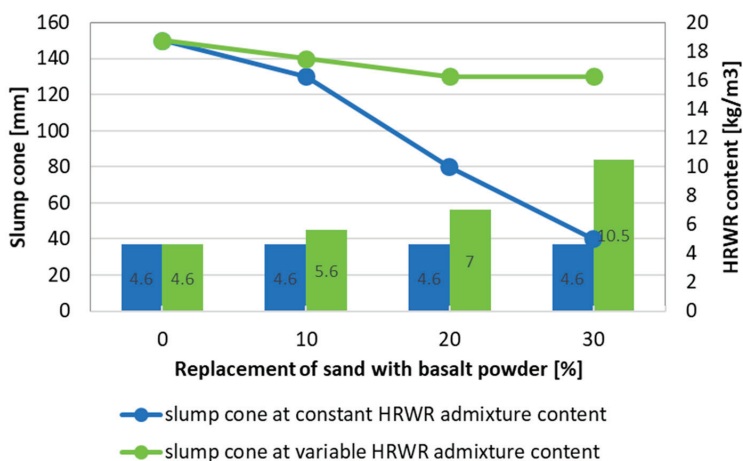


Figure 6. Change of the value of concrete mix slump cone test as a function of basalt dust content at constant and variable HRWR admixture content.

The results of the conducted tests show that a constant content of fluidizing admixture causes the slump cone test to vary from 140 mm, in a mixture without basalt dust, to 40 mm when 30% of sand is replaced with dust. This denotes the change of the concrete mix fluidity from an S3 to S1 consistency class according to European Standard EN-206:2016. The decreased workability of concrete mix with basalt powder addition is attributed to the greater compactness of the concrete mixture. As a result of the significant sorptivity of basalt powder, water is absorbed by its particles when mixing, which leads to a workability reduction of the concrete mixture [37]. Basalt dust features a large specific surface area, which needs more water to obtain proper consistency than in the case of sand. Therefore, when the basalt dust share in the sand mass increases, the concrete mixture fluidity significantly decreases.

When modifying the concrete composition, it was assumed that the same consistency of concrete mixture, characterized by the slump cone (or Abrams cone) test, was maintained within 140 ± 10 mm. Therefore, as sand was gradually replaced with basalt dust, it was necessary to increase the amount of high-range water-reducing (HRWR) admixture. At 30% basalt dust content, the fluidizing admixture content has more than doubled compared to the reference mixture.

The results of studies on the influence of basalt dust on the properties of concrete mixtures with constant consistency with an increasing amount of basalt dust replacing sand are presented in Table 4. As the basalt dust content increases, the air content decreases significantly from 4.1% in the case of the reference mixture to 2.5% in a 30% added dust mixture. The gradual substitution of sand with basalt dust leads to the sealing of aggregate composition, which results in lower air content in the concrete mix and thus a lower porosity of hardened concrete. Along with the increased basalt dust content in the sand mass, the increase in concrete mixture density is observed. The basalt dust density is 2.99 g/cm^3 and is higher than sand density (2.65 g/cm^3), which is the reason why the density of the concrete mixture increases with the dust share increase in the sand mass.

Table 4. Properties of concrete mixes with basalt dust additives.

Concrete Mix	Concrete Slump Test (mm)	Air content (% vol.)	Density (kg/m^3)
M0	150	4.1	2.31
M10	140	3.2	2.41
M20	130	3.0	2.44
M30	130	2.5	2.51

The introduction of dust material into the concrete mix reduces bleeding [38]. The content of very small aggregate grains with a diameter of less than $150 \mu\text{m}$ reduces water bleeding from the concrete mix mainly due to the lower sedimentation rate of fine grains [39].

3.2. Compressive Strength

Obtained results clearly indicate the positive influence of basalt dust as a sand replacement on the concrete strength (Figure 7). With the increase of basalt dust content, the compressive strength of concrete increased in each curing time.

The greatest strength increase in relation to the reference concrete, i.e., 19%, 24%, 25%, and 23% was reported respectively after 14, 28, 90, and 180 days of hardening, when replacing 30% of sand with basalt dust. Then, in the case of early 7-day strength, the highest 13% increase was obtained in concrete with 20% basalt dust additive. Concrete strength with basalt dust after 360 days of hardening does not significantly differ from that of the reference concrete. It is worth mentioning that concrete with 10% basalt dust additive gained 28-day reference concrete strength just after 7 days and 90-day reference concrete strength after only 14 days.

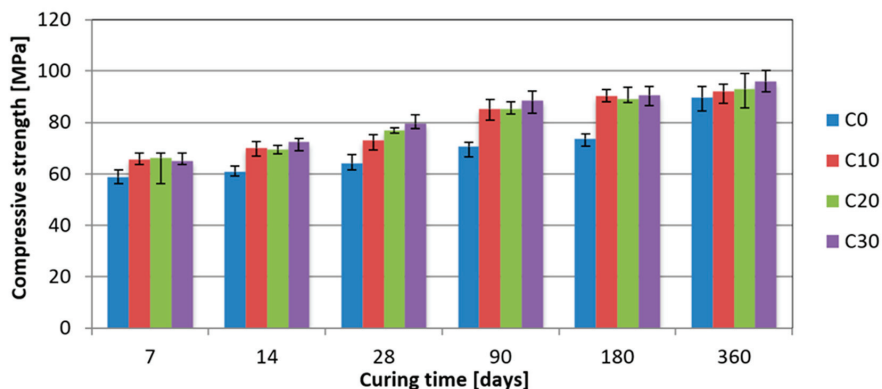


Figure 7. Compressive strength of concrete as a function of time and content of basalt dust as sand replacement (C0–reference concrete, C10–C30–concrete with additive of basalt dust replacing 10–30% of sand).

The beneficial effect of basalt dust on the mechanical properties of concrete is connected with the physical effect of this additive, i.e., with the filler effect. Basalt dust grains fill empty spaces (pores) between sand grains and coarser aggregate. This results in a higher tightness of the aggregate composition, a more compact cement matrix microstructure, and thus lower porosity and higher material strength [24,33]. From the grain size distribution of basalt dust and cement shown in Figure 3, it can be seen that the granularity distribution of both materials is similar. However, basalt dust is of the bimodal grain size type. The largest volume is occupied by grains with a diameter of approximately 20 μm . However, on the basalt dust grain curve, there is another, smaller maximum corresponding to a grain diameter of 1 μm . These very small dust particles were most likely located among slightly larger cement grains, which sealed the microstructure of the cement matrix as well as contributed to improvements in the mechanical properties of mortars and concretes.

The introduction of basalt dust has contributed to an increased level of active centers where it is possible to crystallize hydration products, especially the C–S–H phase, which also has an influence on the increased mortar strength. Cement grains, electrostatically charged differently, tend to attract one another in water slurry, resulting in aggregate creation (flocculation). In this case, water is not able to freely penetrate all the space between cement grains, and not all cement particles are effectively used in the hydration process. Microfiller introduction causes a greater dispersion of cement grains, which contributes to the accelerated hydration of clinker phases and therefore a faster strength increase [12,33].

3.3. Water Absorption

Basalt dust additive has little effect on the water absorption of concrete. The mass absorption of all tested concretes did not exceed the value of 4.5% and decreased with hardening time (Figure 8). After 28 days of hardening, the absorption of all tested concretes was identical. In longer periods, i.e., after 180 and 360 days of hardening, the absorption began to decrease slightly with the increase of basalt dust content. Water absorption decrease with increasing hardening time is attributed to the gradual completing hydration, which leads to the better compactness of cement matrix and the refinement of the pore structure [36,39].

It is worth mentioning that the concrete absorption was determined without evaluating the actual volume of water-saturated material, which may significantly affect the test results. This specific test method uses the mass of water absorbed by the concrete to refer to the mass of the whole dried sample and not only to the mass of the volume of the water-saturated material. It may have a particular effect when determining the absorption of concrete after 28 days of hardening. A longer sample hardening period in wet conditions means a larger volume of water-saturated samples. Therefore, it can be

considered that a more reliable assessment of the impact of basalt dust on the concrete absorption can be performed after a longer hardening period, i.e., after 180 and 360 days of concrete cure.

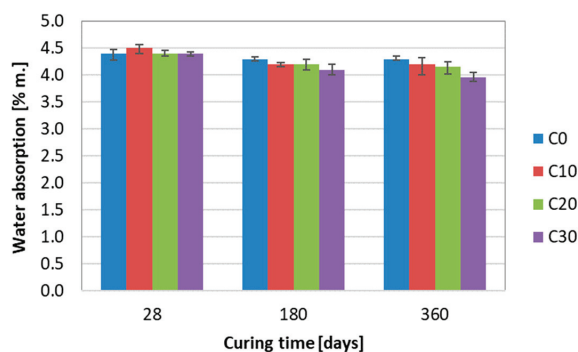


Figure 8. Water absorption of concrete as a function of basalt dust content and hardening time.

3.4. Permeability

The research showed that the penetration depth of pressurized water in all analyzed concretes is very low and is between 10 and 17 mm (Table 5). Here, 50 mm of water penetration allows defining concrete as impermeable. However, concrete in which the depth of water penetration under pressure does not exceed 30 mm meets the requirements of impermeable concrete in corrosive conditions [37].

Table 5. Depth of water penetration in concrete with basalt dust additive.

Concrete	C0	C10	C20	C30
Penetration Depth (mm)	17	15	10	13

Although all concretes feature low permeability, the water penetration depth in concrete with basalt dust additive is slightly lower in comparison with the reference concrete. The pore system has a significant influence on the permeability of concrete. The reduction of permeability is strongly influenced by the pore system. The share and structure of continuous capillary pores is of the greatest importance here [37]. The interruption of capillary pores reduces the penetration and movement of water in the concrete, thus reducing its permeability. Very small basalt dust particles most likely blocked the continuous capillary pores, which undoubtedly reduced the concrete permeability.

3.5. Microstructure

In order to analyze the microstructure, porosity tests of cement mortar samples were performed. Basalt dust was a sand substitute in the amount of 10% and 20%. It was found that as the basalt dust share increases, the total pore volume and porosity decreases. Basalt dust additive reduces mortar porosity in the capillary pore range. On the other hand, the share of fine pores below 50 nm in diameter and of gel pores below 10 nm is significantly increased (Figure 9). This has a positive effect on mortar microstructure sealing, which translates into increased strength and durability. A higher share of fine pores in the total material porosity means greater strength at the given porosity [37,40–43]. This is in line with the results of strength tests of concrete with basalt dust additive as a sand replacement, which show that mortar strength increases with the increase in basalt dust content. The basalt dust used in the study features a bimodal grain size distribution with a small maximum around 1 µm in diameter (Figure 3). These very small particles of basalt dust caused the cement matrix microstructure to be sealed, resulting in lower porosity. The heterogeneous C–S–H nucleation on dust particles, which results in a higher C–S–H content and thus a lower porosity of the basalt dust slurry that replaced sand,

is not to be underestimated. The reduction of porosity across capillary pores undoubtedly reduced the absorption and permeability of concrete with basalt dust additives.

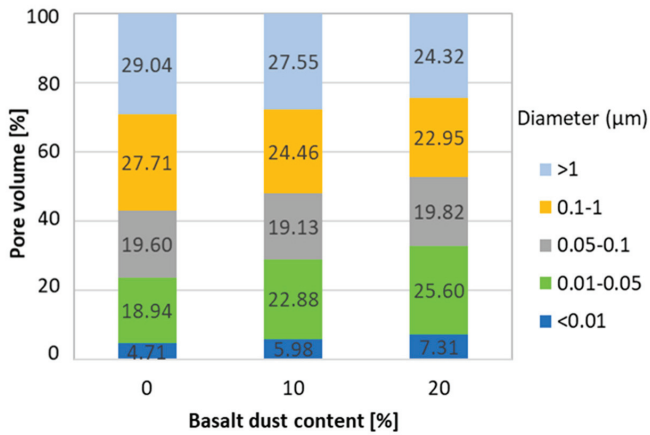


Figure 9. Share of pores of a certain diameter in the total pore volume in cement mortar with basalt dust additive [44].

From SEM observation and EDS analysis, it was found that products of hydration, the C–S–H phase in particular, crystallize on basalt dust particles. Very fine particles of basalt dust act as crystallization centers and provide additional areas where C–S–H nuclei can settle (Figures 10 and 11).

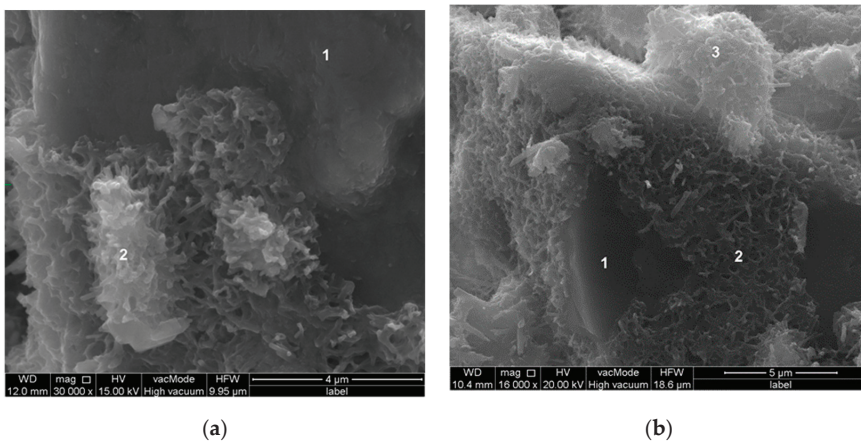


Figure 10. Microstructure of paste with basalt dust: (a) after 2 h of hydration; (b) after 5 h of hydration; point 1—basalt dust grain, points 2 and 3—C–S–H phase.

In cement paste without basalt dust additive, large hexagonal portlandite plates were identified (Figure 12), while these were not found during the research of paste microstructure with basalt dust addition. In many places, large portlandite crystals in the interfacial transition zone between aggregate and paste in concrete without basalt dust were also found (Figure 13), which was not noticed in the case of concrete with dust additive (Figure 14). However, the results of research on the calcium hydroxide content in cement paste did not confirm that the basalt dust additive reduces its content. Therefore, it can be assumed that basalt dust particles finer than cement grains sealed the cement paste microstructure, as a result of which there were no large pores giving space for the formation of larger

portlandite crystals. Much smaller, evenly dispersed portlandite crystals started to form in the cement matrix, and they were more difficult to identify in the images of the SEM microstructure.

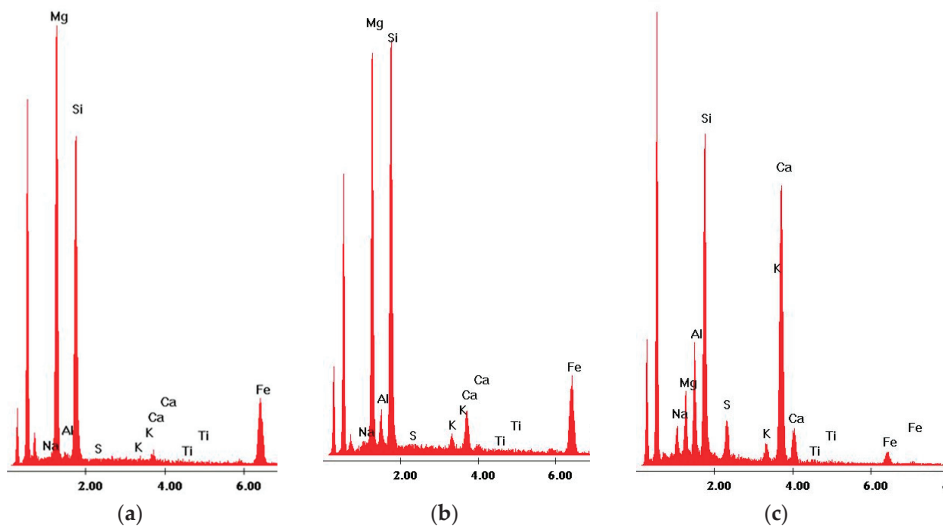


Figure 11. X-ray analysis in the micro-areas indicated in Figure 10: (a) olivine crystal—point 1, (b) and (c) thin layer of C–S–H phase on olivine grain—points 2 and 3.

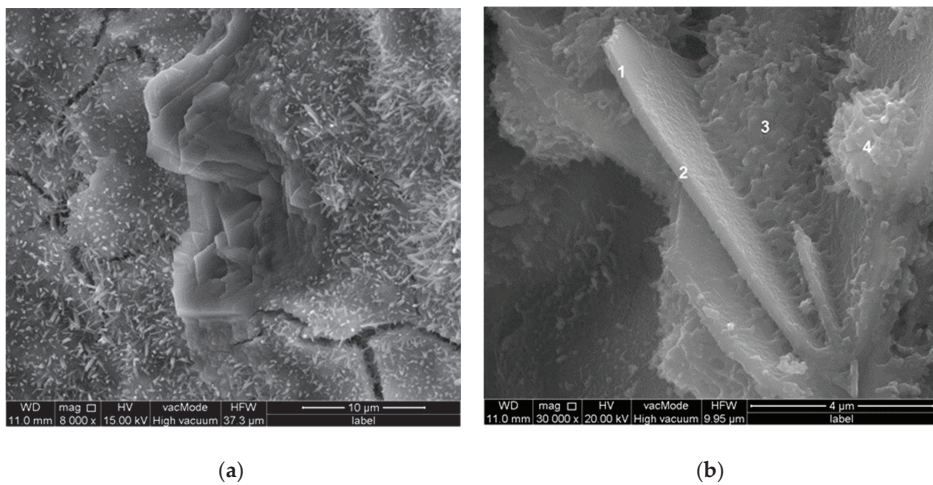


Figure 12. Microstructure of cement paste without basalt dust; (a) After 2 h of hydration; (b) After 5 h of hydration. Large hexagonal portlandite plates are visible: points 1 and 2—portlandite, points 3 and 4—C–S–H phase.

The presented SEM image of a concrete fracture with basalt dust additive (Figure 14) contains a visible compact interfacial transition zone that consists mainly of the C–S–H phase, which adheres tightly to the aggregate grain surface. Within the interfacial transition zone, very small basalt dust grains are visible, which tightly adhere to the mass of hardened cement paste (points 1 and 3 in Figures 14 and 15). The lack of large portlandite crystals indicates the lower porosity of the interfacial transition zone in concrete with basalt dust additive, which, as we know, indicates that this zone has been reinforced.

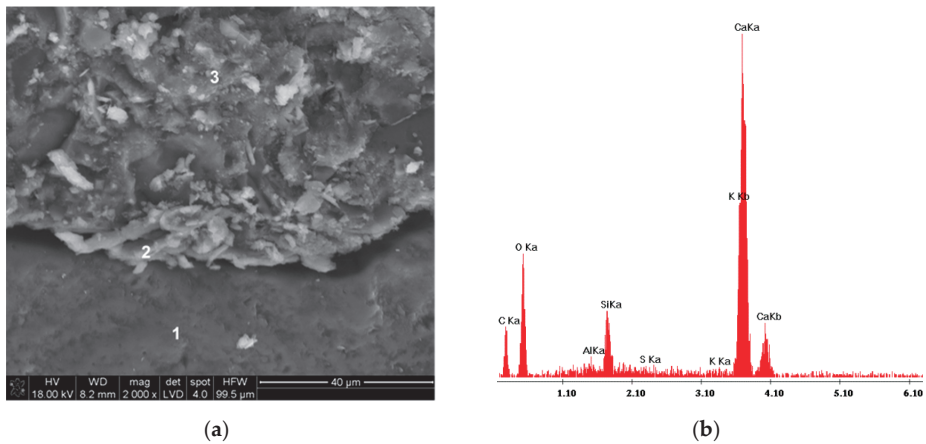


Figure 13. Microstructure of interfacial transition zone: (a) Concrete without basalt dust after 28 days of hydration: point 1—aggregate grain, point 2—portlandite, point 3—C–S–H phase; (b) Analysis in the micro-area defined in point 2.

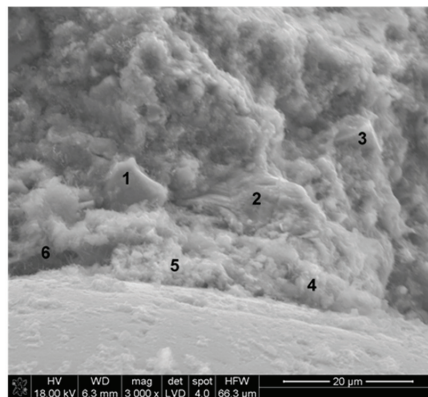


Figure 14. Microstructure of interfacial transition zone: concrete with 10% basalt dust addition after 28 days of hydration: point 1 and 3—basalt dust grain, point 2 and points 4–6—C–S–H phase.

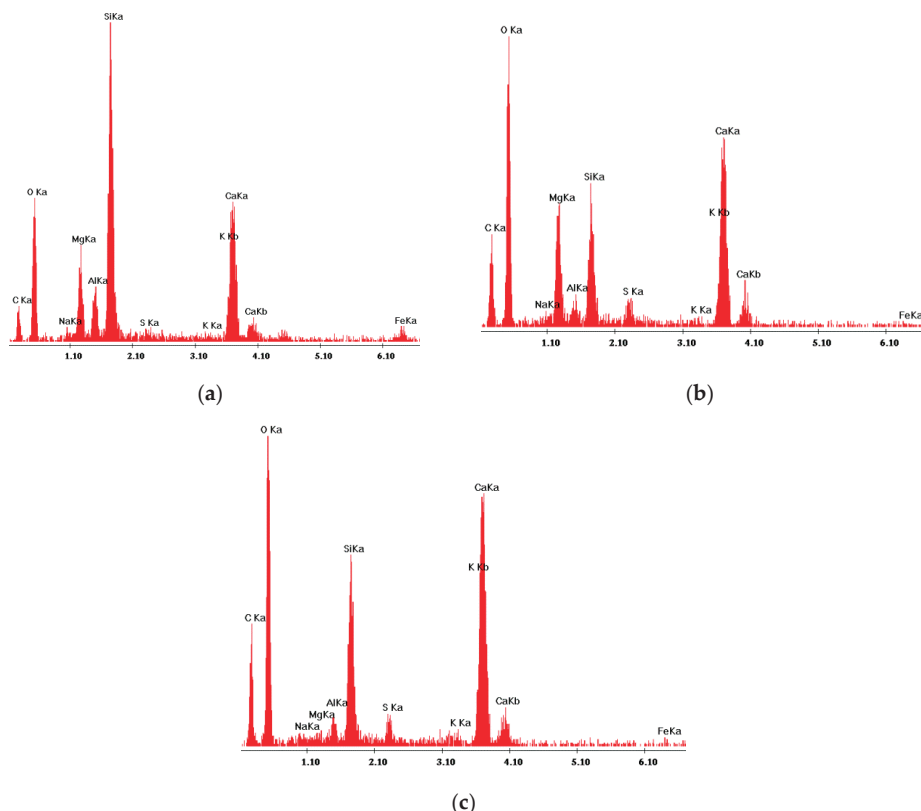


Figure 15. X-ray analysis in micro-areas indicated in Figure 14: (a) and (b) Basalt dust grains—points 1 and 3; (c) C–S–H phase—point 5. C–S–H was also found in points 2, 4, and 6, the X-ray analyses of which were not included.

4. Conclusions

This study discusses an experimental program carried out to investigate the effects of basalt powder replacement on the physical, mechanical, and microstructural properties of concretes. The following conclusions can be drawn based on the results of this study:

Basalt powder affected the workability of fresh concretes. When mixing water is kept constant in concrete mixtures, the workability of concrete mixes decreased with the increase in substitution ratios of basalt powder. When the basalt powder replacement rate was increased to 30%, a 71% decrease in consistency occurred (slump value decreased from 140 to 40 mm). For the production of basalt powder substituted concrete with constant consistency, HRWR should be increased based on the increasing rate of basalt powder substitution. Thus, the consistency of concretes can be maintained by increasing HRWR based on the increase of basalt powder. This increase in water demand can be attributed to the relatively greater surface area of basalt powder.

The amount of air in the reference mixture, which is 4.1%, decreased up to 2.5% with 30% basalt powder addition. This indicates that the use of basalt powder reduces the void rate in the concrete. In addition, concrete densities also increased inversely proportional to the amount of air and supported the improvement in the internal concrete structure. This result can be related to the higher density of basalt powder compared to the sand used in the mixture. This means that the

concrete internal structure has become more compact and the impermeability has increased with basalt powder substitution, and thus a better concrete internal structure has been obtained.

The compressive strength of concretes increased in all mixes based on the concrete curing age. In addition to this well-known result, the substitution of basalt powder instead of sand increased the compressive strength of all substitution rates and curing periods. In concrete mixes containing basalt powder, the increase in compressive strength has been achieved up to 25%. The increase in compressive strength, which is an expected result due to the decrease in the amount of concrete air and the increase in density, can be explained by the fact that the internal structure of the concrete becomes more compact as a result of basalt powder usage.

Although there is no significant relationship between water absorption and basalt substitution rate, very clear information was obtained from the pressurized water penetration depth data. As it is well-known, the pore system has a significant influence on the permeability of concrete. According to the achieved findings, it can be concluded that the relatively small particles of basalt dust blocked the continuous capillary pores and thus reduced the concrete permeability.

Microstructural analyses showed that the presence of basalt powder in concrete mixes is beneficial for cement hydration products. According to the SEM observation and EDX analysis, very fine particles of basalt dust acted as crystallization centers and provided additional areas where C–S–H nuclei can settle. It was observed that the basalt powder well adhered to the hydrated cement paste, and the portlandite crystals did not appear in large quantities between the basalt powder and the C–S–H gels. Contrary to reference mixes, the lack of large portlandite crystals was observed in the microstructures of basalt powder-substituted concrete. This observation indicates that basalt powder-substituted concretes have lower porosity through the interfacial transition zone. This is the result of the reinforcement effect of basalt powder on ITZ (interfacial transition zone).

As a result, the experimental study showed that in addition to improving some physical, mechanical, and microstructural performances of concretes and reducing the usage of natural raw materials, using basalt dust leads to the consumption of this industrial waste, thus providing a twofold benefit.

This study may be extended with new experimental studies related to concrete durability and the steel–concrete bond performance of basalt dust-substituted concretes to better understand the potential of basalt powder usage in concrete production.

Author Contributions: Conceptualization, methodology, investigation, resources, writing—original draft preparation, supervision, M.D.; Methodology, investigation, writing—review and editing, A.B. All authors have read and agreed to the published version of the manuscript.

Funding: This research received no external funding.

Acknowledgments: This article has been supported by the Polish National Agency for Academic Exchange under Grant No. PPI/APM/2019/1/00003.

Conflicts of Interest: The authors declare no conflict of interest. The funders had no role in the design of the study; in the collection, analyses, or interpretation of data; in the writing of the manuscript, or in the decision to publish the results.

References

1. Kozioł, W.; Ciepłiński, A.; Machniak, Ł.; Borcz, A. Kruszywa w Budownictwie. Cz. 1. Kruszywa Naturalne. *Nowoczesne Budownictwo Inżynieryjne Lipiec-sierpień* **2015**, *4*, 98–100. Available online: http://www.nbi.com.pl/assets/NBI-pdf/2015/4_61_2015/pdf/31_Kruszywa_naturalne.pdf (accessed on 3 February 2019).
2. Kozioł, W.; Machniak, Ł.; Borcz, A.; Baic, I. Górnictwo kruszyw w Polsce – szanse i zagrożenia. *Inżynieria Mineralna* **2016**, *17*, 175–182.
3. Kozioł, W.; Ciepłiński, A.; Machniak, Ł.; Jacaszek, C.; Borcz, A. Wydobycie i produkcja kruszyw naturalnych w Polsce i w Unii Europejskiej. *Przegląd Górniczy* **2014**, *70*, 23–29.

4. Koziol, W.; Czaja, P. Górnictwo Skalne w Polsce - Stan Obecny, Perspektywy i Uwarunkowania Rozwoju. *Górnictwo i Geologia* **2010**, *5*, 41–58.
5. Bilir, T. Effects of Non-Ground Slag and Bottom Ash as Fine Aggregate on Concrete Permeability Properties. *Constr. Build. Mater.* **2012**, *26*, 730–734. [CrossRef]
6. Rashad, A.M. A Brief on Blast-Furnace Slag and Copper Slag as Fine Aggregate in Mortar and Concrete Based on Portland Cement. *Rev. Adv. Mater. Sci.* **2016**, *44*, 221–237.
7. Yuksel, I.; Genc, A. Properties of Concrete Containing Nonground Ash and Slag as Fine Aggregate. *ACI Mater. J.* **2007**, *104*, 397–403.
8. Bilir, T.; Gencil, O.; Topcu, I.B. Properties of Mortars with Fly Ash as Fine Aggregate. *Constr. Build. Mater.* **2015**, *93*, 782–789. [CrossRef]
9. Ravina, D. Mechanical Properties of Structural Concrete Incorporating a High Volume of Class F Fly Ash as Partial Fine Sand Replacement. *Mater. Struct.* **1998**, *31*, 84–90. [CrossRef]
10. Siddique, R. Effect of Fine Aggregate Replacement with Class F Fly Ash on the Mechanical Properties of Concrete. *Cem. Concr. Res.* **2003**, *33*, 539–547. [CrossRef]
11. Vardhan, K.; Goyal, S.; Siddique, R.; Singh, M. Mechanical Properties and Microstructural Analysis of Cement Mortar Incorporating Marble Powder as Partial Replacement of Cement. *Constr. Build. Mater.* **2015**, *96*, 615–621. [CrossRef]
12. Vijayalakshmi, M.; Sekar, A.S.S.; Ganesh prabhu, G. Strength and Durability Properties of Concrete Made with Granite Industry Waste. *Constr. Build. Mater.* **2013**, *46*, 1–7. [CrossRef]
13. Soroka, I.; Stern, N. Calcareous Fillers and the Compressive Strength of Portland Cement. *Cem. Concr. Res.* **1976**, *6*, 367–376. [CrossRef]
14. Abdelaziz, M.A.; El-Aleem, S.A.; Menshawy, W.M. Effect of Fine Materials in Local Quarry Dusts of Limestone and Basalt on the Properties of Portland Cement Pastes and Mortars. *Int. J. Eng. Res.* **2014**, *3*, 1038–1056.
15. Binici, H.; Kaplan, H.A.; Yilmaz, S. Influence of Marble and Limestone Dusts as Additives on Some Mechanical Properties of Concrete. *Sci. Res. Essay* **2007**, *2*, 372–379.
16. Çelik, T.; Marar, K. Effects of Crushed Stone Dust on Some Properties of Concrete. *Cem. Concr. Res.* **1996**, *26*, 1121–1130. [CrossRef]
17. Eren, Ö.; Marar, K. Effects of Limestone Crusher Dust and Steel Fibers on Concrete. *Constr. Build. Mater.* **2009**, *23*, 981–988. [CrossRef]
18. Topçu, İ.B.; Uğurlu, A. Effect of the Use of Mineral Filler on the Properties of Concrete. *Cem. Concr. Res.* **2003**, *33*, 1071–1075. [CrossRef]
19. Aliabdo, A.A.; Abd Elmoaty, A.E.M.; Auda, E.M. Re-Use of Waste Marble Dust in the Production of Cement and Concrete. *Constr. Build. Mater.* **2014**, *50*, 28–41. [CrossRef]
20. Alyamaç, K.E.; Aydın, A.B. Concrete Properties Containing Fine Aggregate Marble Powder. *KSCE J. Civ. Eng.* **2015**, *19*, 2208–2216. [CrossRef]
21. Corinaldesi, V.; Moriconi, G.; Naik, T.R. Characterization of Marble Powder for Its Use in Mortar and Concrete. *Constr. Build. Mater.* **2010**, *24*, 113–117. [CrossRef]
22. Arivumangai, A.; Felixkala, T. Strength and Durability Properties of Granite Powder Concrete. *J. Civ. Eng. Res.* **2014**, *4*, 1–6.
23. Felixkala, T.; Partheeban, P. Granite powder concrete. *Indian J. Sci. Technol.* **2010**, *3*, 311–317. [CrossRef]
24. Bonavetti, V.L.; Irassar, E.F. The Effect of Stone Dust Content in Sand. *Cem. Concr. Res.* **1994**, *24*, 580–590. [CrossRef]
25. Chiranjeevi Reddy, K.; Yaswanth Kumar, Y.; Poornima, P. Experimental Study on Concrete with Waste Granite Powder as an Admixture. *Int. J. Eng. Res. Appl.* **2015**, *5*, 87–93.
26. Divakar, Y.; Manjunath, S.; Aswath, M.U. Experimental Investigation on Behaviour of Concrete with the Use of Granite Fines. *Int. J. Adv. Eng. Res. Stud.* **2012**, *1*, 84–87.
27. Unčík, S.; Kmecová, V. The effect of basalt powder on the properties of cement composites. *Concr. Concr. Struct. Conf. Procedia Eng.* **2013**, *65*, 51–56.
28. Soroka, I.; Setter, N. The Effect of Fillers on Strength of Cement Mortars. *Cem. Concr. Res.* **1977**, *7*, 449–456. [CrossRef]
29. Demirel, B. The Effects of Waste Marble Dust Applying as a Fine Sand on the Mechanical Properties of Concrete. *CWB* **2010**, *15*, 259–267.

30. Dobiszewska, M.; Schindler, A.K.; Pichór, W. Mechanical Properties and Interfacial Transition Zone Microstructure of Concrete with Waste Basalt Powder Addition. *Constr. Build. Mater.* **2018**, *177*, 222–229. [CrossRef]
31. Cyr, M.; Lawrence, P.; Ringot, E. Efficiency of Mineral Admixtures in Mortars: Quantification of the Physical and Chemical Effects of Fine Admixtures in Relation with Compressive Strength. *Cem. Concr. Res.* **2006**, *36*, 264–277. [CrossRef]
32. Lawrence, P.; Cyr, M.; Ringot, E. Mineral Admixtures in Mortars Effect of Type, Amount and Fineness of Fine Constituents on Compressive Strength. *Cem. Concr. Res.* **2005**, *35*, 1092–1105. [CrossRef]
33. Kurdowski, W. *Cement and Concrete Chemistry*; Springer: Dordrecht, The Netherlands, 2014.
34. Wong, H.H.C.; Kwan, A.K.H. Packing Density of Cementitious Materials: Part 1—Measurement Using a Wet Packing Method. *Mater. Struct.* **2008**, *41*, 689–701. [CrossRef]
35. Nonat, A.; Courault, A.-C.; Damidot, D. A New Model Describing the Variation of C-S-H Ca/Si Ratio with Lime Concentration in Solution. *CWB* **2001**, *5*, 184–191.
36. Moosberg-Bustnes, H.; Lagerblad, B.; Forsberg, E. The Function of Fillers in Concrete. *Mater. Struct.* **2004**, *37*, 74–81. [CrossRef]
37. Neville, A.M. *Properties of Concrete*, 5th ed.; Pearson Education Limited: London, UK, 2012.
38. Nichols, F.P. Manufactured Sand and Crushed Stone in Portland Cement Concrete. *Concr. Int.* **1982**, *4*, 56–63.
39. Topçu, İ.B.; Bilir, T.; Uygunoğlu, T. Effect of Waste Marble Dust Content as Filler on Properties of Self-Compacting Concrete. *Constr. Build. Mater.* **2009**, *23*, 1947–1953. [CrossRef]
40. Jambor, J. Pore Structure and strength development of Cement Composites. *Cem. Concr. Res.* **1990**, *20*, 948–954. [CrossRef]
41. Mindess, S. Relation between the Compressive Strength and Porosity of Autoclaved Calcium Silicate Hydrates. *J. Am. Ceram. Soc.* **1970**, *53*, 621–624. [CrossRef]
42. Odler, I.; Rößler, M. Investigations on the Relationship between Porosity, Structure and Strength of Hydrated Portland Cement Pastes. II. Effect of Pore Structure and of Degree of Hydration. *Cem. Concr. Res.* **1985**, *15*, 401–410. [CrossRef]
43. Rößler, M.; Odler, I. Investigations on the Relationship between Porosity, Structure and Strength of Hydrated Portland Cement Pastes I. Effect of Porosity. *Cem. Concr. Res.* **1985**, *15*, 320–330. [CrossRef]
44. Dobiszewska, M.; Barnes, R.W. Properties of Mortar Made with Basalt Powder as Sand Replacement. *ACI Mater. J.* **2020**, *117*, 3–9. [CrossRef]



© 2020 by the authors. Licensee MDPI, Basel, Switzerland. This article is an open access article distributed under the terms and conditions of the Creative Commons Attribution (CC BY) license (<http://creativecommons.org/licenses/by/4.0/>).

Article

Drying Shrinkage and Rapid Chloride Penetration Resistance of Recycled Aggregate Concretes Using Cement Paste Dissociation Agent

Sungchul Yang * and Hyewon Lee

School of Architectural Engineering, Hongik University, 2639 Sejong-ro Jochiwon, Sejong 30016, Korea; lhw9473@g.hongik.ac.kr

* Correspondence: scyang@hongik.ac.kr or scyang00@gmail.com; Tel.: +82-44-860-2561; Fax: +82-44-865-2796

Abstract: In the present study, a recycled concrete aggregate (RCA) coating treatment using a cement paste dissociation agent (CPDA) with different mixing methods was newly incorporated in RCA concrete mixtures. First, a preliminary test program was conducted to determine the proper dosage of the CPDA solution throughout its RCA concrete test results from compressive strength, flexural strength, and elastic modulus. Then, a series of experimental tests were carried out to investigate the effect of RCA coating treatment, different mixing method such as the equivalent mortar volume (EMV) method and conventional method, and different RCA replacement ratios on durability test results of RCA concrete such as drying shrinkage values and rapid chloride penetration test (RCPT) values. The test results showed that all RCA concretes mixed with the coated RCAs were found to be workable regardless of different mix methods, with the slump and air contents of all the mixes being almost identical. All the concrete specimens, which were mixed with the coated RCAs with CPDA solution, represented lower drying shrinkage and RCPT values than those mixed without RCA coating treatment, regardless of different mix proportioning methods or RCA replacement ratios. This holds for the concrete specimens proportioned with the EMV method, regardless of different RCA replacement ratios.

Keywords: recycled concrete aggregate; cement paste; dissociation agent; RCA coating; mixture proportioning

Citation: Yang, S.; Lee, H. Drying Shrinkage and Rapid Chloride Penetration Resistance of Recycled Aggregate Concretes Using Cement Paste Dissociation Agent. *Materials* **2021**, *14*, 1478. <https://doi.org/10.3390/ma14061478>

Academic Editor:
Malgorzata Ulewicz

Received: 8 February 2021
Accepted: 11 March 2021
Published: 17 March 2021

Publisher's Note: MDPI stays neutral with regard to jurisdictional claims in published maps and institutional affiliations.



Copyright: © 2021 by the authors. Licensee MDPI, Basel, Switzerland. This article is an open access article distributed under the terms and conditions of the Creative Commons Attribution (CC BY) license (<https://creativecommons.org/licenses/by/4.0/>).

1. Introduction

It is widely acknowledged that various types of waste materials can be transformed into recycled aggregates, powders, or additives and are used in concrete. Ceramic materials have been used as ceramic powder and ceramic aggregates in concrete [1]. This use of glass waste in concrete production and its advantages were summarized well by Zegardo et al. [2], and recent studies related to the use of rubber aggregates and chips were reported by Guetla et al. [3]. Wood chips can also be used for wood plastic composite paver blocks [4].

Recycled concrete aggregate (RCA) is one of many types of recycling aggregates that are used for concrete. RCA is known to be more porous, less dense, and more heterogeneous than natural aggregates. However, the residual mortar (RM) adhering to RCA has a negative impact on the concrete properties. Additionally, it has been reported that RM in RCA reduces the compressive strength and elastic modulus by up to 42% and 45%, respectively [5]. The data reported for Federal Highway Administration (FHWA) also revealed decreases of up to 30% and 50% in the coefficient of thermal expansion and permeability, respectively [6].

Numerous research teams have carried out experimental studies with the goal of enhancing the material properties of RCA concrete. These studies include high-quality RCA produced from precast or preserved quality concrete [7–9], the two-lift paving method [10],

improvement of the mixing process [11,12], the use of oil-contaminated sand [13], new mixture design methods [14–17], strengthening through residual mortar (RM) coating [18–22], and supplementary cementitious materials.

First, high-quality RCA can be obtained from precast concrete [7], concrete sleepers, and returned concrete mixtures [8,9]. RCA acquired from such concrete can produce reliable products of consistent quality and can reduce the cost of sorting aggregates during processing.

Next, two-lift concrete paving has been successfully adopted and employed in Western Europe and the U.S. This method involves the use of low-quality RCA concrete in the lower layer of the concrete pavement. Two-lift construction using recycled concrete in the lower layer has been reported to provide the greatest impact socially and environmentally [10]. In a similar way, it was reported by Siddika et al. [23] that RCAs with other construction by-products can be used with the application of additive manufacturing, so-called, 3D printing.

The application of oil-contaminated sand in concrete was considered effective in enhancing concrete strength properties. Abousning et al. [13] reported that the presence of crude oil up to 4% could improve the properties of mortar compared to the uncontaminated samples.

After the two-stage mixing approach (TSMA) [11] was introduced, a triple mixing procedure [12] was presented for manufacturing strong and durable RCA concrete. The triple mixing process divides the mixing process into 3 steps. The first step involves coating the mixed coarse aggregate with additives and a fixed quantity of water. The second step adds cement and fine aggregates, and the last step mixes in the remaining amount of water and plasticizer. Increased density, water absorption performance, and strength properties were reported.

Improved mixing methods for RCA concrete have also been proposed by a number of other researchers [14–17]. The equivalent mortar volume method was proposed by Fathifazl et al. [14] and received significant interest. In this method, RM was considered part of the total mortar needed for concrete. Additionally, a method that processes a portion of the RM as mortar and the remainder as aggregates was presented [15]. Gupta et al. [16] proposed the equivalent coarse aggregate mass method. The major concept behind this method is processing the mortar adhered to the RCA as sand. New approaches to improving existing mixing methods have continued to be presented and consider the properties of RM of RCA after Fathifazl et al. [14], such as the identical mortar volume design method [17]. Through these new mixing methods, it was shown that the mechanical strength and drying shrinkage of RCA concrete improved to a level similar to the properties of concrete using natural aggregates.

Researchers also investigated the strengthening of RM. Various materials were used to fill pores and interfacial transition zones (ITZs) to improve RCA quality [18–22], including polyvinyl alcohol (PVA) solution [19], siloxane and silane polymer solutions [20], and pozzolanic material slurry [21]. Overall, the surface treatment materials mentioned above helped reduce water absorption in RCA. Recently, the bio-deposition method was introduced as a way to enhance RCA quality [22]. This method used bacteria to produce calcium carbonate on the cell surfaces near the pores of ITZs (when appropriate calcium sources existed). Water absorption and compressive strength were improved using this method.

Drying shrinkage is a very important property of cementitious composites influencing their durability. Several models to predict the concrete drying shrinkage using influential factors have been empirically proposed in terms of slump, air content, fine aggregate, cement content, compressive strength, relative humidity, and volume-to-surface ratio, etc. [24,25]. In addition, it was reported that RCA treatment by PVA solution [19] affects concrete drying shrinkage. It has been widely accepted that the use of more RCA in the conventional concrete mix leads to an increase in drying shrinkage [5,6,8,9,11,17]. Some researchers summarized that drying shrinkage of the RCA concrete exhibited a 6–111% increase in 11 studies [5] while a 20–50% increase for coarse RCA and 70–100% increase for coarse and fine RCA in concrete pavement research areas [6] compared to that of the natural aggregate concrete.

Chloride penetration resistance, which is a measure of concrete durability, is important in reinforced concrete structures as well as plain concrete structures that do not use rebars. The presence of chloride ions was found to affect the spalling of concrete pavement below the freezing temperature of the pore solution and increased the saturation state of rebar corrosion [26]. The Rapid Chloride Penetration Test (RCPT), which is another such test, provides a diffusion-related conductivity measurement and index, where a higher RCPT value indicates greater concrete diffusion [26]. Factors that affect the RCPT include the compressive strength [26]; mineral admixtures such as fly ash [27–29]; aggregates [8,30–33]; curing conditions such as autoclaving, steam curing, and normal curing [34]; pore size [26,27]; RCA replacement ratio [35–37]; specimen temperature [38–40]; regional environment conditions [26]; test conditions [40]; multiple-stage mixing approaches [41,42]; and sodium silicate and silica fume coating of the RCA aggregate [41,42]. Especially, the RCA coating was observed to fill the cracks and pores using the ITZ of the concrete sample through microstructural analysis [41,42].

The above studies highlight the importance of an idealized mixing process, a mix proportioning method, ITZ strengthening, and a coating method to provide enhanced mechanical properties for RCA concretes. However, most previous studies have been limited to investigating the mechanical strength properties of RCA concretes. Readers may notice that, so far, no research determining the effect of RCA coating treatment by cement type solutions has been conducted on durability properties such as drying shrinkage and chloride ion penetration resistance. Thus, in the present study, an RCA coating treatment using a cement paste dissociation agent (CPDA) with different mixing methods was newly incorporated in RCA concrete mixtures. First, a preliminary test program was conducted to determine the proper dosage of CPDA solution using its RCA concrete test results on compressive strength, flexural strength, and elastic modulus. Then, a series of experimental tests were carried out to investigate the effect of RCA coating treatment, different mixing methods such as the equivalent mortar volume (EMV) method and conventional method, and different RCA replacement ratios on the durability test results of RCA concrete such as drying shrinkage values and RCPT values [43]. Therefore, the results of this study provide guidance that can be used to assess the beneficial increment in durability properties by adopting RCA coating treatment with the optimized mix proportioning method.

2. Experimental Program

2.1. RCA Production

This experimental study used RCAs produced from two different sources in South Korea. The RA aggregate was crushed with a maximum size of 25 mm from old runway concrete pavement at an air base reconstruction site. The RP was obtained with a maximum size of 20 mm by crushing the precast concrete (PC) culverts (see Figure 1). It should be noted that the first letter R from RA and RP refers to recycled coarse aggregate and the second letter denotes aggregate types used in this study where A is an arbitrary symbol while P was named since RP was manufactured from precast concretes.



Figure 1. Recycled concrete aggregate (RCA) sources.

The PC culverts had a compressive strength of 35 MPa with a maximum aggregate of 20 mm and a water–cement ratio of 35% or lower according to the Korean Construction Specification [44] and were manufactured by steam curing.

2.2. Aggregate Properties

Table 1 shows the specific gravity, absorption rate, and residual mortar content (RMC) of the RCA and the specific gravity and absorption rate of the natural coarse aggregate and fine aggregate. The specific gravity and absorption ratio of the RA were 2.54 and 4.81%, respectively. The specific gravity and absorption ratio of the RP were 2.60 and 2.62%, respectively.

Table 1. Basic aggregate properties.

Test Items	RA	RP	NCA	Fine Aggregate 1	Fine Aggregate 2
Specific gravity	2.54	2.60	2.69	2.58	2.60
Absorption rate (%)	4.81	2.62	0.54	0.52	0.95
RMC	-	20.0	-	-	-

Crushed granite (which was the same source of aggregate previously used in PC culverts) was used as the natural coarse aggregate, and its specific gravity and absorption rate were 2.69 and 0.54%, respectively. Natural river sand was used as the fine aggregate. RA and fine aggregate 1 were used in the first mix series, while RP and fine aggregate 2 were used in the second mix series. Figure 2 shows the particle size distribution for the RP, natural coarse aggregate (NCA), and fine aggregate 2, satisfying Korean standards.

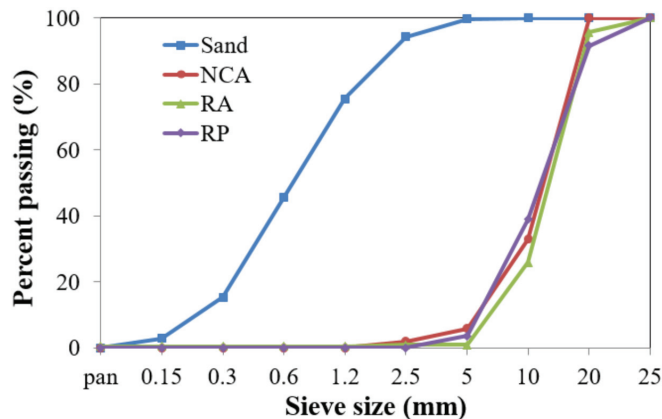


Figure 2. Aggregate gradation for RP, natural coarse aggregate (NCA), and fine aggregate 2.

In order to obtain the RMC value for RP, the heat treatment method proposed by Juan and Gutierrez [45] was used. After heating the prepared RCA samples for 2 h at 500 °C in an electric furnace, the heated samples were removed from the furnace and immersed in ice water to subject the samples to thermal shock and to separate the mortar. The RMC value was calculated by substituting the measured values in Equation (1). The RMC value was 20.0%.

$$\text{RMC} = (W_{\text{RCA}} - W_{\text{OVA}}) / W_{\text{RCA}} \times 100 \quad (1)$$

where W_{RCA} is the weight of the RCA dried in an oven dryer after first collecting the samples and W_{OVA} is the weight of the original virgin aggregate (OVA) dried in an oven dryer after removing residual mortar.

2.3. Cement Paste Dissociation Agent

The cement paste dissociation agent (CPDA) used in this study was a product composed of SiO₂, CaO, NaCl, NaNO₃, Na₂SO₄, and K₂CO₃. The chemical equations below explain the additional hydration reaction of calcium hydroxide from the cement and the CPDA [46]. Free calcium oxide of cement forms calcium hydroxide when mixed with water. Then, calcium hydroxide takes part in the reactions with the second and fourth components to the left in the following equations, which are the main components of the CPDA to further form inorganic crystallization or ettringite around old ITZs or new ITZs.



As a percentage of cement, 1.25% CPDA powder was recommended for conventional cement concretes by the CPDA manufactured company [46]. However, in this study, to coat the weak parts of old ITZs in the RCA concrete, 2.5% CPDA powder as a cement percentage, which is two times higher than the recommended dosages, was selected. Thus, for a preliminary test program (first mix series in Table 2), 0, 2.5, and 5% CPDA powder as a percentage of cement amounts were added in RCA concrete mixes. The test results from Section 4.1 showed that the addition of 2.5% CPDA as chemical admixtures in the RCA concrete mixes helps improve compressive strength, flexural strength, and elastic modulus properties. Thus, in the main test program (second mix series in Table 2), 300 g of CPDA was diluted in 1 L of water instead of powder but with the same dosage and sprayed on the RCA surface as shown in Figure 3. The coated RCAs were poured in a pan and covered with plastic for curing for 2 days. Then, they were used in the concrete mixture.

Table 2. Concrete mixture designs and material quantities.

Test Series	Mix	W/C	S/a	RCA wt %	Mix Proportions (kg/m ³)							
					W	C	S	F/A	NCA	RCA	CPDA	Admixture
1	CRA-0	0.37	38.9	100	138	370	695	-	-	1093	0	-
	CRA-2.5	0.37	38.9	100	138	370	695	-	-	1093	9.25	-
	CRA-5	0.37	38.9	100	138	370	695	-	-	1093	18.5	-
2	CNC	0.36	39.1	0	158	396	675	44.0	1051	0	-	2.56
	CRP-a	0.36	40.4	25	158	396	694	44.0	767	256	-	2.49
	CRP-b	0.36	41.7	50	158	396	712	44.0	499	498	-	2.49
	CRP-aS	0.36	40.4	25	158	396	694	44.0	767	256	-	2.49
	CRP-bS	0.36	41.7	50	158	396	712	44.0	499	498	-	2.49
	ERP-a	0.36	37.0	25	152	380	648	42.3	830	276	-	2.60
	ERP-b	0.36	34.6	50	145	363	619	40.3	584	583	-	2.61
	ERP-aS	0.36	37.0	25	152	380	648	42.3	830	276	-	2.74
	ERP-bS	0.36	34.6	50	145	363	619	40.3	584	583	-	2.62



Figure 3. Spray coating RCAs.

3. Experimental Tests

3.1. Mix Design

In this experiment, type I Portland cement was used with a specific gravity of 3.15 and specific surface area of 3380 cm²/g. The chemical admixture used in this experiment was an air entraining and water reducing agent solution. All of the aggregates were prepared in a saturated surface-dry condition.

Two series of mixes were prepared and tabulated in Table 2. The first series of mixes were designed in order to investigate the optimal amounts of cement paste dissociation agent (CPDA) powder. In the nomenclature from the first mix series, the numbers denote CPDA contents as a percentage of cement amounts.

The second series of mixes were then designed to find whether coating the RCAs with CPDA solution is an effective way to improve the durability properties such as drying shrinkage and chloride penetration resistance as well as mechanical strength properties of recycled aggregate concrete (RAC). This mix series involved nine mixtures. The conventional American Concrete Institute (ACI) mixing method and the equivalent mortar volume (EMV) mixing method were used. In the nomenclature, first, C and E in mix identification denote conventional and equivalent mix design, respectively. Next, R and N denote natural coarse aggregate and RCA, respectively. Thirdly, A refers to type A aggregate while P refers to aggregate manufactured from precast concretes. Fourthly, -a and -b refer to the 25% and 50% RCA replacement ratios per total coarse aggregate, respectively. Lastly, S used in the mixture nomenclature refers to the use of spray coating of the recycled concrete aggregate (RCA) surface in the mixture.

A pan mixer that could perform 60 L volume mixing was available in a research laboratory from Hongik University in Sejong, Korea, which is where the experimentation was conducted. First, the coarse aggregate and fine aggregate were poured in the mixer and mixed together for around 30 s. Then, cement was added and mixed for 30 s. Afterwards, the admixture was diluted sufficiently in water and added to the mixture for additional mixing for around 2 min.

3.2. Specimen Preparation

The specimens for concrete compressive strength measurement were prepared using a 100 mm × 200 mm plastic mold following a predetermined method [47]. The fabricated specimens were removed from the mold after 24 h and moist cured at approximately 20 ± 2 °C until the compressive strength testing. Three specimens were tested for each mixture, and their average values were calculated.

Drying shrinkage experiments were performed using a dial gauge, as suggested by KS (Korean Standards) F 2424 [48], which is equivalent to ASTM (American Society for Testing and Materials) C 157-08 [49]. Two rectangular specimens with 100 × 100 × 400 mm were prepared for each mixture. The drying shrinkage strain was measured by the dial gauge. The specimens were kept inside an environmental chamber, which was controlled at 20 °C and 60% Relative Humidity (RH). Figure 4 shows a schematic diagram and experimental specimens with the dial gauges installed.

In order to test the chloride ion penetration resistance, three cylindrical specimens with a 100 mm diameter and 200 mm height were prepared, followed by fabrication into disc specimens of 50 mm thickness in accordance with ASTM C 1202 [50]. The prepared disc specimens were placed in a vacuum state maintained for 3 h; then, the specimens were immersed in distilled water for 18 h to fulfill the saturation state pretreatment. For the 100 mm diameter and 50 mm thickness specimens, the cathode was filled with 3% NaCl aqueous solution and the anode was filled with 0.3 M NaOH aqueous solution followed by the application of 60 V for 6 h. Figure 5 shows a schematic diagram for the Rapid Chloride Penetration Test (RCPT) setup. After the initial current measurement, the passing current value was measured in 30-min intervals and the total passed charge was calculated using Equation (5).

$$Q = 900(I_0 + 2I_{30} + 2I_{60} + \dots + 2I_{300} + 2I_{330} + I_{360}) \quad (5)$$

where Q refers to the total passed charge and I_n refers to the current at n minutes.

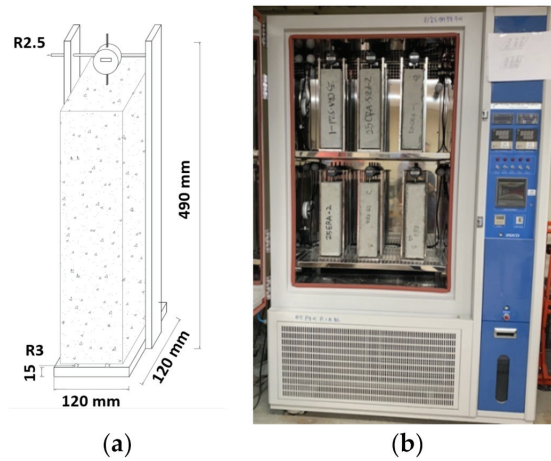


Figure 4. Experimental specimens with a dial-gauge installed: (a) schematic diagram and (b) picture.

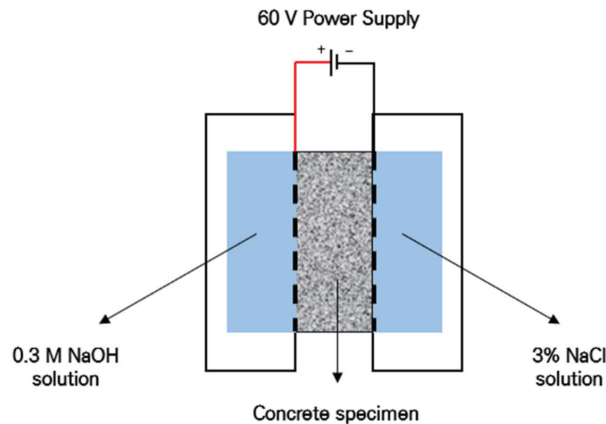


Figure 5. Chloride ion penetration resistance test setup.

4. Experimental Test Results

4.1. Preliminary Test Results from First Mix Series

Figure 6 shows average mechanical concrete strength properties such as compressive strength, flexural strength, and elastic modulus with error bars of the first mix series. In Figure 6a, the compressive strengths increased by 32% and 24% at 7 and 28 days, respectively, in CRA-2.5 mix compared to CRA-0 mix (control specimen). On the other hand, the compressive strengths in CRA-5 mix decreased by 27% and 24% at 7 and 28 days, respectively. The flexural strength test results showed a similar pattern to the compressive strength test results. The flexural strengths increased by 56% and 18% at 7 and 28 days, respectively, in CRA-2.5 mix compared to the control mix, whereas the flexural strengths in CRA-5 mix decreased by 21% and 3% at 7 and 28 days, respectively. Figure 6c shows the elastic modulus of the concrete test results at 28 days. In a similar manner to the compressive and flexural strength test results, elastic modulus increased by 3% in CRA-2.5 mix but decreased by 9% in CRA-5 mix compared to the control specimen. Thus, it appears that the addition of 2.5% of cement paste dissociation agent (CPDA) in the recycled concrete aggregate (RCA) concrete mixes helps improve the mechanical strength properties.

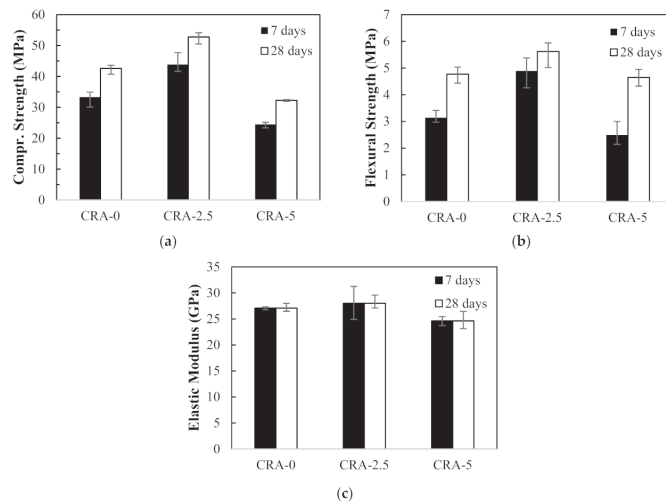


Figure 6. Mechanical strength results of first mix series: (a) compressive strength, (b) flexural strength, and (c) elastic modulus.

4.2. Test Results from Second Mix Series

4.2.1. Fresh and Hardened Properties

It is commonly accepted that concrete durability is thoroughly related to fresh and hardened properties. Table 3 presents the measured fresh and hardened concrete properties from the second mix series. Generally, concrete, which is prepared with workable slump and proper air content and is compacted with high density, is expected to be durable with reasonable compressive strength. It was observed from Table 3 that all RCA concrete mixes proportioned with the conventional mix design method and the equivalent mortar volume (EMV) design method were found to be workable, with their slump ranging between 150 and 160 mm. The air contents of all the mixes were almost identical, ranging from 3.9% to 4.2%. Thus, it can be inferred that slump or air content of RCA concretes from the second mix series does not affect the mechanical strength or durability of RCA concretes.

Table 3. Fresh and hardened properties of the mixes.

Mix iD	Fresh Property			Hardened Property		
	Slump (mm)	Air Content (%)	Density (kg/m ³)	Density (kg/m ³)	Compressive Strength (MPa)	Coefficient of Variation (%)
CNC	155	3.9	2414	2334	32.2	3.00
CRP-a	150	4.0	2333	2428	31.6	2.60
CRP-b	155	4.1	2360	2332	30.8	3.67
CRP-aS	155	4.0	2364	2301	30.3	4.84
CRP-bS	150	4.2	2389	2389	31.6	2.25
ERP-a	160	4.1	2294	2267	27.7	2.00
ERP-b	150	4.2	2336	2336	30.5	3.68
ERP-aS	155	4.1	2354	2306	30.1	2.53
ERP-bS	150	4.3	2314	2249	24.8	2.48

Table 3 summarizes density values at the fresh state and hardened state. While there were some deviations depending on the degree of aggregate coating, RCA substitution ratio, and fresh or hardened state, it seems that the densities of the ERP mixes are 1–2% lower values compared to that of the CNC and CRP mixes.

The compressive strength values at 28 days are represented in Table 3. Excluding ERP-a and ERP-bS, the compressive strength values were similar, at around 30.1–32.2 MPa. It was predicted [14,15] that the concrete that uses the EMV mixing method would exhibit higher strength than concrete that uses the conventional volume mixing method. However, in the case of the RCA used in this mixture, its quality was excellent, with a specific gravity of 2.60 and absorption rate of 2.62%, resulting in favorable strength even when the conventional ACI volume mixing method was used.

Figure 7 shows the average Young's modulus of the concrete samples at 28 days. All the elastic modulus values ranged from 26.3–27.7 GPa within 5% difference, regardless of different mixing methods or use of coating treatment method.

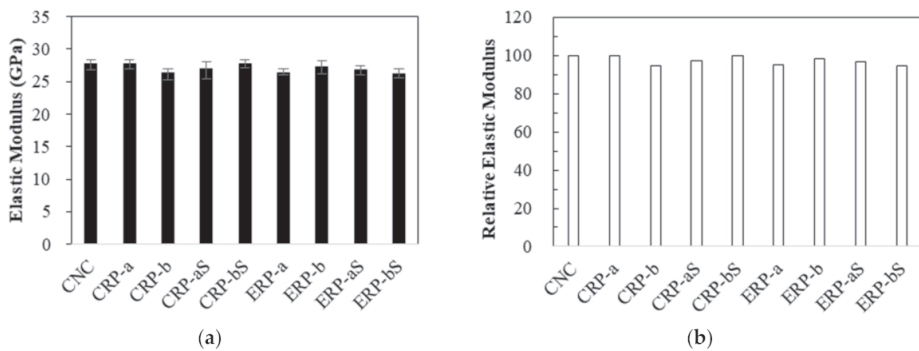


Figure 7. Elastic modulus and relative values: (a) elastic modulus and (b) relative elastic modulus.

4.2.2. Drying Shrinkage

The drying shrinkage test results are shown in Figure 8. Drying shrinkage tests were conducted for all the specimens initially for 111 days, as shown in Figure 8a. It must be noted that the initial wet curing period of 8 days instead of the standard wet curing period of 7 days was employed for the control specimen (CNC) and CRP specimens by malfunction of the environmental chamber. Therefore, it can be seen in Figure 8a that the ERP-a specimen produced higher drying shrinkage test values at early ages compared to the CRP specimens. However, previous researches [5,9,15] revealed that the EMV mixing method yielded a drying shrinkage property of the RCA concrete lower than that of the RCA concrete mixed with the conventional mixing method. Therefore, to verify that this comparatively higher shrinkage value of the ERP at early stages becomes a gradually lower value than that of the CRP specimens, drying shrinkage strains of the CNC, CRP-a, CRP-b, and ERP-a specimens were further measured for 648 days, as shown in Figure 8b. The test results are subsequently discussed in terms of three influencing factors: (1) mix proportioning method, (2) with and without RCA coating treatment, and (3) RCA replacement ratio.

Dependence of Mix Proportioning Method

The effect of different mix proportioning methods on drying shrinkage was studied, and their average test results are plotted with error bars in Figure 9. First, as shown in Figure 9a, the drying shrinkage values of CRP-a and ERP-a specimens were almost identical at 111 days, as mentioned before, but the drying shrinkage of the ERP-a specimen decreased by 4.6% at 648 days compared to that of CRP-a specimen. Likewise, in Figure 9b–d, the drying shrinkage values of the ERP-aS, ERP-b, and ERP-bS specimens decreased by 5.1%, 9.6%, and 0.1% compared to those of the CRP-aS, CRP-b, and CRP-bS specimens at 111 days, respectively. Hence, a lower drying shrinkage of RCA concrete can be achieved using the EMV mix proportion method compared to the RCA concrete proportioned by the conventional mix design method. This was confirmed by Fathifazl et al. [5] that drying

shrinkage is proportional to the total volume of the mortar and that the conventional RCA concrete mix contains a higher volume of mortar due to residual mortar.

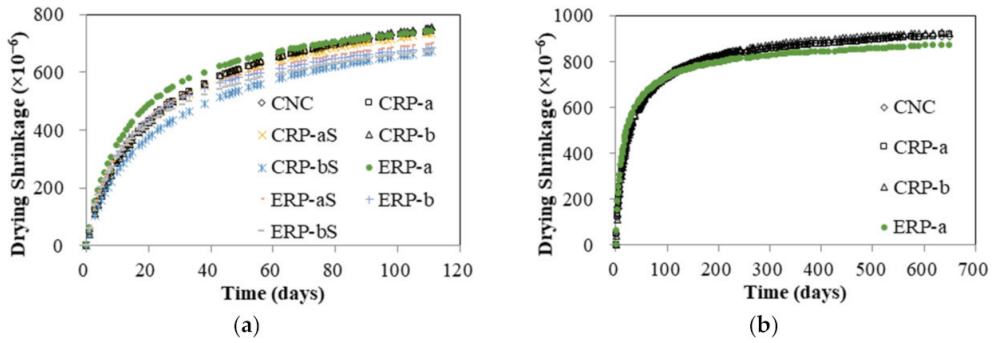


Figure 8. Drying shrinkage test results: (a) all specimens tested for 111 days and (b) some specimens tested for 648 days.

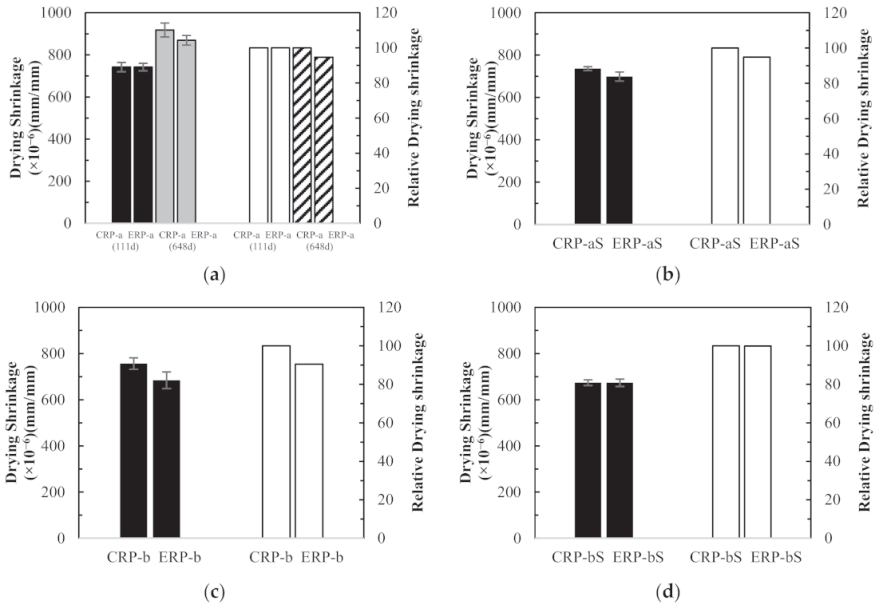


Figure 9. Concrete drying shrinkage results and relative values between different mix design method: (a) CRP-a versus ERP-a, (b) CRP-aS versus ERP-aS, (c) CRP-b versus ERP-b, and (d) CRP-bS versus ERP-bS.

Dependence of Coating Treatment

The effect of RCA coating on drying shrinkage was studied, and their average test results are plotted in Figure 10. Figure 10a–d show that the drying shrinkage values of CRP-aS, CRP-bS, ERP-aS, and ERP-bS mixes at 111 days decreased by 1%, 11%, 6%, and 2%, respectively, compared to those of CRP-a, CRP-b, ERP-a, and ERP-b. Thus, all the concrete specimens, which were mixed with coated RCA, represented better drying shrinkage performance than those mixed without RCA coating treatment, regardless of different mix proportioning methods and RCA replacement ratios.

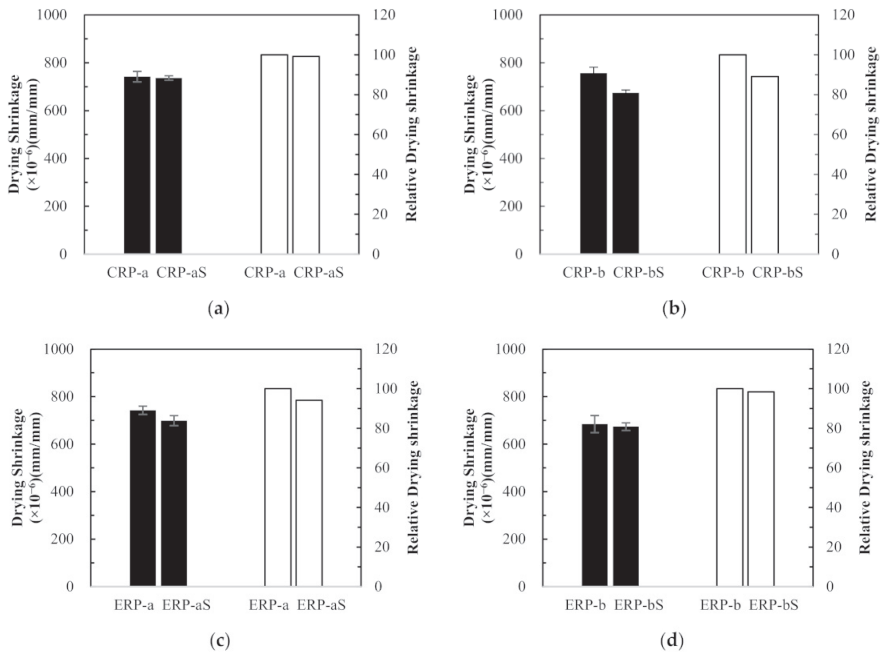


Figure 10. Concrete drying shrinkage results and relative values with and without recycled concrete aggregate coating treatment: (a) CRP-a versus CRP-aS, (b) CRP-b versus CRP-bS, (c) ERP-a versus ERP-aS, and (d) ERP-b versus ERP-bS.

Dependence of RCA Replacement Ratio

The test results were compared to investigate the effect of the RCA replacement ratios on the drying shrinkage of RCA concretes. In Figure 11a, compared to the drying shrinkage value of the CRP-a concrete specimen, which is made with 25% RCA replacement ratio, that of the CRP-b concrete specimen with 50% RCA replacement ratio was increased marginally by 2% at 111 days. However, reversed test results were observed in Figure 11b–d. In Figure 11b, CRP-bS specimens resulted in an 8.5% drop in concrete drying shrinkage compared to CRP-aS specimens. Although CRP-bS specimens were mixed with a 50% RCA replacement ratio using the conventional mix proportioning method, double the amount of coated RCAs led to a drop in drying shrinkage value compared to CRP-aS specimens. It is generally accepted that more RCA replacement in concrete mix leads to inferior drying shrinkage performance. However, the little increase or reversed result of drying shrinkage in concrete made with double the amount of RCA replacement may be attributed to the good-quality RCA adopted in this study. In Figure 11c, an 8% drop in concrete drying shrinkage of the ERP-b specimen was obtained with a 50% RCA replacement ratio compared to that of the ERP-a specimen with a 25% RCA replacement ratio. It should be remembered that the drying shrinkage values of the EMV mixes are expected to be similar regardless of different RCA replacement ratios incorporated in the EMV mix design, as the total mortar is the same. In a similar manner, about a 4% decrease in drying shrinkage for the ERP-bS specimen was observed in Figure 11d compared to the ERP-aS specimen.

4.2.3. Chloride Ion Penetration Resistance

Figure 12 shows the chloride ion penetration resistance experiment results for the concrete specimens. In the same manner as in Section 4.2.2, the test results are subsequently discussed in terms of three influencing factors: (1) mix proportioning method, (2) with and without RCA coating treatment, and (3) RCA replacement ratio.

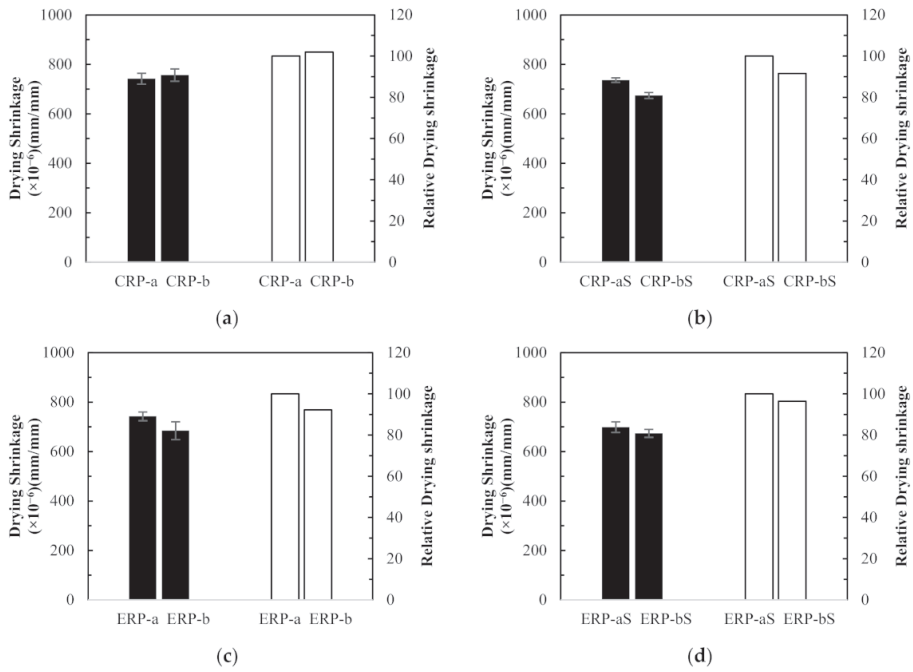


Figure 11. Concrete drying shrinkage results and relative values between different recycled concrete aggregate replacement ratios: (a) CRP-a versus CRP-b, (b) CRP-aS versus CRP-bS, (c) ERP-a versus ERP-b, and (d) ERP-aS versus ERP-bS.

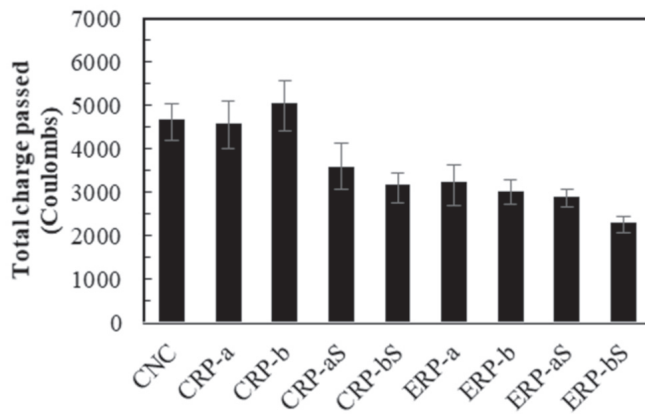


Figure 12. Chloride ion penetration resistance experiment results.

ASTM C 1202 [50] recommends the total charge passed between 2000 to 4000 C to be a moderate condition for concrete specimens. From this recommendation, except for CNC, CRP-a, and CRP-b, all other mixes in Figure 12 represented good resistance against the chloride ion penetration resistance. Thus, it may be said that the ERP mixes have unparalleled resistance regardless of RCA coating treatment, but combined with the RCA coating treatment, it produced the finest performance against chloride ion penetration.

Mix Proportioning Method

The effect of different mix proportioning methods on chloride ion penetration resistance was studied and their Rapid Chloride Penetration Test (RCPT) results are plotted in Figure 13. In Figure 13a–d, the RCPT values of the ERP-a, ERP-aS, ERP-b, and ERP-bS specimens decreased remarkably by 30%, 19%, 40%, and 28%, compared to those of the CRP-a, CRP-aS, CRP-b, and CRP-bS specimens, respectively. In fact, the RCPT values for RCA concrete specimens proportioned by the EMV method were substantially lower than those of the specimens made of a mixture proportioned by the conventional method. Thus, it may be inferred that the RCPT values are related to the total mortar volume of the RCA concrete mix since the total mortar volume in the ERP mixes is reduced due to the residual mortar attached to the RCAs.

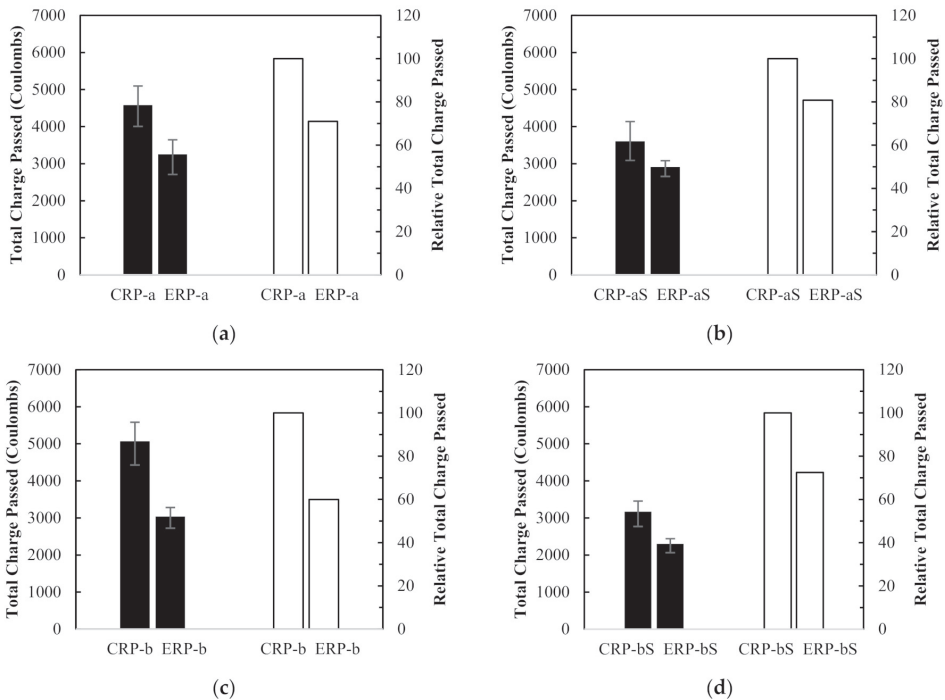


Figure 13. Rapid Chloride Penetration Test results and relative values between different mix design method: (a) CRP-a, (b) CRP-aS, (c) CRP-b, and (d) CRP-bS.

Coating Treatment

The effect of RCA coating on the RCPT results was studied, and their average test results are plotted in Figure 14. Figure 14a–d show that the RCPT values of CRP-aS, CRP-bS, ERP-aS, and ERP-bS mixes decreased by 21%, 37%, 10%, and 24%, respectively, compared to those of CRP-a, CRP-b, ERP-a, and ERP-b. Thus, all the concrete specimens, which were mixed with the coated RCAs, represented reduced RCPT values compared to those mixed without RCA coating treatment, regardless of different mix proportioning methods or RCA replacement ratios. In fact, implementing the RCA coating treatment using the CPDA solution before concrete mixing resulted in better performance for drying shrinkage as well as chloride ion penetration resistance.

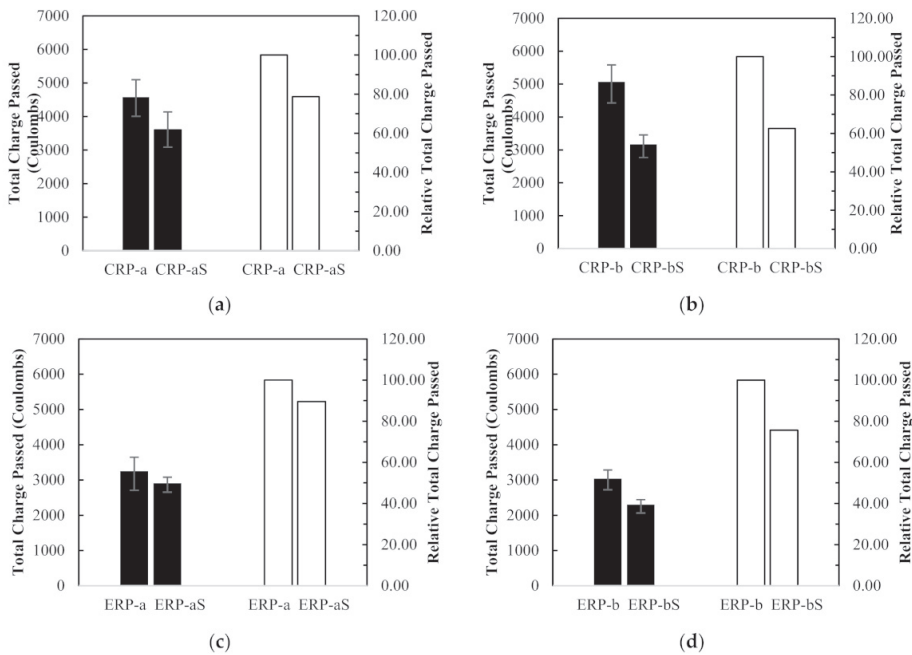


Figure 14. Rapid Chloride Penetration Test results and relative values between different mix design method with and without recycled concrete aggregate coating: (a) CRP-a, (b) CRP-b, (c) ERP-a, and (d) ERP-b.

RCA Replacement Ratio

The test results were compared to determine the effect of RCA replacement ratios on the RCPT values of RCA concretes, as shown in Figure 15. In Figure 15a, compared to the RCPT value of the CRP-a concrete specimen, which is made with 25% RCA replacement ratio, that of the CRP-b concrete specimen with 50% RCA replacement ratio increased by 11%. It is also widely accepted that more RCA replacement in concrete mix leads to inferior chloride ion penetration resistance. However, contrary test results were observed in Figure 15b–d. In Figure 15b, the CRP-bS specimens resulted in a 12% drop in the RCPT value compared to CRP-aS specimens. Although CRP-bS specimens were mixed with 50% RCA replacement ratio, using the conventional mix proportioning method, double the amount of coated RCAs led to a drop in the RCPT value compared to CRP-aS specimens. In Figure 15c, a 6% drop in the RCPT value of the ERP-b specimen was obtained with 50% RCA replacement ratio compared to that of the ERP-a specimen with 25% RCA replacement ratio. As mentioned before, those two test values were supposed to be similar, regardless of different RAC replacement ratios, since their total mortar is the same. Likewise, about a 20% drop in the RCPT value for the ERP-bS specimen was observed in Figure 15d compared to ERP-aS specimen. Similar to the test results from Section 4.2.2 Drying Shrinkage, the reversed result of the RCPTs in concrete made with double the amount of RCA replacement except for CRP-a versus CRP-b may be attributed to the good-quality RCA adopted in this study. Further study on this effect is necessary.

4.2.4. Micro Structural Analysis of RCA

A scanning electronic microscope (SEM) was used to observe the microstructural characteristics of RCA concretes. In this study, CRP-b and CRP-bS samples only were tested to check whether the CPDA coating effect was seen in the image analysis. In Figure 16b, the darker area is the original virgin aggregate, while the lighter part in Figure 16b is old mortar. The strip area between aggregate and old mortar is the interfacial transition zone

(ITZ). It can be seen that the old ITZ in CRP-b (Figure 16a) is different from the old ITZ in CRP-bs (Figure 16b). The old ITZ width in Figure 16a ranges between 22 to 47 μm , while the old ITZ width in Figure 16b ranges between 7 to 11 μm . This implies that the coating effect of the CPDA can modify the microstructure of ITZs. Further research is needed to explore image analysis related to this topic.

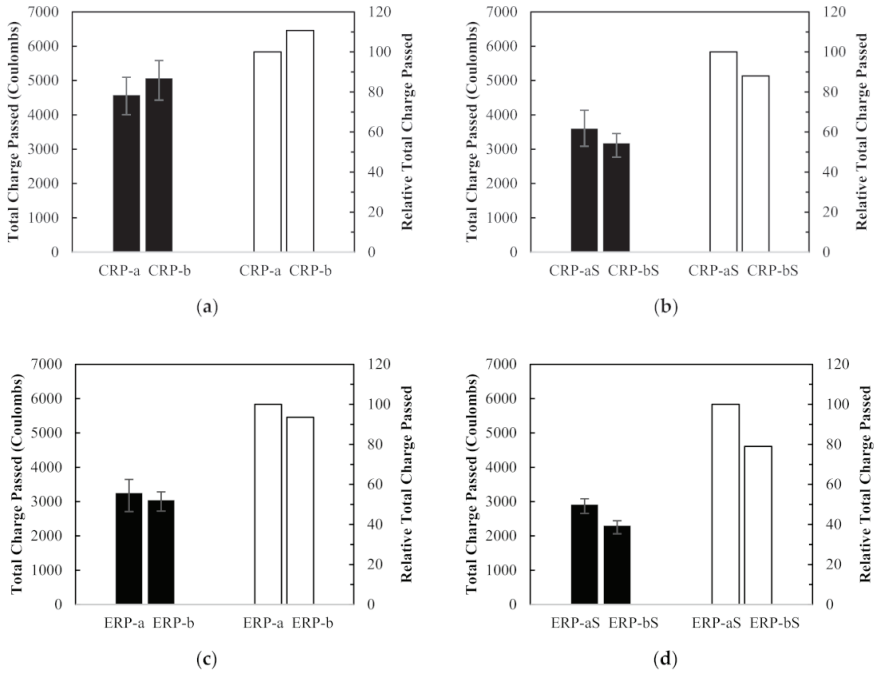


Figure 15. Rapid Chloride Penetration Test results and relative values between different recycled concrete aggregate replacement ratios: (a) CRP-a, (b) CRP-b, (c) ERP-a, and (d) ERP-b.

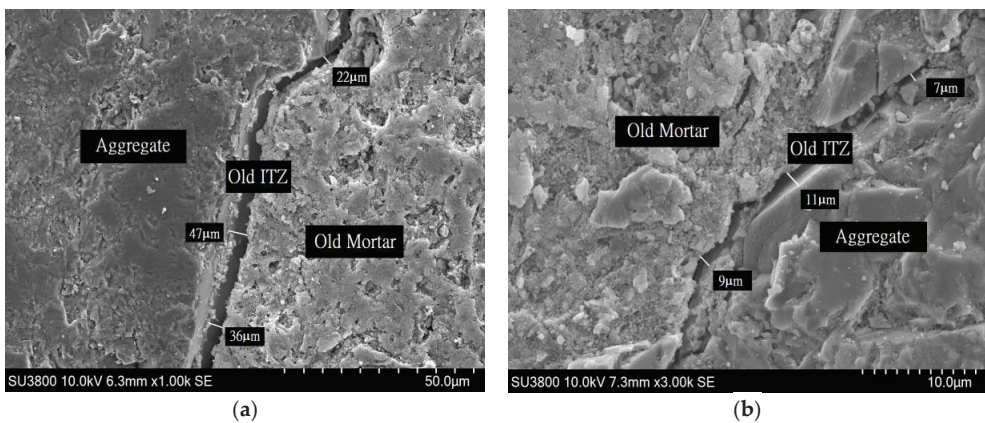


Figure 16. Scanning electronic microscope in the interfacial transition zone (ITZ) of different RCAs: (a) CRP-b and (b) CRP-bs.

5. Conclusions

In this study, recycled concrete aggregate (RCA) manufactured from precast concrete (PC) culvert was used to carry out durability experiments on concrete fabricated using

the conventional ACI volume mixing method and the equivalent mortar volume (EMV) mixing method. Moreover, a cement paste dissociation agent (CPDA) was used to coat the RCA surface followed by curing to investigate the drying shrinkage and the chloride ion penetration resistances of the concrete coated at the RCA surface with CPDA compared with concrete that did not. The following conclusions were obtained from the experimental results.

1. From the preliminary test, it appears that the addition of 2.5% of CPDA in the RCA concrete mixes helps improve the mechanical strength properties such as compressive strength, flexural strength, and elastic modulus. The test results showed that about 24%, 18%, and 3% increases were observed for compressive strength, flexural strength, and elastic modulus, respectively, at 28 days.
2. All RCA concretes mixed with coated RCA were found to be workable regardless of different mix methods, with the slump and air contents of all the mixes being almost identical. Additionally, all the concrete specimens that were mixed with the coated RCAs with CPDA solution had lower drying shrinkage values and RCPT (Rapid Chloride Penetration Test) values than those mixed without RCA coating treatment, regardless of different mix proportioning methods or RCA replacement ratios. The variation in compressive strength and density of the RCA concrete did not affect drying shrinkage or RCPT values.
3. This holds for the concrete specimens proportioned with the EMV method, regardless of different RCA replacement ratios. Especially, it may be inferred that the RCPT values are related to total mortar volume of RCA concrete mix since total mortar volume in the ERP mixes is reduced due to the residual mortar attached to the RCAs.
4. For the conventional RCA mixes, in comparison to test results from the 25% RCA replacement ratio, the little increase or reversed test result of drying shrinkage values and RCPT values in concrete made with 50% RCA replacement ratio may be attributed to the good-quality RCA adopted in this study. Further study on this effect is necessary.

Author Contributions: Conceptualization, S.Y. and H.L.; methodology, S.Y. and H.L.; validation, S.Y.; formal analysis, H.L.; investigation, H.L.; resources, H.L.; data curation, S.Y. and H.L.; writing—original draft preparation, S.Y.; writing—review and editing, S.Y.; supervision, S.Y.; project administration, H.L.; funding acquisition, S.Y. All authors have read and agreed to the published version of the manuscript.

Funding: This research was funded by the Ministry of Land, Infrastructure, and Transport (MOLIT) and the Korea Agency for Infrastructure Technology Advancement (KAIA), grant number 21POQW-B152690-03.

Institutional Review Board Statement: Not applicable.

Informed Consent Statement: Not applicable.

Data Availability Statement: The data presented in this study are available on request from the corresponding author.

Conflicts of Interest: The authors declare no conflict of interest.

References

1. Rahid, K.; Razzaq, A.; Dhmad, M.; Rashid, T.; Tariq, S. Experimental and analytical selection of sustainable recycled concrete with ceramic waste aggregate. *Constr. Build. Mater.* **2017**, *154*, 829–840. [CrossRef]
2. Szelag, M.; Zegardło, T.; Andrzejuk, W. The use of fragmented, worn-out car side windows as an aggregate for cementitious composites. *Materials* **2019**, *12*, 1467. [CrossRef]
3. Ramdani, S.; Guettala, A.; Benmalek, M.; Agular, J. Physical and mechanical performance of concrete made with waste rubber aggregate, glass powder and silica sand powder. *J. Build. Eng.* **2019**, *21*, 302–311. [CrossRef]
4. Yang, S. A feasibility study of wood-plastic composite paver block for basic rest areas. *J. Korean Wood Sci. Technol.* **2019**, *47*, 51–65.
5. Fathifazl, G. Structural Performance of Steel Reinforced Recycled Concrete Members. Ph.D. Thesis, Carleton University, Ottawa, ON, Canada, January 2008.

6. Snyder, M. Recycling concrete pavements. In Proceedings of the ACPA Pennsylvania Chapter Presentation, Harrisburg, PA, USA, 27 January 2010.
7. Thomas, C.; Setien, J.; Polanco, J. Structural recycled aggregate concrete made with precast wastes. *Constr. Build. Mater.* **2016**, *114*, 536–546. [CrossRef]
8. Andal, J.; Shehate, M.; Zacarias, P. Properties of concrete containing recycled concrete aggregate of preserved quality. *Constr. Build. Mater.* **2016**, *125*, 842–855. [CrossRef]
9. Yang, S.; Lim, Y. Mechanical strength and drying shrinkage properties of RCA concretes produced from old railway concrete sleepers using by a modified EMV method. *Constr. Build. Mater.* **2018**, *185*, 499–507. [CrossRef]
10. Shi, X.; Mukhopadhyay, A.; Zollinger, D. Sustainability assessment for portland cement concrete pavement containing reclaimed asphalt pavement aggregates. *J. Clean. Prod.* **2018**, *192*, 569–581. [CrossRef]
11. Tam, V.; Tam, C. Assessment of durability of recycled aggregate concrete produced by two-stage mixing approach. *J. Mater. Sci.* **2007**, *42*, 3592–3602. [CrossRef]
12. Sicakova, A.; Urban, K. The influence of discharge time, kind of additive and kind of aggregate on the properties of three-stage mixed concrete. *Sustainability* **2018**, *10*, 3862. [CrossRef]
13. Abousnina, R.; Manalo, A.; Ferdous, W.; Lokugel, W.; Benabed, B.; Al-Jabri, W. Characteristics, strength development and microstructure of cement mortar containing oil-contaminated sand. *Constr. Build. Mater.* **2020**, *252*, 119155. [CrossRef]
14. Fathifazl, G.; Abbas, A.; Razaqpur, A.G.; Isgor, O.B.; Fournire, B.; Foo, S. New mixture proportioning method for concrete made with coarse recycled concrete aggregate. *J. Mater. Civ. Eng. ASCE* **2009**, *21*, 601–611. [CrossRef]
15. Yang, S.; Lee, H. Mechanical properties of recycled aggregate concrete proportioned with modified equivalent mortar volume method for paving applications. *Constr. Build. Mater.* **2017**, *136*, 9–17. [CrossRef]
16. Gupta, P.; Khaudhair, Z.; Ahuja, A. A new method for proportioning recycled concrete. *Struct. Concr.* **2016**, *4*, 677–687. [CrossRef]
17. Kiskun, N.; Raijand, P.; Panda, S.; Nayak, S.; Pandey, V. Development of durable concrete from C&D waste by adopting identical mortar volume method in conjunction with two-stage mixing procedure. *Constr. Build. Mater.* **2020**, *256*, 119361.
18. Wu, C.; Zhu, Y.; Zhang, X.; Kou, S. Improving the properties of recycled concrete aggregate with bio-deposition approach. *Cem. Concr. Compos.* **2018**, *94*, 248–254. [CrossRef]
19. Kou, S.; Poon, C. Properties of concrete prepared with PVA-impregnated recycled concrete aggregates. *Cem. Concr. Compos.* **2010**, *32*, 649–654. [CrossRef]
20. Speath, V.; Teggner, A. Improvement of recycled concrete aggregate properties by polymer treatment. *Int. J. Sustain. Built Environ.* **2013**, *2*, 143–152. [CrossRef]
21. Kong, D.; Lei, T.; Zheng, J.; Ma, C. Effect and mechanism of surface coating pozzolanics materials around aggregate on properties and ITZ microstructure of recycled aggregate concrete. *Constr. Build. Mater.* **2010**, *24*, 701–708. [CrossRef]
22. ACI Manual of Concrete Practice 209R-92. In *Prediction of Creep, Shrinkage, and Temperature Effects in Concrete Structures*; American Concrete Institute: Farmington Hills, MI, USA, 1997; pp. 1–47.
23. Siddika, A.; Mamun, M.; Ferdous, W.; Saha, A.; Alyousef, R. 3D Printed Concrete: Applications, Performance, and Challenges. *J. Sustain. Cem. Based Mater.* **2019**, *9*, 127–164. [CrossRef]
24. CEB 1990, “Evaluation of the Time Dependent Properties of Concrete”, *Bulletin d’Information No.199*; Comité Européen du Béton/Fédération Internationale de la Précontrainte: Lausanne, Switzerland, 1991; p. 201.
25. Wang, J.; Vandevyvere, B.; Vanhessche, S.; Schoon, J. Microbial carbonate precipitation for the improvement of quality of recycled aggregates. *J. Clean. Prod.* **2017**, *156*, 355–366. [CrossRef]
26. Mohr, P.; Hansen, W.; Jensen, E.; Pane, I. Transport properties of concrete pavements with excellent long-term in-service performance. *Cem. Concr. Res.* **2000**, *30*, 1903–1910. [CrossRef]
27. Li, S.; Roy, D.M. Investigation of relations between porosity, pore structure, and Cl diffusion of fly ash and blend cement pastes. *Cem. Concr. Res.* **1986**, *16*, 749–759. [CrossRef]
28. Wee, T.; Suryavanshi, A.; Tin, S.S. Evaluation of rapid chloride permeability test (RCPT) results for concrete containing mineral admixtures. *ACI Mater. J.* **2000**, *97*, 221–232.
29. Moffatt, E.; Thomas, M.; Fahim, A. Performance of high-volume fly ash concrete in marine environment. *Cem. Concr. Res.* **2017**, *102*, 127–135. [CrossRef]
30. Wee, T.; Suryavanshi, A.; Tin, S. Influence of aggregate fraction in the mix on the reliability of the rapid chloride permeability test. *Cem. Concr. Compos.* **1999**, *21*, 59–72. [CrossRef]
31. Asbridge, A.; Chadbourne, G.; Page, C. Effects of metakaoline and the interfacial transition zone on the diffusion of chloride ions through cement mortars. *Cem. Concr. Res.* **2001**, *31*, 1567–1572. [CrossRef]
32. Grattan-Bellew, P. Alkali contribution from limestone aggregate to pore solution of old concrete. *ACI Mater.* **1994**, *91*, 173–177.
33. Xie, P.; Beaudoin, J.; Brousseau, R. Effect of aggregate size on transition properties at the portland cement paste interface. *Cem. Concr. Res.* **1991**, *21*, 999–1005.
34. Aldea, C.; Young, F.; Wang, K.; Shah, S. Effect of curing conditions on properties of concrete using slag replacement. *Cem. Concr. Res.* **2000**, *30*, 465–472. [CrossRef]
35. Sasanipour, H.; Aslani, F. Effect of specimen shape, silica fume, and curing age on durability properties of self-compacting concrete incorporating coarse recycled concrete aggregate. *Constr. Build. Mater.* **2019**, *228*, 117054. [CrossRef]

36. Khodair, Y.; Bommareddy, B. Self-consolidating concrete using recycled concrete aggregate and high volume of fly ash and slag. *Constr. Build. Mater.* **2017**, *15*, 307–316. [CrossRef]
37. Faella, C.; Lima, C.; Martinelli, E.; Pepe, M.; Realfonzo, R. Mechanical and durability performance of sustainable structural concretes: An experimental study. *Cem. Concr. Res.* **2016**, *71*, 85–96. [CrossRef]
38. Moore, W. *Physical Chemistry*, 4th ed.; Prentice-Hall: Englewood Cliffs, NJ, USA, 1972.
39. Julio-Betancourt, G.; Hooton, R. Study on the Joule effect on rapid chloride permeability values and evaluation of related electrical properties of concretes. *Cem. Concr. Res.* **2004**, *34*, 1007–1015. [CrossRef]
40. Yang, C.; Cho, S.; Huang, R. The relationship between charge passed and the chloride-ion concentration in concrete using steady-state chloride migration test. *Cem. Concr. Res.* **2001**, *32*, 217–222. [CrossRef]
41. Rajhans, P.; Gupta, P.; Kumar, R.; Panda, S.; Nayak, S. EMV mix design method for preparing sustainable self compacting recycled aggregate concrete subjected to chloride environment. *Constr. Build. Mater.* **2019**, *199*, 705–716. [CrossRef]
42. Rajhans, P.; Chand, G.; Kisku, N.; Panda, S.; Nayak, S. Propose mix design method for producing sustainable self compacting heat cured recycled aggregate concrete and its microstructural investigation. *Constr. Build. Mater.* **2019**, *218*, 568–581. [CrossRef]
43. Yang, S.; Lee, H.; Oh, I.; Lee, H.; Hwang, I. Properties of RCA Concretes Mixed with Cement Paste Dissociation Agent. In Proceedings of the 3rd International Conference on Bio-Based Building Materials, Belfast, UK, 26–28 June 2019.
44. *KCS 11 40 05: Reinforced Concrete Culverts*; Korean Construction Specification; KICT: Goyang, Gyeonggi-do, Korea, 2016.
45. Juan, M.; Gutierrez, P. Study on the influence of attached mortar content on the properties of recycled concrete aggregate. *Constr. Build. Mater.* **2009**, *23*, 872–877. [CrossRef]
46. Rusinoff, A. Composition for protecting a body of concrete, a process for preparing same and a method for the protection of a body of concretes. U.S. Patent 5,728,428, 17 March 1998.
47. *ASTM C192: Standard Practice for Making and Curing Concrete Test Specimens in the Laboratory*; American Society for Testing Materials: West Conshohocken, PA, USA, 2012.
48. *KS F 2424: Standard Test Method for Length Change of Mortar and Concrete*; KATS: Seoul, Korea, 2015.
49. *ASTM C157: Standard Test Method for Length Change of Hardened Hydraulic-Cement Mortar and Concrete*; ASTM International: West Conshohocken, PA, USA, 2012.
50. *ASTM C1202: Standard Test Method for Electrical Indication of Concrete's Ability to Resist Chloride ion Penetration*; American Society for Testing Materials: West Conshohocken, PA, USA, 2019.

Article

Corrosion Behavior of Steel-Reinforced Green Concrete Containing Recycled Coarse Aggregate Additions in Sulfate Media

Abigail Landa-Sánchez ¹, Juan Bosch ², Miguel Angel Baltazar-Zamora ^{3,*}, René Croche ⁴, Laura Landa-Ruiz ³, Griselda Santiago-Hurtado ⁵, Victor M. Moreno-Landeros ⁵, Javier Olguín-Coca ⁶, Luis López-Léon ⁶, José M. Bastidas ⁷, José M. Mendoza-Rangel ^{8,*}, Jacob Ress ² and David. M. Bastidas ^{2,*}

¹ Facultad de Ingeniería Mecánica y Eléctrica, Doctorado en Ingeniería, Universidad Veracruzana, Xalapa 91000, Veracruz, Mexico; liagiba07@hotmail.com

² National Center for Education and Research on Corrosion and Materials Performance, NCERCAMP-UA, Department of Chemical, Biomolecular, and Corrosion Engineering, The University of Akron, 302 E Buchtel Ave, Akron, OH 44325, USA; jlb394@zips.uakron.edu (J.B.); jtr45@zips.uakron.edu (J.R.)

³ Facultad de Ingeniería Civil—Xalapa, Universidad Veracruzana, Lomas del Estadio S/N, Zona Universitaria, Xalapa 91000, Veracruz, Mexico; lalanda@uv.mx

⁴ Facultad de Ingeniería Mecánica y Eléctrica, Universidad Veracruzana, Xalapa 91000, Veracruz, Mexico; rcroche@uv.mx

⁵ Facultad de Ingeniería Civil—Unidad Torreón, UADEC, Torreón 27276, Mexico; grey.shg@gmail.com (G.S.-H.); vmmorlan@gmail.com (V.M.M.-L.)

⁶ Grupo de Investigación DICSO, Instituto de Ciencias Básicas e Ingeniería, UAEH, Hidalgo 42082, Mexico; jolguin77@gmail.com (J.O.-C.); luis_lopez@uaeh.edu.mx (L.L.-L.)

⁷ National Centre for Metallurgical Research (CENIM), CSIC, Ave. Gregorio del Amo 8, 28040 Madrid, Spain; bastidas@cenim.csic.es

⁸ Facultad de Ingeniería Civil, Universidad Autónoma de Nuevo León, Ave. Pedro de Alba S/N, Ciudad Universitaria, San Nicolás de los Garza 66455, Mexico

* Correspondence: mbaltazar@uv.mx (M.A.B.-Z.); jmmr.rangel@gmail.com (J.M.M.-R.); dbastidas@uakron.edu (D.M.B.); Tel.: +52-2282-5252-94 (M.A.B.-Z.); +1-330-972-2968 (D.M.B.)

Received: 18 August 2020; Accepted: 25 September 2020; Published: 29 September 2020

Abstract: Novel green concrete (GC) admixtures containing 50% and 100% recycled coarse aggregate (RCA) were manufactured according to the ACI 211.1 standard. The GC samples were reinforced with AISI 1080 carbon steel and AISI 304 stainless steel. Concrete samples were exposed to 3.5 wt.% Na₂SO₄ and control (DI-water) solutions. Electrochemical testing was assessed by corrosion potential (E_{corr}) according to the ASTM C-876-15 standard and a linear polarization resistance (LPR) technique following ASTM G59-14. The compressive strength of the fully substituted GC decreased 51.5% compared to the control sample. Improved corrosion behavior was found for the specimens reinforced with AISI 304 SS; the corrosion current density (i_{corr}) values of the fully substituted GC were found to be 0.01894 $\mu\text{A}/\text{cm}^2$ after Day 364, a value associated with negligible corrosion. The 50% RCA specimen shows good corrosion behavior as well as a reduction in environmental impact. Although having lower mechanical properties, a less dense concrete matrix and high permeability, RCA green concrete presents an improved corrosion behavior thus being a promising approach to the higher pollutant conventional aggregates.

Keywords: corrosion; AISI 304 SS; AISI 1018 CS; green concrete; recycled coarse aggregate; sugar cane bagasse ash; Na₂SO₄

1. Introduction

Traditionally, the world's most widely used building material is hydraulic concrete that, when combined with AISI 1018 carbon steel (CS) rebars, forms a system known as reinforced concrete. Reinforced concrete structures are known for their long-lasting service life and low-maintenance requirements. However, due to the corrosion of the steel reinforcement, billions of dollars are spent in the repair and maintenance of bridges, tunnels, roads and docks, among others, by each country [1–5]. The corrosion of steel embedded in concrete is an electrochemical process in which the oxidation of iron occurs at the anode, whereas at the cathode, oxygen reduction takes place. Corrosion occurs due to several factors that promote passivity breakdown, primarily the carbonation or the ingress of aggressive ions [6,7]. The aggressive depassivating ions are chlorides, present in marine environments [8–10] and sulfates from inorganic salts normally present in both groundwater and in surface water. However, the concentration of aggressive agents in these environments can be highly variable [11–14]. The presence of sulfates in contact with a hardened cement paste can significantly increase the solubility of matrix components and cause degradation of concrete through leaching, thus decreasing the degree of protection of the reinforcement [15–17]. In other studies, laboratory simulations also show that the galvanized reinforcements outperform traditional carbon steel reinforcements not only in aggressive environments, but also in contact with contaminants found in the concrete mixture [18–21].

Presently, the use of ordinary Portland cement (OPC) is responsible for 10% of global CO₂ emissions, a value that can increase up to 15% in the near future [22]. As a solution to this highly pollutive binder, different approaches combining reduced greenhouse emissions and acceptable corrosion resistance properties have been proposed, such as new alkali-activated materials. Some examples of these novel binders are fly ash (FA), slags, metakaolin sugar cane bagasse ash (SCBA) or rice husks ashes (RHA), among others [19,20]. Interest in SCBA and RHA has recently increased due to the fact that both are an agricultural waste product with a similar corrosion performance to OPC [23,24]. After being treated, the SCBA shows pozzolanic activity, making it a suitable binder to replace OPC [24]. However, the required post-treatment to obtain the binder can increase the greenhouse emissions or decrease the workability of the concrete, apart from the mechanical and chemical properties as presented by Franco-Luján et al. [25]. Regarding corrosion behavior, few studies can be found considering these novel binders. For instance, FA in some studies presents a lower diffusion coefficient than OPC [26,27]. Although SCBA presents lower workability, substitution of OPC ranging between 10% and 30% reduces not only the diffusion coefficient of chloride ions, but also the permeability [25,28–32]. As a result, their use has been limited to supplementary cementitious materials (SCMs) as a conservative solution due to the lack of agreement on their corrosion performance [26–38]. This partial replacement of the OPC presents an environmentally friendly and cost-effective approach due to the by-product's nature of the novel binders [39–42].

Furthermore, the recycling of concrete is considered a key process in the current sustainable development trends. This is because concrete is widely used as a construction material. Its manufacturing consumes a large amount of nonrenewable natural resources: aggregates (80%), OPC (10%), SCM (3%) and water (7%). The natural aggregates (NA) used in the manufacturing of concrete are inert granular materials such as sand, gravel, or crushed stone. Gravel and natural sand are generally obtained from a well, river, lake, or seabed [43]. Currently, the global production of aggregates is estimated to be 40 trillion tons, which leads to the exhaustion of natural resources, high energy consumption and extreme impacts on the environment [44].

For the aforementioned reasons, recycled coarse aggregate (RCA) as a replacement for natural coarse aggregate (NCA), in addition to replacing OPC by 20% with SCBA, represents a substantial reduction in the environmental impact of concrete manufacturing [44]. This topic is of great concern in Europe and in developed countries such as the USA and Canada, among others [45]. A total of 78,000 tons of RCA were used in the Netherlands in 1994, due to the fact that the use of 20% RCA thick did not differentiate properties of fresh or hardened concrete, according to the corresponding

national organization [46]. The increasing trend of research efforts of RCA for the manufacturing of new concrete has also increased the interest in the production of high-performance, high-strength concrete [47]. It should be noted that the use of thick RCA (up to 30%) is usually recommended, but it is often considered necessary to add superplasticizers [48] to achieve the required workability of the new concrete. These materials can improve the durability of concrete [44–54]. Due to the scarce works found in the literature, further research efforts are needed to determine the effect of the RCA as well as the partial substitution of OPC with SCBA in the corrosion performance of these novel concretes [55–57].

The aim of this work was to study the effect of the substitution of NCA by the environmentally friendly RCA on the GC embedding AISI 1018 carbon steel (CS) and AISI 304 SS rebars. This GC was also partially substituted with SCBA to further decrease the environmental impact of the traditional OPC concrete. Furthermore, the mechanical strength of the new GC was investigated to describe its future real-world applications. Five different concrete mixtures were prepared according to the ACI 211.1 standard [58], two reinforcement alloys, AISI 304 SS and carbon steel 1018, were investigated under control and aggressive environments. Corrosion monitoring techniques, such as open circuit potential (OCP) and linear polarization resistance (LPR), were used to elucidate the corrosion behavior of the novel green concretes. This work contributes to the corrosion performance knowledge as there is not a clear mechanism on how RCA affects the corrosion phenomenon. Furthermore, it presents concrete mixtures with a substantial reduction in the environmental impact due to the partial substitution not only of OPC with SCBA, but also the natural aggregates by the RCA, thus reducing the CO₂ emissions substantially [22].

2. Materials and Methods

2.1. Green Concrete (GC)

Three different concrete mixtures were made: a conventional concrete control mixture (MC) made with 100% OPC following the standard for Portland blended cement (CPC 30R, NMX-C-414-ONNCCE-2014) [59], natural fine (NFA) and coarse (NCA) aggregates and two mixtures of green concrete (GC)—the first green concrete with a 50% substitution of NCA for RCA and with a partial 20% substitution of cement for SCBA, and the second green concrete with a 100% substitution of RCA and the same SCBA ratio. The SCBA was obtained from Mahuixtlan sugar mills, located in Coatepec, Mexico. The characterization of the physical properties of aggregates, NCA, NFA and RCA, was made in accordance with the ASTM standards, the tests were relative density (specific gravity) [60,61], bulk density (unit weight, kg/m³) [62], absorption (%) of coarse aggregate and fine aggregate [63], maximum aggregate size and fineness modulus [58]. Figure 1 shows the proposed experimental testing procedure to determine the optimal mixture design. Table 1 shows the physical properties of the materials in this research.

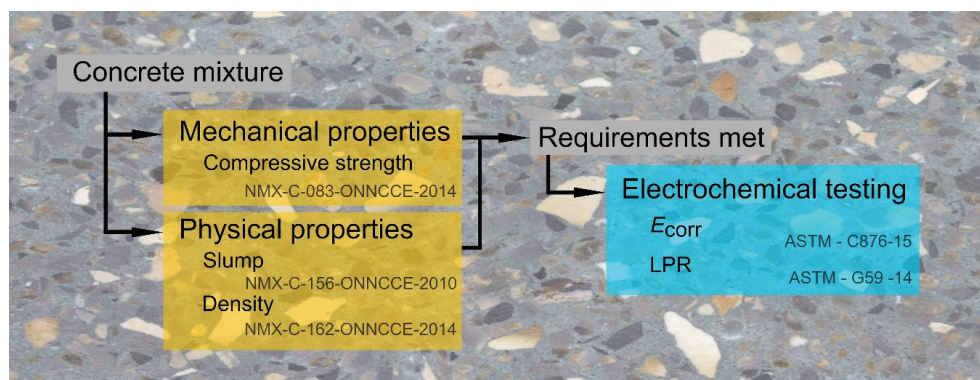


Figure 1. Experimental testing procedure schematic.

Table 1. Physical properties of the natural coarse aggregate (NCA), natural fine aggregate (NFA) and recycled coarse aggregate (RCA).

Type of Aggregates	Relative Density (Specific Gravity)	Bulk Density (Unit Weight, kg/m ³)	Absorption (%)	Fineness Modulus	Maximum Aggregate Size (mm)
NCA	2.62	1433	1.73	-	19
NFA	2.24	1695	1.85	2.2	-
RCA	2.20	1367	12.00	-	19

2.2. Design Mixtures of Conventional Concrete (MC) and GC

The design of concrete mixtures for MC and GC created according to the standard ACI 211.1 [58]. This standard describes a method that is based on the physical properties of coarse and fine aggregates (see Table 1). The proportioning of the concrete mixture indicates the amount of material needed to produce a meter cubic of concrete. In this case, the manufacture of the three concrete mixes used a water/cement ratio of 0.65 for a specified compressive strength of concrete ($f'_c = 22.5$ MPa according to ACI 214R-11 [64]). Table 2 summarizes the proportions for the MC and the two GC mixtures (M50 and M100).

Table 2. Proportioning of concrete mixtures in kg for 1 m³ of concrete ($f'_c = 22.5$ MPa).

Materials	MC	M50	M100
	(100% CPC)	(50% RCA)	(100% RCA)
Kg/m ³			
Cement	315	252	252
Water	205	205	205
SCBA	0	63	63
NCA	917	458.5	0
NFA	914	914	914
RCA	0	458.5	917

2.3. Physical and Mechanical Properties of Concrete Mixtures (Fresh and Hardened State)

For the evaluation of the physical properties of fresh-state concrete mixtures, tests of slump [65], freshly mixed concrete temperature [66] and density [67] were carried out according to the ONNCCE and ASTM standards. Table 3 shows the results obtained for the two concrete mixtures.

Table 3. Physical properties of concrete mixtures.

Concrete Mixture	Slump (cm)	Temperature (°C)	Density (kg/m ³)
MC	10 cm	24	2220
M50	3 cm	19	2187
M100	2 cm	22	2040

To determine the mechanical strength (compressive strength, f'_c) of the concrete mixtures in the hardened state, compression tests were carried out according to the standard NMX-C-083-ONNCCE-2014 [68], at the ages of 14 and 28 days. Table 4 shows the results obtained.

Table 4. Compressive strength at 14 and 28 days (f'_c in MPa).

Concrete Mixture	Compressive Strength (MPa)	
	14 Days	28 Days
MC	14.02	19.91
M50	7.71	11.54
M100	6.75	9.66

The compressive strength decreased as the content of recycled coarse aggregate (RCA) present in GC increased. The GC mix with 50% RCA and 20% SCBA was substituted for the cement CPC 30R (M50) and showed a compressive strength of 11.54 MPa at 28 days. This represents a decrease of 42% with respect to the MC, and a decrease of 51.5% for GC with 100% RCA and 20% SCBA replacing cement CPC 30R, reporting a compressive strength of only 9.66 MPa at an age of 28 days. The decrease in compressive strength in GC mixes is related to the incorporation of RCA. This behavior agrees with that reported in various investigations. Ali et al. found in their investigation of glass fibers incorporated in concrete with RCA that when RCA completely replaces NCA, it reduces the compressive strength, split tensile strength and flexure strength by about 12%, 11% and 8%, respectively [69]. Kurda et al. concluded that both materials, FA and RCA, are detrimental to the mechanical properties of concrete. For instance, compressive strength, splitting tensile strength and modulus of elasticity are negatively affected. The SiO₂ present in the FA and the Ca(OH)₂ present in the RCA experience a pozzolanic reaction that increases the rate of concrete strength development over time [70]. The SiO₂ is also present in the SCBA according to previous results [71], thus being a likely source of this detrimental behavior. Li et al. explained in their research in the structural area that there is a reasonable consensus regarding the structural behavior of composite members combined with RCA. Mechanical strength is slightly lower compared with OPC with no RCA additions. Nevertheless, the manufacturing of composite materials using RCA presents a safe and feasible approach [72]. However, the compressive strength observed for GC was sufficient for use in structures that do not require high strength, such as houses, parks, sidewalks, floors, etc.

2.4. Specifications, Characteristic and Nomenclature of Specimens for Electrochemical Tests

The MC and the two mixtures of GC (M50 and M100) were made with a water/cement ratio of 0.65. The specimens were prisms with dimensions of 15 × 15 × 15 cm. In all the specimens, AISI 304 SS and AISI 1018 CS rebars were embedded with a length of 15 cm and a diameter of 9.5 mm; the AISI 304 SS and AISI 1018 CS rebars were cleaned to remove any impurities [73]. In addition, each rebar was coated 4 cm from the top and 4 cm from the bottom using insulating tape in order to limit the exposed area with a length of 5 cm, as reported previously [74,75].

The specimens were manufactured in accordance with the standard ASTM C 192 [76] and the curing stage of all specimens was carried out water immersion according to the NMX-C-159 standard [77]. After the curing period, the eight specimens were placed in the exposure media, a control medium (DI-water) and 3.5 wt.% Na₂SO₄ solution for 364 days, simulating a sulfate aggressive medium such as contaminated soils, marine and industrial environments [78,79]. The specimens were then subjected to electrochemical tests. Figure 2 shows the compressive strength tests of the different GC mixtures and the electrochemical test to determine the corrosion behavior after exposure to 3.5 wt.% Na₂SO₄ solution.

Table 5 shows the elemental composition of the austenitic AISI 304 stainless steel and AISI 1018 carbon steel.

The nomenclature used for the electrochemical monitoring of AISI 304 SS and AISI 1018 CS embedded in the MC and the two GC (M50 and M100) exposed in a control medium (DI-water) and 3.5 wt.% Na₂SO₄ solution is shown in Table 6, which has the following meaning:

- MC, M50 and M100 indicate the concrete mixture (conventional and green concrete);
- W indicates exposed DI-water (control medium);
- S indicate exposed to 3.5 wt.% Na₂SO₄ solution (aggressive medium);
- 18 for rebars of AISI 1018 CS;
- 304 for rebars of AISI 304 SS.

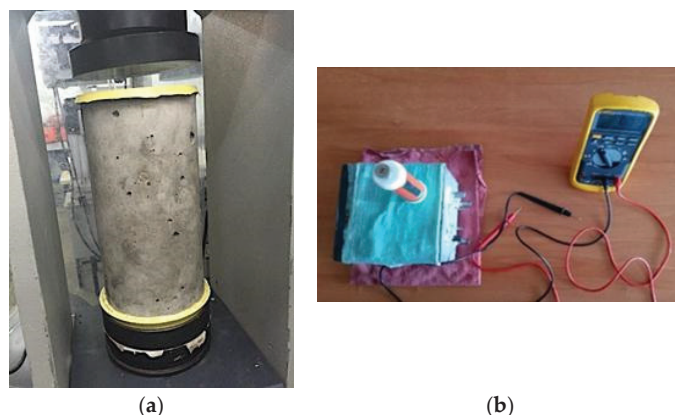


Figure 2. Experimental test conducted on green concrete: (a) compressive strength and (b) electrochemical corrosion monitoring.

Table 5. Elemental composition (wt.%) of the reinforcements tested, AISI 1018 carbon steel (CS) and austenitic AISI 304 SS.

Material	Element, wt.%									
	C	Si	Mn	P	S	Cr	Ni	Mo	Cu	Fe
AISI 1018	0.20	0.22	0.72	0.02	0.02	0.13	0.06	0.02	0.18	Balance
AISI 304	0.04	0.32	1.75	0.03	0.001	18.20	8.13	0.22	0.21	Balance

Table 6. Nomenclature of the reinforced green concrete specimens for electrochemical monitoring.

Mixtures Concrete	Nomenclature of Specimens Exposed DI-Water (Control Medium)		Nomenclature Specimens Exposed to 3.5 wt.% Na ₂ SO ₄ Solution (Aggressive Medium)	
MC (Conventional Concrete: 100% NA and 100% CPC)	MC-W-18	MC-W-304	MC-S-18	MC-S-304
M50 (Green Concrete: 50% RCA and 20% SBCA)	M50-W-18	M50-W-304	M50-S-18	M50-S-304
M100 (Green Concrete: 100% RCA and 20% SBCA)	M100-W-18	M100-W-304	M100-S-18	M100-S-304

MC and GC specimens were exposed to two different media, the control medium (DI-water) and 3.5 wt.% Na₂SO₄ solution, for a period of 364 days. The corrosion behavior was characterized by corrosion potential (E_{corr}) and corrosion current density (i_{corr}) measurements. The electrochemical cell setup used was AISI 304 SS or AISI 1018 CS rebars with a diameter of 9.5 mm for working electrodes (WE). AISI 314 SS rebars were used as counter electrodes (CE; see Figure 3) and standard copper–copper sulfate (Cu/CuSO₄, CSE) as the reference electrode (RE). i_{corr} was monitored using the linear polarization resistance (LPR) technique. The sweep potential range was ± 20 mV with respect to the E_{corr} and the sweep rate was 10 mV/min according to standard ASTM-G59 [80]. Electrochemical measurements were performed in a Gill AC Galvanostat/Potentiostat/ZRA (ACM Instruments, Cark in Cartmel, UK). The results were analyzed using Version 4 Analysis specialized software from ACM Instruments [81,82]. All tests were carried out at room temperature. E_{corr} and i_{corr} were monitored every four weeks and all experimental measurements were performed in triplicate.

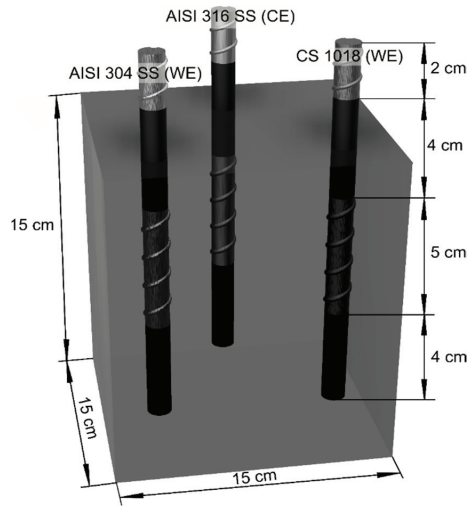


Figure 3. Specifications of specimens for electrochemical tests.

The i_{corr} and the corrosion rate (v_{corr}) were estimated from the LPR technique using the Stern and Geary relation (see Equation (1)) [83]:

$$i_{corr} = \frac{B}{R_p} \tag{1}$$

where B is the proportionality constant equal to 26 and 52 mV/dec for active and passive corrosion state rebars, respectively, and R_p is the polarization resistance [84,85].

E_{corr} was used to assess the degree of deterioration of reinforced concrete specimens according to ASTM C-876-15 [86], which presents the criteria or ranges that relate the E_{corr} values with the probability of corrosion for embedded steel specimens made with MC and GC (see Table 7).

Table 7. The measured half-cell corrosion potential (E_{corr}) versus a Cu/CuSO₄ in reinforcement concrete [86].

E_{corr} (mV _{CSE})	Corrosion Condition
$E_{corr} > -200$	Low (10% of risk corrosion)
$-200 > E_{corr} > -350$	Intermediate corrosion risk
$-350 > E_{corr} > -500$	High (<90% of risk corrosion)
$E_{corr} < -500$	Severe corrosion

To determine the v_{corr} values of steels embedded in the mixtures of MC and GC, the i_{corr} values were used. The criteria used to analyze the i_{corr} results are based on the state of corrosion of CS in OPC reported in the literature [84], as shown in Table 8.

Table 8. Level of corrosion in concrete, corrosion current density (i_{corr}) and the corrosion rate (v_{corr}) [84].

i_{corr} (μA/cm ²)	v_{corr} (mm/d)	Corrosion Level
$i_{corr} \leq 0.1$	$v_{corr} \leq 0.001$	Negligible (Passivity)
$0.1 < i_{corr} < 0.5$	$0.001 < v_{corr} < 0.005$	Low Corrosion
$0.5 < i_{corr} < 1$	$0.005 < v_{corr} < 0.010$	Moderate Corrosion
$i_{corr} > 1$	$v_{corr} > 0.010$	High Corrosion

3. Results and Discussion

3.1. Half-Cell Potential—Corrosion Potential

Half-cell potential monitoring (E_{corr}) and interpretation of the corrosion state were performed using the criteria presented in Table 7, which is in accordance with ASTM C876-15 [86].

3.1.1. E_{corr} Specimens Exposed DI-Water (Control Medium)

Figure 4 shows the results obtained from monitoring the E_{corr} of the specimens MC-W-18, M50-W-18 and M100-W-18. It is observed that the MC-W-18 specimen presents corrosion potentials in the curing stage ranging from -260 to -160 mV_{CSE}, moving from Days 7 to 28 from the intermediate corrosion risk to 10% risk, according to ASTM C-876-15. The trend towards more positive values continued throughout the evaluation period, reaching values up to -45 mV_{CSE} on Day 196, and finally reaching values in the range of -60 to -75 mV_{CSE}, which indicates a 10% of risk corrosion. For the M50-W-18 specimen, the behavior is very similar to the MC-W-18 specimen, with E_{corr} values in the curing stage of -250 mV_{CSE}, reaching a value of -140 mV_{CSE} on Day 28, maintaining a trend towards more positive values until Day 196, reaching an E_{corr} value of -45 mV_{CSE}. At the end of the monitoring period, more negative E_{corr} values are found ranging between -120 and -145 mV_{CSE}, thus indicating a 10% corrosion risk.

The M100-W-18 specimen shows a more unfavorable behavior from Day 196, from E_{corr} values lower than -200 to -330 mV_{CSE} for Day 280, until values of -300 mV_{CSE} observed at the end of the monitoring period. Therefore, the specimens indicate intermediate corrosion risk according to ASTM C-876-15 and with a tendency to more negative values of E_{corr} , which agrees with the findings of Al-Yaqout et al.; the corrosion potential for normal mixtures decreases as the RCA replacement level increases compared to the control mixture. This behavior shows the same trend for the compressive strength, decreasing as the amount of RCA increased in all normal and slag mixtures and under all exposure conditions [87].

The MC-W-304 (MC, 100% CPC-100% natural aggregates), M50-W-304 (GC with 50% RCA and 80% CPC-20% SCAB) and M100-W-304 (GC with 100% RCA and 80% CPC-20% SCAB) specimens were reinforced with AISI 304 SS steel rebars. The E_{corr} results obtained after more than 360 days of monitoring show the following behavior. The MC-W-304 specimen presented a tendency to more noble E_{corr} values from the curing stage, presenting values from -192 mV_{CSE} on Day 7 to -84 mV_{CSE} on Day 28, continuing with a tendency to passive E_{corr} values in the range of -80 to -75 mV_{CSE} from Day 196 [88,89], presenting values below or more positive than -200 mV_{CSE}, which indicates, according to the ASTM C-876-15, a 10% corrosion risk or passivity of the steel–concrete system analyzed.

The M50-W-304 specimen behaves similarly to the control MC-W-304, with corrosion potentials in the curing stage ranging from -218 mV_{CSE} on Day 7 to -95 mV_{CSE} on Day 28, presenting a small activation on Day 56 with an E_{corr} value of -143 mV_{CSE}. From this point to the present, a stage of stability in the E_{corr} values is observed from Days 84 to 364, in the range of -90 and -120 mV_{CSE}, interpreted according to the ASTM C-876-15 as a 10% corrosion risk. The M100-W-304 specimen, presented a similar behavior to the two MC-W-304 and M50-W-304 specimens in the curing stage, showing an E_{corr} value of -183 mV_{CSE} on Day 7 and -97 mV_{CSE} on Day 28. From this point on, the E_{corr} values become -82 and -124 mV_{CSE} until the end of the testing, indicating according to the ASTM C-876-15 as a 10% corrosion risk. The behavior in the E_{corr} values is less than -200 and congruent with the nonaggressive medium of exposure, which is also interpreted as the passivity of the AISI 304 SS steel used as reinforcement in GC and MC.

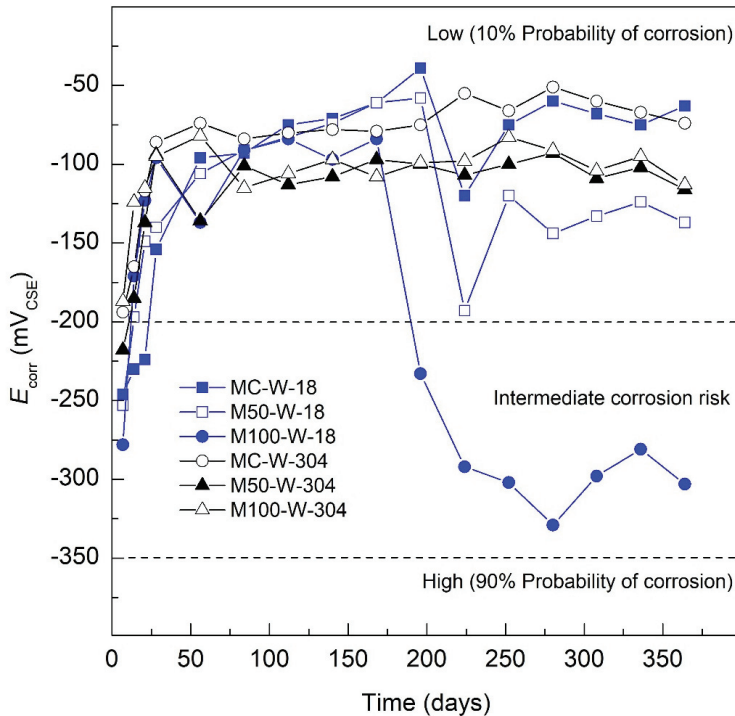


Figure 4. E_{corr} specimens exposed DI-water (control medium).

3.1.2. E_{corr} Specimens Exposed 3.5 wt.% Na_2SO_4 Solution (Aggressive Medium)

Figure 5 presents the results obtained from the E_{corr} monitoring of the specimens when exposed for 364 days to 3.5 wt.% Na_2SO_4 solution (aggressive medium). The evaluated specimens were MC-S-18 (MC, 100% CPC-100% natural aggregates), M50-S-18 (GC with 50% RCA and 80% CPC-20% SCAB) and M100-S-18 (GC with 100% RCA and 80% CPC-20% SCAB). The MC-S-18 specimen in the curing stage presented an E_{corr} value of $-217 \text{ mV}_{\text{CSE}}$ on Day 7 and $-180 \text{ mV}_{\text{CSE}}$ for Day 28. These E_{corr} values indicate, according to the ASTM C-876-15, a 10% corrosion risk. Later, the specimen presents E_{corr} values in the range from -173 to $-159 \text{ mV}_{\text{CSE}}$ after Day 112, from this point to the present, an activation occurs with E_{corr} values from -203 to $-256 \text{ mV}_{\text{CSE}}$ from Day 140 to 224, which would indicate intermediate corrosion risk according to ASTM C-876-15. For Days 252 and 280, E_{corr} values are lower than $-200 \text{ mV}_{\text{CSE}}$, which would be associated with a passivity stage or a 10% corrosion risk; however, after Day 280, there is a trend towards more negative values of $-200 \text{ mV}_{\text{CSE}}$, reaching $-239 \text{ mV}_{\text{CSE}}$ on the last day of monitoring. The M50-S-18 specimen presents more negative values of E_{corr} in the curing stage than those presented by the control MC-S-18 specimen, with an E_{corr} value of $-261 \text{ mV}_{\text{CSE}}$ on Day 7 and $-218 \text{ mV}_{\text{CSE}}$ for Day 28, showing from Days 56 to 140 E_{corr} values that ranged between -189 and $-243 \text{ mV}_{\text{CSE}}$. Then, the specimen shows a decreasing trend towards lower values until the end of the testing, with values reaching $-284 \text{ mV}_{\text{CSE}}$, after Day 140 and until the end of monitoring, Day 364, the E_{corr} values for the M50-S-18 specimen when exposed in 3.5 wt.% Na_2SO_4 solution (aggressive medium) indicate intermediate corrosion risk according to the ASTM C-876-15.

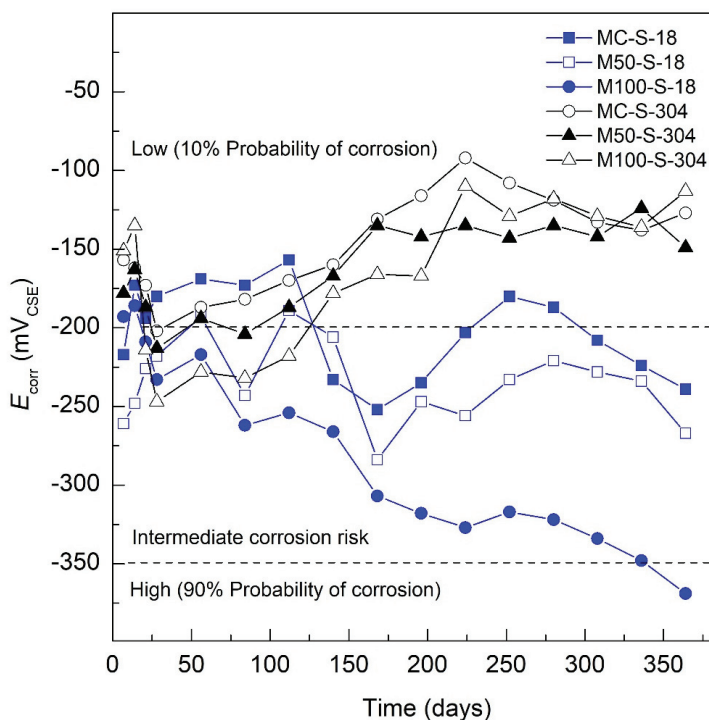


Figure 5. E_{corr} specimens exposed 3.5 wt.% Na_2SO_4 solution (aggressive medium).

The specimen that presented the worst performance when exposed to 3.5 wt.% Na_2SO_4 solution (aggressive medium) was M100-S-18, presenting a tendency to lower E_{corr} values with an E_{corr} value of $-193 \text{ mV}_{\text{CSE}}$ on Day 7 of the curing stage and $-233 \text{ mV}_{\text{CSE}}$ for Day 28, continuing with the negative trend throughout the entire exposure period, reaching a potential of $-348 \text{ mV}_{\text{CSE}}$ on Day 336 and ending on Day 364 with a corrosion potential of $-369 \text{ mV}_{\text{CSE}}$. This indicates a $<90\%$ corrosion risk according to the ASTM C-876-15 standard. This behavior of more negative corrosion potentials (E_{corr}) coincides with that reported in other investigations when evaluating AISI 1018 steel in sustainable concrete made with SCBA and exposed to sulfates [24]. However, the M100-S-18 specimen presents more negative values, which is associated with lower corrosion resistance of the specimens made with GC (M50-S-18 and M100-S-18) when exposed to sulfates, related to a less dense matrix and higher permeability due to the presence of 50% and 100% RCA, as well as the substitution of Portland cement in 20% by SCBA. This decrease in the mechanical properties and durability when RCA has been used was reported by Lovato et al. [90], indicating that the durability properties are also negatively affected by the increment of RCA in concrete. In order to achieve the required workability, the water-to-cement ratio must be increased. This not only leads to an increased demand for water during the manufacturing stage, but also an increase in the porosity of the matrix and consequently reducing the durability of the concretes [90].

The specimens with AISI 304 SS steel were MC-S-304 (MC, 100% CPC-100% natural aggregates), M50-S-304 (GC with 50% RCA and 80% CPC-20% SCAB) and M100-S-304 (GC with 100% RCA and 80% CPC-20% SCAB), exposed for 364 days to 3.5 wt.% Na_2SO_4 solution (aggressive medium). The MC-S-304 specimen presented an E_{corr} value of $-157 \text{ mV}_{\text{CSE}}$ on Day 7 of the curing stage and $-202 \text{ mV}_{\text{CSE}}$ for Day 28, from this point, the specimen presents a trend towards higher E_{corr} values, related to the passivity of AISI 304 SS steel, and reached a minimum E_{corr} of $-92 \text{ mV}_{\text{CSE}}$ on Day 224 of exposure. Then, the specimen showed E_{corr} values in the range from -108 to $-138 \text{ mV}_{\text{CSE}}$ until

the end of the monitoring period, all the E_{corr} values of the MC-S-304 specimen during the entire period of exposure to the aggressive medium were less than $-200 \text{ mV}_{\text{CSE}}$, thus indicating a 10% corrosion risk according to the ASTM C-876-15. The M50-S-304 specimen presented a behavior similar to MC-S-304, with corrosion potentials in the curing stage with a decreasing trend. The M50-S-304 specimen displays an E_{corr} value of $-178 \text{ mV}_{\text{CSE}}$ on Day 7 and $-213 \text{ mV}_{\text{CSE}}$ for Day 28, then increases and become more passive to $-138 \text{ mV}_{\text{CSE}}$ by Day 168 and remains stable in the range of -135 and $-149 \text{ mV}_{\text{CSE}}$ until the final measurement, maintaining E_{corr} values below $-200 \text{ mV}_{\text{CSE}}$ throughout the exposure period, thus indicating, according to ASTM C-876-15, a 10% corrosion risk. Finally, the M100-S-304 specimen presents a similar behavior to the two previous specimens in the curing stage, with corrosion potentials ranging from less to more negative, with an E_{corr} value of $-151 \text{ mV}_{\text{CSE}}$ on Day 7 and $-247 \text{ mV}_{\text{CSE}}$ on Day 28. Unlike the MC-S-304 and M50-S-304 specimens, the M100-S-304 specimen presents E_{corr} values less than $-200 \text{ mV}_{\text{CSE}}$ until Day 112, which would indicate intermediate corrosion risk according to the ASTM C-876-15. Thereafter, the specimen shows a trend towards higher E_{corr} values, reaching an E_{corr} value of $-110 \text{ mV}_{\text{CSE}}$ for Day 224 and remaining stable in the range between -136 and $-113 \text{ mV}_{\text{CSE}}$ until the end of the testing. Like the previous specimens, the M100-S-304 specimen presented E_{corr} values less than $-200 \text{ mV}_{\text{CSE}}$ during almost the entire exposure time to 3.5 wt.% Na_2SO_4 solution (aggressive medium), which indicates a 10% corrosion risk according to ASTM C-876-15. The previous results agree with those reported in the literature, where the excellent corrosion resistance of stainless steel grades AISI 304, AISI 316, etc., has been demonstrated when used as reinforcement in conventional concrete, sustainable concrete, green concrete, and when exposed to aggressive environments such as marine, sulfated and industrial environments [91,92].

3.2. Corrosion Current Density, i_{corr}

The i_{corr} results of the AISI 304 SS and AISI 1018 CS reinforcement in MC and both GC mixtures (M50 and M100) exposed to control medium (DI-water) and 3.5 wt.% Na_2SO_4 solution were interpreted according to the criterion of Table 8.

3.2.1. i_{corr} Specimens Exposed DI-Water (Control Medium)

Figure 6 shows the i_{corr} results of the conventional concrete and GC specimens reinforced with AISI 1018 CS and AISI 304 SS steel exposed in water as a control medium. The MC-W-18 specimen presents an i_{corr} value of $0.67 \mu\text{A}/\text{cm}^2$ for Day 7 of the curing stage, decreasing on Day 28 to a value of $0.21 \mu\text{A}/\text{cm}^2$. For Day 56, a passive i_{corr} value of $0.095 \mu\text{A}/\text{cm}^2$ was observed, and subsequently, values remained less than $0.091 \mu\text{A}/\text{cm}^2$ until the end of monitoring in the range of 0.09 to $0.05 \mu\text{A}/\text{cm}^2$. The i_{corr} values obtained from the MC-W-18 specimen indicate passivation of the reinforcing steel and, according to Table 8, a negligible level of corrosion (absence of corrosion). The M50-W-18 specimen presents a similar passivation behavior as MC-W-18; however, with higher i_{corr} values from the curing stage, presenting on Day 7 an i_{corr} value of $0.58 \mu\text{A}/\text{cm}^2$ and $0.29 \mu\text{A}/\text{cm}^2$ for Day 28. From Day 56 to the end of monitoring, i_{corr} values were below $0.1 \mu\text{A}/\text{cm}^2$ in the range of 0.07 to $0.04 \mu\text{A}/\text{cm}^2$, indicating a negligible level of corrosion. The M100-W-18 specimen had a similar behavior to the two previous specimens with an i_{corr} on Day 7 of 0.64 to $0.26 \mu\text{A}/\text{cm}^2$ for Day 28 and presenting an i_{corr} value of $0.067 \mu\text{A}/\text{cm}^2$ until Day 140. From Day 168 until the end of monitoring, i_{corr} values were in the range of 0.144 to $0.214 \mu\text{A}/\text{cm}^2$, indicating a low level of corrosion according to Table 8 and supporting the corrosion potential monitoring technique. The corrosion potentials presented by the same M100-W-18 specimen, after Day 168 were in the range of -200 to $-340 \text{ mV}_{\text{CSE}}$, indicating corrosion uncertainty according to ASTM C-876-15. With the LPR test, the i_{corr} could be determined, confirming the activation of the system with the presence of a low level of corrosion from Day 196 for the M100-W-18 specimen in a nonaggressive environment. The corrosion present in the M100-W-18 specimen exposed to a nonaggressive medium is related to the less dense and more permeable matrix of green concrete (M100), as indicated by the low compressive strength at 28 days with $f'_c = 9.66 \text{ MPa}$. This decrease in the durability of concrete made with RCA has been demonstrated in

various investigations, Kurda et al. found that the water absorption increases and electrical resistivity decreases with the increasing incorporation level of RCA; the opposite occurs with the addition of FA for both tests [93]. The behavior of the i_{corr} of the other two specimens, MC-W-18 and M50-W-18, indicated a negligible level of corrosion (passivity).

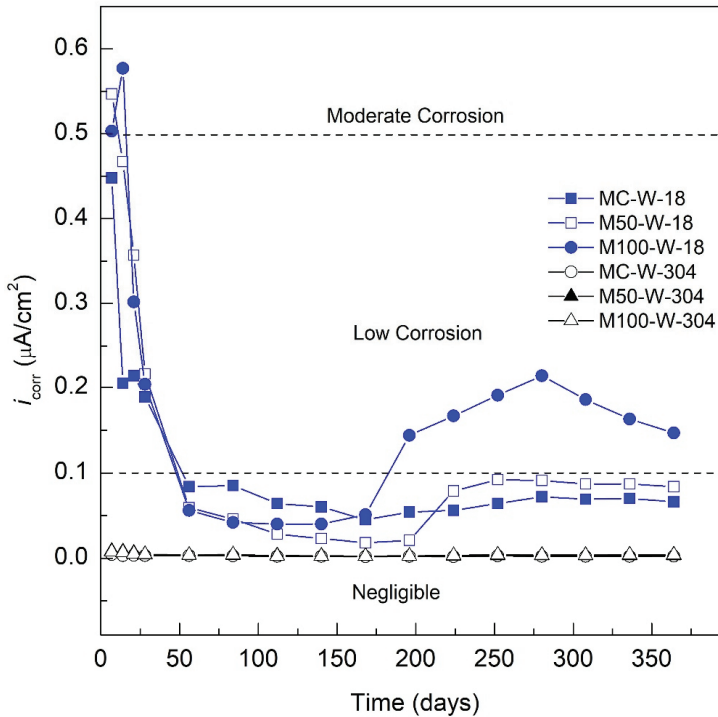


Figure 6. i_{corr} specimens exposed DI-water (control medium).

The MC-W-304 specimen in the curing stage showed an i_{corr} value of $0.0043 \mu\text{A}/\text{cm}^2$ on Day 7 with a trend towards more passive values, presenting an i_{corr} value of $0.0031 \mu\text{A}/\text{cm}^2$ on Day 28. A trend to lower i_{corr} values is observed until Day 224 with an i_{corr} value of $0.0018 \mu\text{A}/\text{cm}^2$. Then, the specimen exhibits a small increase of i_{corr} to $0.0028 \mu\text{A}/\text{cm}^2$ for Day 252 and from i_{corr} values of $0.0021 \mu\text{A}/\text{cm}^2$ on Day 280 to $0.0023 \mu\text{A}/\text{cm}^2$ for the last monitoring on Day 364. All i_{corr} values of the MC-W-304 specimen indicate a negligible or null corrosion level according to that indicated in Table 8. It is also found that this specimen presents the lowest i_{corr} values, followed by the M50-W-304 specimen, which presented i_{corr} values of $0.0085 \mu\text{A}/\text{cm}^2$ on Day 7 to $0.0041 \mu\text{A}/\text{cm}^2$ for Day 28, then continues with a decrease in i_{corr} until Day 168 with a value of $0.0023 \mu\text{A}/\text{cm}^2$. Subsequently, the i_{corr} increases from 0.0026 to $0.0032 \mu\text{A}/\text{cm}^2$ from Days 196 to 364, respectively. Finally, the M100-W-304 specimen (100% RCA and 20% SCBA) presented the highest i_{corr} values, presenting an i_{corr} value of $0.0045 \mu\text{A}/\text{cm}^2$ on Day 28, decreasing to $0.0024 \mu\text{A}/\text{cm}^2$ on Day 168. Following, i_{corr} increases from $0.0027 \mu\text{A}/\text{cm}^2$ on Day 196 to a value of $0.0040 \mu\text{A}/\text{cm}^2$ for the last day of monitoring, Day 364. A clear difference is observed in the i_{corr} values presented by the three studied specimens, the lowest i_{corr} values are shown for the MC-W-304 specimen, followed by the M50-W-304 specimen, and finally the M100-W-304 specimen, the i_{corr} range of the three specimens is more than 10 times less than $0.1 \mu\text{A}/\text{cm}^2$, which indicates that all the specimens present a negligible level of corrosion throughout the period of exposure to the control medium according to Table 8. The results coincide with what is reported in the literature [21,94,95].

3.2.2. i_{corr} Specimens Exposed 3.5 wt.% Na_2SO_4 Solution (Aggressive Medium)

Figure 7 presents the v_{corr} and i_{corr} results of the specimens with AISI 304 SS and AISI 1018 CS steel bars embedded in MC and GC exposed to 3.5 wt.% Na_2SO_4 solution (aggressive medium) for a period of 364 days. The v_{corr} and i_{corr} of the control specimen, MC-S-18, decreased from an i_{corr} value of $0.2435 \mu\text{A}/\text{cm}^2$ on Day 7 to an i_{corr} value of $0.1144 \mu\text{A}/\text{cm}^2$ for Day 28. This behavior is attributed to being in the curing stage where the i_{corr} values tend to decrease due to the formation of the passive layer and the increase in the protection of the concrete. The i_{corr} values decrease until Day 140 of exposure with a value of $0.0729 \mu\text{A}/\text{cm}^2$, indicating a negligible level of corrosion or passivity according to Table 8. However, after Day 168, the activation of the system occurs with a constant increase in i_{corr} values greater than $0.1 \mu\text{A}/\text{cm}^2$ on Day 196 with an i_{corr} value of $0.1656 \mu\text{A}/\text{cm}^2$ and reaching $0.2148 \mu\text{A}/\text{cm}^2$ at the end of monitoring. This indicates that, as of Day 196, the MC-S-18 specimen presented corrosion at a low level due to the exposure to sodium sulfate solution as an aggressive medium. In the case of the M50-S-18 specimen, the curing stage showed decreasing i_{corr} values, reporting $0.3375 \mu\text{A}/\text{cm}^2$ on Day 7 to $0.1844 \mu\text{A}/\text{cm}^2$ for Day 28. This trend continued to decrease until Day 56, reaching an i_{corr} value of $0.1506 \mu\text{A}/\text{cm}^2$. However, after Day 84, the i_{corr} values begin to increase, becoming more active due to exposure to the aggressive environment and a decreased matrix density and increased permeability because it contains 50% of RCA. The values increase to $0.2779 \mu\text{A}/\text{cm}^2$ and remain stable in an i_{corr} range of 0.2419 and $0.3386 \mu\text{A}/\text{cm}^2$ until the end of monitoring. From Day 84, the M50-S-18 specimen presents i_{corr} values that indicate a low level of corrosion according to Table 8. Finally, the M100-S-304 specimen, although showing a tendency for lower i_{corr} values in the curing stage, displays an i_{corr} value of $0.4175 \mu\text{A}/\text{cm}^2$ on Day 7 and $0.2482 \mu\text{A}/\text{cm}^2$ for Day 28. For Day 86, the activation of the system with an increase in its i_{corr} is shown, reaching a value of $0.3417 \mu\text{A}/\text{cm}^2$. On Day 140, an i_{corr} value of $0.519 \mu\text{A}/\text{cm}^2$ indicates a moderate level of corrosion according to Table 8. The i_{corr} increases for the M100-S-18 specimen continued irregularly from Day 168 to 308, ending on Day 364 with an i_{corr} value of $0.7389 \mu\text{A}/\text{cm}^2$. The influence of the 100% RCA in the specimen is observed, influencing the mechanical properties and durability of GC due to a more permeable concrete matrix, lower density and a low resistance to compression compared to the control concrete (concrete with 50 and 100% of coarse natural aggregate). However, the use of mineral admixture (SF, MK, FA and ground granulated blast slag) resulted in a decrease in the charge passed through the concrete specimens [96]. According to Alhawat et al., not only the corrosion initiation process happened faster in RCA concrete, but also a higher corrosion rate was observed as the RCA content increased due to the higher porosity and water absorption [97].

The MC-S-304 specimen presents the best performance against corrosion when exposed for 364 days to 3.5 wt.% Na_2SO_4 solution (aggressive medium), reporting i_{corr} values in the curing stage of $0.0047 \mu\text{A}/\text{cm}^2$ on Day 7 to reach an i_{corr} value of $0.0034 \mu\text{A}/\text{cm}^2$ on Day 28, observing a decrease associated with the increase in concrete protection due to the hydration process of said stage. The decrease in the corrosion rate occurs until Day 56, when the MC-S-304 specimen reports a minimum i_{corr} of $0.0028 \mu\text{A}/\text{cm}^2$, from this point, the values stabilize in the range between 0.0039 and $0.0047 \mu\text{A}/\text{cm}^2$ between Days 112 and 196 of exposure the aggressive medium. Subsequently, the i_{corr} increases gradually from $0.0054 \mu\text{A}/\text{cm}^2$ on Day 224 to the highest value in the entire exposure period at the end of monitoring, Day 364, with an i_{corr} value of $0.0106 \mu\text{A}/\text{cm}^2$. As indicated previously, its performance was excellent in the presence of sodium sulfates, with i_{corr} values well below $0.1 \mu\text{A}/\text{cm}^2$, which is the limit that would indicate the onset of corrosion according to Table 8. This resistance to corrosion of AISI 304 steel embedded in concrete exposed to aggressive media has been demonstrated in various studies [98–100].

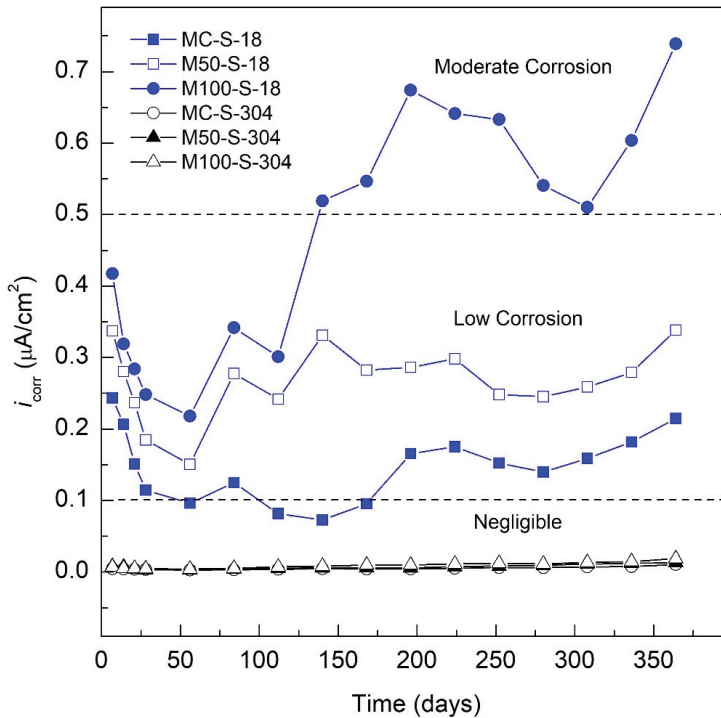


Figure 7. i_{corr} specimens exposed 3.5 wt.% Na_2SO_4 solution (aggressive medium).

In the case of the M50-S-304 specimen, it has a much higher anticorrosive efficiency than that presented by the specimen reinforced with AISI 1018 CS steel (M50-S-18). The M50-S-304 specimen presents i_{corr} values in the curing stage ranging from 0.0080 and 0.0031 $\mu\text{A}/\text{cm}^2$ from Days 7 to 28, respectively. Day 56 shows an i_{corr} value of 0.0032 $\mu\text{A}/\text{cm}^2$, an increase in i_{corr} from Day 56 to 196, with constant increases from Days 56 to 112 going from an i_{corr} value of 0.0032 and 0.0052 $\mu\text{A}/\text{cm}^2$, from there to stabilize and oscillate in the range of 0.0058 and 0.0061 $\mu\text{A}/\text{cm}^2$. From Day 140 to 196, there is a constant increase until the end of the monitoring period, from an i_{corr} value of 0.0077 $\mu\text{A}/\text{cm}^2$ on Day 224 to 0.1321 $\mu\text{A}/\text{cm}^2$ for the Day 364. Like the MC-S-304 specimen, the i_{corr} values are much lower than 0.1 $\mu\text{A}/\text{cm}^2$, which indicates that its corrosion level is negligible, or passivity occurs, according to the provisions of Table 8. However, it can be observed that the M50-S-304 specimen presents higher values than those reported by the MC-S-304 specimen. This behavior is associated with a less dense and more permeable concrete matrix due to the presence of RCA, as reported by Cakir et al. The compressive strength of the concrete decreases by incorporating RCA and that the presence of RCA causes the concrete to have a higher porosity and lower density [101]. However, another study concluded that the RCA content in the concrete is found to have a detrimental effect in the compressive strength, but at low replacement concentrations <20%, this effect is negligible [102]. The monitored i_{corr} values for AISI 304 SS during the curing period were 0.0071 and 0.0047 $\mu\text{A}/\text{cm}^2$ on Days 7 and 28, respectively, during the curing stage. Next, the i_{corr} increases from 0.0041 to 0.0098 $\mu\text{A}/\text{cm}^2$ for Days 56 to 168, respectively. A second period of increase occurs from Days 196 to 280, from an i_{corr} value of 0.00989 to 0.1143 $\mu\text{A}/\text{cm}^2$. Finally, the third period with near-constant i_{corr} of 0.01346 $\mu\text{A}/\text{cm}^2$ on Day 308 to i_{corr} of 0.01894 $\mu\text{A}/\text{cm}^2$ on Day 364. The i_{corr} values during all the periods of exposure showed values less than 0.1 $\mu\text{A}/\text{cm}^2$, which indicates an excellent performance against sulfate corrosion for the M100-S-304 specimen with 100% of RCA and 20% of SCBA.

The corrosion resistance was not influenced by the high permeability, low density and low mechanical resistance of the GC with which the M100-S-304 specimen was made. By data fitting, the durability properties generally decrease linearly with the increase of RCA replacement and the average water absorption rate [103]. The concrete containing NA and RCA showed a carbonation rate of 1.8 times higher [104]. The increase in the carbonation depth observed in samples containing RCA could be attributed to the higher permeability of RCA due to the presence of old mortar adhering to the NA and the old interfacial transition zone (ITZ) [105]. The geopolymer RCA, with a higher content of granulated blast furnace slag, had a lower mass loss and a higher residual compressive strength after the sulfate exposure [106]. The results indicate a direct influence between the percentage of aggregate used in the GC mixes and the level of corrosion that all the specimens present in both the control medium and the aggressive medium. Higher contents of RCA lead to higher i_{corr} in both AISI 1018 CS and AISI 304 SS steels. This behavior is the opposite of the reported behavior in another research, where it was found that the influence on the performance against most usual corrosion processes displayed similar results under a natural chloride attack [107]. Therefore, it is of great importance to continue to study different types of reinforcing steels as an alternative to AISI 1018 steel [108,109] that can increase the resistance to corrosion of GC based on recycled aggregates and alternative materials to OPC, such as SCBA, FA and SF.

4. Conclusions

According to the results from the study, the following conclusions were reached:

GC samples showed a significant decrease in the slump in their fresh state, GC-M50 with a slump of 3 cm and GC-M100 with a slump of 2 cm, decreasing their workability compared to conventional concrete (MC) which presented a slump of 10 cm.

The compressive strength shows a decreasing trend as the content of RCA present in GC increases. The GC-M50 mix with 50% RCA and 20% SCBA must be substituted for the CPC 30R. A compressive strength of 11.54 MPa was observed at 28 days, which represents a decrease of 42% with respect to the MC. A decrease of 51.5% for GC with 100% RCA and 20% SCBA replacing CPC 30R. A compressive strength of only 9.66 MPa was seen for Day 28.

The results obtained in the present investigation indicate a direct influence between the percentage of aggregate used in the GC mixes and the level of corrosion that all the specimens present in both the control medium and the aggressive medium, the higher the content of RCA, the higher the corrosion rate in both CS 1018 and AISI 304 SS reinforcements.

The i_{corr} values of the GC specimens reinforced with AISI 304 SS exposed to Na_2SO_4 were found to be $0.01894 \mu\text{A}/\text{cm}^2$ on Day 364, two orders of magnitude lower than the i_{corr} values ($0.7389 \mu\text{A}/\text{cm}^2$) obtained for CS 1018 in the same period. Therefore, it is shown that even with low mechanical properties, less dense concrete matrix and high permeability, the durability of GC is increased by presenting excellent resistance to corrosion when exposed to 3.5 wt.% Na_2SO_4 for more than 364 days, associated with the excellent corrosion performance of AISI 304 SS as reinforcement in concrete exposed to aggressive media.

Author Contributions: Conceptualization, M.A.B.-Z., J.M.M.-R. and D.M.B.; methodology, A.L.-S., J.B., G.S.-H., V.M.M.-L., J.O.-C., L.L.-R., L.L.-L., M.A.B.-Z., J.R. and D.M.B.; data curation, A.L.-S., J.B., R.C., J.M.M.-R., M.A.B.-Z., J.M.B., J.R. and D.M.B.; writing—review and editing, M.A.B.-Z., J.M.M.-R., J.B. and D.M.B. All authors have read and agreed to the published version of the manuscript.

Funding: This research was funded by PRODEP for the support granted by the SEP, to the Academic Body UV-CA-458 “Sustainability and Durability of Materials for Civil Infrastructure”, within the framework of the 2018 Call for the Strengthening of Academic Bodies with IDCA 28593. Funding support from The University of Akron, Fellowship Program FRC-207367.

Acknowledgments: The authors thank Aldo Canek Garcia-Ramirez, Sabino Márquez-Montero and Mario Ivan Velásquez-Hernández for the technical support.

Conflicts of Interest: The authors declare no conflict of interest.

References

1. Cramer, S.D.; Covino, B.S.; Bullard, S.J.; Holcomb, G.R.; Russell, J.H.; Nelson, F.J.; Laylor, H.M.; Soltesz, S.M. Corrosion prevention and remediation strategies for reinforced concrete coastal bridges. *Cem. Concr. Compos.* **2002**, *24*, 101–117. [CrossRef]
2. Koch, G.H.; Brongers, M.; Neil, G.; Thompson, C.C.; Virmani, P.; Payer, J.H. *Corrosion Costs and Preventive Strategies in the United States*; Publication No. FHWA-RD-01-156; NACE International: Houston, TX, USA, 2002.
3. Güneş, E.; Ozturan, T.; Gesoglu, M. A study on reinforcement corrosion and related properties of plain and blended cement concretes under different curing conditions. *Cem. Concr. Compos.* **2005**, *27*, 449–461. [CrossRef]
4. Pin Gu, S.; Beaudoin, J.J.; Arsenaault, B. Corrosion resistance of stainless steel in chloride contaminated concrete. *Cem. Concr. Res.* **1996**, *26*, 1151–1156.
5. Saricimen, H.; Mohammad, M.; Quddus, A.; Shameem, M.; Barry, M.S. Effectiveness of concrete inhibitors in retarding rebar corrosion. *Cem. Concr. Compos.* **2002**, *24*, 89–100. [CrossRef]
6. De Rincon, O.T.; Montenegro, J.; Vera, R.; Carvajal, A.; De Gutiérrez, R.M.; Saborio, E.; Acosta, A.A.T.; PáRez-Quiroz, J.; Martínez-Madrid, M.; Martínez-Molina, W.; et al. Reinforced concrete durability in marine environments DURACON Project: Long-term exposure. *Corrosion* **2016**, *72*, 824–833. [CrossRef]
7. Baltazar, M.A.; Márquez, S.; Landa, L.; Croche, R.; López, O. Effect of the type of curing on the corrosion behavior of concrete exposed to urban and marine environment. *Eur. J. Eng. Res. Sci.* **2020**, *5*, 91–95. [CrossRef]
8. Ormellese, M.; Berra, M.; Bolzoni, F.; Pastore, T. Corrosion inhibitors for chlorides induced corrosion in reinforced concrete structures. *Cem. Concr. Res.* **2006**, *36*, 536–547. [CrossRef]
9. Baltazar, M.A.; Santiago, G.; Moreno, V.M.; Croche, R.; De la Garza, M.; Estupiñan, F.; Zambrano, P.; Gaona, G. Electrochemical behaviour of galvanized steel embedded in concrete exposed to sand contaminated with NaCl. *Int. J. Electrochem. Sci.* **2016**, *11*, 10306–10319. [CrossRef]
10. Gowripalan, N.; Mohameda, H.M. Chloride-ion induced corrosion of galvanized and ordinary steel reinforcement in high-performance concrete. *Cem. Concr. Res.* **1998**, *28*, 1119–1131. [CrossRef]
11. Liang, M.; Lan, J.J. Reliability analysis for the existing reinforced concrete pile corrosion of bridge substructure. *Cem. Concr. Res.* **2005**, *35*, 540–550. [CrossRef]
12. Santiago, G.; Baltazar, M.A.; Galindo, A.; Cabral, J.A.; Estupiñan, F.H.; Zambrano, P.; Gaona, C. Anticorrosive Efficiency of Primer Applied in Carbon Steel AISI 1018 as Reinforcement in a Soil Type MH. *Int. J. Electrochem. Sci.* **2013**, *8*, 8490–8501.
13. Elias, V.; Fishman, K.L.; Christopher, B.R.; Berg, R.R. *Corrosion/Degradation of Soil Reinforcements for Mechanically Stabilized Earth Walls and Reinforced Soil Slopes*; U.S. Department of Transportation Publication No. FHWA-NHI-09-087; Federal Highway Administration: Washington, DC, USA, 2009.
14. Ismail, A.I.M.; El-Shamy, A.M. Engineering behaviour of soil materials on the corrosion of mild steel. *Appl. Clay Sci.* **2009**, *42*, 356–362. [CrossRef]
15. Santiago, G.; Baltazar, M.A.; Galván, R.; López, L.; Zapata, F.; Zambrano, P.; Gaona, C.; Almeraya, F. Electrochemical evaluation of reinforcement concrete exposed to soil type SP contaminated with sulphates. *Int. J. Electrochem. Sci.* **2016**, *11*, 4850–4864. [CrossRef]
16. Baltazar, M.A.; Santiago, G.; Gaona, C.; Maldonado, M.; Barrios, C.P.; Nunez, R.; Perez, T.; Zambrano, P.; Almeraya, F. Evaluation of the corrosion at early age in reinforced concrete exposed to sulfates. *Int. J. Electrochem. Sci.* **2012**, *7*, 588–600.
17. Baltazar-Zamora, M.A.; Landa-Ruiz, L.; Rivera, Y.; Croche, R. Electrochemical evaluation of galvanized steel and AISI 1018 as reinforcement in a soil type MH. *Eur. J. Eng. Res. Sci.* **2020**, *5*, 259–263. [CrossRef]
18. Bellezze, T.; Malavolta, M.; Quaranta, A.; Ruffini, N.; Roventi, G. Corrosion behaviour in concrete of three differently galvanized steel bars. *Cem. Concr. Compos.* **2006**, *28*, 246–255. [CrossRef]
19. Kayali, O.; Yeomans, S. Bond of ribbed galvanized reinforcing steel in concrete. *Cem. Concr. Compos.* **2000**, *22*, 459–467. [CrossRef]
20. Cheng, A.; Huang, R.; Wu, J.K.; Chen, C.H. Effect of rebar coating on corrosion resistance and bond strength of reinforced concrete. *Constr. Build. Mater.* **2005**, *19*, 404–412. [CrossRef]
21. Martin, U.; Röss, J.; Bosch, J.; Bastidas, D.M. Stress corrosion cracking mechanism of AISI 316LN stainless steel rebars in chloride contaminated concrete pore solution using the slow strain rate technique. *Electrochim. Acta* **2020**, *335*, 135565. [CrossRef]

22. Mahasanen, N.; Smith, S.; Humphreys, K. The cement industry and global climate change: Current and potential future cement industry CO₂ emissions. In *Greenhouse Gas Control Technologies, Proceedings of the 6th International Conference, Kyoto, Japan, 1–4 October 2002*; Elsevier: Amsterdam, The Netherlands, 2003; pp. 995–1000.
23. Habert, G.; d’Espinose de Lacaillerie, J.B.; Roussel, N. An environmental evaluation of geopolymer based concrete production: Reviewing current research trends. *J. Clean. Prod.* **2011**, *19*, 1229–1238. [CrossRef]
24. Ariza-Figueroa, H.A.; Bosch, J.; Baltazar-Zamora, M.A.; Croche, R.; Santiago-Hurtado, G.; Landa-Ruiz, L.; Mendoza-Rangel, J.M.; Bastidas, J.M.; Almeraya-Calderón, F.; Bastidas, D.M. Corrosion behavior of AISI 304 stainless steel reinforcements in SCBA-SF ternary ecological concrete exposed to MgSO₄. *Materials* **2020**, *13*, 2412. [CrossRef] [PubMed]
25. Franco-Luján, V.A.; Maldonado-García, M.A.; Mendoza-Rangel, J.M.; Montes-García, P. Chloride-induced reinforcing steel corrosion in ternary concretes containing fly ash and untreated sugarcane bagasse ash. *Const. Build. Mater.* **2019**, *198*, 608–618. [CrossRef]
26. Kupwade-Patil, K.; Allouche, E.N. Examination of chloride-induced corrosion in reinforced geopolymer concretes. *J. Mater. Civil Eng.* **2013**, *25*, 1465–1476. [CrossRef]
27. Gunasekara, C.; Law, D.W.; Setunge, S. Long term permeation properties of different fly ash geopolymer concretes. *Const. Build. Mater.* **2016**, *124*, 352–362. [CrossRef]
28. Ganesan, K.; Rajagopal, K.; Thangavel, K. Evaluation of bagasse ash as corrosion resisting admixture for carbon steel in concrete. *Anti-Corros. Methods Mater.* **2007**, *54*, 230–236. [CrossRef]
29. Amin, N.U. Use of bagasse ash in concrete and its impact on the strength and chloride resistivity. *J. Mater. Civil Eng.* **2011**, *23*, 717–720. [CrossRef]
30. Somna, R.; Jaturapitakkul, C.; Rattanachu, P.; Chalee, W. Effect of ground bagasse ash on mechanical and durability properties of recycled aggregate concrete. *Mater. Des.* **2012**, *36*, 597–603. [CrossRef]
31. Cordeiro, G.C.; Toledo Filho, R.D.; Tavares, L.M.; Fairbairn, E.M.R. Experimental characterization of binary and ternary blended-cement concretes containing ultrafine residual rice husk and sugar cane bagasse ashes. *Constr. Build. Mater.* **2012**, *29*, 641–646. [CrossRef]
32. Rukzon, S.; Chindaprasirt, P. Utilization of bagasse ash in high-strength concrete. *Mater. Des.* **2012**, *34*, 45–50. [CrossRef]
33. Baltazar-Zamora, M.A.; Ariza-Figueroa, H.; Landa-Ruiz, L.; Croche, R. Electrochemical evaluation of AISI 304 SS and galvanized steel in ternary ecological concrete based on sugar cane bagasse ash and silica fume (SCBA-SF) exposed to Na₂SO₄. *Eur. J. Eng. Res. Sci.* **2020**, *5*, 353–357. [CrossRef]
34. Padhi, R.; Mukharjee, B. Effect of rice husk ash on compressive strength of recycled aggregate concrete. *J. Basic Appl. Eng. Res* **2017**, *4*, 356–359.
35. Joshaghani, A.; Moeini, M.A. Evaluating the effects of sugar cane bagasse ash (SCBA) and nanosilica on the mechanical and durability properties of mortar. *Constr. Build. Mater.* **2017**, *152*, 818–831.
36. Jagadesh, P.; Ramachandramurthy, A.; Murugesan, R.; Karthik Prabhu, T. Adaptability of sugar cane bagasse ash in mortar. *J. Inst. Eng. India Ser. A* **2019**, *100*, 225–240.
37. Praveenkumar, S.; Sankarasubramanian, G. Mechanical and durability properties of bagasse ash-blended high-performance concrete. *SN Appl. Sci.* **2019**, *1*, 1664.
38. Ojeda, O.; Mendoza, J.M.; Baltazar, M.A. Influence of sugar cane bagasse ash inclusion on compacting, CBR and unconfined compressive strength of a subgrade granular material. *Rev. Alconpat* **2018**, *8*, 194–208.
39. Ganesan, K.; Rajagopal, K.; Thangavel, K. Evaluation of bagasse ash as supplementary cementitious material. *Cem. Concr. Compos.* **2007**, *29*, 515–524.
40. Chusilp, N.; Jaturapitakkul, C.; Kiattikomol, K. Effects of LOI of ground bagasse ash on the compressive strength and sulfate resistance of mortars. *Constr. Build. Mater.* **2009**, *23*, 3523–3531.
41. Turner, L.K.; Collins, F.G. Carbon dioxide equivalent (CO₂-e) emissions: A comparison between geopolymer and OPC cement concrete. *Constr. Build. Mater.* **2013**, *43*, 125–130.
42. Talha Junaid, M.; Kayali, O.; Khennane, A.; Black, J. A mix design procedure for low calcium alkali activated fly ash-based concretes. *Constr. Build. Mater.* **2015**, *79*, 301–310.
43. Pawluczuk, E.; Kalinowska-Wichrowska, K.; Boltryk, M.; Ramón, J.; Fernandez, J. The influence of heat and mechanical treatment of concrete rubble on the properties of recycled aggregate concrete. *Materials* **2019**, *12*, 367.

44. Fraile García, E.; Ferreiro-Cabello, J.; López-Ochoa, L.M.; López Gonzáles, L.M. Study of the technical feasibility of increasing the amount of recycled concrete waste used in ready-mix concrete production. *Materials* **2017**, *10*, 817. [CrossRef]
45. Dhir, R.; Henderson, N.; Limbachiya, M. *Proceedings of International Symposium: Sustainable Construction: Use of Recycled Concrete Aggregate*; Thomas Telford Ltd.: London, UK, 2015.
46. De Vries, P. Concrete recycled: Crushed concrete aggregate. In *Concrete in the Service of Mankind. I. Concrete for Environment Enhancement and Protection, Proceedings of the International Conference, Dundee, UK, 24–26 June 1996*; E & FN Spon: London, UK; New York, NY, USA, 1996; pp. 121–130.
47. Limbachiya, M.C.; Leelawat, T.; Dhir, R.K. Use of recycled concrete aggregate in high-strength concrete. *Mater. Struct.* **2000**, *33*, 574–580.
48. Oikonomou, N.D. Recycled concrete aggregates. *Cem. Concr. Compos.* **2005**, *27*, 315–318.
49. Berndt, M.L. Properties of sustainable concrete containing fly ash, slag and recycled concrete aggregate. *Constr. Build. Mater* **2009**, *23*, 2606–2613.
50. Landa-Gómez, A.E.; Croche, R.; Márquez-Montero, S.; Villegas Apaez, R.; Ariza-Figueroa, H.A.; Estupiñan López, F.; Gaona Tiburcio, G.; Almeraya Calderón, F.; Baltazar-Zamora, M.A. Corrosion behavior 304 and 316 stainless steel as reinforcement in sustainable concrete based on sugar cane bagasse ash exposed to Na₂SO₄. *ECS Trans.* **2018**, *84*, 179–188. [CrossRef]
51. Chusilp, N.; Jaturapitakkul, C.; Kiattikomol, K. Utilization of bagasse ash as a pozzolanic material in concrete. *Constr. Build. Mater.* **2009**, *23*, 3352–3358. [CrossRef]
52. Khan, K.; Ullah, M.F.; Shahzada, K.; Amin, M.; Bibi, T.; Wahab, N.; Aljaafari, A. Effective use of micro-silica extracted from rice husk ash for the production of high-performance and sustainable cement mortar. *Constr. Build. Mater.* **2020**, *258*, 119589.
53. Akram, T.; Memon, S.; Obaid, H. Production of low cost self compacting concrete using bagasse ash. *Constr. Build. Mater.* **2009**, *23*, 703–712.
54. Yashwanth, M.K.; Naresh, B.G.; Sandeep, D.S. Potential of bagasse ash as alternative cementitious material in recycled aggregate concrete. *Int. J. Innov. Technol. Explor. Eng.* **2019**, *8*, 271–275.
55. Zhao, Y.; Dong, J.; Wu, Y.; Wang, H.; Li, X.; Xu, Q. Steel corrosion and corrosion-induced cracking in recycled aggregate concrete. *Corros. Sci.* **2014**, *85*, 241–250.
56. Liang, C.; Ma, H.; Pan, Y.; Ma, Z.; Duan, Z.; He, Z. Chloride permeability and the caused steel corrosion in the concrete with carbonated recycled aggregate. *Constr. Build. Mater.* **2019**, *218*, 506–518. [CrossRef]
57. Qing, X.; Tao, J.; San-Ji, G.; Zhengxian, Y.; Nengsen, W. Characteristics and Applications of Sugar Cane Bagasse Ash Waste in Cementitious Materials. *Materials* **2019**, *12*, 1–19.
58. *ACI 211.1-91 Standard. Standard Practice for Selecting Proportions for Normal, Heavyweight, and Mass Concrete*; ACI: Farmington Hills, MI, USA, 2002.
59. *NMX-C-414-ONNCCE-2014-Industria de la Construcción—Cementantes Hidráulicos—Especificaciones y Métodos de Ensayo*; ONNCCE, Cd.: Mexico City, Mexico, 2014.
60. *ASTM C127-15—Standard Test Method for Relative Density (Specific Gravity) and Absorption of Coarse Aggregate*; ASTM International: West Conshohocken, PA, USA, 2015.
61. *ASTM C128-15—Standard Test Method for Relative Density (Specific Gravity) and Absorption of Fine Aggregate*; ASTM International: West Conshohocken, PA, USA, 2015.
62. *ASTM C29/C29M-07—Standard Test Method for Bulk Density (“Unit Weight”) and Voids in Aggregate*; ASTM International: West Conshohocken, PA, USA, 2007.
63. *ASTM C33/C33M-16e1—Standard Specification for Concrete Aggregates*; ASTM International: West Conshohocken, PA, USA, 2016.
64. *ACI 214R-11 Standard, Guide to Evaluation of Strength Test Results of Concrete*; ACI: Farmington Hills, MI, USA, 2011.
65. *NMX-C-156-ONNCCE-2010—Determinacion de Revenimiento en Concreto Fresco*; ONNCCE, Cd.: Mexico City, Mexico, 2010.
66. *ASTM C 1064/C1064M-08—Standard Test Method for Temperature of Freshly Mixed Hydraulic-Cement Concrete*; ASTM International: West Conshohocken, PA, USA, 2008.
67. *NMX-C-162-ONNCCE-2014-Industria de la Construcción—Concreto Hidráulico—Determinación de la Masa Unitaria, Cálculo del Rendimiento y Contenido de Aire del Concreto Fresco por el Método Gravimétrico*; ONNCCE, Cd.: Mexico City, Mexico, 2014.

68. NMX-C-083-ONNCCE-2014—*Industria de la Construcción—Concreto—Determinación de la Resistencia a la Compresión de Especímenes—Método de Ensayo*; ONNCCE, Cd.: Mexico City, Mexico, 2014.
69. Ali, B.; Qureshi, L.; Raza, A.; Nawaz, M.; Rehman, S.; Rashid, M. Influence of glass fibers on mechanical properties on concrete with recycled coarse aggregate. *Civil Eng. J.* **2019**, *5*, 1007–1019. [CrossRef]
70. Kurda, R.; De Brito, J.; Silvestre, J. Combined economic and mechanical performance optimization of recycled aggregate concrete with high volume of fly ash. *Appl. Sci.* **2018**, *8*, 1189. [CrossRef]
71. Castaldelli, N.; Moraes, J.C.B.; Akasaki, J.L.; Melges, J.L.P.; Monzó, J.; Borrachero, M.V.; Soriano, L.; Payá, J.; Tashima, M.M. Study of the binary system fly ash/sugarcane bagasse ash (FA/SCBA) in SiO₂/K₂O alkali-activated binders. *Fuel* **2016**, *174*, 307–316. [CrossRef]
72. Li, W.; Xiao, J.; Shi, C.; Poon, C. Structural behaviour of composites members with recycled aggregate concrete—An overview. *Adv. Struct. Eng.* **2015**, *18*, 919–938. [CrossRef]
73. Landa, A.E.; Croche, R.; Márquez, S.; Galván, R.; Gaona, C.; Almeraya, F.; Baltazar, M.A. Correlation of compression resistance and rupture module of a concrete of ratio w/c = 0.50 with the corrosion potential, electrical resistivity and ultrasonic pulse speed. *ECS Trans.* **2018**, *84*, 217–227. [CrossRef]
74. Volpi-León, V.; López-León, L.D.; Hernández-Ávila, J.; Baltazar-Zamora, M.A.; Olguín-Coca, F.J.; López-León, A.L. Corrosion study in reinforced concrete made with mine waste as mineral additive. *Int. J. Electrochem. Sci.* **2017**, *12*, 22–31. [CrossRef]
75. Santiago, G.; Baltazar, M.A.; Olguín, J.; López, L.; Galván, R.; Ríos, A.; Gaona, C.; Almeraya, F. Electrochemical evaluation of a stainless steel as reinforcement in sustainable concrete exposed to chlorides. *Int. J. Electrochem. Sci.* **2016**, *11*, 2994–3006. [CrossRef]
76. *ASTM C192/C192M-16a—Standard Practice for Making and Curing Concrete Test Specimens in the Laboratory*; ASTM International: West Conshohocken, PA, USA, 2016.
77. NMX-C-159-ONNCCE-2004, *Industria de la Construcción—Concreto—Elaboración y Curado de Especímenes en ONNCCE S.C., Cd.*; ONNCCE, Cd.: Mexico City, Mexico, 2004.
78. Liang, M.; Lin, L.; Liang, C. Service Life Prediction of Existing Reinforced Concrete Bridges Exposed to Chloride Environment. *J. Infrastruct. Syst.* **2002**, *8*, 76–85. [CrossRef]
79. Pradhan, B. Corrosion behavior of steel reinforcement in concrete exposed to composite chloride–sulfate environment. *Constr. Build. Mater.* **2014**, *72*, 398–410.
80. *ASTM G 59-97 (2014)—Standard Test Method for Conducting Potentiodynamic Polarization Resistance Measurements*; ASTM International: West Conshohocken, PA, USA, 2014.
81. Fajardo, S.; Bastidas, D.M.; Criado, M.; Romero, M.; Bastidas, J.M. Corrosion behaviour of a new low-nickel stainless steel in saturated calcium hydroxide solution. *Constr. Build. Mater.* **2011**, *25*, 4190–4196.
82. Baltazar, M.A.; Maldonado, M.; Tello, M.; Santiago, G.; Coca, F.; Cedano, A.; Barrios, C.P.; Nuñez, R.; Zambrano, P.; Gaona, C.; et al. Efficiency of galvanized steel embedded in concrete previously contaminated with 2, 3 and 4% of NaCl. *Int. J. Electrochem. Sci.* **2012**, *7*, 2997–3007.
83. Andrade, C.; Alonso, C. Corrosion rate monitoring in the laboratory and on-site. *Constr. Build Mater.* **1996**, *10*, 315–328.
84. Feliu, S.; González, J.A.; Andrade, C. Electrochemical Methods for On-Site Determinations of Corrosion Rates of Rebars. In *Techniques to Assess the Corrosion Activity of Steel Reinforced Concrete Structures*; ASTM STP 1276; Berke, N.S., Escalante, E., Nmai, C.K., Whiting, D., Eds.; ASTM International: West Conshohocken, PA, USA, 1996; pp. 107–118.
85. González, J.A.; Ramírez, E.; Bautista, A.; Feliú, S. The behaviour of pre-rusted steel in concrete. *Cem. Concr. Res.* **1996**, *26*, 501–511. [CrossRef]
86. *ASTM C 876-15 (2015)—Standard Test Method for Corrosion Potentials of Uncoated Reinforcing Steel in Concrete*; ASTM International: West Conshohocken, PA, USA, 2015.
87. Al-Yaqout, A.; El-Hawary, M.; Nouh, K.; Khan, P. Corrosion resistance of recycled aggregate concrete incorporating slag. *ACI-Mater. J.* **2020**, *117*, 111–122.
88. Baltazar, M.A.; Landa, A.; Landa, L.; Ariza, H.; Gallego, P.; Ramírez, A.; Croche, R.; Márquez, S. Corrosion of AISI 316 stainless steel embedded in sustainable concrete made with sugar cane bagasse ash (SCBA) exposed to marine environment. *Eur. J. Eng. Res. Sci.* **2020**, *5*, 127–131.
89. García-Alonso, M.C.; González, J.A.; Miranda, J.; Escudero, M.L.; Correia, M.J.; Salta, M.; Bennani, A. Corrosion behaviour of innovative stainless steels in mortar. *Cem. Concr. Res.* **2007**, *37*, 1562–1569. [CrossRef]

90. Lovato, P.; Possan, E.; Coitinho, D.; Masuero, A. Modeling of mechanical properties and durability of recycled aggregate concretes. *Constr. Build. Mater.* **2012**, *26*, 437–447.
91. Bautista, A.; Blanco, G.; Velasco, F. Corrosion behaviour of low-nickel austenitic stainless steels reinforcements: A comparative study in simulated pore solutions. *Cem. Concr. Res.* **2006**, *36*, 1922–1930.
92. Alonso, M.C.; Luna, F.J.; Criado, M. Corrosion behavior of duplex stainless steel reinforcement in ternary binder concrete exposed to natural chloride penetration. *Constr. Build. Mater.* **2019**, 385–395. [CrossRef]
93. Kurda, R.; De Brito, J.; Silvestre, J. Water absorption and electrical resistivity of concrete with recycled concrete aggregates and fly ash. *Cem. Concr. Compos.* **2019**, *95*, 169–182. [CrossRef]
94. Hren, M.; Kosec, T.; Legat, A. Characterization of stainless steel corrosion processes in mortar using various monitoring techniques. *Constr. Build. Mater.* **2019**, *221*, 604–613. [CrossRef]
95. Serdar, M.; Valek, L.; Bjelogovic, D. Long-term corrosion behaviour of stainless reinforcing steel in mortar exposed to chloride environment. *Corros. Sci.* **2013**, *69*, 149–157. [CrossRef]
96. Kou, S.; Poon, C.; Agrela, F. Comparasions of natural and recycled aggregate concretes prepared with addition of different mineral admixtures. *Cem. Concr. Compos.* **2011**, *33*, 788–795. [CrossRef]
97. Alhawati, M.; Ashour, A. Bond strength between corroded steel reinforcement and recycled aggregate concrete. *Structures* **2019**, *19*, 369–385. [CrossRef]
98. Bautista, A.; Velasco, F.; Torres-Carrasco, M. Influence of the alkaline reserve of chloride-contaminated mortars on the 6-year corrosion behavior of corrugated UNS S32304 and S32001 stainless steels. *Metals* **2019**, *9*, 686. [CrossRef]
99. Baltazar, M.A.; Bastidas, D.M.; Santiago, G.; Mendoza, J.M.; Gaona, C.; Bastidas, J.M.; Almeraya, F. Effect of silica fume and fly ash admixtures on the corrosion behavior of AISI 304 embedded in concrete exposed in 3.5% NaCl solution. *Materials* **2019**, *12*, 4007. [CrossRef]
100. Criado, M.; Bastidas, D.M.; Fajardo, S.; Fernández-Jiménez, A.; Bastidas, J.M. Corrosion behaviour of a new low-nickel stainless steel embedded in activated fly ash mortars. *Cem. Concr. Compos.* **2011**, *33*, 644–652. [CrossRef]
101. Cakir, O. Experimental analysis of properties of recycled coarse aggregate (RCA) concrete with mineral additives. *Constr. Build. Mater.* **2014**, *68*, 17–25. [CrossRef]
102. Li, X. Recycling and reuse of waste concrete in China: Part I. Material behaviour of recycled aggregate concrete. *Resour. Conserv. Recycl.* **2008**, *53*, 36–44. [CrossRef]
103. Ma, Z.; Tang, Q.; Yang, D.; Ba, G. Durability studies on the recycled aggregate concrete in China over the past decade: A review. *Adv. Civil Eng.* **2019**, *2019*, 4073130. [CrossRef]
104. Pacheco, F.; Miraldo, S.; Labrincha, J.; De Brito, J. An overview on concrete carbonation in the context of eco-efficient construction: Evaluation, Use of SCMs and/or RAC. *Constr. Build. Mater.* **2012**, *36*, 141–150. [CrossRef]
105. Roa, A.; Jha, K.; Misra, S. Use of aggregates from recycled construction and demolition waste in concrete. *Resour. Conserv. Recycl.* **2007**, *50*, 71–81.
106. Xie, J.; Zhao, J.; Wang, J.; Wasn, C.; Huang, P.; Fang, C. Sulfate resistance of recycled aggregate concrete with GGBS and fly ash-based geopolymer. *Materials* **2019**, *12*, 1247. [CrossRef] [PubMed]
107. Gurdian, H.; García, E.; Baeza, F.; Garcés, P.; Zornoza, E. Corrosion behavior of steel reinforcement in concrete with recycled aggregate, fly ash and spent cracking catalyst. *Materials* **2014**, *7*, 3176–3197. [CrossRef]
108. Baltazar, M.A.; Mendoza, J.M.; Croche, R.; Gaona, C.; Hernández, C.; López, L.; Olgúin, F.; Almeraya, F. Corrosion behavior of galvanized steel embedded in concrete exposed to soil type MH contaminated with chlorides. *Front. Mater.* **2019**, *6*, 257. [CrossRef]
109. Saravanan, K.; Sathiyarayanan, S.; Muralidharan, S.; Syed-Azim, S.; Venkatachari, G. Performance evaluation of polyaniline pigmented epoxy coating for corrosion protection of steel in concrete environment. *Prog. Org. Coat.* **2007**, *59*, 160–167. [CrossRef]



Article

Mechanisms Accompanying Chromium Release from Concrete

Anna Król

Department of Environmental Engineering, Faculty of Mechanical Engineering, Opole University of Technology, Prószkowska Str. 76, 45-758 Opole, Poland; a.krol@po.edu.pl

Received: 11 March 2020; Accepted: 15 April 2020; Published: 17 April 2020

Abstract: The use of mineral additives from the power and metallurgy industries in the production of building materials still raises questions about the ecological safety of such materials. These questions are particularly associated with the release of heavy metals. The article presents research related to the leaching of chromium from concretes made of Portland cement CEM I and slag cement CEM III/B (containing 75% of granulated blast furnace slag). Concrete was evaluated for leaching mechanisms that may appear during tank test over the long term (64 days). It has been presented that the dominating process associated with the leaching of chromium from both types of concrete is surface wash-off. Between the 9th and 64th day of the test, leaching of Portland cement concrete can be diffusion controlled. It has been proven that the participation of slag in the composition of concrete does not affect the level of leaching of chromium into the environment from concrete.

Keywords: chromium; leaching; concrete; Portland cement; slag cement; tank test

1. Introduction

In the European cement industry, waste materials are used in the production of Portland clinker and cement. At present, alternative fuels (composed of the combustible parts of industrial and municipal waste) are used on a large scale as partial substitutes for natural fuels, and waste from other industries as an alternative to raw materials naturally extracted from the environment. In addition, cement plants significantly reduce the production and use of Portland clinker (the most expensive component of cement) by introducing so-called mineral additives into the composition of cement as main components. Among the most commonly used are wastes from the power industry and metallurgy, such as silica fly ash, granulated blast furnace slag and silica dust [1–3].

They enable the adjustment of concrete properties so that this composite can meet increasingly difficult requirements in applications such as communication and underground infrastructure; engineering and mining works; and environmental protection facilities [3,4].

The use of waste in the cement industry and construction has therefore become an irreversible process, consistent with the idea of sustainable development. Over time, this solution has raised questions not only about the quality of the end products, but also about their impact on the environment. In many countries, various organizations have begun establishing a system for the environmental assessment of materials used in construction, which is to take particular account of the degree of release of heavy metals into the environment. The process of performing an environmental assessment on a material (concrete) is extremely difficult and complex. It requires consideration of factors related to the internal structure of the composite and external factors affecting concrete objects and structures in their working environment (usually in the natural environment), which may affect the release of hazardous substances. Attention should be paid to the level of release of heavy metals from concrete (concrete objects and structures), depending on the application conditions, considering the “life cycle” of the composite [5,6].

An important aspect, from the scientific point of view, is to know the processes that accompanies the release of heavy metals from building materials, especially during exposure to external factors

(variable temperatures, chemically aggressive liquids, carbon dioxide). The materials may then release additional portions of heavy metals or lose their functional properties (e.g., strength properties) [7].

From a point of view of the author, it is wise to control the content of heavy metals at every “stage of life” of the mineral material, from production to application in the environment. Such a modern approach will protect the environment against the uncontrolled spread of metals. Only knowledge of the processes affecting the level of leaching can strengthen this control and predict the development of the situation under certain concrete application scenarios. A modern approach is needed to show the mechanisms that accompany release from these structures. The comprehensive leaching assessment system will give information on how concrete will behave over a long period of time in a given application environment and whether it will affect both its structure and the leaching of heavy metal. Only such a modern approach will give full control and environmental protection in the future. There are not many publications worldwide that would present this approach. Such publications most often concern only Portland cement.

The author of paper would like to emphasize the importance of research of heavy metal leaching from mineral matrices using diffusion tests; e.g., a tank test. Such tests allow the evaluation of the release in aqueous conditions of the long residence time of the sample. Construction materials are considered neutral to the environment. However, this external environment (natural or anthropogenic changed) is not without influence on concrete. During long-term exposure of concrete in water or an environment with reduced pH or under the influence of carbonation (CO_2 impact), structural, physical and chemical changes may occur in the concrete matrix, which contributes to the release of larger portions of heavy metals. Available literature data show very few sources that would describe the relationship of leaching and the mechanisms associated with it. The author has therefore attempted to determine the mechanisms that accompany the long-term leaching from concrete. The author’s research can be used to predict long-term heavy metal leaching. Such research also would allow one to avoid the destruction of concrete during the leaching process.

In this paper, the author presents the state of knowledge about the incorporation of chromium ions into the structures of mineral composites and the factors and processes that may affect the release of heavy metals from such matrices. The author also presented the results of her own research related to the leaching of chromium from concrete produced with Portland cement CEM I and with slag cement CEM III/B. The author found out what mechanisms accompany the leaching of chromium during the hydration process taking place at the same time and whether the composition of the matrix has a decisive effect on the chromium release level.

1.1. Immobilization of Chromium Ions in Cement Composites

Studies on the mechanism of heavy metal bonding and their influence on the physical and mechanical properties of mineral binders are widely discussed in the literature [8–14]. The authors of these works agree that each heavy metal has different characteristics in terms of the level of immobilization in the structures of mineral composites and the accompanying processes and products of hydration. Therefore, in many issues, researchers have different opinions in the literature, which gives the impression that the knowledge about the incorporation of heavy metal ions into the structures of mineral binders has not been systematized yet.

Mattus and Gilliam [15] and de Korte and Broewers [16] placed particular emphasis on the dependence of the level of heavy metal leaching on the metals’ valencies, indicating, for example, that chromium (III) obtains a higher level of binding in the hydrated phases of mineral binding materials than chromium (VI). Very often, the environment has a reducing effect and Cr (VI) is reduced to Cr (III). The reduction of Cr (VI) to Cr (III) enables the formation of insoluble Cr (OH)₃ hydroxide in an alkaline environment.

It is also known that hexavalent chromium is permanently bonded by substituting the sulphate group in ettringite structures ($\text{C}_3\text{A}\cdot 3\text{CaCrO}_4\cdot 32\text{H}_2\text{O}$). According to Glasser [17], such a reaction is also possible, but to a lesser extent, with calcium monosulfate aluminate hydrate ($\text{C}_3\text{A}\cdot \text{CaCrO}_4\cdot 12\text{H}_2\text{O}$). Replacement of SO_4^{2-} by CrO_4^{2-} is possible, but for a high degree of chromium oxidation. Therefore, immobilization of

chromium is difficult and usually does not exceed 80%. Glasser [17] also claims that the relatively worse binding of hexavalent chromium may also be caused by the fact that it forms very soluble chromates.

Cr (III), on the other hand, is ingrained into the structures of phase C-S-H (hydrated calcium silicates), where substitution takes place [11,12,18]

The effect of this reaction is to stabilize the disturbed structure of the C-S-H phase and to inhibit its transition into crystalline phases [18]. The researchers do not agree on the influence of chromium ions on the hydration process. According to [19], the introduction of small amounts of chromium into the cement paste gives the effect of accelerated hydration regardless of whether Cr cation occurs at the third or sixth degree of oxidation. Wang and Vipulanandan [20] added K_2CrO_4 in amounts ranging from 0.5% to 5% in relation to the weight of Portland cement in binders and observed the delay of setting time of cement paste hydration along with the increase of potassium chromate additive. Tamás et al. [21] demonstrated that the introduction of trivalent chromium into cement pastes reduces the total porosity and volume of air pores, and the volume of capillary pores does not change. They claim that the reduction in pore volume may be caused by the precipitation of insoluble chromium (III) hydroxide in the space occupied by the liquid phase. However, a different thesis on the effect of chromium on the porosity of matrices is given in the paper [22]. Namely, that chromium reduces capillary porosity, but increases total porosity.

1.2. Processes Influencing the Leaching of Heavy Metals from Cement Composites

On the basis of the works [23–25], it should be concluded that the level of immobilization of heavy metals in cement matrices depends on many physical and chemical factors, which include the form of the sample (monolith or crushed sample) and environmental factors (soil, water, sewage, chemically aggressive environments, variable temperature and humidity). The level of leaching of heavy metals from a cement composite is also influenced by its composition and the water to cement ratio (w/c) a given composite was made with. The water to cement ratio (w/c); the selection of concrete components; and the amount and type of cement are the factors determining water resistance; resistance to chemical aggression; frost resistance; and strength, i.e., durability of concrete, and thus influencing the leachability of heavy metals to the environment during the whole concrete life cycle [23]. Factors and processes responsible for the release of heavy metals from construction materials are schematically presented in Figure 1. The knowledge about those factors is based on [24].

External factors include, among others, application scenario, liquid to solid ratio (L/S), time of contact with the leaching medium, ambient pH, temperature and mechanical influences (e.g., abrasion, erosion, frost).

The internal factors characterizing the tested structural material include: the porosity, thermal conductivity, shape, specific surface area, size and reactivity of the material (carbonatization susceptibility, alkalinity), and its age [12].

Much attention is paid in literature to the influence of pH on the release of heavy metals [23–26]. Both the reaction of the environment surrounding the structural material (water, soil) and the reaction of the pore water of the material are important. Each heavy metal has pH-dependent solubility [27]. An example is presented in Figure 2 based on information in [27].

As a result of the decreasing pH of cement mortar (e.g., in the carbonatization process), the solubilities of heavy metals change. They usually form slightly soluble compounds in a strongly alkaline environment, whereas at a lower pH they show an increased solubility. Amphoteric metals (e.g., lead) have the lowest solubility at pH between 8 and 10 [27,28]. Studies carried out by van Gerven and others [28] have shown that elements such as magnesium, nickel and copper have the lowest solubility at pH slightly above 7. On the other hand, barium is much more easily soluble at neutral pH than at an alkaline pH.

The results of van der Sloot's works [29] also indicate, as a result of carbonatization (which reduces the pH of cement composites), an increased leaching of heavy metals; i.e., lead, arsenic, cobalt, zinc, molybdenum and cadmium.

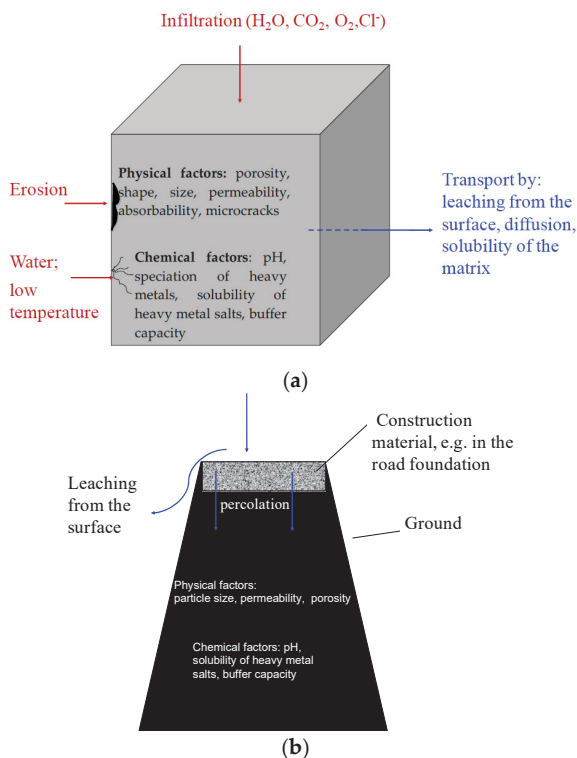


Figure 1. Factors and processes influencing the release of heavy metals from monolith (a) and crushed (b) mineral materials.

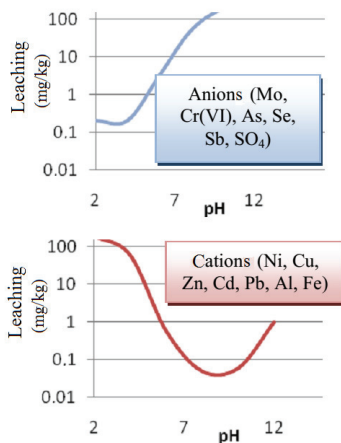


Figure 2. pH-dependent release of anions and cations of heavy metals.

2. Materials and Methods

The author conducted research on the leaching of chromium from concrete on Portland cement CEM I 32,5R (abbreviation: CEM I) and on slag cement CEM III/B 32,5N-LH-HSR/NA (abbreviation: CEM III/B). The content of granulated blast furnace slag in slag cement was 75%. Table 1 shows the chemical compositions of cements, and Table 2 shows the heavy metal contents.

Table 1. Chemical compositions of cements used in the tests.

Component	Content [Weight %]	
	CEM I	CEM III/B
Ignition losses	3.46	0.42
Insoluble parts	0.44	0.48
CaO	64.60	49.75
SiO ₂	19.20	32.92
Al ₂ O ₃	4.69	6.96
Fe ₂ O ₃	3.04	1.80
MgO	1.22	5.04
SO ₃	2.65	1.44
K ₂ O	0.81	0.83
Na ₂ O	0.09	0.28
Cl ⁻	0.047	0.067

Table 2. Heavy metal contents of cements used in the tests [30].

Heavy Metal	Content [mg/kg]	
	CEM I	CEM III B
Cr	54	31
Zn	316	105
Cd	<1	<1
Pb	24	39
Co	7	3
Ni	18	11
Mn	288	1638
V	34	31
Cu	60	27
As	6	0.3
Hg	<0.08	0.08
Tl	<5	<5

In the research, concrete was designed and made using both cements. The composition of the concrete mix was as follows: cement—300.0 kg/m³; sand—685.2 kg/m³; gravel 2–8 mm—600.4 kg/m³; gravel 8–16 mm—628.6 kg/m³; water—180.0 kg/m³; water/cement ratio (w/c)—0.6. The gravels we used were natural aggregates with a density 2.63 kg/dm³.

Cubes measuring 10 cm × 10 cm × 10 cm were formed from the obtained concrete mixes. After 24 h the concrete cubes were subjected to leaching tests taking into account the form of the material (integral form), time (up to 64 days of the test) and the impact of water.

The assessment of inorganic component leaching from mineral materials in the monolithic form involves tank tests, often referred to as diffusion tests. The Netherlands Standardization Institute (NEN), European Committee for Standardization (CEN) and Environmental Protection Agency (EPA) have created a leaching test for different types of materials (building materials, stabilized waste, compacted granular materials). The most common test is based on the EA NEN 7375 standard [31]. The test procedure involves the placing of a sample with a given capacity in a vessel filled with demineralized water. The volume of water in the vessel should be two to five times greater from the volume of the sample. It is also important to place the sample at the distance of at least 2 cm from the vessel walls and to ensure that it is completely immersed in the leachant (Figure 3). The materials are then subjected to leaching over the period of 64 days. The tank test [32] allows assessing the impact of the duration of contact between the leachant and the material on the leaching of pollutants, and the analysis of the cumulative leachability of a given component per specific unit of waste surface. Thanks to the application of the tank test, it is also possible to determine the nature of the leaching; i.e., whether it is dominated by diffusion, surface wash-off, depletion or dissolution.

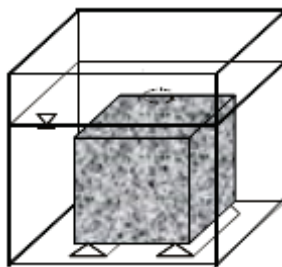


Figure 3. Principle of sample placement in the tank according to EA NEN 7375.

The test was performed at the temperature range 19–21 °C. The eluates used in the test were extracted according to the following time schedule: after 0.25, 1, 2.25, 4, 9, 16, 36 and 64 days. After each extraction of the eluate, the liquid was completely replaced and the samples were immersed in the liquid again. The eluates were filtered through the membrane filters with the pore size of 0.45 µm. The concentrations of $C_{r_{total}}$ in eluates were determined with an inductively-coupled plasma-mass spectrometer (ICP MS) by Perkin Elmer. Each measurement was carried out with three repetitions holding relative standard deviation (RSD) <5%.

3. Results and Discussion

In each of the eight eluates, the concentration of chromium was analyzed.

In the course of the study, the level of leaching per eluate fraction, total leachability per unit of surface area and the emerging leaching processes were determined according to [31].

In the course of calculations for the analyzed heavy metal, the leachability in particular fractions was determined using the Equation [31]:

$$E_i^* = \frac{c_i V}{f A} \quad (1)$$

where:

E_i^* —leaching of the component in fraction i (mg/m²);

c_i —concentration of the component in fraction i (µg/dm³);

V —volume of eluate (dm³);

A —sample surface area (m²);

f —factor: 1000 (µg/mg).

Table 3 shows the leaching of chromium calculated in individual fractions. Measured cumulative leaching (ε_n^*) of a component was calculated (Table 3) according to the formula [31]:

$$\varepsilon_n^* = \sum_{i=1}^n E_i^* \quad \text{for } n = 1 \text{ to } N \quad (2)$$

where ε_n^* is the measured cumulative leaching of a component for period n comprising fraction $i = 1$ to n , in mg/m² of sample surface area; E_i^* is the measured leaching of the component in fraction i , in mg/m²; and N is the total number of leachant replenishment periods.

Derived cumulative leaching ε_n of a component was calculated using the formula [31]:

$$\varepsilon_n = E_i^* \frac{\sqrt{t_i}}{\sqrt{t_i} - \sqrt{t_{i-1}}} \quad (3)$$

where ε_n is the derived cumulative leaching of a component for period n comprising fraction $i = 1$ to n , in mg/m² of sample surface area; E_i^* is the measured leaching of the component in fraction i , in mg/m²; t_i is the replenishment time of fraction i , in s; and t_{i-1} is the replenishment time of fraction $i-1$, in s.

Table 3. Chromium leaching out of concrete with CEM I and CEM III/B cement.

Eluate Fraction	Time [h]	Chromium Leachability E_i^* [mg/m ²]		Measured Cumulative Leachability of Chromium ϵ_n^* [mg/m ²]	
		CEM I Concrete	CEM III/B Concrete	CEM I Concrete	CEM III/B Concrete
1	6	0.0045	0.0031	0.0045	0.0032
2	24	0.0037	0.0015	0.0082	0.0046
3	54	0.0020	0.0016	0.0102	0.0063
4	96	0.0020	0.0014	0.0122	0.0077
5	216	0.0020	0.0014	0.0142	0.0091
6	384	0.0022	0.0017	0.0163	0.0107
7	846	0.0023	0.0028	0.0187	0.0136
8	1536	0.0072	0.0070	0.0258	0.0206

Based on the above calculations, it can be determined which mechanisms accompany heavy metal leaching; i.e., whether each is dominated by diffusion (DIF) or other mechanisms, such as:

- Surface wash-off (SWO);
- Depletion (DEP);
- Dissolution (DIS);
- Delayed diffusion or dissolution (DDD).

For such an analysis, it is recommended [31] that the cumulative leaching (ϵ_n^* and ϵ_n) should be shown graphically. For this purpose, the logarithm of the cumulative leaching ϵ_n obtained in relation to the time logarithm t_i for $n = 1$ to N should be plotted in order to visually assess the measurements obtained. In the same graph, the logarithm of the calculated total leaching ϵ_n^* should be plotted. Graphical analyses are shown in Figures 4 and 5.

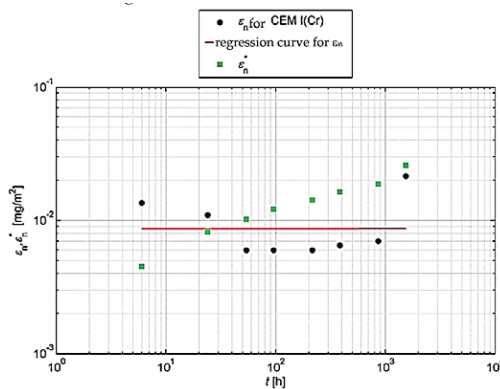


Figure 4. Cumulative leaching ϵ_n of chromium with a determined regression curve for concrete with CEM I.

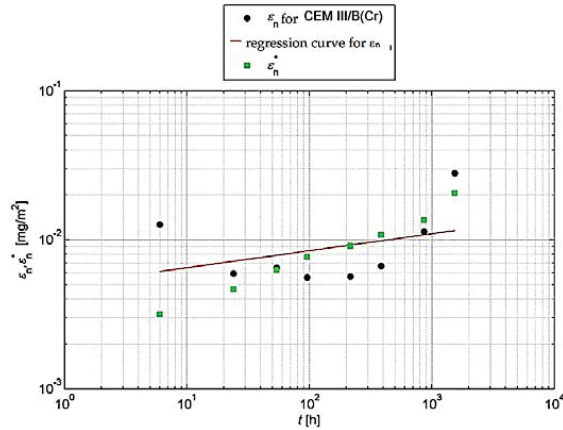


Figure 5. Cumulative leaching ε_n of chromium with a determined regression curve for concrete with CEM III/B.

The eluate fractions obtained and tested during periods 1–8 should be divided into increments long enough to recognize the mechanisms involved in release of heavy metals. Eluate fractions collected in periods 1–8 should be grouped into the ranges like shown in Table 4 [31].

Table 4. Ranges of eluates and increments.

Number of Range	Eluate Fraction	Increments a–b
1	Fractions 2 to 7	Increment 2–7
2	Fractions 5 to 8	Increment 5–8
3	Fractions 4 to 7	Increment 4–7
4	Fractions 3 to 6	Increment 3–6
5	Fractions 2 to 5	Increment 2–5
6	Fractions 1 to 5	Increment 1–4

The CF_{a-b} concentration factor (Equation (4)), slope (rc) of linear regression line of $\log \varepsilon$ versus $\log t$ and the standard deviation (sd_{rc}) shall be determined for a given heavy metal under assessment and for each of the ranges identified.

$$CF_{a-b} = \frac{\text{Mean concentration in the increment}}{\text{Lowest limit of determination of a heavy metal}} \quad (4)$$

On the basis of the slope of the regression function in individual increments (Table 5), it can be specified which mechanisms control the release of heavy metals from the test sample.

Table 5. Interpretation of rc slopes within individual increments [31].

Increment a–b	Slope, rc		
	≤ 0.35	$> 0.35 \text{ i} \leq 0.65$	> 0.65
Increment 2–7	Surface Wash-off (SWO)	Diffusion (DIF)	Dissolution (DIS)
Increment 5–8	Depletion (DEP)	Diffusion (DIF)	Dissolution (DIS)
Increment 4–7	Depletion (DEP)	Diffusion (DIF)	Dissolution (DIS)
Increment 3–6	Depletion (DEP)	Diffusion (DIF)	Dissolution (DIS)
Increment 2–5	Depletion (DEP)	Diffusion (DIF)	Dissolution (DIS)
Increment 1–4	Surface Wash-off (SWO)	Diffusion (DIF)	Delayed diffusion or dissolution (DDD)

Graphical representations of the results obtained for chromium are shown in Figures 6 and 7.

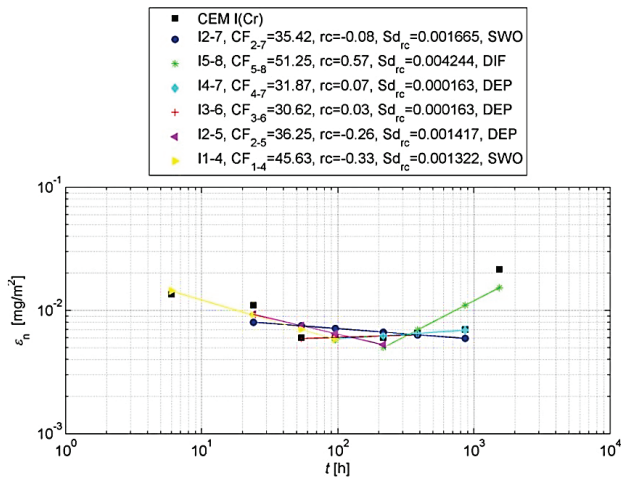


Figure 6. Cumulative leaching ϵ_n of chromium with determined regression curve in increments, for concrete with CEM I.

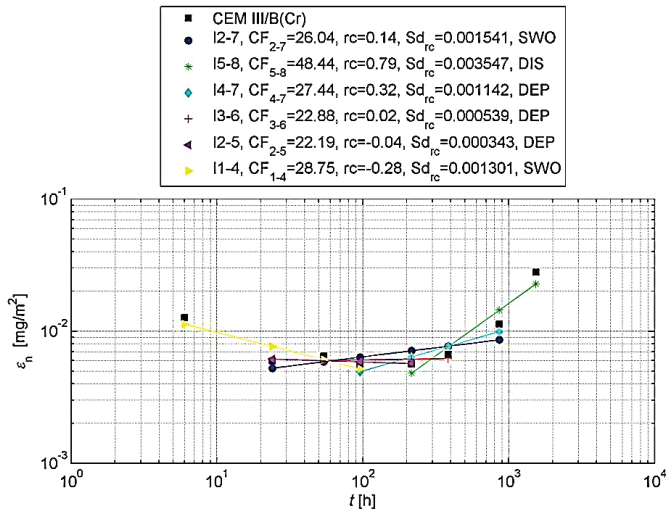


Figure 7. Cumulative leaching ϵ_n of chromium with determined regression curve in increments, for concrete with CEM III/B.

On the basis of the above analyses, it can be concluded that the leachability of chromium from concrete with Portland cement and with slag cement is not controlled during the entire test cycle by one leaching mechanism. However, it can be claimed that the release of chromium in both the longest (increments 2–7) and the shortest and earliest test period (increment 1–4) occurs by surface wash-off (SWO). The tests also showed that the matrix with CEM I does not dissolve, which means that the matrix did not deteriorate during long (64 days) chromium leaching tests. In later test periods (between the 9th and 64th day of the test) the leaching of chromium from concrete may be accompanied by diffusion processes.

Dissolution occurs in the case of concrete with CEM III/B (increment 5–8), which may indicate the destruction of the concrete during long-term exposure to water. However, during this time there are

no increased doses of released chromium per area unit, compared to concrete with Portland cement (Table 3). Studies have shown that the achieved level of chromium release from concrete with CEM III/B can be even lower compared to concrete on Portland cement. This may be related to the caulking structure of concrete affected by granulated blast furnace slag. Composites made of slag cement are characterized by a smaller number of capillary pores, and greater tightness of the structure, and thus a reduction in the permeability and penetration of aggressive substances and water [32,33].

4. Conclusions

The use of alternative fuels and by-products from the power and metallurgy industries as valuable components of clinkers, cements and mineral composites has become in the last twenty years a fully intentional activity of the cement and construction industry, consistent with the idea of sustainable development. This has led to the development of a wide range of industrial by-products that are able to meet the challenges of modern construction. On the other hand, however, the system of environmental assessments has become extremely topical, which should cover the difficult subject of releasing heavy metals from mineral composites into the environment through research procedures. Concrete is commonly present in the environments surrounding people. Therefore, it must not affect the quality of the environment with which it is in contact, and particularly, it must not impair human health.

The paper presents considerations on the mechanisms accompanying the leaching of heavy metals from building materials, focusing on the release of chromium from concrete produced with Portland cement and slag cement.

The results of chromium leaching from concrete seasoned up to 64 days were obtained. Processes accompanying the release of chromium from concrete matrices were evaluated. It was found that the dominant process which controls the leaching of chromium from the analyzed concretes is surface wash-off. It has also been proven that the use of large amounts of granulated blast furnace slag in the cement composition does not release additional portions of chromium from concretes in long contact with water. Concrete with slag cement can be influenced by dissolution. In practice, therefore, more tight concrete of this type should be used (e.g., by lowering the w/c ratio of the concrete), which would allow obtaining a compact structure with a lower capillary content. This can protect slag concrete from dissolving during long term contact with water. As a result, this will contribute to not releasing further portions of chromium into the environment.

There is not much research in the literature on the mechanisms controlling the leaching process; hence, the author took up this subject. However, this issue should be further developed considering other concrete exposure conditions and other kinds of concrete. If such complex tests are carried out, it will be possible to plot the matrices of the use of individual concretes in various application scenarios, so additional heavy metal concentrations are not released.

Funding: This research received no external funding.

Conflicts of Interest: The author declares no conflict of interest.

References

1. Wzorek, M. Assessment of leachability of harmful components from alternative fuels prepared with the use of sewage sludge/Ocena wymywalności szkodliwych składników z paliw alternatywnych wytworzonych z osadów ściekowych. *Ecol. Chem. Eng. S* **2012**, *19*, 617–627. [CrossRef]
2. Wzorek, M.; Baran, T.; Ostrowski, M. The influence of fly ash absorption from secondary fuels combustion on clinkering process and hydraulic activity of Portland cement clinker. *Cem. Wap. Bet.* **2013**, *18*, 207–215.
3. Król, A.; Filipowicz, M.; Dudek, M.; Olkusi, T.; Styszko, K. The role of the silica fly ash in sustainable waste management. *E3S Web Conf.* **2016**, *10*, 49. [CrossRef]
4. Klemczak, B.; Batog, M.; Giergiczny, Z.; Żmij, A. Complex Effect of Concrete Composition on the Thermo-Mechanical Behaviour of Mass Concrete. *Materials* **2018**, *11*, 2207. [CrossRef]

5. Kuterasińska, J.; Król, A. Mechanical properties of alkali activated binders based on copper slag. *Archit. Civil Eng. Environ.* **2015**, *8*, 61–67.
6. Król, A.; Mizerna, K. Directions of development of research methods in the assessment of leaching of heavy metals from mineral waste. *E3S Web Conf.* **2016**, *10*, 50. [CrossRef]
7. Król, A.; Jagoda, D. Carbonation and the durability of cement composites immobilizing heavy metals (Zn²⁺, Cr⁶⁺, Pb²⁺). *Cem. Wap. Bet.* **2012**, *17*, 90–101.
8. Bhunia, P.; Pal, A.; Bandyopadhyay, M. Assessing arsenic leachability from pulverized cement concrete produced from arsenic-laden solid Ca/Si/Co-sludge. *J. Hazard. Mater.* **2007**, *141*, 826–833. [CrossRef]
9. Hekal, E.; Hegazi, W.S.; Kishar, E.A.; Mohamed, M.R. Solidification/stabilization of Ni(II) by various cement pastes. *Constr. Build. Mater.* **2011**, *25*, 109–114. [CrossRef]
10. Da Luz, C.A.; Rocha, J.; Cheriaf, M.; Pera, J. Use of sulfoaluminate cement and bottom ash in the solidification/stabilization of galvanic sludge. *J. Hazard. Mater.* **2006**, *136*, 837–845. [CrossRef]
11. Moulin, I.; Rose, J.; Stone, W.; Bottero, J.-Y.; Mosnier, F.; Haehnel, C. Lead, zinc and chromium (III) and (VI) speciation in hydrated cement phases. In Proceedings of the International Conference on the Science and Engineering of Recycling for Environmental Protection, Harrogate, UK, 31 May–2 June 2000; pp. 269–280.
12. Nagataki, S.; Yu, Q.; Hisada, M. Effect of leaching conditions and curing time on the leaching of heavy metals in fly ash cement mortars. *Adv. Cem. Res.* **2002**, *14*, 71–83. [CrossRef]
13. Serclérat, I.; Moszkowicz, P.; Pollet, B. Retention mechanisms in mortars of the trace metals contained in Portland cement clinkers. *Waste Manag.* **2000**, *20*, 259–264. [CrossRef]
14. Yu, Q.; Nagataki, S.; Lin, J.; Saeki, T.; Hisada, M. The leachability of heavy metals in hardened fly ash cement and cement-solidified fly ash. *Cem. Concr. Res.* **2005**, *35*, 1056–1063. [CrossRef]
15. Mattus, C.; Gilliam, T. *A Literature Review of Mixed Waste Components: Sensitivities and Effects upon Solidification/Stabilization in Cement-Based Matrices*; ORNL/TM-12656; Office of Scientific and Technical Information (OSTI): Oak Ridge, TN, USA, 1994.
16. De Korte, A.; Brouwers, H. Production of non-constructive concrete blocks using contaminated soil. *Constr. Build. Mater.* **2009**, *23*, 3564–3578. [CrossRef]
17. Glasser, F.P. Immobilization potential of cementitious materials. In Proceedings of the International Conference on Environmental Implication of Construction Materials and Technology Developments Environmental Aspects of Construction with Waste Materials, Maastricht, The Netherlands, 1–3 June 1994; pp. 77–86.
18. Takahashi, S.; Daimon, M.; Sakai, E. Sorption of CrO₄²⁻ for cement hydrates and the leaching from cement hydrates after sorption. In Proceedings of the 11th International Congress on the Chemistry of Cement Cement's Contribution on the Development in the 21st Century, Durban, South Africa, 11–16 May 2003; pp. 2166–2172.
19. Rossetti, V.; Medici, F. Inertization of toxic metals in cement matrices: Effects on hydration, setting and hardening. *Cem. Concr. Res.* **1995**, *25*, 1147–1152. [CrossRef]
20. Wang, S.; Vipulanandan, C. Solidification/stabilization of Cr (VI) with cement leachability and XRD analyses. *Cem. Concr. Res.* **2000**, *30*, 385–389. [CrossRef]
21. Tamas, F.; Csetenyi, L.; Tritthart, J. Effect of adsorbents on the leachability of cement bonded electroplating wastes. *Cem. Concr. Res.* **1992**, *22*, 399–404. [CrossRef]
22. Opoczky, L.; Gavel, V. Effect of certain trace elements on the grindability of cement clinkers in the connection with the use of wastes. *Int. J. Miner. Process.* **2004**, *74*, S129–S136. [CrossRef]
23. Dijkstra, J.J.; Sloot, H.A.V.d.; Spanka, G.; Thielen, G. *How to Judge Release of Dangerous Substances from Construction Products to Soil and Groundwater*; ECN-C-05-045; Energy Research Centre of The Netherlands ECN: Petten, The Netherlands, 2005.
24. Sloot, H.A.V.d.; Dijkstra, J.J. *Development of Horizontally Standardized Leaching Tests for Construction Materials: A Material Based or Release Based Approach?* ECN-C-04-060; Energy Research Centre of The Netherlands ECN: Petten, The Netherlands, 2004. [CrossRef]
25. Sloot, H.A.V.d. Comparison of the characteristic leaching behaviour of cements using standard (EN 196 1) cement mortar and an assessment of their long term environmental behaviour in construction products during service life and recycling. *Cem. Concr. Res.* **2000**, *30*, 1079–1096. [CrossRef]
26. Król, A.; Mizerna, K.; Bożym, M. An assessment of pH-dependent release and mobility of heavy metals from metallurgical slag. *J. Hazard. Mater.* **2020**, *384*, 121502. [CrossRef]

27. Sloot, H.A.V.d.; Dijkstra, J.; Seignette, P.; Hjelmar, O.; Spanka, G. *Characterisation Leaching Tests as Basis of Reference for Quality Control and Decisions on Acceptability of Alternative Materials in Construction*; Energy Research Centre: Lyon, France, 2009.
28. Gerven, T.V.; Baelen, D.V.; Dutré, V.; Vandecasteele, C. Influence of carbonation and carbonation methods on leaching of metals from mortars. *Cem. Concr. Res.* **2004**, *34*, 149–156. [CrossRef]
29. Sloot, H.A.V.d. Characterization of the leaching behavior of concrete mortars and of cement–stabilized wastes with different waste loading for long term environmental assessment. *Waste Manag.* **2002**, *22*, 18–186.
30. Król, A. The Role of the Granulated Blast Furnace Slag in Sustainable Cement Production and Waste Management. *Econ. Environ. Stud.* **2017**, *17*, 613–624. [CrossRef]
31. European (EN) and national (NEN) standards accepted in The Netherlands. *EA NEN 7375:2004 Leaching Characteristics of Moulded or Monolithic Building and Waste Materials. Determination of Leaching of Inorganic Components with the Diffusion Test. The Tank Test*; European (EN) and National (NEN) Standards Accepted in The Netherlands: Delft, The Netherlands, 2004.
32. Divsholi, B.S.; Lim, T.Y.D.; Teng, S. Durability Properties and Microstructure of Ground Granulated Blast Furnace Slag Cement Concrete. *Int. J. Concr. Struct. Mater.* **2014**, *8*, 157–164. [CrossRef]
33. Schuldyakov, K.; Kramar, L.; Trofimov, B. The Properties of Slag Cement and its Influence on the Structure of the Hardened Cement Paste. *Procedia Eng.* **2016**, *150*, 1433–1439. [CrossRef]



© 2020 by the author. Licensee MDPI, Basel, Switzerland. This article is an open access article distributed under the terms and conditions of the Creative Commons Attribution (CC BY) license (<http://creativecommons.org/licenses/by/4.0/>).

Article

Post-Pyrolytic Carbon as a Phase Change Materials (PCMs) Carrier for Application in Building Materials

Michał Ryms ^{1,*}, Katarzyna Januszewicz ¹, Paweł Kazimierski ², Justyna Łuczak ³,
Ewa Klugmann-Radziemska ¹ and Witold M. Lewandowski ¹

¹ Department of Energy Conversion and Storage, Faculty of Chemistry, Gdansk University of Technology, G.Narutowicza 11/12, PL-80-233 Gdańsk, Poland; katarzyna.januszewicz@pg.edu.pl (K.J.); ewa.klugmann-radziemska@pg.edu.pl (E.K.-R.); wlew@pg.edu.pl (W.M.L.)

² Institute of Fluid Flow Machinery, Polish Academy of Sciences, Fiszerka 14, PL 80-231 Gdańsk, Poland; pawel.kazimierski@imp.gda.pl

³ Department of Process Engineering and Chemical Technology, Faculty of Chemistry, Gdansk University of Technology, G.Narutowicza 11/12, PL-80-233 Gdańsk, Poland; justyna.luczak@pg.edu.pl

* Correspondence: michal.ryms@pg.edu.pl; Tel.: +48-58-347-23-22

Received: 30 January 2020; Accepted: 8 March 2020; Published: 11 March 2020

Abstract: This article covers new application for char as a carrier of phase-change materials (PCM) that could be used as an additive to building materials. Being composed of bio-char and PCM, the granulate successfully competes with more expensive commercial materials of this type, such as Micronal[®] PCM. As a PCM carrier, char that was obtained from the pyrolysis of chestnut fruit (*Aesculus hippocastanum*) with different absorbances of the model phase-change material, Rubitherm RT22, was tested. DSC analysis elucidated several thermal properties (such as enthalpy, phase transition temperature, and temperature peak) of those mixtures and the results were compared with a commercial equivalent, Micronal DS 5040 X. Comparative research, approximating realistic conditions, were also performed by cooling and heating samples in a form of coatings that were made from chars with different content of RT22. These results indicated that the use of char as a PCM carrier was not only possible, but also beneficial from a thermodynamic point of view and it could serve as an alternative to commercial products. In this case, adsorption RT22 into char allowed for temperature stabilization comparable to Micronal DS 5040 X with ease of use as well as the economic advantages of being very low cost to produce due to microencapsulation. Other advantage of the proposed solution is related with the application of char obtained from waste biomass pyrolysis as a PCM carrier, and using this product in building construction to improve thermal comfort and increase energy efficiency.

Keywords: PCM; phase-change materials; activated carbon; PCM carriers; biomass pyrolysis; thermal stability; building materials modification

1. Introduction

Analyzing the development directions of modern building construction, there is a clear effort to build with attention towards a reduction in energy consumption without sacrificing comfort [1–3]. We increasingly seek to develop new materials with better thermal and insulation properties that could be used in building construction because we attach so much importance to reduce energy consumption, optimizing its use and searching for new, pro-ecological ways to obtain it. Current building materials do result in significant energy consumption reduction; however, they are still relatively expensive and require new solutions not only to reduce energy consumption, but also to be more cost effective [4–7]. As conventional building material selection occurs primarily with cost in mind, one such example comes from buildings in Central and Eastern Europe, which are primarily made from silicate blocks

with moderate thermodynamic properties. Styrofoam is also a popular supportive building material that works with silicate blocks and also lowers energy consumption, but, due to the possibility of thermal bridges between the contacting blocks, lowers energy consumption to a certain level. In low-energy, and especially passive building constructions, materials with better insulation properties should be used, but those materials are more expensive and drive up investment/construction costs. In addition to improving the insulation of materials used in energy-efficient buildings, they can be modified by addition of phase-change materials (PCM), which further improves the energy balance of that building [8]. Unfortunately, despite commercial availability, these solutions have not been widely adopted, due to their high price. Therefore, it is necessary to look for opportunities to develop inexpensive building materials, which can not only prevent energy loss in the first place, but temporarily store excess energy (like solar energy) for release in a timely manner. Such solutions have already been analyzed many times [9–14]; with several proposed solutions [15–18]. However, ongoing research in this area is still critical and valued in the building construction industry.

There are many known methods for the practical use of phase-change materials, especially in building construction, where microcapsules are most commonly used [19–27] (e.g., Micronal 5040X, i.e., Rubitherm RT22 trapped inside a polyethylene coating). These microcapsules, mixed with gypsum, cement, or mortar, are included in gypsum walls, mortars, screeds, or plasters. The disadvantages that are associated with these materials include: high price (due to difficulty obtaining the Micronal product), low thermal conductivity, and low mechanical strength. At higher loads, those problems result in cracking and the depressurization of polymer coatings and pouring of the PCM after exceeding its melting point.

This last drawback does not appear in the solution using metal, ceramic, glass, or other hermetic containers filled with PCM, the mechanical strength of which can be adjusted by wall thickness. However, they have a high thermal inertia, due to the low thermal conductivity of materials that are solidified within. This limits their application in heat storages and regenerators, in which fast-changing thermal energy occurs. Additionally, in building construction, due to the need to redesign traditional building material shapes (bricks, hollow bricks, etc.) to utilize PCM materials within them has hampered the development of this approach.

There are some known attempts of using lightweight aggregate (LWA), e.g., Pollytag[®] as a carrier [28,29] with PCM (Ceresin) completed with a patent [30]. PCM that was trapped in the LWA pores was able to stabilize the temperature of the asphalt road surface in laboratory conditions at a lower level, when compared to a surface without PCM. This behavior could theoretically protect the asphalt mineral mixture from softening and rutting under real conditions. However, this solution has not yet been put into practical use due to implementation difficulties related to the mechanical strength of the resulting products. A relatively low amount of Ceresin (3% by weight) adsorbed into the pores of Pollytag[®] construction aggregate; however, achieving the required stabilization temperature necessitated the addition of large amounts of modified aggregate into the asphalt mixture, which lowered its mechanical strength when compared to the traditional mineral aggregate and reduced the pavement surface hardness. Research on the use of LWA and PCM was also conducted relative to traditional building materials [14], but, as a carrier, its use has encountered some limitations due to the specificity of Pollytag[®]. First, the air remaining in its pores hindered heat exchange and inhibited PCM phase changes. The second limitation was the relatively large granulate size, which poses an obstacle when adding it or filling traditional building materials with it (holes, hollow bricks, etc.). However, filling with this granulate gypsum wall or plaster, as well as covering the surface with it, was already problematic.

In this paper, the use of post-pyrolytic carbonate that was obtained from waste biomass as a PCM carrier is proposed. The effects of the above solution were verified in an experimental way, examining the heating and cooling time of the coatings that were applied to the temperature sensors made of char containing various amounts of Rubitherm (PCM), wherein one of the coatings, made from the char without PCM, was taken as a reference sample. Although the experiments presented in this

manuscript were mainly limited to coatings, the material can also be implicitly used in a wide range in construction.

2. Theoretical Background

The starting point for these considerations were studies on the possibility of heat accumulation using phase change materials that were previously mentioned, as it related to modified asphalt pavement for its temperature stabilization [28,29]. Lightweight aggregate was then used as the PCM carrier and it provided a porosity that was high enough to absorb a sufficient amount of PCM with acceptable strength. This solution has patent protection [30] and it paves the way for other similar applications such as classic building construction, in which solutions based on the PCM sealing modification in containers, capsules, bags, or microgranules as a protection against potential leakage had been most common. In these solutions, PCM was trapped in porous aggregate and, thanks to the van der Waals forces, remained in LWA, even at high temperatures and it was experimentally confirmed [14]. Those experiments showed that use of PCM mixtures with an aggregate additive had a positive effect on temperature stabilization of other building materials and improved the thermal comfort of rooms. For hollow blocks and gypsum blocks that were modified with the aggregate and PCM mixture, a significant extension of the temperature stabilization period (thermal comfort) was achieved, but depended on the initial conditions [14]. Aside from cost reduction, this modification additionally resulted in resource savings through the replacement of expensive yet easy to use Micronal DS 5040 X with a less expensive and more durable alternative—Rubitherm RT22 adsorbed on a cheap and mechanically durable carrier, which would be difficult to apply directly in liquid form. This new solution enables the easy implementation of phase-change materials in construction.

A natural consequence of research on PCM carriers is the search for novel materials with high porosity and environmental friendliness. One of those novel materials might be char, which, through activation and increased absorption capacity, has potential as an excellent PCM carrier. Another advantage is its production via pyrolytic utilization as both waste biomass and municipal waste combustion (RDF; tires, sewage sludge, etc.). The possibility of valorization and use of waste products that are currently incinerated is a commercially attractive research direction.

The purpose of the research described is the use of char obtained after pyrolysis as a PCM carrier. It was assumed the simplest solution would involve adsorption that was carried out above the PCM melting point. The same char was used in this study; however, the resulting product was comprehensively examined for its physical and thermodynamic properties as well as its potential in practical application by comparing synthesized materials with commercially available microcapsules containing the same PCM due to different activation methods showing a different specific surface areas and different absorption capacities. Heating and cooling this modified char allowed for a determination of the hysteresis and repeatability of the process as well as its durability, which certainly impact potential applications, such as building, road construction, and even gardening.

The amount of PCM, relative to the total weight of building materials, determines the effectiveness of temperature stabilization within a building. For example, in tests that were carried out with a 3% (by weight) addition of ceresin trapped in LWA [29], the decrease in surface temperature, as compared to parallel measurements for surfaces without ceresin, was ~5 K. In this work, in which the PCM share the biocarbonate, should be 5–7 times higher, which represents an adequate increase in the thermodynamic effect or a reduction in the amount of modified PCM carbonate added to building materials (gypsum, cement, mortar, etc.).

In this study, a product of waste biomass pyrolytic decomposition was used; in this case, it was the fruit of inedible chestnut (*Aesculus hippocastanum*), although the general source of the char might originate from any type of waste biomass, which increases the rationale for undertaking research in this area. It is worth emphasizing that the formation of the adsorptive structure of the char begins during the thermal, anaerobic biomass degradation. Parameters, such as temperature, presence of inert gas, heating rate, and reactor type, have a significant impact on the quantity and quality of

pyrolysis products [31,32]. The wide range of available pyrolyzers for both laboratory and technical scale applications allows for their selection in terms of the desired product properties.

A muffle furnace was used due to the laboratory scale of this work. It was assumed that the char that was obtained after these processes might not have sufficiently developed a surface, which negatively impacted its adsorption properties. Therefore, several activation pathways were examined to improve the carbonate sorption parameters. These pathways unblocked their pores, being often blocked by gaseous and liquid post-pyrolytic residues, which resulted in porosity and specific surface increases. Char, like any activated carbon, has a specific surface area, depending on its porosity (macro-meso and micropores), which can be increased by activation. The greater the ratio of the total area of all pores to the mass of activated carbon, the more extensive its structure and the greater its absorption potential.

Activation is divided into two classifications—physical, where the activator can be carbon dioxide, steam, and/or oxygen at temperatures from 800–1000 °C; and, chemical, where the activator is sodium hydroxide, zinc chloride, and phosphoric acid (V) at temperatures from 400–1000 °C. An advantage of chemical activation is that it is a one step process in conjunction with biomass pyrolysis previously impregnated with the activator. In the tests described below, the effect of the surface area development and pore size on PCM adsorption was assessed; chemically and physically activated samples were used.

It is expected that the insertion of PCM in place of air into porous char will increase its mechanical strength, especially pressure and hardness; where strength, depending on the type of PCM, might even surpass that of the biomass itself, e.g., wood from which this char can be obtained. These features, in addition to better thermal conductivity, should also provide a definite advantage for the char as a PCM carrier, relative to other carriers (Pollytag[®], Leca[®] KERAMZYT, aerated concrete, porous gypsum to name a few), and over encapsulated PCM, foil, or placed in containers.

3. Methodology and Experimental Study

The methodology in this work is difficult to formally describe without reference to individual experiments, as it was different for each test. Utilized methodologies include:

- pyrolysis of various types of waste biomass (N₂—inert gas, temperature: 800 °C, time: 90 min.—Section 3.1);
- determining the composition, as well as physical and sorption properties of the obtained biochar (proximate and elementary analysis);
- methods used to activate the biochar (Section 3.2) and study the effects of increasing the sorption surface (BET surface and pore size analysis);
- PCM sorption procedure in biochar (typical vacuum sorption in liquid Rubitherm RT22 for approx. 30 min., and thermal draining at 80 °C in the same time period);
- testing and selecting biomass in terms of the sorption capacity of the biochar that was obtained from it, from currently available biomass types: coconut shell, walnut shell, chestnuts (validation of the sorption capacity of various types of activated and inactivated biochars, based on DSC analysis—Section 3.3); and,
- conducting experimental studies of thermodynamic properties of a material obtained from selected biochar (chestnuts), modified by PCM (Section 3.4).

In this situation, while considering the accessibility and readability of the work, the authors decided to provide information on the methodology successively, within the individual descriptions of the experiments.

3.1. Preparation of Post-Pyrolytic Carbon

Biomass is required to obtain char as a PCM carrier, which can be obtained from various sources. From ecological and economical points of view, this should be waste biomass that is intended for disposal.

Therefore, chestnut fruits (*Aesculus hippocastanum*), often referred to simply as chestnuts—an inedible resource often subjected in Poland to waste disposal—was selected as the biomass example for this study.

The process of obtaining char was as follows. Chestnuts were dried for 12 h at 105 °C and ground using a knife mill (3 mm mesh diameter). Pyrolysis of ~100 g of the granulate was carried out without an inert gas flow for 90 min. at 800 °C in a steel reactor with an outlet tube placed in a muffle furnace. The solid recovery after pyrolysis was 25% of the initial mass.

After mixing several batches, the elemental analysis of chestnut fruit and the char obtained from it was determined (Thermo Scientific™ FLASH 2000 CHNS/O Analyzer, Thermo Fisher Scientific Inc., Waltham, MA, USA) as well as basic property tests (Table 1). Elemental analysis showed an increase in elemental carbon (relative to the original biomass), while the hydrogen, oxygen, and sulfur levels all decreased, which indicated the release of volatile compounds. Precursors with a high levels of elemental carbon enable effective activation.

Table 1. Raw waste material properties.

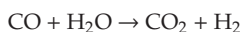
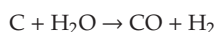
Sample	Proximate Analysis (wt.%)			Elemental Analysis (wt.%)				
	Moisture	Ash	Volatiles	C	H	N	O	S
<i>Chestnut</i>	3.5	3.5	74.6	43.6	6.6	1.4	47.8	0.2
<i>Chestnut char</i>	-	-	-	74.3	1.1	1.8	24.3	0.0

Table 1 presents the proximate (moisture, ash, volatiles) and elemental analysis (CHNSO) of the raw material (chestnut) used for the pyrolysis experiments. The moisture content was about 3.5 wt.% (the sample was dried before analysis). The volatile matter was detected to be 74.6 wt.%, whereas the ash content was 3.5 wt.%. For comparison purposes, in the same table (Table 1), the results that were obtained for the solid product of the pyrolysis (char) were also included. The thermal degradation of raw material removed the volatile compounds from the sample (CO_x, H₂O, H₂), which resulted in lower hydrogen and oxygen content.

3.2. Char Activation and Surface Analysis

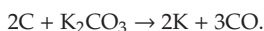
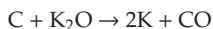
The carbonate was chemically activated using KOH and physically with carbon dioxide to improve sorption parameters. Chemical activation consisted of mixing the char with KOH in a 3:1 weight ratio, followed by heating in a tubular furnace at 800 °C for approximately 90 min.; this mixture was comminuted in a mortar. Unlike pyrolysis, the activation process took place under a stream of nitrogen. The mass ratio of the activating agent to char was chosen based on previous results from our own work. After adding 50 mL of deionized water, the sample was purified in an ultrasonic bath (30 min.) from excess KOH, washed with 5 M HCl and deionized water until pH 7, and then dried for 24 h at 105 °C.

The activation mechanism of KOH char is described, depending on the temperature, by the following primary reactions [33]:



which may also be accompanied by secondary reactions:





Physical activation of ~20 g samples were carried out in a tubular furnace at 800 °C under a stream of carbon dioxide (10 dm³/h). Two physical activation series of CO₂ carbonized char were performed; the difference between them was the washing times with the activating agent (1 h, 10 dm³ of CO₂; 2 h, and 20 dm³ of CO₂). The physical activation mechanism is described by an endothermic ($\Delta H_{298}^\circ = +172.42$ kJ/mol) Boudouard reaction:



The simultaneous assessments of sorption properties and the effectiveness of the activation process were performed using surface and pore size analysis; the Brunauer-Emmett-Teller (BET) was determined by N₂ absorption-desorption isotherms at 77 K while using a Micromeritics Gemini V200 Shimadzu analyzer (Table 2).

Table 2. Surface area (S_{BET}) and pore size (V_p) of activated carbon obtained from the chestnut.

No	Material	Chestnut	
	Activation Method	S_{BET} [m ² /g]	V_p [cm ³ /g]
I, II	Reference Samples	31.6	0.016
III	CO ₂ (1 h)	58.7	0.030
IV	CO ₂ (2 h)	143.3	0.073
V	KOH	1252.5	0.643

The biochar samples were activated using two main methods, namely chemical and physical activation (10 and 20 dm³ of CO₂ used in 1 h and 2 h of activation process). The amount of activating agent was calculated proportionally to the carbon content in the sample (taken from the elemental analysis, Table 1). In this regard, CO₂-to-carbon molar ratio was set to be 1:0.5 and 1:1. The efficiency of activation was evaluated by the BET surface analysis (Table 2). As the reference sample, inactivated biochar with a surface area of 31.6 m²/g was used. It was found that the surface area and volume of pores of biochar after physical activation performed at 1000 °C using CO₂ (sample III) increased with the amount of CO₂ used in the experiment (sample IV). Nevertheless, the highest S_{BET} was obtained for the sample that was chemically activated with KOH. The surface area achieved was 1252.5 m²/g with the pore volume of 0.64 cm³/g.

The significantly improved performance was observed when KOH was applied while analyzing the effect of developing the porous structure due to the activation. However, the physical activation process was more economical, as the amount of activator and its cost (exhaust gas) is negligible.

3.3. Thermal Calorimetry Study

Another component of this research was a PCM introduction (commercially available Rubitherm RT22) to various samples of the carbonate: II—inactivated, III—activated 1 h with CO₂, IV—activated 2 h with CO₂, and V—activated with KOH. Char sample I, as a reference, was neither activated nor containing PCM. The synthesis began with ~2 g of the char was added to the molten Rubitherm RT22 and stirred for 1 h at 80 °C. The excess Rubitherm was vacuum filtered and the samples were dried on paper at 80 °C for 12 h. This procedure was utilized for all samples, except sample I. In this way, only PCM remained permanently adsorbed by the van der Waals forces in samples II–V.

Thermal comparison tests were performed using a DSC (Differential Scanning Calorimeter Q20, TA Instruments-Waters LLC, USA) from –90 to 450 °C with a temperature accuracy of ±0.1 °C, precision of ±0.01 °C, and enthalpy precision of ±0.1%. A preliminary comparison was carried out for six

different carrier types of post-pyrolytic biomass carbonate (chestnut fruit, coconut, and walnut shells), without activation, or activated by four different methods. A 90 min. CO₂ activation was added in addition to the methods of physical activation discussed above. Three different samples of the same substance were tested each time for DSC tests. These were subjected to six complete runs (three times cooling and three times heating) in the temperature range between −10 and 40 °C. Figure 1 shows the averaged results of those comparisons for heating cycle (exo down).

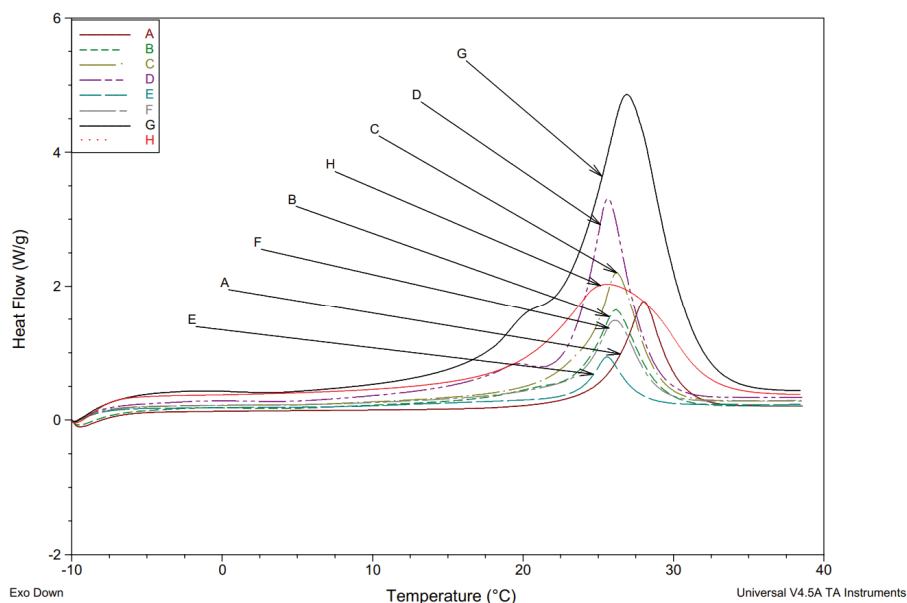


Figure 1. DSC diagram presenting results of testing char samples soaked with Rubitherm RT22 and reference samples, including; carbonate from chestnut fruit: A (sample II)—not activated, B (sample III)—activated with CO₂ (1 h), C (sample IV)—activated with CO₂ (2 h), D (sample V)—activated with KOH; char from: E)—coconut shell activated with CO₂ (1/2 h), F)—walnut shell activated with CO₂ (1/2 h); and, reference samples: G)—pure Rubitherm RT22 and H)—Micronal DS 5040 X.

The comparative analysis of thermographs that is shown in Figure 1 indicated, as expected, that pure Rubitherm RT22 showed the best heat storage properties. The commercial product Micronal DS 5040 X was next, despite a drop in heat capacity of ~60%. However, results obtained for chestnut char that were subjected to KOH activation showed similar heat capacities (~50% relative to RT22) and an almost identical temperature per peak maximum of 25 °C. Table 3 summarizes a detailed summary of DSC test results for individual samples, the biomass origin, and how it was activated.

Table 3. Comparison of DSC results for different char samples, including; carbonate from chestnut fruit: A—not activated, B—activated with CO₂ (1 h), C—activated with CO₂ (2 h), D—activated with KOH; char from: E—coconut shell activated with CO₂ (1/2 h), F—walnut shell activated with CO₂ (1/2 h), and reference samples: G—pure Rubitherm RT22 and H—Micronal DS 5040 X.

	A	B	C	D	E	F	G	H
Sample Weight [mg]	5.27	5.48	5.78	5.59	5.51	6.16	6.52	6.45
Enthalpy ΔH [kJ/kg]	49.2	67.1	84.0	125.7	42.9	66.2	256.4	150.4
Onset Temp. T^* [°C]	25.3/24.6	23.0/22.9	23.4/23.7	22.8/22.3	23.3/22.9	23.2/22.3	21.7/21.6	18.6/17.7
Peak Temp. T^{**} [°C]	28.0/23.6	26.2/21.1	26.2/21.4	25.6/21.3	25.3/22.0	26.1/21.8	26.9/17.8	25.5/15.3

(*) measured at phase change onset for heating/cooling process (**) heating/cooling process.

3.4. Thermodynamic Study

The DSC results confirmed that, from a thermodynamic point of view, it is possible to use char as a PCM carrier and also indicated the most beneficial type of biomass based on the method to activate the char. However, it was decided to conduct tests on a laboratory scale to confirm these DSC results before executing expensive and time-consuming tests on a technical scale using real building materials.

For this purpose, a measuring station (Figure 2) was built to study the heating and cooling times of coatings made using the most thermodynamically promising char that was obtained from pyrolysis of common nut fruit. This was, as shown by earlier DSC tests, the absorption of Rubitherm RT22 and depended on the activation type or lack thereof.

Five different coatings were synthesized from the same chestnut char. Coatings corresponding to samples I and II contained non-activated char. Sample I was the reference sample, did not contain PCM (Rubitherm RT 22), and sample II did. The remaining samples all contained PCM; their char were activated, as follows: sample III—with CO₂ (for 1 h), sample IV—with CO₂ (for 2 h), and sample V—with KOH. The coating numbers correspond to the sample numbers in Figures 3–5.

All of the coatings were conducted in the same manner. The same amount of char (0.2 g) with differing amounts, depending on the type of activation, of RT22 were ground in a mortar with one drop of saponin and seven drops of liquid PVA (poly(vinyl alcohol)) glue. After obtaining a homogeneous semi-liquid mass, it was applied to temperature sensors, placed in a stainless-steel cover (5 mm diameter, 30 mm long).

After the coatings dried, the samples were attached between two slats (250 mm × 30 mm × 10 mm), according to the method that is shown in Figure 2, and subjected to two tests. The first procedure consisted of heating (0.5–1.0 h) samples with a solar simulator (infrared radiator in the form of a special reflector) in a thermostatic room, then cooling them (1.0 h) after switching off the radiator (Figures 3 and 4). In the second procedure, the heating times and temperatures of samples previously cooled in the refrigerator were measured several times in a thermostatic room (Figure 5).

The infrared radiator that was used in these tests was located 0.5 m from the strip with the samples attached. The value of light intensity incident on the samples was $E_f = 18.5$ klux, and irradiation measured in the same place $E_{ir} = 385$ W/m².

The measuring system consisted of eight DS18B20 temperature sensors. Five measured the coating temperatures; the other three measured temperatures in non-disturbed areas at distances between 1.5 and 2 m from the coatings. The temperature sensor cables were connected to the AVT 5330 module as well as the data processing and counting system. The obtained results were recorded on a computer that was equipped with the station.

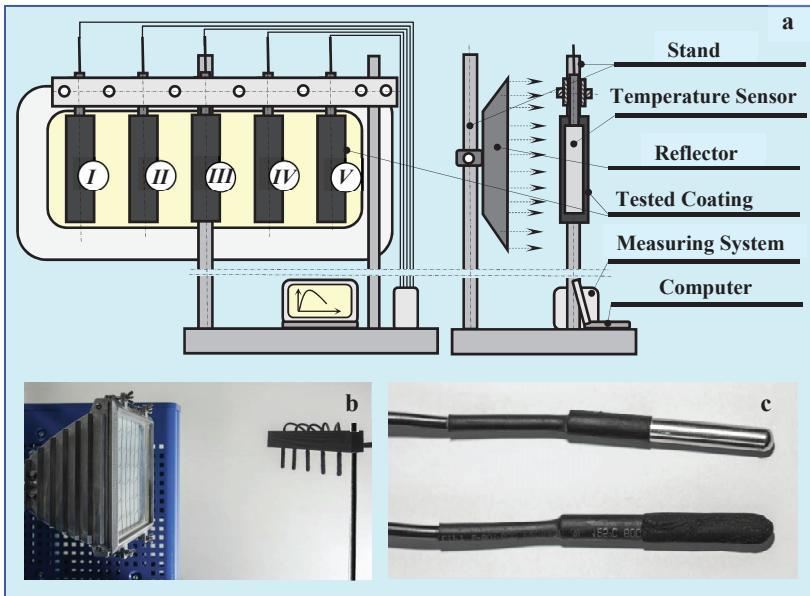


Figure 2. Measuring the heating and cooling times of the tested coatings with infrared radiation. (a) Scheme of measuring station, (b) view of the reflector and stand, (c) temperature sensors without and with coating. For cooling, after placing, exposing and heating the samples, no simulator was needed. Composition of individual char coatings: I—without RT22, II—with RT22, III—activated with CO₂ (1 h), including RT22, IV—activated with CO₂ (2 h), including RT22, V—activated with KOH, including RT22.

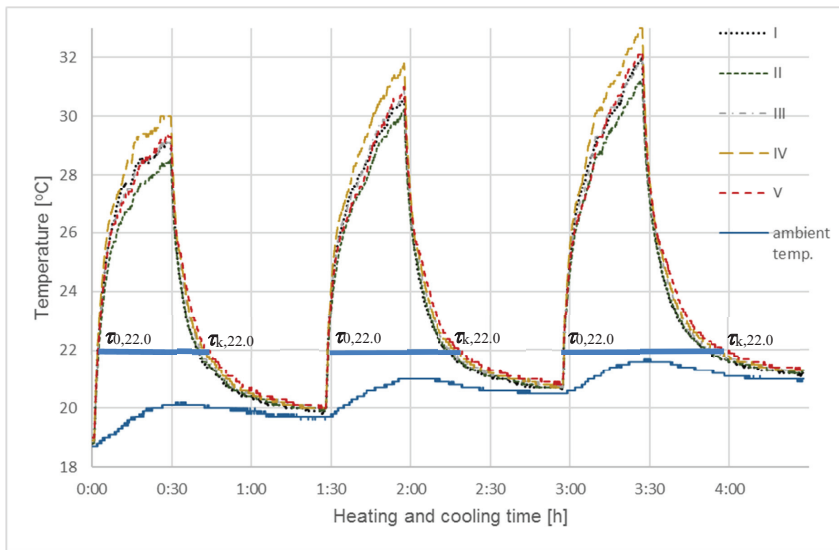


Figure 3. Testing of coatings using a solar lighting simulator - SI. The diagram shows results of the heating and cooling steps, for 0.5 h and 1 h, respectively, for five chestnut char samples: I—without activation and without RT22, II—without activation with RT22, III—activation with CO₂ (1 h) with RT22, IV—activation with CO₂ (2 h) with RT22, V—activation with KOH with RT22.

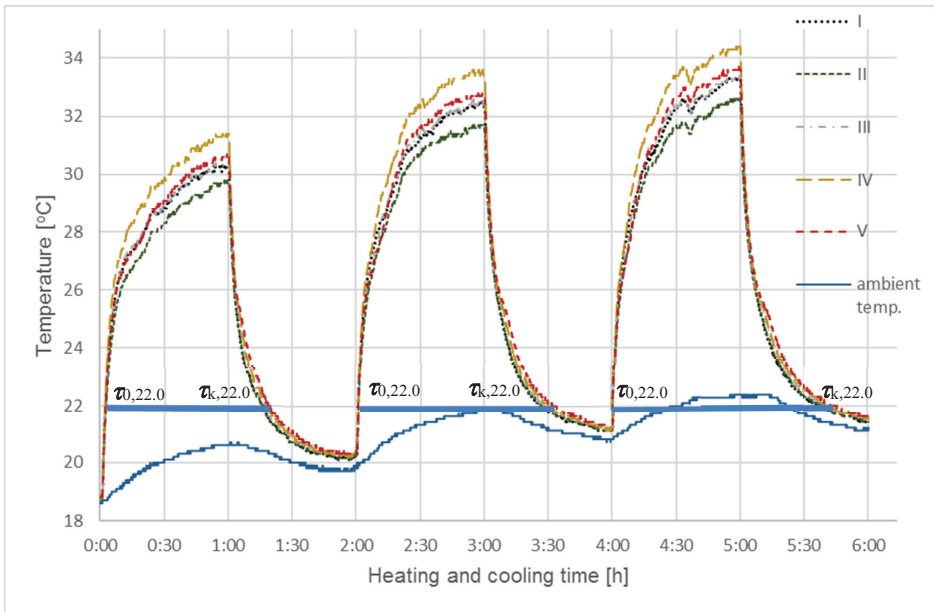


Figure 4. Testing of coatings using a solar lighting simulator - SI. The diagram shows the results of the heating and cooling process for each of five chestnut char samples for 1 h: I—without activation and without RT22, II—without activation with RT22, III—activation with CO₂ (1 h) with RT22, IV—activation with CO₂ (2 h) z RT22, V—activation with KOH with RT22.

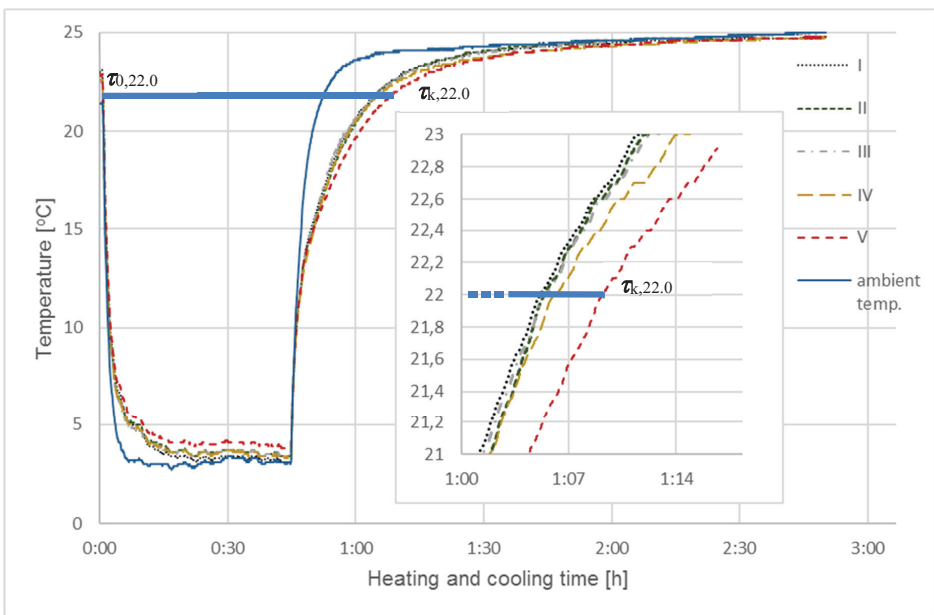


Figure 5. Results of natural heating for five chestnut char samples—SI: I—without activation and without RT22, II—without activation with RT22, III—activation with CO₂ (1 h) with RT22, IV—activation with CO₂ (2 h) with RT22, V—activation with KOH with RT22.

Measurement uncertainties that were related to sensor accuracy were specified by the manufacturer as 0.25 °C. The standard deviation calculated for the sensors was 0.6 °C; the total measurement uncertainty was estimated as 0.85 °C.

The temperature of each sample was determined as a function of time, both during heating and cooling, based on these results. Figure 2 shows the overall diagram of the test stand.

4. Results of Thermodynamic Properties of the Obtained Material

In the first series of simulation tests (SI), all of the samples were exposed to infrared radiation for a period of 0.5 h. This made it possible to heat the sample coatings to a temperature approximating hot summer days (ambient temperature > 30 °C). After heating, the samples were allowed to cool to ambient temperature; the cooling times increased slightly during subsequent cycles (from ~19.7 °C (I cycle), 20.8 °C (II cycle) to 21.0 °C (III cycle)). The ambient temperature was taken as the average temperature from three sensors that were positioned at 1.5–2.0 m from the measuring station. The final temperature of the heated samples also increased during subsequent cycles and ranged from 28.5–30.0 °C in cycle I, 30.5–32 °C in cycle II, and 31.0–33.0 °C in cycle III. The heating and cooling tests in this and subsequent series were conducted in triplicate; Figure 3 presents the aggregate results that were obtained in the initial heating/cooling tests. The thick horizontal sections in the figure represent the three cycle times ($\Delta\tau = \tau_{k,22.0} - \tau_{0,22.0}$), measured for each of the samples upon exceeding 22.0 °C, ($\tau_{0,22}$), during heating until 22.0 °C was reached during cooling $\tau_{k,22}$. Table 4 summarizes the cycle lengths obtained for this series (SI) and the next three (SII).

It was decided to compare the cycle times that were measured from τ_0 , i.e., the moment when the sample exceeded the set initial temperature T_0 to the final time τ_k —i.e., the moment of the last reading of the set final temperature T_k . The temperatures were selected, so that the results of all measurement series could be compared, and their values were as close as possible to the phase transition temperature, which for Rubitherm RT22 is 22 °C.

In this study, instead of measuring the temperature increase ΔT in given time frames (τ_0 , τ_k), the time intervals between the transition of sample temperatures from T_0 to T_k were measured, due to greater accuracy of time measurement than the accuracy of temperature increase measurement, especially in fast-changing processes.

This procedure was repeated for a second series of tests (SII) with an increase in the sample heating time to 1 h (Figure 4). This resulted in a slight final temperature increase that was nearly identical to the results that were obtained for heating for 30 min. The final ambient temperatures at the end of each cycle in both procedures were practically the same; however, fluctuations in ambient temperatures during individual cycles in the second series were greater. This slightly influenced the maximum coating temperature level, but proved that a longer exposure time in this case is not intentional and the assumed cooling time of one hour was sufficient for describing the cooling phenomenon; after that one hour, all of the samples reached the same temperature and they also cooled at the same rate.

Table 4. Summary of individual heating and cooling cycle durations for coatings made from the tested char with different Rubiterm RT22 content.

Samples	I	II	III	IV	V
SI—First Heating-Cooling Cycle					
$\tau_{k,22,0}$	00:39:44	00:39:44	00:39:44	00:39:44	00:39:44
$\tau_{0,22,0}$	00:02:10	00:02:32	00:02:14	00:02:04	00:02:16
$\Delta\tau = \tau_{k,22,0} - \tau_{0,22,0}$	00:37:34	00:37:12	00:37:30	00:37:40	00:37:28
Percentage	100	99.7	103.1	106.6	108.6
SI—Second Heating-Cooling Cycle					
$\tau_{k,22,0}$	02:14:10	02:14:16	02:15:14	02:16:54	02:18:26
$\tau_{0,22,0}$	01:29:10	01:29:20	01:29:12	01:29:06	01:29:10
$\Delta\tau = \tau_{k,22,0} - \tau_{0,22,0}$	00:45:00	00:44:56	00:46:02	00:47:48	00:49:16
Percentage	100	99.8	102.3	106.2	109.5
SI—Third Heating-Cooling Cycle					
$\tau_{k,22,0}$	03:51:11	03:51:11	03:53:05	03:55:31	03:57:57
$\tau_{0,22,0}$	02:58:21	02:58:25	02:58:21	02:58:19	02:58:21
$\Delta\tau = \tau_{k,22,0} - \tau_{0,22,0}$	00:52:50	00:52:46	00:54:44	00:57:12	00:59:36
Percentage	100	99.9	103.6	108.3	112.8
SII—First Heating-Cooling Cycle					
$\tau_{k,22,0}$	01:15:38	01:15:26	01:16:18	01:17:30	01:18:32
$\tau_{0,22,0}$	00:02:28	00:02:46	00:02:30	00:02:18	00:02:32
$\Delta\tau = \tau_{k,22,0} - \tau_{0,22,0}$	01:13:10	01:12:40	01:13:48	01:15:12	01:16:00
Percentage	100	99.3	100.9	102.9	103.9
SII—Second Heating-Cooling Cycle					
$\tau_{k,22,0}$	03:26:29	03:26:41	03:28:05	03:30:07	03:31:57
$\tau_{0,22,0}$	02:01:21	02:01:29	02:01:21	02:01:17	02:01:21
$\Delta\tau = \tau_{k,22,0} - \tau_{0,22,0}$	01:25:08	01:25:12	01:26:44	01:28:50	01:30:36
Percentage	100	100.1	101.9	104.3	106.4
SII—Third Heating-Cooling Cycle					
$\tau_{k,22,0}$	05:36:53	05:38:07	05:40:05	05:40:59	05:43:23
$\tau_{0,22,0}$	04:01:01	04:01:05	04:01:01	04:01:01	04:01:01
$\Delta\tau = \tau_{k,22,0} - \tau_{0,22,0}$	01:35:52	01:37:02	01:39:04	01:39:58	01:42:22
Percentage	100	101.2	103.3	104.8	106.8
SIII—Heating-Cooling Cycle					
$\tau_{k,22,0}$	01:05:02	01:05:18	01:05:14	01:05:54	01:09:10
$\tau_{0,22,0}$	00:00:42	00:00:42	00:00:42	00:00:42	00:00:42
$\Delta\tau = \tau_{k,22,0} - \tau_{0,22,0}$	01:04:20	01:04:36	01:04:32	01:05:12	01:08:28
Percentage	100	100.4	100.3	101.3	106.4
Average	100	100.2	102.4	105.2	107.5

Both of the studies on the heating and cooling process of char containing RT22 confirmed that there was a clear difference between temperature changes as a function of time obtained for the individual samples. Differences in the cooling rates were more pronounced than the heating rates. Radiative heat exchange during heating was more intense than during convection cooling, which steepens the

heating curves of individual samples and differences in the heat exchange time between individual samples become less visible. The coatings were thin, as were the amounts and mass of char, and Rubitherm RT22 contained in them in relation to the weight of the temperature sensors. However, the effect of the absorbed RT22 on the heat capacity of the modified char turned out to be sufficiently clear, especially on the cooling curves. It was concluded that, for larger amounts of PCM modified carbonate, in relation to the mass of the sensor, this effect will be even greater due to the change of heat accumulation from the surface to the interior.

The comparative analyses shown in Figures 3 and 4 indicated that extended sample heating time did not impact the cooling curve shape, which were almost identical for every cycle in the first two testing series. However, longer heating times did cause greater dissection and flattening of the heating curves for individual samples, especially after exceeding the phase transition temperature of Rubitherm RT22 (22 °C, according to manufacturer specifications and the results in Table 3). However, after heating the thin char coating, additional heating was carried using a temperature sensor with a much higher mass and heat capacity than the tested coatings.

Differences in individual sample final temperatures, which are visible in all test cycles carried out in both series, come from the termination of the sample heating process after exceeding the phase transition temperature of Rubitherm RT22, but before they reach thermodynamic equilibrium.

A most interesting aspect of this research corresponds to temperatures near the phase transition temperature, at which the storage and release of thermal energy occurs. This was observed and measured for both series, though the impact of Rubitherm RT22 was only sufficiently clear for sample cooling. The excessively high sample heating rate masked the effects of differences that are caused by phase change in Rubitherm. As such, a third series of tests (SIII) was devised, during which the heating rate was reduced and the final temperature was lowered to better correspond to the RT22 phase transition temperature.

The SIII series was carried out using only one cooling and heating cycle, as the results that were obtained in the previous SI and SII series showed that repeating the cycles resulted in no changes. For this series, samples were initially cooled to 3 °C for 30 min., placed in a room maintained at 25 °C, and were then heated automatically and at a much slower rate than radiant heating. Those results, together with the enlarged fragment, enabled a more accurate analysis of the heating curves and a more qualitative assessment of the differences that were obtained for individual samples; those are presented in Figure 5.

As expected, the heating curve that was obtained in this experiment was more inclined, which made it easier to analyze differences in the sample process times.

The results that were obtained for SI and SII for all three test cycles, determining the total time of full cycles measured from the initial temperature $T_0 = 22$ °C, by heating-cooling, until the individual samples reach the final temperature $T_k = 22$ °C, are summarized in Table 4. Table 4 also shows the results obtained in SIII over the same temperature range, though that cycle involved cooling the samples prior to heating them. A graphical illustration of the results that are listed in Table 4 are thick horizontal sections in Figures 3–5, determining the cumulative times for full heating and cooling cycles or cooling/heating for all samples.

5. Analysis and Discussion

Analyzing curves in Figures 3–5, and combined with results collected in Table 4, selected at one temperature (22 °C), clearly indicated the impact of different Rubitherm RT22 amounts in the char on the cycle time length $\Delta\tau = \tau_{k,22.0} - \tau_{0,22.0}$ of heat exchange processes taking place in individual samples. Differences in the process times are visible, even though the amount of Rubitherm RT22 adsorbed was small relative to the much higher mass and thermal capacity of the temperature sensors.

When compared to the reference sample (I) with no Rubitherm RT22, the total cooling and heating times ($\Delta\tau = \tau_{0,22.0} - \tau_{k,22.0}$) of all samples with differing levels of Rubitherm RT22 were longer. For

sample V (activated with KOH), this time was extended by 7.5%, 5.2% for sample IV, 2.4% for III, and only 0.2% for sample II (non-activated char).

It was decided to reanalyze the obtained results to better understand the effect of char with different contents of Rubitherm RT22 on the mechanism of heat exchange occurring in the samples. It was conducted by eliminating fast-changing heat exchange processes and only focusing on the cooling times of the samples in the SI and SII series (Table 5), and their heating times in SIII (Table 6).

Table 5. Summary of cooling times of coatings from temperature $T_0 = 28.5\text{ }^\circ\text{C}$ to temperature $T_k = 21.5\text{ }^\circ\text{C}$ for series SI and SII.

Samples	I	II	III	IV	V
SI—First Cooling Cycle					
$\tau_{0,28.5}$	00:29:58	00:29:44	00:30:02	00:30:22	00:30:06
$\tau_{k,21.5}$	00:42:36	00:43:20	00:44:58	00:46:20	00:47:44
$\Delta\tau = \tau_{k,21.5} - \tau_{0,28.5}$	00:12:38	00:13:36	00:14:56	00:15:58	00:17:38
Percentage	100	107.6	118.2	126.4	139.6
SI—Second Cooling Cycle					
$\tau_{0,28.5}$	01:58:48	01:58:40	01:58:58	01:59:22	01:59:06
$\tau_{k,21.5}$	02:19:38	02:20:08	02:21:40	02:22:54	02:26:04
$\Delta\tau = \tau_{k,21.5} - \tau_{0,28.5}$	00:20:50	00:21:28	00:22:42	00:23:32	00:26:58
Percentage	100	103.0	100.0	113.0	129.4
SI—Third Cooling Cycle					
$\tau_{0,28.5}$	03:29:27	03:29:13	03:29:35	03:29:59	03:29:47
$\tau_{k,21.5}$	04:03:27	04:04:33	04:09:15	04:09:09	04:13:37
$\Delta\tau = \tau_{k,21.5} - \tau_{0,28.5}$	00:34:00	00:35:20	00:39:40	00:39:10	00:43:50
Percentage	100	103.9	116.7	115.2	128.9
SII—First Cooling Cycle					
$\tau_{0,28.5}$	01:01:18	01:01:08	01:01:26	01:01:48	01:01:32
$\tau_{k,21.5}$	01:19:00	01:18:56	01:20:04	01:22:12	01:23:36
$\Delta\tau = \tau_{k,21.5} - \tau_{0,28.5}$	00:17:42	00:17:48	00:18:38	00:20:24	00:22:04
Percentage	100	100.6	105.3	115.2	124.7
SII—Second Cooling Cycle					
$\tau_{0,28.5}$	03:02:47	03:02:31	03:02:55	03:03:21	03:03:15
$\tau_{k,21.5}$	03:36:47	03:37:55	03:40:51	03:41:23	03:45:19
$\Delta\tau = \tau_{k,21.5} - \tau_{0,28.5}$	00:34:00	00:35:24	00:37:56	00:38:02	00:42:04
Percentage	100	104.1	111.6	111.9	123.7
SII—Third Cooling Cycle					
$\tau_{0,28.5}$	05:03:35	05:03:19	05:03:41	05:04:09	05:04:07
$\tau_{k,21.5}$	05:54:12	05:55:04	05:59:16	05:58:16	06:00:58
$\Delta\tau = \tau_{k,21.5} - \tau_{0,28.5}$	00:50:37	00:51:45	00:55:35	00:54:07	00:56:51
Percentage	100	102.2	109.8	106.9	112.3
Average	100	103.6	111.7	114.8	126.4

Table 6. Summary of coating heating times during the third round of measurements from $T_0 = 5.0\text{ }^\circ\text{C}$ to $T_k = 23.5\text{ }^\circ\text{C}$ and their cooling from $T_0 = 23.5\text{ }^\circ\text{C}$ to $T_k = 5.0\text{ }^\circ\text{C}$ for SIII.

Samples	I	II	III	IV	V
SIII—heating round					
$\tau_{0,5.0}$	00:45:12	00:45:10	00:45:12	00:45:12	00:45:10
$\tau_{k,23.5}$	01:18:12	01:18:00	01:19:34	01:23:28	01:25:28
$\Delta\tau = \tau_{k,23.5} - \tau_{0,5.0}$	00:33:00	00:32:50	00:34:22	00:38:16	00:40:18
Percentage	100	99.5	104.1	116.0	122.1

The results obtained in SI and SII included in Table 5 were selected because they featured the widest temperature range of all cycles (between 21.5–28.5 °C). The results obtained in SIII, because they cover a different temperature range (5.0–23.5 °C) and in a different heating/cooling order, are separately presented in Table 6.

The results in Tables 4–6 indicated that Rubitherm RT22 contained in char affected heat exchange during the heating and cooling of the samples. However, during cooling, as the RT22 content in char increased, the sample cooling time also increased relative to the reference sample (I), which did not contain Rubitherm. This is clearly seen in the last row of Table 5, which clearly shows the average cooling time extensions for all SI and SII cycles, which are: 26.4% for sample V, 14.8% for sample IV, 11.7% for sample III, and 3.6% for sample II, relative to sample I. The cooling time differences of individual samples are greater than differences in full cycle times (Table 4). This is due to the much larger heat capacity of the temperature sensor relative to the mass of the RT22 char tested. The extension of the total heating and cooling times caused by this resulted in a reduction of the differences in the individual samples. The results collected in Table 5 were analyzed at shorter cooling times, limited by a lower temperature range (28.5–21.5 °C). This elimination of the effect on the heating time results allowed for an observation of larger differences in cooling times between individual samples.

Fearing that the rapid heating rate of the samples in SI and SII might affect result interpretations, which may be ambiguous, accidental, and contradictory, a modified SIII experiment was planned and carried out.

The order of heating and cooling processes was changed with the rate and final heating temperature lowered. Consequently, it was possible to obtain less steep heating curves (Figure 5), from which it was easier to observe heating time differences of individual samples.

At high rates of temperature change, e.g. steep heating curves in Figures 3 and 4, as well as cooling curves in Figure 5, fast temperature changes take place in a short period. As time was measured in these studies, the shorter it was, the less accurate the results were. On less steep cooling (Figures 3 and 4) or heating (Figure 5) curves, differences in the time to reach the same temperature could already be measured with much greater accuracy that allowed for the differences between individual samples to be determined.

The results obtained in SIII, as summarized in Table 6 for heating time, show a similar, but inverse, trend to those in Table 5; the effect of Rubitherm RT22 on changes in heat transfer times for individual samples. This time, cooling curves obtained in SIII—opposite to those in SI and SII—were too steep to determine the effect of Rubitherm RT22 levels; therefore, they were excluded from consideration. Table 6, instead, focuses on results that are related to heating times.

The interpretation of the heating process time results was unambiguous and consistent with the results obtained in SI and SII, which are presented in the bottom row of Table 5. As the levels of Rubitherm RT22 in the char increased, so did the sample heating times: by 22.1% (V), 16.0% (IV), and 4.1% (III). Only for sample II was there a slight, within the margin of error (0.5%) heating time decrease relative to the reference sample (I).

These results obtained for SI and SII and collected in Table 5, as well as the results obtained in SIII for the heating process (Table 6), are unambiguous and clearly indicate that Rubitherm RT22 contained

in the carbonate directly impacts the thermal processes occurring in it. During phase transitions (melting-solidification), thermal energy is stored and then released; this work clearly documents the extension of heat transfer times.

6. Conclusions

A novelty in this work is the research and testing of a new carrier for phase-change material. Thus far, no one has tried to utilize pyrolytic biochar with a well-developed internal surface for permanent PCM adsorption (due to the van der Waals forces).

The proposed and conducted research procedure of cooling during SI and SII series and heating in SIII, designed for small masses of tested char RT22 carrier (about 0.2 g) and small thicknesses of coatings (0.1–0.15 mm), proved to be so accurate that it provided unambiguous results that were consistent with data obtained at the remaining stages of the study. These measurements, as well as the measurements of the degree of activation for various methods of activated carbon obtaining, and the adsorption studies showed that the amount of Rubiterm RT22 is the highest in the activated KOH carbonate (sample V), smaller in activated 2 h CO₂ (sample IV), even smaller in activated 1 h CO₂ (sample III), and the smallest in non-activated carbonate (sample II).

The results showed that the use of char as a PCM carrier meets expectations regarding accumulation and slower heat release to the environment. Heating and cooling tests both showed similar dynamics of increases/decreases during heat exchange and represent a function of its accumulation and release during phase transitions.

Thermal analysis tests using DSC confirmed the potential of using carbonate as a potential PCM carrier. Further simulation studies, consisting of measuring heating/cooling times of coatings made of RT22 modified char, further confirmed that properly activated char that was obtained from waste biomass had similar thermodynamic parameters to commercial materials of this type upon the absorption of PCM, but were much less expensive than commercial products.

In addition, it has been shown that PCM impregnated carbonate materials have significant pro-ecological values because:

- it is a recycled product of waste biomass subjected to torification or pyrolysis;
- char as a PCM carrier is an inexpensive, chemically, and environmentally neutral product; and,
- the PCM used in these studies is a hydrocarbon derived from the distillation of crude oil, a type of paraffin that is chemically unreactive and, therefore, environmentally neutral.

Thanks to its well-developed surface and high absorption capacity, the activated char permanently adsorbs such an amount of PCM that obtaining up to 50% greater heat capacity in relation to RT22 is possible and, due to van der Waals forces, the PCM will not be desorbed, even in liquid state.

The use of the char modified in the above manner, in the form of plaster addition, paints, screeds, asphalt mixtures, etc., in addition to stabilizing the temperature, storing temporary excess energy, and releasing it in a timely fashion, also prevents local overheating, both on the surface and within an object. Overheating can lead to softening, flowing, thermal deformation and degradation by oxidation, drying, or cracking; all of which can lead to material damage as well as objects that are made of them.

Research conducted in this work proves that the development of such a building material, which, when compared to commercial products, will be much cheaper, equally effective, and possible to use in the production of gypsum boards, plasters, screeds, etc., just as Micronal, is only a matter of time. However, detailed research on the implementation of this new material will be the subject of a separate paper.

The continuation of this research topic is justified because the research showed that biochar can be a PCM carrier, and even a coating created from it clearly affects the time of heat transfer. Heat transfer studies should be conducted—no longer on the surficial scale (2D), however, but on the capacitively-volumetric (3D) scale. Larger amounts of PCM modified biochar will be required to carry

out this research and, thus, the scale of research conducted in this work (pyrolysis, activation, sorption) should be increased from a laboratory scale to a technical or semi-technical one.

Author Contributions: Conceptualization, M.R. and W.M.L.; Data curation, P.K. and J.Ł.; Formal analysis, M.R. and E.K.-R.; Investigation, M.R., K.J. and W.M.L.; Methodology, M.R., K.J. and W.M.L.; Project administration, M.R.; Resources, K.J. and P.K.; Supervision, W.M.L.; Validation, M.R., K.J., J.Ł., E.K.-R. and W.M.L.; Writing—original draft, M.R., K.J. and W.M.L.; Writing—review & editing, J.Ł. and E.K.-R. All authors have read and agreed to the published version of the manuscript.

Funding: This work was supported by the Ministry of Science and Higher Education, Poland, SUBVENTION 2019—MINI GRANT. The APC was funded by Gdansk University of Technology, Poland.

Acknowledgments: This work was supported by the Ministry of Science and Higher Education, Poland, SUBVENTION 2019—MINI GRANT.

Conflicts of Interest: The authors declare no conflict of interest.

References

1. EPC. Directive 2010/31/EU of the European Parliament and of the Council of 19 May 2010 on the energy performance of buildings. *Off. J. Eur. Union* **2010**, *153*, 13–35. [CrossRef]
2. Bastani, A.; Haghighat, F. Expanding heisler chart to characterize heat transfer phenomena in a building envelope integrated with phase change materials. *Energy Build.* **2015**, *106*, 164–174. [CrossRef]
3. Ahangari, M.; Maerefat, M. An innovative PCM system for thermal comfort improvement and energy demand reduction in building under different climate conditions. *Sustain. Cities Soc.* **2019**, *44*, 120–129. [CrossRef]
4. Aditya, L.; Mahlia, T.M.I.; Rismanchi, B.; Ng, H.M.; Hasan, M.H.; Metselaar, H.S.C.; Muraza, O.; Aditiya, H.B. A review on insulation materials for energy conservation in buildings. *Renew. Sustain. Energy Rev.* **2017**, *73*, 1352–1365. [CrossRef]
5. Shen, H.; Tan, H.; Tzempelikos, A. The effect of reflective coatings on building surface temperatures, indoor environment and energy consumption—an experimental study. *Energy Build.* **2011**, *43*, 573–580. [CrossRef]
6. Kuta, M.; Matuszewska, D.; Wójcik, T.M. The role of phase change materials for the sustainable energy. *E3S Web Conf.* **2016**, *10*, 6. [CrossRef]
7. Amoruso, G.; Donevska, N.; Skomedal, G. German and norwegian policy approach to residential buildings' energy efficiency—a comparative assessment. *Energy Effic.* **2018**, *11*, 1375–1395. [CrossRef]
8. Stritih, U.; Tyagi, V.V.; Stropnik, R.; Paksoy, H.; Haghighat, F.; Joybari, M.M. Integration of passive PCM technologies for net-zero energy buildings. *Sustain. Cities Soc.* **2018**, *41*, 286–295. [CrossRef]
9. Lachheb, M.; Younsi, Z.; Naji, H.; Karkri, M.; Nasrallah, S.B. Thermal behavior of a hybrid PCM/plaster: A numerical and experimental investigation. *Appl. Therm. Eng.* **2017**, *111*, 49–59. [CrossRef]
10. Sharifi, N.P.; Shaikh, A.A.N.; Sakulich, A.R. Application of phase change materials in gypsum boards to meet building energy conservation goals. *Energy Build.* **2017**, *138*, 455–467. [CrossRef]
11. Shukla, N.; Fallahi, A.; Kosny, J. Performance characterization of PCM impregnated gypsum board for building applications. *Energy Procedia* **2012**, *30*, 370–379. [CrossRef]
12. Jaworski, M. Thermal performance of building element containing phase change material (PCM) integrated with ventilation system—experimental study. *Appl. Therm. Eng.* **2014**, *70*, 665–674. [CrossRef]
13. Jaworski, M.; Abeid, S. Thermal conductivity of gypsum with incorporated phase change material (PCM) for building applications. *J. Power Technol.* **2011**, *91*, 49–53.
14. Ryms, M.; Klugmann-Radziemska, E. Possibilities and benefits of a new method of modifying conventional building materials with phase-change materials (PCMs). *Constr. Build. Mater.* **2019**, *211*, 1013–1024. [CrossRef]
15. Tyagi, V.V.; Buddhi, D. PCM thermal storage in buildings: A state of art. *Renew. Sustain. Energy Rev.* **2007**, *11*, 1146–1166. [CrossRef]
16. Nkwetta, D.N.; Haghighat, F. Thermal energy storage with phase change material—a state-of-the art review. *Sustain. Cities Soc.* **2013**, *10*, 87–100. [CrossRef]
17. Mankel, C.; Caggiano, A.; König, A.; Schicchi, D.S.; Sam, M.N.; Koenders, E. Modelling the thermal energy storage of cementitious mortars made with PCM-recycled brick aggregates. *Materials* **2020**, *13*, 1064. [CrossRef]

18. Xu, L.; Yang, R. Stearic acid/inorganic porous matrix phase change composite for hot water systems. *Molecules* **2019**, *24*, 1482. [CrossRef]
19. Cabeza, L.F.; Castellon, C.; Nogues, M.; Medrano, M.; Leppers, R.; Zubillaga, O. Use of microencapsulated PCM in concrete walls for energy savings. *Energy Build.* **2007**, *39*, 113–119. [CrossRef]
20. Kheradmand, M.; Azenha, M.; de Aguiar, J.L.; Krakowiak, K.J. Thermal behavior of cement based plastering mortar containing hybrid microencapsulated phase change materials. *Energy Build.* **2014**, *84*, 526–536. [CrossRef]
21. Thiele, A.M.; Sant, G.; Pilon, L. Diurnal thermal analysis of microencapsulated PCM-concrete composite walls. *Energy Convers. Manag.* **2015**, *93*, 215–227. [CrossRef]
22. Li, C.; Yu, H.; Song, Y. Experimental investigation of thermal performance of microencapsulated PCM-contained wallboard by two measurement modes. *Energy Build.* **2019**, *184*, 34–43. [CrossRef]
23. Jamekhorshid, A.; Sadrameli, S.M.; Barzin, R.; Farid, M.M. Composite of wood-plastic and micro-encapsulated phase change material (MEPCM) used for thermal energy storage. *Appl. Therm. Eng.* **2016**, *112*, 82–88. [CrossRef]
24. Bahrar, M.; Djamai, Z.I.; Mankibi, M.E.; Larbi, A.S.; Salvia, M. Numerical and experimental study on the use of microencapsulated phase change materials (PCMs) in textile reinforced concrete panels for energy storage. *Sustain. Cities Soc.* **2018**, *41*, 455–468. [CrossRef]
25. Nejman, A.; Gromadzińska, E.; Kamińska, I.; Cieślak, M. Assessment of thermal performance of textile materials modified with PCM microcapsules using combination of DSC and infrared thermography methods. *Molecules* **2020**, *25*, 122. [CrossRef]
26. Hu, Q.; Chen, Y.; Hong, J.; Jin, S.; Zou, G.; Chen, L.; Chen, D.Z. A smart epoxy composite based on phase change microcapsules: Preparation, microstructure, thermal and dynamic mechanical performances. *Molecules* **2019**, *24*, 916. [CrossRef]
27. Agrawal, R.; Hanna, J.; Gunduz, I.E.; Luhrs, C.C. Epoxy-PCM composites with nanocarbons or multidimensional boron nitride as heat flow enhancers. *Molecules* **2019**, *24*, 1883. [CrossRef]
28. Ryms, M.; Lewandowski, W.M.; Klugmann-Radziemska, E.; Denda, H.; Wcisło, P. The use of lightweight aggregate saturated with PCM as a temperature stabilizing material for road surfaces. *Appl. Therm. Eng.* **2015**, *81*, 313–324. [CrossRef]
29. Ryms, M.; Denda, H.; Jaskuła, P. Thermal stabilization and permanent deformation resistance of LWA/PCM-modified asphalt road surfaces. *Constr. Build. Mater.* **2017**, *142*, 328–341. [CrossRef]
30. Politechnika, G.; Lewandowski, W.M.; Ryms, M.; Wcisło, P.; Denda, H.; Klugmann-Radziemska, E. Stabilizing Temperature of Asphalt Road Surface, Comprises Introducing Mixture of Asphalt Mineral, Substructure and/or Substrates, and a Phase Change Material Comprising Mixture of Hydrocarbons, Preferably Ceresin on to the Road. Poland Patent PL409634, 29 September 2014.
31. Lewandowski, W.M.; Januszewicz, K.; Kosakowski, W. Efficiency and proportions of waste tyre pyrolysis products depending on the reactor type—A review. *J. Anal. Appl. Pyrolysis* **2019**, *140*, 25–53. [CrossRef]
32. Ryms, M.; Januszewicz, K.; Lewandowski, W.M.; Klugmann-Radziemska, E. Pyrolysis proces of whole tires as a biomass energy recycling. *Ecol. Chem. Eng. S* **2013**, *20*, 93–107. [CrossRef]
33. Otowa, T.; Nojima, Y.; Miyazaki, T. Development of KOH activated high surface area carbon and its application to drinking water purification. *Carbon* **1997**, *35*, 1315–1319. [CrossRef]



© 2020 by the authors. Licensee MDPI, Basel, Switzerland. This article is an open access article distributed under the terms and conditions of the Creative Commons Attribution (CC BY) license (<http://creativecommons.org/licenses/by/4.0/>).

Article

The Influence of Calcareous Fly Ash on the Effectiveness of Plasticizers and Superplasticizers

Jacek Gołaszewski, Tomasz Ponikiewski *, Aleksandra Kostrzanowska-Siedlarz and Patrycja Miera

Department of Building Processes and Building Physics, Faculty of Civil Engineering, Silesian University of Technology, 44-240 Gliwice, Poland; Jacek.Golaszewski@polsl.pl (J.G.); Aleksandra.Kostrzanowska-Siedlarz@polsl.pl (A.K.-S.); Patrycja.Miera@polsl.pl (P.M.)

* Correspondence: Tomasz.Ponikiewski@polsl.pl

Received: 9 April 2020; Accepted: 11 May 2020; Published: 13 May 2020

Abstract: Due to the rational shaping of the environment and the management of environmental resources in accordance with the principle of sustainable development, calcareous fly ash (CFA)—high-calcium as a by-product of lignite combustion—is a valuable addition to concrete. This additive, however, due to its high-water demand lowers the workability of the concrete mix, which is a problem, especially in the first 90 min after mixing the components of the mix. In order to meet this challenge, plasticizers (P) and superplasticizers (SP) for concrete are used with various effects which are designed to reduce the yield value and plastic viscosity. To check the technical efficiency of admixtures P and SP with different chemical bases, the main objective of this research was to investigate the influence of raw and ground CFA on the rheological properties and other side effects of admixtures, such as the amount of air in the mixture and the amount of heat of hydration. The use of P, particularly SP, effectively improves the workability of the mortar containing CFA, especially ground CFA. With these admixtures, it is possible to obtain mortars containing ground CFA with similar rheological properties to mortars without its addition. To obtain a specific workability of mortar with CFA, it is usually necessary to introduce a higher dose of P or SP than used for mortars without CFA. The presence of raw CFA does not alter the effectiveness of P and strongly reduces the effectiveness of SP. The reduced effectiveness of SP manifests primarily as a high workability lost. The presence of ground CFA does not change the effectiveness of P (or is higher). The effectiveness of the superplasticizer SNF (with a chemical base of naphthalene sulfonate) and PE (with a chemical base of polycarboxylate ether) is slightly lower or does not change. The effectiveness of the superplasticizer SMF (with a chemical base of melamine sulfonates) is significantly lower. We found that the presence of ash affects the efficiency of P and SP, while processing via the grinding of ash makes the effect negligible. These results are novel in both their cognitive and practical aspects.

Keywords: calcareous fly ash; plasticizer; superplasticizer; rheological properties; fly ash processing methods; cement mortars, workability

1. Introduction

Waste management for the coal fired power plants is gaining key importance in connection with threats to the environment and health. Such power plants in Poland alone produce millions of tons of fly ash per year, whose properties depend on the type of coal (lignite or hard coal) and the method of combustion. The reuse of this fly ash in the composition of concrete relates to sustainable development by reducing the amount of cement and thereby reducing cement production, which is associated with a reduction in the amount of CO₂ released into the atmosphere. In addition to this ecological aspect, there is also an economic one, as fly ash can provide measurable benefits to investors by replacing cement and clinker with waste materials. Fly ash from the combustion of hard coal is characterized by

its pozzolanic properties, and due to its beneficial effect on the properties of concrete, it is a valued and widely used addition to concrete. When lignite is burned, calcareous fly-ash (CFA) is produced—i.e., fly ash that contains large amounts of calcium compounds. However, due to its composition and physical properties, not every CFA is suitable for concrete [1]. The studies carried out to date [2] show that, among the CFA available in Poland, only the CFA from the Bełchatów power plant has properties that allow it to be used as an additive to cement and concrete. This CFA has high pozzolanic and hydraulic activity and meets the requirements of the EN 197-1 standard [3] for the main constituents of common cement. After the grinding process, it can also be used as an active mineral additive to concrete [1,3–5]. As established in several studies [6–12], the use of this CFA in up to 30% of cement as an additive to concrete or as the main component of cement, in general, does not negatively influence the strength and durability of the concrete. Notably, it is necessary to use CFA processed by grinding, not in a raw state. Moreover, the authors in [13] investigated the effects of nanoclay additions on the fresh properties, mechanical performance, and microstructure properties of high volume fly ash mixes designed for 3D printing. The results in [13] showed that the addition of high volume fly ash improved the thixotropic properties of the mixtures, thus increasing its suitability for concrete printing applications.

Unfortunately, the use of CFA as a concrete additive is significantly hindered by problems related to fresh concrete's workability. In a raw state, CFA is characterized by very high water demands, much higher than those of cement [5,14]. These demands can be reduced by processing, preferably by grinding [2,14]. Even then, the water demands remain higher than those of cement [2,6]. The high water demands of CFA make it difficult to obtain fresh concrete with the required stable workability in the long term, whether it is used as an additive to cement or as an additive to concrete [6,12–18]. The processing of CFA solves this problem to some extent, but it should be noted that the use of ground CFA undoubtedly has a beneficial effect on the rheological properties of mortars and their variability [12,14,16–18].

Therefore, to obtain the required workability of CFA containing concrete, it is necessary to use plasticizers (P) or superplasticizers (SP). Indeed, the possibility of using CFA is conditional on the use of these admixtures [12,14,18]. Therefore, the effectiveness of these admixtures in the presence of CFA is particularly important. However, the experimental data on this topic has been limited. In general, to obtain a specific workability of fresh concrete with CFA, it is necessary to use more P or SP than for of the corresponding compositions without CFA [16–22]. This is likely due primarily to the higher water demand of fresh concrete with CFA. Consequently, there is a smaller amount of free water in the mixture [23]. The potentially lower efficiency of P and SP in the presence of CFA is indicated by the faster loss of workability of mixes with CFA [6], but such effects do not occur in every case [16,17,22]. To date, there has been no in-depth study on how different types of P and SP work with CFA with different properties, both in terms of the primary effect—the rheological properties of the mortars—and the secondary effects—setting time, air entrainment, or hydration heat. Generally, this indicates that present knowledge of the impact of CFA on the effectiveness of P and SP is very limited and not systematic; thus, further studies are needed.

The main objective of this research was to investigate the influence of raw and ground CFA on the effectiveness of P and SP activity. The basic effect of P and SP on rheological properties was studied using rheometric techniques. The secondary effects of the admixture's effects, such as setting time, heat of hydration, and air content, were also studied.

2. Effectiveness of Plasticizers and Superplasticizer Action

The effectiveness (efficiency) of concrete admixtures is a criterion based on the characteristics of the quality of its effects in its given function and its associated primary effect [24]. The primary effect is defined here as an effect of the admixture corresponding to its function as a direct consequence of the physical mechanism of its action. Typically, the assessment of the effectiveness of an admixture and its applications should take into account secondary effects because of the possible adverse impact of the

admixture on the important properties of the concrete and (or) the hardened concrete. The types and primary and secondary effects of P and SP are summarized in Table 1.

Table 1. Types, primary and secondary effects of plasticizers (P) and superplasticizers (SP) [24].

Admixture	Type	Primary Effect	Secondary Effects-Side Effects
P	<ul style="list-style-type: none"> lignosulfonates and its salts (Ca, Na, Mg, NH₄); hydroxy-carboxylate acids and its salts (containing groups (OH), (COOH)). 	Influence on rheological properties of cement mixtures enabling:	<ul style="list-style-type: none"> influence on cement setting time influence on air content in mixture influence on heat of cement hydration
SP	<ul style="list-style-type: none"> salts of sulfonated naphthalene formaldehyde polymers (SNF); salts of sulfonated melamine formaldehyde polymers; (SMF); polycarboxylate acrylic acids polymers and cross-linked polymers (PC and CLPC) polycarboxylate ethers polymers (PE); Rother substances in example modified lignosulfonates. 	<ul style="list-style-type: none"> increase in workability (fluidity) of mixture (constant w/b ratio) decrease in w/b ratio at given workability of cement mixture (enabling increase in compressive strength and durability of hardened cement composite) decrease in cement content at given fresh and hardened cement mixture properties 	

The effectiveness of P and SP should be considered from technical, technological, and economic perspectives. Technical effectiveness determines the changes in the rheological properties of the fresh concrete in terms of the minimum dosage of admixture needed for its effects to take place in the intended time needed for transporting and arranging the mix at the installation site; the conventionally adopted time is 90 min. Economic effectiveness refers to the cost of obtaining certain changes in the rheological properties using the above additives. Technological effectiveness is the ease and safety of using the admixture and the sensitivity of its effects to changes in environmental conditions. This article focuses on the technical and rheological aspects of the effectiveness of P and SP in the presence of CFA. In practice, the choice of admixture also depends on economic and technological factors. The fulfilment of these factors will achieve the desired effect of the admixture at the lowest cost and in a safe manner.

The aim of using P and SP is to adequately modify the rheological properties of the fresh concrete according to the technology used and the conditions for the implementation process of concreting. The basis for evaluating the effectiveness of these additives is measuring their impact on the changes of their rheological properties and workability. Therefore, the effectiveness tests of these admixtures focus primarily on the identification effect on the rheology of fresh concrete under certain technological conditions and the possibility of side effects of the admixtures, such as changes in the aeration of the mix or changes in the heat release curve during cement hydration. For this purpose, it is necessary to adopt a rheological model of the fresh concrete, and then measure the changes in its rheological parameters alongside the air content in the mix and changes in the nature of heat release during the hydration process, as a result of the addition of an admixture in terms of the variable factors and type of the concrete components.

Physically, mortar and concrete are similar. Both are a mixture of cement, water, aggregate, admixtures, and additives. Numerous studies show that the tests carried out on mortars can also be used to predict the rheological properties of fresh concrete. Simple mathematical relationships between the rheological properties of fresh mortars and fresh concrete mixes are presented in past studies [25–33]. Thus, it is commonly accepted that mortars can be used to test the effectiveness of P and SP. Thanks to this, the cost of research can be significantly reduced, and its scope can be increased.

Therefore, studies on the effects of CFA on the performance of plasticizers and superplasticizers were also performed on mortars.

3. Experimental Section

3.1. Variables and Research Plan

The research plan is presented in Table 2. The research was conducted for three batches of CFA (raw fly ash; batches: A, B, C, and ground fly ash; batches: AG, BG, and CG), sampled in a time range of a half year from the intermediate reservoirs of the Bełchatów Power Plant. We used both raw and ground CFA, which were added as a substitute for 20% of the cement mass. The effectiveness of different admixtures was assessed by testing changes in the rheological properties of the mortars and the testing side effects of the admixture, including the heat of hydration and air content, with and without CFA. We selected two P and four SP that are typically used and represent the main types of this admixture. Admixtures were also selected based on their different chemical bases that were representative of the given admixture group: For P: lignosulfonates, iminodietanol, bis ethanol, phosphate (V) tri butyl acetate, formaldehyde, methanol, and (Z)-octadec-9-enyloamine; for SP: polycarboxylate ether, melamine sulfonates, and naphthalene sulfonate.

Table 2. Research plan—type of calcareous fly ash (CFA), w/b ratio, admixture dosage and tested properties.

Type and Batches of Calcareous Fly Ash (CFA)	w/b Ratio	Symbol of Admixture	For Testing Rheological Properties [% b.m]	For Testing Air Content [% b.m]	For Testing Heat of Hydration [% b.m]
Raw CFA: A, B, C	0.55	P	P1	0, 0.25, 0.5%	x
	0.55		P2	0, 0.25, 0.5%	0, 0.25%
Ground CFA: AG, BG, CG CFA content: 20% as cement mass replacement	0.55	SP	SMF	0, 0.6, 1.15, 2.3%	0, 1.15%
	0.45		SNF	1.8, 2.4, 3.6%	1.8%
	0.45		PE1	1.0, 1.25, 2.0, 2.5%	1.25%
	0.45		PE2	0.5, 0.75, 1.0%	0.5%

The maximum amount of P and SP corresponded to the maximum amount recommended by the producer of the admixture. The maximum content of admixture also did not exceed the saturation point, which was verified in preliminary studies.

This study was conducted on mortars, but due to the similarity of the rheology of mortars and concrete mixes, it can also be used to design the workability of a concrete mix.

3.2. Materials and the Composition

The composition and selected physical properties of the raw and ground CFA used in this research are compiled in Table 3. Blaine specific surface was tested according to [34].

Table 3. Chemical composition of CFA.

CFA	LOI	SiO ₂	Al ₂ O ₃	Fe ₂ O ₃	CaO	SO ₃	K ₂ O	Na ₂ O	CaO _w	Bulk Density [kg/m ³]	Fineness		Blaine Specific Surface [34] [cm ² /g]	
											Raw	Ground G	Raw	Ground G
A	2.56	33.47	19.19	5.37	31.18	4.33	0.11	0.31	3.43	1098	36.4	23	2860	3500
B	2.12	40.98	19.00	4.25	25.97	3.94	0.14	0.13	1.07	1028	46.3	20.8	2370	3520
C	2.67	45.17	20.79	4.58	20.6	2.5	0.19	0.23	1.18	960	57.2	16.7	1900	3700

Ground CFA was created by subjecting raw CFA to a grinding process in a laboratory ball mill. The residue on the 45 µm sieve was taken as the measure of grinding. Due to its coarse granulation and

value of fineness (minimum, 36%; average, 50%), the tested CFA did not meet the basic requirements set by the ASTM C618 standard [35] (retention on a 45 μm sieve at a maximum of 34.0%) and PN-EN 450-1 standard [36] (retention on a 45 μm sieve at a maximum of 40%). The other requirements for the CFA composition were, however, met. Fluctuations in the chemical composition and properties of the ash are significant, especially the amount of CaO , SO_3 , and Na_2O . However, it should be noted that CFA is characterised by a relatively low changeability in the amount of SiO_2 and Al_2O_3 and a low loss on ignition. The X-ray diffraction (XRD) pattern of CFA is presented in Figure 1. The differential thermal analysis (DTA) pattern of CFA is presented in Figures 2–4. The cumulative distribution of ash grain size is presented in Figure 5. This ash contains above 25% reactive silica and above 10% reactive calcium oxide, which shapes its pozzolano–hydraulic properties. The results of the supplementary tests in terms of phase composition and granulation confirm the above-mentioned observations on the usefulness of calcareous fly ash as a pozzolan–hydraulic component of cement for batches of materials with different phase compositions (see the diffractograms and thermograms in Figures 1–4) and variable particle sizes within the fluctuations shown during intensive monitoring, as shown in Figure 5. Observations of calcareous fly ash using scanning electron microscopy showed the presence of grains with a spherical shape and a smooth surface, as well as irregularly shaped porous grains, as displayed in Figures 6–8.

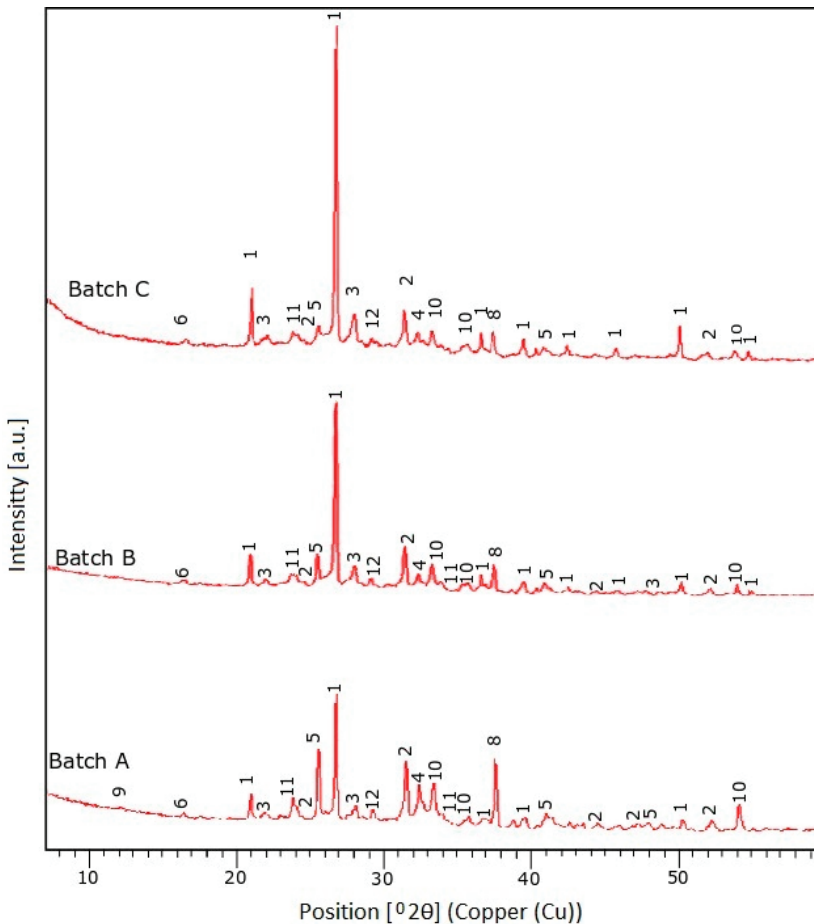


Figure 1. Cont.

Symbol in diffractograms	Quantitative Phase Composition of CFA												
	Component share [% by mass]												
	Amorphous phase (non-crystalline)	Quartz SiO ₂	Gehlenite Ca ₂ A ₁₂ Si ₇ O ₇	Anorthite	Belite β-Ca ₂ SiO ₄	Anhydrite CaSO ₄	Mullite Al ₆ Si ₂ O ₁₃	Aluminate Tricalcium	CaO	Brownmillerite Ca ₂ (Al,Fe) ₂ O ₅	Hematite Fe ₂ O ₃	Ye'elemite Ca ₄ A ₆ O ₁₂ SO ₄	Calcite
Batch A	-	1	2	3	4	5	6	7	8	9	10	11	12
Batch A	41.1	18.2	7.8	6.3	6.5	5.8	3.4	5.8	3.4	0.5	0.5	0.4	<0.1
Batch B	52.8	16.8	7	8.8	5.5	46	6.1	5.6	1.5	0.6	0.5	0.3	<0.1
Batch C	43.5	22.2	7	9.8	2.9	3.4	8.1	1.5	1.2	0.9	0.5	0.2	<0.1

Figure 1. The X-ray diffraction (XRD) pattern of CFA batch A, B, C.

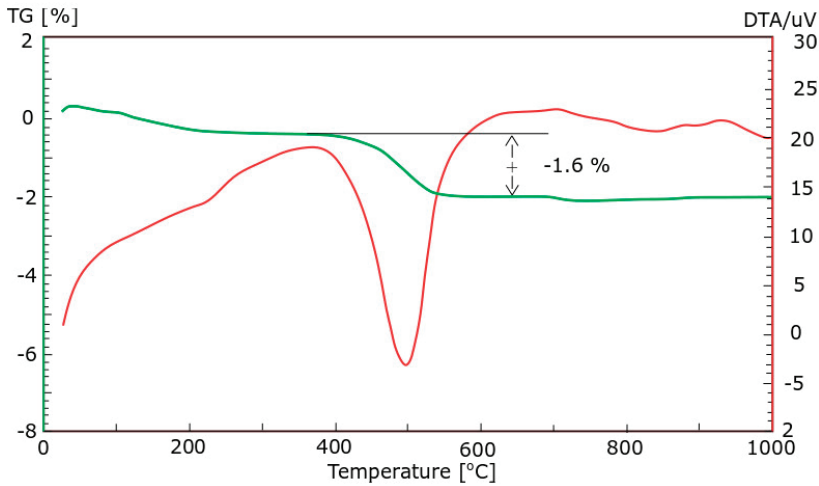


Figure 2. The differential thermal analysis (DTA) pattern of CFA batch A.

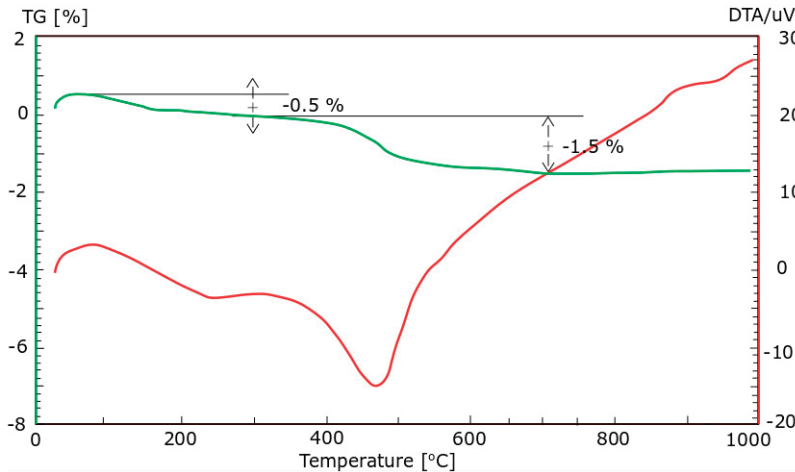


Figure 3. The differential thermal analysis (DTA) pattern of CFA batch B.

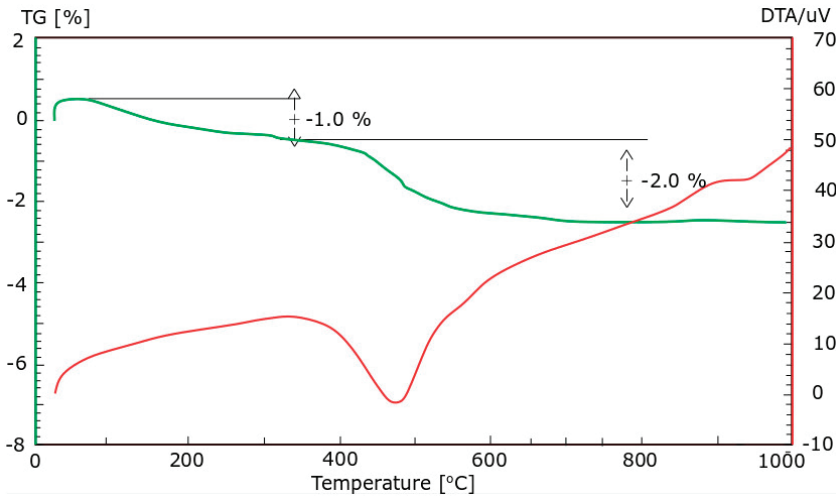


Figure 4. The differential thermal analysis (DTA) pattern of CFA batch C.

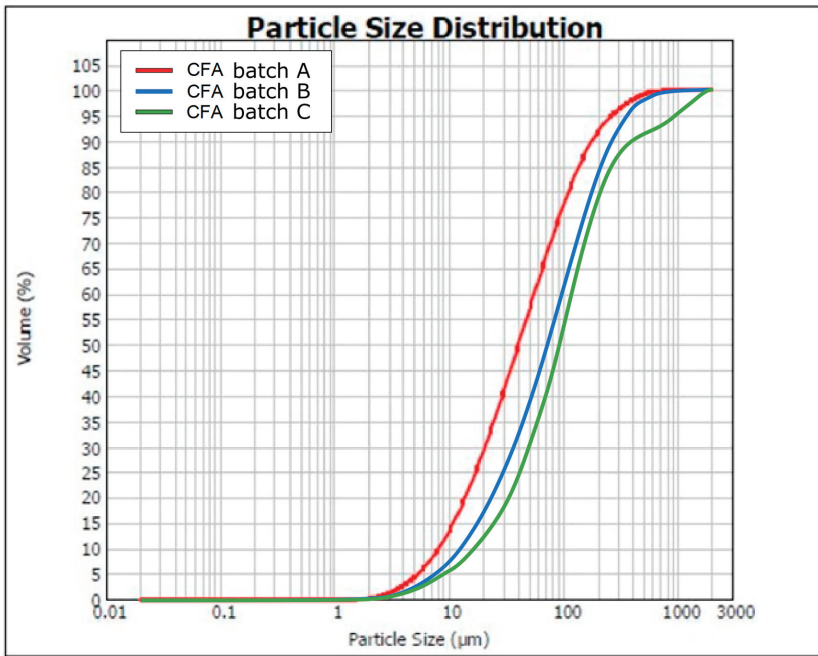


Figure 5. Cumulative distribution of ash grain size of CFA batch A, B, C.

After processing by grinding, the requirement of fineness under 34µ is always met, and the Blaine specific surface is 3500–3700 cm²/g. The water demand of the tested CFA is high. Replacing 20% of the cement with CFA causes the water demand to increase from 8% to 12% (on average, 10%) (the test procedure according to PN EN 450-1 [36]). Processing of the CFA by grinding causes the water demand to decrease. Replacing 20% of the cement with ground CFA causes the water demand to increase from 2% to 6% (on average, 4%).

The properties used for P and SP are presented in Table 4. The properties of the CEM I 42.5 cement used in this research are presented in Table 5. The mortar proportions are shown in Table 6. In order to eliminate the influence of the type and grading of sand on the rheological properties of the mortars, normal sand (2 mm maximum with a bulk density of 2.65 g/cm³, according to PN-EN 196-1 [37]) was used. The grading curve of the normal sand is presented in Figure 9. The proportions of the mortar mixture were based on standard mortar proportioning according to PN-EN 196-1 [37] but with the w/b ratio changed to 0.45 or 0.55.

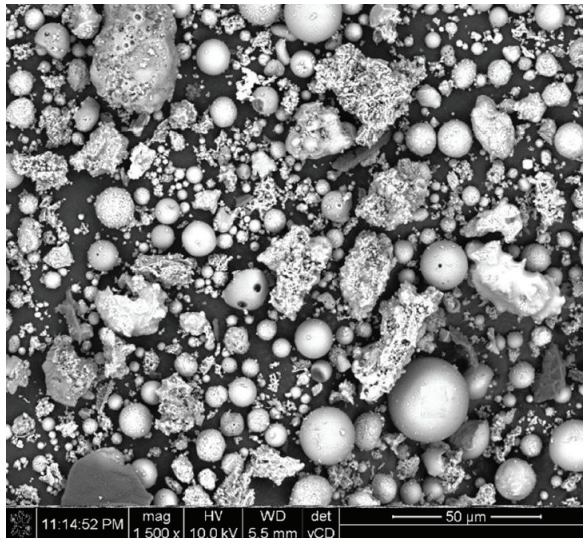


Figure 6. Morphology of calcareous fly ash grains batch A (magnification of 1500 times).



Figure 7. Morphology of calcareous fly ash grains batch B (magnification of 1500 times).

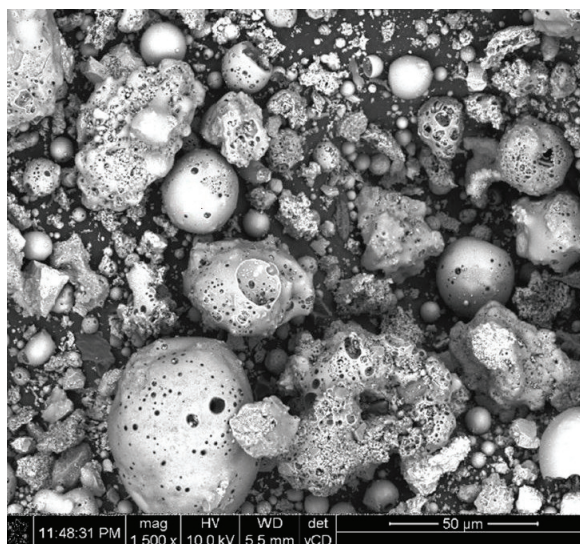


Figure 8. Morphology of calcareous fly ash grains batch C (magnification of 1500 times).

Table 4. The type, chemical base, density and volume of chemical admixtures. Date obtained from the manufacturer of admixture.

Symbol of Admixture	Chemical Base	Density at 20 °C, [g/cm ³]	Maximum Recommended Dosage, [% b.m]
P1	lignosulfonates	1.00+/-0.01	0.5%
P	iminodietanol, bis ethanol, phosphate (V) tri butyl acetate, formaldehyde, methanol, (Z)-octadec-9-enyloamine	1.07+/-0.01	0.5%
PE1	polycarboxylate ether	1.07+/-0.02	2.5%
PE2	polycarboxylate ether	1.07+/-0.02	1.0%
SP	SMF melamine sulfonates	1.20+/-0.03	2.3%
	SNF naphthalene sulfonate	1.15+/-0.03	3.6%

Table 5. Properties of cement CEM I 42.5. Data obtained from the cement producer.

SiO ₂ [%]	Al ₂ O ₃ [%]	Fe ₂ O ₃ [%]	CaO [%]	SO ₃ [%]	Na ₂ O _e [%]	C ₃ S [%]	C ₂ S [%]	C ₃ A [%]	C ₄ AF [%]	Spec. Surf., [34] [cm ² /g]
20.5	4.89	2.85	63.3	2.76	0.73	65	10	8.1	8.7	3500

Table 6. Composition of mortars for testing the rheological properties.

Constituent	Amount, [g/batch]
Cement	450/405/360/315
Calcium Fly Ash w/(c + CFA)	-/45/90/135
Water	0.45/0.55
Standard sand	202.5/247.5
	1350

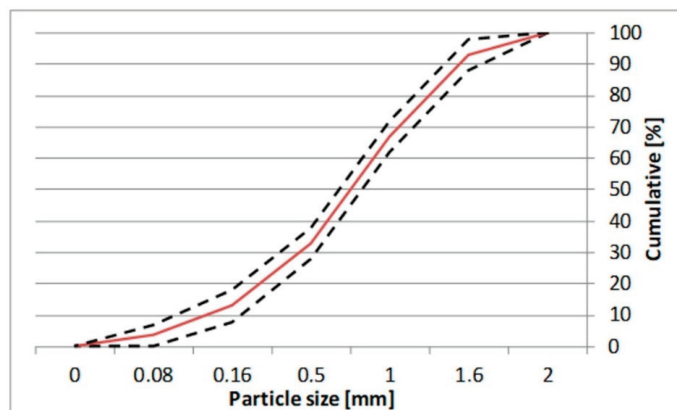


Figure 9. The grading curve of normal sand [34].

3.3. Testing Effectiveness of the Plasticizer and Superplasticizer Action

3.3.1. Rheological Properties

The rheological behaviour of mortar and concrete is commonly described by the Bingham model using the parameters of yield value and plastic viscosity.

The yield value determines the shear stress necessary for initiating flow. When the shear stress is higher than the yield value, the mixture starts to flow at a speed inversely proportional to the plastic viscosity. The yield value controls the workability of ordinary fresh concrete, while the role of plastic viscosity is secondary. In the case of self-compacting concrete characterized by a low yield value, the plastic viscosity determines the flowability, stability, and ability to self-deaerate. Problems with the rheology of mortars and concretes are discussed in detail in [28,38,39].

The mortars for testing the rheological properties were prepared according to PN-EN 196-1 [37], and the mixer and mixing procedures were compliant with PN-EN 196-1 [34]. CFA was added together with cement, and the admixtures were added to water (PE) and delayed for 30 s (P, SNF, and SMF). After the end of mixing, the mortar samples were transferred to a Viskomat NT rotational rheometer. The rheological parameters g (Nm) and h (Nm s), corresponding to yield value and plastic, were then determined. The values of g and h can be presented in physical units, but the measurement constants of the rheometer have to be defined. According to [29], in an apparatus like the one used in this work, $\tau_0 = 7.9$ g and $\eta_{pl} = 0.78$ h. However, since the rheometer constants were not verified, the results are presented as g and h . The mean relative errors of determination of the rheological parameters g and h of the mortars containing CFA were, respectively, 4.4% and 4.5%, which are identical to other studies. This proves that the Bingham model is acceptable for describing the rheological properties of mortars with CFA and P or SP. The general basis and rules for rheological measurements are detailed in [38,39]. The tested mortars were prepared and stored between measurements under conditions that allowed its temperature to remain at 20 °C. During the measurements, the required temperature was maintained with an automatic thermostatic controller.

3.3.2. Air Content

The air content in the mortar was determined by PN-EN 1015-7 [40].

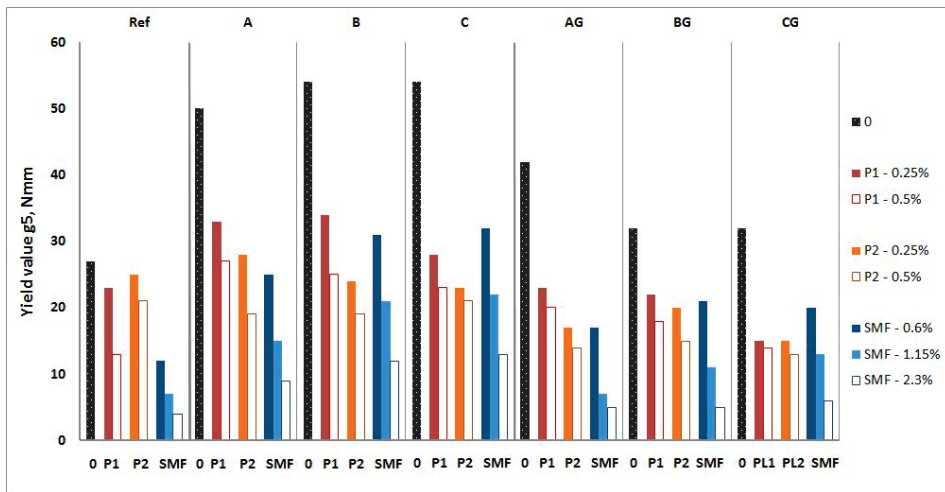
3.3.3. Heat of Hydration

The heat of hydration for the cement–CFA–admixture systems was determined using an isothermal microcalorimeter (TamAir). This apparatus measures the amount of heat (in J/g) that is emitted under

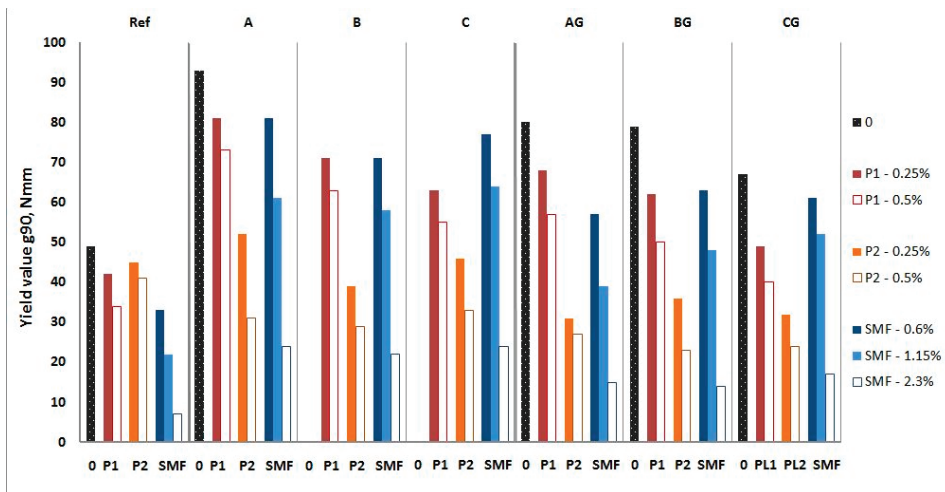
isothermal conditions during binder hydration (CFA and CEM I) from the moment of its contact with water and admixture in relation to an inert referential sample with an analogous heat capacity. The water–binder ratio (w/b) of the tested cement paste was 0.45 (P, SMF) or 0.55 (SNF, PE). This measurement was conducted on a binder sample weighting 5 g, mixed with 2.25 g or 2.75 g of water. During the measurement, the temperature of the cement paste was 20 °C. The measurement of the heat of hydration lasted 12 h.

4. Results and Discussion

The influence of P and SP on the rheological properties of CFA mortars is shown in Figures 10–13, and their influence on the air content and heat of hydration is shown in Tables 7 and 8, respectively.

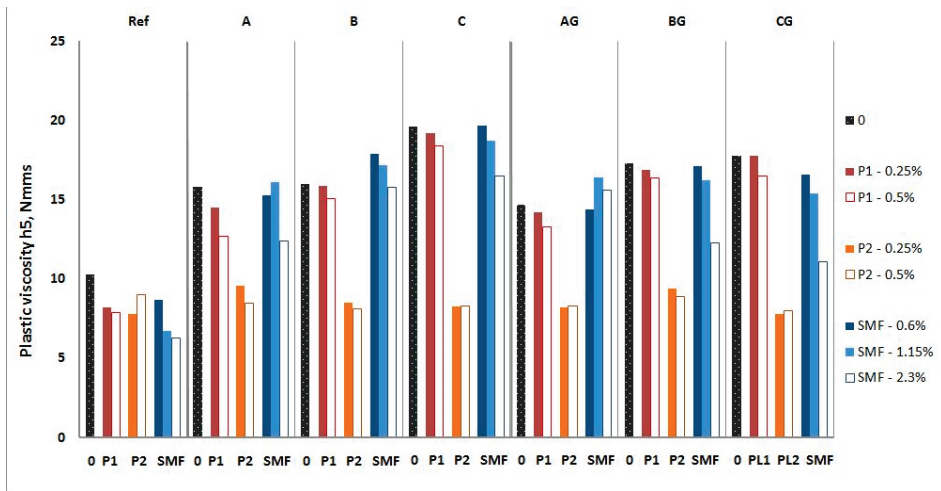


(a) after 5 min

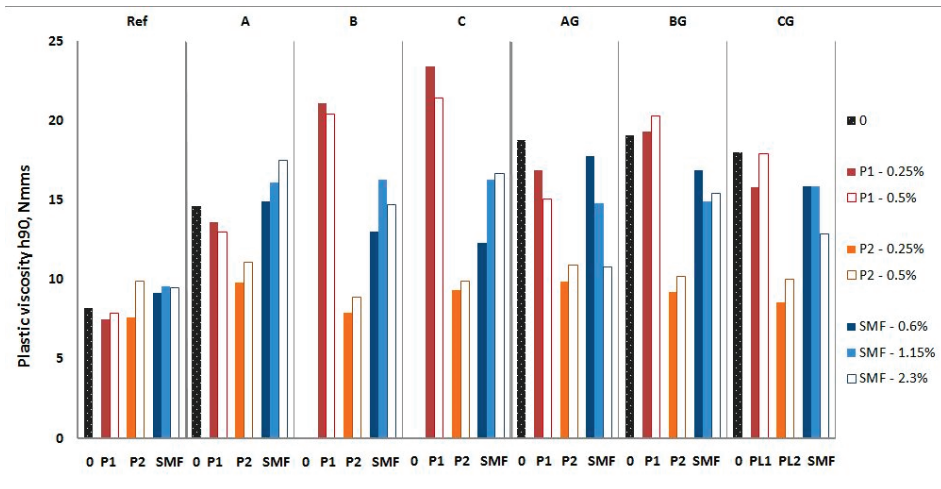


(b) after 90 min

Figure 10. Influence of P1 and P2 and SMF on yield value g of mortars with raw and ground CFA. (a) after 5 min; (b) after 90 min.



(a) after 5 min



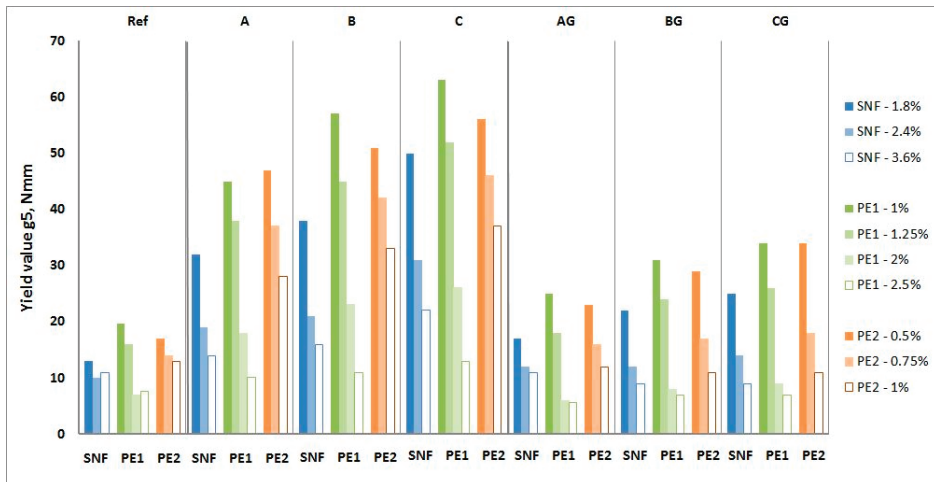
(b) after 90 min

Figure 11. Influence of P1 and P2 and SMF on plastic viscosity h of mortars with raw and ground CFA. (a) after 5 min; (b) after 90 min.

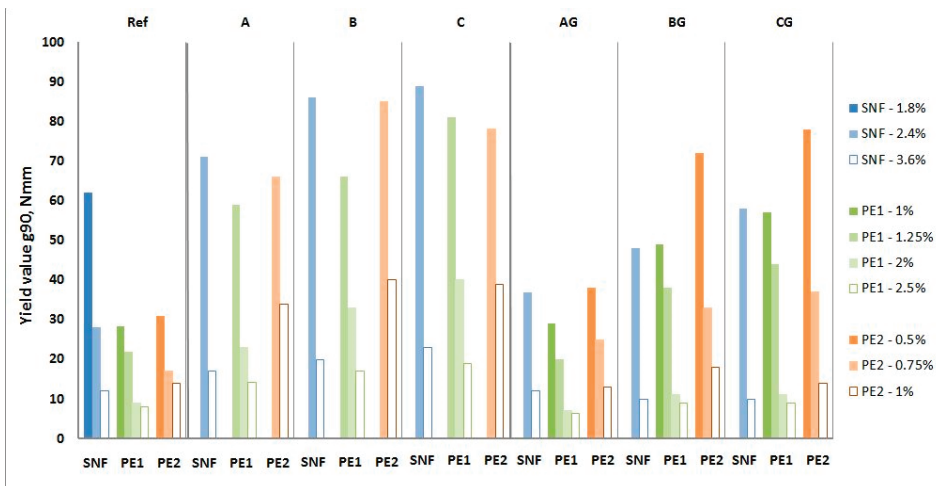
The PL and SP used in this study liquefied the cement mortars containing CEM I without the addition of CFA. Studies have shown that the workability and stability of mortar are retained for a period of 90 min. Thus, the admixtures used are compatible with the cement used in the study.

Adding raw CFA to mortars as a cement replacement causes a significant increase in the yield value g and plastic viscosity h , depending on the type of CFA. The range of changes in the yield value g of mortars increases over time, but the presence of CFA insignificantly affects changes in the plastic viscosity h over time. The nature of the influence of ground CFA on the rheological parameters of mortars is the same as that of raw CFA. It also worsens the workability of mortar, however, to a much lesser extent than raw CFA. The influence of CFA type and processing method is presented and discussed in [14,19].

In order to determine the significance of the influence of the compositional factors and their interactions on the rheological properties, an analysis of variance (ANOVA) was carried out using one-dimensional significance tests for the rheological parameters (g_5 , g_{90} , h_5 , and h_{90}) of the mortars with P and SP. The results are shown in Tables 9 and 10, which present the ANOVA with parameterization, sigma-restrictions, and a decomposition of the effective hypotheses. The ANOVA statistical analysis showed that the largest statistical effects on rheological parameters were yield value and plastic viscosity, regardless of the time at which the measurement was made, and the type of batch. The rheological parameters of the mortars with P were also affected by the type of batches and type of P. However, the rheological parameters of the mortars with SP were affected by the dosage of SP.

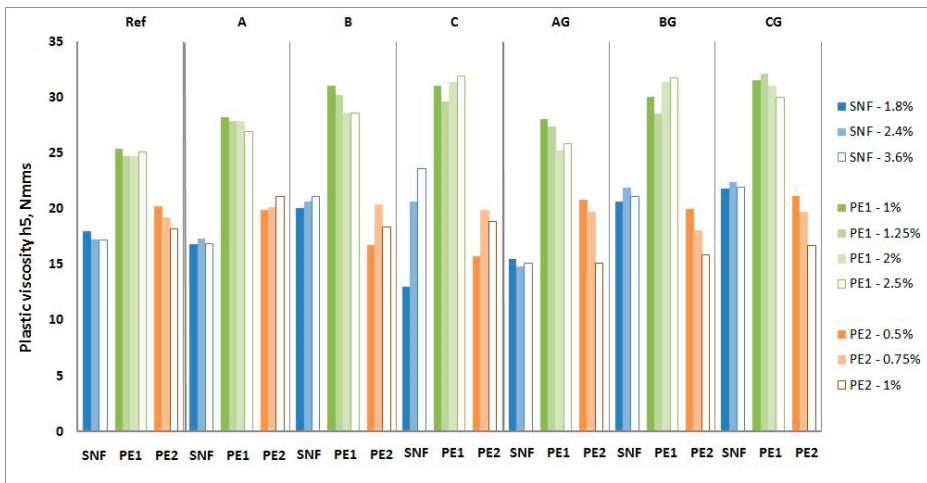


(a) after 5 min

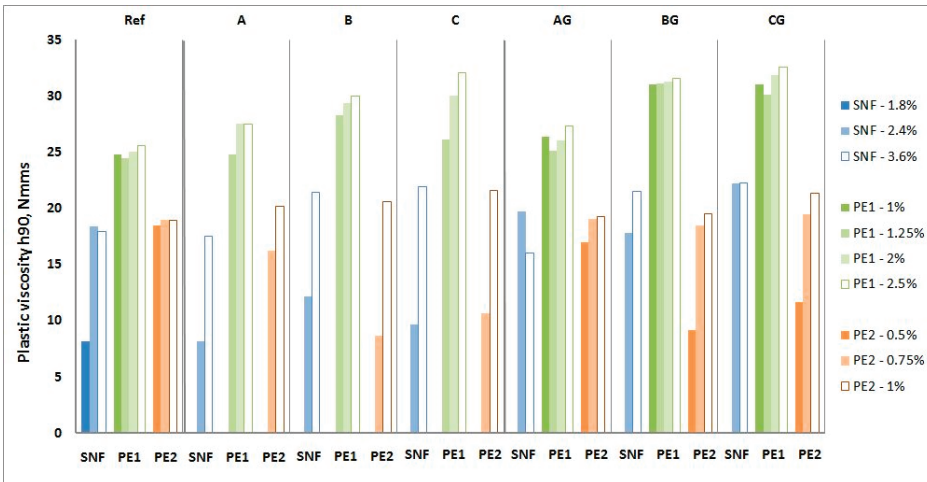


(b) after 90 min

Figure 12. Influence of SNF, PE1 and PE2 on yield value g of mortars with raw and ground CFA. (a) after 5 min; (b) after 90 min.



(a) after 5 min



(b) after 90 min

Figure 13. Influence of SNF, PE1 and PE2 on plastic viscosity h of mortars with raw and ground CFA. (a) after 5 min; (b) after 90 min.

Table 7. Influence of P and SP on air content in mortars with and without CFA.

CFA	Air Volume [%]						
	without Admixture	0.25% P1	0.25% P2	1.15% SMF	1.8% SNF	1.25% PE1	0.5% PE2
CEM I	5.2	4.6	19.0	2.5	13.5	2.8	9.5
A	2.8	2.4	16.6	3.3	13.1	2.4	13.2
AG	2.5	1.4	15.1	2.3	12.1	2.0	14.4
B	3.5	2.7	16.3	2.6	12.5	3.0	12.3
BG	2.9	2.4	17.5	1.2	11.9	4.0	11.2
C	4.2	2.1	17.2	2.7	12.9	2.0	11.6
CG	2.2	1.7	18.0	1.0	11.0	3.8	10.5

Table 8. Heat of hydration of cement and CFA paste with P2 and SMF, SNF and PE1 [J/g] during 12 h.

Heat of Hydration, [J/g]							
Sample	10 min	1.5 h	12 h	Sample	10 min	1.5 h	12 h
w/b = 0.55				w/b = 0.45			
CEM I	0.166	3.600	50.315	CEM I	0.177	3.619	51.764
CEM I + 1/2 max P2	0.011	1.588	20.520	CEM I + 1/2 max SNF	-0.121	0.904	5.977
CEM I + 1/2 max SMF	0.122	1.295	19.330	CEM I + 1/2 max PE1	-0.109	1.313	4.712
A	0.850	7.336	47.157	A	0.753	6.909	47.032
A + 1/2 max P2	0.885	6.697	32.721	A + 1/2 max SNF	0.627	5.854	21.384
A + 1/2 max SMF	0.852	6.277	34.699	A + 1/2 max PE1	0.650	4.583	14.576
AG	1.433	9.018	49.557	AG	1.230	8.596	69.799
AG + 1/2 max P2	1.252	7.032	35.273	AG + 1/2 max SNF	0.991	6.437	21.983
AG + 1/2 max SMF	1.297	7.139	36.311	AG + 1/2 max PE1	1.034	6.101	18.514
B	0.876	6.843	44.860	B	0.876	6.843	44.860
B + 1/2 max P2	0.652	5.212	27.130	B + 1/2 max SNF	0.853	5.766	19.844
B + 1/2 max SMF	0.684	5.645	32.767	B + 1/2 max PE1	0.506	4.462	13.293
BG	1.095	7.994	49.350	BG	1.095	7.994	49.350
BG + 1/2 max P2	0.715	5.627	30.805	BG + 1/2 max SNF	0.723	6.021	21.042
BG + 1/2 max SMF	0.882	5.913	33.511	BG + 1/2 max PE1	0.765	5.660	17.697
C	0.907	6.905	46.781	C	0.849	6.526	47.159
C + 1/2 max P2	0.770	5.363	31.955	C + 1/2 max SNF	0.644	4.716	14.542
C + 1/2 max SMF	0.578	4.511	27.013	C + 1/2 max PE1	0.606	3.880	10.974
CG	1.335	7.049	46.999	CG	1.256	6.838	48.463
CG + 1/2 max P2	1.493	7.253	40.282	CG + 1/2 max SNF	1.150	6.224	17.704
CG + 1/2 max SMF	1.105	5.631	32.095	CG + 1/2 max PE1	0.945	5.244	10.189

Table 9. Analysis of Variance (ANOVA). One-dimensional significance tests for rheological parameters of mortar with P.

Impact of CFA and P on Rheological Parameters of Mortars	g5 [Nmm]		g90 [Nmm]		h5 [Nmms]		h90 [Nmms]	
	The Value of F	Level of Significance p	The Value of F	Level of Significance p	The Value of F	Level of Significance p	The Value of F	Level of Significance p
Raw and ground CFA; type of batches	55.97577	0.000000	59.9000	0.004932	53.69909	0.000000	25.33230	0.000009
Type of P	1.25945	0.120692	19.5596	1.85693	1.89624	0.190867	1.69624	0.255697
Dosage of P, [% b.m.]	1.95367	0.100815	13.5963	2.26472	1.69185	0.300257	1.23665	0.30236
Raw and ground CFA; batches and Type of P	9.68102	0.000205	56.5476	0.00998	17.53595	0.000009	9.16799	0.000270
Raw and ground CFA; batches and Dosage of P, [% b.m.]	1.89637	0.140802	20.0119	1.01307	2.19993	0.093236	1.89624	0.140827
Type of P and Dosage of P, [% b.m.]	2.71871	0.111022	12.5952	3.37841	1.19355	0.336703	1.10185	0.363647

Significant statistical influence is marked in bold italics.

Table 10. ANOVA. One-dimensional significance tests for rheological parameters of mortar with SP.

Impact of CFA and SP on Rheological Parameters of Mortars	g5 [Nmm]		g90 [Nmm]		h5 [Nmms]		h90 [Nmms]	
	The Value of F	Level of Significance p	The Value of F	Level of Significance p	The Value of F	Level of Significance p	The Value of F	Level of Significance p
Raw and ground CFA; type of batches	549.774	0.0178	18.4861	0.000027	3.937173	0.020769	4.84901	0.010359
Type of SP	25.263	5.3485	5.7630	0.006398	2.536958	0.096357	2.5693	0.019653
Dosage of SP, [% b.m.]	1854.023	0.000000	512.1678	0.000000	52.2563	0.000569	23.45659	0.000215
Raw and ground CFA; batches and Type of SP	33.214	8.3383	1.6148	0.188646	3.094208	0.034357	2.33994	0.045490
Raw and ground CFA; batches and Dosage of SP, [% b.m.]	54.996	13.8065	1.7850	0.015218	1.021517	0.498316	2.09643	0.081593
Type of SP and Dosage of SP, [% b.m.]	10.816	25.5603	1.3870	0.025324	1.315541	0.304389	2.76971	0.016045

Significant statistical influence is marked in bold italics.

In the presence of P1 and especially P2, the negative influence of raw CFA on the yield value g of mortars is clearly lower. After the addition of 0.5% P1 or P2, the yield value g of the mortars with ground CFA is usually lower than that of mortar without CFA. For P1, this effect disappears over time, while for P2, it remains strong after 90 min. P1 has an insignificant effect on the plastic viscosity h of

the CFA mortar. P2 significantly reduces plastic viscosity h . The addition of plasticizers makes the changes in the plastic viscosity h of the CFA mortars less significant over time. The results obtained are consistent with the results of the tests on cements containing CFA in [16,17].

However, the increased SMF addition yield value g of the CFA mortars generally remains higher than that of the mortar without CFA until the maximum recommended dose of SMF is applied (only for mortars with ground CFA). The presence of SMF accelerates the increase in yield value g for mortars over time. This increase is greater for mortars containing CFA. In general, the impact of SMF on the plastic viscosity h of the tested mortars is insignificant from a workability point of view.

The test results agree with those in [24,41,42], in which it appears that admixtures based on melamine sulfonates demonstrate a possible decrease in the water content in concrete by up to 20%–30% compared to synthetic polymers, such as polycarboxylates and acrylic copolymers (PCEs), which have versatile chemical structures and can achieve up to 40% water reduction.

Obtaining consistent CFA mortars to measure their rheological properties requires the addition of 1.8% SNF. When raw CFA is used, the yield values of these mortars range from 2.5 to 3.5 times higher than the yield values g of the reference mortars, but when ground CFA is used, the yield value g of mortars only ranges from 1.5 to 2 times higher. Increasing the amount of SNF to 3.6% causes the yield value g of the mortars with ground CFA to drop lower than that in the reference mortar (an average of 15%). Mortars with raw CFA are then characterized by an average yield value g higher than 75%. At a dose of up to 2.4%, the SNF range of changes over time for the yield value g of mortars with CFA is clearly higher than that of the reference mortar. When 3.6% SNF is used, the increase in the yield value g over time for the reference mortar and mortars with ground CFA is negligible. To a small extent, the amount of SNF in the mortars with and without CFA influences the plastic viscosity h . The range of changes in the plastic viscosity h over time for the mortar and mortars with ground CFA is low and shows no clear trend; the workability these changes can thus be considered negligible. For mortars with raw CFA, with 2.4% SNF, they show a large decline in their plastic viscosity h resulting from stiffening of the mixture [26].

Obtaining consistent CFA mortars to measure the rheological properties requires the addition of 1% PE1 or 0.5% PE2. When raw CFA is used, the yield value of these mortars ranges from 2.2 to 3.4 times higher than the yield value g of the reference mortars, but when the ground CFA is used, the yield value g of the mortars only ranges from 1.25 to 2 times higher. The increase in the yield value g over time for the raw CFA mortars is very high, and after 90 min, these mortars are too stiff to perform rheological measurements. The increase in the yield value g of ground CFA mortars is usually clearly higher than that of the reference mortar (from 1.5 up to 2 times), but in some cases, it can be similar (PE1 or AG). The plastic viscosity h of the mortars with both ground and raw CFA is similar to or slightly higher than that of the reference mortar, and the plastic viscosity h of the PE1 mortars is higher than that of the PE2 mortars. The plastic viscosity h of the P1 mortars generally does not change in 90 min, while that of the PE2 mortars decreases.

Further increasing the amount of PE1 and PE2 reduces the yield value g and plastic viscosity h . This reduction is higher for mortars containing CFA. With the addition of 2% PE1 and 1% PE2, the rheological properties of the reference mortar and the mortars with ground CFA are similar (sometimes the yield value g of ground CFA is even lower), and the mortars do not show significant changes in their yield value over time. For the raw CFA mortars, the yield value g and its growth over time are reduced by increasing the SP addition but remain considerably higher than those of the reference mortar. Increasing the dose of PE1 insignificantly influences the plastic viscosity h of the mortars. This is due to the properties of raw CFA and the high water demands, which were confirmed in [16,22]. Increasing the dose of PE2 lowers the plastic viscosity h of the mortars with ground CFA and increases the plastic viscosity h of the mortars with raw CFA. The plastic viscosity h of the mortars with raw CFA with PE2 at a dose of 0.75% significantly decreases, and with a dose of 1.0% PE2, it insignificantly increases.

The effects of P and SP action are affected by the type of CFA. On the basis of the conducted studies, it is not possible to identify clear trends. However, the use of P and SP reduces the influence

of the type of CFA (particularly when the CFA is ground) on the rheological properties of mortars (particularly when large amounts of P and SP), but the influence of CFA type may still be noticeable even if the maximum recommended dose is used.

The introduction of P1, SMF, and PE1 does not aerate the mortars, while the use of P2, SNF, and PE2 does aerate the mortars, both with and without CFA, as shown in Table 7. This effect may be partially responsible for the relatively smaller plastic viscosity of the mortars with the addition of P2, SNF, and PE2.

The introduction of P2, SMF, SNF, and PE1 reduces the cement hydration heat emitted after 2 h by 60–80%, as shown in Table 8. These results are consistent with those of other studies in this field [43]. In the presence of CFA, the reduction in the amount of heat released by adding these admixtures is smaller and ranges from 10% to 45%, depending on the nature and processing of the CFA (without showing clear trends). This indicates the retarding effect of admixtures, which is lower in the presence of CFA. The reasons for this can also be seen in the mechanism of the increased absorption of P and SP described above by large, irregular CFA grains. This phenomenon causes a smaller amount of P and SP to act in the cement paste, thereby exerting a smaller effect on the hydration process. It should be noted that a reduction in the heat generated after 2 h and 12 h by PE1 is higher than that for SMF and SNF. This indicates the strong retarding effect of PE1.

5. Evaluation of the Effectiveness of Plasticizers and Superplasticizers in the Presence of CFA

Evaluation of the effectiveness of P and SP in the presence of CFA was focused on the changes in the yield value g of mortars. Thus, the initial yield value g and its changes over time were taken into account. Plastic viscosity h , as indicated earlier, is normally of secondary importance to the mixture's workability. Additionally, as shown in this research, the range of plastic viscosity h changes in mortars due to the addition of P or SP with or without CFA is, in most cases, insignificant.

The obtained results for PL and SP activity do not indicate that the presence of CFA significantly affects their mechanisms of action described in [24,44]. The introduction of CFA as a cement replacement, due to its increased water demands, reduces the amount of free water in the mixture. Accordingly, mortars with CFA are characterized by a much higher yield value g and a faster increase in the yield value g over time than in mortar without CFA. Thus, to obtain a certain yield value g of mortars with CFA, it is necessary to use a higher addition of P or SP than for similar mortars without CFA. The amounts of P1 and P2 and SNF, SMF, and PE necessary to obtain a mortar yield g equal to 20 Nm are shown in Figures 14a and 15a. These relationships demonstrate the beneficial effect of using ground CFA. Obtaining the specific yield value g of ground CFA mortars requires a significantly lesser amount of admixture than that of raw CFA mortars. Importantly, it also shows that immediately after mixing, in the presence of ground CFA, plasticizers P1 and P2 are more effective, while the superplasticizers SNF, PE1, and PE2 and SMF are significantly less effective than in mortars without CFA. Only the effectiveness of P1 and SMF depend on the type of CFA; the effectiveness of the other types of admixtures, to a lesser extent, depends on the type of CFA, especially when the CFA is ground. The increase in the yield value g of mortars with an initial yield of 20 Nm is shown in Figures 14b and 15b. This increase is generally much higher for mortars with CFA, especially when raw CFA and SMF and PE2 are used. Only for P2 and PE1 is the increase in the yield value g over time for mortars with ground CFA less than or similar to that for mortars without CFA. This means that the effectiveness of P and SP with respect to time of action is generally reduced in the presence CFA. Analyzing the available literature [1,24,42,44,45] shows that the morphology of CFA grains affects the lower efficiency of P and SP. Raw CFA is characterized by large, porous grains with a large developed surface, which also contain large porous residues of unburned coal. This is the reason for the increased absorption of P and SP on CFA grains. This phenomenon significantly reduces the amount of admixtures that can work effectively in a cement mix. During processing by grinding, large grains are destroyed, which both reduces the CFA's water demand [14] and contributes to an increase in the amount of active P

or SP. The CFA processed by grinding increases the effects of the admixtures in comparison with the operations in cement mixes modified by raw CFA.

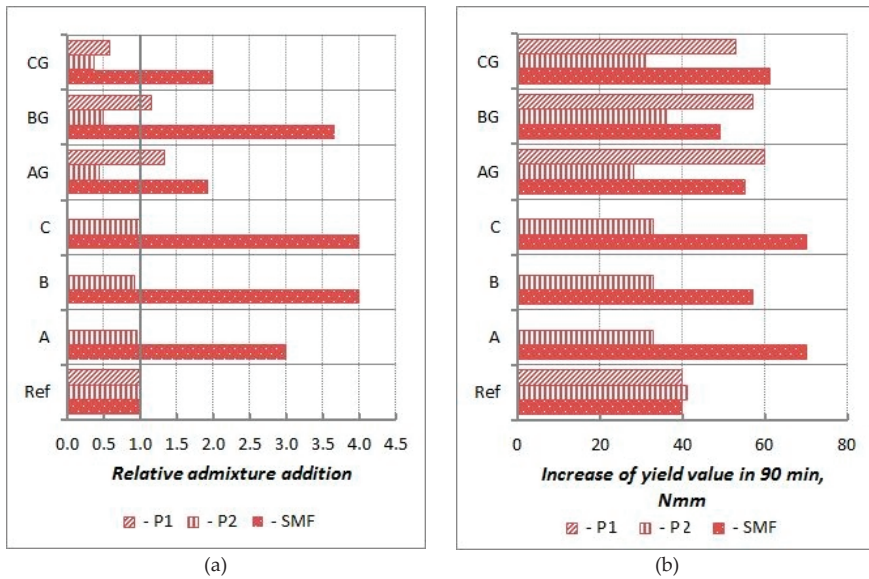


Figure 14. Influence of CFA on effectiveness of P1, P2 and SMF (mortars of w/b = 0.55); (a) relative admixture content (in relation to reference mortar without CFA) necessary to be added to obtain mortar with $g_5 = 20$ Nmm; (b) increase in yield value g of mortars with initial yield value g equal 20 Nmm in time.

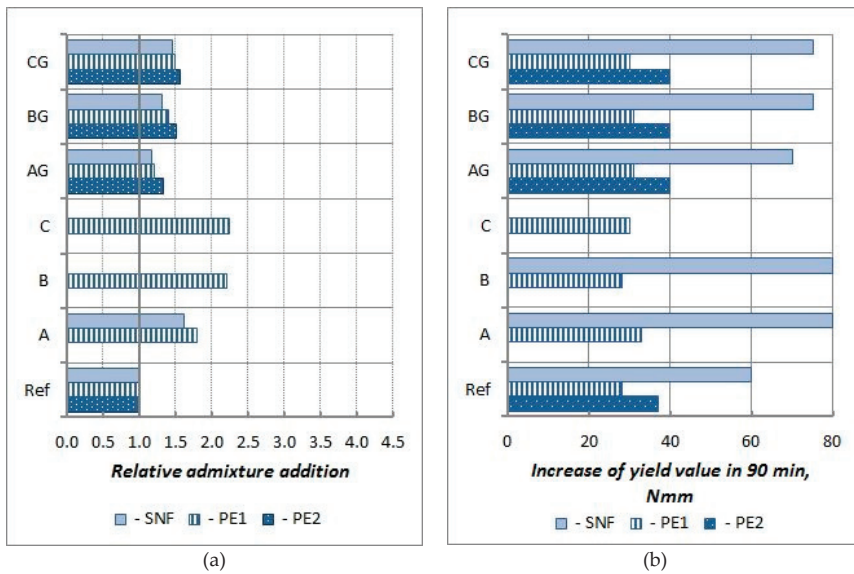


Figure 15. Influence of CFA on effectiveness of SNF, PE1 and PE2 (mortars of w/b = 0.45); (a) relative admixture content (in relation to reference mortar without CFA) necessary to be added to obtain mortar with $g_5 = 20$ Nmm; (b) increase in yield value g of mortars with initial yield value g equal 20 Nmm in time.

For mortars with CFA, the effectiveness of P and SP in the presence of CFA was also analyzed according to the changes in the initial yield value g_5 and the increase in the yield value g over time of up to 90 min ($g_{90}-g_5$) caused by the addition of these admixtures compared to the analogous changes of (i) the reference mortar (without CFA) and (ii) the CFA mortar without an admixture. The relative influence of CFA type and processing on the effectiveness of P and SP is shown in Figures 16 and 17.

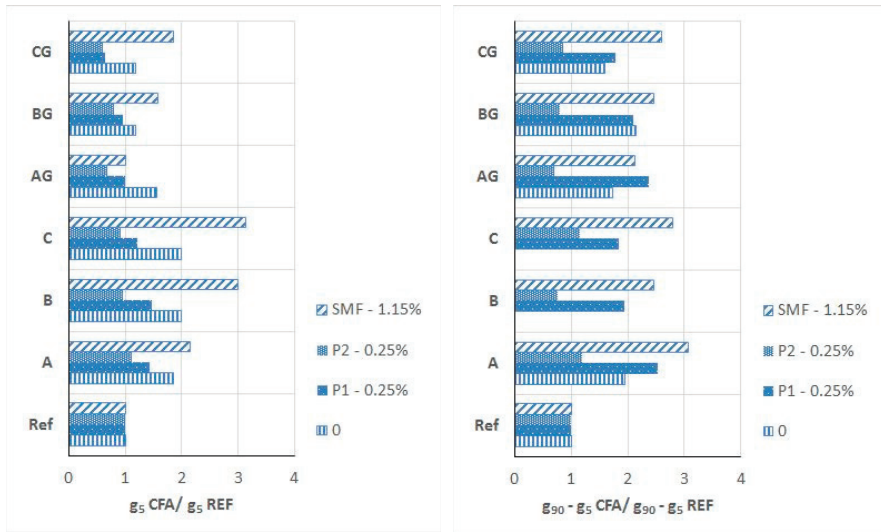


Figure 16. Relative effect of CFA presence on initial yield value g (g_5) and yield value g increase in time ($g_{90}-g_5$) of mortars in respect to reference mortars REF without CFA (Mortars without and with P1 or P2 or SMF – 1/2 of recommended maximum dosage, $w/b = 0.55$).

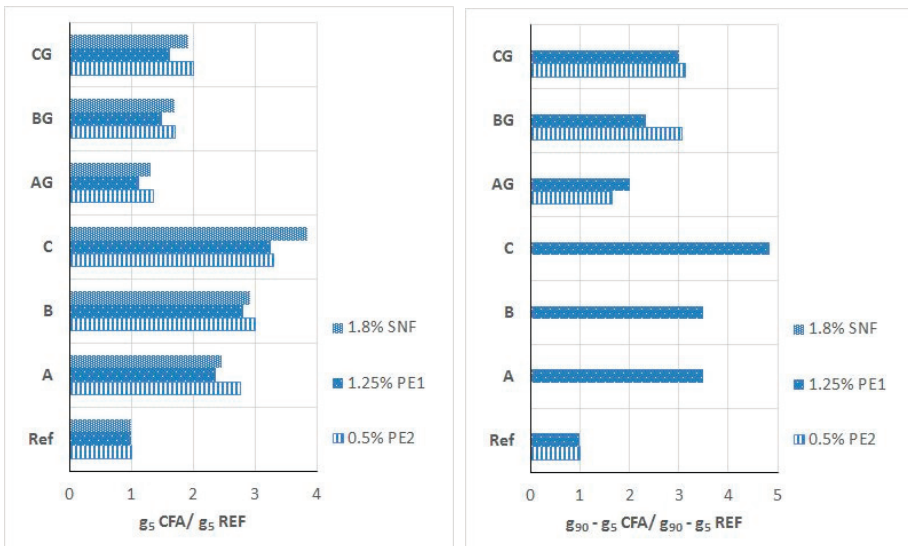


Figure 17. Relative effect of CFA presence on initial yield value g (g_5) and yield value g increase in time ($g_{90}-g_5$) of mortars in respect of reference mortars without CFA. (Mortars with SNF or PE1 or PE2 – 1/2 of recommended maximum dosage, $w/b = 0.45$).

The presence CFA favourably impacts the initial effectiveness of P1 and P2. The range of the reduction of the yield value g caused by the addition of P is higher in the mortars with CFA, particularly in mortars with ground CFA. The yield value g of the ground CFA mortars with a P addition of 0.25% is always lower than that of the mortars without CFA. The presence of CFA negatively affects the effectiveness of P1 with respect to workability changes over time. The relative increase in the yield value g over time for all mortars with CFA and P1, but especially those with raw CFA, is significantly higher than that for analogical mortar without CFA. At the same time, the presence of CFA favourably impacts the effectiveness of P2. The relative increase in the yield value g over time for mortars with P2 and with unprocessed and (particularly) ground CFA is lower than that of the mortar without CFA. Thus, using processing with CFA increases the effectiveness of P.

The effectiveness of SMF in the presence of CFA is clearly lower. The relative reduction of the initial yield value g of the CFA mortars is lower than of the mortar without CFA, even when the ground CFA is used. It should be noted, however, that despite lower effectiveness in the presence of CFA, the effects of SMF action remain higher than those of P1 and P2. The effects that adding SMF have quickly disappear over time (faster than for P1 and P2), which is typical for this type of admixture [24]. With the addition of 1.15%, the SMF increase in the yield value g of the mortars with ground CFA is clearly higher than that in the reference mortar and even higher than that in mortars without the addition of SMF. This means that the effectiveness of SMF with respect to time is vulnerable to CFA, especially raw CFA.

The initial effectiveness of the SNF in the presence of ground CFA does not reduce significantly but, at the same time, is reduced in the presence of raw CFA. Thus, at an SNF dose close to maximum, the mortar with ground CFA has a lower yield value g than the mortar without CFA. For workability loss, the effectiveness of SNF in the presence of CFA (both raw and ground) is reduced. Only at a dose of 3.6% SNF (the maximum recommended dose) was it possible to obtain ground CFA mortars with the range of changes in yield value g over time analogous to those of the mortar without CFA. In conclusion, the presence of CFA reduces the effectiveness of SNF. This reduction is lower when ground CFA is used.

The initial effectiveness of PE1 in the presence of ground CFA is higher but decreased in the presence of raw CFA. At 2% and higher dosages of PE1, the mortars with ground CFA achieve a similar yield to the mortars without CFA. In terms of workability loss, the effectiveness of PE1 in the presence CFA is lower. However, it should be noted that at high PE1 dosages, the workability loss of the ground CFA mortars and the reference mortar is negligible. On the other hand, the mortars with raw CFA show a considerable loss of workability even when the maximum recommended dose of PE1 is used. Thus, the presence of raw CFA reduces the effectiveness of PE1, but the presence of ground CFA affects it much less significantly.

The effectiveness of PE2 is generally lower than that of PE1. The presence of CFA, especially raw CFA, reduces the effectiveness of PE2. At a dose of 0.50%, PE2 was able to fluidize the raw CFA mortar only to a small extent. The mortars with raw and ground CFA present a rapid workability loss—much faster than that of the reference mortar. Increasing the dose of PE2 slightly reduces the yield value g of mortars with raw CFA, but even at its maximum recommended dose, such mortars show a rapid workability loss. An increased dose of PE2 strongly influences the reduction of the yield value g of mortars with ground CFA. At the maximum dosage, the yield values of these mortars are smaller than those of the reference mortar. The mortar with ground CFA still shows a rapid loss of workability. Therefore, in general, the presence of CFA negatively impacts the effectiveness of PE2, but to a lesser degree when ground CFA is used.

The type of CFA affects the efficiency of all tested SP. However, based on the current research, it is not possible to identify clear trends (SP usually works clearly better in the presence of CFA-type A and worse with CFA type C, but this effect cannot be clearly linked to the specific properties of the CFA). With an increased amount of SP, the influence of the type of CFA on the rheological parameters of the

mortar is reduced. However, for raw CFA, even at the maximum recommended dosage, this influence remains evident.

6. Conclusions

We confirmed that the use of raw CFA has a very negative impact on the workability of mortars. This effect is much less if ground CFA is used. The practical application of this ash without the simultaneous use of plasticizers or superplasticizers can be difficult in many cases.

The use of an admixture, particularly SP, allows one to effectively control the workability of mortar containing CFA, especially ground CFA. With these admixtures, it is possible to obtain mortars containing ground CFA with similar rheological properties to mortars without this addition. To obtain a specific workability of mortar with CFA, it is usually necessary to introduce a higher dose of a P or SP than found in mortar without CFA.

The presence of CFA also influences the effectiveness of the P and SP. This effect depends mostly on the rheological admixture type and CFA processing. Table 11 presents the general results of the impact of raw and ground CFA additions on the technical effectiveness of P and SP. With a value of (−1) for obtaining the specified effect of mix workability, a higher admixture dosage is necessary, and with a value of (−2), a higher admixture dosage is necessary (or the specified mix's workability may be impossible).

Table 11. Influence of raw and ground CFA addition on the technical effectiveness level of P and SP action.

Type of Admixture	In Raw CFA Presence	In Ground CFA Presence
P:	Technical effectiveness of P action	
P1- lignosulfonates (max 0.5%)	−2 *	0 *
P2- iminodietanol, bis ethanol, phosphate (V) tri butyl acetate, formaldehyde, methanol, (Z)-octadec-9-enyloamine (max 0.5%)	2 *	2 *
SP:	Technical effectiveness of SP action	
SMF- melamine sulfonates (max 2.3%)	−2 *	−2 *
SNF- naphthalene sulfonate (max 3.6%)	−2 *	−1 *
PE1- polycarboxylate ether (max 2.5%)	−2 *	0 *
PE2- polycarboxylate ether (max 1.0%)	−2 *	−1 *

Explanation of symbols in the table: *−2- significantly reduced efficiency compared to operation without CFA; −1- slightly reduced efficiency compared to operation without CFA; 0- unchanged efficiency compared to operation without CFA; 1- slightly increased efficiency compared to operation without CFA; 2- significantly increased efficiency compared to operation without CFA.

The properties of CFA have an impact on the effectiveness of P and SP; this effectiveness is clearly lower when ground CFA is used. In the presence of CFA, the secondary effects of using P or SP for air entrainment or setting the time are similar. However, the effects of these admixtures on the heat of hydration are lower in the presence of CFA.

The obtained results may be used as an indicator for admixture selection or for the workability design of fresh mortars and concretes containing CFA. The use of P or SP allow one to effectively use CFA in concrete technology as a concrete or cement additive and thereby obtain significant environmental benefits. However, the selection of specific P or SP should always be verified experimentally while taking into account the CFA and cement's properties, as well as the specific demands of the mixture's workability and the secondary effects of the admixture.

Author Contributions: The authors declare equal participation in the research and preparation of manuscript. All authors have read and agreed to the published version of the manuscript. Conceptualization, J.G. and T.P.; methodology, T.P. and A.K.-S.; software, J.G., T.P. and A.K.-S.; validation, J.G., T.P. and A.K.-S.; formal analysis, J.G.; investigation, A.K.-S. and P.M.; resources, A.K.-S. and P.M.; data curation, A.K.-S. and P.M.; writing—original draft preparation, J.G.; writing—review and editing, T.P. and A.K.-S.; visualization, A.K.-S.; supervision, J.G.; project administration, J.G.; funding acquisition, T.P. and J.G.

Funding: This research was funded by the European Union from the European Regional Development Fund. No. POIG 01.01.02-24-005/09, Innovative cement based materials and concrete with high calcium fly ashes.

Conflicts of Interest: The authors declare no conflict of interest.

References

- Giergiczny, Z. Fly ash and slag. *Cem. Concr. Res.* **2019**, *124*, 1–18. [CrossRef]
- Baran, T.; Drozd, W. Evaluation of properties of domestic calcareous fly ash and its processing methods. *Roads Bridges Drog. Mosty* **2013**, *12*, 5–15.
- EN 197-1. *Cement—Part 1: Composition, Specifications and Conformity Criteria for Common Cements*; British Standards Institution (BSI): London, UK, 2011.
- Dziuk, D.; Giergiczny, Z.; Garbacik, A. Calcareous fly ash as a main constituent of common cements. *Roads Bridges Drog. Mosty* **2013**, *12*, 57–69.
- Giergiczny, Z.; Garbacik, A.; Ostrowski, M. Pozzolanic and hydraulic activity of calcareous fly ash. *Roads Bridges Drog. Mosty* **2013**, *12*, 71–81.
- Giergiczny, Z.; Synowiec, K.; Żak, A. Suitability evaluation of calcareous fly ash as an active mineral additive to concrete. *Roads Bridges Drog. Mosty* **2013**, *12*, 83–97.
- Czopowski, E.; Łaźniewska-Piekarczyk, B.; Rubinska-Jonczy, B.; Szwabowski, J. Properties of concretes based on cements containing calcareous fly ash. *Roads Bridges Drog. Mosty* **2013**, *12*, 31–40.
- Dąbrowska, M.; Giergiczny, Z. Chemical resistance of mortars made of cements with calcareous fly ash. *Roads Bridges Drog. Mosty* **2013**, *12*, 131–146.
- Drożdż, W.; Giergiczny, Z. The resistance of mortars and concrete with calcareous fly ash on alkaline corrosion. *Roads Bridges Drog. Mosty* **2013**, *12*, 147–158.
- Jóźwiak-Niedźwiedzka, D.; Sobczak, M.; Gibas, K. Carbonation of concretes containing calcareous fly ashes. *Roads Bridges Drog. Mosty* **2013**, *12*, 223–236.
- Gibas, K.; Glinicki, M.A.; Nowowiejski, G. Evaluation of impermeability of concrete containing calcareous fly ash in respect to environmental media. *Roads Bridges Drog. Mosty* **2013**, *12*, 157–172.
- Gołaszewski, J.; Kostrzanowska, A.; Ponikiewski, T.; Antonowicz, G. Influence of calcareous fly ash on rheological properties of cement pastes and mortars. *Roads Bridges Drog. Mosty* **2013**, *12*, 99–112.
- Panda, B.; Ruan, S.; Unluer, C.; Tan, M.J. Improving the 3D printability of high volume fly ash mixtures via the use of nano attapulgite clay. *Compos. Part B Eng.* **2019**, *165*, 75–83. [CrossRef]
- Gołaszewski, J.; Giergiczny, Z.; Ponikiewski, T.; Kostrzanowska-Siedlarz, A.; Miera, P. Effect of calcareous fly-ash processing methods on rheological properties of mortars. *Period. Polytech. Civil Eng.* **2018**, *62*, 643–652. [CrossRef]
- Giergiczny, Z. *Rola Popiołów Lotnych Wapniowych i Krzemionkowych w Kształtowaniu Właściwości Współczesnych Spoiw Budowlanych i Tworzyw Cementowych (The Role of Calcareous and Silicious Fly Ash in the Shaping of Modern Construction and Cement Binders Properties)*; Monografia, Politechnika Krakowska: Kraków, Poland, 2006. (In Polish)
- Gołaszewski, J.; Kostrzanowska-Siedlarz, A.; Ponikiewski, T.; Miera, P. Influence of Cements Containing Calcareous Fly Ash as a Main Component Properties of Fresh Cement Mixtures. *IOP Conf. Ser. Mater. Sci. Eng.* **2017**, *245*, 022099. [CrossRef]
- Gołaszewski, J.; Kostrzanowska-Siedlarz, A.; Ponikiewski, T.; Miera, P. Influence of Multicomponent and Pozzolanic Cements Containing Calcareous Fly Ash and Other Mineral Admixtures on Properties of Fresh Cement Mixtures. *IOP Conf. Ser. Mater. Sci. Eng.* **2019**, *471*, 112024. [CrossRef]
- Nowoświat, A.; Gołaszewski, J. Influence of the Variability of Calcareous Fly Ash Properties on Rheological Properties of Fresh Mortar with Its Addition. *Materials* **2019**, *12*, 1942. [CrossRef]
- Wei, S.; Handong, Y.; Binggen, Z. Analysis of mechanism on water-reducing effect of fine ground slag, high-calcium fly ash, and low-calcium fly ash. *Cem. Concr. Res.* **2003**, *33*, 1119–1125. [CrossRef]

20. Yazıcı, H. The effect of silica fume and high-volume Class C fly ash on mechanical properties, chloride penetration and freeze–thaw resistance of self-compacting concrete. *Constr. Build. Mater.* **2008**, *22*, 456–462. [CrossRef]
21. Felekoğlu, B.; Türkel, S.; Kalyoncu, H. Optimization of fineness to maximize the strength activity of high calcium ground fly ash—Portland cement composites. *Constr. Build. Mater.* **2009**, *23*, 2053–2061. [CrossRef]
22. Gołaszewski, J.; Ponikiewski, T.; Kostrzanowska, A. The influence of High Calcium Fly Ash on rheological properties of cement mixtures. In *Non-Traditional Cement & Concrete IV, Proceedings of the International Conference, Brno, Czech Republic, 27–30 June 2011*; Bilek, V., Keršner, Z., Eds.; University of Technology: Brno, Czech Republic, 2011; pp. 410–419.
23. Ponikiewski, T.; Gołaszewski, J. The influence of high-calcium fly ash on the properties of fresh and hardened self-compacting concrete and high performance self-compacting concrete. *J. Clean. Prod.* **2014**, *72*, 212–221. [CrossRef]
24. Ramachandran, V.S. *Concrete Admixtures Handbook. Properties, Science and Technology*, 2nd ed.; Noyes Publications: Park Ridge, NJ, USA, 1995; ISBN 0-8155-1373-9.
25. Gołaszewski, J. Correlation between Rheology of Superplasticized Fresh Mortars and Fresh Concretes. In *Superplasticizers and other Admixtures in Concrete, Proceedings of the 9th ACI International Conference Superplasticizers and Other Chemical Admixtures, Seville, Spain, 13–17 October 2009*; Malhotra, V.M., Ed.; American Concrete Institute (ACI): Farmington Hills, MI, USA, 2009; pp. 215–236, SP-262-16.
26. Gołaszewski, J. The influence of cement paste volume in mortar on the rheological effects of the addition of superplasticizer. In *Brittle Matrix Composites 8*; Brandt, A.M., Li, V.C., Marshall, I.H., Eds.; Woodhead Publishing: Cambridge, UK, 2007; pp. 441–450. ISBN 978-1-8456-9031-1.
27. Gołaszewski, J. Influence of cement properties on new generation superplasticizers performance. *Constr. Build. Mater.* **2012**, *35*, 586–596. [CrossRef]
28. Banfill, P.F.G. The rheology of fresh cement and concrete—A review. In *Proceeding of the 11th International Cement Chemistry Congress, Durban, South Africa, 11–16 May 2003*; pp. 50–63.
29. Banfill, P.F.G. The rheology of fresh mortar. *Mag. Concr. Res.* **1991**, *43*, 13–21. [CrossRef]
30. Norberg, J.; Peterson, O.; Billberg, P. Effects of a New Generation of Superplasticizers on the Properties of Fresh Concrete. In *Superplasticizers and other Admixtures in Concrete, Proceedings of the 5th ACI International Conference Superplasticizers and Other Chemical Admixtures, Rome, Italy, 9 January 1997*; Malhotra, V.M., Ed.; American Concrete Institute (ACI): Farmington Hills, MI, USA, 1997; pp. 583–598.
31. Helm, M.; Hornung, F. Rheological test procedure in the ready-mixed concrete bath plant. *Annu. Trans. Nord. Rheol. Soc.* **1997**, *5*, 106–108.
32. Petit, J.Y.; Khayat, K.H.; Wirquin, E. Yield stress and viscosity equations for mortars and self-consolidating concrete. *Cem. Concr. Res.* **2007**, *37*, 655–670. [CrossRef]
33. Gołaszewski, J.; Kostrzanowska-Siedlarz, A.; Cygan, G.; Drewniok, M. Mortar as a model to predict self-compacting concrete rheological properties as a function of time and temperature. *Constr. Build. Mater.* **2016**, *124*, 1100–1108. [CrossRef]
34. PN-EN 196-6:2011 Methods of testing cement. Determination of fineness.
35. ASTM C618 Standard Specification for Coal Fly Ash and Raw or Calcined Natural Pozzolan for Use in Concrete.
36. PN-EN 450-1:2012. Fly ash for concrete. Definition, specifications and conformity criteria.
37. PN-EN 196-1:2006. Methods of testing cement. Determination of strength.
38. Tattersall, G.H.; Banfill, P.F.G. *The Rheology of Fresh Concrete*; Pitman Advanced Publishing Program: Boston, MA, USA, 1983; ISBN 0-273-08558-1.
39. Roussel, N. *Understanding the Rheology of Concrete*; Woodhead Publishing: Cambridge, UK, 2011; p. 384.
40. PN-EN 1015-7:2000. Methods of test for mortar for masonry. Determination of air content of fresh mortar.
41. Gelardi, G.; Mantellato, S.; Marchon, D.; Palacios, M.; Eberhardt, A.B. Chemistry of chemical admixtures. In *Science and Technology of Concrete Admixtures*, 1st ed.; Aitcin, P.C., Flatt, R., Eds.; Woodhead Publishing: Cambridge, UK, 2016; pp. 149–218. ISBN 978-0-0810-0696-2.
42. Nkinamubanzi, P.C.; Mantellato, S.; Flatt, R.J. Superplasticizers in practice. In *Science and Technology of Concrete Admixtures*, 1st ed.; Aitcin, P.C., Flatt, R., Eds.; Woodhead Publishing: Cambridge, UK, 2016; pp. 353–377. ISBN 978-0-0810-0696-2.

43. Nocuń-Wczelik, W.; Trybalska, B. Wpływ wybranych domieszek chemicznych na szybkość hydratacji i mikrostrukturę zaczynu cementowego. *Cem. Wapno Beton* **2007**, *6*, 284–289.
44. Kurdowski, W. *Cement and Concrete Chemistry*; Springer: Berlin/Heidelberg, Germany, 2016; ISBN 9789402405941.
45. Urban, M. Wpływ wielkości strat prażenia popiołu lotnego krzemionkowego na parametry reologiczne mieszanek nowej generacji. *Cem. Wapno Beton* **2007**, *4*, 193–200.



© 2020 by the authors. Licensee MDPI, Basel, Switzerland. This article is an open access article distributed under the terms and conditions of the Creative Commons Attribution (CC BY) license (<http://creativecommons.org/licenses/by/4.0/>).

Article

Use of GRP Pipe Waste Powder as a Filler Replacement in Hot-Mix Asphalt

Ahmet Beycioğlu ¹, Orhan Kaya ¹, Zeynel Baran Yıldırım ¹, Baki Bağrıaçık ²,
Magdalena Dobiszewska ^{3,*}, Nihat Morova ⁴ and Suna Çetin ⁵

¹ Department of Civil Engineering, AAT Science and Technology University, Adana 01250, Turkey; abeycioglu@atu.edu.tr (A.B.); okaya@atu.edu.tr (O.K.); zbyildirim@atu.edu.tr (Z.B.Y.)

² Department of Civil Engineering, Çukurova University, Adana 01250, Turkey; bbagriacik@cu.edu.tr

³ Faculty of Civil and Environmental Engineering and Architecture, UTP University of Science and Technology, 85–796 Bydgoszcz, Poland

⁴ Department of Civil Engineering, Isparta University of Applied Science, Isparta 32260, Turkey; nihatomrova@isparta.edu.tr

⁵ Department of Ceramics, Çukurova University, Adana 0125, Turkey; cetins@cu.edu.tr

* Correspondence: magdalena.dobiszewska@utp.edu.pl

Received: 1 September 2020; Accepted: 12 October 2020; Published: 16 October 2020

Abstract: There is an increasing global trend to find sustainable, environmentally friendly and cost-effective materials as an alternative to limited natural raw materials. Similarly, the use of waste materials has been gaining popularity in the production of hot-mix asphalt (HMA). In this study, the sustainable use of glass-fiber-reinforced polyester (GRP) pipe waste powder (GRP-WP), gathered from the cutting and milling process of GRP pipe production, utilizing it in asphalt mixes as a filler, is evaluated based on lab testing to find out: (i) if it produces similar or better performance compared to the most conventionally available filler material (limestone) and, (ii) if so, what would be the optimum GRP-WP filler content to be used in asphalt mixes. For this reason, an experimental test matrix consisting of 45 samples with three different amounts of binder content (4%, 4.5% and 5.0%), and a 5% filler content with five different percentages of the GRP-WP content (0%, 25%, 50%, 75% and 100% replacement by weight of the filler), was prepared to figure out which sample would produce the similar Marshall stability and flow values compared to the control samples while also satisfying specification limits. It was found that the samples with 4.5% binder content, 3.75% GRP-WP and 1.25% limestone filler content produced the results both satisfying the specification requirements and providing an optimum mix design. It is believed that use of GRP-WP waste in HMA production would be a very useful way of recycling GRP-WP.

Keywords: hot-mix asphalt; GRP composite pipe; manufacturing waste powder; filler replacement; sustainability

1. Introduction

The World Bank has announced that our global waste production is increasing day by day. By 2030, the world is expected to generate 2.59 billion tons of waste annually. By 2050, the world is expected to increase its waste generation by 70 percent, from 2.01 billion tons of waste in 2016 to 3.40 billion tons of waste annually [1]. Recycling and disposal are two current waste management options [2]. When the current amounts of waste and its potential increase are considered, recycling wastes instead of disposing of them is more important for sustainability.

Asphalt concrete is one of the vital structures in terms of civil engineering and is used in very large-scale applications including roads and waterproofing due to its high resistance to durability, water resistance and good stability properties [3]. The global road network consists of more than

36 million km of unpaved and paved road network. Since this is an engineering field with such a great production potential, highway construction is a dominant industry consuming substantial amounts of natural resources, especially mineral aggregates derived from quarry extraction. In the last few decades, recycling of industrial waste materials in pavement preservation, maintenance and reconstruction has been a very popular way to achieve sustainable solutions. Billions of tons of waste materials have been produced annually around the world, and pavement applications can be one of the best ways to consume these wastes by reducing the accumulation of landfills, saving raw materials extracted from the environment and consuming lower amounts of energy [4–9].

As is well known, asphalt concrete is a composite material itself, containing asphalt cement as binder, coarse and fine aggregates and fillers [3]. In the United States and India, powder materials passing through a 0.075 mm sieve are defined as fillers, while in Europe, powder materials passing through a 0.063 mm sieve are classified as fillers [9]. Despite being used in limited concentrations, the inclusion of fillers in asphalt mix has significant influences on the properties of asphalt mixes. As a result of a comprehensive literature review, Choudhary et al. [9] summarized the benefits of using fillers in the asphalt mix as follows: satisfying the aggregate gradation specification and influencing the strength and volumetric requirements of the mix; reducing optimum bitumen content and material cost of the mix; stiffening bitumen to improve the mechanical properties of the mix and increasing not only the ability of mixes to resist permanent deformation at high temperatures but also cracking resistance at low temperatures and fatigue life at intermediate temperatures; influencing the “bond” in the aggregate–bitumen system, which further affects the moisture sensitivity of the mix; slowing down the aging process of asphalt mixes by either catalyzing oxidation or by hindering the diffusion of oxygen in mastic; influencing the thermal performance of asphalt mixes; affecting the constructability of a mix by influencing its mixing and compaction temperature. Hence, the choice of suitable filler is a primary concern amongst field engineers [10–22].

The conventional mineral fillers are directly supplied by mining from natural resources. The filler is a material that is consumed continuously as it is one of the basic materials used in asphalt road construction. This continuous use may even cause difficulties in material supply in some regions, leading to the imposition of restrictions on mining in several regions and reducing the availability of good-quality aggregates at shorter haul distances. If this situation is evaluated in terms of the overall cost of projects, providing the aggregates from longer distances increases their transportation cost as well as the overall cost of pavement constructions. Recycling the waste materials as fillers by using them in place of conventional fillers looks very effective for sustainability practices in pavement construction.

The concept of sustainability is very important and no natural materials are unlimited. For this reason, it will always be desirable to find affordable and environmentally friendly alternative materials in asphalt mixtures. Moreover, studies on the use of waste materials in asphalt mixes will be very valuable to meet the demands of the various agencies’ environmental rating systems (such as LEED and BREEAM, which are the construction project certification programs that signify a certain level of environmentally friendly design achievement of a building) [4]. The current literature shows that the use of waste materials in pavement designs has been studied for many years. Especially, the waste materials used as fillers include tire-derived fuel fly ash [23], rice husk ash [24,25], recycled waste lime [26], andesite waste [27], fly ash [28], red mud waste [29], construction and demolition waste, brick powder [30], Kota Stone [31], bauxite residue [32] and waste glass powder [33], etc. The reutilization of the fine glass-fiber-reinforced polyester (GRP) powder as a partial cement replacement, partial fine aggregate replacement and filler addition for self-compacting concrete, as well as its influence on the durability of the cementitious products, has already been widely exploited [34–41]. However, there are not many studies found in the literature investigating the use of GRP waste as a filler in asphalt mixes [42].

GRP using thermosetting resins is increasingly utilized for a wide range of applications, such as transportation, construction and energy. Indeed, the diversity in the manufacturing, possibilities ranging from unidirectional laminates to randomly oriented fiber compounds and their attractive

mechanical properties make these materials very appealing [43]. The GRP industry by way of the manufacturing process produces considerable quantities of waste materials such as fibers, polymers, particle pipe powder, etc., and to landfill such solid wastes would cause a major environmental hazard.

According to the literature, there is no clear statistical information on the amount of pipe powder that emerged in GRP pipe manufacturing. The GRP factory which supported this research reported that the amounts of pipe powder (PP) produced in its manufacturing were 31.89 tons in 2015, 41.22 tons in 2016, 73.1 in 2017, 134.42 tons in 2018 and 1333.62 tons until October in 2019.

One of the biggest problems in the GRP pipe industry is waste recycling. The variety of solutions for recycling GRP manufacturing wastes with effective technologies is increasing as landfilling these wastes has negative environmental impacts [44–46]. Reducing the waste by mechanical, thermal and chemical approaches has been implemented by various industrial sectors [47]. Industrial companies have to focus on industrial scale composite recycling to improve acceptable waste management solutions to meet the expectations of sustainability [48,49].

The waste management of GRP materials, particularly those made with thermosetting resins, is a critical issue for the composites industry because these materials cannot be reprocessed. Therefore, most thermosetting GRP waste is presently sent to landfills, in spite of the significant environmental impact caused by their disposal in this way. The limited GRP waste recycling worldwide is mostly due to its intrinsic thermosetting properties, lack of characterization data and the unavailability of viable recycling and recovery routes.

In this study, sustainable use of glass-fiber-reinforced polyester pipe waste powder (GRP-WP), utilizing them in asphalt mixes as fillers, will be evaluated based on lab testing to find out: (i) if it produces similar or better performance compared to the most conventionally available filler material (limestone) and, (ii) if so, what would be the optimum GRP-WP filler content to be used in asphalt mixes. It is believed that the use of GRP-WP waste in asphalt mixes would be a very useful way of recycling the huge amount of GRP pipe waste powders. Considering the existence of a wide variety of industrial sectors and the potential hazards posed by the wastes, the potential use of waste in hot-mix asphalt or other engineering materials should continue to be explored for many years to come.

2. Materials and Methods

2.1. Materials

In this study, crushed limestone aggregates obtained from a quarry located in the southern region of Turkey, namely from Adana Province, that have been commonly used in asphalt pavement applications, were used. In terms of gradation of the mix, a coarse aggregate of 58%, passing between 25–4.75 mm sieves, a fine aggregate of 37%, passing between 4.75–0.075 mm sieves, and a filler of 5% were used. Sieve analysis results of the mix was within the limits specified by Turkish Highway Construction Specifications (HTS) [50]. Table 1 shows sieve analysis results of the mix used in this study as well as the specification limits.

Physical, mechanical and durability properties of the aggregates used in this study were also determined based on American (ASTM) standards (Table 2).

As part of this study, along with limestone-based coarse and fine aggregates, GRP-WP (Figure 1), a waste material produced during the cutting and milling of GRP pipes, was used as a replacement for filler in different ratios. In order to use GRP-WP as filler, GRP-WP was first sieved through a 0.075 mm sieve and the powder passing through the sieve was used as filler in asphalt mixes.

Table 1. Gradation and specification limits.

Sieve Diameter (mm)	Limit Values (HTS) % Passing [50]	Gradation of Mixture % Passing	Weight (g)
25 mm	100	100	0
19 mm	80–100	91.0	103.0
12.5 mm	58–80	67.5	270.9
9.5 mm	48–70	59.9	86.8
4.75 mm	30–52	42.1	205.5
2.00 mm	20–40	26.0	185.3
0.425 mm	8–22	11.0	172.3
0.180 mm	6–14	7.4	41.4
0.075 mm	2–7	5.0	27.3
Filler	0	0	57.5
Total	100%	100%	1150

Table 2. Physical, mechanical and durability properties of aggregates.

Properties	Results	Tests Standards
Specific gravity (g/cm^3)		
Coarse aggregate	Apparent specific gravity	2.771
	Bulk specific gravity	2.729
Fine aggregate	Apparent specific gravity	2.766
	Bulk specific gravity	2.646
Filler	Bulk specific gravity	2.778
	Dry rodded unit weight (g/cm^3)	1.914
Unit weight (bulk density) (g/cm^3)	1.725	ASTM C 29
Abrasion loss (%) (Los Angeles)	26.12	ASTM C 131
Flatness index (%)	14.65	ASTM D 4791
Resistance to disintegration by sulfate (weight loss %)	4.67	ASTM C 88



(a)



(b)

Figure 1. (a) Cutting and (b) milling process of GRP pipes.

GRP-WP and its scanning electron microscopy (SEM) image are shown in Figure 2. As can be seen in Figure 2, the SEM image reveals that GRP-WP contains a considerable amount of micro-sized chopped glass fibers (CGF). Considering these micro-CGFs, one of the motivations of this study was that GRP-WP would be a good candidate to be used as filler, potentially improving the performance of asphalt concretes.

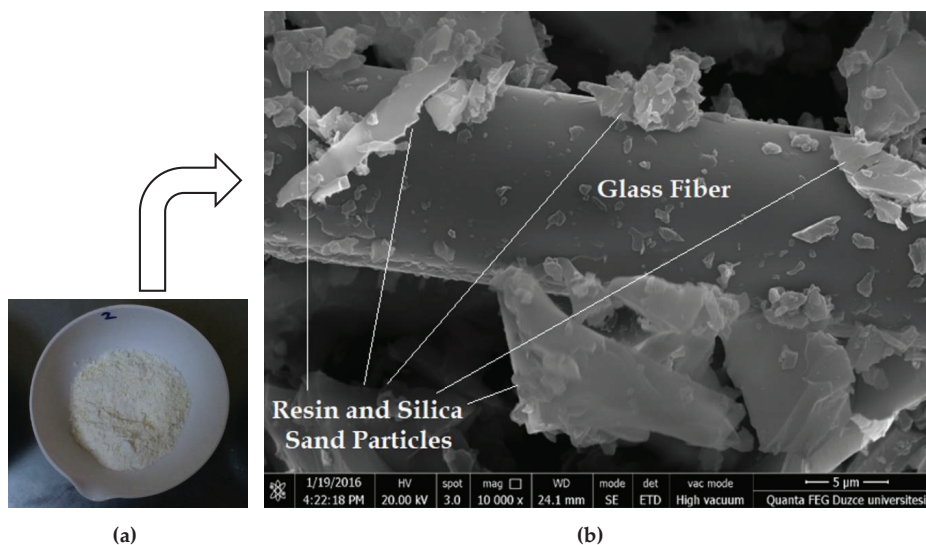


Figure 2. (a) GRP-WP and (b) SEM image of GRP-WP.

To prepare the Marshall samples, an asphalt binder with a 50–70 penetration grade (found as 58 in this study) was used. The physical properties of this binder are provided in Table 3.

Table 3. Physical properties of the asphalt binder.

Properties	Results	Test Standards
Source of the Binder	Kırkkale, Turkey	-
Penetration Grade (25 °C)	58 (50/70)	ASTM D 5
Softening Point (°C)	48.5	ASTM D 36/D 36 M
Specific Gravity (g/cm ³)	1.040	ASTM D 70–09 e 1
Ductility (25 °C)	>100 cm	ASTM D 113–07
Loss on Heating (%)	0.43	ASTM D 6–95
Flash Point (°C)	280	ASTM D 92–05 a
Viscosity (at 135 °C, cP)	430.23	ASTM D 4402–06
Viscosity (at 165 °C, cP)	120.95	ASTM D 4402–06

2.2. Methodology

In this study, asphalt concrete samples were prepared by using various amounts of binder content (3.5%, 4%, 4.5%, 5% and 5.5%) and 5% filler content, based on the limits specified by HTS [49]. For each binder content amount, three samples were prepared, making a total of 15 samples (3 × 5). All the produced samples were tested based on Marshall stability (MS) test (ASTM D 6927) and stability, flow as well as bulk specific gravity (Gsb), air content (Va), voids in mineral aggregate (VMA) and voids filled with asphalt (VFA) results were obtained so that optimum binder content could be determined (Figure 3a–f).

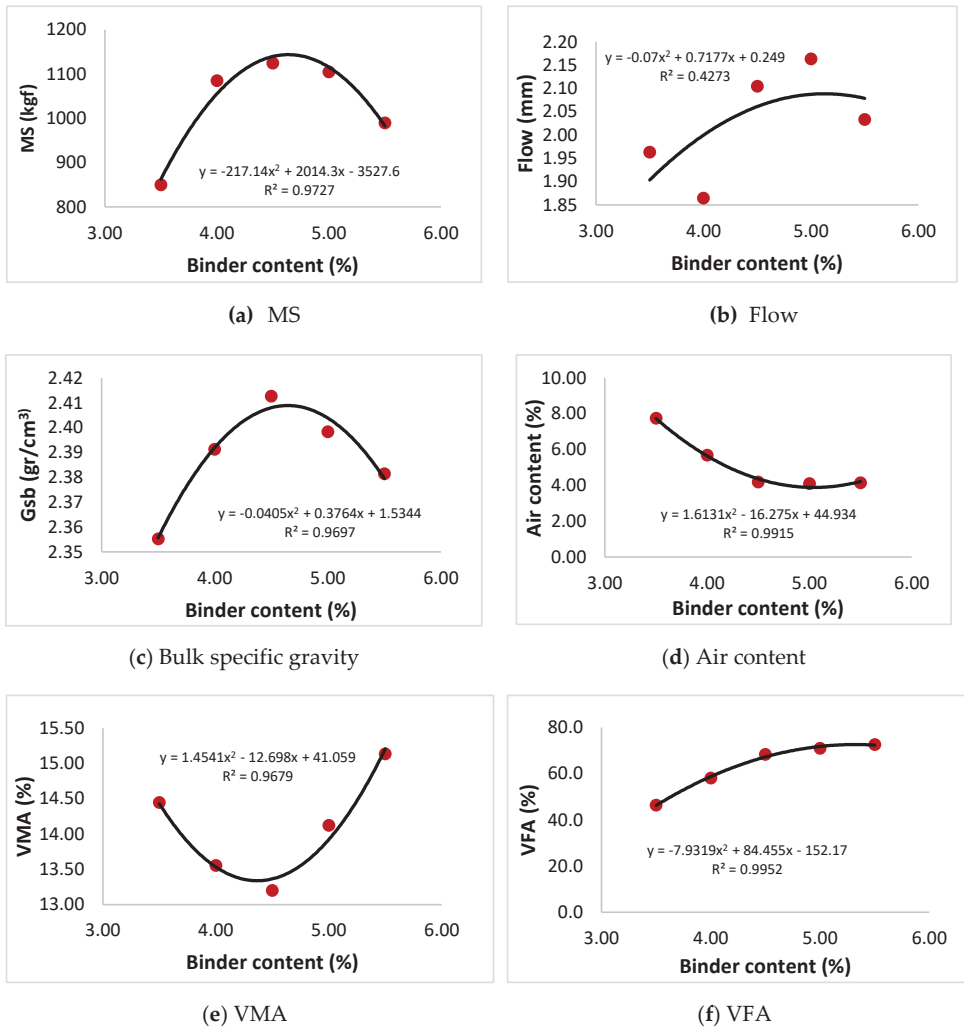


Figure 3. Test results for various binder content values.

The optimum binder content for the mix design was determined by taking the average value of the four binder content amounts obtained based on the following criteria and the graphs shown in Figure 3.

1. Binder content corresponding to the maximum stability (found as 4.64 for MS = 1143)
2. Binder content corresponding to the maximum bulk specific gravity (found as 4.65 for Gsb = 2409).
3. Binder content corresponding to the median value of the specification design limits of air content in the total mix (found as 4.21 for Va = 5%) [50].
4. Binder content corresponding to the median value of the specification design limits of VFA in the total mix (found as 4.51 for VFA = 67.5%) [50].

Based on the criteria above, the optimum binder content was calculated as:

$$\frac{(4.64 + 4.65 + 4.21 + 4.51)}{4} = 4.45\% \tag{1}$$

Thereafter, an experimental test matrix consisting of 45 samples with three different amounts of binder content (4%, 4.5% and 5.0%) and a 5% filler content with five different amounts of GRP-WP content (0%, 25%, 50%, 75% and 100% filler replacement) was prepared to determine which sample would produce the highest Marshall stability and flow values as well as satisfying specification limits (Table 4). As can be seen in Table 4, the control sample contained only limestone as filler while other samples contained GRP-WP in different ratios as a replacement for limestone filler. The samples containing GRP-WP were named pipe powder asphalt concrete (PPAC) (Table 4).

Table 4. Experimental test matrix used in this study.

Sample Name	Aggregates %			Limestone in Filler (%)	GRP-WP in Filler (%)
	Coarse	Fine	Filler		
Control Sample	60	35	5	5	0
PPAC 1	60	35	5	3.75	1.25
PPAC 2	60	35	5	2.5	2.5
PPAC 3	60	35	5	1.25	3.75
PPAC 4	60	35	5	0	5

3. Results

In this part of the paper, 45 Marshall samples explained in Table 4 are tested for Marshall stability (MS), flow, VMA, VFA and Va. Figure 4 shows mean values of the MS results along with the standard deviation distributions for the samples tested. As can be seen in Figure 4, the highest MS value was obtained for the samples with 2.5% GRP-WP and 2.5% limestone (LS) filler content. MS results tend to increase as GRP-PP content increases until a GRP-WP content of 2.5% is reached, and then they start to decrease. Moreover, the highest MS value of 1373.9 kgf was observed for the sample with 4% binder content, 2.5% GRP-WP and 2.5% LS filler content, whereas the lowest MS value of 939.4 kgf was observed for the sample with 4.5% binder content, 5% GRP-WP and no LS filler content. Compared to the control samples, all samples except for the samples with 5% GRP-WP and no LS filler content produced higher MS values.

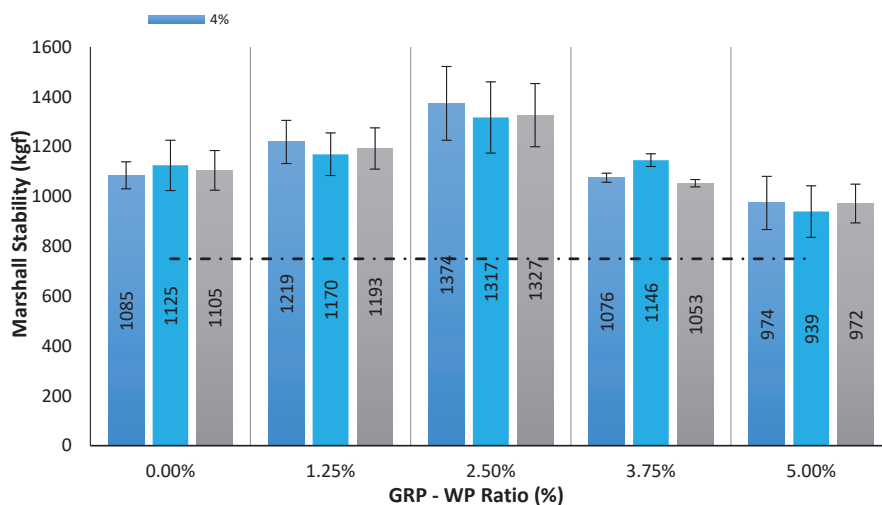


Figure 4. Comparison of MS results for the 45 samples tested.

In Turkey, all state highways under the jurisdiction of the General Directorate of Highways are designed to consist of three stabilized layers (an asphalt wear course at the very top, another asphalt

layer (called a binder course) underneath it and an asphalt stabilized base course under the binder course) and a granular subbase course laying on a subgrade. Overall, considering the MS test results, all 45 samples were found to produce adequate MS values to meet the strength requirement needed for binder courses [50].

The flow value is a measure evaluating the behavior of asphalt mixes subjected to traffic loadings and representing the plasticity and elasticity properties of the mixes. Furthermore, the flow value, the vertical deformation value at the maximum load, is a parameter related to the internal friction and cohesion of the compacted asphalt mixes, where it is inversely proportional to the internal friction value [51]. Figure 5 shows mean values of the flow results along with the standard deviation distributions for the samples tested. As can be seen in Figure 5, the lowest flow value was obtained as 1.22 mm for the sample with 4% binder content, 5% GRP-WP and no LS filler content, while the highest flow value was obtained as 2.04 mm for the sample with 4.5% binder content, 3.75% GRP-WP and 1.25% LS filler content. HTS [50] requires asphalt mixes to have at least 2 mm flow value to be used in binder courses. It was observed that the samples with 4.5% and 5% binder content and 3.75% GRP-WP and 1.25% LS filler content as well as the control samples with 4% and 4.5% binder content produced sufficient flow value to meet the specification limits (Figure 5).

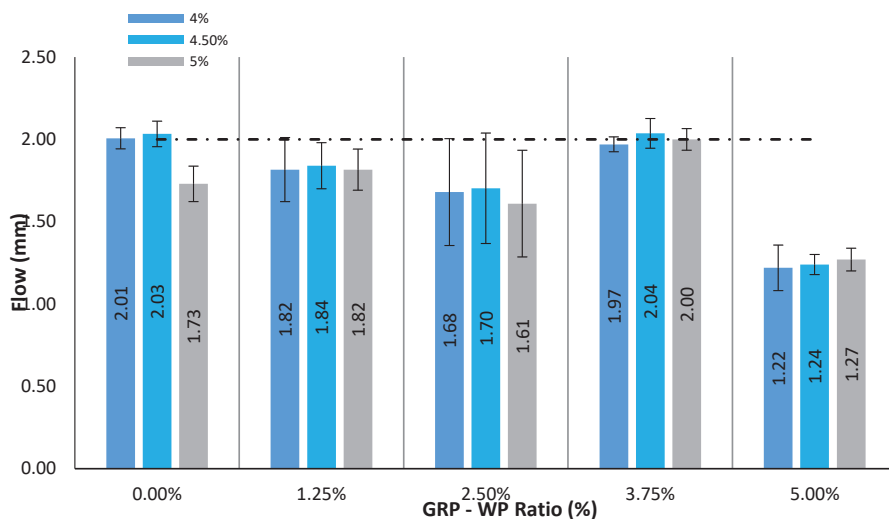


Figure 5. Comparison of flow results for the 45 samples tested.

Figure 6 shows mean values of the VMA results along with the standard deviation distributions for the samples tested. As can be seen in Figure 6, VMA results were found to increase as GRP-WP content increased. While VMA results of the control samples were in the range of 12.92% to 14.60%, VMA results of the samples with GRP-WP fillers linearly increased as GRP-WP content increased, reaching its maximum value of 16.27% for the sample with 5% binder content, 5% GRP-WP and no LS filler content. Compared to the control samples, VMA results of the samples with 5% GRP-WP and no LS filler content increased by 19.97%, 18.90% and 11.44% for the binder content amounts of 4%, 4.5% and 5%, respectively.

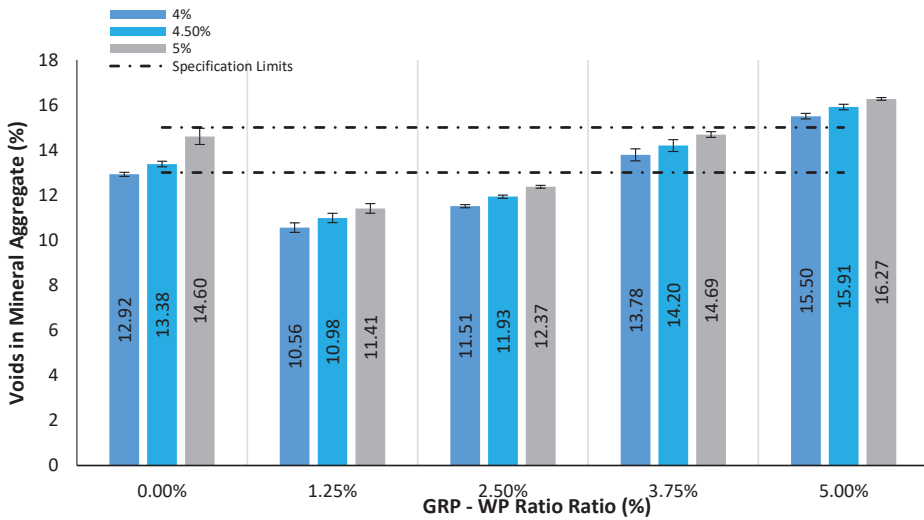


Figure 6. Comparison of VMA results for the 45 samples tested.

Figure 7 shows mean values of the VFA results along with the standard deviation distributions for the samples tested. As can be seen in Figure 7, VFA results tend to decrease as GRP-WP content increases. While VFA results of the control samples with 4%, 4.5% and 5% binder content were 61.51%, 67.38% and 68.33%, respectively, they decrease as GRP-WP content increases, reaching its minimum value for the samples with 5% GRP-WP and no LS filler content. VFA results of the samples with 5% GRP-WP and no LS filler content and 4%, 4.5% and 5% binder content were found to be 49.74%, 55.01% and 60.15%, respectively.

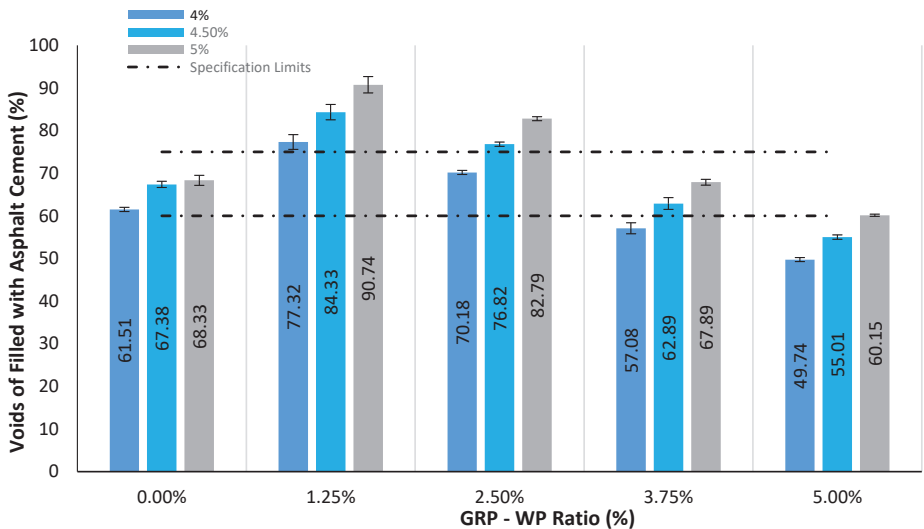


Figure 7. Comparison of VFA results for the 45 samples tested.

Figure 8 shows mean values of the air content (Va) results along with the standard deviation distribution results for the samples tested. As can be seen in Figure 8, Va results tend to increase as GRP-WP content increases. Moreover, Va results of the control samples with 4%, 4.5% and 5% binder

content were 4.97%, 4.36% and 4.63%, respectively. It was observed that Va results increase as GRP-WP content increases. However, Va results of the control samples were between those of the samples with 2.5% GRP-WP and 2.5% LS filler content and 3.75% GRP-WP and 1.25% LS filler content. Furthermore, Va results of the samples with 5% GRP-WP and no LS filler content and 4%, 4.5% and 5% binder content were 7.79%, 7.16% and 6.48%, respectively. Samples with the Va results within the limits of the specification were as follows: all control samples and all samples with 3.75% GRP-WP and 1.25% LS filler content. However, no samples with 5% GRP-WP and no LS filler content amounts were found to meet the Va requirements [50].

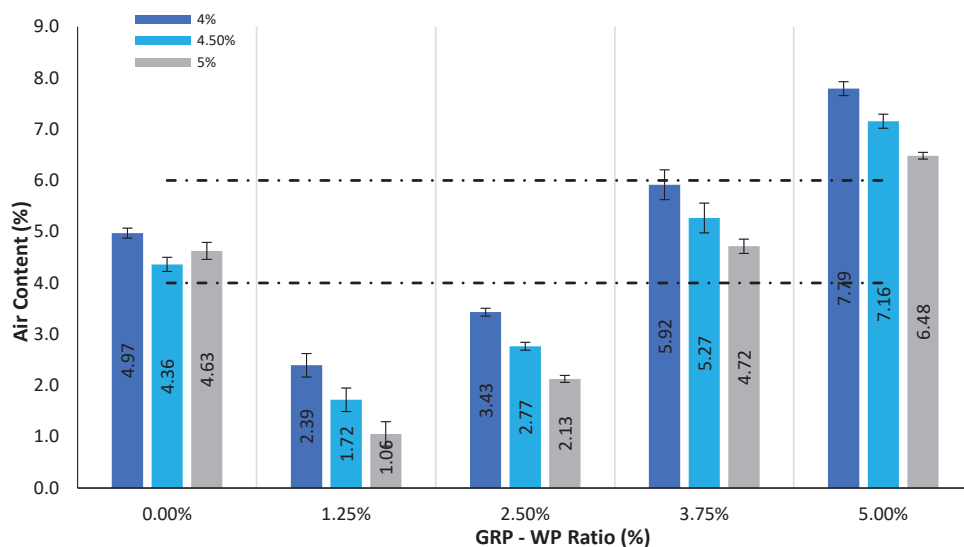


Figure 8. Comparison of air content (Va) results for the 45 samples tested.

4. Discussion and Conclusions

In this study, the potential use of GRP-WP as a filler was evaluated. First, the optimum binder content was determined for the asphalt mixes with 5% filler content fully composed of LS fillers. The optimum binder content was calculated as 4.5% by taking the average value of corresponding binder content amounts producing maximum values of MS and Gsb as well as median values of specification limits for Va and VFA (Va value of 5% and VFA value of 67.5%). Then, an experimental test matrix consisting of 45 samples with three different amounts of binder content (4%, 4.5% and 5.0%), and a 5% filler content with five different percentages of GRP-WP content (0%, 25%, 50%, 75% and 100% replacement by weight of the filler), was prepared in order to determine which sample would produce the highest Marshall stability while satisfying specification limits for flow and volumetric results. Considering the all test results for MS, flow, VMA, VFA and Va, it was observed that the samples with 4.5% binder content, 3.75% GRP-WP and 1.25% LS filler content produced the results both satisfying the specification requirements and providing an optimum mix design.

The main objective of this study was to identify if GRP-WP, a waste material, could be used as a filler replacement by evaluating if it produces similar performance compared to the LS filler. In this way, a sustainable, environmentally friendly and cost-effective use of this material could be found. One of the ways to evaluate if a mixture provides similar performance is to compare the MS and flow results of the mixtures with the control samples. MS is measure of strength in asphalt mixtures. Higher values of MS results of the asphalt mixtures are desirable in order to show that they resist showing and rutting [51]. Therefore, a minimum MS value is specified for the asphalt mixtures, considering the level of traffic the mixture is designed for. In terms of flow results, the maximum allowable flow

values in the specifications control the plasticity and maximum allowable binder content, while the lowest flow values control the brittleness and strength of the mixes [51]. Therefore, it is required that the flow results of the asphalt mixtures must be between the lower and upper specification limits. Overall, it was found that the samples prepared with GRP-WP filler replacement produced similar MS and flow values compared to the control samples as well as satisfying the specification limits, except for the case when all LS fillers were replaced with GRP-WP. The samples with 5% GRP-WP and no LS filler produced consistently poorer performance compared to the control samples. One of the main objectives of this study was satisfied in that there was no significant loss of performance of the samples with GRP-WP, except for the case with 5% GRP-WP and no LS filler, compared to the control samples.

In order to identify how GRP-WP filler replacement changes the micro-structure and behavior of the mix, scanning electron microscope (SEM) images of the asphalt mixes were also analyzed. It is known that GRP is a well-designed high-performance composite containing glass fiber, silica sand and polyester resin in its structure [48]. Having these materials in its structure, GRP is a very well-interlocked and tightly bonded material. It is known that when mixed with asphalt binder, filler and asphalt binder creates a filler–asphalt mastic, a high-consistency matrix, cementing larger aggregate particles together and so affecting the mechanical and physical properties of the asphalt mixtures [52]. GRP-WP contains a considerable amount of micro-size chopped glass fibers (CGF), silica sand particles and polyester resin particles on the CGF's surface. When it is mixed with asphalt binders, due to its fibrous properties, it might have produced a stiff mastic that binds aggregate particles together and produces a mixture with a similar performance as the mixtures with LS fillers. This might explain why the samples with GRP-WP exhibited similar MS and flow values compared to the control samples.

Numerous studies showed that there are correlations between volumetric properties of the mixes and their performance [53,54]. The durability of an asphalt mixture is highly affected by its V_a . Too low V_a may lead to flushing, whereas too high V_a might cause water damage and rutting in the mixtures. On the other hand, VMA shows the amount of space needed to accommodate the effective volume of binder and the volume of air voids needed in the asphalt mixture. In order to achieve a durable binder film thickness, a minimum VMA value is required [53]. VFA, the total amount of voids between aggregate particles in the compacted mixture that are filled with asphalt binder, is specified to avoid less durable asphalt mixes. It was also shown that a decrease in V_a and increase in VFA are some of the ways to reduce the cracking potential of the mixtures [54]. In order to produce a well-performing asphalt mixture, all volumetric properties of the mixes must satisfy corresponding specification limits.

There was a general trend among the samples with GRP-WP that as GRP-WP content increases, VMA and V_a results increase but VFA results decrease. Higher V_a results with increasing GRP-WP content might be due to the lower level of adsorption and chemical exchange between silica and asphalt, causing more free binder in the mixtures [55]. In other words, as found by some other studies [4], GRP-WP has lower porosity compared to LS. Lower porosity of GRP-WP causes lower absorbance of bitumen in the mixture, leading to more free binder in the mixtures. Therefore, as GRP-WP filler content increases, the amount of free binder in the mixture increases, causing the higher level of V_a of the mixes [4,55]. In order to solve this issue, an optimum asphalt binder content could be determined for each GRP-WP filler content to avoid excessive V_a .

It was also observed during the compaction of the mixtures that even though the same number and level of Marshall hammer blows were used in all samples, a noticeable decrease in the level of compaction occurred as GRP-WP content increased. Zulkati et al. [13] demonstrated that stiffened asphalt–filler mastic produces a tougher mix that is hard to compact. The role of filler in the asphalt–binder mastic is that fillers act as tiny rollers during the compaction, similar to the role of friction-lubricate agents, given that they have regular and spherical shapes. The asphalt–filler mastic with regular-shaped fillers, such as LS [13], leads to a faster and smoother orientation of the larger aggregates, causing less compaction resistance. As discussed earlier based on Figure 2, the SEM image of the GRP-WP reveals that GRP-WP contains a considerable amount of micro-sized chopped glass fibers (CGF). Due to the irregular shapes of these CGFs, they have significantly longer lengths

compared to their widths, and they might have negatively impacted the workability of the asphalt mixtures, causing a reduction in compaction, as discussed by several other studies, such as those presented by Melotti et al. [56] and Wróbel et al. [57]. Resistance to compaction might be one of the main reasons why Va results increase as GRP-WP content increases. A similar trend was observed in some other studies that [58,59] reduction in compaction might cause an increase in Va.

It was observed in this study that the samples with 5% GRP-WP content with no LS filler exhibited significantly higher levels of Va and VMA as well as significantly lower levels of VFA compared to the control samples. As a result, the same samples produced significantly lower MS and flow results compared to the control samples. This shows that the volumetric properties of the samples are one of the key factors in determining the performance of asphalt mixtures.

Volumetric properties of asphalt mixtures are related to each other. VFA is inversely related to Va and VMA: as Va and VMA increase, the VFA decreases. This is why, as GRP-WP content increases, Va and VMA results increase but VFA results decrease [58].

This study demonstrated that GRP-WP, a sustainable material, could be successfully used as a filler replacement, not only satisfying speciation limits but also performing as well as an LS filler when it is used in its optimum content. It is believed that use of GRP-WP waste in asphalt mixes would be a very useful way of recycling the huge amount of GRP pipe waste powders. Therefore, it is imperative that, like any other newly introduced material, a systematic study like this study should be carried out to find out its optimum content and identify if it produces as successful performance as its conventionally available counterpart, such as LS in this case. Considering the existence of a wide variety of industrial sectors and the potential hazards posed by the wastes, the potential use of waste in asphalt concrete or other engineering materials should continue to be explored for many years to come.

Author Contributions: A.B.: funding acquisition, conceptualization, formal analysis, writing—review and editing; O.K.: formal analysis, conceptualization, supervision, writing—review and editing; B.B.: investigation, methodology, experimental works, writing; M.D.: conceptualization, formal analysis, writing—review and editing; Z.B.Y.: investigation, methodology, experimental works, writing; N.M.: supervision, conceptualization, writing—review and editing; S.C.: formal analysis, experimental works, writing. All authors have read and agreed to the published version of the manuscript.

Funding: This research received no external funding.

Acknowledgments: This article has been supported by the Polish National Agency for Academic Exchange under Grant No. PPI/APM/2019/1/00003. The authors would like to thank to Superlit Pipe Industry Inc. for providing the glass-fiber-reinforced polyester (GRP) pipe waste powder (GRP-WP).

Conflicts of Interest: The authors declare no conflict of interest. The funders had no role in the design of the study; in the collection, analyses, or interpretation of data; in the writing of the manuscript, or in the decision to publish the results.

References

1. Urban Development USA. A Global Snapshot of Solid Waste Management to 2050. Washington, DC, USA. Available online: <https://openknowledge.worldbank.org/handle/10986/30317> (accessed on 10 May 2020).
2. Hassan, H.F. Recycling of municipal solid waste incinerator ash in hot-mix asphalt concrete. *Constr. Build. Mater.* **2005**, *19*, 91–98. [CrossRef]
3. Loaiza, A.; Colorado, H.A. Marshall stability and flow tests for asphalt concrete containing electric arc furnace dust waste with high ZnO contents from the steel making process. *Constr. Build. Mater.* **2018**, *166*, 769–778. [CrossRef]
4. Choudhary, J.; Kumar, B.; Gupta, A. Application of waste materials as fillers in bituminous mixes. *Waste Manag.* **2018**, *78*, 417–425. [CrossRef] [PubMed]
5. Singh, S.K.; Rekha, P.; Surya, M. Utilization of Linz–Donawitz slag from steel industry for waste minimization. *J. Mater. Cycles Waste Manag.* **2020**, *22*, 611–627. [CrossRef]
6. Jahanbakhsh, H.; Karimi, M.M.; Naseri, H.; Nejad, F.M. Sustainable asphalt concrete containing high reclaimed asphalt pavements and recycling agents: Performance assessment, cost analysis, and environmental impact. *J. Clean. Prod.* **2020**, *244*, 118837. [CrossRef]

7. Aljassar, A.H.; Al-Fadala, K.B.; Ali, M.A. Recycling building demolition waste in hot-mix asphalt concrete: A case study in Kuwait. *J. Mater. Cycles Waste Manag.* **2005**, *7*, 112–115. [CrossRef]
8. Xiaodan, C.; Wang, H. Life cycle assessment of asphalt pavement recycling for greenhouse gas emission with temporal aspect. *J. Clean. Prod.* **2018**, *187*, 148–157.
9. Choudhary, J.; Kumar, B.; Gupta, A. Laboratory evaluation on recycling waste industrial glass powder as mineral filler in hot mix asphalt. In Proceedings of the Civil Engineering Conference—Innovation for Sustainability, Hamirpur, India, 9–10 September 2016; pp. 352–359.
10. Wang, T.; Xiao, F.; Zhu, X.; Huang, B.; Wang, J.; Amirkhani, S. Energy consumption and environmental impact of rubberized asphalt pavement. *J. Clean. Prod.* **2018**, *180*, 139–158. [CrossRef]
11. Wei, Y.; Chai, J.; Qin, Y.; Xu, Z.; Zhang, X. Performance evaluation of green-concrete pavement material containing selected C&D waste and FA in cold regions. *J. Mater. Cycles Waste Manag.* **2019**, *21*, 1550–1562.
12. Aljassar, A.H.; Metwali, S.; Ali, M.A. Effect of filler types on marshall stability and retained strength of asphalt concrete effect of filler types on marshall stability and retained strength of asphalt concrete. *Int. J. Pavement Eng.* **2016**, *5*, 47–51. [CrossRef]
13. Zulkati, A.; Diew, W.; Delai, D. Effects of Fillers on Properties of Asphalt-Concrete Mixture. *J. Transp. Eng.* **2012**, *138*, 902–910. [CrossRef]
14. Faheem, A.; Cloutier, C.; Bautista, E.G.; Sobolev, K. Impact of Coal Combustion Product Incorporation in Asphalt Mixture Performance. In Proceedings of the 97th Annual Meeting of Transportation Research Board, Washington DC, USA, 8–12 January 2017.
15. Wang, H.; Al-Qadi, I.; Faheem, A.; Bahia, H.; Yang, S.H.; Reinke, G. Effect of mineral filler characteristics on asphalt mastic and mixture rutting potential. *Trans. Res. Rec. J. Transp. Res. Board* **2011**, *2208*, 33–39. [CrossRef]
16. Airey, G.D.; Liao, M.C.; Thom, N.N. Fatigue behaviour of bitumen-filler mastics. In Proceedings of the 10th International Conference on Asphalt Pavements, Quebec City, QC, Canada, 12–17 August 2006; pp. 485–495.
17. Modarres, A.; Bengar, P.A. Investigating the indirect tensile stiffness, toughness and fatigue life of hot mix asphalt containing copper slag powder. *Int. J. Pavement Eng.* **2017**, *20*, 977–985. [CrossRef]
18. Pasandín, A.R.; Pérez, I. The influence of the mineral filler on the adhesion between aggregates and bitumen. *Int. J. Adhes. Adhes.* **2015**, *58*, 53–58. [CrossRef]
19. Anderson, D.A.; Goetz, W.H. Mechanical behavior and reinforcement of mineral filler-asphalt mixes. *Proc. Assoc. Asph. Paving Technol.* **1973**, *42*, 37–66.
20. Gubler, R.; Liu, Y.; Anderson, D.A.; Partl, M.N. Investigation of system and asphalt binders by rheological means. *J. Asph. Paving Technol.* **1999**, *68*, 284–304.
21. Recasens, R.M.; Martínez, A.; Jiménez, F.P.; Bianchetto, H. Effect of filler on the aging potential of asphalt mixtures. *Trans. Res. Rec. J. Trans. Res. Board* **2005**, *1901*, 10–17. [CrossRef]
22. Chen, M.Z.; Lin, J.T.; Wu, S.P.; Liu, C.H. Utilization of recycled brick powder as alternative filler in asphalt mixture. *Constr. Build. Mater.* **2011**, *25*, 1532–1536. [CrossRef]
23. Matos, P.; Micaelo, R.; Duarte, C.; Quaresma, L. Influence of bitumen and filler on the selection of appropriate mixing and compaction temperatures. *Int. J. Pavement Res. Technol.* **2014**, *7*, 237–246.
24. Choi, M.J.; Kim, Y.J.; Kim, H.J.; Lee, J.J. Performance evaluation of the use of tire-derived fuel fly ash as mineral filler in hot mix asphalt concrete. *J. Traffic Transp. Eng.* **2020**, *7*, 249–258. [CrossRef]
25. Al-Hdabi, A. Laboratory investigation on the properties of asphalt concrete mixture with rice husk ash as filler. *Constr. Build. Mater.* **2016**, *12*, 544–551. [CrossRef]
26. Sargin, Ş.; Saltan, M.; Morova, N.; Serin, S.; Terzi, S. Evaluation of rice husk ash as filler in hot mix asphalt concrete. *Constr. Build. Mater.* **2013**, *48*, 390–397. [CrossRef]
27. Do, H.S.; Mun, P.H.; Keun, R.S. A study on engineering characteristics of asphalt concrete using filler with recycled waste lime. *Waste Manag.* **2008**, *28*, 191–199.
28. Uzun, İ.; Terzi, S. Evaluation of andesite waste as mineral filler in asphaltic concrete mixture. *Constr. Build. Mater.* **2012**, *31*, 284–288. [CrossRef]
29. Woszuk, A.; Bandura, L.; Franus, W. Fly ash as low cost and environmentally friendly filler and its effect on the properties of mix asphalt. *J. Clean. Prod.* **2019**, *520*, 493–502. [CrossRef]
30. Zhang, J.; Sun, C.; Li, P.; Liang, M.; Yao, Z. Experimental study on rheological properties and moisture susceptibility of asphalt mastic containing red mud waste as a filler substitute. *Constr. Build. Mater.* **2019**, *211*, 159–166. [CrossRef]

31. Antunes, A.C.; Freire, L.; Micaelo, Q.R. Evaluation of waste materials as alternative sources of filler in asphalt mixtures. *Mater. Struct.* **2017**, *50*, 254. [CrossRef]
32. Singh, S.; Choudhary, J.; Kumar, B.; Gupta, A. Effects of Using Kota Stone as Filler on Mechanical Properties of Asphalt Concrete Mixes. In *Recent Developments in Waste Management, Lecture Notes in Civil Engineering*; Kalamdhad, A., Ed.; Springer: Singapore, 2020; Volume 57, pp. 249–259.
33. Choudhary, R.; Kumar, A.; Rahman, G. Rheological and mechanical properties of bauxite residue as hot mix asphalt filler. *Int. J. Pavement Res. Technol.* **2019**, *12*, 623–631. [CrossRef]
34. Howarth, J.; Mareddy, S.S.; Mativenga, P.T. Energy intensity and environmental analysis of mechanical recycling of carbon fibre composite. *J. Clean. Prod.* **2014**, *81*, 46–50. [CrossRef]
35. Tittarelli, F.; Moriconi, G. Durability of cementitious products made with blended cements based on GRP industrial waste. In Proceedings of the Atti del VII Congresso Nazionale AIMAT, Associazione Italiana d'Ingegneria dei Materiali, Ancona, Italy, 29 Giugno–2 Luglio 2004.
36. Tittarelli, F.; Moriconi, G. Re-use of GRP industrial waste in cementitious products. In *Young Researchers' Forum, Proceedings of the 6th International Congress on Global Construction: Ultimate Concrete Opportunities*. Dundee, Scotland, 5–7 July 2005; Dhir, R.K., Halliday, J.E., Csetenyi, E., Eds.; Thomas Telford: London, UK, 2005; pp. 153–164.
37. Tittarelli, F.; Moriconi, G. Effect of GRP industrial waste on durability of cement mortars. In *Sustainable Construction Materials and Technologies, Proceedings of the First International Conference*. Coventry, UK, 11–13 June 2007; Chun, Y.M., Claisse, P., Naik, T.R., Ganjian, E., Eds.; Taylor & Francis/Balkema: Leiden, The Netherlands, 2007; pp. 35–39.
38. Tittarelli, F.; Moriconi, G. Re-use of GRP industrial by-product as filler for SCC. In Proceedings of the SCC2008: Challenges and Barriers to Application, The Third North American Conference on the Design and Use of Self-Consolidating Concrete, Chicago, IL, USA, 10–12 November 2008.
39. Tittarelli, F.; Moriconi, G. Use of GRP industrial by-products in cement based composites. *Cem. Concr. Compos.* **2019**, *32*, 219–225. [CrossRef]
40. Tittarelli, F.; Moriconi, G.; Pauri, M.G.; Favoni, O. Re-use of GRP industrial waste in new blended cements. In Proceedings of the Atti del VII Congresso Nazionale AIMAT, Associazione Italiana d'Ingegneria dei Materiali, Ancona, Italy, 29 Giugno–2 Luglio 2004; Volume 43.
41. Osmani, M.; Pappu, A. Utilisation of Glass Reinforced plastic waste in concrete and cement composites. In Proceedings of the Second International Conference on Sustainable Construction Materials and Technologies, Ancona, Italy, 28–30 June 2010.
42. Coffey, D.; Sanders, M.; Steuerwald, G. System and Method for Recycling Scrap Fiberglass Products in Concrete and Asphalt Construction. U.S. Patent 2004/0132842 A1, 8 July 2014.
43. Asthana, G.; Choudhary, J.; Kumar, B.; Gupta, A. Experimental Investigation of Waste Glass Powder as Filler in Asphalt Concrete Mixes. In *Recent Developments in Waste Management, Lecture Notes in Civil Engineering*; Kalamdhad, A., Ed.; Springer: Singapore, 2020; Volume 57, pp. 261–270.
44. Beauson, J.; Bech, J.; Brondsted, P. Composite recycling: Characterizing end of life wind turbine blade material. In Proceedings of the 19th International Conference on Composite Materials, Montreal, QC, Canada, 28 July–2 August 2013.
45. Jacob, A. Composites can be recycled. *Reinf. Plast.* **2011**, *55*, 45–46. [CrossRef]
46. Liu, Y.; Farnsworth, M.; Tiwari, A. A review of optimization techniques used in the composite recycling area: State-of-the-art and steps towards a research agenda. *J. Clean. Prod.* **2017**, *140*, 1775–1781. [CrossRef]
47. Oliveux, G.; Bailleul, J.L.; La Salle, E.L.G. Chemical recycling of glass fibre reinforced composites using subcritical water. *Compos. Part A Appl. Sci. Manuf.* **2012**, *43*, 1809–1818. [CrossRef]
48. Mazzoli, A.; Moriconi, G. Particle size, size distribution and morphological evaluation of glass fiber reinforced plastic (GRP) industrial by-product. *Micron* **2014**, *67*, 169–178. [CrossRef] [PubMed]
49. Mikhailenko, P.; Kakar, M.R.; Piao, Z.; Bueno, M.; Poulikakos, L. Incorporation of recycled concrete aggregate (RCA) fractions in semi-dense asphalt (SDA) pavements: Volumetrics, durability and mechanical properties. *Constr. Build. Mater.* **2020**, *264*, 120166. [CrossRef]
50. General Directorate of Highways. *State Highways Technical Specifications (HTS)*; General Directorate of Highways: Ankara, Turkey, 2006.
51. Umar, F.; Ađar, E. *Pavement Structure*; Istanbul Technical University Civil Engineering Faculty Press: Istanbul, Turkey, 1991.

52. Nciri, N.; Shin, T.; Lee, H.; Namjun, C. Potential of Waste Oyster Shells as a Novel Biofiller for Hot-Mix Asphalt. *Appl. Sci.* **2018**, *8*, 415. [CrossRef]
53. Hislop, W.P.; Coree, B.J. VMA as a design parameter in hot mix asphalt. In *Mid-Continent Transportation Symposium*; Iowa State University: Ames, IA, USA, 2000.
54. Zhang, W.; Shen, S.; Wu, S.; Chen, X.; Xue, J.; Mohammad, L. Effects of in-place volumetric properties on field rutting and cracking performance of asphalt pavement. *J. Mater. Civ. Eng.* **2019**, *31*, 04019150. [CrossRef]
55. Simone, A.; Mazzotta, F.; Eskandarsefat, S.; Sangiorgi, C.; Vignali, V.; Lantieri, C.; Dondi, G. Experimental application of waste glass powder filler in recycled dense-graded asphalt mixtures. *Road Mater Pavement Des.* **2019**, *20*, 592–607. [CrossRef]
56. Melotti, R.; Santagata, E.; Bassani, M.; Salvo, M.; Rizzo, S. A preliminary investigation into the physical and chemical properties of biomass ashes used as aggregate fillers for bituminous mixtures. *Waste Manag.* **2013**, *33*, 1906–1917. [CrossRef]
57. Wróbel, M.; Wozuk, A.; Franus, W. Laboratory Methods for Assessing the Influence of Improper Asphalt Mix Compaction on Its Performance. *Materials* **2020**, *13*, 2476. [CrossRef]
58. Chen, H.; Xu, Q.; Chen, S.; Zhang, Z. Evaluation and design of fiber-reinforced asphalt mixtures. *Mater. Des.* **2008**, *30*, 2595–2603. [CrossRef]
59. Morova, N. Investigation of usability of basalt fibers in hot mix asphalt concrete. *Constr. Build. Mater.* **2013**, *47*, 175–180. [CrossRef]

Publisher’s Note: MDPI stays neutral with regard to jurisdictional claims in published maps and institutional affiliations.



© 2020 by the authors. Licensee MDPI, Basel, Switzerland. This article is an open access article distributed under the terms and conditions of the Creative Commons Attribution (CC BY) license (<http://creativecommons.org/licenses/by/4.0/>).

Article

The Chemical-Mineralogical Characterization of Recycled Concrete Aggregates from Different Sources and Their Potential Reactions in Asphalt Mixtures

Edgar H. Sánchez-Cotte ¹, Carlos Albeiro Pacheco-Bustos ², Ana Fonseca ², Yaneth Pineda Triana ³, Ronald Mercado ⁴, Julián Yepes-Martínez ^{2,*} and Ricardo Gabriel Lagares Espinoza ²

¹ Facultad Tecnológica, Universidad Distrital Francisco José de Caldas, Cl. 68D Bis A Sur, Bogotá 49F-70, Colombia; esanchez@udistrital.edu.co

² División de Ingeniería, Universidad del Norte-km 5 Vía Puerto Colombia, Barranquilla, Colombia; cbustosa@uninorte.edu.co (C.A.P.-B.); fonsecama@uninorte.edu.co (A.F.); lagaresr@uninorte.edu.co (R.G.L.E.)

³ Facultad de Ingeniería, Universidad Pedagógica y Tecnológica de Colombia, Avenida Central del Norte 39-115, Tunja 150003, Colombia; yaneth.pineda@uptc.edu.co

⁴ Grupo de Investigación en Fenómenos Interfaciales, Reología y Simulación de Transporte (FIRST), Universidad Industrial de Santander, Cl. 9 Bucaramanga, Cra 27 Santander, Bucaramanga, Colombia; ramerca@uis.edu.co

* Correspondence: juliany@uninorte.edu.co

Received: 5 November 2020; Accepted: 20 November 2020; Published: 8 December 2020

Abstract: The incorporation of a recycled concrete aggregate (RCA) as a replacement of natural aggregates (NA) in road construction has been the subject of recent research. This tendency promotes sustainability, but its use depends mainly on the final product's properties, such as chemical stability. This study evaluates the physical and chemical properties of RCAs from two different sources in comparison with the performance of NA. One RCA was obtained from the demolition of a building (recycled concrete aggregate of a building—RCAB) and another RCA from the rehabilitation of a Portland cement concrete pavement (recycled concrete aggregate from a pavement—RCAP). Characterization techniques such as X-ray fluorescence (XRF), X-ray diffraction (XRD), UV spectroscopy, and atomic absorption spectrometry were used to evaluate the RCAs' coarse fractions for chemical potential effects on asphalt mixtures. NA was replaced with RCA at 15%, 30%, and 45% for each size of the coarse fractions (retained 19.0, 12.5, 9.5, and 4.75 sieves in mm). The mineralogical characterization results indicated the presence of quartz (SiO₂) and calcite (CaCO₃) as the most significant constituents of the aggregates. XFR showed that RCAs have lower levels of CaO and Al₂O₃ concerning NA. Potential reactions in asphalt mixtures by nitration, sulfonation, amination of organic compounds, and reactions by alkaline activation in the aggregates were discarded due to the minimum concentration of components such as NO₂, (–SO₃H), (–SO₂Cl), and (Na) in the aggregates. Finally, this research concludes that studied RCAs might be used as replacements of coarse aggregate in asphalt mixtures since chemical properties do not affect the overall chemical stability of the asphalt mixture.

Keywords: recycled concrete aggregate (RCA); natural aggregates (NA); chemical characterization

1. Introduction

Waste generation during the execution of construction activities (construction and demolition waste—CDW) has prompted researchers from several countries to develop projects aimed at making construction waste reuse viable [1–5]. A material that can form part of this waste is Portland cement concrete

(PCC), which, when crushed, is transformed into a recycled concrete aggregate (RCA). Re-incorporating an RCA into the productive cycle reduces its final disposal volume and the exploitation of quarry to obtain stone materials. Waste minimization complies with the principles of efficiency and Sustainable Development Goals 7, 12, and 13, promulgated by the United Nations—the UN. However, RCAs differ in some physical, chemical, and mechanical properties in relation to natural aggregates (NA), mostly due to the presence of bonded mortar [6]. The presence of mortar, which originates at a weaker interfacial zone between the binder and RCA, increases the porosity and water absorption of RCAs, and also reduces their strength and mechanical performance when used in the production of asphalt mixtures [7]. In Figure 1, the different conformations of RCA are shown, taking into account the fractionation due to the crushing process. These conformations indicate that the structure of the RCA is heterogeneous since it can be made up of natural aggregate, mortar, or a combination of both.

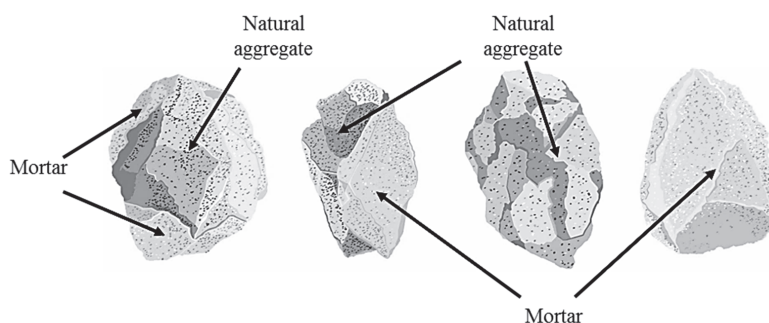


Figure 1. Typical conformations of the recycled concrete aggregate (RCA).

Standard physical and mechanical laboratory tests for checking the quality of NA are used to evaluate RCAs and their potential performances in asphalt mixtures [8,9]. However, the study of the chemical and mineralogical properties of RCAs provides further information about the phenomena occurring in mixtures of RCAs and other materials [10]. Besides, the chemical laboratory tests evaluate the presence of undesirable substances or elements in these aggregates, such as chlorides, sulfates, carbonates, and the contaminants absorbed from their original project sources [6,8,9].

The chemical and mineralogical compositions of RCAs are varied and do not follow a general pattern in terms of its elements, compounds, and concentrations due to the various RCA sources and the different dosages of their original concrete components [6,8,11]. Further, the chemical composition of RCAs has not been researched extensively [6,8], which makes it challenging to achieve a standardized procedure for their use [12]. On the other hand, studies highlight the importance of applying image analysis to determine aspects such as residual mortar after the use of RCAs in concrete mixtures, estimation of porosity distribution, and degradation characteristics within concrete [13–15].

Cement is a constituent of PCC. Cement has a significant effect on the chemical composition of an RCA because cement is present in the attached mortar, which is considered the weakest part of PCC. Cement is produced from mineral materials such as limestone and gypsum, an alumina base, and silica naturally found as clay or shale [16]. Limestone, which is the cement base, is composed of 60% calcium carbonate (CaCO_3) and the rest (40%) include clay, silica, and dolomite. However, RCAs can contain salts formed from potassium (K) and cobalt (Co), and potassium (K) and iron (Fe), which can cause aging in asphalt pavements, as they can oxidize asphalt cement [17]. Based on the chemical and mineralogical composition, the following concepts from previous investigations explain the effects of RCAs on asphalt mixtures: (a) The presence of salts in the aggregate indicates that there is a higher electrical conductivity. Therefore, a lower electrical resistivity makes the aggregate susceptible to the penetration of chloride ions when embedded in concrete [16,17]. (b) When there are manganese salts in the aggregates, and the aggregates enter into contact with air, an oxidizing effect occurs in the asphalt cement, generating premature aging [17]. (c) The presence of iron oxides

can cause aging and deterioration of the asphalt pavement when catalytic reactions are generated in the asphalt cement [18,19]. (d) The presence of magnesium in a mineral form called periclase can cause a volume increase in contact with water, owing to its hygroscopic property, causing stresses on the internal structure [20]. (e) The carbonates of calcium and magnesium (dolomites) are prone to generate an alkali-carbonate expansive reaction through the dedolomitization process. This process forms brucite $Mg(OH)_2$ and regenerates the alkaline hydroxide in the concrete. Generally, $Mg(OH)_2$ formation weakens the cement paste junction and the porous zone in the periphery of the aggregate, which generates hygroscopic characteristics and affects its physical properties. (f) The regeneration of the alkali ion $(OH)^-$ in a solution makes dedolomitization a continuous process that can affect the recycled aggregates, since it produces an increase in volume and possible generation of fissures [21], hence the need to incorporate aggregates with low alkaline reactivity [22]. (g) The carbonation process occurs when the concrete is exposed to atmospheric contaminants, which favors the appearance of microfractures. It reduces the material strength due to the cycles of crystallization and carbonation expansion related to the alternate wetting and drying of the material [23]. (h) The different conditions and environmental factors to which the RCA concrete is exposed to during its useful life are other factors that can cause weakening and increase porosity. These exposures tend to favor chloride and sulfate attacks [16]. (i) A property of the RCA that affects the adherence behavior with asphalt cement is pH [24,25]. Adhesion is favored at a higher pH (alkaline), as is the case for limestone aggregates. Adhesion decreases when the aggregates are acidic or neutral, such as aggregates containing aluminates and silica (i.e., basalts or granites).

Based on the information presented above, Table 1 summarizes the results of physical property tests, and Table 2 summarizes the results of XRF tests reported by several researchers. The results of these tests depend on the RCA sources.

Table 1. Summary of the literature review on the results of RCA physical properties tests.

Reference	Test				
	Specific Gravity Bulk (Fine Aggregate)	Specific Gravity Bulk (Coarse Aggregate)	LA Abrasion Test (%)	Absorption of Fine Aggregate, <4 mm (%)	Absorption of Coarse Aggregate (>4 mm) (%)
[26]	2.37	2.45–2.48	32–38	7.9	3.9–4.1
[27]	2.092	2.412	22	–	–
[28]	2.63	2.63	34	6.1	6.1
[29]	2.32	2.32	32	4.9	4.9
[30]	2.591	2.591	33.6	6.91	6.91
[31]	2.32	2.32	32.3	8.52	4.88
[32]	2.28	2.28	31	5.8	5.8

Table 2. Summary of the literature review on the results of the XRF test.

Reference	XRF Test									
	SiO ₂	CaO	Al ₂ O ₃	Fe ₂ O ₃	Na ₂ O	MgO	SO ₃	K ₂ O	TiO ₂	MnO
[33]	42.95–38.65	22.8–19.24	8.85–7.26	3.63–3.09	1.06–0.94	5.11–4.63	–	1.6–1.31	0.39–0.29	0.15–0.12
	68.4	5.8	11.2	3.3	1.7	1	0.2	3.2	–	–
[8]	68.6	6.5	10.2	3.3	1.6	1.2	0.3	2.8	–	–
	65.3	8.2	10.1	3.3	1.4	1.6	0.2	2.6	–	–
	65.6	8.8	9.3	3.2	0.9	1.2	0.2	2.7	–	–
[11]	58.29	13.27	7.69	6.12	1.45	2.28	0.92	0.8	0	0.16
[34]	62.56	12.01	12.52	5.82	2.69	1.83	–	1.3	0.62	0.12

To understand more about the chemical and physical behavior of RCAs in asphalt, it was necessary to carry out some laboratory tests to identify their relationships.

RCA has been investigated in various proportions, sizes, and fractions as a replacement for NA in asphalt mixtures. However, the performance results obtained for the mixtures do not show a tendency to affirm acceptable behavior when RCA is included. The design characteristics of the mixture containing recycled concrete, and the mineralogy of its aggregates, mark the properties of RCAs such as density, absorption, and wear [35]. The replacement ratio affects the behavior of the resulting concrete. In general, the aggregates are subjected to physical and mechanical tests to evaluate

the quality of the aggregates used in asphalt mixtures. However, as mentioned earlier, there are chemical and mineralogical characteristics that affect these mixtures.

Reference [9], reported the mineralogy of RCA in different areas of Portugal, with predominant results of quartz, calcite, K feldspar, and sodium feldspar; they also identified a high concentration of polluting species such as chlorides and sulfates that were not suitable for RCAs to be reused [9].

Reference [33] provided important data to be considered in the development of correct recycling strategies, based on the chemical and mineralogical compositions of different granulometric fractions of RCAs [8]. Reference [6] identified that replacements up to 30% of coarse RCAs in concrete mixtures do not influence the chemical composition in terms of the main components (SiO_2 , Al_2O_3 , and CaO), revealing a direct correlation between the chemical composition of solids and the leaching of ions through ICP-AE analysis of eluates. That highlighted the importance of a correct characterization of the leaching behavior of these new materials [33]. Given the importance of the chemical characterization of RCAs, the present study aimed to analyze the chemical properties of RCAs from two demolition sources in an area of the Colombian Caribbean and a source of NA (recycled concrete aggregate of a building—RCAB; recycled concrete aggregate from a pavement—RCAP; natural aggregate—NA) to evaluate their potential influences on the behavior of asphalt mixtures. This should make a contribution to the knowledge about the characterization of these concrete residues according to the area to which they are exposed within their useful lives. Chemical stability was analyzed from the concentrations of the reactants that could be involved in potential asphalt–mineral reactions. The study presents an alternative approach that involves the chemical properties of RCAs as a criterion for defining the behavior of asphalt mixtures. The samples were evaluated by different techniques to identify the properties of the NA and RCAs (RCAP and RCAB). The characterization tests carried out were: X-ray fluorescence spectrometry (XRF), diffraction spectrometry, X-ray diffraction (XRD), soluble ion analysis by UV–Vis spectrophotometry, atomic absorption analysis, loss on ignition (LOI), determination of mass, percentage of organic impurities, and pH. Figure 2 shows the flow chart used to characterize, analyze, and evaluate the properties of the NA, RCAB, and RCAP aggregates for use in asphalt mixtures.

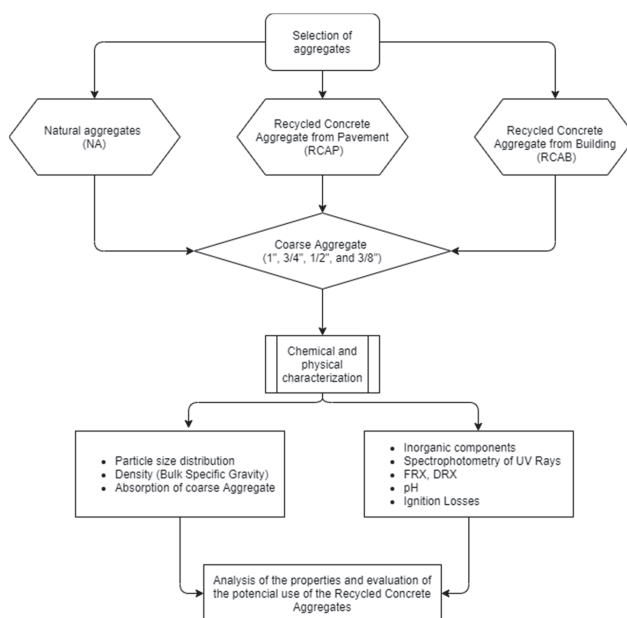


Figure 2. Flow chart of the study plan.

2. Materials and Methods

2.1. Materials

The aggregates were obtained from three different sources: a natural commercial aggregate of the research area (NA), an aggregate from the demolition of a concrete road (RCAP), and an aggregate from the demolition of a building (RCAB). The natural aggregate (NA) is representative of the typical materials used in the Department of Atlántico (municipality of Arroyo de Piedra), Barranquilla, Colombia. The RCAP was sourced from the reconstruction of the PCC pavement of the access road to the area port of Barranquilla, Avenida Hamburgo. The RCAB originated from the demolition of the Tomás Arrieta Stadium, in Barranquilla, Colombia. The crushing was carried out at a company plant dedicated to the exploitation and commercialization of stone aggregates located in the area of study. The grain size distribution of all the aggregates followed the Colombian technical specifications for highway construction [36] for an HMA-25 (nominal maximum aggregate size—NMAS—of 25 mm). The analyzed aggregates were coarse fractions. To evaluate the physical, chemical, and mineralogical properties of the aggregates, the following tests were carried out.

2.2. Physical Characterization

2.2.1. Particle Size Distribution

One of the fundamental characteristics of aggregates to be used in asphalt mixtures is related to the distribution of aggregate particle sizes. The granulometric range to be obtained by combining the different fractions must be selected to avoid segregation, and thus, guarantees the levels of compaction and strength required. RCAs replace NA in different percentages according to the characteristics of the aggregates. It is, therefore, necessary to generate combinations for optimizing the substitution percentages and obtaining the best functional behavior. Table 3 shows the size distribution ranges of the aggregates (NA and RCA).

Table 3. Distribution size of HMA-25 [36].

HMA-25	Sieve (mm)	25	19	12.5	9.5	4.75	2	0.425	0.18	0.075
% pass	Upper Limit	100	95	85	77	59	45	25	17	8
	Lower Limit	100	80	67	60	43	29	14	8	4

The size obtained after the crushing process is related to the type and technology of the machinery used, and the aggregate gradation parameter. Figure 3 shows the processes of collecting, crushing, sifting, and storing used in obtaining the aggregates (NA, RCAP, and RCAB). Figure 4 displays the size distribution of the aggregates.



Figure 3. Crushing processes to obtain the RCA.



Figure 4. Crushed size distribution of the recycled concrete aggregate from a pavement.

In Table 4, it is possible to observe the percentage distribution for each material used in the granulometric spindle with NA and the mixtures, including RCAs, in different percentages of coarse and fine sizes (mass replacement).

Table 4. Aggregate mixes.

Sieve (mm)	Fraction	100% NA	85% NA–15% RCA		70% NA–30% RCA		55% NA–45% RCA	
			NA %	RCA %	NA %	RCA %	NA %	RCA %
19	Coarse	14	11.9	2.1	9.8	4.2	7.7	6.3
12.5		17	14.5	2.6	11.9	5.1	9.4	7.7
9.5		8.5	7.2	1.3	6	2.6	4.7	3.8
4.75		10	8.5	1.5	7	3	5.5	4.5
NS	Fine	4	4	0	4	0	4	0
NWS		43	43	0	43	0	43	0
Filler	–	3.5	3.5		3.5		3.5	

Note: NS = natural sand, NWS = natural washed sand.

2.2.2. Density, Relative Density (Specific Gravity), and Absorption of Coarse Aggregate

The technique used to establish the mass ratio (dry to the furnace, saturated superficially dry, and submerged), and to measure the relative density and absorption of the coarse aggregate followed the ASTM C 127-07 standard, which indicates how to measure the masses of the aggregates in the mentioned conditions, and how to establish the corresponding relationships between them.

2.3. Chemical Characterization

2.3.1. Ignition losses

The loss ignition technique was used to determine the organic and inorganic fractions of the RCAs [16]: 550 °C for the organic matter content and 1000 °C for the inorganic fractions of the samples. The samples were prepared according to NTC-ISO 11464 requirements. This methodology involves different stages: 1. Selection and sample preparation. 2. Drying of the sample according to ASTM D 2216-10 (method A) for 24–36 h in a JeioTech Model 55 L oven. 3. Ignition of the sample at 550 °C for 4 h in a Vulcan S, Model 550 muffle, in which the organic matter was gasified, resulting in a difference from the original weight. 4. Final ignition continued at 1000 °C for 2 h more, in which the inorganic carbon was gasified, and the new weight and difference were determined using a Precisa Model 180A analytical balance.

2.3.2. pH

pH is essential because it has a direct effect on the reaction with the asphalt, altering the ideal conditions. NTC-ISO 11464 and NTC 5264-2008 (method A) standards were followed to determine the pH values. Samples weighing 10.0 g each were diluted in a 1.0:1.2 ratio after obtaining dense

mixtures with 1.0: 1.0 ratios; the samples were manual mixed, and two replicates were made for the trials. For the tests, 25 mL beakers were used. A multi-parameter equipment WTW brand model Multi 3420 was used to obtain the conductivity, pH, and temperature measurement in compliance with NTC 5264-2008 standard.

The chemical composition of the RCA was determined by X-ray fluorescence (XRF) of the coarse fraction particle sizes (retained 19.0, 12.5, 9.5, and 4.75 sieves in mm), which were crushed until they passed through sieve #200 (<0.075 mm). Semi-quantitative and semi-qualitative analysis were carried out using a PANalytical Minipal2 spectrometer, with a source of rhodium radiation and energy parameters of 1 to 30 keV.

The elemental content of the RCA was determined by atomic absorption spectrometry, using samples having sizes less than 44 μm (Sieve #200). The samples were treated by digestion with an acid mixture according to EPA 3051A in a microwave digester Mars 6 under standard methods SM: 3030E, 3111B, 3111D for elemental analysis in Shimadzu 7000 flame atomic absorption spectrometer.

The concentrations of SO_4^{2-} , Cl^- , NO_3^- , and PO_4^{3-} ions present in the RCA were determined by the turbidimetric method (EPA 9038), standard method 4500-Cl-B, cadmium reduction (EPA-353.3), and the ascorbic acid method (EPA 365.1), respectively. Subsequently, the Hach DR 6000 visible UV spectrophotometer was read.

2.4. Mineralogical Characterization

The mineralogical composition of each RCA was determined by X-ray diffraction (XRD), with 10.0 g samples, which were crushed until they passed through sieve #200 (<0.075 mm). Effervescence tests and magnetic field tests were carried out. A Phillips x'pert pro PANalytical diffractometer was used with CuK α radiation (40 kV and 35 mA) at 2 θ -angular within a range of 10°–80° with a 0.5 s/step sweep speed. The analysis was carried out through the X'pert High Score plus[®] program, taking the diffraction patterns of the Inorganic Crystal Structure Database (ICSD) as the reference.

3. Results and Discussion

3.1. Physical Characterization

3.1.1. Particle Size Distribution

The particle size distribution of coarse aggregate materials plays an important role in the design and performance of asphalt mixtures. The coarse fraction was defined considering that, in general, the fine fraction of the RCA has higher absorption and lower density compared to the coarse fraction [28], since the optimum asphalt content (OAC) will increase to a lesser extent [12]. Figure 5 displays the particle size-distribution curves of the coarse fractions of NA, RCAP, and RCAB. The particle sizes of the three materials were not within the limits of HMA-25, which indicates that the NA and RCAs should be combined with the fine fraction and filler to meet the specifications.

3.1.2. Density and Absorption

Although the regulations do not establish maximum values of absorption or minimum density, it is convenient to avoid highly absorbent aggregates in asphalt mixtures [37]. Some authors consider highly absorbing aggregates as those that exceed 5% water absorption; for instance: in Belgium, the maximum absorption allowed for coarse aggregate is 10%, while in Japan, it is 7% [38]. Table 5 presents the values of the density and water absorption of the aggregates within the coarse size fractions for NA, RCAP, and RCAB. When the aggregate size decreases, its absorption increases due to the larger surface area, and its specific gravity decreases owing to the smaller quantity of mortar as a consequence of the crushing. It is also observed that RCA has higher absorption and lower density than NA; the mixtures manufactured with RCA will have a higher OAC (optimum asphalt content).

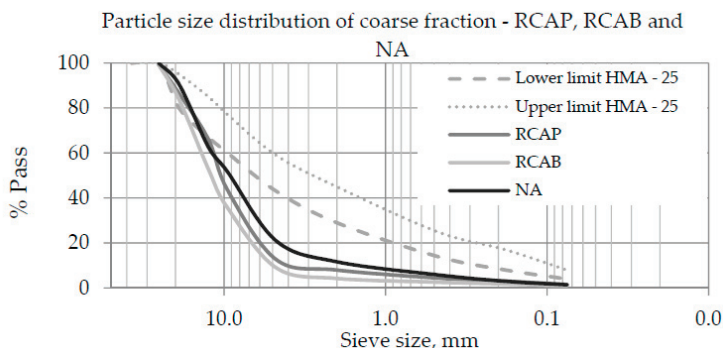


Figure 5. Particle size distribution curves of the coarse fractions of the recycled concrete aggregate from a pavement, aggregate from the demolition of a building (RCAB), and natural aggregate (NA).

Table 5. Specific gravity and water absorption of coarse NA, RCAP, and RCAB.

Sieve Size (mm)	NA		RCAP		RCAB	
	Specific Gravity	Water Absorption (%)	Specific Gravity	Water Absorption (%)	Specific Gravity	Water Absorption (%)
25.0–19.0	2.671	1.105	2.342	4.663	2.306	5.95
19.0–12.5	2.669	1.11	2.338	4.9	2.302	6.257
12.5–9.5	2.671	1.139	2.278	5.604	2.281	6.423
9.5–4.75	2.641	1.202	2.258	6.074	2.275	6.617

3.2. Chemical Characterization

3.2.1. Loss of Ignition (550 °C and 1000 °C)

The coarse fractions of the aggregates were characterized based on their weight loss when subjected to 550 °C and 1000 °C. These ignition losses were directly related to the organic matter content and thermal decomposition of the aggregates. When the test was performed at 550 °C, the moisture evaporated, and the organic material was volatilized. Figure 6 shows the mass loss at 550 °C for the 19.0 mm, 12.5 mm, 9.5 mm, 4.75 mm, and 2.0 mm sieve sizes. It can be noticed that recycled aggregates experienced greater weight loss than the natural aggregate. We affirm that the RCAB and the RCAP have higher contents of volatile organic material (VOM). This higher content was directly related to the longer environmental exposure time of the recycled aggregates. As for the RCAB, the VOM and humidity contents ranged from 3.18% to 3.80%, with a tendency to increase when the particle size decreased. For RCAP, these contents ranged between 3.45% and 3.78%. By comparing these results with those of the natural aggregate, the amount of VOM was about 1% to 2% lower in NA.

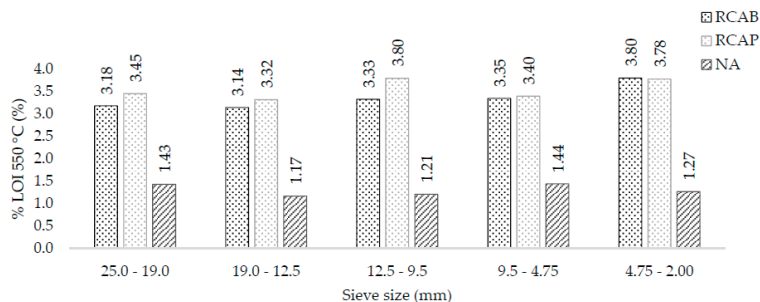


Figure 6. LOI550 °C of NA, RCAP, and RCAB by size.

Ignition losses at 1000 °C initially involved the evaporation of moisture from the aggregates, followed by the vaporization of VOM. Above 900 °C, decomposition reactions of the carbonates present in the aggregates were produced. This test gives an idea of the content of dolomite and other carbonate minerals, such as ankerite. Figure 7 presents the mass loss at 1000 °C in each of the 19.0, 12.5, 9.5, 4.75, and 2.0 mm sieve sizes. The ignition loss at 1000 °C was around 20% to 25% for the RCA, and between 7% and 8% for the NA. This difference reflects on the origins of both materials. Regardless of whether the recycled aggregates had been exposed to environmental effects, their origin appeared to be different from that of the NA. It is possible to say that the content of the carbonated minerals (mainly dolomite) was higher in the RCAs, which can be evidenced by the XRD tests. Besides, the mineralogy of the RCA seemed to be similar, presenting equivalent carbonate contents of calcium, magnesium, and manganese, whereas the NA had higher silicate content. Therefore, the results indicate that the chemical stability of RCA will not be compromised, although from the mineralogical point of view, the difference may imply a change in mechanical behavior.

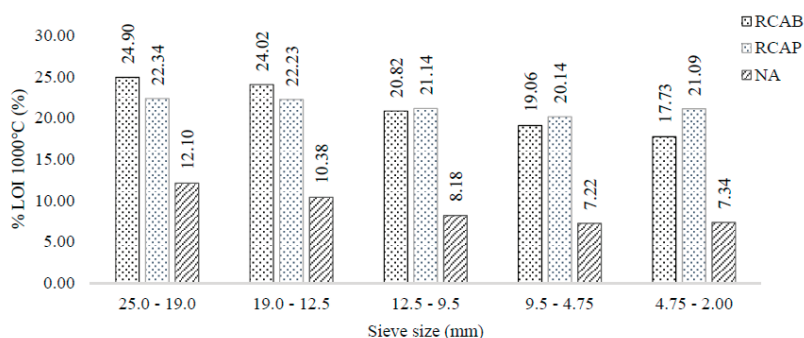


Figure 7. LOI 1000 °C of NA, RCAP, and RCAB by size.

3.2.2. pH of NA, RCAP, and RCAB

As seen in Figure 8, both the NA and RCA indicated alkaline pH values. However, RCAs did not exhibit a statistically significant difference with 95% confidence in the pH as the particle size changed, whereas the NA tended to have lower pH with the decrease in size.

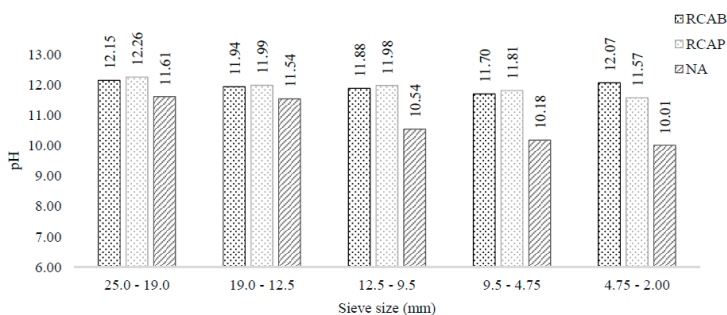


Figure 8. pH of NA, RCAP, and RCAB by particle size.

These results agree with what is expected for a natural aggregate and can be interpreted as the absence of a calcareous binder in these small-sized natural aggregates. The natural aggregate does not contain binders such as cement, which may explain the tendency towards neutral pH of the solutions that come in contact with particles below 9.5 to 4.75 mm.

The results suggest that larger natural aggregates (above the 4.75 mm) have water-soluble alkaline compounds beyond the carbonates from minerals such as limestone. Thus, an RCA could influence the asphalt mixture behavior and reduce the adhesion between the aggregates and asphalt.

However, the obtained results suggest that coarse RCAs have water-soluble alkaline components beyond mineral carbonates, such as limestone and dolomite. Therefore, those constituents can influence the behavior of asphalt mixtures and reduce their adhesion in the mixture.

3.2.3. X-ray Fluorescence (XRF)

Table 6 shows the chemical compositions of NA, RCAP, and RCAB obtained by XRF analysis expressed in weight (%). The main oxides were Al_2O_3 (6.85–12.00%), SiO_2 (32.13–49.88%), and CaO (20.85–43.10%). The SO_3 content was less than 0.75% for the RCAs, which is critical to avoid the formation of nitration reactions.

Table 6. XRF chemical compositions of NA, RCAP, and RCAB.

Main Constituents	(%)		
	NA	RCAB	RCAP
Na_2O	5.45	7.1	7.1
MgO	2.73	5.73	4.85
Al_2O_3	12	8.65	7.85
SiO_2	49.88	34.43	32.13
SO_3	1.6	0.7	0.75
K_2O	0.99	1.03	1.05
CaO	20.85	39.08	43.1
TiO_2	0.33	0.16	0.13
MnO	0.17	0.05	0.05
Fe_2O_3	5.85	3.06	3.01

Figure 9 shows the representation of the CaO – Al_2O_3 – SiO_2 system as a ternary phase diagram for the proportions of these compounds present in the coarse aggregates. NA has high SiO_2 content and low levels of CaO and Al_2O_3 , whereas RCAP and RCAB have similar CaO and SiO_2 contents but low Al_2O_3 content. The closeness of RCAB and RCAP in Figure 9 indicates similarity in their composition, which is related to the initial structure of the concrete from where they were sourced.

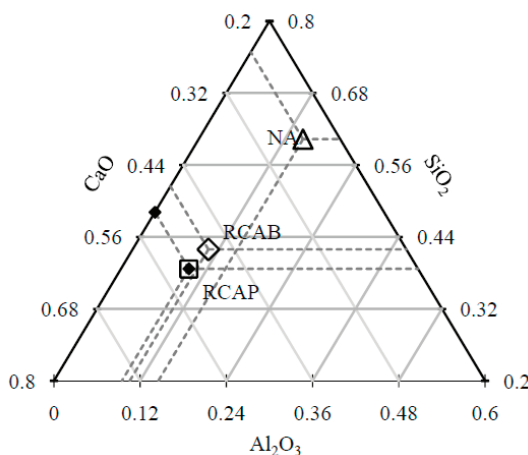


Figure 9. Positions of the NA, RCAB, and RCAP on the CaO – SiO_2 – Al_2O_3 ternary diagram.

According to the results of Table 6 and Figure 9, the increases in CaO and MgO contents in the RCAs with respect to the NA can be attributed: (a) to the origins of the RCAs and (b) samples of calcite from cement mortars or rubble from bricks, a product of demolition. Likewise, the SiO₂ contents of the RCAs in a lower proportion than the NA, show a more basic and therefore more hydrophobic tendency, which could favor their use in asphalt mixtures [39].

Figure 10 shows the chemical analysis patterns for the NA, RCAB, and RCAP samples of the semi-quantitative type presented as predominant peaks of quartz mineral (SiO₂) and calcite (CaCO₃). The NA and RCAB had sodium silico-aluminates (NaAlSi₃O₈) called albite, belonging to the family of feldspars, with peaks of lower intensity.

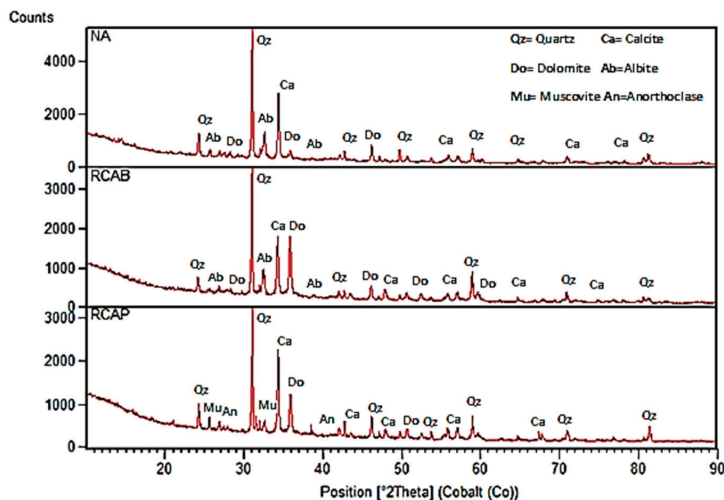


Figure 10. XRD patterns of NA, RCAP, and RCAB.

RCAB had a higher content of dolomite [CaMg(CO₃)₂] (34.3%) compared to RCAP (27.3%). This higher content can be attributed to the nature of the aggregate and the cement composition used in the concrete manufacturing.

In the case of RCAP, both muscovite KAl₂(AlSi₃)O₁₀(OH)₂ and anorthoclase (6SiO₂Al₂O₃(K, Na)₂O), were present in proportions of less than 5%. Similarly, the presence of pyroxenes or steatite was demonstrated, which can be attributed to traces of pozzolans in the residues.

Figures 11 and 12 show the amounts of CaO, SiO₂, and Al₂O₃ in each of the mixtures produced with NA, RCAB, and RCAP. A more significant presence of silicon dioxide (SiO₂) was observed when there was no RCA mixture (RCAP and RCAB). The SiO₂ reduced from 24.3% to 22.7% such that the percentage of RCAB increased, and between 24.3% to 22.3% for the increase in RCAP content, because of the lower presence of mortar. Calcium oxide (CaO) increased with recycled aggregate content in the mixture, while the aluminum oxide (Al₂O₃) did not show any significant difference.

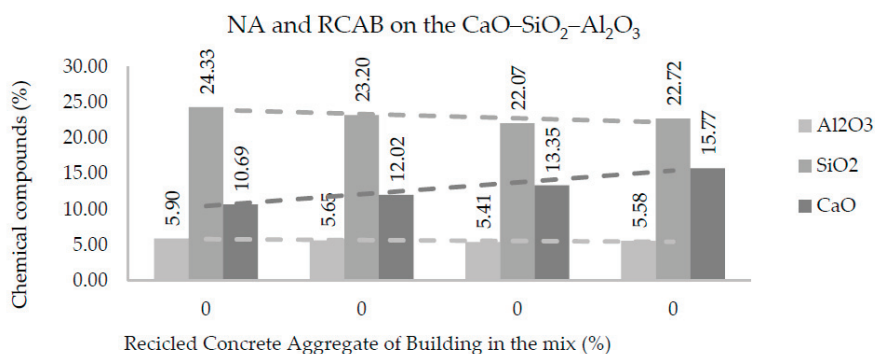


Figure 11. Effects of RCAB percentage on Al₂O₃, SiO₂, and CaO contents in the mixtures of aggregates.

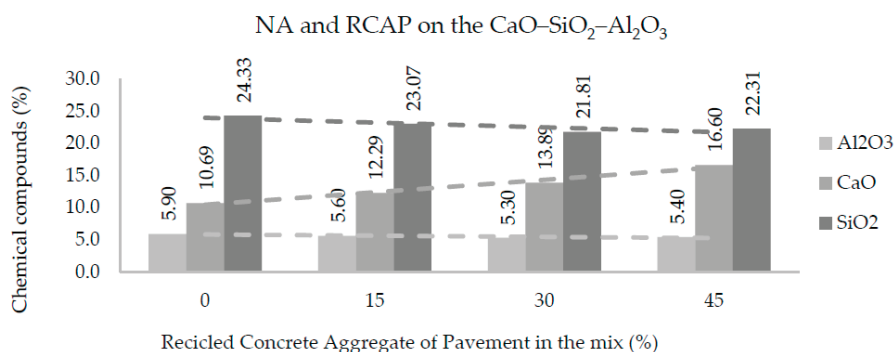


Figure 12. Effects of RCAP percentage on Al₂O₃, SiO₂, and CaO contents in the mixtures of aggregates.

Table 7 shows the results obtained from the ions dissolved in the NA and RCA using visible ultraviolet spectroscopy. The chloride content in the RCA considerably exceeded that of NA, with a more significant presence in RCAP that may be associated with its origin corresponding to a road located near the coast. Moreover, the chloride content in the RCA was higher for the coarse fraction (25.0–9.5 mm), which can be attributed to a larger exposed surface area of mortar adhered to Cl⁻ present. On the other hand, the sulfate content in the natural aggregate was higher than for RCAs for sizes 25.0–19.0, 19.0–12.5, and 12.5–9.5 mm, which can be associated with the aggregate source. The sulfate content in RCAB was higher for all the fractions compared to RCAP, which may cause susceptibility to degradation attributable to the expansion and cracking in the concrete of corresponding asphalt mixtures [40]. The presence of nitrates in both NA and RCAs were similar. However, the highest content was reported for RCAP for the 25.0–19.0 mm, which may be associated with group concentrations NO₃⁻ of surface water in contact with the material in service.

To determine the environmental impact related to ionic leaching in the asphalt mixtures, an analysis was performed using atomic absorption spectrometry for the different fractions of the three aggregates. In Table 8, Si and Ca are the most representative elements due to the mineralogical nature of the aggregates. In addition, chemically analyzed RCA samples contained different types of sand and cement, whose main compositions were CaO and SiO₂. The heavy metal values were insignificant in the leaching process. For example, the lead content did not exceed 0.3 mg/L. This condition means that RCAs will not become sources of environmental pollution, a vital criterion to be subsequently used without toxic risk. The presence of mercury in one of the fractions (9.5–4.75 mm) of RCAB with a value of 11.56 mg/L is explained by the existence of mercury in soils. Reactions with some complex compounds in organic matter (especially fulvic and humic acids) and soil clays cause the mercury to

remain for some time. These compounds can reach the RCAs by the exploitation of river sands or soils contaminated with mercury [34]. In the atmosphere, mercury can be found due to natural causes (such as volcanic eruptions, volatilization of aquatic and marine environments) or anthropogenic factors (industrial processes). Depending on the way mercury is found, it can remain in the atmosphere for a considerable period. Thus, depending on the location of the RCA's origin, the aggregates may contain mercury. In the case of RCAB, the proximity to the sea and industrial zone means that the concrete had been exposed to the mercury present in the atmosphere and absorbed the mercury in its base matrix [34].

Table 7. Results of the physicochemical analysis (UV spectrophotometer).

Aggregate	Size (mm)	NO ₃ ⁻ (mg/L)	SO ₄ ⁻² (mg/L)	Cl ⁻ (mg/L)
NA	25.0–19.0	0.7	114	21
	19.0–12.5	1	113	135
	12.5–9.5	0.8	63	43.75
	9.5–4.75	1.4	43	35.75
RCAB	25.0–19.0	1.1	37	242
	19.0–12.5	0.8	33	166
	12.5–9.5	0.9	49	153
	9.5–4.75	0.9	45	154
RCAP	25.0–19.0	3.13	16	482.5
	19.0–12.5	1.6	31	217
	12.5–9.5	1	33	269
	9.5–4.75	0.8	44	213

Table 8. Atomic absorption spectrometry of water-soluble elemental contents (mg/L).

Aggregate	Size (mm)	Fe	Al	Si	Ti	Ca	Pb	Zn	Ni	Mg	Mn	Hg
NA	25.0–19.0	135.5	13.9	1777	1.89	172.9	<0.3	0.3	<0.1	16.9	5.2	–
	19.0–12.5	173.2	16.2	1966	1.18	230.2	<0.3	0.4	<0.1	17.1	5.7	<10
	12.5–9.5	184.5	15.2	2008	1.18	177.6	<0.3	0.4	<0.1	11	5.3	<10
	9.5–4.75	169.8	16.5	2460	1.09	139.2	<0.3	0.3	<0.1	9.32	5.1	<10
RCAB	25.0–19.0	54.62	15.9	854.4	1.45	314.7	<0.3	0.2	<0.1	62.1	1.2	<10
	19.0–12.5	60.87	17.8	1886	1.18	317.4	<0.3	0.2	<0.1	61.3	1.5	<10
	12.5–9.5	46.48	18.6	1476	1.36	327.5	<0.3	0.2	<0.1	40.2	1.6	<10
	9.5–4.75	73.09	19.8	1415	<1.00	389.8	<0.3	0.3	<0.1	38.8	1.5	11.6
RCAP	25.0–19.0	73.31	22.4	1142	<1.00	359.5	<0.3	0.2	<0.1	54.5	1.5	<10
	19.0–12.5	61.38	13	1236	<1.00	320.2	<0.3	0.1	<0.1	45.1	1.6	<10
	12.5–9.5	53.38	14.2	1123	1.8	284.7	<0.3	0.1	<0.1	39.8	1.4	<10
	9.5–4.75	54.04	10.8	1316	<1.00	305.5	<0.3	0.1	<0.1	36	1.3	<10

Another important indicator is iron (Fe) found in natural aggregates, and its value in RCA decreases to approximately 50%. This can be associated with the nature of the area where the natural aggregates were exploited and now as part of the RCA.

3.2.4. Potential Reactions of RCAs in Asphalt Mixtures

This section seeks to analyze the chemical stability and possible interactions between the aggregates and the asphalt cement, assuming that these aggregates are used in the manufacture of asphalt mixtures.

It should be noted that the temperature at which the asphalt mixture works depends on environmental factors and the frequency and type of traffic once it begins its service. The only time where this mixture is exposed to high temperatures (above 150 °C) is during its manufacturing and storage. Likewise, the type of technology used in manufacturing the mixture (traditional or by emulsion) does not significantly affect the time because the system is subjected to high temperatures for a few hours [41]. The reactions that may take place to depend on several factors, among which the most important are temperature and reactant concentration [42,43].

The first reaction to be considered is the nitration of hydrocarbon compounds, which consists of the inclusion of a nitro group (NO_2) to the hydrocarbon chain [44]. However, both a nitrating agent (nitric acid) and a catalyst (sulfuric acid) are needed for this reaction to occur. Although the presence of SO_3 in the aggregates could indicate the presence of sulfuric acid, its concentration and nitric acid together are not sufficient to induce these reactions. Therefore, the only fixed nitrogen in the aggregates is in the form of nitrates (probably as sodium or potassium salts; see Table 7). These salts are stable compounds, which will not tend to react with the hydrocarbon. Additionally, as can be seen in Table 7, the nitrate content is in parts per million, which minimizes its possible reaction with the organic compounds. On the other hand, although the nitration reactions are exothermic [44], the conditions of the heavy hydrocarbon and asphalt mixture are such that there is no greater chemical potential (Gibbs free energy) for the nitration reaction to occur. Therefore, discard it among the series of reactions that this research intends to analyze.

The second reaction is the sulfonation of the compounds present in asphalt. This possible reaction consists of the inclusion of the sulfonic acid group ($-\text{SO}_3\text{H}$), or the corresponding salt or halogen group of sulfonic acid ($-\text{SO}_2\text{Cl}$) in an organic compound [44]. For this reaction to occur, the organic compound must contact a sulfonating agent, which may be sulfur trioxide, oleum, or concentrated sulfuric acid. In this case, the product formed would have amphiphilic properties, that is, a double affinity for both water and hydrocarbon, which could even improve the accession between the aggregate and asphalt [44]. However, the reaction with sulfur trioxide occurs in the gas phase; the sulfur present as SO_3 indicates that there could be sulfuric acid present in the aggregates (Table 6), but this concentration in combination with the temperature conditions is not sufficient to stimulate the reaction. Therefore, although these types of reactions take place at low temperatures, they are conditioned to very high concentrations of sulfuric acid, which is a scenario far from the asphalt mixing systems. In this study, the SO_3 content in the aggregates did not exceed 3% by weight of the samples, as can be seen in Table 6. Equally, the higher content of SO_3 indicates that these types of reactions (with shallow conversion) could occur. Besides, the content of SO_3 could even act as an adhesion-improving agent.

The third reaction considered in this analysis is the amination of the organic compounds present in the asphalt. This reaction involves the addition of the amine group by reducing nitro, nitroso, hydroxylamino, azoxy, azi, and hydrazo organic compounds. Amines may also be formed by reacting compounds containing certain labile groups (i.e., halogens, hydroxyl, and sulfonic) with ammonia [44]. Although the production of these compounds could improve the final adhesion between the aggregate and binder (in the same way as sulfonated surfactant compounds), these reactions are discarded in asphalt mixtures. The main reason is that there is no evidence of the presence or production of nitrated compounds (as discussed above), which makes impossible the amination reactions by reduction. Similarly to the nitration reactions, the fixed nitrogen in the system only exists as nitrates (salts), which are compounds that only ionize in aqueous solutions and are inert in a solid-state form when in contact with hydrocarbons.

Before considering the possible oxidation reactions, it should be noted that the halogenation reactions of the asphalt binder are not spontaneous under the temperature and concentration conditions where the mixture is found. In these reactions, halogen atoms are introduced into the hydrocarbon chain [44]. Although it is possible to determine the presence of halogens such as chlorine in the aggregates forming chlorides (Table 7), chlorine is found to form stable salts that are unreactive with the organic compounds present in the asphaltic binder. Likewise, as can be seen in Table 7, the chloride concentrations in the aggregates are in hundreds of parts per million for the recycled aggregates (RCAB and RCAP), whereas the level in the natural aggregate is in parts per million. The higher concentrations in the RCAs may be attributable to their exposure to environmental factors (atmospheric pollutants). However, in none of the cases can it be stated that they generated halogenation reactions with the binder compounds.

For the fourth reaction case, reactions could occur by alkali activation, which can improve the production of the binder and binder material. In Table 6, we find that the molar proportions do not

suggest the generation of alkaline activation solutions, which require a molar ratio of 3.4 between SiO_2 and Na_2O [45]. In addition, there is no use of sodium hydroxide NaOH in the mixture as a reactive material that promotes the generation of alkaline activation solution. According to Figures 11 and 12, the proportions of SiO_2 and CaO (alkaline oxides) can be approximated in a molar proportion as the substitution percentage of the RCA (RCAP and RCAB) in the mixture increases. The proportion of SiO_2 decreases while that of CaO increases when more RCA is added, without reaching the required values of molar proportion. There are aggregates with significant silicon and calcium contents such as quartz (SiO_2) and calcite (CaCO_3) in addition to other silicates (silico-aluminates) such as albite ($\text{NaAlSi}_3\text{O}_8$), muscovite $\text{KAl}_2(\text{AlSi}_3\text{O}_{10})(\text{OH})_2$, and anorthoclase ($6\text{SiO}_2\text{Al}_2\text{O}_3(\text{K}, \text{Na})_2\text{O}$). These aggregate types have proportions lower than 5% and require generating the necessary conditions by adding other solutions to increase the molar amount of sodium species (Na) and promote alkaline reactions.

Finally, it is important to underline that even though in this work the evolution of the chemical composition of an asphalt mixture (using RCAs) was not monitored, some research allows us to affirm that the mixture is sufficiently stable over time. Asphalt binders have been used before as stabilization matrices for non-hazardous and hazardous wastes [46–48]. Besides, other recycled solid-asphalt mixtures have been developed, including hazardous solid effluents from the oil refining industry [49–51]. In this case, despite solids containing heavy metals, they remain stable in the asphalt matrix, preventing their escape through leaching into the environment [52]. These are some examples that allow us to conclude that the reactivity of the system over time can be neglected when using asphalt-RCAs mixtures.

4. Conclusions and Recommendations

Based on the results of the study, it can be concluded that:

- The physical characterization showed that the RCAs have lower density and higher absorption than NA. This result can be explained by the presence of mortar adhered in RCAs. As an RCA replaces the NA, the optimal asphalt content (OAC) increases due to higher absorption of the RCA, which ultimately increases the cost of the asphalt mixture.
- Coarser RCAs (25.0–19.0 to 9.5–4.75 mm) primarily contain quartz, calcite, and dolomite, which provide chemical and mineralogical characteristics suitable for use in asphalt mixtures.
- The increase in the concentration of CaO in the RCA, the decrease in SiO_2 concerning the NA, and pH higher than 11.7, all promote the adhesion with the binder in the asphalt mixtures.
- The ratio of SiO_2 to Na_2O found in the RCAs, the reduction in the ratio between SiO_2 and CaO (alkaline) in the replacements (15%, 30%, and 45%) of RCAs, and the absence of NaOH in non-asphalt mixtures promote alkaline activation reactions, which favor the chemical stability of the mixture.
- Although the exposure time of the RCAs to the coastal environment led to a high concentration of Cl^- ions—up to 482 mg/L, some of Cl^- ions came from stable salts that were not reactive with the organic compounds present in the asphalt binder.
- The nitrate and sulfate contents in RCAs do not promote nitration and sulfonation reactions owing to the absence of catalytic agents such as nitric and sulfuric acids, which favor chemical stability in asphalt mixtures.
- Dissolved metals in RCAs support the use of RCAs in asphalt mixtures because the lead and mercury contents do not generate adverse environmental impacts.
- Based on the chemical, mineralogical, and physical characteristics of the RCAs, the replacement of NA with an RCA in the manufacture of hot mix asphalt is an alternative viable. According to the results of this study, it is suggested to improve regulations to promote the use of RCAs in the manufacture of asphalt mixtures with less environmental impact in relation to conventional aggregates.

Despite having very good and interesting results in this research, the authors think that more experiments are necessary to obtain a more robust average of the results. For example, more analysis with different sources is necessary to obtain the RCAs and to understand the performance in the mixture. Other important laboratory experiment should analyze the absorption of the asphalt with different RCAs in order to assess the asphalt consumption and the costs of implementation in projects of roads. Future studies should also include the formulation of analysis guides for RCAs, where the way to chemically study them is standardized, and thus obtain indices and potential reactions between aggregates and asphalt mixtures, which should give standard data and reactions.

Author Contributions: Conceptualization, E.H.S.-C. and C.A.P.-B.; methodology, A.F., R.G.L.E., and E.H.S.-C.; validation, Y.P.T., E.H.S.-C., and A.F.; formal analysis, J.Y.-M., R.M., E.H.S.-C., A.F., and C.A.P.-B.; investigation, R.G.L.E. and E.H.S.-C.; resources, E.H.S.-C.; data curation, E.H.S.-C., J.Y.-M., and A.F.; writing—original draft preparation, E.H.S.-C.; writing—review and editing, A.F., J.Y.-M., R.M., E.H.S.-C., and C.A.P.-B.; visualization, E.H.S.-C., J.Y.-M., and A.F.; supervision, E.H.S.-C. and C.A.P.-B.; project administration, C.A.P.-B. All authors have read and agreed to the published version of the manuscript.

Funding: This research was funded by Administrative Department of Science, Technology, and Innovation-Colciencias-research grants 745/2016, contract 037 of 2017/code 1215-745-59105.

Acknowledgments: The authors thank the Universidad del Norte for sponsoring this research, and the Universidad Distrital Francisco José de Caldas. The authors are also grateful to INGECOST Company for its collaboration in crushing the recycled material and providing the natural aggregate. In addition, the authors extend their gratitude to Aconstruir S.A. company for supplying the concrete waste. Finally, the authors thank the Institute for Materials Research and Innovation—INCITEMA—for evaluating the RCA with its technological infrastructure. Special thanks also go to all those who helped in one way or another during both the course of this research and documentation of this paper.

Conflicts of Interest: The authors declare no conflict of interest. The funders had no role in the design of the study; in the collection, analyses, or interpretation of data; in the writing of the manuscript, or in the decision to publish the results.

References

1. Behera, M.; Bhattacharyya, S.; Minocha, A.; Deoliya, R.; Maiti, S.N. Recycled aggregate from C&D waste & its use in concrete—A breakthrough towards sustainability in construction sector: A review. *Constr. Build. Mater.* **2014**, *68*, 501–516.
2. Kumar, R. Influence of recycled coarse aggregate derived from construction and demolition waste (CDW) on abrasion resistance of pavement concrete. *Constr. Build. Mater.* **2017**, *142*, 248–255. [CrossRef]
3. Ossa, A.; Garcia, J.; Botero, E. Use of recycled construction and demolition waste (CDW) aggregates: A sustainable alternative for the pavement construction industry. *J. Clean. Prod.* **2016**, *135*, 379–386. [CrossRef]
4. Bustos, C.A.P.; Pumarejo, L.G.F.; Cotte, É.H.S.; Quintana, H.A.R. Construction demolition waste (CDW), a perspective of achievement for the city of Barranquilla since its management model. *Ing. Desarro.* **2017**, *35*, 533–555. [CrossRef]
5. Cotte, E.S.; Bustos, C.A.P.; Páez, C. Una visión de Ciudad sostenible desde el modelo de gestión de los residuos de construcción y demolición (Rcd) caso De estudio: Barranquilla. *Tecnura* **2020**, *24*, 68–83. [CrossRef]
6. Limbachiya, M.C.; Marrocchino, E.; Koulouris, A. Chemical–mineralogical characterisation of coarse recycled concrete aggregate. *Waste Manag.* **2007**, *27*, 201–208. [CrossRef] [PubMed]
7. Tam, V.W.; Tam, C.; Le, K. Removal of cement mortar remains from recycled aggregate using pre-soaking approaches. *Resour. Conserv. Recycl.* **2007**, *50*, 82–101. [CrossRef]
8. Angulo, S.C.; Ulsen, C.; John, V.M.; Kahn, H.; Cincotto, M.A. Chemical—mineralogical characterization of C & D waste recycled aggregates from São Paulo, Brazil. *Waste Manag.* **2009**, *29*, 721–730.
9. Rodrigues, F.; Carvalho, M.T.; Evangelista, L.; Jorge, D.B. Physical–chemical and mineralogical characterization of fine aggregates from construction and demolition waste recycling plants. *J. Clean. Prod.* **2013**, *52*, 438–445. [CrossRef]
10. Courard, L.; Rondeux, M.; Zhao, Z.; Michel, F. Use of Recycled Fine Aggregates from C&DW for Unbound Road Sub-Base. *Materials* **2020**, *13*, 2994.

11. Medina, C.; Zhu, W.; Howind, T.; Frias, M.; De Rojas, M.I.S. Effect of the constituents (asphalt, clay materials, floating particles and fines) of construction and demolition waste on the properties of recycled concretes. *Constr. Build. Mater.* **2015**, *79*, 22–33. [CrossRef]
12. Sanchez-Cotte, E.H.; Fuentes, L.; Martinez-Arguelles, G.; Quintana, H.A.R.; Walubita, L.F.; Cantero-Durango, J.M. Influence of recycled concrete aggregates from different sources in hot mix asphalt design. *Constr. Build. Mater.* **2020**, *259*, 120427. [CrossRef]
13. Abbas, A.; Fathifazl, G.; Fournier, B.; Isgor, O.; Zavadil, R.; Razaqpur, A.; Foo, S. Quantification of the residual mortar content in recycled concrete aggregates by image analysis. *Mater. Charact.* **2009**, *60*, 716–728. [CrossRef]
14. Chung, S.-Y.; Sikora, P.; Rucinska, T.; Stephan, D.; Elrahman, M.A. Comparison of the pore size distributions of concretes with different air-entraining admixture dosages using 2D and 3D imaging approaches. *Mater. Charact.* **2020**, *162*, 110182. [CrossRef]
15. Štátná, A.; Šachlová, Š.; Pertold, Z.; Prikryl, R.; Leichmann, J. Cathodoluminescence microscopy and petrographic image analysis of aggregates in concrete pavements affected by alkali—Silica reaction. *Mater. Charact.* **2012**, *65*, 115–125. [CrossRef]
16. Lagares, R. Determinación de la Influencia de las Características Químicas de los Agregados Reciclados de Concreto Como Llenante en Concretos Hidráulicos y Asfálticos (Determination of the Influence of the Chemical Characteristics of Recycled Concrete Aggregates as Fillers in Hydraulic and Asphalt Concretes). Master's Thesis, Universidad del Norte, Barranquilla, Colombia, 2017.
17. Moschopedis, S.E.; Speight, J.G. Influence of metal salts on bitumen oxidation. *Fuel* **1978**, *57*, 235–240. [CrossRef]
18. Ebberts, A.R. Oxidation of Asphalt in Thin Films. *Ind. Eng. Chem.* **1942**, *34*, 1048–1051. [CrossRef]
19. Herold, M.; Roberts, D.; Noronha, V.; Smadi, O. Imaging spectrometry and asphalt road surveys. *Transp. Res. Part C Emerg. Technol.* **2008**, *16*, 153–166. [CrossRef]
20. Qing, Y.; Yu, K.; Zhang, Z. Expansion of ordinary Portland cement paste varied with nano-MgO. *Constr. Build. Mater.* **2015**, *78*, 189–193.
21. Segarra Foradada, J. *Envejecimiento de Presas por Reacciones Expansivas en Hormigón (Aging in the Dam Due to Expansive Reactions in the Concrete)*; Universitat Politècnica de Catalunya: Barcelona, Spain, 2005.
22. Santos, M.B.; De Brito, J.; Silva, A.S. A Review on Alkali-Silica Reaction Evolution in Recycled Aggregate Concrete. *Materials* **2020**, *13*, 2625. [CrossRef]
23. He, Z.; Tang, S.; Zhao, G.; Chen, E. Comparison of three and one dimensional attacks of freeze-thaw and carbonation for concrete samples. *Constr. Build. Mater.* **2016**, *127*, 596–606. [CrossRef]
24. Xu, S.; Xiao, F.; Amirkhani, S.; Singh, D. Moisture characteristics of mixtures with warm mix asphalt technologies—A review. *Constr. Build. Mater.* **2017**, *142*, 148–161. [CrossRef]
25. Andrzejuk, W.; Szewczak, A.; Fic, S.; Lagód, G. Wettability of Asphalt Concrete with Natural and Recycled Aggregates from Sanitary Ceramics. *Materials* **2020**, *13*, 3799. [CrossRef] [PubMed]
26. Won, M. *Performance of Continuously Reinforced Concrete Pavement Containing Recycled Concrete Aggregate*; Texas Department of Transportation: Austin, TX, USA, 2001.
27. Bhusal, S.; Li, X.; Wen, H. Evaluation of Effects of Recycled Concrete Aggregate on Volumetrics of Hot-Mix Asphalt. *Transp. Res. Rec. J. Transp. Res. Board* **2011**, *2205*, 36–39. [CrossRef]
28. Pérez, I.; Pasandín, A.R.; Gallego, J. Stripping in hot mix asphalt produced by aggregates from construction and demolition waste. *Waste Manag. Res.* **2012**, *30*, 3–11. [CrossRef]
29. Zulkati, A.; Wong, Y.D.; Sun, D.D. Mechanistic Performance of Asphalt-Concrete Mixture Incorporating Coarse Recycled Concrete Aggregate. *J. Mater. Civ. Eng.* **2013**, *25*, 1299–1305. [CrossRef]
30. Wu, S.; Zhong, J.; Zhu, J.; Wang, D. Influence of demolition waste used as recycled aggregate on performance of asphalt mixture. *Road Mater. Pavement Des.* **2013**, *14*, 679–688. [CrossRef]
31. Chen, M.J.; Wong, Y.D. Porous Asphalt Mixture with a Combination of Solid Waste Aggregates. *J. Mater. Civ. Eng.* **2015**, *27*, 04014194. [CrossRef]
32. Qasrawi, H.; Asi, I. Effect of bitumen grade on hot asphalt mixes properties prepared using recycled coarse concrete aggregate. *Constr. Build. Mater.* **2016**, *121*, 18–24. [CrossRef]
33. Bianchini, G.; Marrochino, E.; Tassinari, R.; Vaccaro, C. Recycling of construction and demolition waste materials: A chemical—mineralogical appraisal. *Waste Manag.* **2005**, *25*, 149–159. [CrossRef]

34. Bui, N.K. Enhancement of Recycled Aggregate Concrete Properties by a New Treatment Method. *Int. J. Geomate* **2018**, *14*, 68–76. [CrossRef]
35. Martínez-Arguelles, G.; Coll, M.D.; Pumarejo, L.G.F.; Cotte, E.H.S.; Rondon, H.; Pacheco, C.A.; Martínez, J.Y.; Espinoza, R.G.L. Characterization of Recycled Concrete Aggregate as Potential Replacement of Natural Aggregate in Asphalt Pavement. In *IOP Conference Series: Materials Science and Engineering*; IOP Publishing: Bristol, UK, 2019; Volume 471, p. 102045.
36. INVIAS. *Artículo 450, Mezclas Asfálticas en Caliente de Gradación Continua, Especificaciones Generales Para la Construcción de Carreteras (Article 450, Continuous Grade Hot Asphalt Mixes, General Specifications for Road Construction)*; INVIAS: Bogotá, Colombia, 2013.
37. Paranavithana, S.; Mohajerani, A. Effects of recycled concrete aggregates on properties of asphalt concrete. *Resour. Conserv. Recycl.* **2006**, *48*, 1–12. [CrossRef]
38. Sánchez de Juan, M. Estudio Sobre la Utilización de Árido Reciclado Para la Fabricación de Hormigón Estructural (Study on the Use of Recycled Aggregate for the Manufacture of Structural Concrete). Ph.D. Thesis, Escuela Técnica Superior de Ingenieros de Caminos, Canales y Puertos, Madrid, Spain, 2004.
39. Huang, Q.; Qian, Z.; Hu, J.; Zheng, D.; Chen, L.; Zhang, M.; Yu, J. Investigation on the properties of aggregate-mastic interfacial transition zones (ITZs) in asphalt mixture containing recycled concrete aggregate. *Constr. Build. Mater.* **2020**, 121257. [CrossRef]
40. Zhao, G.; Li, J.; Shao, W. Effect of mixed chlorides on the degradation and sulfate diffusion of cast-in-situ concrete due to sulfate attack. *Constr. Build. Mater.* **2018**, *181*, 49–58. [CrossRef]
41. Mercado, R.; Fuentes, L. Asphalt emulsions formulation: State-of-the-art and dependency of formulation on emulsions properties. *Constr. Build. Mater.* **2016**, *123*, 162–173.
42. Petersen, J.C.; Harnsberger, P.M. Asphalt Aging: Dual Oxidation Mechanism and Its Interrelationships with Asphalt Composition and Oxidative Age Hardening. *Transp. Res. Rec. J. Transp. Res. Board* **1998**, *1638*, 47–55. [CrossRef]
43. Petersen, J.C. Asphalt oxidation -An overview including a new model for oxidation proposing that physicochemical factors dominate the oxidation kinetics. *Fuel Sci. Technol. Int.* **1993**, *11*, 57–87. [CrossRef]
44. Groggins, P.H. *Unit Processes in Organic Synthesis*; McGraw Hill: New York, NY, USA, 1958.
45. Bassani, M.; Tefa, L.; Coppola, B.; Palmero, P. Alkali-activation of aggregate fines from construction and demolition waste: Valorisation in view of road pavement subbase applications. *J. Clean. Prod.* **2019**, *234*, 71–84. [CrossRef]
46. Bednarik, V.; Vondruska, M.; Koutny, M. Stabilization/solidification of galvanic sludges by asphalt emulsions. *J. Hazard. Mater.* **2005**, *122*, 139–145. [CrossRef]
47. Cervinkova, M.; Vondruska, M.; Bednarik, V.; Pazdera, A. Stabilization/solidification of munition destruction waste by asphalt emulsion. *J. Hazard. Mater.* **2007**, *142*, 222–226. [CrossRef]
48. Modarres, A.; Ayar, P. Coal waste application in recycled asphalt mixtures with bitumen emulsion. *J. Clean. Prod.* **2014**, *83*, 263–272. [CrossRef]
49. Al-Futaisi, A.; Jamrah, A.; Yaghi, B.; Taha, R. Assessment of alternative management techniques of tank bottom petroleum sludge in Oman. *J. Hazard. Mater.* **2007**, *141*, 557–564. [CrossRef] [PubMed]
50. Hu, G.; Li, J.; Zeng, G. Recent development in the treatment of oily sludge from petroleum industry: A review. *J. Hazard. Mater.* **2013**, *261*, 470–490. [CrossRef] [PubMed]
51. Da Silva, L.J.; Alves, F.C.; De França, F.P. A review of the technological solutions for the treatment of oily sludges from petroleum refineries. *Waste Manag. Res.* **2012**, *30*, 1016–1030. [CrossRef]
52. Karamalidis, A.K.; Voudrias, E.A. Release of Zn, Ni, Cu, SO₄²⁻ and CrO₄²⁻ as a function of pH from cement-based stabilized/solidified refinery oily sludge and ash from incineration of oily sludge. *J. Hazard. Mater.* **2007**, *141*, 591–606. [CrossRef]

Publisher's Note: MDPI stays neutral with regard to jurisdictional claims in published maps and institutional affiliations.



© 2020 by the authors. Licensee MDPI, Basel, Switzerland. This article is an open access article distributed under the terms and conditions of the Creative Commons Attribution (CC BY) license (<http://creativecommons.org/licenses/by/4.0/>).

Review

An Analytical Mini-Review on the Compression Strength of Rubberized Concrete as a Function of the Amount of Recycled Tires Crumb Rubber

Luca Lavagna *, Roberto Nisticò ^{*,†}, Matteo Sarasso and Matteo Pavese

Polytechnic of Torino, Department of Applied Science and Technology DISAT, C.so Duca degli Abruzzi 24, 10129 Torino, Italy; matteo.sarasso@studenti.polito.it (M.S.); matteo.pavese@polito.it (M.P.)

* Correspondence: luca.lavagna@polito.it (L.L.); roberto.nistico0404@gmail.com (R.N.);

Tel.: (+39)-011-090-4598 (L.L.); Fax: (+39)-011-090-4624 (L.L.)

† Current address: Independent Researcher, Via Borgomasino 39, 10149 Torino, Italy.

Received: 14 February 2020; Accepted: 6 March 2020; Published: 9 March 2020

Abstract: Since waste tires constitute a serious environmental concern, several studies are devoted to the use of finely divided recycled rubber for the production of rubberized concrete by partial substitution of the mineral aggregate fraction. The introduction of rubber into concrete presents several advantages (e.g., improvement of toughness and thermal/electrical/acoustic insulation capacities). Unfortunately, the addition of a high content of rubber into concrete causes an important loss of mechanical resistance of the final composite. In this context, several scientific studies are devoted to investigate the best technical solutions for favoring the interfacial adhesion between rubber and cement paste, but the interpretation of the literature is often misleading. To overcome this issue, the metadata extrapolated from the single scientific works were critically re-analyzed, forming reference diagrams where the variability fields of the different rubber concrete formulations (in terms of mechanical responses as a function of the rubber content) were defined and the best performances discussed. This study evidenced the twofold role of reference diagrams, able in both presenting the data in an unambiguous manner (for a successful comparison) and providing the guidelines for future works in this research field.

Keywords: concrete; composite materials; rubber concrete; mechanical properties; recycling; rubber

1. Introduction

Along with human activities, the solid waste increment in landfills opened a Pandora's box related to the end-of-life waste management, prompting worldwide researchers to identify the best technologies for favoring waste disposal and (if possible) their recycling, aiming at environmental and economic sustainability [1–7]. Nowadays, significant effort has been directed toward the recovery and reuse of waste materials as new resources (based on green chemistry and circular economy guidelines) for the production of value-added products [8–15]. Among the different waste types, end-of-life waste rubber tires are one of the most voluminous wastes in terms of both shape and quantity (the European consumption of tires is about 3.2 million tons per year) [16,17]. From the chemical viewpoint, the composition of tires is mainly organic (rubber/elastomers and carbon black about 70%), with a small amount of inorganic components (about 17%), textiles and other additives (about 13%) [18]. Used tires can be either reused or wasted, and end-of-life tire waste can be either landfilled, thermally converted to produce energy (via combustion) or re-processed to obtain raw materials [19]. Regarding the waste tires management, the first two options (namely, landfilling and burning) can cause several environmental concerns (e.g., serving as habitat for the proliferation of disease-carrying insects and rodents during landfilling, or being a source of dioxins and other volatile pollutants during combustion)

with serious risk to human health [20,21]. Thus, for all these reasons, rubber tires are preferentially treated via milling to produce granulates, chips, powders and textiles, thus making them exploitable in several advanced applications [19].

In this context, the possibility of partially substituting the mineral aggregate (sand and gravel) fraction in concrete with recycled tires crumb rubber is a technical solution that is extremely appealing, as it leads to cement-based composite materials that can have significantly improved ductility, tenacity, impact resistance and thermal/electrical/acoustic insulation capacities [22]. Additionally, the development of rubber-containing concrete allows to reach a twofold environmental benefit, since it reduces both the environmental impact due to tire disposal (landfilling and burning) and the excavation processes for recovering the mineral aggregate fraction from quarries or along rivers courses.

Despite the many benefits given by the introduction of rubber in concrete, a significant reduction of both the mechanical resistance and specific mass has been registered. These side-effects are attributable not only to the different mechanical response of the rubber component compared to the mineral aggregates, but mainly to the poor interfacial adhesion between the rubber element with the cement paste [23,24], which significantly reduces the loadable quantity of rubber in concrete.

Nevertheless, promising mechanical properties (mostly the increased toughness) encouraged the evaluation of structural performances of rubber concrete where high resistance to dynamic stress is required, such as in the case of earthquake-resistant structures [25]. However, in order to make feasible the structural uses of rubber concrete, it is necessary to select formulations able to guarantee an adequate level of mechanical resistance, thus overcoming the interfacial adhesion concerns. A very recent review by Roychand and co-workers presents the current panorama of the research on the substitution of aggregates with recycled rubber [26], together with the possibilities envisaged in the literature of rubber treatment or fiber insertion to guarantee acceptable mechanical properties to the cement-based composite.

In the current literature, rubber concrete is presented with very different formulations that are sometimes improperly compared. In fact, the literature suggests that typical parameters affecting the mechanical response of rubber concrete are (i) the rubber content (expressed either as aggregate substitution level or as volume/weight percentage), (ii) the granulometry of both the substituted mineral aggregate (coarse or fine) and the added rubber, (iii) the introduction of additives (e.g., pozzolana, silica) and (iv) the quantities of all components within the formulation and the water-to-cement ratio, (v) the effects of appropriate pre-treatments (e.g., NaOH washing) and surface functionalization (or coatings) of the rubber to favor the interface interaction with the inorganic matrix (cement paste).

In this study we aim at improving the ease of comparison between the different procedures, formulations and strategies that are currently employed to improve the properties of rubber-containing concrete. We provide a rational evaluation of the experimental results reported in the literature, first by building a reference diagram that shows the variability of mechanical response of different rubber concrete formulations. Then, we evidence the effect of different approaches used in the published literature on the final properties of rubber concrete. The final goal is to provide a preliminary assessment tool (to be adopted in future research) that allows a rapid estimation of the mechanical behavior of the produced material relative to the performance of current state-of-the-art tools.

2. Analysis of Bibliography

Some works focused on the use of end-of-life tires have been selected from electronic databases (i.e., Scopus, Science Direct), others from the recent review by Roychand et al. [26].

A list of studies focused on the mechanical properties of different rubber concrete formulations was produced. From the initial list, 46 publications [19,23,24,27–67] were selected since they followed both criteria of inclusion adopted in this research, namely (i) tests should be performed on different mixtures of rubber concrete and compared with a similar concrete composition without rubber; and (ii) numerical data of the mechanical (mostly, flexural and compression) strength should be provided.

The selected case studies were further analyzed in depth by verifying the effective relevance of their content with the aim of this study. Following this exclusion principle, 11 publications [28–33,35,36,38–40] were not included in this research as follows: Naito et al. and Kashani et al. [28,30] did not indicate the type of cement and aggregate used in their study. Kaloush et al. [29], Ismail et al. [31] and Raffoul et al. [35] did not keep constant the mix design when adding the rubber to concrete, so that the comparison with the reference material is not possible. Kaloush et al. and Raffoul et al. changed the w/c ratio, while Ismail et al. added polymer fibers. Xue et al and Najim et al. [32,33] did mechanical characterization for other purposes. Mendis et al. [36] and Elghazouli et al. [40] did not make compression tests. Aslani et al. [38] and Wang et al. [39] used iron or steel fibers to enhance the mechanical performance. Whereas six publications [19,23,34,41–43] were not included for other specific reasons, namely the study by Rahman et al. [41] was excluded since it focused on the effect of different plasticizers, the one by He et al. [23] because it is mainly focused on the adhesion phenomena occurring between concrete and rubber, the two studies by Najim et al. [19,42] together with the one by Siddique et al. [43] and Roychand et al. [26] since they are review articles, and lastly the one written by Taha et al. [34] because it presents issues related to the mix design and the relative composition quantification.

After this preliminary screening, the publications effectively analyzed in this study were 27. Since, in some cases, more than one series of samples per publication has been considered, detailed acronyms have been adopted to unequivocally recognize a specific data series in the reference diagrams. To simplify the comprehension (and the readability) of the diagrams, Table 1 reports the acronyms adopted in the present study and the corresponding description from the original study.

Table 1. Case studies selected for the data analysis.

Acronyms Adopted in the Present Study	Description (and Acronyms) from the Original Work	Original Works	References
1A	Substitution of fine aggregate (SCRC30)	Yung et al. (2013)	[44]
1B	Substitution of fine aggregate (SCRC50)	Yung et al. (2013)	[44]
2A	Substitution of fine aggregate (F1)	Boudaoud et al. (2012)	[45]
2B	Substitution of coarse aggregate (F2)	Boudaoud et al. (2012)	[45]
3A	Substitution of fine aggregate, powder rubber	Kumar et al. (2014)	[46]
3B	Substitution of fine aggregate, powder and chipped rubber	Kumar et al. (2014)	[46]
4A	Substitution of fine aggregate	Issa et al. (2013)	[47]
5A	Substitution of fine aggregate (M7)	Youssif et al. (2016)	[48]
5B	Substitution of fine aggregate, rubber treated with NaOH at different time (M6, M8, M9)	Youssif et al. (2016)	[48]
6A	Substitution of fine aggregate (RC)	Ly et al. (2015)	[49]
7A	Substitution of fine aggregate (CF)	Liu et al. (2016)	[50]
7B	Substitution of both fine and coarse aggregates (CM)	Liu et al. (2016)	[50]
8A	Substitution of coarse aggregate, rubbers with different sizes (TC, CR, FCR, TC-CR, TC-FCR)	Cesoglu et al. (2014)	[51]
9A	Substitution of fine aggregate (mix 16-20)	Mohammed et al. (2014)	[52]
9B	Substitution of fine aggregate (mix 21-25)	Mohammed et al. (2014)	[52]
10A	Substitution of coarse aggregate, ground rubber (GR-8)	Zheng et al. (2008)	[53]
10B	Substitution of coarse aggregate, crushed rubber (CR-40)	Zheng et al. (2008)	[53]
11A	Substitution of fine aggregate (RC)	Feng et al. (2018)	[54]
12A	Substitution of both fine and coarse aggregates (M25-R)	Tiwari et al. (2008)	[55]
13A	Substitution of fine aggregate (mix 2)	Gerges et al. (2018)	[56]
13B	Substitution of fine aggregate (mix 4)	Gerges et al. (2018)	[56]
14A	Substitution of fine aggregate (RC)	Liu et al. (2013)	[58]
15A	Substitution of fine aggregate (series I)	Thomas et al. (2016)	[59]
16A	Substitution of aggregate with fine rubber (FRC)	Topcu (1995)	[27]
16B	Substitution of aggregate with coarse rubber (CRC)	Topcu (1995)	[27]
17A	Substitution of fine aggregate (CR)	Kardos et al. (2015)	[60]
18A	Substitution of fine aggregate (RSCC)	Khalil et al. (2015)	[61]
19A	Substitution of fine aggregate (pre-treatment of rubber with NaOH) (CRC)	Li et al. (2018)	[62]
20A	Substitution of fine aggregate (RC-0.35)	Zhou et al. (2018)	[63]
21A	Substitution of fine aggregate (CR)	Bisht et al. (2017)	[64]
22A	Substitution of fine aggregate (R)	Yousif et al. (2017)	[65]
23A	Substitution of fine aggregate (OH-)	Guo et al. (2017)	[66]
24A	Substitution of fine aggregate (RC-0.35)	Xue et al. (2018)	[67]
25A	Substitution of fine aggregate (01-RT)	Sgobba et al. (2015)	[24]
25B	Substitution of fine aggregate (pre-treatment of rubber with NaOH) (01-RTL)	Sgobba et al. (2015)	[24]
26A	Substitution of coarse aggregate (SCRC)	Aslani et al. (2018)	[37]
27A	Substitution of fine aggregate (FR)	Najim et al. (2012)	[57]
27B	Substitution of coarse aggregate (CR)	Najim et al. (2012)	[57]
27C	Substitution of both fine and coarse aggregates (FCR)	Najim et al. (2012)	[57]

3. Bibliography Data Manipulation

The main relevant mechanical test for evaluating the mechanical response of concrete is the evaluation of the compression strength. All the case studies considered present compression strength results, with most following ASTM C39/C39M [68] as the reference standard, while a few do not report the standard adopted for the measurement.

The first step in the analysis was the extraction of numerical values from the compression tests of each publication. In some cases, such values were not directly reported in the text, but graphically represented in a diagram. To extrapolate the numerical values from plots and graphics, the software WebPlotDigitizer 3.8 (Austin, Texas, USA) has been employed.

The data extracted from the selected publications were plotted in Figure 1, which reports the compression strength declared by the authors against the declared volumetric percentage of substitution of the mineral aggregate fraction with rubber. As expected, Figure 1 reports a significant reduction of the mechanical resistance of the materials when the rubber content within the composites increases. An objective comparison of the performance of the different rubber concrete formulations is, however, hampered by two factors: first, the control concrete presents very different compression strength values, which are comprised in the very wide 22–72 MPa range. Second, most papers have different ways of declaring the substitution of the mineral aggregate fraction with rubber. Thus, both the *x*-axis and the *y*-axis do not present comparable data.

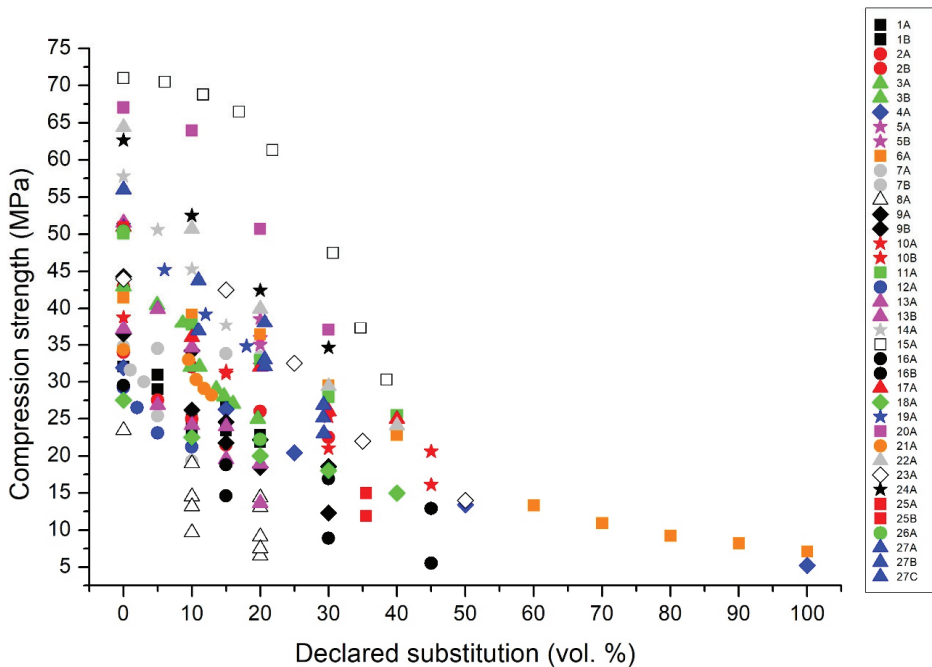


Figure 1. Reference diagram: compression strength (expressed in MPa) vs. the declared volumetric percentage of substitution of the mineral aggregate with rubber (expressed in vol.%).

Considering the compression strength, it is evident in Figure 1 that, for instance, the values at 10% rubber substitution that are in the 50–70 MPa range (series 15A, 20A, 22A, 24A [59,63,65,67]) are very high mostly due to the use of high-strength concrete. Other series, for instance 7A and 7B [50], have a much lower reduction in strength, but since their reference concrete has a lower strength, they seem less performing with strength values in the 20–35 MPa range. The same issue happens at all

percentages of rubber substitution. For instance, at 30% declared substitution, the series 20A [63] or 24A [67] seem more performing than the series 18A [61], even if the latter has a much lower strength reduction with respect to the control concrete.

The effect of the control concrete value is very evident, but also the differences in the declared substitutions have a profound effect on the lack of clarity of Figure 1. For instance, series 6A [49] declares up to 100% rubber substitution, but this substitution refers to a specific fraction of aggregates and not to the total aggregate content. This effect expands the curve toward very high values, suggesting a smaller strength reduction than the real one.

The revision of the stated formulation pointed out a significant inconsistency among the analyzed papers in the mode to declare the reference quantities. Hence, all the declared formulations were analyzed case-by-case in order to obtain the principal components of the mix design and the characterizing parameters (i.e., quantity, size, density). In most cases, in fact, the percentage of substitution did not refer unequivocally to the total volume of the aggregates, but it preferentially refers to a type (or portion) of aggregate (e.g., either coarse or fine). To guarantee uniformity in the data interpretation, the substitution level in the composites was “normalized” by referring always to the total volume of aggregates present in the control mixture.

Additionally, the vis-a-vis revision of the selected publications revealed a further remarkable inconsistency that affected the data interpretation. In fact, some authors chose the weight parameters as either specific weight or bulk density. Moreover, the choice of these parameters for every formulation was different case-by-case, often showing inconsistent values, thus making the numerical values here extrapolated extremely wide and difficult to compare. For instance, Youssf et al. [65], series 22A, declared a specific gravity for crumb rubber equal to 0.85, which is outside the values observed in the literature for vulcanized rubber. As another example, Gesoğlu et al. [51], series 8A, use tire chips with specific gravity 1.02 and crumb rubber with specific gravity of 0.83 and 0.48. It seems to us that also these values are too low with respect to the literature data of rubber density [69–77]. It is difficult to hypothesize the origin of these values, but it could be possible that some values are apparent density or bulk density. Other cases are those of Boudaud et al. [45], series 2A/B, who did not mention the rubber density, and of Feng et al. [54], series 11A, who cited only the bulk density of 539 kg/m³, which cannot be used to quantify the volume substitution.

To overcome this issue, the composition of the formulations that were not clearly defined or outside a reasonable range was further recalculated by using, for the specific weight, the average value of all the studies where the data were clear and consistent with literature values. These weight parameters are reported in Table 2. If the weight parameters provided by the original authors were comparable with the ones selected in Table 2, the declared values were maintained in our data elaboration.

Table 2. Weight parameters adopted for the data analysis.

Components	Average Specific Weight for All the Data analyzed (kg m ⁻³) ± St. Dev.
Rubber	1120 ± 64
Fine mineral aggregate	2649 ± 25
Coarse mineral aggregate	2672 ± 33

Therefore, the aggregate content and the relative volumetric percentage of substitution with rubber were recalculated for all compositions using, when needed, the reference values reported in Table 2. In this way, rubber concrete mixtures considered in this study present the highest level of comparability in terms of parameters and mechanical performances registered.

Despite this, it is important to notice that the analyzed formulations still show a considerable variability of the components used, namely (i) type of cement paste and aggregates adopted, (ii) presence/absence of additives, fly ashes, slags, silica and other additional components and (iii) amount and proportion of each component within the concrete formulation. For all these reasons, even after this

consistent data homogenization, resulting case studies still present a significant degree of heterogeneity. However, at the end of this elaboration process, all case studies are coherent among each other.

Figure 2 reports the recalculated compression strength, normalized with respect to the control samples, against the volumetric percentage of substitution of the mineral aggregate fraction with rubber. It is interesting to note that the maximum substitution shown on the *y*-axis becomes 37% and is no longer 100% as in Figure 1. Moreover, all series start at 100% for the reference concretes without rubber.

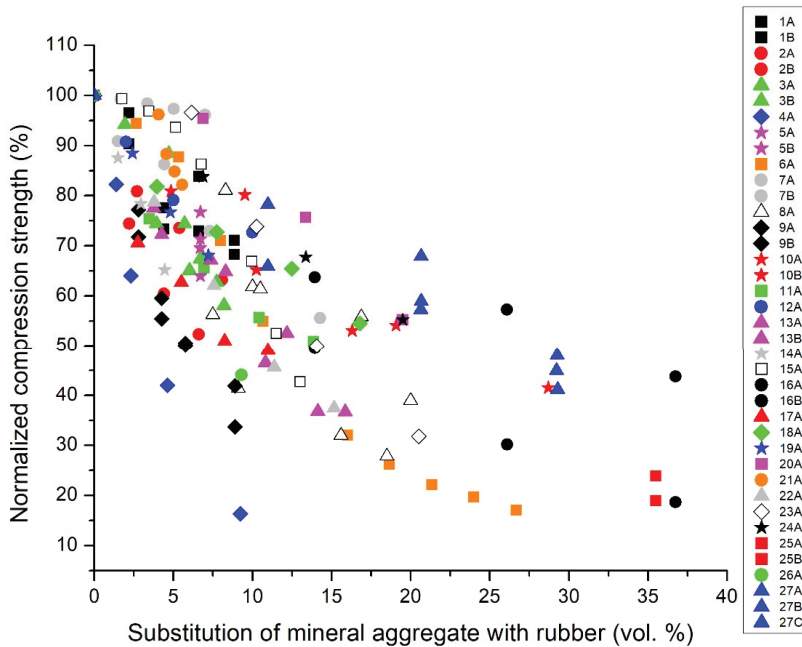


Figure 2. Reference diagram: normalized compression strength (expressed in %) vs. the volumetric percentage of substitution of the mineral aggregate with rubber (expressed in vol.%) recalculated using the fixed values of reference specific weight.

By using the diagram presented in Figure 2 it is possible to compare the different rubber concretes proposed by the different authors, without the risk of being misled by the different ways of presenting the experimental data. For instance, it is evident that series 7A/B, 20A, and 23A present good results at low rubber substitution, and series 27A/B/C and 16A/B at high rubber substitution; while series 4A and 9A/B lose strength rapidly with the increase of rubber content. To discriminate which parameters have a significant effect on the compression strength of rubber concrete, a complete analysis of the outputs coming from the reference diagrams obtained after this important elaboration process is reported in the following paragraphs.

4. Reference Diagrams and Their Critical Interpretation

The reference diagram relative to compression tests (Figure 2) clearly shows a reduction of the compression strength by increasing the rubber content (as expected). Moreover, going more in detail, it is possible to highlight different trends. Liu et al. 7B [50] obtained a reduction of only 4% of the compression strength with a substitution of the aggregate fraction with rubber of 7 vol.%, whereas other studies reported at least 15% reduction for the same amount of rubber (1AB, 3AB, 5AB, 6A, 8A, 11A, 12A, 13AB [44,46,48,49,51,54–56]). The works written by Zheng et al., 10AB, [53] and Najim et al., 27ABC, [57] also report interesting performances, with a lower reduction of compression strength than

most of the case studies here analyzed (moreover, this difference is more evident when increasing the amount of rubber inside the composites). Conversely, the formulations proposed by Issa et al., 4A, [47] and Mohammed et al., 9AB, [52] are characterized by poor mechanical responses (below the other case studies considered) with a remarkable depletion of the compression strength with just 15 vol.% rubber substitution.

In general, the data described in Figure 2 show a mean compression strength reduction of around 20% for substitution of ca. 5 vol.%, around 40% for ca. 10 vol.%, and around 60% for ca. 20 vol.%.

In order to rationalize these trends, the diagrams were further analyzed, studying specific aspects of the formulations reported in the literature that could have beneficial or detrimental effects on the mechanical properties of the rubber concrete. Figure 3 reports the same data of Figure 2, but highlighting the effects due to rubber pre-treatments/modifications. The surface modification of the crumb rubber by means of appropriate pre-treatments (e.g., NaOH washing, controlled oxidation) and/or further surface functionalization (e.g., coatings deposition) is a technical solution investigated by worldwide researchers to overcome the interfacial adhesion concerns with the other inorganic components (mostly the cement paste), principally responsible for the loss of mechanical properties in rubberized concrete [48]. Few data are available; however, four series (5B, 29A, 23A and 25B) can be separated from the others, since the rubber in these cases underwent a chemical treatment with NaOH. This treatment, however, showed no significant effect on the mechanical performances of the composites: the normalized compression strength values experimentally obtained are widely distributed and mainly in the central part of the measured range.

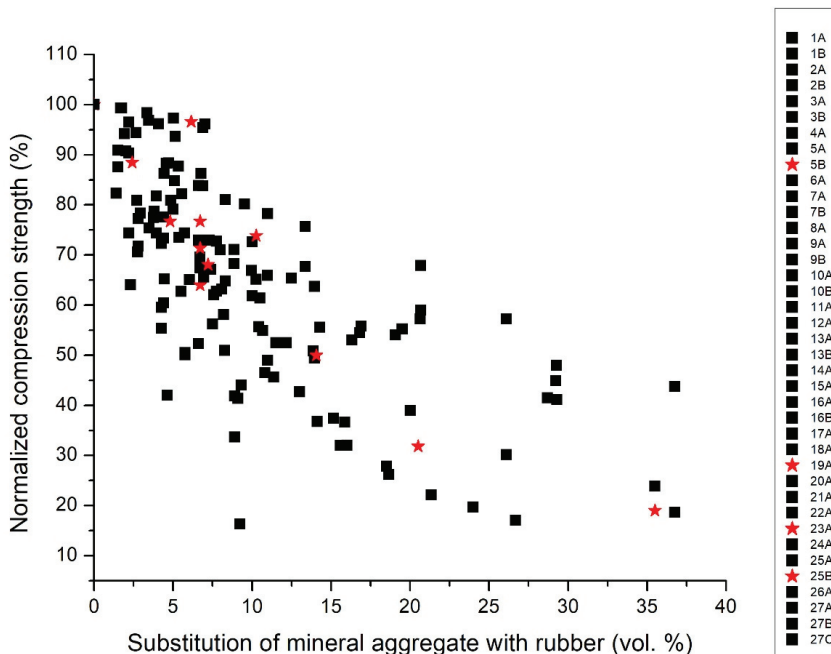


Figure 3. Reference diagram: normalized compression strength (expressed in %) vs. the volumetric percentage of substitution of the mineral aggregate with rubber (expressed in vol.%) recalculated using the fixed values of reference specific weight. Effect of the rubber pre-treated in NaOH (red stars) and rubber without any treatment in NaOH (black squares).

Another important parameter that could affect the rubber concrete performance is the type of aggregate that is substituted—fine, coarse, or both—and it is reported in Figure 4a, where black squares represent substitution of fine aggregate, red stars substitution of coarse aggregate, and green circles both fine and coarse aggregate. In this case, the data are again widely distributed, suggesting the absence of very significant trends of improvement or deterioration of the mechanical properties depending on the substituted aggregate, but at high rubber content it seems that the substitution of both fine and coarse aggregate entails a lower reduction of mechanical properties.

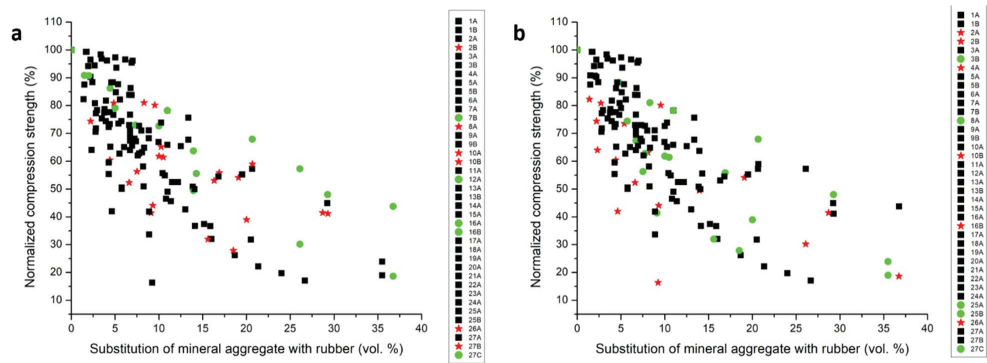


Figure 4. Reference diagram: normalized compression strength (expressed in %) vs. the volumetric percentage of substitution of the mineral aggregate with rubber (expressed in vol.%) recalculated using the fixed values of reference specific weight. (a) Effect of replacing fine aggregate (black squares), replacing coarse aggregate (red stars), replacing both fine and coarse aggregate (green circles). (b) Effect of using for aggregate replacement fine rubber (black squares), coarse rubber (red stars), fine and coarse rubber (green circles).

Figure 4b shows instead the effect of the replacement of the aggregate according to the size of the rubber used to replace it. From the figure it seems that using coarse rubber is less effective than using fine rubber or a mixture of fine and coarse rubber.

However, it is very interesting to study in bigger detail the effect of the substitution of the different size fractions on the mechanical properties. In most cases, the coarse aggregate was replaced with coarse rubber and the fine aggregate with fine rubber, but there are cases where different sizes were used for the substitution. In the 2A [45] and in the 4A [47] series, the fine aggregate was replaced with large size rubber, leading to a drastic decrease in the mechanical strength. Similarly, when a smaller aggregate fraction was substituted with a larger rubber one, the mechanical results were generally not very good (series 3B [46], 25A and 25B [24], 16B [27]). On the contrary, when a bigger aggregate fraction was substituted with smaller rubber one, the mechanical results were from average to very good. An average performance was observed in the case of series 7B [50], 10A [53] and 12A [55], while a very good one in the case of series 8A [51], 16A [27] and 27B [57].

In Figure 5 the comparison of ordinary Portland cement (black squares) vs high-performance cement (red squares) is presented. The use of a high-performance cement seems to improve the mechanical performance of the composite, both at low and at high aggregate replacement volumes.

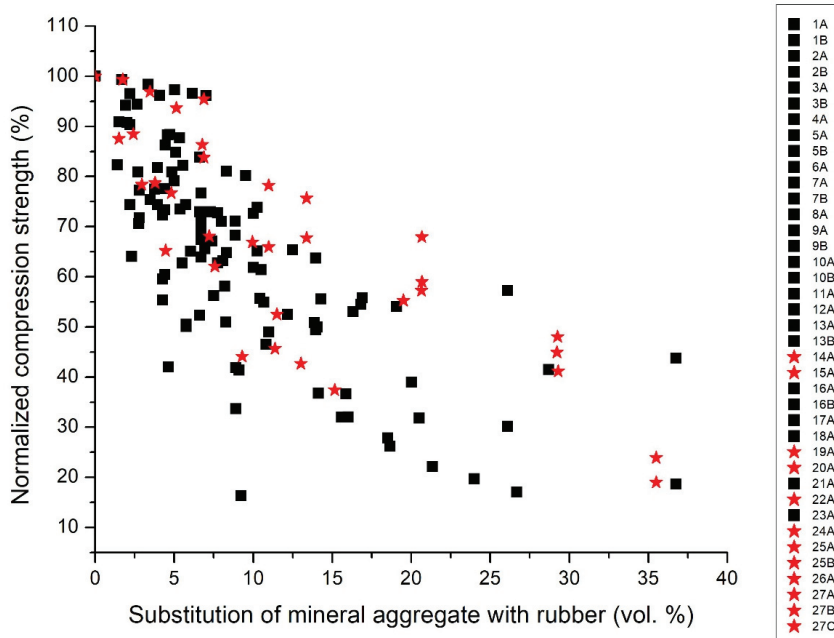


Figure 5. Reference diagram: normalized compression strength (expressed in %) vs. the volumetric percentage of substitution of the mineral aggregate with rubber (expressed in vol.%) recalculated using the fixed values of reference specific weight. Comparison using high-performance concrete (red stars) vs normal cement (black squares).

5. Considerations on Specific Case Studies

In order to rationally unveil the reason why some particular case studies present better mechanical responses than the others, here we reported a brief technical analysis of the best formulations selected. Additionally, on the basis of the reference diagrams proposed in this study, a critical analysis of the formulations and of the boundary conditions has been reported, with the aim of better understanding and proposing new guidelines for favoring the development of high-performance rubber concrete.

Among the different case studies here analyzed, the three series proposed by Najim et al. [57] and Topçu [27] (indicated in this study as 27A, 27B, 27C, 16A and 16B) seem to give the best performances at higher substitution of rubber. For the study of Najim et al., the authors selected a high-strength cement as cementitious matrix, using only a single fraction of rubber with sizes ranging between 2 and 14 mm. One hint adopted by the authors is to favor the dispersion components by premixing the solid ingredients in absence of water. As highlighted in Figure 4a, the best results were reached when both fine and coarse aggregates were replaced with rubber. Topçu [27] suggests using fine rubber for substituting both fine and coarse aggregate. Moreover, in his work it is evident that rubberized concretes in contrast to the normal ones have higher plastic energy capacities.

The results obtained by the series from Zheng et al. [53] (indicated in this study as 10B) seems also very promising, since a lower resistance cement has been selected as cementitious matrix. However, in this case the best results were reached by replacing only the coarse aggregate fraction. Compared to the previous procedure adopted by Najim et al., 27ABC [57], the procedure employed by Zheng and co-workers 10AB [53] for the specimen preparation has not been fully described; thus, it is impossible to point out any further hints to follow. On the other hand, the only element in common between these two studies seems to be the size of the rubber adopted for high level of substitution that is around 5–14 mm size, which confirms the trend suggested by Topçu 16AB [27].

When considering the substitution of only small quantities of mineral aggregate, the best performances were reached by Liu et al. [50] (indicated in this study as 7A). As highlighted in this study, authors selected rubber powders with a small size distribution (i.e., 2–4 mm), finding more advantageous to substitute only the fine aggregate fraction. Interestingly, in this study Liu and co-authors pointed out that the use of rubber already used in the construction field allows to obtain a significant improvement of the adhesion between rubber and the cementitious paste.

It is also evident that the use of a high-performance cement helps to reduce the loss of mechanical properties as shown in Figure 5, in particular with high percentages of aggregate substitution.

Given the graphs of reference, some points are evident to obtain good mechanical results for high percentages of substitution of the aggregate.

- (i) It seems that the substitution of the aggregate with a larger fraction of rubber is not effective [45,47], while good results were obtained with rubber with a smaller size with respect to the aggregate [27,57]. The use of coarse rubber seems less effective than the use of small rubber, as shown in Figure 4.
- (ii) Prior to proceeding with the addition of water, the cement paste, the mineral aggregates and rubbers should be premixed to favor the homogeneous dispersion of the components within the final composite [50].
- (iii) As pointed out by He et al., Liu et al. and Sgobba et al. [23,24,50], the adhesion problems between the components can be partially overcome by imposing a light chemical treatment on the rubber, before introducing it into the desired cement paste. However, it is worth noting that, based on data analysis, the chemical treatment of rubber with chemical agents (e.g., NaOH) has almost no tangible effects on the mechanical performance of the cement composite even when using high-performance cement [24,48,62,66].
- (iv) Lastly, using a high-performance cement as matrix can significantly reduce the loss of mechanical properties for high substitution degree of the mineral aggregate fraction [24,37,57–59,62,63,65,67].

6. Conclusions

Quite recently, several efforts were realized for trying to minimize the anthropogenic impact on the natural environment, and promising results were obtained in term of sustainability. Among the different classes of human-derived technological wastes, end-of-life rubber tires caught the attention of worldwide experts since, from one side, they are potentially dangerous for both environment and human health if normally landfilled or thermally converted, whereas from the other side they can be extremely appealing if re-processed to produce useful products. In this context, the possibility of partially substituting the mineral aggregate fraction in concrete with recycled rubber tires to produce cement-based composite materials with significantly improved toughness, impact resistance, and thermal/electrical/acoustic insulation capacities is an exceptionally promising solution. Unfortunately, this solution presents some technical limitations, such as the decline of the composite mechanical resistance at high content of rubber.

On the basis of the most recent results reported in the literature, we reported here a literature survey coupled with a critical analysis of the metadata extrapolated from scientific papers. Reference diagrams showing the variability fields of the different rubber concrete formulations in terms of mechanical responses as a function of the rubber content were presented and best performances (in terms of both mechanical resistance and loading of rubber) critically discussed. This study evidenced the twofold role of reference diagrams able to i) present the data in an unambiguous manner (for a successful comparison) and ii) provide the guidelines for improving the interaction between rubber and cement paste. Results obtained pointed out the importance of i) correlating the crumb rubber size with the one of the relative mineral aggregate fraction that has been substituted, ii) premixing the solid elements for homogenizing the final composition, iii) pre-treating the rubber prior to use in the composite and iv) selecting a cement paste able to guarantee a reduction of the loss of mechanical properties in the final composite. Additionally, this study evidenced also how it is important to use a

common language in science for a correct interpretation of the data. Therefore, in order to significantly reduce any misleading conclusions, authors hope that the approach here proposed will be extendedly adopted in the future.

Author Contributions: Conceptualization, M.P., L.L. and R.N.; methodology, M.P.; validation, L.L. and R.N.; formal analysis, L.L. and M.S.; investigation, M.S.; data curation, L.L.; writing—original draft preparation, R.N. and L.L.; writing—review and editing, L.L., R.N. and M.P.; visualization, L.L.; supervision, M.P.; project administration, M.P. and R.N.; funding acquisition, M.P., L.L. and R.N. All authors have read and agreed to the published version of the manuscript.

Funding: This research received no external funding.

Conflicts of Interest: The authors declare no conflicts of interest.

References

1. Gálvez-Martos, J.-L.; Styles, D.; Schoenberger, H.; Zeschmar-Lahl, B. Construction and demolition waste best management practice in Europe. *Resour. Conserv. Recycl.* **2018**, *136*, 166–178. [CrossRef]
2. Menegaki, M.; Damigos, D. A review on current situation and challenges of construction and demolition waste management. *Reuse Recycl. UN SGDs Can Sustain. Chem. Contrib. Green Chem. Educ.* **2018**, *13*, 8–15. [CrossRef]
3. Yadav, P.; Samadder, S.R. A critical review of the life cycle assessment studies on solid waste management in Asian countries. *J. Clean. Prod.* **2018**, *185*, 492–515. [CrossRef]
4. Cucchiella, F.; D’Adamo, I.; Gastaldi, M. Sustainable management of waste-to-energy facilities. *Renew. Sustain. Energy Rev.* **2014**, *33*, 719–728. [CrossRef]
5. Dutta, T.; Kim, K.-H.; Deep, A.; Szulejko, J.E.; Vellingiri, K.; Kumar, S.; Kwon, E.E.; Yun, S.-T. Recovery of nanomaterials from battery and electronic wastes: A new paradigm of environmental waste management. *Renew. Sustain. Energy Rev.* **2018**, *82*, 3694–3704. [CrossRef]
6. Nisticò, R. Aquatic-derived biomaterials for a sustainable future: A European opportunity. *Resources* **2017**, *6*, 65. [CrossRef]
7. Nisticò, R.; Lavagna, L.; Versaci, D.; Ivanchenko, P.; Benzi, P. Chitosan and its char as fillers in cement-base composites: A case study. *Bol. Soc. Esp. Cerámica Vidr.* **2019**. (In Press)
8. Andreola, F.; Barbieri, L.; Lancellotti, I.; Leonelli, C.; Manfredini, T. Recycling of industrial wastes in ceramic manufacturing: State of art and glass case studies. *Ceram. Int.* **2016**, *42*, 13333–13338. [CrossRef]
9. Meng, Y.; Ling, T.-C.; Mo, K.H. Recycling of wastes for value-added applications in concrete blocks: An overview. *Resour. Conserv. Recycl.* **2018**, *138*, 298–312. [CrossRef]
10. Oliveux, G.; Dandy, L.O.; Leeke, G.A. Current status of recycling of fibre reinforced polymers: Review of technologies, reuse and resulting properties. *Prog. Mater. Sci.* **2015**, *72*, 61–99. [CrossRef]
11. Maris, J.; Bourdon, S.; Brossard, J.-M.; Cauret, L.; Fontaine, L.; Montebault, V. Mechanical recycling: Compatibilization of mixed thermoplastic wastes. *Polym. Degrad. Stab.* **2018**, *147*, 245–266. [CrossRef]
12. Nisticò, R.; Evon, P.; Labonne, L.; Vaca-Medina, G.; Montoneri, E.; Vaca-Garcia, C.; Negre, M. Post-harvest tomato plants and urban food wastes for manufacturing plastic films. *J. Clean. Prod.* **2017**, *167*, 68–74. [CrossRef]
13. Nisticò, R.; Evon, P.; Labonne, L.; Vaca-Medina, G.; Montoneri, E.; Francavilla, M.; Vaca-Garcia, C.; Magnacca, G.; Franzoso, F.; Negre, M. Extruded poly(ethylene-co-vinyl alcohol) composite films containing biopolymers isolated from municipal biowaste. *ChemistrySelect* **2016**, *1*, 2354–2365. [CrossRef]
14. Soroudi, A.; Jakubowicz, I. Recycling of bioplastics, their blends and biocomposites: A review. *Eur. Polym. J.* **2013**, *49*, 2839–2858. [CrossRef]
15. Franzoso, F.; Vaca-Garcia, C.; Rouilly, A.; Evon, P.; Montoneri, E.; Persico, P.; Mendichi, R.; Nisticò, R.; Francavilla, M. Extruded versus solvent cast blends of poly(vinyl alcohol-co-ethylene) and biopolymers isolated from municipal biowaste. *J. Appl. Polym. Sci.* **2016**, *133*. [CrossRef]
16. Sienkiewicz, M.; Kucinska-Lipka, J.; Janik, H.; Balas, A. Progress in used tyres management in the European Union: A review. *Waste Manag.* **2012**, *32*, 1742–1751. [CrossRef]
17. Rashad, A.M. A comprehensive overview about recycling rubber as fine aggregate replacement in traditional cementitious materials. *Int. J. Sustain. Built Environ.* **2016**, *5*, 46–82. [CrossRef]
18. ETRMA - Statistics. Available online: <http://www.etrma.org/statistics-2> (accessed on 11 December 2019).

19. Najim, K.B.; Hall, M.R. A review of the fresh/hardened properties and applications for plain- (PRC) and self-compacting rubberised concrete (SCRC). *Constr. Build. Mater.* **2010**, *24*, 2043–2051. [CrossRef]
20. Cardo, M.V.; Rosin, P.; Carbajo, A.E.; Vezzani, D. Artificial container mosquitoes and first record of *Aedes aegypti* in the islands of the Paraná Lower Delta, Argentina. *J. Asia-Pac. Entomol.* **2015**, *18*, 727–733. [CrossRef]
21. Aylón, E.; Murillo, R.; Fernández-Colino, A.; Aranda, A.; García, T.; Callén, M.S.; Mastral, A.M. Emissions from the combustion of gas-phase products at tyre pyrolysis. *J. Anal. Appl. Pyrolysis* **2007**, *79*, 210–214. [CrossRef]
22. Fattuhi, N.I.; Clark, L.A. Cement-based materials containing shredded scrap truck tyre rubber. *Constr. Build. Mater.* **1996**, *10*, 229–236. [CrossRef]
23. He, L.; Ma, Y.; Liu, Q.; Mu, Y. Surface modification of crumb rubber and its influence on the mechanical properties of rubber-cement concrete. *Constr. Build. Mater.* **2016**, *120*, 403–407. [CrossRef]
24. Sgobba, S.; Borsa, M.; Molfetta, M.; Marano, G.C. Mechanical performance and medium-term degradation of rubberised concrete. *Constr. Build. Mater.* **2015**, *98*, 820–831. [CrossRef]
25. Youssf, O.; ElGawady, M.A.; Mills, J.E. Experimental Investigation of Crumb Rubber Concrete Columns under Seismic Loading. *Structures* **2015**, *3*, 13–27. [CrossRef]
26. Roychand, R.; Gravina, R.J.; Zhuge, Y.; Ma, X.; Youssf, O.; Mills, J.E. A comprehensive review on the mechanical properties of waste tire rubber concrete. *Constr. Build. Mater.* **2020**, *237*, 117651. [CrossRef]
27. Topçu, I.B. The properties of rubberized concretes. *Cem. Concr. Res.* **1995**, *25*, 304–310. [CrossRef]
28. Naito, C.; States, J.; Jackson, C.; Bewick, B. Assessment of crumb rubber concrete for flexural structural members. *J. Mater. Civ. Eng.* **2014**, *26*, 04014075. [CrossRef]
29. Kaloush, K.E.; Way, G.B.; Zhu, H. Properties of crumb rubber concrete. *Transp. Res. Rec.* **2005**, *1914*, 8–14. [CrossRef]
30. Kashani, A.; Ngo, T.D.; Hemachandra, P.; Hajimohammadi, A. Effects of surface treatments of recycled tyre crumb on cement-rubber bonding in concrete composite foam. *Constr. Build. Mater.* **2018**, *171*, 467–473. [CrossRef]
31. Ismail Mohamed, K.; Sherir Mohamed, A.A.; Siad, H.; Hassan Assem, A.A.; Lachemi, M. Properties of self-consolidating engineered cementitious composite modified with rubber. *J. Mater. Civ. Eng.* **2018**, *30*, 04018031. [CrossRef]
32. Xue, J.; Shinozuka, M. Rubberized concrete: A green structural material with enhanced energy-dissipation capability. *Constr. Build. Mater.* **2013**, *42*, 196–204. [CrossRef]
33. Najim, K.B.; Hall, M.R. Crumb rubber aggregate coatings/pre-treatments and their effects on interfacial bonding, air entrapment and fracture toughness in self-compacting rubberised concrete (SCRC). *Mater. Struct.* **2013**, *46*, 2029–2043. [CrossRef]
34. Reda Taha, M.M.; El-Dieb, A.S.; Abd El-Wahab, M.A.; Abdel-Hameed, M.E. Mechanical, fracture, and microstructural investigations of rubber concrete. *J. Mater. Civ. Eng.* **2008**, *20*, 640–649. [CrossRef]
35. Raffoul, S.; Garcia, R.; Pilakoutas, K.; Guadagnini, M.; Medina, N.F. Optimisation of rubberised concrete with high rubber content: An experimental investigation. *Constr. Build. Mater.* **2016**, *124*, 391–404. [CrossRef]
36. Mendis, A.S.M.; Al-Deen, S.; Ashraf, M. Flexural shear behaviour of reinforced Crumbed Rubber Concrete beam. *Constr. Build. Mater.* **2018**, *166*, 779–791. [CrossRef]
37. Aslani, F.; Ma, G.; Yim Wan, D.L.; Muselin, G. Development of high-performance self-compacting concrete using waste recycled concrete aggregates and rubber granules. *J. Clean. Prod.* **2018**, *182*, 553–566. [CrossRef]
38. Wang, X.; Xia, J.; Nanayakkara, O.; Li, Y. Properties of high-performance cementitious composites containing recycled rubber crumb. *Constr. Build. Mater.* **2017**, *156*, 1127–1136. [CrossRef]
39. Elghazouli, A.Y.; Bompa, D.V.; Xu, B.; Ruiz-Teran, A.M.; Stafford, P.J. Performance of rubberised reinforced concrete members under cyclic loading. *Eng. Struct.* **2018**, *166*, 526–545. [CrossRef]
40. Atahan, A.O.; Yücel, A.Ö. Crumb rubber in concrete: Static and dynamic evaluation. *Constr. Build. Mater.* **2012**, *36*, 617–622. [CrossRef]
41. Rahman, M.M.; Usman, M.; Al-Ghalib, A.A. Fundamental properties of rubber modified self-compacting concrete (RMSCC). *Constr. Build. Mater.* **2012**, *36*, 630–637. [CrossRef]
42. Najim, K.B.; Hall, M.R. Workability and mechanical properties of crumb-rubber concrete. *Proc. Inst. Civ. Eng. Constr. Mater.* **2013**, *166*, 7–17. [CrossRef]

43. Siddique, R.; Naik, T.R. Properties of concrete containing scrap-tire rubber – an overview. *Waste Manag.* **2004**, *24*, 563–569. [CrossRef] [PubMed]
44. Yung, W.H.; Yung, L.C.; Hua, L.H. A study of the durability properties of waste tire rubber applied to self-compacting concrete. *Constr. Build. Mater.* **2013**, *41*, 665–672. [CrossRef]
45. Boudaoud, Z.; Beddar, M. Effects of recycled tires rubber aggregates on the characteristics of cement concrete. *Open J. Civ. Eng.* **2012**, *02*, 193–197. [CrossRef]
46. Kumar, G. N.; Sandeep, V.; Sudharani, C. Using tyres wastes as aggregates in concrete to form rubcrete—Mix for engineering application. *Int. J. Res. Eng. Technol.* **2014**, *03*, 500–509.
47. Issa, C.A.; Salem, G. Utilization of recycled crumb rubber as fine aggregates in concrete mix design. *Constr. Build. Mater.* **2013**, *42*, 48–52. [CrossRef]
48. Youssf, O.; Mills, J.E.; Hassanli, R. Assessment of the mechanical performance of crumb rubber concrete. *Constr. Build. Mater.* **2016**, *125*, 175–183. [CrossRef]
49. Lv, J.; Zhou, T.; Du, Q.; Wu, H. Effects of rubber particles on mechanical properties of lightweight aggregate concrete. *Constr. Build. Mater.* **2015**, *91*, 145–149. [CrossRef]
50. Liu, H.; Wang, X.; Jiao, Y.; Sha, T. Experimental Investigation of the Mechanical and Durability Properties of Crumb Rubber Concrete. *Materials* **2016**, *9*, 172. [CrossRef]
51. Gesoğlu, M.; Güneyisi, E.; Khoshnaw, G.; İpek, S. Investigating properties of pervious concretes containing waste tire rubbers. *Constr. Build. Mater.* **2014**, *63*, 206–213. [CrossRef]
52. Mohammed, B.S.; Azmi, N.J. Strength reduction factors for structural rubbercrete. *Front. Struct. Civ. Eng.* **2014**, *8*, 270–281. [CrossRef]
53. Zheng, L.; Huo, X.S.; Yuan, Y. Strength, modulus of elasticity, and brittleness index of rubberized concrete. *J. Mater. Civ. Eng.* **2008**, *20*, 692–699. [CrossRef]
54. Feng, W.; Liu, F.; Yang, F.; Li, L.; Jing, L. Experimental study on dynamic split tensile properties of rubber concrete. *Constr. Build. Mater.* **2018**, *165*, 675–687. [CrossRef]
55. Tiwari, A.; Panigrahi, B.L.; Sahu, R. Study of the behaviour of concrete after partial replacement of coarse aggregates by waste tyre rubber fibres and addition of admixtures. *Int. J. Civ. Eng. Tech.* **2018**, *9*, 203–213.
56. Gerages, N.N.; Issa, C.A.; Fawaz, S.A. Rubber concrete: Mechanical and dynamical properties. *Case Stud. Constr. Mater.* **2018**, *9*, e00184. [CrossRef]
57. Najim, K.B.; Hall, M.R. Mechanical and dynamic properties of self-compacting crumb rubber modified concrete. *Constr. Build. Mater.* **2012**, *27*, 521–530. [CrossRef]
58. Liu, F.; Zheng, W.; Li, L.; Feng, W.; Ning, G. Mechanical and fatigue performance of rubber concrete. *Constr. Build. Mater.* **2013**, *47*, 711–719. [CrossRef]
59. Thomas, B.S.; Chandra Gupta, R. Properties of high strength concrete containing scrap tire rubber. *J. Clean. Prod.* **2016**, *113*, 86–92. [CrossRef]
60. Kardos, A.J.; Durham, S.A. Strength, durability, and environmental properties of concrete utilizing recycled tire particles for pavement applications. *Constr. Build. Mater.* **2015**, *98*, 832–845. [CrossRef]
61. Khalil, E.; Abd-Elmohsen, M.; Anwar, A.M. Impact resistance of rubberized self-compacting concrete. *Water Sci.* **2015**, *29*, 45–53. [CrossRef]
62. Li, D.; Zhuge, Y.; Gravina, R.; Mills, J.E. Compressive stress strain behavior of crumb rubber concrete (CRC) and application in reinforced CRC slab. *Constr. Build. Mater.* **2018**, *166*, 745–759. [CrossRef]
63. Zhou, M.; Cao, M.; Pei, Z.; Xue, G. Assessment of strengths of crumb rubber concrete at low temperature. *Adv. Civ. Eng. Mater.* **2018**, *7*, 20170116. [CrossRef]
64. Bisht, K.; Ramana, P.V. Evaluation of mechanical and durability properties of crumb rubber concrete. *Constr. Build. Mater.* **2017**, *155*, 811–817. [CrossRef]
65. Youssf, O.; Hassanli, R.; Mills, J.E. Mechanical performance of FRP-confined and unconfined crumb rubber concrete containing high rubber content. *J. Build. Eng.* **2017**, *11*, 115–126. [CrossRef]
66. Guo, S.; Dai, Q.; Si, R.; Sun, X.; Lu, C. Evaluation of properties and performance of rubber-modified concrete for recycling of waste scrap tire. *J. Clean. Prod.* **2017**, *148*, 681–689. [CrossRef]
67. Xue, G.; Pei, Z. Experimental study on axial compressive properties of rubber concrete at low temperature. *J. Mater. Civ. Eng.* **2018**, *30*, 04017301. [CrossRef]
68. *C01 Committee Test Method for Compressive Strength of Hydraulic Cement Mortars (Using 2-in. or [50-mm] Cube Specimens)*; ASTM International: West Conshohocken, PA, USA, 2020.
69. Ikeda, Y.; Kato, A.; Kohjiya, S.; Nakajima, Y. *Rubber Science—A Modern Approach*; Springer: Singapore, 2018.

70. Forrest, M. *Rubber analysis: characterization, failure diagnosis and reverse engineering*; Smithers Rapra: Shrewsbury, UK, 2018.
71. Kreps, B.S. Verification of the specific gravity of rubber before and after vulcanization. *India Rubber J.* **1932**, *84*, 293–294. [CrossRef]
72. Rodgers, B. (Ed.) *Rubber Compounding. Chemistry and Applications*; CRC Press: Boca Raton, FL, USA, 2016.
73. Mark, J.E.; Erman, B.; Roland, C.M. *The Science and Technology of Rubber*; Academic Press: Boston, MA, USA, 2013.
74. Forrest, M. *Recycling and Re-use of Waste Rubber*; Smithers Rapra: Shrewsbury, UK, 2014.
75. Simpson, R.B. *Rubber Basics*; Smithers Rapra: Shrewsbury, UK, 2002.
76. Dick, J.S. *Rubber Technology. Compounding and Testing for Performance*; Carl Hanser Verlag GmbH & Co. KG: München, Germany, 2009.
77. Evans, M.S. *Tyre Compounding for Improved Performance*; Smithers Rapra Review: Shrewsbury, UK, 2010.



© 2020 by the authors. Licensee MDPI, Basel, Switzerland. This article is an open access article distributed under the terms and conditions of the Creative Commons Attribution (CC BY) license (<http://creativecommons.org/licenses/by/4.0/>).

Review

Current Applications of Recycled Aggregates from Construction and Demolition: A Review

Glaydson Simões dos Reis ^{1,2}, Marco Quattrone ³, Wesley Monteiro Ambrós ⁴, Bogdan Grigore Cazacliu ¹ and Carlos Hoffmann Sampaio ^{5,*}

- ¹ Université Gustave Eiffel, MAST, GPEM, F-44344 Bouguenais, France; glaydsonambiental@gmail.com (G.S.d.R.); bogdan.cazacliu@univ-eiffel.fr (B.G.C.)
 - ² Biomass Technology Centre, Department of Forest Biomaterials and Technology, Swedish University of Agricultural Sciences, SE-901 83 Umeå, Sweden
 - ³ National Institute on Advanced Eco-Efficient Cement-Based Technologies, Department of Construction Engineering, Escola Politécnica, University of São Paulo, São Paulo 05508-070, Brazil; MARCO.QUATTRONE@lme.pcc.usp.br
 - ⁴ Mineral Processing Laboratory, Federal University of Rio Grande do Sul, 9500 Bento Gonçalves Avenue, Porto Alegre 91501-970, Brazil; weslei.ambros@ufrgs.br
 - ⁵ Departament d'Enginyeria Minera, Industrial i TIC, Universitat Politècnica de Catalunya, Barcelona Tech. Av. Bases de Manresa 61–63, Manresa, 08242 Barcelona, Spain
- * Correspondence: carlos.hoffmann@upc.edu

Abstract: A literature review comprising 163 publications published over a period of 26 years from 1992 to 2018 is presented in this paper. This review discusses the generation and recycling of construction and demolition waste (CDW) as well as its main uses as raw materials for the construction engineering sector. This review pays attention to the use of CDW aggregates for sand, pavements/roads, bricks, ceramics, cementitious materials, and concrete productions, as well as its uses as eco-friendly materials for water decontamination. The physical-chemical and mechanical characteristics of recycled aggregates play an important role in their correctly chosen applications. The results found in this literature survey allow us to conclude that recycled aggregates from CDW can be successfully used to produce construction materials with quality comparable to those produced with natural aggregates. We concluded that the use of CDWs as raw materials for manufacturing new construction materials is technically feasible, economical, and constitutes an environmentally friendly approach for a future construction and demolition waste management strategy.

Keywords: construction and demolition waste (CDW); CDW recycling; construction materials from CDW; recycled concretes; CDW adsorbents

Citation: Reis, G.S.d.; Quattrone, M.; Ambrós, W.M.; Grigore Cazacliu, B.; Hoffmann Sampaio, C. Current Applications of Recycled Aggregates from Construction and Demolition: A Review. *Materials* **2021**, *14*, 1700. <https://doi.org/10.3390/ma14071700>

Academic Editor: F. Pacheco Torgal

Received: 23 February 2021

Accepted: 27 March 2021

Published: 30 March 2021

Publisher's Note: MDPI stays neutral with regard to jurisdictional claims in published maps and institutional affiliations.



Copyright: © 2021 by the authors. Licensee MDPI, Basel, Switzerland. This article is an open access article distributed under the terms and conditions of the Creative Commons Attribution (CC BY) license (<https://creativecommons.org/licenses/by/4.0/>).

1. Introduction

Waste management is one of the most challenging problems of the 21st century. Among the main types of wastes, construction and demolition waste (CDW) has received important attention in the waste concern [1,2]. CDW is one of the heaviest and most voluminous waste streams generated in the European Union and across the world. CDW is usually defined as the waste materials from operations of construction, reconstruction, alteration, extension, maintenance, and demolition of buildings and other infrastructure [3].

The construction and demolition industries generate around 900 million tons of waste per year, in the European Union alone [3]. CDW is produced in virtually all activities related to the construction and demolition sectors, such as the construction of buildings, houses, roads, bridges, flyovers, etc. These residues consist of distinct types of materials and are a heterogeneous residue that can contain any constituent that is part of a building or infrastructure, as well as any other materials used during construction work [1,4]. In this way, it is comprised mostly of inert and non-biodegradable material such as sand, gravel,

concrete, metal, plastic, glass, etc. Therefore, inert fraction waste represents between 40 and 85% of the overall waste volume, discounting excavation soils from this waste [3].

Figure 1 shows a generic schema of CDW classification based on its sources of origins [1]. It is well known that the amount and composition of any residue, and in particular, CDW, can vary widely according to the regions in which they are generated, mainly depending on factors such as population growth, regional planning, legislation, soil characteristics, topography, construction materials, and technologies, etc. [1,3].

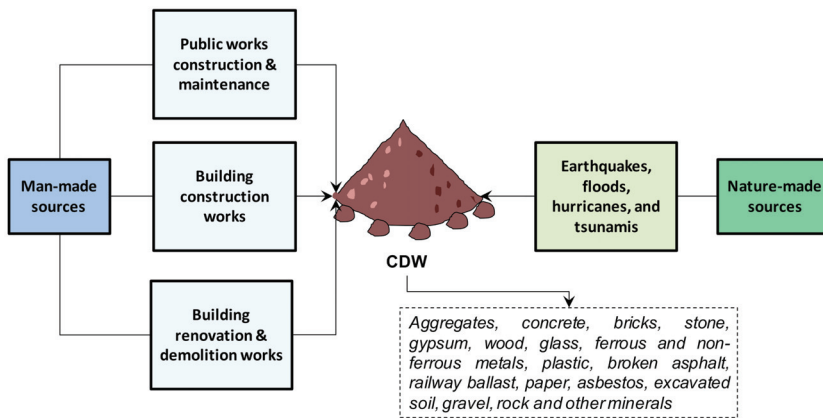


Figure 1. Classification of construction and demolition waste (CDW) according to the source of origin. Adapted from Menegaki and Damigos [1].

The CDW amount is expected to increase in Europe every year; therefore, within this scenario, new strategies for its reuse and recycling need to be implemented correspondingly. Table 1 shows the CDW quantities produced in the E.U. and other countries in the world, as well their recovery/recycling rates indexes. According to the E.U. Waste Framework Directive (2008/98/EC) [5], member states were required to set a target for the recycling of non-hazardous CDW at a minimum of 70% of its weight by 2020. According to the final report published by European Union [2], it showed that fourteen member states already achieved the 70% target (see Table 1), and six other countries were very close, with a recovery rate higher than 60%. On the other hand, some member states showed very low recycling rates, such as Greece, Finland, and Bulgaria [2].

The potential for the recycling and reuse of CDW is high. There is a huge market interest to reuse and recycle aggregates derived from CDW in construction materials and projects [6–17]. Over the last decades, many studies have been performed to evaluate the feasibility of using CDW in projects, such as:

- ✓ Concrete, mortar, and ceramic materials [4,7];
- ✓ Eco-friendly concrete blocks [8,10];
- ✓ Geopolymers synthesis [11,13];
- ✓ Geotechnical applications [14];
- ✓ Use in sea-wall foundations [15];
- ✓ Landfill cover layer [16];
- ✓ Alternative pipe backfilling materials [17];
- ✓ Asphalt and roads [18–20].

Within the aforementioned context, the main goal of this review is to fill the information gap regarding the use of CDW in the production of construction materials, particularly concrete blocks, concrete, cement, ceramic bricks, and roads, as well their uses for environmental applications. Special attention is given to the quantification and properties of CDW generated in Europe and worldwide. Moreover, we hope that the current study may

help to promote the good management of CDW, which is still a challenge to the global construction industry. Open atmospheres about the treatment and utilization of CDW should be built in the international industrial community.

Table 1. Total CDW generation and CDW recovery indexes, 2017 [1,2].

Countries	CDW Generation (10 ⁶ tons)	Recovery Rate (%)
Europe Union		
France	246.70	59.00
Germany	201.00	85.00
United Kingdom	100.23	91.00
Italy	39.00	97.00
Spain	27.70	68.00
The Netherlands	25.71	99.00
Finland	16.00	12.00
Czech Republic	13.80	60.00
Portugal	11.40	74.00
Austria	8.30	92.00
Sweden	7.70	79.00
Belgium	6.95	86.00
Poland	3.51	68.00
Ireland	3.31	74.00
Hungary	3.00	65.00
Denmark	2.89	87.00
Estonia	1.94	75.00
Bulgaria	1.54	12.00
Romania	1.33	67.00
Slovakia	0.80	39.00
Greece	0.81	0.40
Croatia	0.68	52.00
Luxembourg	0.58	99.00
Lithuania	0.56	87.00
Slovenia	0.53	91.00
Malta	0.52	19.00
Latvia	0.40	96.00
Cyprus	0.14	45.00
Other countries		
China	1020.00	40.00
India	530.00	n.a.
U.S.A.	519.00	48.00
Brazil	101.00	6.14
Japan	77.00	80.50
Taiwan	63.00	91.00
Hong Kong	24.30	28.00
Australia	19.50	62.20
Thailand	10.00	32.00
Switzerland	7.00	28.00
South Africa	4.70	16.00
Norway	1.30	67.30

2. Composition and Properties of Recycled Materials

2.1. Composition and Chemical Characteristics of Recycled Aggregates (RAs)

Recycled aggregates (RA) composition is mainly dependent on its sources (concrete, masonry, bricks, roads, etc.), which can vary by location. In some countries, fired bricks are the main construction material, while in others, masonry and wood are the main materials [3]. Building and construction technology has a large influence on the chemical composition of CDW. For instance, the presence of sulfate from interior rendering or glass from glazed ceramic tiles can seriously affect the use of RA produced from contaminated CDW.

Figure 2 shows the general characteristics and composition of the solid wastes generated in Europe according to the waste category. It shows that the fraction of the mineral and solidified wastes (concrete, masonry, bricks, ceramics, earth, etc.) are very high, reaching up to 76%, and coming mainly from construction and demolition activities. However, many other types of wastes are generated and sometimes mixed with CDW. This can affect the composition of CDW and the recycled aggregates (RAs) from CDW, which also affect its reuse and recycling, which will be further discussed in the paper. An example is given in Table 2, which indicates that the general composition of CDW aggregates (Recycled Ceramics (RC) siliceous and limestone and recycled mixed aggregates (RMA) and recycled mixed ceramic aggregates (RMCA)) varies in terms of its main oxides. The aggregates' compositions largely depend on the nature of the aggregates used in their manufacture, such as type of cement, sand, or siliceous aggregates.

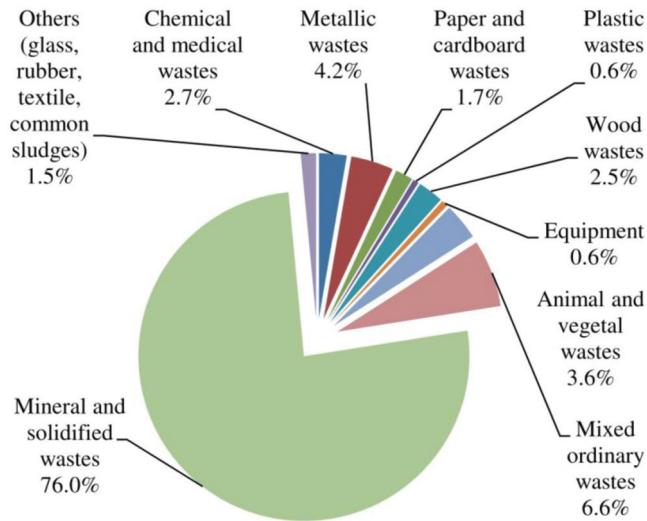


Figure 2. Total waste generated in the European Union according to the waste category, 2017 [3,21].

Table 2. Chemical characterization of different recycled aggregates according to Jiménez [22]. RC: recycled ceramic aggregates; RMA: recycled mixed aggregates; RMCA: recycled mixed ceramic aggregates.

	RC—Siliceous	RC—Limestone	RMA and RMCA
SiO ₂	45–60%	4–5%	40–50%
Al ₂ O ₃	15–20%	1–2%	6–8%
Fe ₂ O ₃	2–5%	1–2%	2–4%
CaO	5–7%	52–54%	20–28%
MgO	0.5–1.5%	0.2–0.8%	0–1%

2.2. Water Absorption

Water absorption (WA) is a key factor affecting the durability of a material and its resistance to the natural environment. The durability of construction materials is mainly dependent on permeability, which is the capacity of a fluid to penetrate their structures. High permeability leads to the penetration of water and ions molecules that react with, i.e., harden, cement paste microstructures, destroying their chemical stability [23]. On the other hand, and considering the service-life of construction, low permeability improves the resistance of the construction materials because it can avoid or impede the degradation agent attacks [23,24].

Natural aggregates have WA values between 0.5% and 1.5%, which is normally omitted for most concrete applications. However, more precautions must be taken when using RAs because their greater porosity can lead to WA values up to 12%, which therefore might lead to mixtures containing 1000 kg of RA in 1 m³ of concrete easily containing 100 liters of absorbed water [25,26].

The high WA of RA is related to the presence of old mortar. The ability of a recycled aggregate to absorb more water is due to the high presence of the adhered mortar onto the aggregate's surface which, consequently, leads to a higher porosity of aggregate; this can affect the amount of water available for mixing, also influencing the cement hydration and therefore leading to problems related to the loss of concrete workability at the fresh state and the loss of mechanical and durability performances in the long-term [27]. The high presence of attached mortar enhances the porosity and WA of the aggregate, which is responsible for the concrete density and durability reduction. RAs have higher WA compared to natural aggregates (NA); therefore, there is also a critical disadvantage of reusing it in new construction materials, which is the heterogeneous nature of RA [28]. Although NA generally comes from the same resource, RA has several origins and qualities, leading to quality variation between different batches [28].

Peng et al. [29] performed an experiment evaluating the recycled concrete properties made with RAC. The WA of RCA was much higher than that of NA. The WA of RCA decreased from 4.07% to 2.89% and from 7.89% to 2.77%, respectively, after removing the attached mortar. Additionally, the authors stated that the microcracking of original gravel in RCA is also responsible for increasing the WA.

Taking into consideration the cementitious aggregates, its fine fractions contain higher cement mortar amounts than coarse fractions, which leads to much higher WA. If used in new concretes, high WA will affect the water/cement ratio, workability of concrete mix, and physical properties such as water absorption and carbonation. Therefore, it is important to remove the old mortar adhered in the RA that will be used in the new cementitious material.

2.3. Density

As well as the water absorption, the density of an aggregate is an important property. It defines the quality of the material and is important for proportioning concrete mixes and controlling several properties of the hardened recycled aggregate concrete [30]. The recycled concrete aggregate's density is proved to be lower than that of natural aggregate. This is due to the presence of adhered cement mortar [31] and peculiar characteristic of the recycled concrete aggregates with respect to natural ones. This adhered material makes the aggregate density lower: typical values range between 2.2 g/cm³ and 2.6 g/cm³ [32].

De Juan et al. [33] showed the influence of the amount of adhered mortar on recycled concrete aggregate density. It was shown that depending on the liberation degree, density can vary along with the different grain size fractions, i.e., fine fraction, where the old cement paste is concentrated, it can show a different density of coarse fraction [34].

The strength of the original crushed concrete only marginally influences the density of the resulting aggregate [35–37]. Topçu and Sengel [38] evaluated the influence of the addition of recycled aggregates in new concrete production. The fresh-state results showed, as expected, a decrease in the density and workability caused by the replacement of the NA by RA. Limbachiya et al. [39] found that the variation of the particle density of the RA was 7–9% lower than that of the NA, which resulted in recycled concrete with worse mechanical properties.

When the material is composed of crushed concrete and masonry rubble, the density values are lower than for recycled concrete aggregate [40]. Red ceramics density is not only lower than concrete density [41–43], but also varies with the manufactured temperatures [44]. In this context, homogenization of the feed mixed recycled aggregate [45] becomes of major importance in producing secondary raw materials.

Mortar, of which density is generally lower than 2.1 g/cm^3 , is another RA component that could drastically influence density, but its content is generally limited by the RA producer, as is the case for other impurities such as wood, gypsum, glass.

2.4. Environmental Limitations of the Use of CDW in Relation to Its Constituents

Ascertaining the physical and chemical composition of RAs is important, because based on these data, future approaches for their reuse will be evaluated and proposed. Some factors determine the potential reuse and recyclability of CDW into RA for any specific situation. CDW can contain high concentrations of harmful substances that sometimes exceed regulatory limits and therefore they can be environmentally incompatible to be used as RA. In that case, they could require appropriate disposal or segregation by a separation technology able to remove/reduce the amount of such contaminants.

If it is not properly managed, CDW might contain small amounts of several hazardous substances such as metal-based paints, adhesives, phenols, resins, aromatic hydrocarbons, and others [21]. Once these substances are in the CDW and those are used as RAs for construction materials such as concrete, bricks, and roads, they can pose particular risks to the environment by contact with rainwater or infiltration, which can leach out these harmful elements (including organic compounds, anions, and metals). Such leaching represents a potential risk to the environment.

Leaching tests on construction materials containing waste [46,47] are being conducted in view to better understand the effect of incorporating recycled aggregates in concrete, especially on the increase in metal trace element (Cr, Pb, As, Ba, Cu, Mo, Sb, Ni, and Zn) and anion (sulfates and chlorides) amounts, and consequently, their potential release.

Engelsen and co-workers [48] showed that when the value pH was high, the amount of metal trace element leaching was low because of the interactions with hydrate constituents. Oxyanion-forming elements could be integrated into the structure of the hydrated phases, ettringite or hydrocalumite, hence limiting the leaching process [49]. After modelling the leaching behavior, Engelsen et al. (2010) [50] concluded that there was no difference between the leaching behavior of classical and recycled concrete.

2.5. Limitations on CDW Composition in Relation to Its Applications

The variety of contaminants that can be found in RA from CDW might also put structures at risk because many of these elements can severely degrade the strength of concrete made with RA from CDW. Such materials include asphalt, glass, gypsum, metals, plastic, rubber, soil, or wood. For instance, Hansen [51] reported that the addition of 30% by volume of asphalt in recycled concretes can reduce its compressive strength by about 30%. Huang [52] reported that 75% compressive strength of recycled concrete was lost with a replacement level of 64% of asphalt aggregates, by weight of total aggregate content. According to the European Standard EN 12,620 [53], the maximum allowed bituminous material content in RA is about 10%.

Other constituents such as glass are commonly found in CDW, even though it is usually removed from buildings and houses before demolition. Organic materials, for example, wood and plastic, are also often found in CDW and can be removed through density separation techniques [54]. It is known that the presence of these constituents in CDW provokes a very harmful effect on the qualities of the construction materials concerning their mechanical properties; therefore, their separation is needed. According to the European Standard EN 12,620 [53], the glass content must not exceed 1% by mass, and wood and plastic, which float in water, are classified separately as floating non-stone material; content is limited to a maximum of 0.1% by mass [21].

Ascertaining the correct quantification of constituents in CDWs is important for understanding their chemical compositions, and therefore their possible applications or processing needs. Considering the vast range of environments and conditions to which these materials made from CDW can be exposed, their chemical composition (e.g., sulfate

and chloride content) could compromise the performance of recycled concrete, bricks, and roads made from CDW.

For instance, in road aggregates, the amount of sulfur compounds is very limited to ensure its chemical stability and avoid pathologies in adjacent structures of concretes or pavement layers made with cement. Gypsum is the main source of soluble sulfates in RA, and there is a linear relationship between the total sulfur content measured according to EN 1744-1 [55].

Agrela et al. [56] studied the soluble sulfate (SO_3) in natural aggregate and mixes of CDW (crushed concrete and crushed masonry). They found values of 0.05% for NA and values from 0.69 to 0.72 in different mixes of CDW; these values are below the limit for soluble sulfate, and the total sulfate content must not exceed the specified limit of 1% for pavement structural layer materials according to UNE EN 103,201 and EN 1744-1 specifications [57]. Agrela et al. [58] found total sulfur values from 0.37 to 1.58 and soluble sulfates varying from 0.22 to 1.09%. Vegas et al. (2011) studied CDW aggregates for roads and showed that those aggregates which presented soluble sulfate contents below 3.74% did not cause dimensional stability problems for the roads.

However, in the presence of easily mobilizable sulfates, an internal sulfate attack manifested by a delayed swelling of hydraulic mixtures may happen. This is due to the formation of a significant amount of secondary or delayed ettringite [59]. It appears that this reaction requires simultaneous specific conditions such as a moist environment, high temperature of the concrete at early age, and presence of aluminates.

Recycled aggregate could also contain significant quantities of soluble alkalis and potentially reactive silica and may present a risk for alkali–silica reactions (ASRs) [60,61] when used for producing new concrete. This chemical mechanism [62,63] can induce cracking and severe damage in concrete structures [64–66]. Methods have been proposed in order to limit the risk of ASRs when using natural aggregates [67,68], although their adaptability to RA has not yet been clarified.

3. Recycled CDW Materials Applications

3.1. Sand Production

In the construction sector, river sand is the most commonly used aggregate in cementitious materials. On one hand, there is a worldwide shortage of good-quality natural sand, whereas in countries where the availability of sand is sufficient, the mining costs and environmental impacts related to extraction, processing, and transport are other major concerns with the ever-growing usage of this natural resource [69].

Based on cement usage and engineering computations (i.e., cement consumption and the ratio of cement to sand for various construction purposes), sand demand for 2007 was estimated to be 17.37 million cubic meters, and since then its usage has grown [70]. Additionally, the last UNEP (United Nations Environmental Program) report “*Sand and sustainability: Finding new solutions for environmental governance of global sand resources*” [71] estimated a sand demand of about 50 billion tons per year, an average of 18 kg per person per day.

Along with these issues, the European Parliament (according to Waste Framework Directive 2008/98/EC) stated that EU countries should achieve 70% of CDW minimum recycling rate by 2020. In this regard, over the last few years, studies have been carried out into using CDW materials as a replacement for sand in concrete materials.

Silva et al. [72] studied the addition of fine crushed red clay brick to a siliceous sand mortar. Three different ratios were tested (0%, 5% and 10%). In general, the authors reported that the addition of red clay brick waste up to 10% improved the mortar properties in comparison with the reference mortar.

In another study [73], a comparative analysis of mortars prepared with three natural sands and three recycled sands was performed. The properties of these mortars were fully evaluated and compared. The shrinkage and water absorption were higher in mortars with recycled sands, while compressive strength was lower when compared to reference mortars.

From an environmental perspective, the use of fine RA as sand can bring several advantages such as: (i) it reduces the sand mining, which it causes huge environmental impacts worldwide; (ii) it reduces the consumption of energy and CO₂ emissions; and (iii) it prevents illegal deposits and landfill of the fine fractions of CDW.

However, the main issue concerning the quality of recycled aggregates from CDW for sand production is the presence of the porous and low strength phases (adhered mortar), and specifically to the patches of hardening cement paste attached to the surface of natural aggregates. This produces sand with low quality which, when used in cementitious materials (concrete or mortar), harms workability and the mechanical and durability performance at hardened state [74]. For those reasons, in most countries, recycled sands (made from CDW) are not allowed in structural cementitious material production.

Therefore, the removal of adhered mortar is a crucial factor for the improvement of aggregate performances; however, this is not a simple task. Thus far, it is seen in the literature that for the separation of cement paste from CDW successive comminution stages [75] and thermal treatments [76] are necessary which, due to their costs, are not generally employed, and in some cases increase the environmental impact of the final product [77].

3.2. Use of CDW for Pavements/Roads Construction

Pavements are one of the most energy-intensive infrastructure assets depending on non-renewable natural resources. Therefore, the application of recycled aggregates from CDW in the construction of embankments, sub-bases, and foundations for roads, where unbound materials are used, is an excellent management idea for increasing recycling rates and creating a market opportunity for recycled aggregates.

Currently, the main utilization of CDW aggregates is for pavement construction. Recycled aggregates from construction and demolition waste have often been used in pavement layers, from small percentages to the full replacement of materials [4,57,78]. In several countries, management and experimental testing technologies containing information about executive procedures and their performance have been gaining ground in the discussion of the environmentally correct reuse of materials.

In European countries and Japan, there are elaborate and consolidated policies regarding the control and management of waste due to the high demographic density and little storage space [4]. That is why these countries have pioneered the development of knowledge about how to handle CDW. Some countries in the world, such as Italy, have specifications for the control of production and application of recycled aggregates for paving, considering the shape and heterogeneity of the grains. Ekanayake and Ofori [79] reported that, in the United States, more than 20 individual states use CDW as aggregate in highway construction. In Brazil, The Netherlands, and Japan the recycling of CDW materials in paving and road works is mandatory, and a huge amount of CDW is used for this purpose [1,80].

Leite et al. [78] evaluated the feasibility of using RA for pavement applications. The behavior of the recycled materials was compared with the behavior of limestone aggregates. The authors concluded that RA from CDW, which has higher densities, might be utilized as a coarse base and sub-base layer for low-volume roads. In addition, RA rich in cementitious materials also helps to improve the layer performances.

Molenaar and van Niekerk [81] evaluated the effect of the composition, degree of compaction, and grading on the mechanical characteristics of crushed concrete and crushed masonry on unbound base. The authors found that all three factors influence the mechanical characteristics of pavement, but it was the degree of compaction that affected it the most. In practice, this is an interesting outcome, because the degree of compaction is much easier to control than other factors such as gradation and composition. In another study [82], the performance of RCA in the base and sub-base was studied. The results showed that a mixture of 25% RCA with 75% NA obtained the same resilient response and permanent

deformation properties as a dense-graded coarse aggregate base, which is used in base and sub-base layers.

Although the use of CDW for road construction has been widely performed, the standardization of the RA used in roads is currently under way. Most countries are implementing standardized limits on the use of NA in roads. For instance, the presence of sulfur compounds is a limiting factor, not only for concrete but also in road aggregates, to ensure the dimensional stability of the section and avoid potential pathologies in adjacent concrete structures or cement-treated pavement layers [83].

Agrela et al. [56] studied the soluble sulfate (SO_3) in natural aggregate and mixtures of CDW (crushed concrete and crushed masonry). They found values of 0.05% for NA and values from 0.69 to 0.72% in different mixes of CDW; these values are below the 1% limit for soluble sulfate which the total sulfate content must not exceed for materials used as pavement structural layer according to UNE EN 103,201 and EN 1744-1 standards [57]. The recycled aggregates used in the rural road met the limit of 1% for sulfur compounds set by the technical specification. However, Vegas et al. [84] have questioned this limit. Vegas et al. [85] studied CDW aggregates for roads and showed that these aggregates which presented soluble sulfates content below 3.74% did not cause dimensional stability problems for the roads. Many other parameters including maximum aggregate size, particle shape, grading (especially fines content), density, etc., have been identified as affecting the road performance [4].

Another important method of CDW reutilization is to use reclaimed asphalt pavement (RAP) in new roads and or pavements. RAP has become a reality in many countries such as the United States, China, Egypt, Japan, and Australia, among others [86,87]. This practice is becoming popular due to both environmental and economical attractiveness. For instance, Vidal et al. [88] showed that the incorporation of 15% RAP into new asphalt mixtures could reduce the total cumulative energy requirement, climate change, and use of fossil fuels by 13 to 14%. Edil [89] reported that up to 30% of savings could be achieved by using RAP as a base material for pavements. Asphalt binder is the most expensive material; therefore, using RAP material in pavements it means that less binder is required.

Mousa et al. [87] studied the application of RAP in the construction of unbound base and sub-base layers in Egypt. The authors studied what the optimal amount of RAP (0%, 20%, 60%, 80% and 100%) was which could be blended with NA. It was concluded that mixing up to 60% of RAP in road sub-base and 20% in road base construction could be used. Much other research has been conducted in this regard.

In another investigation, extensive research was performed in Florida, U.S.A. [90], related to the use of RAP to build sub-base layers below rigid pavements. The RAP layer performances were evaluated and compared (over one year) to a lime rock control section. The authors stated that the mechanical performance of a sub-base layer constructed with RAP was similar or even better than the one constructed with lime rock. Moreover, it was concluded that no environmental impact was detected when RAP was used as a pavement material for highways.

3.3. Ready Mix Concrete

Concrete made with RA is no longer only a research field and, in many countries, it is a practical reality [91,92]. Various pilot projects have been implemented in countries such as China, the United States, Portugal, Germany, France, and Brazil with encouraging results [43,57,59]. Such use is becoming so widespread that several countries have developed or are developing normative documents to address the specificities of using recycled aggregates for concrete [93,94]. This conveys the significance of studies researching the suitability and performance levels of these residues in high-level recycled applications, i.e., structural concrete.

Over the last few years, CDW has been extensively studied for recycling and the application as aggregates for producing new concrete [74,92,94–96]. However, despite many types of research involving CDW for concrete production, there is still a lack of

confidence in the construction sector about using the RA in real concrete applications because of its “poor” mechanical performance compared with natural aggregates.

Concrete is composed of three components: aggregate, hardened cement paste, and an interfacial transition zone (ITZ) between the cement paste and the aggregate [93]. Usually, the ITZ is the weakest part because of its higher porosity and cracks than in the other components [97,98]. Concrete made with RCA results in more ITZs than in concrete made with NA. Shi et al. [93] found that the adhered original mortar was the weakest portion in recycled concrete. The presence of the residual mortar in RA can vary up to 60% depending on the aggregate grain size. Indeed, the most distinguishing feature of RA is the presence of old adhered mortar, which makes it significantly porous due to the high porosity of hardened cement paste, resulting in an inhomogeneous and less dense aggregate, and, consequently, in a poor quality of the concrete.

Butler et al. [97] indicated that RCA with good quality should meet certain criteria to be suitable for use in reinforced concrete. The relative density of the aggregate should be 2.3 or higher, and a maximum mortar content and water absorption of 50% and 3%, respectively. This limit in water absorption is hard to follow in practice, and the effects of RA in concrete appear both at fresh and hard states. The higher water absorption is responsible for difficulties in maintaining workability, especially during transportation [99] and casting [100]. At hard state, the water absorption and porosity of RA affect concrete characteristics in rather complex manners. For instance, the ITZ microstructure of recycled aggregate concrete can be strengthened by carbonation treatment of recycled concrete aggregate [101]. The adhered cement paste of the RAs can generate a higher creep or drying shrinkage in concrete [102,103]. Additionally, although the durability could be affected [104], the RA excess water could act by internally curing the concrete [105,106].

Another aspect that should be addressed is the risk of contamination of using CDW aggregates. Because the RCA comes from debris of concrete elements, the risk that this material be contaminated with chloride exists. Studies showed the presence of chloride in recycled aggregates but always below the limits specified by standards [107,108]. With regard to the effect of RCAs on the chloride penetration resistance of RAC, published results showed that the RCA content affects the chloride penetration resistant. For a 100% replacement of coarse natural aggregates by recycled ones, the chloride penetration resistance can double the value of the correspondent reference concrete with natural aggregates [74,109–111]. Chloride resistance can be improved by reducing the permeability, i.e., reduction in porosity.

An alkali–silica reaction (ASR) is a harmful reaction generating expansion, cracking, and damages to concrete structures [112]. The incorporation of RCAs coming from concrete debris affected by ASR can initiate the expansion reaction in new RAC. The magnitude of the expansion is usually the same as the original concrete but can be larger due to the higher water absorption of the RCAs [113–115].

3.4. Concrete Blocks

Concrete blocks (CBs) are one of the main building materials used in the construction industry, and they are made using cement as a binder. A concrete block is one of several precast concrete products used in construction. It is made from a mixture of powdered Portland cement, sand, gravel, and water, and is responsible for high energy expenditure and a large carbon footprint [116,117]. Therefore, aiming for more environmental protection and sustainable development, several studies have been carried out on the production of CB from waste materials, in particular CDW aggregates, which are interesting materials for CB production [116,118].

Re-utilization of inert CDW as an additive for manufacturing concrete blocks is a winning strategy because it not only recycles the waste product, but also reduces the pressure concerning waste disposal as well as overcoming the shortages of clay in many parts of the world. Moreover, recycling CDW by incorporating them into CB for building materials is a practical solution for the pollution problem and reduces costs in the building

sector. Therefore, the use of CDW waste as aggregates for concrete block production has attracted much interest in recent years, and few reports have been published dealing with the use of CDW as the main additive for fired brick production.

Besides the characteristics of the materials, the quality of the CB also depends on the fabrication method, drying and curing procedure, firing procedure, etc. [117]. These factors will affect the quality of the final product properties such as compressive strength, water absorption, impact and abrasion, low tensile strength, etc. Good quality CB has high compressive strength and low water absorption. Compressive strength is highly affected by firing temperature, method of production, and physical, chemical, and mineralogical properties of the raw material [117,119]. CB made of CDW with different compositions can also present different properties.

Poon et al. (2002) [12] produced CB by using cementing recycled aggregates and fly ash as main additives and found that replacing NA with RA at levels of 25% and 50% exhibited marginal impacts on the CB compressive strength. In relation to the compressive strength of the CB, some studies have reported that there was a very low effect when CB contains up to 50% of RCA in its composition [12,117]. Moreover, research has demonstrated that RCA with a higher cement content is needed for it to be a good additive to make CB with higher compressive strength [117]. In addition, regarding RA and RCA replacement ratios in CB, these wastes can be used in large quantities (up to 100%) because of their properties such as high hardness, high strength, chemical inertness, etc. Besides, these wastes are among the most popular recycled materials used in CB and could reduce the demand for NA in the CB industry.

The production of CB by firing is also an interesting alternative. Kou et al. [119] explored the feasibility of using fresh concrete waste for manufacturing wall blocks under different temperatures (300, 500, 800 °C). All the blocks were burnt after 28 days of curing. It was concluded that the compressive strength of all manufactured blocks increased when exposed to 300 °C, which was due to the acceleration of cement hydration. However, as the fire temperature rose (up to 800 °C), the compressive strength of the wall blocks significantly decreased. This happened because at high temperatures, the hydrated cement paste might be disintegrated (e.g., the hydration products such as $\text{Ca}(\text{OH})_2$ are decomposed at 500 °C and calcium silicate hydrates are decomposed at 800 °C) [12].

The production of concrete blocks by firing has the advantage of easy execution by using well-known processes. However, it has the disadvantages of consuming a significant amount of energy and releasing a large amount of greenhouse gases. Despite many studies which have been carried out for producing bricks from RA, the commercial production of bricks from waste materials (specially from CDW) is still very limited. Some drawbacks related to brick production include the absence of relevant standards, the potential contamination from the waste materials used, and the slow acceptance of waste material-based bricks by industry and the public [117]. Therefore, boosting the production and utilization of CBs made from CDW materials requires studies not only on the technical, economic, and environmental aspects, but also on standardization, government policy, and public education [117].

3.5. Cement

Cement an essential material for the economic development of cities because it is the most consumed material by construction industries. However, its production is extremely energy-intensive and leads to excessive pollution including SO_2 and CO_2 emissions. According to the Cement Technology Roadmap [120], the UNEP report on low- CO_2 eco-efficient cement-based materials [121,122], the cement industry contributes to about 5–8% of the global CO_2 emissions, which are mainly released from the calcination of limestone; therefore, it is one of the most impacting sectors to be duly considered in “green strategies”.

In 2010, 3.3 billion tons of cement were produced worldwide, with an increase of 7% in the preceding year [123], reaching 4.13 billion tons, in 2016 [124]. In 2020, the cement production increased to 4.13 billion of tons, and a production of 4.83 billion of

tons is expected by 2030 [124]. However, considering the infrastructure development in Asia and other emerging economies, such as Turkey and Brazil, cement production will further increase. Therefore, efforts have been made to produce environmentally friendly cementitious materials from waste materials [125].

The main raw materials for Portland cement production include limestone (CaCO_3); clay, as a source of alumina (Al_2O_3); silica (SiO_2); and ferrous oxide (Fe_2O_3). Therefore, theoretically, any material which has all these oxides can be used as a raw material to produce Portland clinker. This is the case with CDW, which is mainly composed of these minerals. These can also include recycled concrete aggregates, especially the fine fraction rich in old, hydrated cement paste [126] and other waste coming from cementitious products [127].

Another field of application of RA is the alkali-activated cement, so-called geopolymers. Allahverdi and Kani [128] developed a geopolymer using waste from a brick production plant and activated it with NaOH in a proportion of 8% Na_2O in the binder. This cement had a compressive strength of 40 MPa after 28 days of curing. In another study, Allahverdi and Kani [128] reported compressive strengths of up to 50 MPa using a mixture of 60% concrete waste and 40% red clay brick waste activated with a solution of NaOH and water glass.

Puertas et al. [129] produced cementitious materials by using ceramic waste made from red and white clays, where the residue was activated with NaOH and water glass. The authors found that the samples cured for eight days exhibited compressive and flexural strengths up to 13 MPa. Komnitsas et al. [11] evaluated using various construction residues including bricks, tiles, and concrete for manufacturing geopolymer cement, and reported compressive strengths of up to 57.8 MPa. In another published work, geopolymer cement was manufactured by using ceramic wastes, and after 28 days of curing, the specimens exhibited a compressive strength up to 71 MPa [130].

Impurities and contaminants that can be found in CDW are one of the main issues for cement production because they can affect its properties. According to Duxson et al. [131] and Luukkonen et al. [132], the content of SiO_2 and Al_2O_3 plays an important role in the performance of cementitious materials. According to the authors, increasing the $\text{SiO}_2/\text{Al}_2\text{O}_3$ molar ratio increases the compressive strength and elasticity up to a certain ratio. Porosity, in contrast, increases at low $\text{SiO}_2/\text{Al}_2\text{O}_3$ ratios. Hajimohammadi and van Deventer [133] reported an opposite trend; a $\text{SiO}_2/\text{Al}_2\text{O}_3$ ratio of 1.8 resulted in a higher compressive strength than $\text{SiO}_2/\text{Al}_2\text{O}_3$ of 2.25. These studies show that the trend of compressive strength as a function of the composition (in terms of $\text{SiO}_2/\text{Al}_2\text{O}_3$ ratio) is not constant across materials and depends on other additional factors.

Despite the important achievements of the cement industry, the technology of cement production will, without doubt, be developed further in future. However, it will be necessary to overcome certain challenges which remain, such as reducing production costs and keeping a strong focus on quality, performance, influence of cement on concrete durability, and the decrease in CO_2 emissions related to its production.

3.6. Ceramics and Bricks

The utilization of solid wastes as additives to manufacture ceramic bricks and products has attracted huge attention over the last few years. It is interesting to both the enterprises generating wastes and the producers of ceramic bricks, stones, tiles, etc. Ceramic materials show an extensive range of chemical composition, resulting in products with heterogeneous characteristics [134]. This attribute enables easy incorporation of different types of waste materials into its products, which is the case of the inert CDW [117].

In general, inert CDW minerals are very heterogeneous but contain almost always the same main components as those of natural ceramic raw materials such as mortar, ceramics, concrete, rocks, natural gravel, masonry, sand, and soil, depending on the place they are generated and characteristics of each construction [134]. These characteristics might qualify

it as a good additive for ceramic material production. Thus far, very few studies have dealt with the use of CDW as an additive for ceramic material construction [135–138].

Acchar and coworkers [139] investigated the effects of the incorporation of CDW on the properties of clay-based ceramics. The results demonstrated that a high content (approximately 50 wt.%) of CDW can be added into red tiles and bricks ceramics without causing changes in the processing routine and without causing harm to their characteristics.

Gaspareto and Texeira [140] proposed to produce ceramic bricks by using crushed CDW as a de-plasticizing material and mixing it with natural clay with high plasticity, to adjust the properties of the fresh mixture. The physical properties of the ceramic mass were evaluated after burning, aiming for its application in the production of solid bricks. The results indicate that it is possible to use CDW with this clay to produce massive ceramic bricks, obtaining a ceramic material with good physical properties. In the tests of compressive strength, it was possible to conclude that adding 40% (wt.%) had a compressive strength higher than 4 MPa, considered very good for the Brazilian standards.

Bianchini et al. [135] also studied the effect of the incorporation of CDW on the sintering/densification and mechanical behavior of a commercial clay-based ceramic mixture for ceramic brick production. The obtained results showed that high contents (approximately 20 wt.%) of CDW can be incorporated into an industrial clay mixture for ceramic products without significant changes in its properties.

Dos Reis et al. [141] prepared fired bricks by using sludge from the inert mineral part of the construction and demolition waste with different proportions (0%, 30%, 50%, 70%, and 100% by weight). The results showed that this waste can successfully be used as the main additive for brick production. The brick made with 70% of the waste presented the highest compressive strength value (16.8 MPa) in comparison with the other proportions. Furthermore, the addition of the waste improved the insulation properties compared to the clay brick.

However, some concerns need to be addressed before inert CDW or any waste can be incorporated as an additive in ceramic products; such as, the chemical composition and size and shape of the additives. For example, the presence of Fe_2O_3 can lead to problems of efflorescence when the clay is homogenized for a long time, and thus it is recommended not to exceed 10% of Fe_2O_3 . The presence of CaO can also be a problem. During firing, CaCO_3 is broken down, producing CO_2 and CaO, and if free CaO does not bond, it can produce expansion in bricks by moisture absorption, and due to this, cracks or chipping may be produced [117].

The presence of carbon is also an issue of concern. When the carbon is not completely burned out during the firing of the ceramic products, it is coked inside the samples and that can lead to poor strength of the ceramic product [84]. The size and shape of the materials used as additives can also play an important role in the quality of ceramic products because such characteristics of additives may lead to a bad and/or cold compaction and thus to the low physical quality of the ceramic products [117,134]. Additionally, large grains are subjected to stresses beyond their limits and fracture, making the rest of the structure less resistant.

3.7. Environmental Application for CDW—Adsorbent Material to Clean Up Polluted Waters

As mentioned before, there are many possibilities for CDW recycling and reuse, most of them related to the use of CDW in construction materials. However, the uses of CDW as raw materials for environmental applications as eco-friendly materials have grown significantly, such as its use as an adsorbent for the uptake of pollutants in aqueous media [141–146]. A compilation of cementitious adsorbents derived from CDW and their conditions of application for pollution removal from aqueous media is shown in Table 3.

Table 3. Comparison of adsorption capacities of different cementitious adsorbents from CDW.

Adsorbent	Adsorbate	Q_{\max} (mg g ⁻¹)	Isotherm Model	Conditions	Ref.
Cellular concrete-supported	Arsenic	16.0	Langmuir	0.2 g of adsorbent in 50 mL with initial concentration from 10 to 100 mg L ⁻¹ ; pH from 6.5 to 7.2	Martemianov et al. [145]
Cellular concrete-supported	Copper	53.0	Langmuir	0.07 g of adsorbent in 100 mL of at 180 rpm; pH of 5.0 and equilibrium time of 120 min	Martemianov et al. [145]
Hydrated cement	Fluoride	2.7	Freundlich	Initial ion concentration of 15.8, pH of 6.7, adsorbent dosage of 10 g/L, shaking speed of 150 rpm, contact time of 24 h	Kagne et al. [147]
Recycled concrete	Phosphate	6.88	Langmuir	pH of 5.0; particle size 2–5 mm; 2.0 g of adsorbent in 100 mL of solution	Deng and Wheatley [148]
Aerated autoclaved light concrete	Arsenic(III)	15.5	Freundlich	Temperature of 24 °C, adsorbent dose of 1.0 g/L, contact time of 30 min, pH of 7.0	Mondal et al. [149]
Burnt Crushed Concrete Granules (700 C)	Phosphate	21.55	Langmuir	pH 7.0; Equilibrium time of 30 min; Adsorbent dosage of 5 g/L	Kang et al. [150]
Burnt Crushed Concrete Granules (900 C)	Phosphate	8.47	Langmuir	pH 7.0; Equilibrium time of 30 min; Adsorbent dosage of 5 g/L	Kang et al. [150]
Carbonated concrete	Phosphate	30.6	-	pH 12.4; 22 °C, Equilibrium time of 104 min; Adsorbent dosage of 5 g/L	Dos Reis et al. [146]
Non-carbonated concrete	Phosphate	47.6	-	pH 12.4; 22 °C, Equilibrium time of 72 min; Adsorbent dosage of 5 g/L	Dos Reis et al. [146]
CSW	Phosphate	24.04	Liu	pH 9.4; 22 °C, Equilibrium time of 212 min; Adsorbent dosage of 5 g/L	Dos Reis et al. [151]
CSW-C	Phosphate	57.64	Liu	pH 9.4; 22 °C, Equilibrium time of 136 min; Adsorbent dosage of 5 g/L	Dos Reis et al. [151]
Functionalized CDW	Ciprofloxacin	138	Liu	Temperature of 40 °C, adsorbent dose of 1.5 g/L, contact time of 70 min, pH = 7.0	Caicedo et al. [152]
Concrete sludge	Borate	50.0	-	Temperature of 25 °C, adsorbent dose of 1.5 g/L, contact time of 70 min, pH = 7.0	Sasaki et al. [153]
Portland Pozzolana Cement	Fluoride	0.25	-	Temperature of 40 °C, adsorbent dose of 50 g/L, contact time of 27 h, pH = 2.0	Shyamal and Ghosh [154]
Concrete powder	Cesium	96.97	Langmuir	Temperature of 21 °C, contact time of 8 min, pH = 12.0	Kang et al. [155]
Cement carbon composite	Methylene blue	9.6	Langmuir	Temperature of 30 °C, adsorbent dose of 1.0 g/L, contact time of 3 h	Manjunath et al. [156]
Cement carbon composite	Methyl orange	20.20	Langmuir	Temperature of 30 °C, adsorbent dose of 1.0 g/L, contact time of 3 h	Manjunath et al. [156]
Portland cement derived adsorbent	Copper	145.8	Langmuir	Temperature of 25 °C, adsorbent dose of 10.0 g/L, contact time of 3 h, pH = 5.0	Lim et al. [157]
Portland cement derived adsorbent	Cadmium	177.9	Langmuir	Temperature of 25 °C, adsorbent dose of 10.0 g/L, contact time of 3 h, pH = 5.0	Lim et al. [157]

Adsorption processes represent a cost-effective approach for solving many problems of the treatment of wastewaters [158,159]. Adsorption is a surface process where pollutants are transferred from the effluent to a solid phase. One advantage of adsorption technology is that the adsorbents can be regenerated and reutilized. This merit makes it a low-cost process, even cheaper when used with wastes such as CDW.

To date, some adsorbents made by CDW have been reported in the international literature (see Table 3). These adsorbents have been employed in the removal of several pollutants from aqueous solutions, such as heavy metals, arsenate, dyes, drugs, and fluoride, etc. The maximum adsorption capacity (Q_{\max}) was used to evaluate the effectiveness of these CDW adsorbents. From Table 3, it can be observed that the Q_{\max} varies according to the pollutant used, as well as the characteristics of the adsorbents. Moreover, the adsorption studies have used different experimental conditions such as different initial concentrations of pollutants, varied contact time, temperatures, and pH conditions. It is well known that these conditions play a huge influence on the efficiency of uptake amount of the selected pollutant. However, the data show that even using different pollutants, different adsorption conditions and different CDW characteristics as adsorbents, they can be successfully employed in the adsorption process.

Kagne et al. [147] studied the removal of fluoride in synthetic and real wastewaters on hydrated cement and demonstrated that its uptake mechanism was due to chemisorption and precipitation. The same findings were found and related by Bibi et al. [160]. Sasaki et al. [143], using concrete wastes for the removal of arsenate, found that its removal mechanism involved the precipitation of arsenate in the form of calcium arsenate ($\text{Ca}_3(\text{AsO}_4)_2$) and by ion exchange with ettringite present in the concrete matrix. Littler et al. [161] studied phosphate adsorption and have shown that, in the presence of cement (or similar), the dissolution of calcium into phosphate-bearing waters results in the precipitation of calcium phosphate solids. The same phenomenon was observed and related by Park et al. [162].

However, the main concern of using concrete materials as an adsorbent for effluent treatment is that they are not completely inert materials. Generally, they present potential hazardous elements such as heavy metals, basic elements, and other toxic constituents that can be leached into the soil, leading to environmental risks. Therefore, investigating metal speciation and leaching behavior is an important way to determine and minimize risks to the environment.

Barbudo et al. [163] evaluated the leaching potential of NA and RA from CDW and the results showed that neither of these aggregates released detectable quantities of heavy metals. However, a high concentration of SO_3 compounds was detected which can cause the pollution of superficial and/or groundwater. Martemianov et al. [145] applied concrete adsorbent for removing metals and arsenic in water and the results showed that the leaching of arsenic, copper, and lead met the requirements of drinking water standards, but the leaching of cadmium was high compared to the other metals.

These results have demonstrated that CDW exhibits good adsorption capacities towards different types of pollutants. Additionally, these data strengthen the potential of CDW materials to be applied as adsorbents to diminish the level of pollutants from wastewaters.

4. Conclusions, Remarks and Future Trends

Environmental concerns about CDW generation and accumulation rise every year, which reinforces the need to reuse it as recycled aggregate for construction industries, because the sector has a great potential to absorb most of the CDW generation. In this context, this paper provides a thorough literature review on the current situation and challenges in the application of recycled aggregates from CDW considering a worldwide scenario. CDW generation, composition, properties, and alternative uses are reviewed in detail. Seven main applications for recycled aggregates obtained from CDW are presented and discussed: sand production, pavement/road construction, ready mix concrete, concrete blocks, cement, ceramics/bricks, and low-cost adsorbent for wastewater treatment. The data found in this literature survey indicate that recycled aggregates from CDW can be successfully used to produce construction materials with quality comparable to those produced with natural aggregates and constitute an environmentally friendly approach for a future construction and demolition waste management strategy.

Three main issues have been identified for future actions and studies oriented to the recycling of CDW in new construction materials: (i) the development of standardized tests to orient specific regulations for using RA from CDW in new materials; (ii) investigating the environmental risks associated with the use of RA from CDW as well as ways to potentialize its application in high added-value sectors, such as ceramics and pollutant adsorbents; (iii) looking deeper at aspects related to political strategies to boost the confidence and acceptance of materials derived from CDW by professionals and society. The more knowledge about the capabilities of using recycled aggregates, the better one can arrive at solutions to overcome the current challenges.

Author Contributions: Conceptualization, G.S.d.R.; investigation, G.S.d.R.; data curation, G.S.d.R., M.Q., and W.M.A.; writing—original draft preparation, G.S.d.R.; funding acquisition, B.G.C. and C.H.S.; writing—review and editing, G.S.d.R., M.Q., W.M.A., B.G.C. and C.H.S. All authors have read and agreed to the published version of the manuscript.

Funding: This research was funded by the French Ministry for the Ecological and Solidary Transition under the FastCarb research program (fastcarb.fr) and by Serra Hünter fellow. The APC was partially funded by the authors.

Institutional Review Board Statement: Not applicable.

Informed Consent Statement: Not applicable.

Data Availability Statement: Data sharing not applicable.

Conflicts of Interest: The authors declare no conflict of interest.

References

- Menegaki, M.; Damigos, D. A review on current situation and challenges of construction and demolition waste management. *Curr. Opin. Green Sustain. Chem.* **2018**, *13*, 8–15. [CrossRef]
- Deloitte. Study on Resource Efficient Use of Mixed Wastes, Improving management of construction and demolition waste—Final Report. *Prep. Eur. Comm. DG ENV* **2017**, *2*, 152–162.
- Monier, V.; Hesstin, M.; Impériale, A.; Prat, L.; Hobbs, G.; Ramos, K.A.M. *Resource Efficient Use of Mixed Wastes: Improving Management of Construction and Demolition Waste*; European Union: Luxembourg, 2017; ISBN 978-92-79-76478-3.
- Cardoso, R.; Silva, R.V.; de Brito, J.; Dhir, R. Use of recycled aggregates from construction and demolition waste in geotechnical applications: A literature review. *Waste Manag.* **2016**, *49*, 131–145. [CrossRef] [PubMed]
- Directive, E. Directive 2008/98/EC of the European Parliament and of the Council of 19 November 2008 on waste and repealing certain Directives. *Off. J. Eur. Union* **2008**, *312*, 3.
- Huang, B.; Wang, X.; Kua, H.; Geng, Y.; Bleischwitz, R.; Ren, J. Construction and demolition waste management in China through the 3R principle. *Resour. Conserv. Recycl.* **2018**, *129*, 36–44. [CrossRef]
- Jones, R.; Zheng, L.; Yerramala, A.; Rao, K.S. Use of recycled and secondary aggregates in foamed concretes. *Mag. Concr. Res.* **2012**, *64*, 513–525. [CrossRef]
- Favaretto, P.; Hidalgo, G.E.N.; Sampaio, C.H.; Silva, R.D.A.; Lermen, R.T. Characterization and Use of Construction and Demolition Waste from South of Brazil in the Production of Foamed Concrete Blocks. *Appl. Sci.* **2017**, *7*, 1090. [CrossRef]
- Poon, C.S.; Lam, C.S. The effect of aggregate-to-cement ratio and types of aggregates on the properties of pre-cast concrete blocks. *Cem. Concr. Compos.* **2008**, *30*, 283–289. [CrossRef]
- Allahverdi, A.; Kani, E.N. Construction wastes as raw materials for geopolymer binders. *Int. J. Civ. Eng.* **2009**, *7*, 154–160.
- Komnitsas, K.; Zaharaki, D.; Vlachou, A.; Bartzas, G.; Galetakis, M. Effect of synthesis parameters on the quality of construction and demolition wastes (CDW) geopolymers. *Adv. Powder Technol.* **2015**, *26*, 368–376. [CrossRef]
- Poon, C.-S.; Kou, S.-C.; Wan, H.-W.; Etxeberria, M. Properties of concrete blocks prepared with low grade recycled aggregates. *Waste Manag.* **2009**, *29*, 2369–2377. [CrossRef]
- Vásquez, A.; Cárdenas, V.; Robayo, R.A.; de Gutiérrez, R.M. Geopolymer based on concrete demolition waste. *Adv. Powder Technol.* **2016**, *27*, 1173–1179. [CrossRef]
- Vieira, C.S.; Pereira, P.M. Use of recycled construction and demolition materials in geotechnical applications: A review. *Resour. Conserv. Recycl.* **2015**, *103*, 192–204. [CrossRef]
- Yeung, A.T.; Mok, K.; Tham, L.; Lee, P.; Pei, G. Use of inert C&D materials for seawall foundation: A field-scale pilot test. *Resour. Conserv. Recycl.* **2006**, *47*, 375–393. [CrossRef]
- Rahardjo, H.; Satyanaga, A.; Harnas, F.R.; Leong, E.C. Use of Dual Capillary Barrier as Cover System for a Sanitary Landfill in Singapore. *Indian Geotech. J.* **2016**, *46*, 228–238. [CrossRef]
- Rahman, M.A.; Imteaz, M.; Arulrajah, A.; Disfani, M.M. Suitability of recycled construction and demolition aggregates as alternative pipe backfilling materials. *J. Clean. Prod.* **2014**, *66*, 75–84. [CrossRef]
- Pourkhorshidi, S.; Sangiorgi, C.; Torreggiani, D.; Tassinari, P. Using Recycled Aggregates from Construction and Demolition Waste in Unbound Layers of Pavements. *Sustainability* **2020**, *12*, 9386. [CrossRef]
- Tataranni, P.; Sangiorgi, C.; Simone, A.; Vignali, V.; Lantieri, C.; Dondi, G. A laboratory and field study on 100% Recycled Cement Bound Mixture for base layers. *Int. J. Pavement Res. Technol.* **2018**, *11*, 427–434. [CrossRef]
- Gomez-Meijide, B.; Perez, A.P.I. Recycled construction and demolition waste in Cold Asphalt Mixtures: Evolutionary properties. *J. Clean. Prod.* **2016**, *112*, 588–598. [CrossRef]
- Silva, R.V.; De Brito, J.; Dhir, R.K. Properties and composition of recycled aggregates from construction and demolition waste suitable for concrete production. *Constr. Build. Mater.* **2014**, *65*, 201–217. [CrossRef]
- Jiménez, J.R. Recycled aggregates (RAs) for roads. In *Handbook of Recycled Concrete and Demolition Waste*; Elsevier: Amsterdam, The Netherlands, 2013; pp. 351–377.

23. Zhang, R.; Panesar, D.K. Water absorption of carbonated reactive MgO concrete and its correlation with the pore structure. *J. CO₂ Util.* **2018**, *24*, 350–360. [CrossRef]
24. Eckert, M.; Oliveira, M.J. Mitigation of the negative effects of recycled aggregate water absorption in concrete technology. *Constr. Build. Mater.* **2017**, *133*, 416–424. [CrossRef]
25. Belin, P.; Habert, G.; Thiery, M.; Roussel, N. Cement paste content and water absorption of recycled concrete coarse aggregates. *Mater. Struct.* **2013**, *47*, 1451–1465. [CrossRef]
26. Quattrone, M.; Cazacliu, B.; Angulo, S.; Hamard, E.; Cothenet, A. Measuring the water absorption of recycled aggregates, what is the best practice for concrete production? *Constr. Build. Mater.* **2016**, *123*, 690–703. [CrossRef]
27. García-González, J.; Rodríguez-Robles, D.; Juan-Valdés, A.; Morán-del Pozo, J.M.; Guerra-Romero, M.I. Pre-saturation technique of the recycled aggregates: Solution to the water absorption drawback in the recycled concrete manufacture. *Materials* **2014**, *7*, 6224–6236. [CrossRef]
28. Joseph, M.; Boehme, L.; Sierens, Z.; Vandewalle, L. Water absorption variability of recycled concrete aggregates. *Mag. Concr. Res.* **2015**, *67*, 592–597. [CrossRef]
29. Peng, G.-F.; Huang, Y.Z.; Wang, H.S.; Zhang, J.F.; Liu, Q.B. Mechanical Properties of Recycled Aggregate Concrete at Low and High Water/Binder Ratios. *Adv. Mater. Sci. Eng.* **2013**, *2013*, 842929. [CrossRef]
30. Agrela, F.; de Juan, M.S.; Ayuso, J.; Geraldés, V.; Jiménez, J. Limiting properties in the characterisation of mixed recycled aggregates for use in the manufacture of concrete. *Constr. Build. Mater.* **2011**, *25*, 3950–3955. [CrossRef]
31. Pedro, D.; de Brito, J.; Evangelista, L. Influence of the use of recycled concrete aggregates from different sources on structural concrete. *Constr. Build. Mater.* **2014**, *71*, 141–151. [CrossRef]
32. De Brito, J.; Saikia, N. Construction and Demolition Waste Aggregates. In *Smart and Sustainable Planning for Cities and Regions*; Springer: London, UK, 2013; pp. 81–113.
33. De Juan, M.S.; Gutiérrez, P.A. Study on the influence of attached mortar content on the properties of recycled concrete aggregate. *Constr. Build. Mater.* **2009**, *23*, 872–877. [CrossRef]
34. Angulo, S.C.; Carrizo, P.M.; Figueiredo, A.D.; Chaves, A.P.; John, V.M. On the classification of mixed construction and demolition waste aggregate by porosity and its impact on the mechanical performance of concrete. *Mater. Struct.* **2009**, *43*, 519–528. [CrossRef]
35. Hansen, T.; Narud, H. Strength of recycled concrete made from crushed concrete coarse aggregate. *Concr. Int.* **1983**, *5*, 79–83.
36. Andreu, G.; Miren, E. Experimental analysis of properties of high performance recycled aggregate concrete. *Constr. Build. Mater.* **2014**, *52*, 227–235. [CrossRef]
37. Nagataki, S.; Gokce, A.; Saeki, T.; Hisada, M. Assessment of recycling process induced damage sensitivity of recycled concrete aggregates. *Cem. Concr. Res.* **2004**, *34*, 965–971. [CrossRef]
38. Topçu, I.B.; Şengel, S. Properties of concretes produced with waste concrete aggregate. *Cem. Concr. Res.* **2004**, *34*, 1307–1312. [CrossRef]
39. Limbachiya, M.C.; Leelawat, T.; Dhir, R.K. Use of recycled concrete aggregate in high-strength concrete. *Mater. Struct.* **2000**, *33*, 574–580. [CrossRef]
40. Martínez-Lage, I.; Vázquez-Burgo, P.; Velay-Lizancos, M. Sustainability evaluation of concretes with mixed recycled aggregate based on holistic approach: Technical, economic and environmental analysis. *Waste Manag.* **2020**, *104*, 9–19. [CrossRef]
41. Debieb, F.; Kenai, S. The use of coarse and fine crushed bricks as aggregate in concrete. *Constr. Build. Mater.* **2008**, *22*, 886–893. [CrossRef]
42. Khalaf, F.M. Using Crushed Clay Brick as Coarse Aggregate in Concrete. *J. Mater. Civ. Eng.* **2006**, *18*, 518–526. [CrossRef]
43. Cahim, P. Mechanical properties of brick aggregate concrete. *Constr. Build. Mater.* **2009**, *23*, 1292–1297. [CrossRef]
44. Richerson, D.W.; Lee, W.E. *Modern Ceramic Engineering: Properties, Processing, and Use in Design*, 4th ed.; CRC Press: Boca Raton, FL, USA, 2018.
45. Khoury, E.; Cazacliu, B.; Cothenet, A.; Remond, S. Homogenization process of field samples of recycled aggregates. *Constr. Build. Mater.* **2020**, *243*, 117991. [CrossRef]
46. Galvín, A.P.; Ayuso, J.; Jiménez, J.R.; Agrela, F. Comparison of batch leaching tests and influence of pH on the release of metals from construction and demolition wastes. *Waste Manag.* **2012**, *32*, 88–95. [CrossRef]
47. Galvín, A.P.; Ayuso, J.; Agrela, F.; Barbudo, A.; Jiménez, J.R. Analysis of leaching procedures for environmental risk assessment of recycled aggregate use in unpaved roads. *Constr. Build. Mater.* **2013**, *40*, 1207–1214. [CrossRef]
48. Engelsens, C.J.; van der Sloot, H.A.; Wibetoe, G.; Petkovic, G.; Stoltenberg-Hansson, E.; Lund, W. Release of major elements from recycled concrete aggregates and geochemical modelling. *Cem. Concr. Res.* **2009**, *39*, 446–459. [CrossRef]
49. Chrysochoou, M.; Dermatas, D. Evaluation of ettringite and hydrocalumite formation for heavy metal immobilization: Literature review and experimental study. *J. Hazard. Mater.* **2006**, *136*, 20–33. [CrossRef]
50. Engelsens, C.J.; van der Sloot, H.A.; Wibetoe, G.; Justnes, H.; Lund, W.; Stoltenberg-Hansson, E. Leaching characterisation and geochemical modelling of minor and trace elements released from recycled concrete aggregates. *Cem. Concr. Res.* **2010**, *40*, 1639–1649. [CrossRef]
51. Hansen, T. *Recycling of Demolished Concrete and Masonry*; CRC Press: Boca Raton, FL, USA, 2004.
52. Huang, B.; Shu, X.; Burdette, E.G. Mechanical properties of concrete containing recycled asphalt pavements. *Mag. Concr. Res.* **2006**, *58*, 313–320. [CrossRef]
53. *Aggregates for Concrete*; British Standards Institution: London, UK, 2002; BS EN 2002, 12620.

54. Coelho, A.; De Brito, J. Preparation of concrete aggregates from construction and demolition waste (CDW). In *Handbook of Recycled Concrete and Demolition Waste*; Elsevier: Amsterdam, The Netherlands, 2013; pp. 210–245.
55. *Tests for Chemical Properties of Aggregates*; British Standards Institution: London, UK, 2009; BS EN 1744-1:2009+A1:2012.
56. Agrela, F.; Barbudo, A.; Ramírez, A.; Ayuso, J.; Carvajal, M.D.; Jiménez, J.R. Construction of road sections using mixed recycled aggregates treated with cement in Malaga, Spain. *Resour. Conserv. Recycl.* **2012**, *58*, 98–106. [CrossRef]
57. Jiménez, J.R.; Ayuso, J.; Agrela, F.; López, M.; Galvín, A.P. Utilisation of unbound recycled aggregates from selected CDW in unpaved rural roads. *Resour. Conserv. Recycl.* **2012**, *58*, 88–97. [CrossRef]
58. Agrela, F.; Cabrera, M.; Galvín, A.; Barbudo, A.; Ramirez, A. Influence of the sulphate content of recycled aggregates on the properties of cement-treated granular materials using Sulphate-Resistant Portland Cement. *Constr. Build. Mater.* **2014**, *68*, 127–134. [CrossRef]
59. Neville, A. The confused world of sulphate attack on concrete. *Cem. Concr. Res.* **2004**, *34*, 1275–1296. [CrossRef]
60. Shehata, M.H.; Christidis, C.; Mikhael, W.; Rogers, C.; Lachemi, M. Reactivity of reclaimed concrete aggregate produced from concrete affected by alkali–silica reaction. *Cem. Concr. Res.* **2010**, *40*, 575–582. [CrossRef]
61. Adams, M.P. Alkali-Silica Reaction in Concrete Containing Recycled Concrete Aggregates. Master’s Thesis, Oregon State University, Corvallis, OR, USA, 2012.
62. Stanton, T.E. Expansion of Concrete through Reaction between Cement and Aggregate. *Trans. Am. Soc. Civ. Eng.* **1942**, *107*, 54–84. [CrossRef]
63. Wang, H.; Gillott, J. Mechanism of alkali-silica reaction and the significance of calcium hydroxide. *Cem. Concr. Res.* **1991**, *21*, 647–654. [CrossRef]
64. Dron, R.; Brivot, F.; Chaussadent, T. Mécanisme de la réaction alcali-silice. *Bull. Liaison Lab. Ponts Chaussées* **1998**, *214*, 61–68.
65. Prezzi, M.; Monteiro, J.M.; Sposito, G. The alkali-silica reaction, Part 1: Use of the double layer theory to explain the behaviour of reaction-products gels. *Acı Mater. J.* **1997**, *94*, 10–17.
66. Glasser, L. Osmotic pressure and the swelling of gels. *Cem. Concr. Res.* **1979**, *9*, 515–517. [CrossRef]
67. Hong, S.H.; Glasser, F.P. Alkali sorption by C-S-H and C-A-S-H gels: Part II Role of alumina. *Cem. Concr. Res.* **2002**, *32*, 1101–1111. [CrossRef]
68. Kawabata, Y.; Yamada, K. Evaluation of Alkalinity of Pore Solution Based on the Phase Composition of Cement Hydrates with Supplementary Cementitious Materials and its Relation to Suppressing ASR Expansion. *J. Adv. Concr. Technol.* **2015**, *13*, 538–553. [CrossRef]
69. Hajimohammadi, A.; Ngo, T.; Kashani, A. Glass waste versus sand as aggregates: The characteristics of the evolving geopolymer binders. *J. Clean. Prod.* **2018**, *193*, 593–603. [CrossRef]
70. Sathiparan, N.; De Zoysa, H. The effects of using agricultural waste as partial substitute for sand in cement blocks. *J. Build. Eng.* **2018**, *19*, 216–227. [CrossRef]
71. UNEP 2019. *Sand and Sustainability: Finding New Solutions for Environmental Governance of Global Sand Resources*; GRID-Geneva. United Nations Env. Programme: Geneva, Switzerland, 2019.
72. Silva, J.; de Brito, J.; Veiga, R. Incorporation of fine ceramics in mortars. *Constr. Build. Mater.* **2009**, *23*, 556–564. [CrossRef]
73. Martínez, I.; Etxeberria, M.; Pavón, E.; Díaz, N. A comparative analysis of the properties of recycled and natural aggregate in masonry mortars. *Constr. Build. Mater.* **2013**, *49*, 384–392. [CrossRef]
74. Evangelista, L.; de Brito, L. Durability performance of concrete made with fine recycled concrete aggregates. *Cem. Concr. Compos.* **2010**, *32*, 9–14. [CrossRef]
75. Ulsen, C.; Antoniassi, J.L.; Martins, I.M.; Kahn, H. High quality recycled sand from mixed CDW e is that possible? *J. Mat. Res. Technol.* **2021**, *12*, 29–42. [CrossRef]
76. Ahn, J.-W.; Kim, H.-S.; Han, G.-C. Recovery of Aggregates from Waste Concrete by Heating and Grinding. *Geosyst. Eng.* **2001**, *4*, 117–122. [CrossRef]
77. Quattrone, M.; Angulo, S.C.; John, V.M. Energy and CO₂ from high performance recycled aggregate production. *Resour. Conserv. Recycl.* **2014**, *90*, 21–33. [CrossRef]
78. Leite, F.D.C.; Motta, R.D.S.; Vasconcelos, K.L.; Bernucci, L. Laboratory evaluation of recycled construction and demolition waste for pavements. *Constr. Build. Mater.* **2011**, *25*, 2972–2979. [CrossRef]
79. Ekanayake, L.L.; Ofori, G. Building waste assessment score: Design-based tool. *Build. Environ.* **2004**, *39*, 851–861. [CrossRef]
80. Ulubeyli, S.; Kazaz, A.; Arslan, V. Construction and Demolition Waste Recycling Plants Revisited: Management Issues. *Procedia Eng.* **2017**, *172*, 1190–1197. [CrossRef]
81. Molenaar, A.A.; van Niekerk, A.A. Effects of gradation, composition, and degree of compaction on the mechanical characteristics of recycled unbound materials. *Transp. Res. Rec.* **2002**, *1787*, 73–82. [CrossRef]
82. Bennert, T.; Papp, W.J.; Maher, A.; Gucunski, N. Utilization of Construction and Demolition Debris Under Traffic-Type Loading in Base and Subbase Applications. *Transp. Res. Rec. J. Transp. Res. Board* **2000**, *1714*, 33–39. [CrossRef]
83. Vázquez, E. *Progress of Recycling in the Built Environment: Final Report of the RILEM Technical Committee 217-PRE*; Springer Science & Business Media: Berlin/Heidelberg, Germany, 2012; Volume 8.
84. Vegas, I.; Ibañez, J.; José, J.S.; Urzelai, A. Construction demolition wastes, Waelz slag and MSWI bottom ash: A comparative technical analysis as material for road construction. *Waste Manag.* **2008**, *28*, 565–574. [CrossRef]

85. Vegas, I.; Ibañez, J.; Lisbona, A.; de Cortazar, A.S.; Frias, M. Pre-normative research on the use of mixed recycled aggregates in unbound road sections. *Constr. Build. Mater.* **2011**, *25*, 2674–2682. [CrossRef]
86. Tarsi, G.; Tataranni, P.; Sangiorgi, C. The Challenges of Using Reclaimed Asphalt Pavement for New Asphalt Mixtures: A Review. *Materials* **2020**, *13*, 4052. [CrossRef]
87. Mousa, E.; Azam, A.; El-Shabrawy, M.; El-Badawy, S. Laboratory characterization of reclaimed asphalt pavement for road construction in Egypt. *Can. J. Civ. Eng.* **2017**, *44*, 417–425. [CrossRef]
88. Vidal, R.; Moliner, E.; Martínez, G.; Rubio, M.C. Life cycle assessment of hot mix asphalt and zeolite-based warm mix asphalt with reclaimed asphalt pavement. *Resour. Conserv. Recycl.* **2013**, *74*, 101–114. [CrossRef]
89. Edil, T.B. *Specifications and Recommendations for Recycled Materials Used as Unbound Base Course*; University of Wisconsin-Madison: Madison, WI, USA, 2011.
90. Cosentino, P.J.; Kalajian, E.H.; Shieh, C.S.; Mathurin, W.J.K.; Gomez, F.; Cleary, E.D.; Treeratukoon, A. Developing Specifications for Using Recycled Asphalt Pavement as Base, Subbase or General Fill Materials, Phase II. Report No. FL/DOT/RMC/06650-7754. 2003. Available online: <https://trid.trb.org/view/660611> (accessed on 12 January 2021).
91. Behera, M.; Bhattacharyya, S.; Minocha, A.; Deoliya, R.; Maiti, S. Recycled aggregate from C&D waste & its use in concrete—A breakthrough towards sustainability in construction sector: A review. *Constr. Build. Mater.* **2014**, *68*, 501–516. [CrossRef]
92. Bui, N.K.; Satomi, T.; Takahashi, H. Mechanical properties of concrete containing 100% treated coarse recycled concrete aggregate. *Constr. Build. Mater.* **2018**, *163*, 496–507. [CrossRef]
93. Shi, C.; Li, Y.; Zhang, J.; Li, W.; Chong, L.; Xie, Z. Performance enhancement of recycled concrete aggregate—A review. *J. Clean. Prod.* **2016**, *112*, 466–472. [CrossRef]
94. Bravo, M.; de Brito, J.; Evangelista, L.; Pacheco, J. Durability and shrinkage of concrete with CDW as recycled aggregates: Benefits from superplasticizer's incorporation and influence of CDW composition. *Constr. Build. Mater.* **2018**, *168*, 818–830. [CrossRef]
95. Lima, P.R.L.; Leite, M.B.; Santiago, E.Q.R. Recycled lightweight concrete made from footwear industry waste and CDW. *Waste Manag.* **2010**, *30*, 1107–1113. [CrossRef]
96. Bravo, M.; De Brito, J.; Evangelista, L.; Pacheco, J. Superplasticizer's efficiency on the mechanical properties of recycled aggregates concrete: Influence of recycled aggregates composition and incorporation ratio. *Constr. Build. Mater.* **2017**, *153*, 129–138. [CrossRef]
97. Butler, L.J.; West, J.S.; Tighe, S.L. Effect of Recycled Concrete Aggregate Properties on Mixture Proportions of Structural Concrete. *Transp. Res. Rec. J. Transp. Res. Board* **2012**, *2290*, 105–114. [CrossRef]
98. Alexandridou, C.; Angelopoulos, G.N.; Coutelieris, F.A. Mechanical and durability performance of concrete produced with recycled aggregates from Greek construction and demolition waste plants. *J. Clean. Prod.* **2018**, *176*, 745–757. [CrossRef]
99. Alhozaimey, A.M. Effect of absorption of limestone aggregates on strength and slump loss of concrete. *Cem. Concr. Compos.* **2009**, *31*, 470–473. [CrossRef]
100. Mefteh, H.; Kebaili, O.; Oucief, H.; Berredjem, L.; Arabi, N. Influence of moisture conditioning of recycled aggregates on the properties of fresh and hardened concrete. *J. Clean. Prod.* **2013**, *54*, 282–288. [CrossRef]
101. Lu, B.; Shi, C.; Cao, Z.; Guo, M.; Zheng, J. Effect of carbonated coarse recycled concrete aggregate on the properties and microstructure of recycled concrete. *J. Clean. Prod.* **2019**, *233*, 421–428. [CrossRef]
102. Sagoe-Crentsil, K.; Brown, T.; Taylor, A. Performance of concrete made with commercially produced coarse recycled concrete aggregate. *Cem. Concr. Res.* **2001**, *31*, 707–712. [CrossRef]
103. Fathifazl, G.; Razaqpur, A.G.; Isgor, O.B.; Abbas, A.; Fournier, B.; Foo, S. Creep and drying shrinkage characteristics of concrete produced with coarse recycled concrete aggregate. *Cem. Concr. Compos.* **2011**, *33*, 1026–1037. [CrossRef]
104. Buyle-Bodin, F.; Hadjieva-Zaharieva, R. Influence of industrially produced recycled aggregates on flow properties of concrete. *Mater. Struct.* **2002**, *35*, 504–509. [CrossRef]
105. Henkensiefken, R.; Castro, J.; Bentz, D.; Nantung, T.; Weiss, J. Water absorption in internally cured mortar made with water-filled lightweight aggregate. *Cem. Concr. Res.* **2009**, *39*, 883–892. [CrossRef]
106. Golias, M.; Castro, J.; Weiss, J. The influence of the initial moisture content of light-weight aggregate on internal curing. *Constr. Build. Mater.* **2012**, *35*, 52–62. [CrossRef]
107. Corinaldesi, V.; Moriconi, G. Influence of mineral additions on the performance of 100% recycled aggregate concrete. *Constr. Build. Mater.* **2009**, *23*, 2869–2876. [CrossRef]
108. Tam, V.W.; Tam, C.M. Crushed aggregate production from centralized combined and individual waste sources in Hong Kong. *Constr. Build. Mater.* **2007**, *21*, 879–886. [CrossRef]
109. Bravo, M.; De Brito, J.; Pontes, J.; Evangelista, L. Durability performance of concrete with recycled aggregates from construction and demolition waste plants. *Constr. Build. Mater.* **2015**, *77*, 357–369. [CrossRef]
110. Bao, J.; Li, S.; Zhang, P.; Ding, X.; Xue, S.; Cui, Y.; Zhao, T. Influence of the incorporation of recycled coarse aggregate on water absorption and chloride penetration into concrete. *Constr. Build. Mater.* **2020**, *239*, 117845. [CrossRef]
111. Guo, H.; Shi, C.; Guan, X.; Zhu, J.; Ding, Y.; Ling, T.-C.; Zhang, H.; Wang, Y. Durability of recycled aggregate concrete—A review. *Cem. Concr. Compos.* **2018**, *89*, 251–259. [CrossRef]
112. Alexander, M.G. *Woodhead Publishing Series in Civil and Structural Engineering*; CRC Press: Boca Raton, FL, USA, 2019; pp. 87–113.
113. Li, X.; Gress, D.L. Mitigating Alkali-Silica Reaction in Concrete Containing Recycled Concrete Aggregate. *Transp. Res. Rec. J. Transp. Res. Board* **2006**, *1979*, 30–35. [CrossRef]

114. Abid, S.R.; Nahhab, A.H.; Al-aayedi, H.K.H.; Nuhair, A.M. Expansion and strength properties of concrete containing contaminated recycled concrete aggregate. *Case Stud. Constr. Mater.* **2018**, *9*, e00201. [CrossRef]
115. Delobel, F.; Bulteel, D.; Mechling, J.; LeComte, A.; Cyr, M.; Rémond, S. Application of ASR tests to recycled concrete aggregates: Influence of water absorption. *Constr. Build. Mater.* **2016**, *124*, 714–721. [CrossRef]
116. Meng, Y.; Ling, T.-C.; Mo, K.H. Recycling of wastes for value-added applications in concrete blocks: An overview. *Resour. Conserv. Recycl.* **2018**, *138*, 298–312. [CrossRef]
117. Matar, P.; El Dalati, R. Using recycled concrete aggregates in precast concrete hollow blocks. *Mater. Werkst.* **2012**, *43*, 388–391. [CrossRef]
118. Matwiss, W. Use of wastes derived from earthquakes for the production of concrete masonry partition wall blocks. *Waste Manag.* **2011**, *31*, 1859–1866.
119. Kou, S.-C.; Zhan, B.-J.; Poon, C.-S. Properties of partition wall blocks prepared with fresh concrete wastes. *Constr. Build. Mater.* **2012**, *36*, 566–571. [CrossRef]
120. World Business Council for Sustainable Development and International Energy Agency. *Cement Technology Roadmap 2009: Carbon Emissions Reductions up to 2050*; World Business Council for Sustainable Development and International Energy Agency: Geneva, Switzerland, 2009.
121. Scrivener, K.L.; John, V.M.; Gartner, E.M. Eco-efficient cements: Potential economically viable solutions for a low-CO₂ cement-based materials industry. *Cem. Concr. Res.* **2018**, *114*, 2–26. [CrossRef]
122. Miller, S.A.; John, V.M.; Pacca, S.A.; Horvath, A. Carbon dioxide reduction potential in the global cement industry by 2050. *Cem. Concr. Res.* **2018**, *114*, 115–124. [CrossRef]
123. Pepe, M. *A Conceptual Model for Designing Recycled Aggregate Concrete for Structural Applications*; Springer: Berlin/Heidelberg, Germany, 2019.
124. Schneider, M. The cement industry on the way to a low-carbon future. *Cem. Concr. Res.* **2019**, *124*, 105792. [CrossRef]
125. Jani, Y.; Hogland, W. Waste glass in the production of cement and concrete—A review. *J. Environ. Chem. Eng.* **2014**, *2*, 1767–1775. [CrossRef]
126. Schoon, J.; De Buysser, K.; Van Driessche, I.; De Belie, N. Fines extracted from recycled concrete as alternative raw material for Portland cement clinker production. *Cem. Concr. Compos.* **2015**, *58*, 70–80. [CrossRef]
127. Schoon, J.; Van Der Heyden, L.; Eloy, P.; Gaigneux, E.M.; De Buysser, K.; Van Driessche, I.; De Belie, N. Waste fibre-cement: An interesting alternative raw material for a sustainable Portland clinker production. *Constr. Build. Mater.* **2012**, *36*, 391–403. [CrossRef]
128. Allahverdi, A.; Kani, E. *Use of Construction and Demolition Waste (CDW) for Alkali-Activated or Geopolymer Cements*. *Handbook of Recycled Concrete and Demolition Waste*; Woodhead publishing: Cambridge, UK, 2013; pp. 439–475.
129. Puertas, F.; Barba, A.; Gazulla, M.F.; Gómez, M.P.; Palacios, M.; Martínez-Ramírez, S. Residuos cerámicos para su posible uso como materia prima en la fabricación de clínker de cemento Portland: Caracterización y activación alcalina. *Materiales De Construcción* **2006**, *56*, 73–84. [CrossRef]
130. Sun, Z.; Cui, H.; An, H.; Tao, D.; Xu, Y.; Zhai, J.; Li, Q. Synthesis and thermal behavior of geopolymer-type material from waste ceramic. *Constr. Build. Mater.* **2013**, *49*, 281–287. [CrossRef]
131. Duxson, P.; Provis, J.L.; Lukey, G.C.; van Deventer, J.S. The role of inorganic polymer technology in the development of ‘green concrete’. *Cem. Concr. Res.* **2007**, *37*, 1590–1597. [CrossRef]
132. Luukkonen, T.; Abdollahnejad, Z.; Yliniemi, J.; Kinnunen, P.; Illikainen, M. One-part alkali-activated materials: A review. *Cem. Concr. Res.* **2018**, *103*, 21–34. [CrossRef]
133. Hajimohammadi, A.; van Deventer, J.S. Characterisation of one-part geopolymer binders made from fly ash. *Waste Biomass Valorization* **2017**, *8*, 225–233. [CrossRef]
134. Boltakova, N.; Faseeva, G.; Kabirov, R.; Nafikov, R.; Zakharov, Y. Utilization of inorganic industrial wastes in producing construction ceramics. Review of Russian experience for the years 2000–2015. *Waste Manag.* **2017**, *60*, 230–246. [CrossRef]
135. Bianchini, G.; Marrocchino, E.; Tassinari, R.; Vaccaro, C. Recycling of construction and demolition waste materials: A chemical–mineralogical appraisal. *Waste Manag.* **2005**, *25*, 149–159. [CrossRef]
136. Acchar, W.; Silva, J.E.; Castanho, S.R.M.; Segadaes, A.M. Properties of Clay-Based Ceramics Added with Construction and Demolition Waste. Available online: <http://repositorio.ipen.br/bitstream/handle/123456789/13188/14823.pdf?sequence=1> (accessed on 12 January 2021).
137. Fiala, L.; Konrád, P.; Fořt, J.; Keppert, M.; Černý, R. Application of ceramic waste in brick blocks with enhanced acoustic properties. *J. Clean. Prod.* **2020**, *261*, 121185. [CrossRef]
138. Gencil, O.; Erdugmus, E.; Sutcu, M.; Oren, O.H. Effects of concrete waste on characteristics of structural fired clay bricks. *Constr. Build. Mater.* **2020**, *255*, 119362. [CrossRef]
139. Acchar, W.; Silva, J.E.; Segadaes, A.M. Increased added value reuse of construction waste in clay based building ceramics. *Adv. Appl. Ceram.* **2013**, *112*, 487–493. [CrossRef]
140. Gaspareto, M.G.T.; Teixeira, S.R. Utilização de resíduo de construção civil e demolição (RCD) como material não plástico para a produção de tijolos cerâmicos. *Cerâmica Ind.* **2017**, *22*, 40–46. [CrossRef]

141. Reis, G.S.d.; Cazacliu, B.G.; Cothenet, A.; Poullain, P.; Wilhelm, M.; Sampaio, C.H.; Lima, E.C.; Ambros, W.; Torrenti, J.-M. Fabrication, microstructure, and properties of fired clay bricks using construction and demolition waste sludge as the main additive. *J. Clean. Prod.* **2020**, *258*, 120733. [CrossRef]
142. Egemose, S.; Sønderup, M.J.; Beinthin, M.V.; Reitzel, K.; Hoffmann, C.C.; Flindt, M.R. Crushed concrete as a phosphate binding material: A potential new management tool. *J. Environ. Qual.* **2012**, *41*, 647–653. [CrossRef]
143. Sasaki, T.; Iizuka, A.; Watanabe, M.; Hongo, T.; Yamasaki, A. Preparation and performance of arsenate (V) adsorbents derived from concrete wastes. *Waste Manag.* **2014**, *34*, 1829–1835. [CrossRef]
144. Wang, X.; Chen, J.; Kong, Y.; Shi, X. Sequestration of phosphorus from wastewater by cement-based or alternative cementitious materials. *Water Res.* **2014**, *62*, 88–96. [CrossRef]
145. Martemianov, D.; Xie, B.-B.; Yurmazova, T.; Khaskelberg, M.; Wang, F.; Wei, C.-H.; Preis, S. Cellular concrete-supported cost-effective adsorbents for aqueous arsenic and heavy metals abatement. *J. Environ. Chem. Eng.* **2017**, *5*, 3930–3941. [CrossRef]
146. dos Reis, G.S.; Thue, P.S.; Cazacliu, B.G.; Lima, E.C.; Sampaio, C.H.; Quattrone, M.; Ovsyannikova, E.; Kruse, A.; Dotto, G.L. Effect of concrete carbonation on phosphate removal through adsorption process and its potential application as fertilizer. *J. Clean. Prod.* **2020**, *256*, 120416. [CrossRef]
147. Kagne, S.; Jagtap, S.; Dhawade, P.; Kamble, S.; Devotta, S.; Rayalu, S. Hydrated cement: A promising adsorbent for the removal of fluoride from aqueous solution. *J. Hazard. Mater.* **2008**, *154*, 88–95. [CrossRef] [PubMed]
148. Deng, Y.; Wheatley, A. Mechanisms of phosphorus removal by recycled crushed concrete. *Int. J. Environ. Res. Public Health* **2018**, *15*, 357. [CrossRef]
149. Mondal, M.; Manoli, K.; Ray, A.K. Removal of arsenic(III) from aqueous solution by concrete-based adsorbents. *Can. J. Chem. Eng.* **2019**, *98*, 353–359. [CrossRef]
150. Kang, K.; Lee, C.-G.; Choi, J.-W.; Hong, S.-G.; Park, S.-J. Application of Thermally Treated Crushed Concrete Granules for the Removal of Phosphate: A Cheap Adsorbent with High Adsorption Capacity. *Water Air Soil Pollut.* **2017**, *228*, 8. [CrossRef]
151. Dos Reis, G.S.; Cazacliu, B.G.; Correa, C.R.; Ovsyannikova, E.; Kruse, A.; Sampaio, C.H.; Lima, E.C.; Dotto, G.L. Adsorption and recovery of phosphate from aqueous solution by the construction and demolition wastes sludge and its potential use as phosphate-based fertiliser. *J. Environ. Chem. Eng.* **2020**, *8*, 103605. [CrossRef]
152. Caicedo, D.F.; dos Reis, G.S.; Lima, E.C.; De Brum, I.A.; Thue, P.S.; Cazacliu, B.G.; Lima, D.R.; dos Santos, A.H.; Dotto, G.L. Efficient adsorbent based on construction and demolition wastes functionalized with 3-aminopropyltriethoxysilane (APTES) for the removal ciprofloxacin from hospital synthetic effluents. *J. Environ. Chem. Eng.* **2020**, *8*, 103875. [CrossRef]
153. Sasaki, T.; Sakai, Y.; Hongo, T.; Iizuka, A.; Yamasaki, A. Preparation of a Solid Adsorbent Derived from Concrete Sludge and its Boron Removal Performance. *Ind. Eng. Chem. Res.* **2012**, *51*, 5813–5817. [CrossRef]
154. Shyamal, D.S.; Ghosh, P.K. Efficiency of Portland Pozzolana Cement as an adsorbent in removing excess fluoride from groundwater. *Groundw. Sustain. Dev.* **2019**, *9*, 100248. [CrossRef]
155. Kang, S.; Lee, J.; Park, S.-M.; Alessi, D.S.; Baek, K. Adsorption characteristics of cesium onto calcium-silicate-hydrate in concrete powder and block. *Chemosphere* **2020**, *259*, 127494. [CrossRef]
156. Manjunath, S.V.; Baghel, R.S.; Kumar, M. Performance evaluation of cement–carbon composite for adsorptive removal of acidic and basic dyes from single and multi-component systems. *Environ. Technol. Innov.* **2019**, *16*, 100478. [CrossRef]
157. Lim, W.-R.; Kim, S.W.; Lee, C.-H.; Choi, E.-K.; Oh, M.H.; Seo, S.N.; Park, H.-J.; Hamm, S.-Y. Performance of composite mineral adsorbents for removing Cu, Cd, and Pb ions from polluted water. *Sci. Rep.* **2019**, *9*, 1–10. [CrossRef]
158. Dos Reis, G.S.; Bin Mahbub, M.K.; Wilhelm, M.; Lima, E.C.; Sampaio, C.H.; Saucier, C.; Dias, S.L.P. Activated carbon from sewage sludge for removal of sodium diclofenac and nimesulide from aqueous solutions. *Korean J. Chem. Eng.* **2016**, *33*, 3149–3161. [CrossRef]
159. Dos Reis, G.S.; Adebayo, M.A.; Sampaio, C.H.; Lima, E.C.; Thue, P.S.; De Brum, I.A.S.; Dias, S.L.P.; Pavan, F.A. Removal of Phenolic Compounds from Aqueous Solutions Using Sludge-Based Activated Carbons Prepared by Conventional Heating and Microwave-Assisted Pyrolysis. *Water Air Soil Pollut.* **2016**, *228*, 33. [CrossRef]
160. Bibi, S.; Farooqi, A.; Hussain, K.; Haider, N. Evaluation of industrial based adsorbents for simultaneous removal of arsenic and fluoride from drinking water. *J. Clean. Prod.* **2015**, *87*, 882–896. [CrossRef]
161. Littler, J.; Geroni, J.N.; Sapsford, D.J.; Coulton, R.; Griffiths, A.J. Mechanisms of phosphorus removal by cement-bound ochre pellets. *Chemosphere* **2013**, *90*, 1533–1538. [CrossRef]
162. Park, J.-Y.; Byun, H.-J.; Choi, W.-H.; Kang, W.-H. Cement paste column for simultaneous removal of fluoride, phosphate, and nitrate in acidic wastewater. *Chemosphere* **2008**, *70*, 1429–1437. [CrossRef]
163. Barbudo, A.; Galvin, A.P.; Agrela, F.; Ayuso, J.; Jiménez, J.R. Correlation analysis between sulphate content and leaching of sulphates in recycled aggregates from construction and demolition wastes. *Waste Manag.* **2012**, *32*, 1229–1235. [CrossRef] [PubMed]

MDPI
St. Alban-Anlage 66
4052 Basel
Switzerland
www.mdpi.com

Materials Editorial Office
E-mail: materials@mdpi.com
www.mdpi.com/journal/materials



Disclaimer/Publisher's Note: The statements, opinions and data contained in all publications are solely those of the individual author(s) and contributor(s) and not of MDPI and/or the editor(s). MDPI and/or the editor(s) disclaim responsibility for any injury to people or property resulting from any ideas, methods, instructions or products referred to in the content.



Academic Open
Access Publishing

[mdpi.com](https://www.mdpi.com)

ISBN 978-3-0365-9543-6